Solar cell degradation: the role of moisture ingress

Oscar Kwame Segbefia

UiA University of Agder

Doctoral Dissertations at the University of Agder 420

Oscar Kwame Segbefia

Solar cell degradation: the role of moisture ingress

Doctoral Dissertation for the Degree *Philosophiae Doctor (Ph.D.)* at
the Faculty of Engineering and Science, Specialisation in Renewable Energy

University of Agder
Faculty of Engineering and Science
2023

Doctoral Dissertations at the University of Agder 420

ISSN: 1504-9272

ISBN: 978-82-8427-136-1

Printed by Make!Graphics

Kristiansand, Norway

In memory of my parents: Nora and Stephen; To God be the glory …

… Moisture is the core of life. Yet, in PV devices, moisture can be the core of degradation.

Acknowledgments

PhD is a journey of solitude, not loneliness. In this thrilling adventure, I have realized that I am never alone. Many people played pivotal roles in the success of this journey. It is therefore my pleasure to acknowledge all who in one way or the other supported me during my PhD journey. Apologies, as this list is not exhaustive.

Most importantly, I would like to thank Tor Oskar Sætre for being a great mentor and a father to me throughout my PhD adventure. Thank you so much for your patience, understanding, and support. To Tore Sandnes Vehus, who took over as my main supervisor when Tor Oskar retired, I am very grateful. Your support, suggestions, and sacrifice are appreciated. I am equally thankful to Anne Gerd Imenes for being supportive and helpful always. I am also grateful to Ingunn Burud and Andreas Svarstad Flø from the Norwegian University of Life Sciences (NMBU). Thank you for being supportive collaborative supervisors. I also wish to express my profound gratitude to Naureen Akhtar, Odin Kvam, and Steve Schading for their immeasurable help and insight during the experimental components of my PhD work.

I also appreciate the Energy Materials Group at UiA for providing a conducive work environment and for invaluable discussions, suggestions, and feedback on my research. Sissel and Alfredo, you made our meetings really memorable. How can I forget my office mates: Saba, Basant, and Madhawa? Thank you for your diverse help and the share of rich experiences. For my Africa brothers: Solomon, Immanuel, and Antoine, am grateful to you for making me to feel the typical African family experience in Norway. Thank you to all colleagues I am lucky enough to meet and share my experiences with during my PhD: Gulshan, Nils, Ghali, Ahmed, Konara, Milad, Bilal, Sinziana, Saga, Juan, Haidar, Foysal, Mohammad, and Jai. I am equally grateful to Emma Elisabeth Horneman and Leif Arne Løhaugen for their efforts and help with administration and other related issues during my stay at UiA. I am also grateful to the UiA football team, especially Professor van Khang Huynh, for making my stay in Grimstad a memorable one. Those memorable moments on the pitch are still fresh in my mind.

Thank you to my family and friends at home for the immense support and encouragement over these years. Selorm, Eric, Dodzi, Patrick, Ceasar, Mawunyo, Mawunyega, Courage, Whoknows, Florence, Mensah, Vincent, Kafui, Zola, Mawuko, Tony, Aaron, and Rev. Fr. Benjamin Gawu: you are special to me.

Last but not least, I am very grateful to my lovely wife: Jennifer Asiwome, for her encouragement, support, love, understanding, and sacrifices. I cannot thank you enough for your role over the years as I embark on the journey to find myself. To my son, Uri Xorse, you are my crown.

Abstract

Moisture ingress is one of the key fault mechanisms responsible for photovoltaic (PV) devices degradation. Moisture and moisture induced degradation (MID) products can attack the solar cell and the PV module components which can lead to solar cell degradation (e.g., microcracks), corrosion, optical degradation, potential induced degradation (PID), etc. These MID mechanisms have dire implications for the performance reliability of PV modules. Understanding the influence of moisture ingress on solar PV device's degradation will boost the interest in investing in solar PV power installations globally, especially in the Nordics. In this thesis, the effect of moisture ingress on 20-years old field-aged multicrystalline silicon (mc-Si) PV modules is investigated. The defective areas in the PV modules were identified using visual inspection, electroluminescence (EL), ultraviolet fluorescence (UV-F), and infrared thermal (IR-T) techniques. Scanning electron microscopy and energy dispersive X-ray spectroscopy (SEM-EDS) analyses were used to elucidate the role of moisture on the observed degradation mechanisms. In addition, temperature coefficient profiling is used as a diagnostic tool to characterize different moisture induced defects.

The ethylene vinyl acetate (EVA) front encapsulation was found to undergo optical degradation and the extracted cells show dark discolored Tedlar®/Polyester/Tedlar® (TPT) backsheets. Corrosion at the solder joint was dominant and is attributed to the dissolution of lead and tin (main components of solder) and the Ag grids in moisture and acetic acid due to galvanic corrosion. Degradation of the EVA encapsulation produces acetic acid, carbon dioxide, phosphorus, sulfur, fluorine, and chlorine. It was observed that under the influence of moisture ingress, leached metal ions e.g., Na, Ag, Pb, Sn, Cu, Zn, and Al migrate to the surface of the solar cells. This led to the formation of oxides, hydroxides, sulfides, phosphates, acetates, and carbonates of silver, lead, tin, copper, zinc, and aluminum. Also, other competing reactions led to the formation of stannates of copper, silver, sodium, and zinc. Similarly, migration of silver and aluminum to the surfaces of the TiO_2 antireflection coating (ARC) nanoparticles (NPs) lead to the formation of titania-alumina and silver-titania complexes. Formation of these titania-metal complexes affects the opto-electrical efficiency of the TiO_2 ARC in the PV module. Additionally, in the presence of moisture and acetic acid, Pb is preferentially corroded (to form lead acetate complexes) instead of the expected sacrificial Sn in the solder. In the EL and UV-F images, these degradation species appear as dark spots, and as hot spots in IR-T images. More importantly, these MID defects and fault modes lead to parasitic resistance and mismatch losses, and hence, degradation in the current-voltage (I-V) characteristics, temperature coefficients, and maximum power (P_{max}) of the field-aged PV modules. The observed temperature sensitivities are characteristic of different moisture-induced defects. Taken together, this work has expounded on the understanding and detection of MID phenomenon in field-deployed solar PV modules.

Sammendrag

Inntrengning av fuktighet er en av de viktigste feilmekanismene som er ansvarlig for nedbrytning av fotovoltaiske (PV) enheter. Fuktighets- og fuktinduserte nedbrytningsprodukter (MID) kan angripe solcellen og PV-modulkomponentene som kan føre til degradering av solcellene (f.eks. mikrosprekker), korrosjon, optisk nedbrytning, potensiell indusert nedbrytning (PID), etc. Disse MID-mekanismene har alvorlige implikasjoner for ytelsespåliteligheten til PV-moduler. Å forstå påvirkningen av fuktighetsinntrengning på nedbrytningen av solcellepaneler vil øke interessen for å investere i solenergiinstallasjoner globalt, spesielt i Norden. I denne tesen undersøkes effekten av fuktinntrengning på 20 år gamle feltaldrede multikrystallinsk silisium (mc-Si) PV-moduler. De defekte områdene i PV-modulene ble identifisert ved bruk av visuell inspeksjon, elektroluminescens (EL), ultrafiolett fluorescens (UV-F) og infrarød termisk (IR-T) teknikker. Skanningelektronmikroskopi og energidispersiv røntgenspektroskopi (SEM-EDS) analyser ble brukt for å belyse fuktighetens rolle på de observerte nedbrytningsmekanismene. I tillegg brukes temperaturkoeffisientprofilering som et diagnostisk verktøy for å karakterisere ulike fuktinduserte defekter.

Frontinnkapslingen bestående av etylenvinylacetat (EVA) ble funnet å gjennomgå optisk nedbrytning, og de ekstraherte cellene viser mørkt misfargede Tedlar®/Polyester/Tedlar® (TPT) baksideark. Korrosjon ved loddeforbindelsen var dominerende og tilskrives oppløsning av bly og tinn (hovedkomponenter i loddemetall) og Ag-gitteret i fuktighet og eddiksyre på grunn av galvanisk korrosjon. Nedbrytning av EVA-innkapslingen produserer eddiksyre, karbondioksid, fosfor, svovel, fluor og klor. Det ble observert at under påvirkning av fuktinntrengning, migrerer utlutede metallioner, f.eks. Na, Ag, Pb, Sn, Cu, Zn og Al, til overflaten av solcellene. Dette førte til dannelsen av oksider, hydroksider, sulfider, fosfater, acetater og karbonater av sølv, bly, tinn, kobber, sink og aluminium. Også andre konkurrerende reaksjoner førte til dannelsen av stannater av kobber, sølv, natrium og sink. På samme måte fører migrering av sølv og aluminium til overflatene til TiO_2 antirefleksjonsbelegg (ARC) nanopartikler (NP) til dannelse av titan-aluminiumoksid og sølv-titanoksid-komplekser. Dannelse av disse titanium-metallkompleksene påvirker den elektrooptisk effektiviteten til TiO_2 ARC i PV-modulen. I tillegg, i nærvær av fuktighet og eddiksyre, korroderes Pb fortrinnsvis (for å danne blyacetatkomplekser) i stedet for det forventede offer-Sn i loddetinn. I EL- og UV-F-bildene vises disse nedbrytningsartene som mørke flekker, og som varme flekker i IR-T-bilder. Enda viktigere er at disse MID-defektene og feilmodusene fører til parasittiske motstandstap og mistilpasningstap, og dermed forringelse av strømspenningskarakteristikkene (I-V), temperaturkoeffisientene og maksimal effekt (P_{max}) til felteldede PV-moduler. De observerte temperaturfølsomhetene er karakteristiske for forskjellige fuktinduserte defekter. Til sammen har dette arbeidet forklart forståelsen og oppdagelsen av MID-fenomener i feltutplasserte solcellepaneler.

Publications

A. O.K. Segbefia, N. Akhtar, T.O. Sætre, Defects and fault modes of field-aged photovoltaic modules in the Nordics, Energy Reports, 9 (2023) 3104-3119. https://doi.org/10.1016/j.egyr.2023.01.126

B. O.K. Segbefia, A.G. Imenes, T.O. Saetre, Moisture ingress in photovoltaic modules: A review, Sol. Energy, 224 (2021) 889-906. https://doi.org/10.1016/j.solener.2021.06.055

C. O.K. Segbefia, N. Akhtar, T.O. Sætre, The effect of moisture ingress on titania antireflection coatings in field-aged photovoltaic modules, in: 2022 IEEE 49th PVSC, IEEE, 2022, pp. 1237-1244. 10.1109/PVSC48317.2022.9938896

D. O.K. Segbefia, N. Akhtar, T.O. Sætre, Moisture induced degradation in field-aged multicrystalline silicon photovoltaic modules. Sol. Energy Mater. Sol. Cells, 258 (2023) 112407. https://doi.org/10.1016/j.solmat.2023.112407

E. O.K. Segbefia, Temperature profiles of field-aged photovoltaic modules affected by optical degradation. Manuscript to be submitted for publication. Preprint: http://dx.doi.org/10.2139/ssrn.4046700

F. O.K. Segbefia, T.O. Sætre, Investigation of the Temperature Sensitivity of 20-Years Old Field-Aged Photovoltaic Panels Affected by Potential Induced Degradation, Energies, 15 (2022) 3865. https://doi.org/10.3390/en15113865

G. O.K. Segbefia, A.G. Imenes, I. Burud, T.O. Sætre, Temperature profiles of field-aged multicrystalline silicon photovoltaic modules affected by microcracks, in: 2021 IEEE 48th Photovoltaic Specialists Conference (PVSC), IEEE, 2021, pp. 0001-0006. 10.1109/PVSC43889.2021.9518939

H. O.K. Segbefia, B.R. Paudyal, I. Burud, T.O. Sætre, Temperature Coefficients of Photovoltaic Modules under Partial Shading Conditions, 38th EU PVSEC, (2021) 1180 - 1186. 10.4229/EUPVSEC20212021-5CV.2.3

Supplementary publication:

- O.K. Segbefia, A.G. Imenes, T.O. Saetre, Outdoor Fault Diagnosis of Field-Aged Multicrystalline Silicon Solar Modules, in: 37th EU PVSEC, 2020.

Contents

List of Figures

List of Tables

Abbreviations

AES: auger electron spectroscopy

AFM: atomic force microscopy

AM: air mass

ARC: antireflection coating

a-Si: amorphous silicon

C Sensor: capacitance embedded sensor

ca.: circa (meaning, approximately)

CdTe: cadmium telluride

CIGS: copper indium gallium (di)selenide

CIS: copper indium diselenide

CMI: climate moisture index

CNC: computer numerical control software

c-Si: crystalline silicon

DH: damp heat

DLIT: dark lock-in thermography

DMA: dynamic mechanical analysis

DSC: differential scanning calorimetry

DSLR: digital single-lens reflex

DVS: dynamic vapor sorption

EDS: energy-dispersive X-ray spectroscopy

EL: electroluminescence spectroscopy

ETFE: ethylene tetrafluoroethylene

EVA: ethylene vinyl acetate

FEG: field emission gun

FEM: finite element methods

FTIR: fourier transform infrared spectroscopy

GaAs: gallium arsenide

GWFID: gas chromatography/flame ionization detection

HF: humidity freeze

HJT: heterojunction

IBC: interdigitated back contact

IEA: International Energy Agency

IEC: International Electrotechnical Commission

IR: infrared

IRENA: International Renewable Energy Agency

IR-T: infrared thermography

I-V: current-voltage

LCOE: levelized costs of electricity/energy

LED: light-emitting diode

LID: light induced degradation

LIT: lock-in thermography

mc-Si: multicrystalline silicon

MI: moisture ingress

MID: moisture induced degradation

MQT: Module Qualification Test

NIR: near infrared

NOCT: normal operating cell temperature

NREL: National Renewable Energy Laboratory

OTR: oxygen transmission rate

PA: polyamide

PCTFE: polychlorotrifluoroethylene

PDMS: polydimethylsiloxane

PERC: passivated emitter rear cell

PET: polyethylene terephthalate

PIB: polyisobutylene

PID: potential induced degradation

PL: photoluminescence spectroscopy

POE: polyolefin elastomer

PPE: PVDF/PET/EVA

PV: photovoltaic(s)

PVB: polyvinyl butyral

PVDF: polyvinylidene fluoride

PVF: polyvinyl fluoride

PVPS: Photovoltaic Power Systems Program

RFID: radio-frequency identification

RH: relative humidity

SC: solar cell

SEM: scanning electron microscopy

SOCT: spectroscopic optical coherence tomography

STC: standard test conditions

TC: temperature cycling

TD-GC/MS: thermal desorption gas chromatography/mass spectrometry

TGA: thermo-gravimetric analysis

TM: melting temperature

TOPCon: tunnel oxide passivated contact

TPO: thermoplastic polyolefin elastomer

TPSE: thermoplastic silicone elastomer

TPT: Tedlar®/PET/Tedlar®

UV: ultraviolet

UV-F: ultraviolet fluorescence spectroscopy

VA: vinyl acetate

VI: visual inspection

WVTR: water vapour transmission rate

XPS: X-ray photoelectron spectroscopy

Symbols

A: preexponential factor

A_c: solar cell area

A_m: PV module's area

$C_{(x)}$: local calibration factor of the PV module at point x

D: diffusivity

D_0: diffusion coefficient at infinity time

E: Young's modulus

E_a: activation energy

E_D: activation energy for diffusivity

E_p: activation energy for permeability

E_s: activation energy for solubility

F: diffusion flux

FF: fill factor

FF_0: ideal fill factor

G_I: in-plane solar irradiance

$I_{(x)}$: local current flowing through point x of the solar cell

I: total current

I_{mpp}: current at maximum power point

I_{sc}: short circuit current

J_{mpp}: current density at maximum power point

J_{sc}: short circuit current density

k: Boltzmann constant

kWh: kilowatt-hour

l: layer thickness

n: number of samples

N_c: number of solar cells

nm: nanometer

P: permeability

P_0: permeability constant

P_{in}: input power

P_{max}: maximum power

P_T: ideal power

R: gas constant

R_{ext}: external resistance

R_{int}: internal resistance

S: solubility

S_0: solubility constant

T: temperature

T_c: cell temperature

T_{cH}: solar cell with the highest temperature

T_{cL}: solar cell with the lowest temperature

T_g: glass transition temperature

T_m: module temperature

T_r: reference temperature

T_{TTF}: test-to-failure in hours

USD: United State Dollar

$V_{(x)}$: local voltage at a point x

V_{mpp}: voltage at maximum power point

V_{oc}: open circuit voltage

V_T: thermal voltage

W_p: peak watt

ΔT: difference in temperature

β_{FF}: temperature coefficient of fill factor

β_{Jmpp}: temperature coefficient of J_{mpp}

β_{Jsc}: temperature coefficient of J_{sc}

β_{Pmax}: temperature coefficient of P_{max}

β_r: module reference temperature coefficient

β_{Vmpp}: temperature coefficient of V_{mpp}

β_{Voc}: temperature coefficient of V_{oc}

β_X: temperature coefficient of parameter X

$\beta_{\eta m}$: module temperature coefficient of efficiency

γ: solar radiation absorption coefficient

η_m: PV module efficiency

η_r: module reference efficiency

μm: micrometer

$\phi_{(x)}$: local luminescence at a point x

Chapter 1

Introduction

1.1 Background

Over the past decades, the campaign for renewable energy sources such as solar energy has intensified. The importance of this transition cannot be overemphasized, with climate change concerns at sight. Adopting renewables e.g., solar photovoltaic (PV) is important for achieving the global net zero emissions since the energy sector contributes to over 75 percent of the greenhouse gas emissions currently [1]. According to the International Renewable Energy Agency (IRENA), the global renewable energy paradigm is underway. In 2021, renewable energy constituted about 38 % of the total installed power capacity worldwide [2]. Also, installation of solar PV energy sources accounted for more than 50 percent of global energy installations in spite of rising prices [3]. In the year 2020, the global economy plummeted to record levels due to the COVID-19 pandemic. Yet, investment in solar PV witnessed the highest rate since the year 2000 [4]. According to IRENA, solar PV recorded the highest employment rate, about 33 %, among all renewable energy technologies in 2020. This suggests that the emergence of a solar energy economy is inevitable. Put simply, solar PV electricity is becoming an integral part of the livelihood of mankind, be it rural or urban.

Solar PV is becoming cost-effective globally, which is expected to attract more investment to the sector in the coming years [3]. According to the IEA Sustainable Recovery Plan, higher investments into renewables can have a positive impact on the global economy, reducing unemployment and putting emissions within acceptable limits [5]. However, both IEA and IRENA believe that more effort is needed to enhance PV cost, efficiency, and performance reliability. This means reliability, affordability, and efficiency of electricity will become the determinant for energy utilization [4]. Over the years, research efforts within the PV community have made gains as regards improving cell efficiency and cost. Yet, performance reliability of PV plants due to defects and fault modes is a major concern [6].

In the field and under several environmental stressors, solar PV panels can be affected by moisture ingress, which can lead to delamination, discolouration of encapsulation, solar cell cracks, potential induced degradation (PID), corrosion, antireflection coating (ARC) degradation, solder bond degradation, bypass diode failure, and front glass degradation [6-9]. These moisture induced degradation (MID) mechanisms lead to decreased photon absorption, parasitic charge carrier recombination, increased series resistance (R_s), and

decreased shunt resistance (R_{SH}) in PV modules [7, 10-12]. MID mechanisms are capable of influencing the temperature coefficients (β_x) [6, 9, 13, 14], and hence, the power output of PV modules [8, 15]. Currently, the average degradation rate of crystalline silicon PV modules is 0.8 percent per year [16-18]. This rate can vary from 0.5 % to 2 % depending on the technology, climate, and age [19].

Defects and fault modes constitute durability and reliability issues and affect efficiency and cost of PV plants directly, see Figure 1.1. Efficiency is a key metric in solar PV cell fabrication and performance monitoring because the cost of a PV module is just a small fraction as compared to the total capital cost of operating a solar PV power plant. This is because as solar PV costs reduce (due to increasing efficiency and reliability), financing costs increase due to several socio-economic factors [20]. Performance reliability influences the payback time and levelized cost of electricity (LCOE) of solar PV plants [19]. This can have different implications for investor confidence in solar PV power. For instance, the LCOE of solar PV dropped from 0.381 to 0.057 United State Dollar per kilowatt-hour (USD/kWh) in 2010 to 2020, respectively [2]. This is a major reason for higher penetration of solar PV power in the past decades [20, 21]. The global market share of crystalline silicon (c-Si) solar panels increased from about 90 % in 2014 to about 94 % in 2019 [22]. The sustained market competitiveness of c-Si technologies is due to improved efficiency and reduced costs.

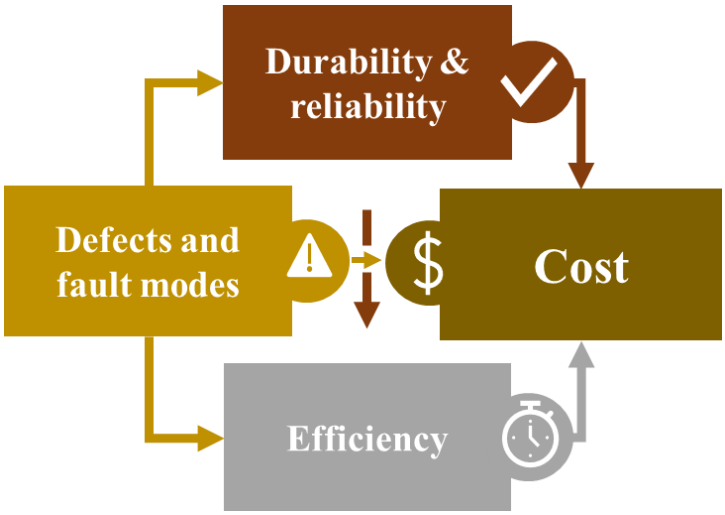

Figure 1. 1. The effect of defects and fault modes on performance reliability, efficiency, and cost of solar PV plants.

It is known that single junction silicon PV cells have efficiency limits less than 33 % in the absence of all intrinsic parasitic absorption and recombination processes [23, 24]. Multijunction solar cells are yet to achieve an efficiency above 34 % [23]. Under concentrated light, the efficiency can be enhanced to exceed 37 % [24]. Yet, the efficiency of the best crystalline silicon PV modules is still below 25 % [23, 24]. However, in the presence of defects and faults modes, lower efficiencies are expected [14, 19].

The maximum power (P_{max}) is related to the maximum power point voltage (V_{mpp}) and maximum power point current (I_{mpp}) as

$$P_{max} = V_{mpp} \cdot I_{mpp} \tag{1.1}$$

The largest rectangular area of the I-V curve of a solar cell is the fill factor (FF). Mathematically, the fill factor can be expressed in terms of the open circuit voltage (V_{oc}) and short circuit current (I_{sc}) as

$$FF = \frac{P_{max}}{V_{oc} \cdot I_{sc}} \tag{1.2}$$

Hence, P_{max} can be rewritten in terms of FF as

$$P_{max} = V_{oc} \cdot I_{sc} \cdot FF \tag{1.3}$$

The fill factor is a measure of the degradation state of the solar cell or the PV module [6]. It is the parameter that compares the P_{max} to the virtual or ideal power (P_T) of a PV module presuming that the $V_{oc} \approx V_{mpp}$ and the $I_{sc} \approx I_{mpp}$. Graphically, the fill factor is the ratio of areas of rectangle A to rectangle B, see Figure 1.2.

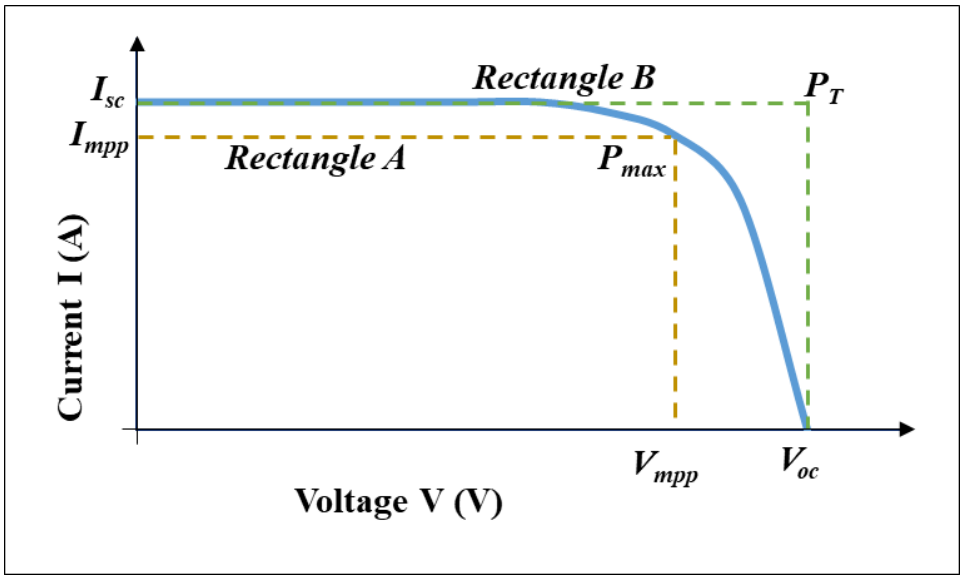

Figure 1. 2. I-V curve of a PV module showing the maximum power (P_{max}), open circuit voltage (V_{oc}), short circuit current (I_{sc}), maximum power point voltage (V_{mpp}), maximum power point current (I_{mpp}), and ideal power (P_T). FF = Area of rectangle (A/B).

Defects and fault modes lead to a decrease in I_{mpp} and/or V_{mpp}, which lead to a decrease in the area of Rectangle A, and hence, in the FF. This results in the degradation of P_{max}. The PV module efficiency (η_m) is related to the P_{max}, module's area (A_m), and the input power (P_{in}) as

$$\eta_m = \frac{P_{max}}{A_m \cdot P_{in}} \tag{1.4}$$

A_m is the product of the solar cell's area (A_c) and the number of solar cells in the module (N_c).

Degradation behaviour of these parameters can be characteristic of different defects and fault modes [25]. They can give valuable information about different failure mechanisms [6]. Defects influence the cell temperature (T_c) of the PV module due to mismatch losses [17]. The temperature difference (ΔT) between the "best" solar cell with the lowest temperature, T_{cL}, and the "worst" solar cell with the highest temperature, T_{cH}, can be an indicator of a specific defect or fault mechanism [26]. This manifests itself in the degradation of the temperature coefficients of P_{max} (β_{Pmax}), V_{oc} (β_{Voc}), I_{sc} (β_{Jsc}), fill factor (β_{FF}), I_{mpp} (β_{Jmpp}), V_{mpp} (β_{Vmpp}), and efficiency ($\beta_{\eta m}$) [27-30]. The prospect of monitoring solar PV module performance reliability (defect types) based on the temperature sensitivity is promising. Do MID defects have distinct temperature sensitivity? For the purpose of this thesis, the focus will be on the characteristics of MID defect mechanisms.

1.2 Motivation

More than 80 % of the electricity production in the Nordic countries comes from renewable sources (mainly hydro and wind) [31]. In Norway, more than 90 % of the electricity comes from hydropower. This makes the Scandinavian countries a leader in the global decarbonization agenda. However, the prospect of solar PV electricity in the Nordic countries is highlighted in Figure 1.3 [8, 21].

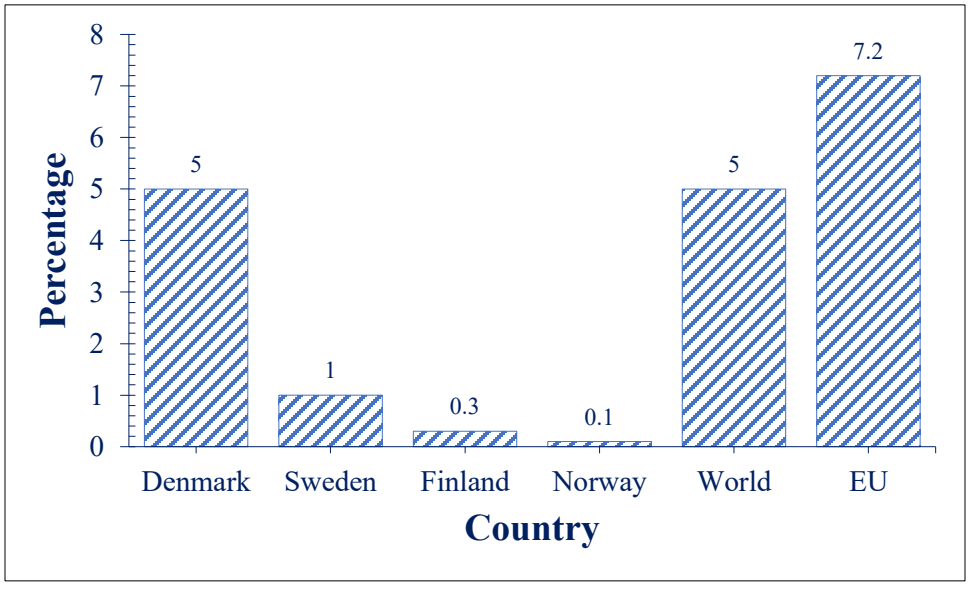

Figure 1. 3. Theoretical electricity contribution of PV to national energy mix, based on the PV capacity installed by the end of 2021 for the Nordics. Extracted from IEA PVPS Snapshot of Global PV markets, 2022 [21], refer to Paper A.

Usually, photovoltaic PV modules are expected to produce at least 90 % and 80 % of their rated power after 10 years and 25 years of operation, respectively [6, 32]. Yet, in the field, solar PV plants fail due to harsh environmental and climatic conditions e.g., temperature, humidity, ultraviolet radiation, wind and snow loads, soiling, etc. [16, 32]. Under these climatic stressors, moisture can enter the PV module from the edges, cracks, voids, and backsheet. This leads to the formation of MID defect and failure mechanisms which is one of the major routes to degradation mechanisms that ultimately make the PV module fail [9, 33]. Details on the effect of moisture ingress and MID mechanisms on solar PV devices are presented in Chapter 3.

This means that solar PV degradation is climate dependent [14, 19]. The existing PV module standards are limited in predicting solar PV module performance reliability in the field [34]. Collecting ample climate specific performance reliability data on solar PV plants can be useful in this regard. Indeed, several studies have been conducted in the climatic zones in order to understand the occurrence of different defects and fault modes in different climates [14, 35]. For now, investigations are based on the Köppen-Geiger climate zones: *A* (tropical), *B* (steppe/arid), *C* (temperate/moderate), *D* (cold/snow), and *E* (alpine/polar). Most of the investigations on the entire PV modules were conducted in climate zones *B* and *C*. An extract of this observation is illustrated in Figure 1.4.

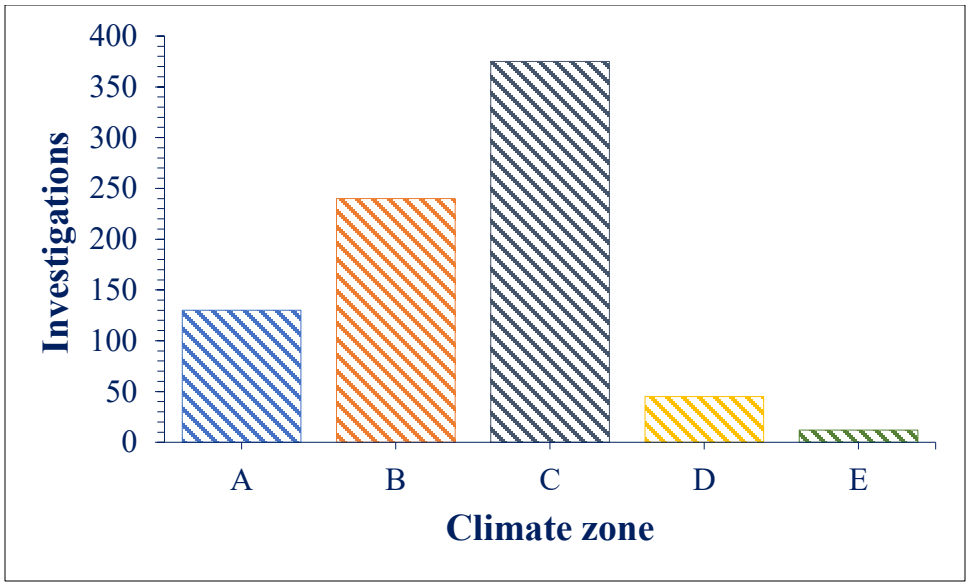

Figure 1. 4. Distribution of reported failure data on PV modules installed from the 1970s to the year 2015. Data is based on investigations that were done on the entire PV module as a unit. Extracted from Halwachs et al. [35], refer to Paper A.

The Nordics fall in climate zone *D*, where the second fewest investigations were done over the study period, as expected. Ample climatic failure data from the cold regions (e.g., southern Norway) becomes ever more important [15, 35]. This will be useful for understanding performance reliability issues of solar PV plants in the Nordics [14, 19]. This will help to reduce LCOE of solar PV plants. Since it is becoming challenging to enhance the

efficiency of solar PV modules substantially, performance reliability monitoring is the key to reducing LCOE of solar PV plants. Moreover, as investments in solar PV plants increase, a corresponding increase in research and development in this sector (especially c-Si, the dominant PV technology) makes a lot of sense.

This thesis presents the main MID defects and failure modes associated with crystalline silicon PV modules deployed in Norway. The work further investigates the underlying causes of the identified failure mechanisms using microstructural techniques. Characterization of MID defects based on their temperature sensitivity has also been explored. To the best of my knowledge, there is no such report from the same region.

1.3 Objectives and research questions

The general aim of this thesis is to extend the knowledge on the role of moisture ingress in the degradation of solar PV modules by

- exploring the dominant defects and fault modes of PV modules in the Nordics,
- investigating microstructural MID mechanisms in solar PV modules, and
- examining the correlation between moisture induced solar PV module defects and temperature sensitivity.

These objectives were explored by answering the following questions:

- What are the dominant defects and fault mechanisms of PV modules deployed in the Nordics?
- What is the role of moisture ingress in PV module degradation?
- Is there any relationship between moisture ingress and microcracks?
- How can we detect moisture ingress in PV modules?
- Is there any relationship between PV module defects and temperature sensitivity?

1.4 Thesis Outline

The thesis is structured under seven chapters as follows:

Chapter 1 contextualizes solar PV modules degradation as regards the importance of solar energy harnessing to the fight against climate change, energy sufficiency, and global economic sustainability. The chapter presents the motivation, objectives, and the research questions for this thesis.

Chapter 2 presents a brief overview of the degradation mechanisms: causes, effects, and detection methods as regards crystalline silicon solar cells and PV modules. A brief overview

of standardized reliability and durability tests methods for solar PV modules is also presented. This chapter puts Chapter 3 and 4 in perspective.

Chapter 3 gives information on moisture ingress in crystalline silicon solar PV devices, which is necessary to understand the appended articles. The predisposing factors and the mechanism behind moisture ingress in solar PV modules is presented. Next, the effects of moisture ingress i.e., MID defects and failure modes are presented. Finally, the detection, prevention, and mitigation techniques for moisture ingress in solar PV devices is discussed.

Chapter 4 discusses the temperature dependence of the electrical parameters of solar PV devices. It examines the relationship between PV module efficiency, degradation, and temperature sensitivity. A special focus is placed on the correlation between moisture induced defects and the temperature sensitivity of solar PV modules.

Chapter 5 presents the main experimental methods used in this PhD project. These methods include standardized solar PV characterization tools, a novel Visual Inspection method and defect characterization using temperature coefficients profiling. In addition, the information on the solar PV modules used in the PhD work is presented.

Chapter 6 summarizes the main contributions of the articles included in this thesis, which are included in the appendices. Figure 1.5 gives an overview of the papers in relation to the main contributions of each of them. In Paper A, the most common defects and fault modes of field deployed solar PV modules are investigated. Moisture ingress was identified as one of the major failure mechanisms in the field-aged PV modules. Hence, a review on moisture ingress in silicon solar PV modules is conducted in Paper B to understand the causes, mechanism, effects, detection, and mitigation of moisture ingress. Next, the effect of moisture ingress on the titanium dioxide (TiO_2) antireflection coating (ARC) and the solar cells and its components are examined in Paper C and Paper D, respectively.

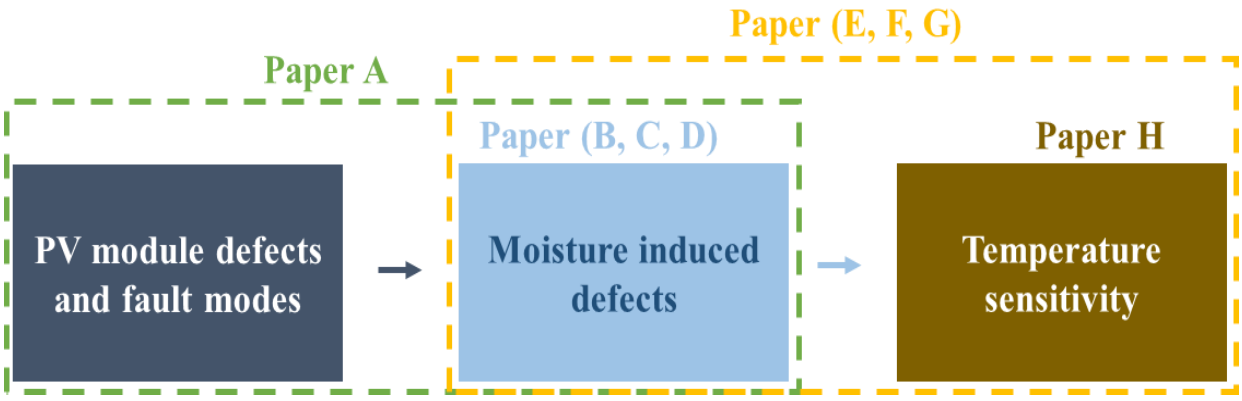

Figure 1. 5. An overview of the research articles as regards the effect of moisture ingress on the field-aged solar PV modules.

The correlation between moisture induced defects and the temperature sensitivity of a set of the filed-aged solar PV modules are investigated in Paper E, F, and G. The temperature

sensitivity of the modules affected by optical degradation (Paper E), potential induced degradation (Paper F), and microcracks (Paper G) are explored. Finally, Paper H investigates the difference between the temperature sensitivity of unshaded and partially shaded PV modules due to mismatch losses. Shading is a typical problem in the Nordics. Hence, this paper explores the similarities and differences between mismatch losses originating from defects and partially shaded PV modules. This paper gives an insight into the temperature sensitivity of modules that can be correlated with mismatch losses due to defects alone, and which is as a result of partial shading.

Chapter 7 presents a brief summary of the main findings and contribution of the present work and their implications for solar PV module performance reliability. In addition, an outlook for future work is presented.

Finally, the eight articles which form the basis for this thesis are included in the Appendices. The appended papers are published or submitted for publication in peer-reviewed international journals and conference proceedings.

Chapter 2

Field degradation of solar PV systems

2.1 Solar PV module degradation in perspective

In the field, solar PV modules are subjected to a variety of environmental and climatic stressors. Gradually, these PV panels can develop defects and faults which can result in failure. A PV module failure is any condition that creates a safety issue or has irreversible effect on the module power [14]. A purely aesthetic issue which does not pose the aforementioned effects is not categorized as a PV module failure [6]. Any anomaly with a solar PV cell/module that is not as it is supposed to be, is a defect. A fault is a defect which can result in a failure if not addressed in time or adequately. A failure can result from a defect, but not always [14]. Some of these defects and failure modes of solar PV modules were reported by Köntges et al. [6].

These degradation and fault modes such as delamination, discolouration, metal grids corrosion, potential induced degradation, solar cell degradation, potential induced degradation (PID), interface adhesion losses, optical losses, and other material degradation affect modules' performance during their guarantee period of approximately 25 years or even more [6, 32, 35]. These defects and fault modes lead to PV module degradation, and hence, power degradation [36]. About 2 % of PV modules are predicted to fail after 11-12 years due to climatic stressors [6]. According to Malik et al. [37], after 4 years of installation, PV module degradation can lead to about 2 % reduction in P_{max} of the solar PV plant.

PV module degradation can also be a function of the PV materials, usage, technology, assembling, and handling of PV modules [16, 19, 35]. From packaging to installation, estimated power loss of up to 1.4 % (mainly due to cracks) was reported [38]. Also, roof mounted PV modules are likely to operate at higher temperatures due to reduced ventilation, and for that matter tend to degrade faster [16, 36]. Bifacial solar PV modules operate at higher T_m due to higher effective heat transfer coefficient [39]. Crystalline silicon solar cells have annual degradation rates of about 0.5 % while thin film technologies show annual degradation rate of 1 % but are predicted to improve over the coming years [16].

In environments with high humidity (such as in the Nordics), the most common PV module defects and fault modes are moisture ingress and solar cell cracks [35, 40]. This is because

the Nordics are characterized by long periods of rainfall and snow. Specifically, the global annual average climate moisture index (CMI) of Norway is reportedly greater than 0.5 [41]. CMI is the measure of moisture availability at a specific place and time based on the precipitation and moisture absorption of the local atmosphere [41]. Hence, the CMI can be an indicator of the degree of moisture exposure of electronic devices (including solar panels) in a particular place. These together with high wind pressure, render the reliability of PV modules in higher altitudes more complicated [6, 35, 40, 42]. Figure 2.1 gives an overview of solar PV module failure mechanisms which are usually observed in the field. Noteworthy in Figure 2.1 is that the core of these failure mechanisms is moisture ingress.

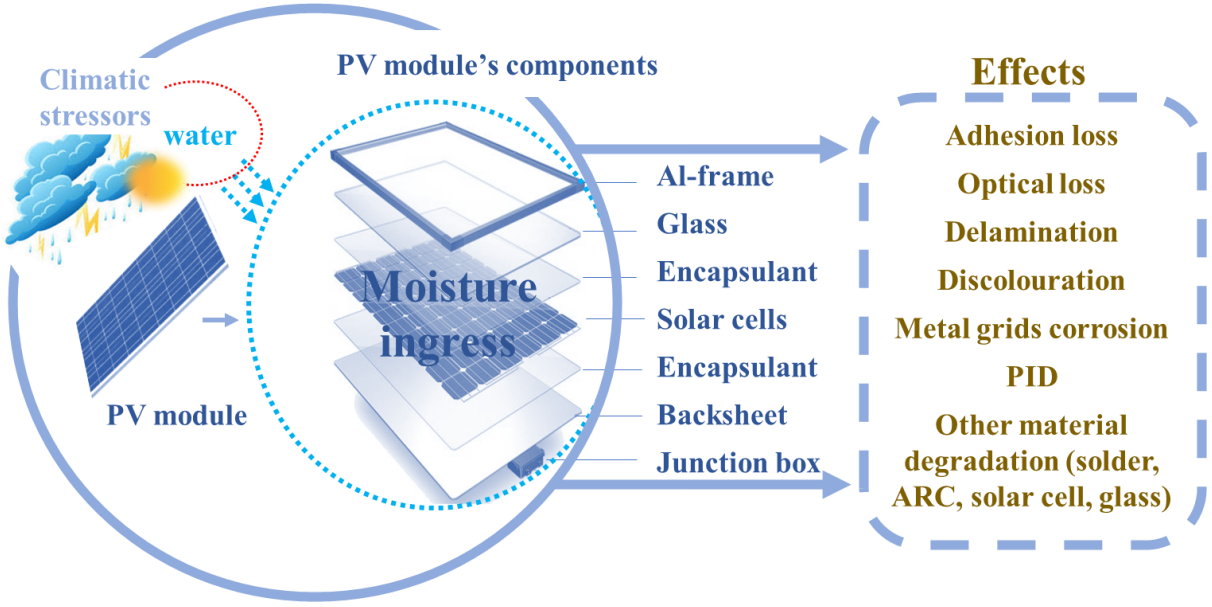

Figure 2. 1. Moisture ingress as the core for different degradation mechanisms in PV modules in the field. Adapted from Paper B [33].

Corrosion can cause parasitic resistance losses, whilst delamination and discolouration of encapsulants can also lead to loss of adhesion and optical efficiency [14, 34, 35]. Moisture ingress can induce several defect and failure modes which lead to PV module degradation and eventual power loss [6]. Some defects and failure modes influence the appearance of the PV module, and are easily detected using visual inspection [32]. However, some others such as microcracks are difficult to detect with the unaided eye and have no effect on the appearance of the module but can affect the power output [6, 26].

For defects and fault modes that cannot be detected with visual inspection, advanced spectroscopic and microscopic techniques are used for their detection. Some of these tools are electroluminescence (EL), photoluminescence (PL), fourier transform infrared (FTIR), ultraviolet fluorescence (UV-F) spectroscopy, infrared thermography (IR-T), scanning electron microscopy (SEM), and energy dispersive X-ray spectroscopy (EDS). In addition, current-voltage (I-V) characteristics are also a useful defect diagnostic tool [6, 14, 19].

However, these tools are often very useful after the defect or fault mode has occurred and some are destructive [14, 26].

A comprehensive standard that forecasts modules durability and reliability over their useful lifetime of about 25 years (+35 years proposed) becomes ever more important [43, 44]. For any of these standards to be representative of real-life operating conditions, understanding of the degradation mechanisms (defects and failure modes) is vital [45, 46]. The existing PV module standards: design qualification and type approval test (IEC 61215), safety requirements test (IEC 61730), and salt mist corrosion testing (IEC 61701) are not sufficient for predicting PV module performance reliability over the 25 years lifetime [34, 44, 47]. Hence, there is an ever-rising need for the adaptation, improving or upgrading of these existing standard testing procedures for PV modules and components [43, 44, 46].

2.2 Performance reliability and durability testing

According to Kurtz et al. [47], qualification tests naturally provide a pass or fail outcome which reflects whether the test artefact exceeds a minimum acceptable key indicator. These tests, in Figure 2.2, are carried on a representative sample of 10 or less modules and the tests are relatively short in duration and are done to minimize cost of testing [44].

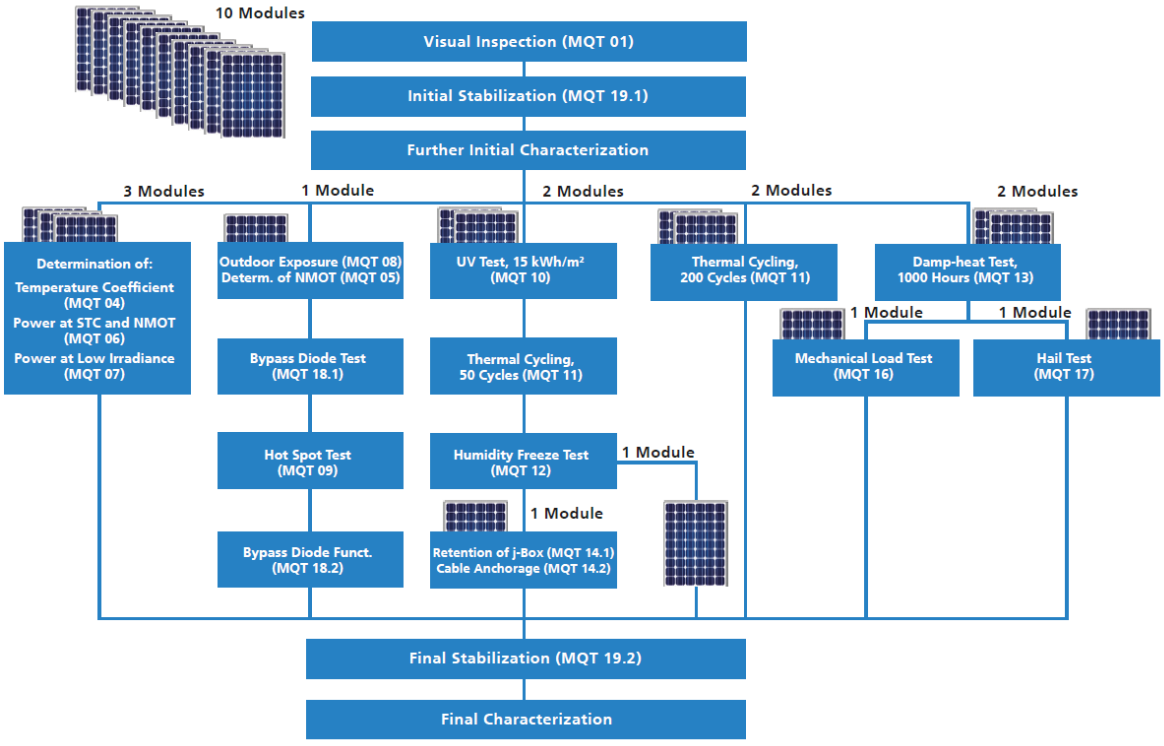

Figure 2. 2. The prototype IEC 61215 Module Qualification Tests, MQT test protocol by Fraunhofer Institute for Solar Energy Systems ISE [48].

Since 1970s, the qualification, testing and standardization for PV cells, modules, and systems have evolved [43, 44]. However, these tests are limited in identifying wear out failures and performance reliability over the lifetime of the PV module [45, 49]. Additionally, they are not reliable in detecting all defects and failure modes e.g., moisture ingress and PID [50]. Accelerated ageing tests are promising in predicting wear out failures [43]. These ageing tests include thermal cycling (TC) tests, ultraviolet (UV) exposure, humidity freeze (HF) tests, damp heat (DH), mechanical load tests or a combination of two or more of these tests in climatic or environmental chambers to identify specific defects and failure modes [43, 44, 51]. Table 2.1 shows some of the defects and failure modes that can be detected with each ageing technique.

Table 2. 1. PV laboratory tests and associated failure modes. Adapted from Wohlgemuth & Kurtz [51].

Laboratory test	Failure mode
Therma cycling	Cell cracks and broken interconnects, junction box adhesion, solder bond failure, open circuits, PID
Damp heat	Corrosion, delamination/adhesion loss and discolouration of encapsulant and other PV components, moisture ingress, PID
Humidity freeze	Delamination of encapsulants, junction box adhesion
UV test	Delamination, discolouration, and adhesion of encapsulants, PID
Mechanical load test	Cell cracks, broken glass and interconnects, solder bond and component failures

The most common tests used to evaluate moisture ingress reliability of solar PV modules are the DH, HF, and TC tests. These tests at times have negative impact on the test modules [34]. Damp heat and humidity freeze tests at elevated temperatures sometimes predispose the polymeric components of the solar PV module to ingress of moisture, reduces the optical properties of the module, and leads to the formation of acetic acid within the PV module bulk. Acetic acid accumulation in PV modules is a major precursor for interconnect corrosion, discolouration of encapsulation, and delamination in solar PV modules [52-54]. TC can induce thermomechanical stresses that can promote loss of adhesion at the encapsulant/PV-cell interfaces, cracks in solar cells, and other material induced degradations which also serve as conduits for moisture ingress [34, 45].

The most common approach is utilizing one or a combination of the above approaches to realize the accelerated degradation of solar PV cells, modules, and systems [49]. This is because one single approach does not test for all degradation modes, rather, other components of the solar PV module end up being aged undesirably during the testing of another factor [34, 46]. The accumulation of acetic acid and lead acetate in the EVA encapsulant after prolonged damp heat exposure which predisposes the cell to corrosion and subsequent degradation is an example [34, 45]. Hence, selecting the most effective ageing approach in order not to over-accelerate or under-accelerate these degradation factors is the key [34, 45, 46]. That is, equating these tests to real life operating conditions remained the greatest challenge. [43, 45, 49]. Moreover, as solar PV modules' reliability and durability has improved in recent years, accelerated testing appears to be losing its effectiveness [19]. The use of physical models to forecast solar PV module's durability and reliability is fast, convenient, and cost-effective. However, these models are amenable to errors in estimating climatic variables, degradation rates, and PV module reliability. This can introduce up to 65 % variation in the estimated degradation rate values [15]. Hence, ensuring solar PV performance reliability by way of real field outdoor monitoring under different climatic conditions becomes more relevant than ever.

Chapter 3

Moisture ingress in solar PV modules

3.1 Overview

Crystalline silicon (c-Si) solar PV panels comprise several components. These components are a front solar glass covering, a front polymeric encapsulation, silicon solar cells, a weatherproof polymeric backsheet, perimetric aluminum frame, junction boxes, and other materials such as metal grids, solder bonds, edge sealants and dielectric coating [13, 55], refer to Figure 2.1. A typical solar PV panel affected by moisture ingress is shown in Figure 3.1. Moisture from the edges of the solar PV panel can lead to corrosion, discolouration of encapsulation, delamination, and degradation of the solder bonds and other components.

Figure 3. 1. Effect of moisture ingress on a solar PV panel from the perimeter. Adapted from Wohlgemuth et al. [32], also refer to Paper B.

The PV module components, especially the polymeric elements play essential functions in ensuring performance reliability and longevity of these devices [56]. Polymeric encapsulation components ensure optical efficiency, provide physical and electrical insulation, ensure mechanical support and cohesion, act as ancillary electrical connectors, and offer protection against climatic and environmental weathering [13, 55-59]. Yet, PV

module polymeric encapsulation materials are not perfectly impermeable to moisture [57, 60]. Moisture includes water (H_2O) vapour, oxygen gas (O_2), carbon mono-oxide (CO), carbon dioxide (CO_2), and other gaseous species in the environment.

Usually, moisture enters the PV module by through the polymeric materials (via capillary action), module edges, and voids created by manufacturing, handling, transportation, installation, and under climatic stressors [34, 61]. The amount of moisture absorbed by a polymeric material depends on the temperature, concentration gradient, and also the material properties [62, 63]. Some of the material properties that influence diffusion are polymer crystallinity, chemical morphology, polarity, free volume, voids in material, degree of cross-linking, ageing, and chemical additives [63]. Another predisposing factor for moisture ingress is the PV module technology and vintage [45, 56, 63]. Current solar PV module encapsulation materials are engineered to resist delamination and discolouration: conduits for moisture ingress [33]. This is achieved by optimizing the vinyl acetate content and other stabilizers (e.g., curing agents, UV absorbers, photo and thermo antioxidants) in the EVA encapsulant [13]. In addition, the use of double glass configurations and a combination of desiccant filled primary edge sealants (e.g., polyisobutylene) and secondary edge sealants (e.g., polysulphide, polyurethane, and silicone) in recent solar PV modules provides superior moisture barrier against moisture ingress [64, 65]. The detailed mechanism of moisture ingress in polymeric c-Si PV modules is presented in Section 3.2.

According to Mon et al. [66], moisture ingress and ambient temperature play vital roles in determining the rate of many life-limiting electrochemical processes e.g., corrosion and material degradation in solar cells and PV devices. In the presence of moisture, the EVA encapsulation can produce carboxylic acids e.g., acetic acid and its related degradation products which lead to corrosion of metal grids, delamination, and discolouration of encapsulants [55, 67]. It has been observed that delamination and discolouration at the edges of the PV module is most critical to power degradation and also a catalyst for other failure modes, including moisture ingress [34, 45, 64]. Moisture ingress can also affect the optical efficiency of the module [53, 58, 68].

3.1.1 Encapsulation material properties

A common limiting factor for the performance reliability and durability of solar PV devices is the moisture diffusion properties of PV encapsulation materials [57, 59, 64]. The most common commercial PV module front encapsulation materials are listed in Table 3.1. They are ethylene vinyl acetate (EVA), ionomer, polyvinyl butyral (PVB), silicone rubber (e.g., polydimethylsiloxane (PDMS), thermoplastic silicone elastomer (TPSE), polyolefin elastomer (POE), thermoplastic polyolefin elastomer (TPO), polyethylene terephthalate (PET), polyamide (PA), polyvinyl fluoride (PVF) or Tedlar®, polyvinylidene fluoride (PVDF) or Kynar®, ethylene tetrafluoroethylene (ETFE) or Halar®, and polychlorotrifluoroethylene

(PCTFE) or Xylan®. The table also summarized the main properties of solar PV encapsulation materials. The diffusivity (D), refractive index (η), glass transition temperature (T_g), and volume resistivity (ρ_v) are very important properties of a good PV encapsulant [33, 56, 58].

Table 3. 1. Properties of some PV module front encapsulation materials, Paper B [33].

Polymer	Parameter			
	D [g/m²/d]	η	T_g [°C]	ρ_v @ 23°C [Ωcm]
EVA	8.38	1.48 to 1.49	-40 to -34	10^{14} to 10^{15}
Silicone rubber (eg. PDMS)	9 to 68	1.38 to 1.58	-120 to -50	10^{14} to 10^{15}
PVB	19.26	1.48	+12 to +20	10^{10} to 10^{12}
Ionomer	0.31	1.49	+40 to +50	10^{16}
TPSE	38.50	1.42	-100 to -5	10^{16} to 10^{17}
TPO	0.89	1.48	-60 to -40	10^{14} to 10^{18}

The first encapsulation material used in the early days of PV industry was PDMS [58]. Currently, EVA is the dominant commercial PV encapsulation material for decades [56, 57]. EVA encapsulants are cost-effective, and in addition, have high optical efficiency, good adhesion properties, high glass transition temperature, and optimal resistance to other climatic stressors [59, 69]. Even though, ionomer encapsulation materials do have the best moisture barrier properties (see Table 3.1), they fall behind EVA encapsulation materials in terms of the other properties mentioned above. Backsheets are composed of 3 main layers namely: a weatherproof outer layer, an electrically insulating inner core layer, and an adhesion promoting cell side layer, see Figure 3.2.

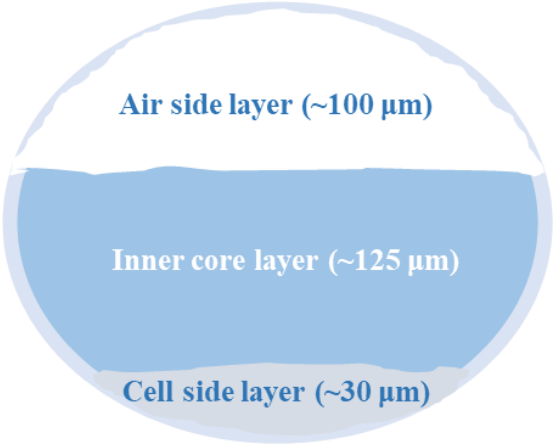

Figure 3. 2. Main components of a multilayered backsheet for solar PV applications.

The choice of a backsheet for a PV application is independent of the front encapsulation used. In Table 3.2, some of the popular material combinations for different backsheet designs are listed [33]. Fluoro-polymer based backsheets comprise about 80 % of the market share [70]. Yet, the non-fluoro-polymer based backsheets are promising [71]. Multilayered PET based backsheets are more common because they are cost-effective and have superior inter-layer adhesion properties, which is the most preferred property for outdoor solar PV applications [52]. However, understanding the degradation behaviour of these polymeric materials under real field stressors is vital [72].

Table 3. 2. The most common commercial backsheet designs. PVF is Tedlar®, PVDF is Kynar®, coating (C) is fluoro-polymer coating (e.g., Kynar, Xylan coatings). New backsheet designs substitute cell side EVA layer with olefins such as POE and TPO, Paper B [33].

Backsheet Design	TPT	TPE	KPK	KPE	PPE	KPC	PPC
Outer Layer	PVF	PVF	PVDF	PVDF	PET	PVDF	PET
Inner core layer	PET	PET	PET	PET	PET	PET	PET
Cell side layer	PVF	EVA	PVDF	EVA	EVA	coating	coating

Water vapour transmission rate, WVTR tests (the most popular) [60], gravimetric [73], capacitance [74, 75], and water immersion methods [76] are usually employed to determine the moisture barrier characteristics of PV encapsulants. With the water vapour transmission rate (WVTR) parameters determined experimentally, the moisture or gaseous barrier properties of a polymeric material can be determined [67, 73]. WVTR or oxygen transmission rate (OTR) is the amount of water or gaseous molecules that diffuse through a strip of polymeric encapsulation material, x, in a given time, t.

3.1.2 Solar PV module technology

Commercial solar PV modules are found in 2 distinct designs based on the type of encapsulation. Solar PV modules with permeable and impermeable encapsulation designs, refer to Figure 3.3. The impermeable encapsulation design, usually referred to as glass-to-glass configuration, is the most resilient to moisture ingress [33]. However, the escape of MID species is also limited. This can therefore lead to accelerated degradation of field deployed solar panels. In the impermeable design, the front and rear are made with glass encapsulation, see Figure 3.3a. In this type of module technology, the most likely routes for moisture ingress is from the edges and cracks in the module [33, 64]. This is the preferred design for thin film PV modules and other emerging technologies such as organic PV technologies due to their higher vulnerability to moisture ingress [60]. Thin films include

cadmium telluride (CdTe), copper indium diselenide (CIS), amorphous silicon (a-Si), gallium arsenide (GaAs), copper indium gallium selenide (CIGS) modules. Recent developments have also led to the growth in the market of bifacial solar PV modules, where glass-glass based c-Si modules are expected to become a leading technology in the coming years [77]. Table 3.3 shows the major commercial solar PV technologies.

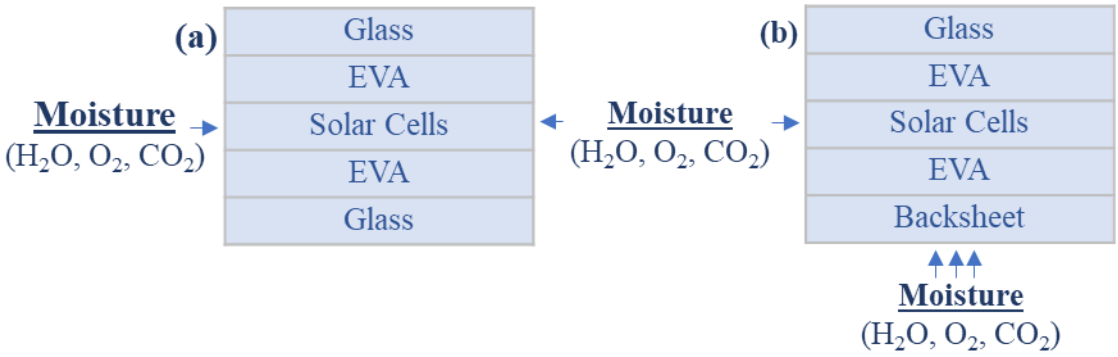

Figure 3. 3. Solar PV module designs: (a) impermeable and (b) permeable encapsulation, in Paper B [33].

Table 3. 3. The major commercial solar PV technologies, Paper B [33].

PV module type	Characteristics	PV Module Design
Monocrystalline (Single crystal/grain)	- about 20 % efficiency - relatively expensive - $\beta_{\eta m}$: -0.3 to -0.5 %/°C - blue in colour	Permeable (Glass-to-polymer)
Multicrystalline (Several grains with grain boundaries and high dislocations density)	- about 15 - 17 % efficiency - relatively low cost - $\beta_{\eta m}$: -0.3 to -0.5 %/°C - black in colour	Permeable (Glass-to-polymer)
Thin film (CdTe, a-Si, CIGS, GaAs, etc.)	- about 7 - 18 % efficiency - lower cost - $\beta_{\eta m}$: -0.1 to -0.4 %/°C - blue/black in colour	Impermeable (Glass-to-glass)
Crystalline silicon bifacial PV modules	- efficiency: about 17 - 24 % (front), 16 - 19 % (rear), 0.70 - 0.9 bifaciality factor - lower LCOE - $\beta_{\eta m}$: -0.3 to -0.4 %/°C	Impermeable (Glass-to-glass)
Emerging PV (e.g., Organic PV, Perovskites, etc.)	- relatively low efficiency - flexible, lightweight, and inexpensive - positive $\beta_{\eta m}$, but poor stability	Impermeable (Glass-to-glass)

For the purpose of this thesis, the focus is on c-Si solar PV technologies. The effect of moisture ingress on the degradation of thin film solar PV modules is provided elsewhere [44, 61]. On the other hand, the permeable design, also known as "breathable" or glass-to-polymer technology are most popular with conventional c-Si technologies, see Figure 3.3b. Permeable designs are more prone to moisture ingress, but reduces acetic acid and moisture accumulation within the PV module [67]. Unfortunately, due to the higher moisture diffusivity properties of EVA encapsulation materials, it is nearly impossible to prevent moisture ingress into PV modules completely [60]. Even the ideal hematic encapsulation is also liable to moisture ingress via cracks, for example [78].

3.1.3 Environmental and climatic factors

MID kinetics are strongly influenced by climatic conditions [79, 80]. High humidity, temperature, ultraviolet (UV) radiation, and soiling expose the PV module to moisture ingress [33]. Among these factors, temperature is known to influence moisture ingress the most. The influence of temperature on the moisture diffusion characteristics of different commercially available solar PV encapsulation materials is illustrated in Figure 3.4. Moisture diffusivity (moisture ingress) increases with increasing ambient temperature. As shown in Table 3.1, ionomer encapsulation materials are the most resilient to moisture ingress while EVA encapsulation materials are poorer in preventing moisture ingress into PV modules.

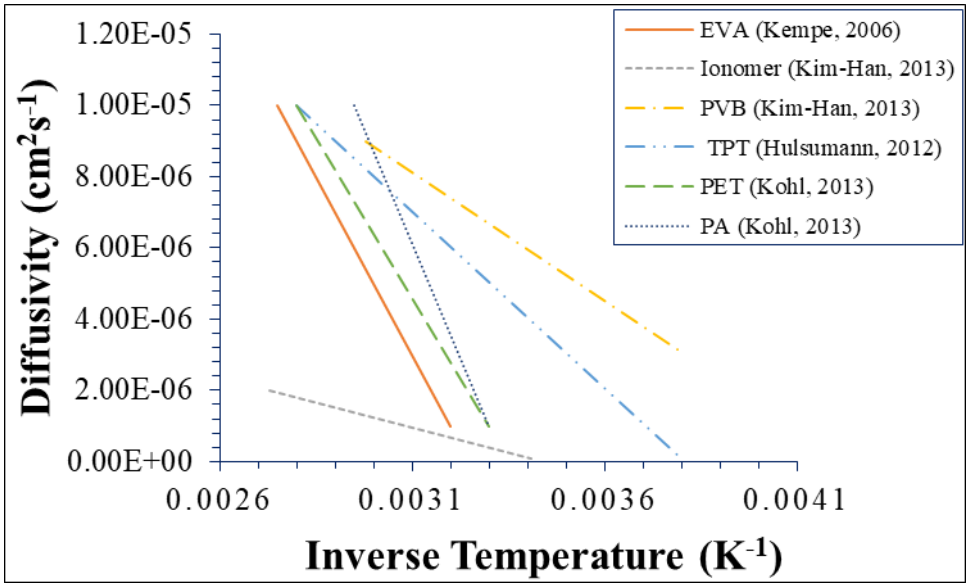

Figure 3. 4. Moisture diffusion as a function of temperature in different encapsulation materials. Adapted from Paper B, Segbefia et al. [33].

It was reported that in hot and humid environments, moisture induced defects (e.g., corrosion, delamination, and discolouration of encapsulants) dominated the degradation modes of field deployed solar PV plants [79, 80]. High humidity and soiling increase the rate

of moisture accumulation on the surface of the PV module [81]. High ambient temperature also increases moisture diffusivity of the module encapsulation [78]. Ultraviolet radiation together with high humidity and temperature induces delamination and discoloration of the PV module encapsulation [54]. These defects and fault modes serve as conduit for moisture ingress, and hence, lead to corrosion, cracks, PID, and optical degradation in the PV module. Moisture ingress is also influenced by pressure and concentration gradients of diffusants, which are also functions of humidity and temperature [63].

Koehl et al. [82] investigated the impact of humidity on PV modules based on monitored climatic data at specific locations. Using phenomenological models, they estimated the moisture concentration at the surfaces of PV modules and concluded that degradation kinetics strongly depend on climatic locations. In another study, Hülsmann et al. [80] using a FEM simulation, studied the moisture ingress into wafer-based photovoltaic modules under extended periods of exposure in four different climatic conditions (namely *moderate climate* - Freiburg, Germany, *arid climate* - Negev desert, Israel, *alpine climate* - Zugspitze, Germany and *tropic climate* - Serpong, Indonesia), using PET based and PA based backsheets and EVA as the encapsulating material. They observed a faster moisture ingress for warmer regions and higher moisture concentrations for moderate climate test sites.

In a related report, Hülsmann and Weiss [79] compared a simulated moisture uptake by PV modules under the standard IEC 61215 type approval ageing tests and moisture ingress into PV modules based on measured data sets from four different climatic zones. They used EVA as an encapsulant and TPT stack as a backsheet. They found that the standard IEC 61215 ageing tests caused twice as much moisture content in encapsulants than 20 years field exposure of modules. This is due to the dependency of diffusion (and solubility) on temperature and humidity and also the type of encapsulants, refer to Figure 3.4. They also compared their results to prior results in literature and found a good agreement among the results. Wisniewski et al. [78] used a finite element model based on experimental data from WVTR tests to comprehend the moisture ingress into double glass modules and concluded that moisture ingress increases with increasing temperature. They also argued that the moisture content of the EVA can affect the diffusivity factor up to two folds.

According to Kempe et al. [54], accumulation of acetic acid (due to moisture ingress and UV radiation) can lead to significant loss of adhesion of EVA encapsulants. Also, Novoa et al. [83] developed a fracture kinetics model based on a quantitative characterization technique to study the effects of moisture, temperature, and mechanical stress on the adhesion characteristics of backsheets using ageing tests. They found that the delamination rate increased with test duration, temperature, and relative humidity. In another related study, the same group with the same model investigated the influence of humidity and temperature on the debonding kinetics of EVA and PVB encapsulants and reported the same trend as observed with backsheets [69]. Similarly, Bosco et al. [34] also investigated the influence of humidity and temperature on the delamination kinetics of the EVA/Si–PV cell boundary and concluded that electrochemical reactions dominated at higher humidity levels.

3.2 Mechanism

Moisture ingress is the diffusion of water and other gaseous species into the bulk of a solar PV module [6, 60]. Moisture is adsorbed onto the surface of a PV module encapsulation, and with suitable concentration gradient, are transported through and desorbed onto other components of the PV module [61]. This process continues until equilibrium is established with the ambient environment [60]. The mechanism for moisture ingress and the associated degradation mechanisms is illustrated in Figure 3.5. The figure illustrates the formation of photoproducts under the action of sunlight and formation of carboxylic acids in the presence of moisture in PV module. The diffused MID species and moisture initiate different degradation processes in the solar PV module [9, 11, 67, 84].

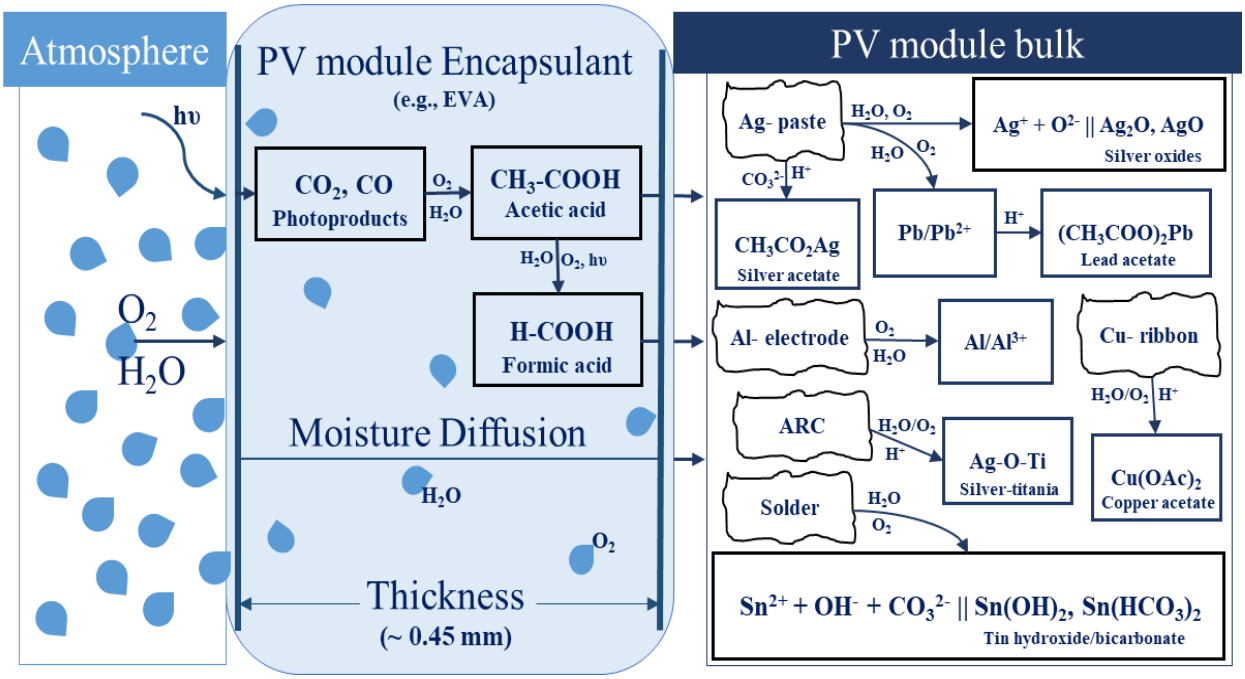

Figure 3. 5. Moisture ingress mechanism and the associated degradation mechanisms in solar PV devices. MID products (e.g., acetic acid) attack the components of the solar PV module, which lead to degradation. Adapted from Paper B, Segbefia et al. [33].

In the presence of sunlight (*hυ*), the encapsulant produces photoproducts e.g., CO_2 and CO [84]. Carboxylic acids e.g., acetic acid is formed when the photoproducts reacts with moisture [67]. Moisture and its degradation products diffuse into the solar PV module bulk and attack the components of the PV module [11]. Silver (Ag) and lead (Pb) comes from the silver paste and the solder, respectively. Tin (Sn) also comes from the solder. The rear aluminum (Al-) electrode is the source of Al and the titanium dioxide (TiO_2) antireflection coating (ARC) undergo degradation to form silver-titania (Ag-O-Ti) complexes [85]. The main degradation products are the acetates, oxides, and carbonates of the metal components [9]. Moisture is the electrolyte which sustains these electrochemical degradation reactions

[11]. According to Li et al. [86], under different, voltage bias conditions, the PV module encapsulation material can degrade to form basic or/and acidic environments in the PV module bulk. This is likely the situation in solar PV modules affected by PID.

In principle, there are two types of diffusion models: Fickian or non-Fickian diffusion models. The models which obey the Fick's laws: Equations (3.1) - (3.3), are known as Fickian diffusion models, otherwise, it is non-Fickian diffusion model [63, 65, 87, 88]. According to Mitterhofer et al. [63], the Fickian diffusion models are the most popular of the two models. However, in some exceptional cases, the non-Fickian models such as dual transport models are more accurate for modelling the behaviour of the actual diffusion process [87, 88]. For an idyllic thin film of a polymer exposed to moisture species (in an ideal environment), the moisture diffusion characteristics can be written as

$$\frac{\partial C}{\partial t} = \nabla \cdot (D \nabla C), \tag{3.1}$$

where t is diffusion time, D is the diffusivity and C is the concentration of the species within the polymeric encapsulant.

Considering a 1-dimensional diffusion where the concentration gradient is dominantly along the horizontal axis, Equation (3.1) can be rewritten in respect of the diffusion flux (F). F is the mass flow rate of permeants per unit area,

$$F = -D \cdot \frac{\partial C}{\partial x}, \tag{3.2}$$

where x is the space coordinate measured normal to the diffusion section, $-\partial C/\partial x$ is the driving force for the diffusion. The value of F (Equation (3.2)) determined experimentally is taken as the *WVTR* of the polymeric encapsulation material [78, 89]. Yet, considering an ideal barrier polymeric encapsulation material without voids, the characteristics of perfect condensable permeating species can be modelled using

$$P = S \cdot D, \tag{3.3}$$

where P is the permeability coefficient and S is the solubility (Henry's coefficient), also known as the concentration proportionality constant. The solubility, S characterizes the partial pressure of a solute-absorbent system [90]. Hence, the equilibrium between saturated moisture concentration (C_{sat}) and ambient vapor pressure (p_v) for a moisture-polymer barrier can be represented with $C_{sat} = S \cdot p_v$, which is the Henry's law. Considering moisture which interacts with polymeric materials easily, P can be written in respect of F and S as per Equations (3.2) and (3.3).

$$P = -\frac{F}{\partial C/\partial x} \cdot S \tag{3.4}$$

Hence, the *WVTR* of solar PV encapsulation materials can be modelled from experimental data using Equation (3.4) [60, 80].

In the case of ideal Fickian diffusion process in PV applications, the transient $WVTR_{(t)}$ can be modelled as in Equation (3.5) [91]

$$WVTR_{(t)} = \frac{D \cdot C_{sat}}{l}\left[1 + 2\sum_{n=1}^{\infty}(-1)^n exp^{\left(\frac{-Dn^2 \cdot \pi^2 \cdot t}{l^2}\right)}\right], \tag{3.5}$$

where n is the number of data points in space per unit time (t), and l is the thickness of the encapsulation material. n = 0, 1, 2, … Usually, experimental data points give $n = 10$, yet, n is more accurate with an ideal model with appropriate error margins [57].

In a homogenous polymeric PV module encapsulation material in the field, D, S, and P are temperature dependent and temperature effects are reliably modelled using the Arrhenius equation. If D, S, and P are generally represented with X, the equation is

$$X = X_0 exp^{\left(-\frac{E_X}{R \cdot T}\right)}, \tag{3.6}$$

where X is the coefficient X with preexponential factor, X_0, *and* activation energy, E_X. R is the universal gas constant, and T is the absolute temperature (in kelvins).

From Equation (3.6), E_X can be determined using a graph of X versus T^{-1} and the properties of D, S, and P can be determined for the polymeric encapsulation material under different ambient conditions. To determine the diffusivity of a polymeric encapsulation material at different module temperatures, Equation (3.7) can be used [60].

$$ln\ D = In\ D_0 - \frac{E_D}{R} \cdot \frac{1}{T} \tag{3.7}$$

One assumption of the Arrhenius equation is that E_D (activation energy) is independent of temperature and the influence of moisture diffusion on the physical properties of the polymeric encapsulation material is negligible [57]. Yet, the properties of the encapsulation material (e.g., chemical structure, morphology, additives and stabilizers, degradation state, etc.) can influence the diffusion characteristics of the PV polymeric encapsulation material [62]. Hence, sometimes, an ideal linear correlation between ($ln\ D$) and T^{-1} becomes impractical [57]. In such situations, the activation energy (E_a) can be determined using two diffusivity values (D_1 and D_2) at two temperature values (T_1 and T_2), respectively [57].

$$ln\ \frac{D_1}{D_2} = \frac{E_a}{R}\left(\frac{1}{T_2} - \frac{1}{T_1}\right) \tag{3.8}$$

The accuracy of the above equation is strongly dependent on the experimental methods and the related error margins. In real field conditions, T, and hence, D can vary over a wide range. Moreover, WVTR measurements depend on the surface conditions of the polymeric strip. In the presence of surface scratches or cracks, delamination, and other defects of the encapsulant, correlating experimental and real field values becomes increasingly challenging.

Kimball et al. [92] proposed a method based on the Fickian and Arrhenius laws for estimating the lifetime (t_{TTF}: test-to-failure in hours) of field-aged solar PV modules. The t_{TTF} is related to the relative humidity (RH) in %, the humidity exponent (n_e), and the preexponential factor, A as

$$t_{TTF} = A \cdot exp^{\left(\frac{E_a}{R \cdot T}\right)} \cdot RH^{(n_e)}. \tag{3.9}$$

However, it was reported that under high humidity and temperature conditions, some PV encapsulation materials can undergo hydrothermal degradation [63].

3.3 Moisture induced defects and fault modes

Figure 3.6 shows the role of moisture in different degradation mechanisms in solar PV modules. Beside attacking the various components of the PV module, the presence of moisture in the PV module initiates different electrochemical degradation pathways leading to several failure modes, refer to Figure 3.5.

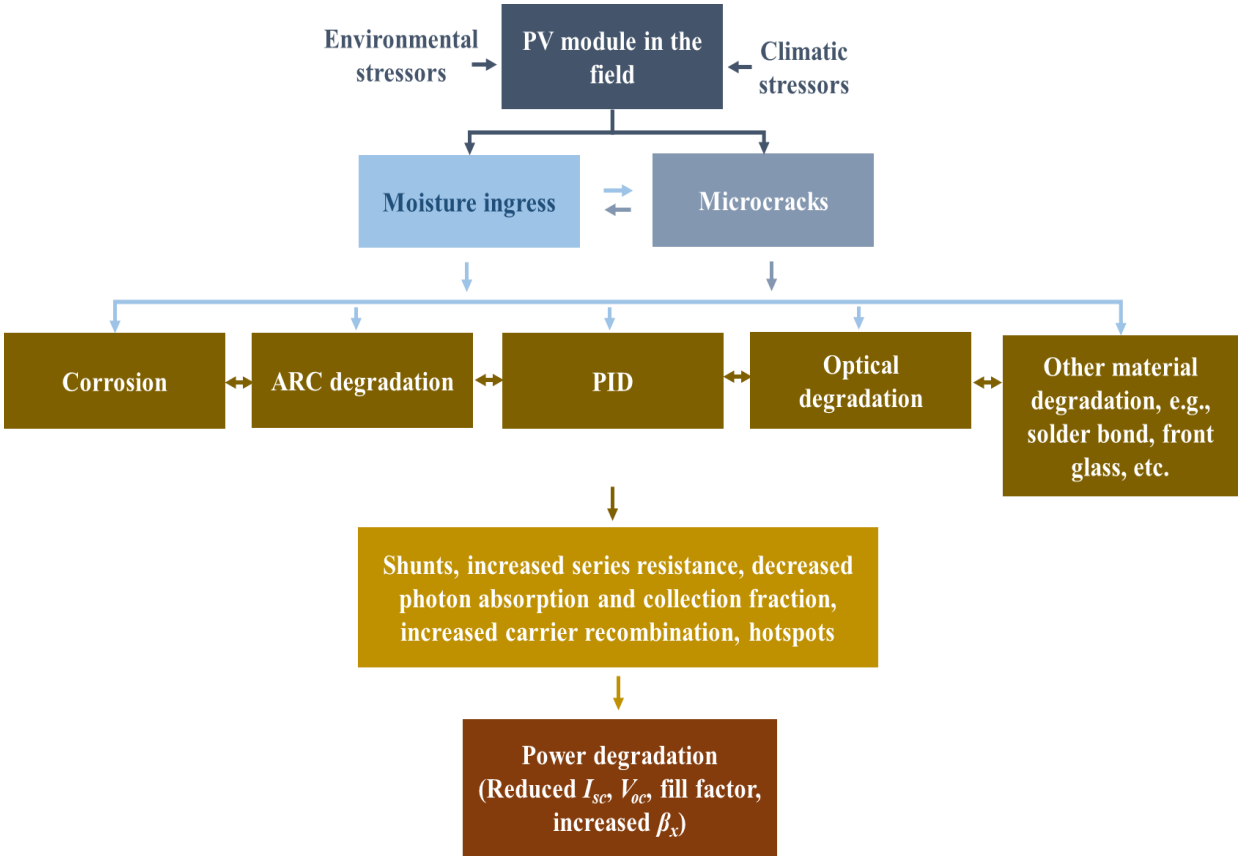

Figure 3. 6. The effects of moisture induced defects and fault modes. Moisture ingress and microcracks are solar PV module co-defects.

Moisture can attack the metal grids to form their respective oxides. EVA encapsulation can degrade into carboxylic acids. These MID mechanisms lead to the formation of MID products, and hence, MID defects and fault modes, see Figure 3.6. These defects and fault modes lead to shunting, increased series resistance, hot spots, decreased optical efficiency, increased charge carrier recombination, and localized hot spots. Of greater concern is that these degradation mechanisms lead to the degradation of the electrical parameters: I_{sc}, V_{oc}, and FF. Figure 3.7 illustrates the current-voltage (I-V) characteristics of a solar PV module affected by defects and fault modes.

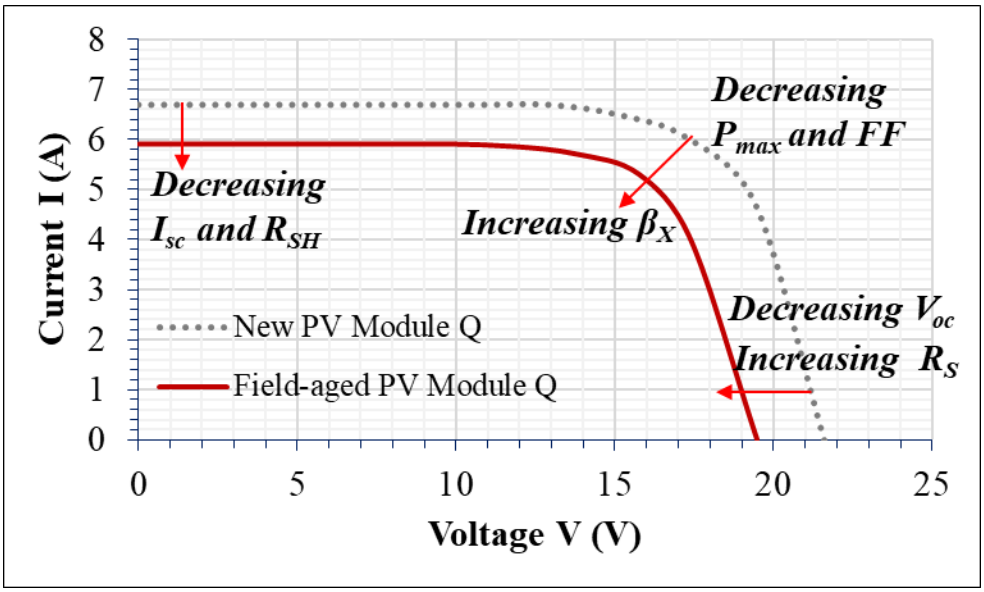

Figure 3. 7. I-V characteristics of a solar PV module affected by defects, Paper D.

Degradation in the parameters can also be witnessed in the degradation of the temperature coefficient (βx) of each electrical parameter. In effect, these degradation mechanisms account for the degradation in P_{max} of the solar PV module. The degradation mechanisms also affect the longevity of the solar PV plants, and hence, return on investment [19]. A good estimate for degradation rates leads to reduced financial risks on investment [16].

3.3.1 Solar cell microcracks

Solar cell cracks is one of the major reliability issues which lead to solar PV modules degradation in the field [14, 93]. Cracks can be classified based on the crack properties, e.g., crack width, see Figure 3.8. Cracks with dimensions less than 30 microns in width are known as microcracks [42, 94]. Cracks can be horizontal, perpendicular, or diagonal to the busbars, while some have multidimension patterns. According to Papargyri et al. [42], crack properties depend strongly on the manner they were initiated. The origin and causes of microcracks in solar PV modules are multidimensional. Microcracks can occur during

manufacturing, handling, transportation, installation, and during field operation [94]. Also, silicon wafer thickness and crystal orientation influence crack initiation, propagation, and development [94].

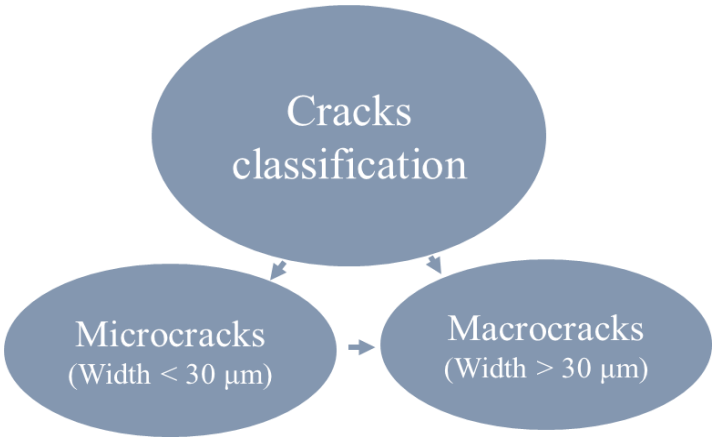

Figure 3. 8. Classification of solar cell microcracks

The thermal processing and etching steps in the manufacturing of the solar PV module also contribute to the formation of microcracks [94]. Figure 3.9 shows two field-aged solar PV modules with different types of microcracks. The effect of solar cell cracks on the power output of a PV module is illustrated in Figure 3.10. Figures 3.10a and 3.10b illustrate the I-V characteristics of a module affected by microcracks. When all solar cell parts are completely isolated due to cracks, a power loss of up to 12 % per year can be expected [14].

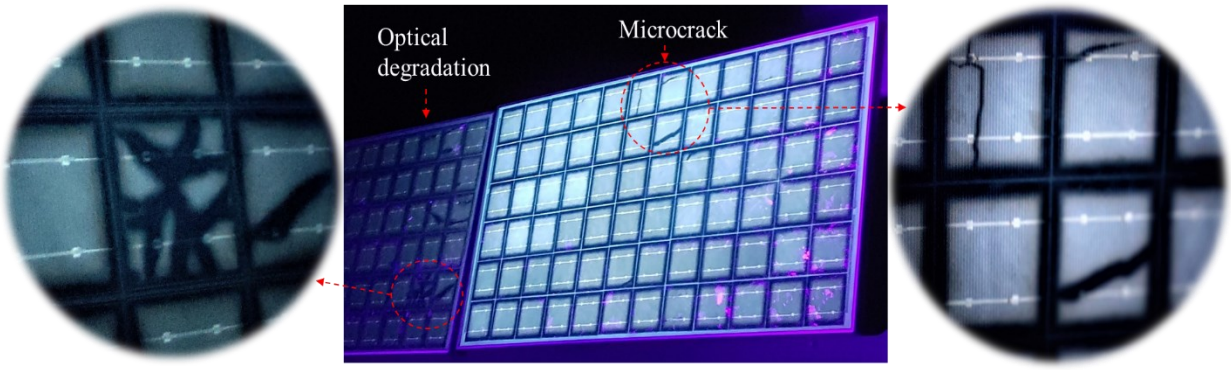

Figure 3. 9. Some types of microcracks in field-aged solar PV modules. PV module on the left side is affected by optical degradation as well, though, both PV modules are affected by microcracks. The module (left) contains multidimensional microcracks whilst the module (right) contains perpendicular and diagonal microcracks. Adapted from Paper A and G.

However, microcracks that do not affect the busbars, or the metal grids of the solar cell do not contribute to more than 2.5 % degradation in power output of the solar cells [42, 93]. The crack geometry: crack position, orientation, and dimension can also account for up to 19 % power degradation [95]. Yet, crack density and population have not been found to have any established correlation with power degradation [42, 93, 95]. Figure 3.10c illustrates the

temperature sensitivity of a PV module due to microcracks. Increased temperature sensitivity leads to power degradation [27, 29].

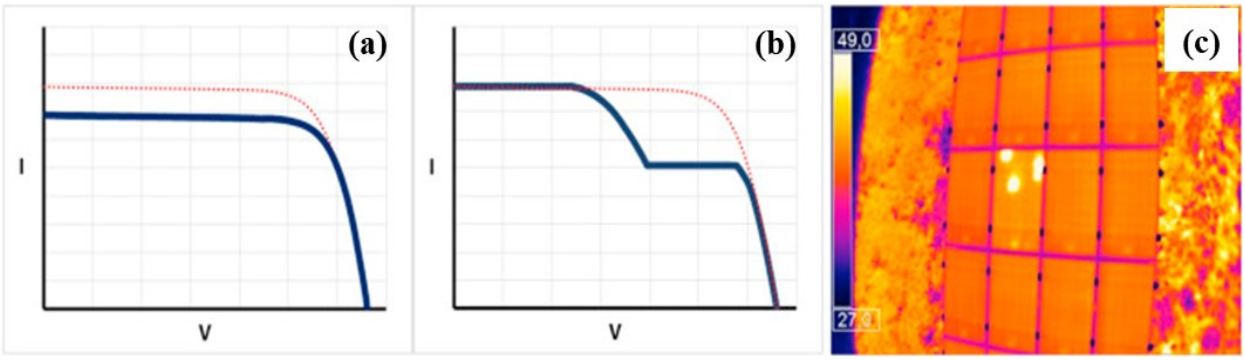

Figure 3. 10. (a) – (b) Characteristic I-V curve, and (c) a thermal image of a solar module with defects due to solar cell cracks. The drop in the maximum power (P_{max}) and fill factor (FF) in (a) and (b) is due to the hot spots in (c). Adapted from Tsanakas et al. [26].

Also, harsh climatic conditions (such as high temperature, humidity, snow, and wind loads) can induce solar cell cracks [42]. Microcracks that were not detected at the manufacturing stages can also degrade further into macrocracks under harsh environmental conditions in the field [6]. The presence of microcracks can induce other MID defect mechanisms e.g., PID, due to increased T_m, [38]. The influence of temperature on the development of cracks in PV modules is well investigated [6, 42]. Yet, the effect of moisture ingress on the development of microcracks is not well understood.

3.3.2 Optical degradation

The front encapsulation material of solar PV modules is expected to possess optimal optical efficiency throughout their lifetime [13, 96, 97]. Yet, in the field, PV panels are exposed to several environmental stressors including high humidity, temperature, soiling, and UV dose [96]. Under these conditions, moisture can enter the solar PV panel from the perimeter and backsheet [33]. Figure 3.11a shows a field-aged solar PV module affected by delamination around the cell edges. Figure 3.11b shows part of the module with trapped moisture and MID species. This results in optical degradation. Voids such as cracks created in the panel can also serve as conduit for moisture ingress and reservoir for moisture and MID species. Ingressed moisture can lead to a variety of degradation mechanisms, including optical degradation [33], refer to Figure 2.1 and Figure 3.6.

Moisture and MID products can lead to corrosion, delamination, discolouration of encapsulation material, snail trails, PID, trapped moisture and MID species, loss of adhesion, and other components of the PV module [96]. These degradation mechanisms have also been found to serve as a precursor for other degradation mechanisms in PV plants [33, 96, 98].

Consequently, these MID defects and fault modes affect the optical efficiency of the front encapsulant, and hence, constitute optical degradation [8].

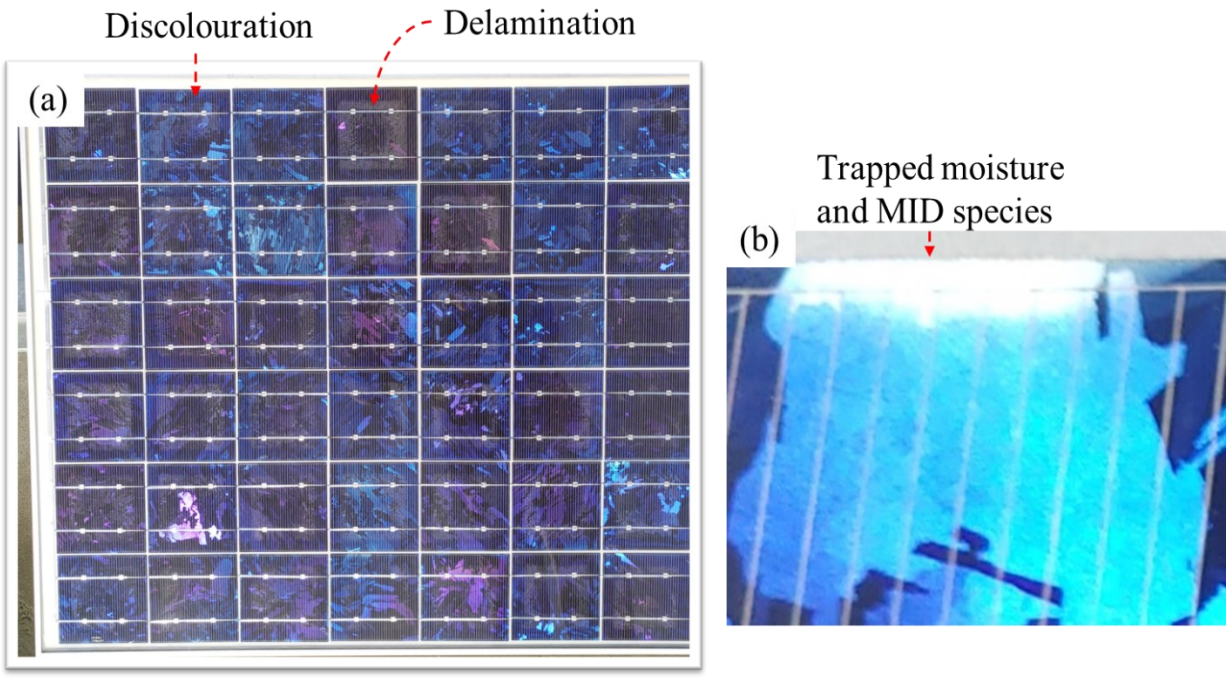

Figure 3. 11. (a) A typical solar PV module affected by optical degradation. (b) Part of a solar PV module showing trapped moisture and MID species. Adapted from Paper A and C.

Over time, the issue of optical degradation becomes more pronounced and can in the most severe cases constitute more than 50 % degradation in the rated power output of the PV module [98]. The loss of power output is due to increased optical reflection and absorption in the encapsulant, with reduced photon absorption in the active PV material [98, 99]. The optical transparency can be quantified by the "yellowness index". According to the International Standards Organization [100], "yellowness index" is a measure of the deviation in polymer hue from colourless or whiteness toward yellow.

Pern et al. [99] observed about 50 % reduction in the efficiency of PV modules as the encapsulant colour changed to dark brown. Rosillo and Alonso-García [101] reported up to 3 % reduction in the maximum power (P_{max}) of silicon crystalline PV modules due to high yellowness index. Dechthummarong et al. [102] investigated the relationship between encapsulant degradation and electrical insulation properties of field-aged single c-Si solar PV modules that were deployed in Thailand. They observed that the modules with lower yellowness index possessed better electrical insulation properties. However, sometimes, the use of the "yellowness index" as a measure of optical degradation can be misleading [103]. For instance, de Oliveira et al. [103] observed up to 0.5 %/year loss in power for ~15 years old PV modules with insignificant discolouration. In addition, degradation in power due to optical degradation also depends on other attendant defects and fault mechanisms within the module [6, 14, 26]. The PV panel (on the left side) in Figure 3.9 shows a field-aged solar

panel affected by optical degradation. The panel shows a weak UV fluorescence signal and some microcracks.

Reports show that optical degradation affects the electrical performance characteristics of solar PV modules, which lead to subsequent power degradation [96, 98]. Optical degradation influences the electronic structure and charge transport properties in the PV module [104]. In addition, optical degradation increases the number of UV absorption chromophoric species in the encapsulant [105]. These chromophores increase the UV absorption efficiency of the encapsulant which can lead to increased T_m [106]. Moreover, the chromophores can also absorb/block visible light, hence, reduce the amount of useable photons reaching the active solar cell materials [98, 107]. This leads to accumulation of current in the affected areas accompanied with high localized inhomogeneous cell temperatures known as hot spots in defective modules [26]. Increased T_m leads to a drop in the PV module power output.

3.3.3 Corrosion of metal grids

Corrosion is the deterioration of materials due to reactions (chemical, electrochemical, physical, or physicochemical) with the environment [108]. Traditionally, corrosion of metals occurs when there is an exchange of electrons between a metal and its environment. In the presence of oxygen and moisture, metals can experience electrochemical corrosion [45, 66, 68]. Corrosion mechanism of the metal grids in solar PV devices when exposed to high humidity is illustrated in Figure 3.5. Additionally, moisture ingress induces adhesion loss and creates voids in encapsulants and backsheets and therefore predisposes all components of the PV module to corrosion [18, 57, 58, 66], see Figure 3.12.

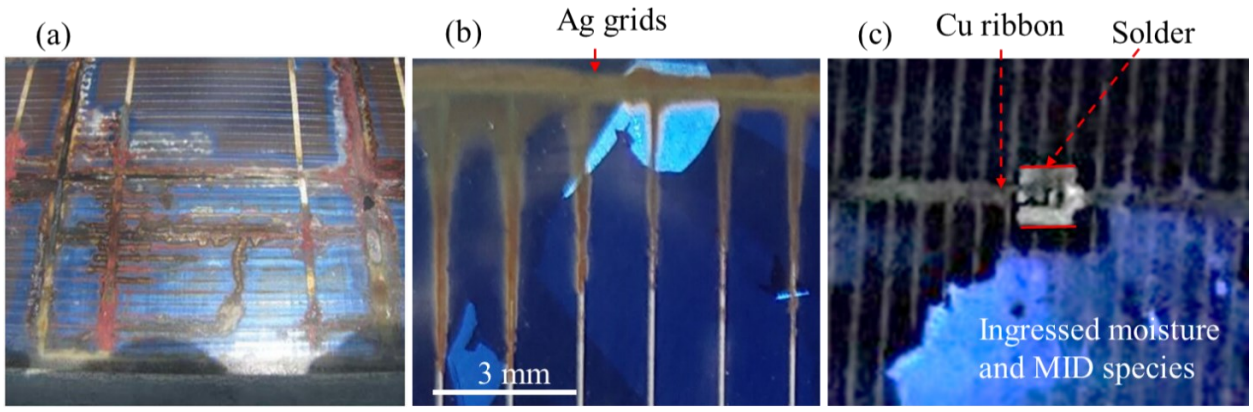

Figure 3. 12. Metal grids corrosion in field-aged solar PV modules due to moisture ingress. (a) is adapted from Wohlgemuth et al. [32]. Degradation of (b) silver grids and (c) copper ribbons, adapted from Paper C and D.

Figure 3.12 shows the corrosion and oxidation of the silver and copper grids in some field deployed solar PV modules due to moisture ingress. The effect of moisture ingress is severest

at the edges of the solar PV module, crack sites, and at the solder joints. Once moisture enters the PV module bulk, electrochemical reactions are initiated. In the presence of excess moisture and light, the acetic acid (due to EVA degradation) can breakdown to formic acid, and the incidence of corrosion is more likely [33]. Moisture and acetic acid can attack the metal grids to form their respective metal oxides, acetates, hydroxides, and bicarbonates [10, 12, 53, 109]. The copper ribbon, lead, and zinc (from the silver paste) can also degrade into copper (Cu), lead (Pb), and zinc (Zn) acetates, respectively in the presence of acetic acid and moisture [12, 109, 110]. Figure 3.13 shows the microstructure of the Ag grids degradation in a PV module affected by moisture ingress.

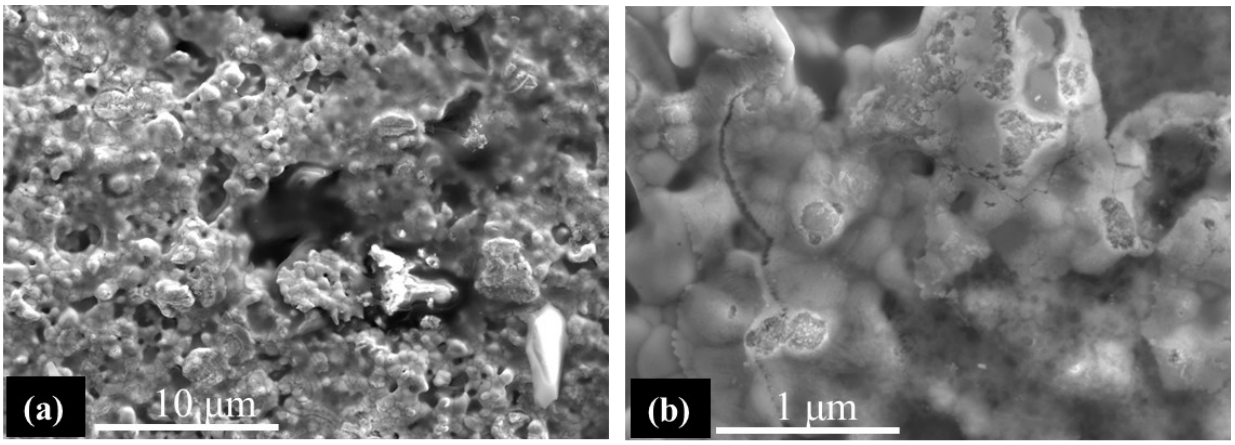

(c)

Element	Atomic %
O	52.6
Si	3.8
Pb	2.0
Ag	36.7
Zn	4.9

(d)

Element	Atomic %
O	59.5
Si	2.3
Pb	5.9
Ag	26.4
Zn	5.9

Figure 3. 13. Moisture induced degradation of the silver (Ag) grids in a field-aged solar PV panel. (a) – (b) SEM micrographs and (c) – (d) corresponding EDS analyses.

Figure 3.13a was acquired from the solder junction, and its high-resolution image is shown in Figure 3.13b. The EDS analyses of the SEM micrographs in Figures 3.13a and 3.13b are shown in Figures 3.13c and 3.13d, respectively. High amount of oxygen (O) indicates moisture ingress. The presence of Pb and Zn (in the EDS analyses) occurs under the influence of moisture ingress. This results in the formation of oxides of these metals, products of corrosion. Recently, Jeffries et al. [109] reported silver acetate as the main product of acetic acid corrosion in PV modules. Moreover, it was reported that the corrosion of intermetallic compounds (IMC) in acetic acid depend on the concentration of Ag in the paste [109]. These degradation products can also lead to the degradation of the solar cells, corrosion, and optical degradation [10-12, 53, 109-111].

Solar cell metal interconnect corrosion is known as a major cause for the overall module performance degradation [18, 34, 57, 112]. Kim et al. [53] studied three crystalline silicon PV modules under accelerated ageing conditions using I-V measurements, SEM-EDS, and Auger Electron Spectroscopy (AES) and found that the major effect of moisture ingress in PV modules is metal contact corrosion. Also, Kraft et al. [113] studied the corrosion of the screen-printed silver front-side contacts of silicon solar cells after damp heat test. They observed that the presence of acetic acid, a decomposition product of moisture ingressed EVA encapsulants, was responsible for the corrosion of the metal grids.

According to Peshek et al. [68], the routes to corrosion are dominated by moisture ingress from the perimeter to the interior of the module. Earlier on, Jorgensen et al. [114] studied the properties of module packaging materials, including moisture ingression, corrosion, and interfacial adhesion characteristics, under damp heat ageing conditions. They deposited an 80-nm-thick aluminum veneers onto a 100-cm^2 glass substrate and observed that the designs with the imbedded Al-glass laminates were effective in trapping deleterious species that catalyze moisture driven corrosion. These species they believed are of low molecular weight PET fragments of carbonyl, carboxylic, and phenolic origins. Also, Wohlgemuth and Kempe [115] performed series of damp heat tests on BP Solar modules to evaluate the effect of temperature and humidity on solar module degradation. They discovered that corrosion was the dominant degradation mechanism identified with the test modules. Later, Peike et al. [56] explored the origin of damp-heat induced cell degradation in c-Si PV modules under (80 % RH at 80 °C and 90 °C) damp heat conditions using EL imaging and EDS. They concluded that the corrosion of the grids is the underlying cause for the degradation.

3.3.4 Potential induced degradation (PID)

Solar PV panels are usually connected serially in grid-connected systems to increase voltage output and for safety purposes, modules frames are grounded [116]. However, several factors can induce high potential difference between solar cells and the PV module frame due to electrochemical interactions [117]. Some of these factors include module encapsulation and design, solar cell's anti-reflection coating, PV system electrical topology and inverter type, environmental/climatic factors (such as humidity, temperature, UV radiation, soiling, etc.), and grounding conditions of the front glass [117].

According to Naumann et al. [118], high surface defect density on interdigitated back contact (IBC) solar cells results in decreased field effect passivation. Decreased field effect passivation leads to high surface recombination, and hence, causes PID of polarization/passivation (PID-p) type. However, PID-p is temporary and reversible [14, 118]. Investigations revealed that transport of mobile ions, especially sodium (Na^+) ions, within the PV module bulk is responsible for the PID of shunting (PID-s) type [17, 116, 119, 120]. High conductivity of sodium ion decorated stacking faults across the solar cell emitter

leads to shunting, hence, PID-s [116, 120]. PID-s manifests itself in the degradation in the open circuit voltage, short circuit current, and fill factor [116]. Hence, PID-s type appears to be the key problem in the field [14].

In the presence of moisture, aluminum and sodium ions can also leach from the Al- frame and the front glass, respectively into emitter regions in the solar cells, hence, cause PID in the PV module [121]. These MID processes can also lead to the incidence of microcracks and/or snail trails, optical degradation, and ARC degradation, among others [108, 122]. These degradation mechanisms affect the efficiency and performance reliability of PV plants [119]. For instance, silver oxides deposited on the metal grids lead to increases series resistance [53, 109, 110]. Degradation of the polymer encapsulation and the silver grids in the presence of moisture can lead to the formation of silver carbonates, sulfides and phosphates which are precursors for snail trails [10]. The silver carbonate can reflect, absorb, and scatter light photons [123]. This influences the charge carrier generation, transport, and recombination in the solar cell and the module bulk. Resistance effects leads to localized hot spots and increased T_m, and hence, a drop in the power output [27]. MID products such as lead, silver, copper oxides, acetates, and carbonates appear as dark spots in EL and UV-F images, and in IR-T images, they are seen as hot spots [7, 11, 53, 109, 111].

In addition to power degradation, PID also induces mismatch losses due to non-uniform degradation [17, 124, 125]. Degraded cells that are affected by PID cause current reverse biasing, which leads to local overheating or joule heating [117]. This triggers hot spots, which influence the PV module operating temperature (T_m), hence, the temperature sensitivity [17, 124, 126]. According to Islam et al. [125], PID in polycrystalline solar panels can accelerate cell crack propagation and can lead to the degradation in the temperature coefficient of efficiency. In addition, Wang et al. [17] observed an increased temperature coefficient of maximum power (P_{max}) in PV modules affected by PID.

There have been efforts to prevent PID at the cell and module manufacturing levels, installation, and during operation [116, 127]. I-V characterization, EL, and IR-T imaging can be used to detect and monitor the onset of PID in PV plants under sunlight or in the dark with external bias conditions [116, 127]. PID-s cells are identified as warmer cells in IR thermal images and darker cells in EL images [119, 128]. According to Carolus et al. [117], I-V and external quantum efficiency (EQE) measurements can be used to differentiate PID-s from PID-p. Figure 3.14 shows an EL image of a field-aged solar PV module acquired under $0.1I_{sc}$ conditions in a dark room. The PID shunted cells appear darker. Proposed methods for reversing the PID effect appears to be saddled with other limitations [129]. Indeed, the TS IEC 62804-1 standard exists to ensure PID reliability of commercial PV modules. However, the PID effect continues to be a challenge for the PV community [17, 116, 128]. These mitigation techniques are yet to be implemented commercially largely due to the complexity of PID [117, 129].

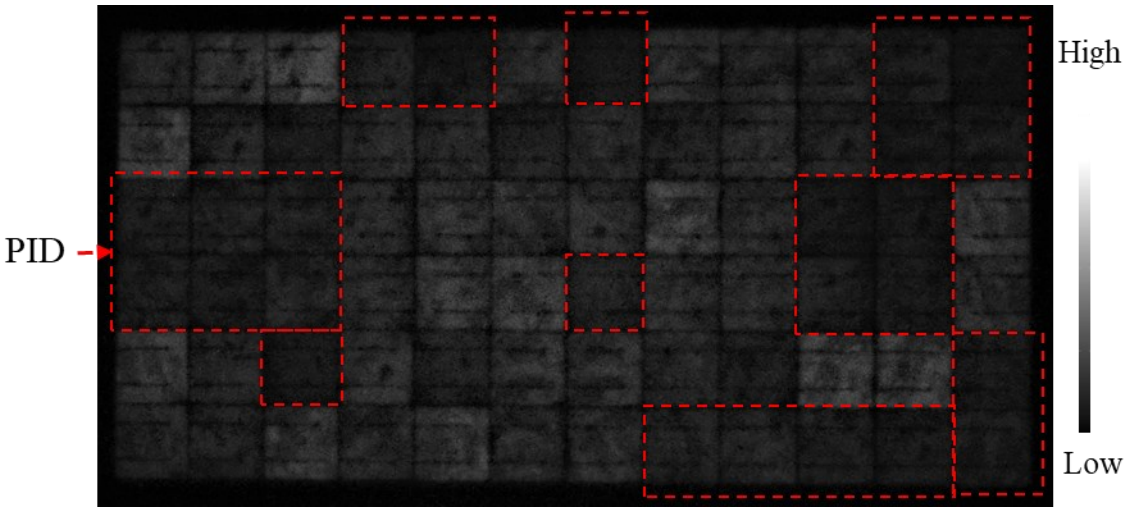

Figure 3. 14. An EL image of a field-aged solar PV module showing PID shunted cells (darker cells). The image was acquired under 0.1I_{sc} forward bias conditions in a dark room.

Also, the so-called PID-free modules may be susceptible to PID after long-term exposure to repeated outdoor weathering. The increasing installations of floating PV power plants represent a challenge even for PID-free modules, as leakage currents increase with increasing localized humidity [33, 116]. This emphasizes the need for early-stage diagnostics of moisture ingress in PV plants.

3.3.5 Solder bond degradation

The solder bond (refer to Figure 3.12) connects the copper ribbons to the silver busbars, and its main components are tin and lead. It is known that solder degradation in the presence of moisture and acetic acid obeys galvanic corrosion reaction [53, 110]. In the presence of moisture and acetic acid, Pb is preferentially corroded [130]. Acetic acid catalyzes the degradation of the Pb in the solder in the presence of moisture [131]. Under atmospheric conditions, a nanometer sized protective lead oxide passive layer is formed on the surface of Pb according to the following reaction mechanisms:

$$\text{Anode (oxidation):} \quad Pb \rightarrow Pb^{+2} + 2e^{-} \tag{3.10}$$

$$\text{Cathode (reduction):} \quad \tfrac{1}{2}O_2 + H_2O + 2e^{-} \rightarrow 2OH^{-} \tag{3.11}$$

$$\text{Passive PbO layer:} \quad Pb^{+2} + 2OH^{-} \rightarrow PbO + H_2O \tag{3.12}$$

The passivation lead oxide (PbO) layer protects the Pb metal from further corrosion and degradation. However, in the presence of moisture and acetic acid, the PbO protective layer is susceptible to dissolution, and hence, degradation. The acidified electrolyte (consisting of MID products) in the PV module permeates into cracks and defects in the PbO protective

layer and reacts with the Pb to form soluble lead acetate complexes according to the following reaction mechanisms [132]:

$$\text{PbO layer dissolution}: PbO + 2CH_3COOH \rightarrow Pb^{+2} + 2CH_3COO^- + H_2O \quad (3.13)$$

$$2PbO + Pb^{+2} + 2CH_3COO^- + H_2O \rightarrow Pb(CH_3COO)_2 \cdot 2PbO \cdot H_2O \quad (3.14)$$

Figure 3.15 shows the microstructural analysis of the solder bond in a field-aged solar PV module due to the effects of moisture ingress.

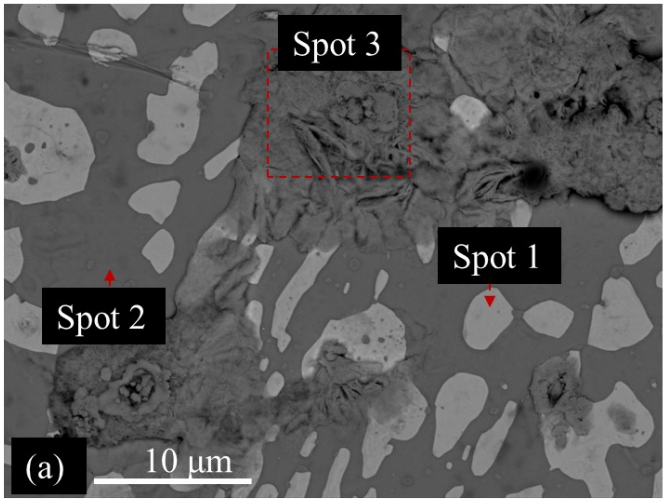

(b)

Element	Atomic %		
	Spot 1	Spot 2	Spot 3
Carbon	4.6	0.0	0.0
Oxygen	23.1	0.0	74.4
Aluminum	0.1	0.0	0.0
Silicon	1.1	2.0	0.0
Lead	69.4	0.0	20.8
Tin	1.8	98.0	4.8

Figure 3. 15. Moisture induced degradation of the solder bond in a solar cell extracted from a field-aged PV module. (a) SEM micrograph and (b) corresponding EDS analysis.

EDS point analysis at Spot 1 shows that Pb has been oxidized. On the other hand, the EDS analysis at Spot 2 shows that Sn is unoxidized. Pb is preferentially oxidized due to the presence of MID species e.g., acetic acid [131]. The presence of carbon in the EDS elemental analysis at Spot 1 suggests that the role of acetic acid in the degradation process cannot be ruled out. Spot 3 shows a loose structure of Pb due to severe oxidation, see Figure 3.15. MID species such as acetic acid served as catalysts for the observed degradation. Hence, carbon is absent from the EDS point analysis acquired from Spot 3.

3.4 Detection methods

EL, PL, IR-T, UV-F, DLIT, I-V, and visual inspection techniques have been used to detect MID defects and fault mechanisms in PV plants [11, 33, 53]. The collective advantage of these techniques is that they are non-destructive. However, these techniques are incapable of establishing the microstructural causes of the observed degradation mechanisms. Hence, investigations to unravel the root causes of these degradation mechanisms (based on degradation products) employ microscopic and spectroscopic methods. MID species can be

detected using SEM, EDS, electron beam induced current (EBIC), FTIR spectroscopy, X-ray photoelectron spectroscopy (XPS), atomic force microscopy (AFM), thermo-gravimetric analysis (TGA), resonance-enhanced Raman spectroscopy (Raman), etc. [11, 13, 33, 108, 112]. Even though these techniques are destructive, they are well established to give more accurate results.

The prospects of employing both the destructive and non-destructive methods to detect MID mechanisms have been reported [11, 12, 53, 108, 123]. In these investigations, efforts were made to understand MID observed in non-destructive methods at the microstructural level. This twin approach employs the strengths of both methods for defects and fault diagnosis. MID products such as lead, silver, copper oxides, acetates, and carbonates appear as dark spots in EL and UV-F images, and in IR-T images, they are seen as hot spots [7, 11, 53, 109, 111]. Figure 3.16 shows the hot spots and dark spots in a PV module affected by defects. The figure shows the corresponding IR-T images (Figure 3.16a), EL image (Figure 3.16b), and UV-F image (Figure 3.16c) in the same PV module. Figure 3.16b and 3.16c are the portion marked red in Figure 3.16a. The SEM-EDS analyses of the marked-out defect areas in Figure 3.16 were shown in Figures 3.13 and 3.15.

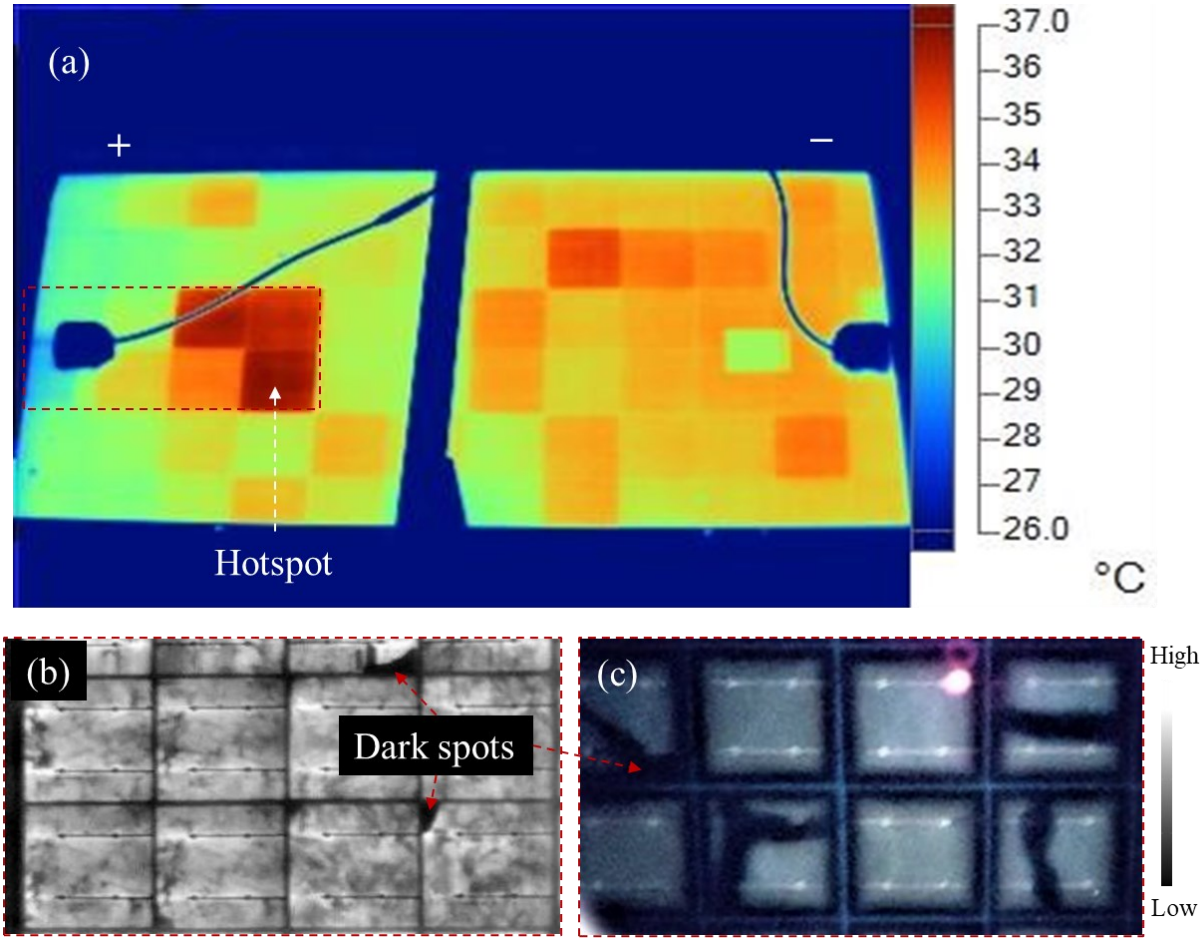

Figure 3. 16. (a) IR thermography of a field-aged solar PV module. Corresponding (b) EL image and (c) UV-F image of the marked-out hotspot area in (a), from Paper D.

3.5 Mitigation techniques for moisture ingress

Controlling moisture ingression into PV modules will ensure the durability and reliability and therefore boost the marketability of PV devices substantially [60]. There has been significant work within the scientific community to understand and develop possible mitigation strategies for preventing or delaying moisture ingress in PV modules. The use of encapsulation materials with high adhesion and moisture barrier qualities, desiccant stacked sealants, and imbedded moisture/humidity sensors are some of the ways of achieving this objective [33, 63, 65, 74, 75, 87, 88]. Other strategies such as developing intricate PV configurations with breathable backsheets [60] and making PV devices with high substrate adhesion and super hydrophobic materials on the surfaces have been explored and are still under serious investigation [33, 34, 69].

Marais et al. [133] investigated the effect of moisture and gas (oxygen and carbon dioxide) transport through various blends of EVA with varying vinyl acetate (VA) contents. They found that, in the case of water, permeation rates increase with higher VA content whilst the gas permeation rate is unaffected even with varying contents of VA. As such, EVA with lower VA contents can limit the ingression of moisture into PV modules. In another study, Czyzewicz and Smith [134] developed ionomer-based encapsulants with superior electrical, mechanical and moisture barrier properties with a possibility of making modules without supplementary edge seals. They argued that their developed ionomer-based encapsulant, with superior moisture barrier properties can be a solution to the problem of moisture ingression into PV modules. Kim and Han [89] studied the permeation rates in various encapsulants and observed that ionomer encapsulants are the best when considering only their lower moisture diffusivity, but EVA comes top when all characteristics and requirements of a good encapsulant are considered.

The moisture barrier properties of encapsulants can be improved significantly when they are used together with edge seals such polyisobutylene (PIB) sealants [65]. However, PA, PET, and TPT encapsulants and backsheet have better moisture barrier properties than even a desiccant stacked edge sealed EVA [80]. A collection of literature on the moisture barrier properties of some popular edge sealants is illustrated in Figure 3.17. The data shows that ionomers possess the best moisture barrier potential, and hence, has better prospects for solar PV applications. In Figure 3.17, the best moisture barrier material is the PIB base edge sealants proposed by Kempe et al. [65], which can perform optimally over a vast temperature range. Additionally, Wisniewski et al. [78] believe that PV modules with EVA films with lower initial water content can delay the time taken by the EVA to reach equilibrium with the ambient environment by two folds.

In an earlier work, Kempe [135] evaluated the performance of desiccant edge-seal materials in a PV module. They employed an optical method where the reaction of water with calcium was used to quantify and compare moisture ingress into a PV module by exposing different test samples to humidity and heat. They concluded that desiccant filled PIB sealants have the

potential to slow down moisture ingress in PV modules. In a related work by the same group, Reese et al. [74] proposed a method of determining the moisture barrier properties of encapsulants based on the resistivity of Ca films when they undergo hydrolysis. In this process, the conductive Ca film changes to an insulator in the presence of moisture, and hence, the resistivity. Also, Miyashita et al. [75] used colour changes in cobalt chloride, $CoCl_2$ paper to investigate moisture ingress into PV modules and found out that moisture ingress occurs from the back to the core of the module, but this also depends on the WVTR of the backsheet.

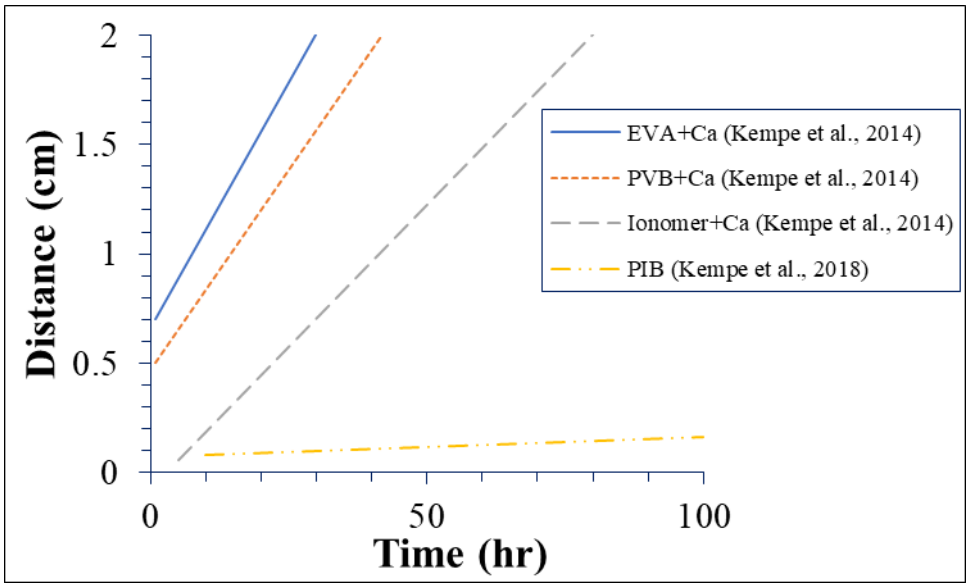

Figure 3. 17. Moisture barrier resilience of some edge sealants. Data extracted from Kempe et al. [64] and Kempe et al. [65]. Adapted from Paper B, Segbefia et al. [33].

Furthermore, Kempe et al. [64] used a thin film of Ca between two laminated glass pieces for a variety of encapsulant and edge-seal materials to evaluate the ability of these configuration to prevent moisture ingress into PV modules. They found that the Ca-embedded structures are capable of preventing moisture ingress just like desiccant-stacked PIB sealants. They argued that since the best encapsulants are still permeable to moisture, low diffusivity encapsulants are reliable in preventing moisture ingress, in case edge sealants fail. In a related work by the same group, they developed permeation models that can be useful for field applications. They concluded that molecular sieve desiccants can serve as a good moisture barrier materials when used in PIB based edge seals [65]. The synopsis of these results and other related reports in literature are illustrated in Figure 3.17. Further, Hardikar et al. [136], using a theoretical framework, studied the moisture barrier performance of edge seals in PV modules based on accelerated testing and historical meteorological data. They concluded that edge sealants are capable of securing modules, even in aggressive environments.

In a related work, Morita et al. [137] investigated the moisture barrier reliability of organic PV modules using the Ca method proposed by Kempe et al. [64] and Reese et al. [74]. Test

samples were connected to a data acquisition system via signal cables in order to test under varying environmental conditions. An edge card connector (with Ca film) was used to connect samples to the barrier material enabling easy switching of samples in and out of test. They observed a high moisture barrier resilience under conditions of 85°C / 85% RH. However, they noticed a degradation (which was thought to be due to products from the encapsulant) of the modules, a condition which they believe can be improved by incorporating a vacuum process into the sample preparation procedure.

In other investigations, Jankovec et al. [87] proposed an in-situ moisture measuring technique for PV modules using miniature digital humidity and temperature sensors embedded in encapsulants. They were able to test different encapsulants, backsheets, and edge sealants in different PV modules. They believed that using their monitoring technique, module's reliability and durability analysis can be done by extracting the diffusion coefficients of encapsulants and backsheets after exposure to high humidity and temperature conditions. In another study, Slapšak et al. [88] developed an in-situ miniature digital relative humidity sensor based on a wireless radio-frequency identification (RFID) technology which can be used for monitoring moisture concentration in PV modules under indoor and outdoor conditions. They believe that the size of the sensors makes it possible to integrate them into any module design conveniently for reliable extraction of required data.

However, most materials used for edge seals are limited by low fracture strength, and therefore are prone to mechanical failure [57, 62]. Hence, delamination or ripping can occur when edge seal environment of the module is subjected to even the slightest stress or strain [34, 45, 133]. Hence, using opto-thermoelectrical properties (e.g., temperature sensitivity) of MID species and defects to monitor and characterize MID failure mechanisms in solar PV devices is promising, expedient, fast, and cost-effective.

Chapter 4

Temperature sensitivity of solar PV modules

Beside power degradation, defects and fault modes also induce mismatch losses due to non-uniform degradation [17, 124, 125]. Degraded cells cause current reverse biasing, which leads to local overheating or joule heating [117]. This triggers hot spots, which influence the PV module operating temperature (T_m), hence, the temperature sensitivity [17, 124, 126]. The cell temperature difference (ΔT) between the cell with the lowest temperature (T_{cL}) and the solar cell with the highest temperature (T_{cH}) can be an indicator of a specific defect or fault mechanism. That is, the nature of the hot spots depends on the characteristics of the defect [26, 97]. It has to be noted, however, that ΔT values are also influenced by several factors including current characteristics and the ambient environment [81, 138].

Also, the thermal profile of the module depends on the degree and the areas affected by the defects [119]. For instance, the ΔT due to optical degradation can be up to 6 °C or even higher depending on the degree of degradation [26]. High T_m affects the efficiency and induces other degradation processes [26, 33]. The formation of PID in modules affected by microcracks is an example [38]. Critical solar cell cracks influence the thermal signatures of cells with ΔT values as high as ~45 °C [26, 97]. Depending on the crack characteristics, power degradation can vary from 0.5 % to 1.43 % per year [38].

Beside defects and fault modes, partial shading of solar PV modules also leads to mismatch losses, and hence, local hot spots [139, 140]. Figure 4.1a and 4.1b are the IR thermal images of the same solar PV module under no shading and partial shading conditions, respectively. From the figure, the effect of partial shading on the development and distribution of hot spots over the PV module is clear. This affects the electrical characteristics of the module [141].

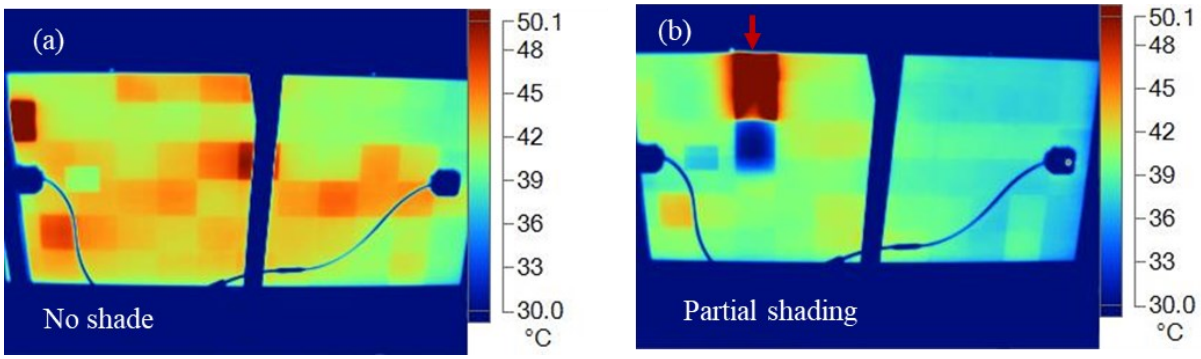

Figure 4. 1. IR thermography of the same field-aged PV module under (a) no shading and (b) partial shading conditions. The red arrow indicates the position of the shade, from Paper H.

Shading of PV plants is an issue in all parts of the world, depending on the local surroundings and/or obstacles near the installation, even under optimum solar irradiation conditions [140]. Moreover, shading can be more difficult to avoid and have a greater impact on yield at high latitudes, due to low solar incidence angles in the winter [142]. Usually, mismatched cells due to shading may become reverse biased which leads to local hot spots or joule heating [143]. Hence, PV modules are equipped with bypass diodes to mitigate the effect of reverse biasing. Yet, bypass diodes are limited in preventing hot spots entirely [139]. Hence, understanding and incorporating the temperature coefficients of PV modules under partial shading conditions in mitigation algorithms has the potential of improving diagnostic methods for solar power plants [27, 144]. This will also help to understand which mismatch loss is due to which defect(s), shading, or both. Under partial shading conditions, the temperature coefficient of J_{mpp} (β_{Jmpp}) and fill factor (β_{FF}) are the most affected [145]. Figure 4.2 shows the temperature sensitivity of the PV module in Figure 4.1 under no shading and partial shading conditions. However, the temperature sensitivity also depends on the ambient conditions and the types of defects [146, 147]. Under partial shading conditions, the β_{Jmpp} shows high negative values. The β_{Pmax} and β_{FF} show higher values (greater than -0.5 %/°C) as well, see Figure 4.2.

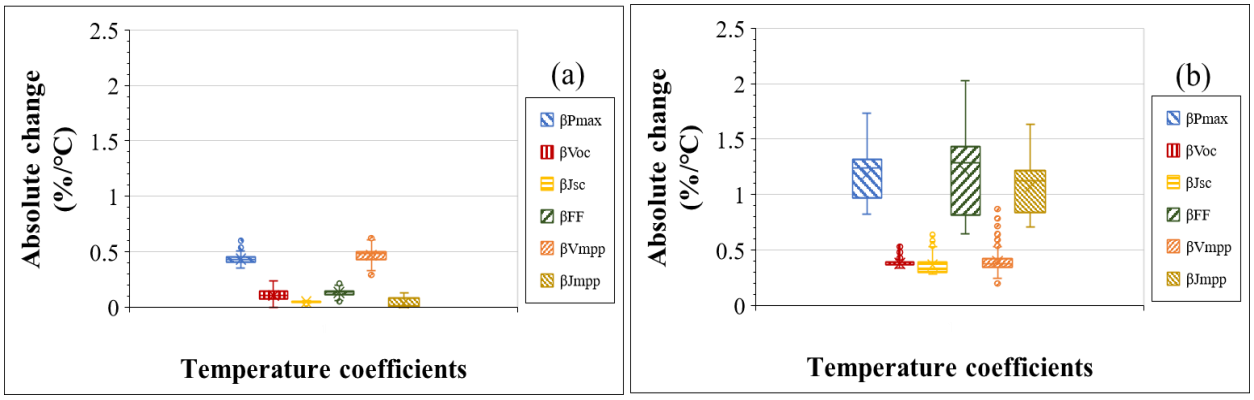

Figure 4. 2. Evolution of temperature coefficients of a field-aged PV module under (a) no shading and (b) partial shading conditions. The ends of the boxes are the lower and upper quartile (interquartile range), the internal lines and *x*-marks indicate the median and mean, respectively. Measurements were done under 960 W/m^2 - 1060 W/m^2 in-plane irradiance conditions, and then normalized to STC.

The temperature sensitivity of PV cells or modules were modeled based on internal device physics and the dominant recombination mechanisms [144, 148]. Even though these investigations provided vital insights into the general trends as regards the temperature behaviour of PV devices, they have failed to provide enough information on how PV systems in real operating conditions respond to temperature changes [28, 148]. That is, theoretical investigations rarely provide information on the "effective" temperature coefficients of PV modules [27, 149]. It has also been observed experimentally that the exposure of thin films such as CIGS to light can modify their temperature coefficients, especially that of fill factor [27]. Berthod et al. [150] observed that the temperature behaviour of compensated silicon

solar cell depends mainly on the net doping and the bulk resistivity. According to Kristensen et al. [151], temperature sensitivity of solar cells also depends on the wafer material. That is, intrinsic crystal defects: grain boundaries and dislocation clusters have varying effects on the temperature sensitivity.

The temperature coefficients of PV modules are computed from the T_m, which is the average value for the individual cells. Hence the solar cell with the least short circuit current (I_{sc}) limits the temperature coefficient of J_{sc} (β_{Jsc}) of the PV module [28, 148]. According to International Electrotechnical Commission (IEC) specifications, a number of temperature sensors are to be attached to the back surface of the PV module at different spots and the average of these taken as the T_m. However, this procedure has been found to be challenging in practical terms due to inhomogeneity of temperature distribution over the entire module [28, 148]. Osterwald et al. [148] proposed a method for measuring the T_c of individual cells but this method is impracticable when dealing with PV modules and plants in the field.

Extensive research on the influence of the temperature sensitivity on PV modules main electrical parameters is available in literature [27-29, 149, 152]. However, investigations on the influence of defects and failure modes on the temperature coefficients of PV modules are rare [17, 124-126]. Moreover, only a few were done on field-aged PV modules [17, 125]. The use of temperature coefficients for PV module fault diagnostics is non-destructive, fast, reliable, cost-effective, and can be done conveniently anytime. In normal operation, the module voltage reduces significantly whilst the current increases but only slightly when temperature increases, see Figure 4.3.

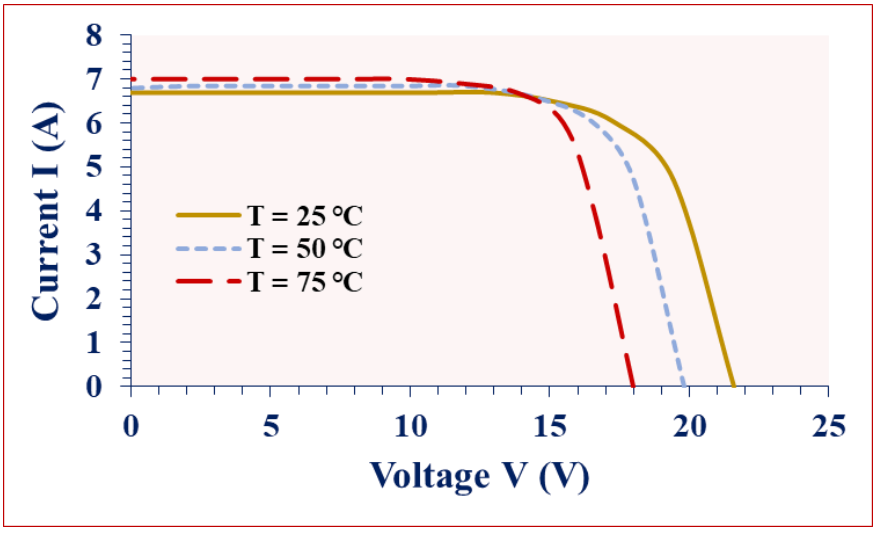

Figure 4. 3. Effect of temperature on electrical characteristics of a PV module, Paper E.

This affects the fill factor and PV module efficiency [27, 29, 152]. Hence, PV module efficiency depends on the PV module temperature characteristics [138, 153]. Moreover, the microscopic effect of temperature can accurately be traced to the temperature coefficients of the PV device [27, 28]. Figure 4.4 illustrates the effect of temperature coefficient (β_X) on the change in P_{max} (ΔP_{max}) of different c-Si solar cell PV module technologies in the field.

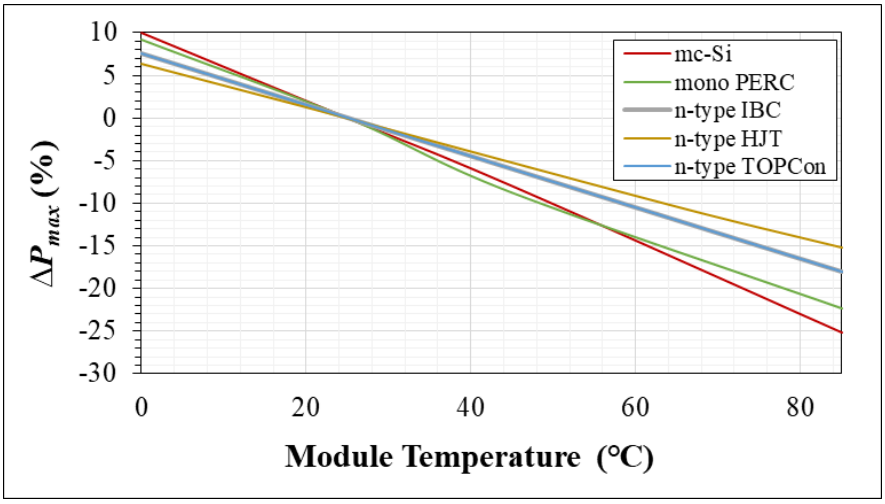

Figure 4. 4. Effect of temperature sensitivity on P_{max} of different PV module technologies.

Solar PV panels in the field can operate far below 25 °C during winter and far above the normal operating cell temperature, NOCT (45 °C) up to about 85 °C during Summer. Under high T_m (e.g., at 85 °C), a power loss of about 25 % can be expected due to the temperature sensitivity of the solar cell technology. Noteworthy is that, techno-economic analyses of solar PV plants are based on location specific T_m using technology specific β_X [22]. The analysis also takes into account the typical meteorological year profile of the location. The reported β_X for mc-Si, monocrystalline passivated emitter rear cell (PERC), n-type interdigitated back contact (IBC), n-type heterojunction (HJT), and n-type tunnel oxide passivated contact (TOPCon) solar cells are approximately -0.42 %/°C, -0.37 %/°C, -0.30 %/°C, -0.26 %/°C, and -0.30 %/°C, respectively. The n-type HJT technology performs well under higher T_m conditions.

Conceptually, the effect of T_m on P_{max} can be derived from Equation (1.3) because PV module parameters (V_{oc}, I_{sc}, FF, V_{mpp}, I_{mpp}) depend linearly on T_m [27]. Hence, it can be represented as

$$\beta_{Pmax} = \beta_{Voc} + \beta_{Jsc} + \beta_{FF} \tag{4.1}$$

Interestingly, each of the parameters in Equation (4.1) depends on different loss mechanisms in the PV module [27, 144]. These loss mechanisms mainly depend on the effects of different defects and fault mechanisms on the charge carrier generation-recombination balances at maximum power point (MPP) [144]. Therefore, under MPP conditions, comparing Equation (1.1) with Equation (4.1), gives

$$\beta_{Pmax} = \beta_{Vmpp} + \beta_{Jmpp} \tag{4.2}$$

The V_{oc} is the charge carrier generation-recombination characteristic of a solar PV module. So, the temperature sensitivity of a PV module improves when the V_{oc} increases [154]. Moreover, the β_{Voc} of a PV module accounts for 80 - 90 % of the β_{Pmax} of the PV module [27]. For that matter, and inferring from Equation (4.2), β_{Vmpp} has the greatest impact on the degradation in β_{Pmax}, and hence, on P_{max} degradation under nominal operating conditions.

For solar PV modules with defect free solar cells, the series resistance is approximately zero [144]. In this case, the β_{FF} mainly varies with β_{Voc} and can be expressed as [27, 154]

$$\frac{1}{FF}\frac{\partial FF}{\partial T} = (1 - 1.02FF_0)\left(\frac{1}{V_{oc}}\frac{\partial V_{oc}}{\partial T} - \frac{1}{T}\right), \tag{4.3}$$

$$\beta_{FF} = (1 - 1.02FF_0)\left(\beta_{V_{oc}} - \frac{1}{T}\right), \tag{4.4}$$

FF_0 is the ideal fill factor.

As shown in Figure 4.3, thermally excited electrons dominate the electrical properties of the semiconductor when temperature increases, and hence, influences both V_{oc} and fill factor. The model for terrestrial solar PV module assumes that, under maximum power point (MPP) conditions, the PV module efficiency (η_m) is a linear function of the T_m, but depends on in-plane solar irradiance (G_I) as:

$$\eta_m = \eta_r[1 - \beta_r(T_m - T_r) + \gamma log_{10} G_I] \tag{4.5}$$

Where η_r and β_r are the module reference efficiency and temperature coefficient, respectively at reference temperature, T_r. γ is the solar radiation absorption coefficient: the ratio of transmitted to incident solar radiation. γ was found to be from 0 to 2 for crystalline silicon solar cells [29]. However, high solar absorptivity is desired of PV devices [155]. So, most often, the γ is considered negligible and taken as zero for crystalline silicon solar cells [29, 30]. Hence, Equation (4.5) approximates to

$$\eta_m = \eta_r[1 - \beta_r(T_m - T_r)] \tag{4.6}$$

The slope of the linear regression plot of η_m versus (T_m - T_r) in Equation (4.6) gives $\eta_r\beta_r$. In that regard, a graph of a parameter X versus T_m fits the linear equation $y = mx + c$, where the slope, $m = \beta_x$ and the intercept, $c = \eta_r$. Hence, the relative temperature coefficient of parameter X (β_x) in %/°C can be calculated by dividing the slope of parameter X by the intercept of parameter X. Mathematically,

$$\beta_x = {}^{m}/_{c} \tag{4.7}$$

The temperature sensitivity of a solar PV module also depends on T_0, the temperature at which η_m reduces to zero [156]. For crystalline silicon solar cells, T_0 is about 270 °C [152]. Mathematically,

$$\beta_r = \frac{1}{T_0 - T_r} \tag{4.8}$$

Hence, for crystalline silicon PV modules, $\beta_r \approx$ -0.4 %/°C, refer to Equation (4.8). However, for substantially degraded cells, T_0 is significantly lower, with increasing β_r, and the effect of $\beta_{\eta m}$ on P_{max} degradation becomes more pronounced.

A major cause of solar PV module defects and failure modes in the field is moisture ingress, especially in cold regions. These defects and failure modes influence the temperature sensitivity of solar PV modules, and hence, their efficiency, performance reliability and costs of operation. High T_m can also induce other degradation mechanisms in the solar PV module. The temperature sensitivity can be a characteristic of specific defect and failure mode. Hence, monitoring the temperature sensitivity of solar PV modules can be useful for faults diagnostics during operation. For instance, defect specific temperature sensitivity characteristics can be integrated into the algorithms of I-V tracers and thermal imagers for defect diagnosis in solar PV plants. Information on temperature sensitivity degradation due to defects and failure mechanisms can be useful for forecasting costs of using solar PV plants. It can also be useful for decision making on the improvement on and development of existing PV technologies and protocols, respectively.

Chapter 5

Materials and Methods

5.1 Materials

The Grimstad Renewable Energy Park was officially commissioned in June 2000 and consists of 96 multicrystalline silicon (mc-Si) PV modules, amorphous silicon (a-Si) panels, and thermal collectors [157]. A section of the park (mc-Si PV modules) and the geographical location of the installation site are shown in Figure 5.1.

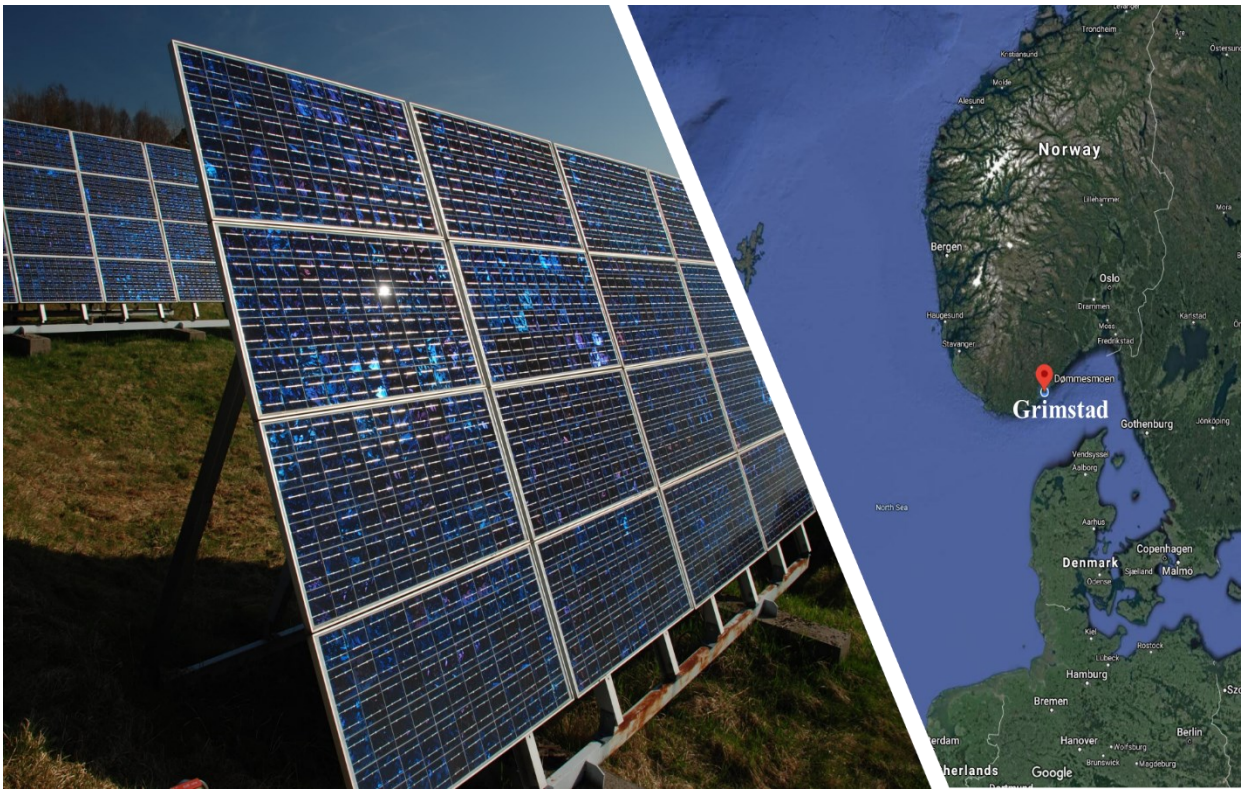

Figure 5. 1. A section of the mc-Si PV modules on the Energy Park at Dømmesmoen, Grimstad, showing the location of the site in southern Norway on the right, from Paper A.

The climate in Grimstad (58.3447° N, 8.5949° E, 50 m above sea level for the installation site) is warm cold with monthly average temperature, relative humidity, and air pressure ranges of −6.71 °C to 21.05 °C, 30 % to 99 %, and 97 kPa to 104 kPa, respectively. According to

Köppen-Geiger climate classification, Grimstad is a humid continental climate, *Dfb* (-10 °C to +30 °C, with less than 90 %), due to the constant stable marine air masses and heavy snow loads in winter [158]. The optimum angle average global irradiation is >2.46 kWh/m^2 per day (>5.5 kWh/m^2 per day in summer), with an average wind speed of 3.4 - 5.3 m/s.

According to the manufacturer, these solar PV modules were certified as per the then existing IEC 1215 (presently, the IEC 61215) standard. Investigation was carried on 43 of the mc-Si modules which were available. The main purpose of the Energy Park was to serve as a resource center for research and education in renewable energy. In 2011, the PV modules were decommissioned and kept securely for research purposes. At the time of decommissioning, the electrical performance data of these modules was investigated by Verma et al. [159], and it was found that the PV modules were producing ~90 % of their rated power. However, their investigation on the mc-Si panels was solely on the electrical performance parameters, hence, the importance of the present study on the underlying defects and fault modes. The technical specification of the solar cells and modules (as provided by the manufacturer in 2000) is summarized in Table 4.1.

Table 5. 1. Solar PV module technical specification, from Paper A.

PV Module Type	NESTE (NP100G12)
Power/efficiency (nameplate)	100 W ± 10 % (1000 W/m^2 and 25 °C) η = 13 % (total area), FF = 70 % V_{oc} = 21.6 V, I_{sc} = 6.7 A, I_{mp} = 6.0 A, V_{mp} = 16.7 V
Cells	Multicrystalline silicon (0.1 x 0.1) m^2
Module dimension	Area: 129.3 × 65 = 8′405 cm^2 Depth: 3.4 cm (w. frame) Weight: 9.1 kg
Electrical layout	(12 x 2) x 3 = 72 cells in series
Front glass	Low iron content 3 mm tempered glass
Encapsulant	EVA
Backsheet	Multi-layered white TPT
Junction box	2 weatherproof plastic casing, accommodating a bypass diode each
Frame	Full perimeter anodized aluminum frame

Each PV module consists of (12 x 2) series connected solar cells and 3 substrings. The solar cells feature a full area screen-printed Al- grid rear surface with dimensions of 100 x 100 mm^2, a titania antireflective coating (ARC), and tinned copper (Cu) ribbons. Details on the solar cells and the electrical layout of the PV panels were reported in Paper C, D, and F [9, 85, 160].

5.2 Experimental methods

In all, 43 field-aged solar PV modules were investigated. Figure 5.2 is the schematic of the experimental methods.

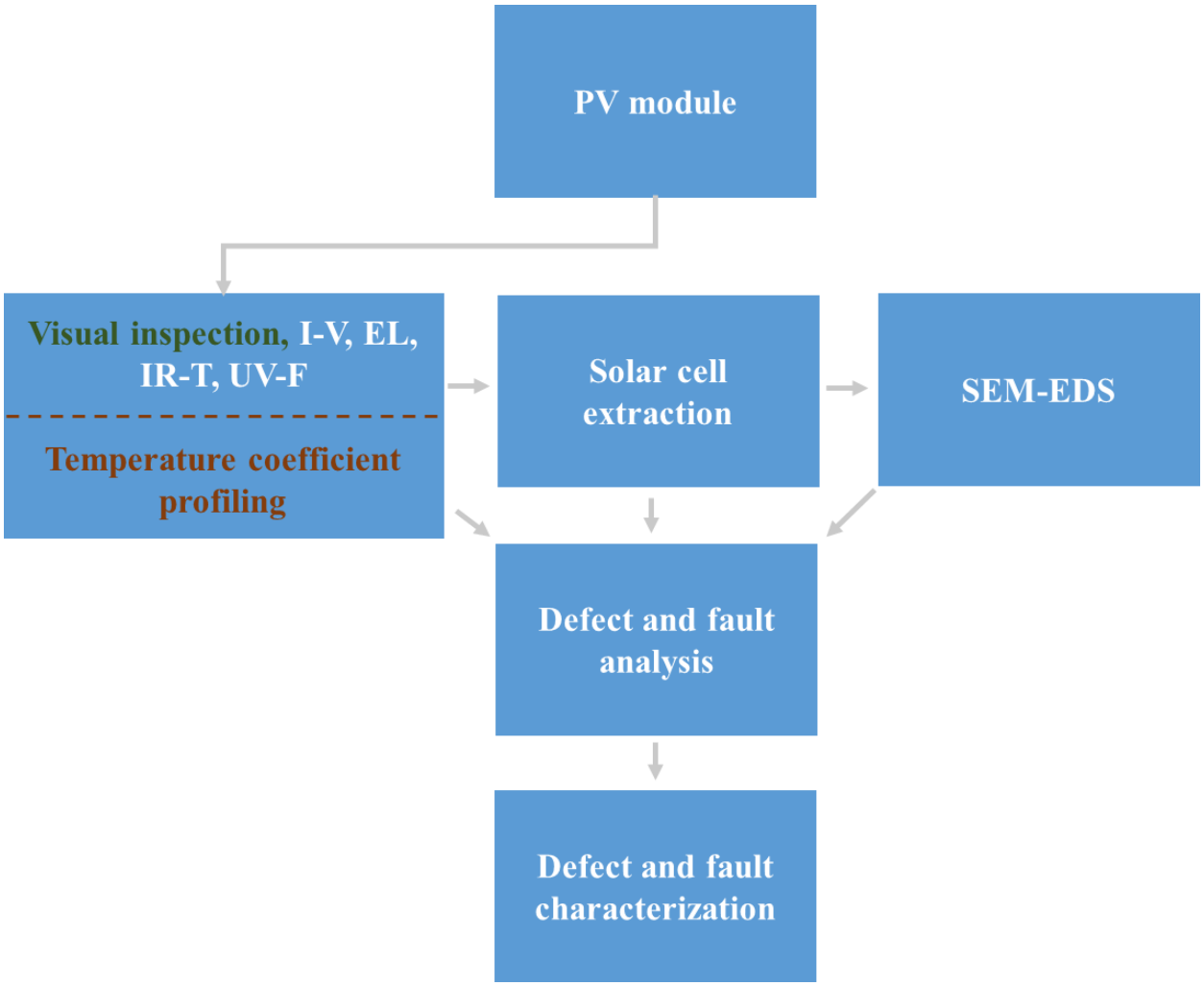

Figure 5. 2. Overview of the experimental methods, from Paper A.

5.2.1 Visual inspection

Visual inspection was conducted on all the PV panels (front and back) under clear sky outdoor and well-controlled light exposure conditions in the dark. This complementary procedure made it possible for a comprehensive logging of a variety of defects and fault modes which would not be possible with the conventional visual inspection alone. The visual inspection was done according to the IEC 61215: 2016 standard.

5.2.2 I-V measurements

The current-voltage (I-V) characteristics of all the PV panels were acquired using a handheld I-V 500w I-V Curve Tracer from HT® Instruments by following the IEC 60904- 1 standard. The electrical parameters acquired via the I-V characterization are the P_{max}, I_{sc}, I_{mpp}, V_{oc}, V_{mpp} and *FF*. The data included information on the G_I, T_m, and the normalized values of all the electrical parameters at STC for each PV module. STC specifies cell temperature (T_c) of 25 °C, solar irradiance of 1000 W/m^2 and air mass 1.5 (AM1.5) spectrum for commercial PV panels. The I-V characterization of all the modules proceeded under clear sky outdoor G_I conditions (960 - 1060 W/m^2), and the STC values were computed automatically by the I-V tracer used to minimize errors associated with data recording. The uncertainty of the Tracer for all the parameters (except the fill factor) measured is to the nearest hundredth. Moreover, the computed uncertainty is less than ±3 % for all parameters measured. Hence, the values of all the parameters were approximated to the nearest tenth to accommodate the uncertainty in measurements. For the same reason, the *FF* and η_m are written in two significant figures. The η_m in the year 2020 was computed by multiplying the ratio of the normalized measured P_{max} values in the year 2020 to the datasheet P_{max} with the datasheet η_m value (13 %).

5.2.3 Ultraviolet fluorescence (UV-F) imaging

For the detection of MID defects and fault modes such as microcracks and optical degradation, the UV-F imaging technique is one of the effective tools. PV components, especially polymeric materials (e.g., EVA) degrade into fluorescent species when exposed to environmental stressors and chemical species. In the presence of ingressed moisture or other gaseous species such as oxygen, the fluorescent degraded species undergo metamorphoses to nonfluorescent species via photobleaching or photoquenching. When these encapsulation materials are exposed to UV light, degraded areas show darker traces. The acquired UV-F information becomes useful for defect cataloguing and mitigation. Each of the PV module was characterized using a portable TROTEC® LED UV TorchLight 15F (λ ≈

365 nm) which is equipped with a Wolf eyes FD45 spectrum filter. The investigation was conducted in the dark by following the IEA recommended procedure [119, 161].

5.2.4 Electroluminescence (EL) imaging

Luminescence signal from electroluminescence or photoluminescence imaging has proven to be a potent tool for detecting and diagnosing material degradation and shunts. When a PV panel is forward biased, the solar cell signals in the near infrared (NIR) region, peaking around 1150 nm for silicon cells [119]. This can provide information on the degradation state of the PV panel. The EL characteristics of the PV panels were acquired in a dark room using a BrightSpot EL Test Kit, see Figure 5.3.

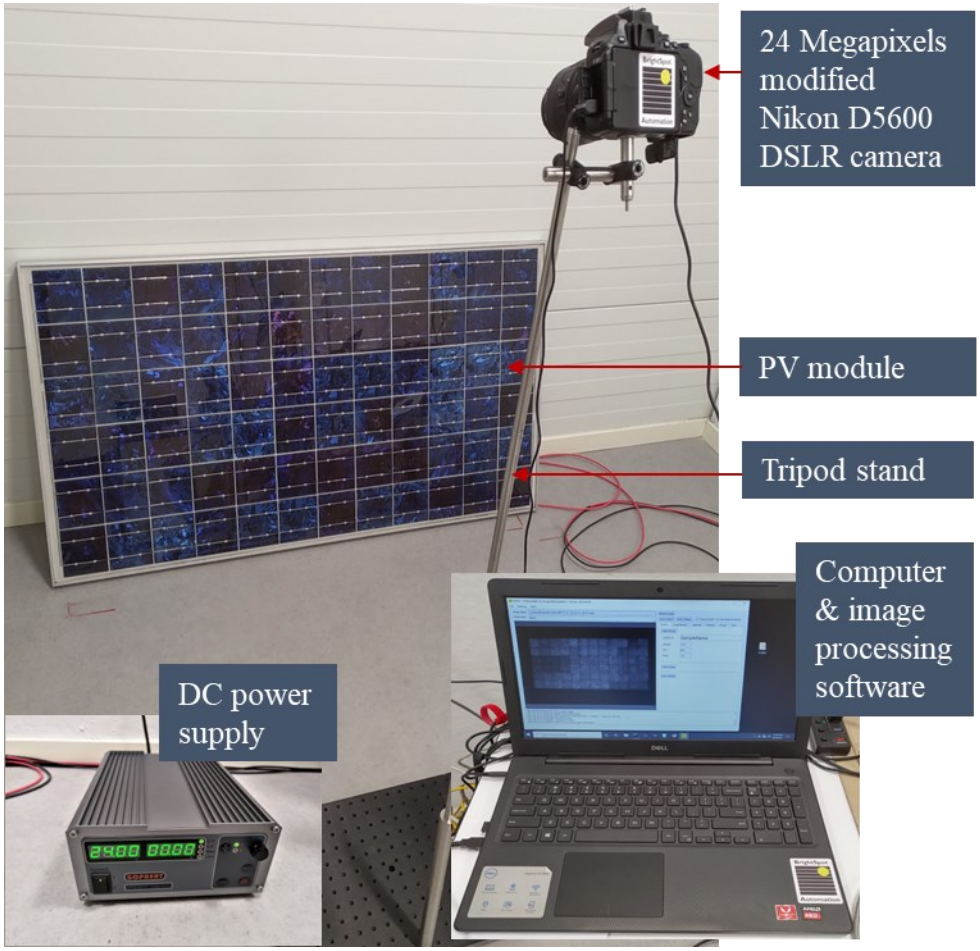

Figure 5. 3. Experimental setup of the EL imaging system, Paper F.

The kit comprises of a 24 megapixels modified DSLR (digital single-lens reflex) Nikon D5600 camera, a DC power supply set, connecting cables, a flexible tripod stand, and computer with data acquisition and processing software. The investigation was conducted by following the

IEC 60904- 13 standard and the IEA procedure [119, 161]. The EL characterization of the PV modules was conducted using forward bias current of $0.1I_{sc}$ and I_{sc}.

According to Potthoff et al. [162], the local luminescence, $\phi_{(x)}$ at a point x of a PV module is related to the local voltage, $V_{(x)}$ and the thermal voltage, V_T as

$$\phi_{(x)} = C_{(x)} exp\left(\frac{V_{(x)}}{V_T}\right), \quad for\ V_{(x)} \gg V_T \tag{5.1}$$

Where $C_{(x)}$ is the optical and material properties of the PV module and the camera system known as the local calibration factor. However, the operating voltage, V depends on $V_{(x)}$, the internal resistance (R_{int}) between the metal grids and the solar cells and external resistance (R_{ext}) between the interconnectors and the solar cells of the module and can be written as

$$V = V_{(x)} + R_{int} I_{(x)} + R_{ext} I \tag{5.2}$$

Where $I_{(x)}$ is the local current flowing through point x of the solar cell and I is the total current supplied to the PV module. If the solar cell or module is in good condition, then $C_{(x)} \approx C$ for all solar cells in series (N_c) and R_{int} is negligible and $R_{ext} \approx R$, the total resistance within the PV module. Then V becomes [162]

$$V = V_T \cdot ln\left(\frac{\phi_{(x)}}{C}\right) + I \cdot \frac{R}{N_c} \tag{5.3}$$

For a defect free solar cell and module, R is negligible at current density below $0.1I_{sc}$ [162]. That is, higher voltages come with higher resistances from electrical contacts rather than bulk material resistances, when the module is in a good condition. But, at lower injection levels, the material properties dominate the luminescence signal of the PV module. However, for bad solar cells at current density below $0.1I_{sc}$, $R \approx R_{int}$, and Equation (5.3) can be written in the form of Equation (4.1) for each solar cell as

$$\phi_{(x)} = C_{(x)} exp\left(\frac{V_{(x)} + IR_{int}}{V_T}\right), \quad for\ V_{(x)} \gg V_T \tag{5.4}$$

In this case, the local luminescence is also influenced by the internal resistances as a result of cell cracks and other cell defects. In other words, when the cell is completely separated due to defects such as cracks, $I \approx I_{(x)} \approx 0$, and $V \approx V_{(x)}$ is maximum for the affected solar cell. However, moisture ingress can influence the luminescence signal due to photoquenching by degradation products, which is possible at open cracks or at the edges of the PV module.

5.2.5 Infrared thermography (IR-T)

Defective PV panels under forward bias conditions can experience increased T_m due to the resistive losses. IR thermal information of the solar cells, and hence, the PV panel is useful for defects diagnostics. The IR thermal images of the PV panels were acquired using the Fluke

Ti400 Infrared Camera (measuring in NIR band: λ = 650 - 1400 nm) by following the IEC 62446- 3 standard. The investigation took place both indoors and outdoors. For the indoor investigation, the PV panels were investigated under I_{sc} forward bias conditions. IR images were taken 0.5, 2, and 5 minutes after current flow was initiated. For the outdoor investigation, the IR thermal images were acquired after soaking the PV panels in the sun for at least 15 minutes. The experimental set up for the outdoor investigation under clear sky outdoor conditions at the Rooftop facility is shown in Figure 5.4.

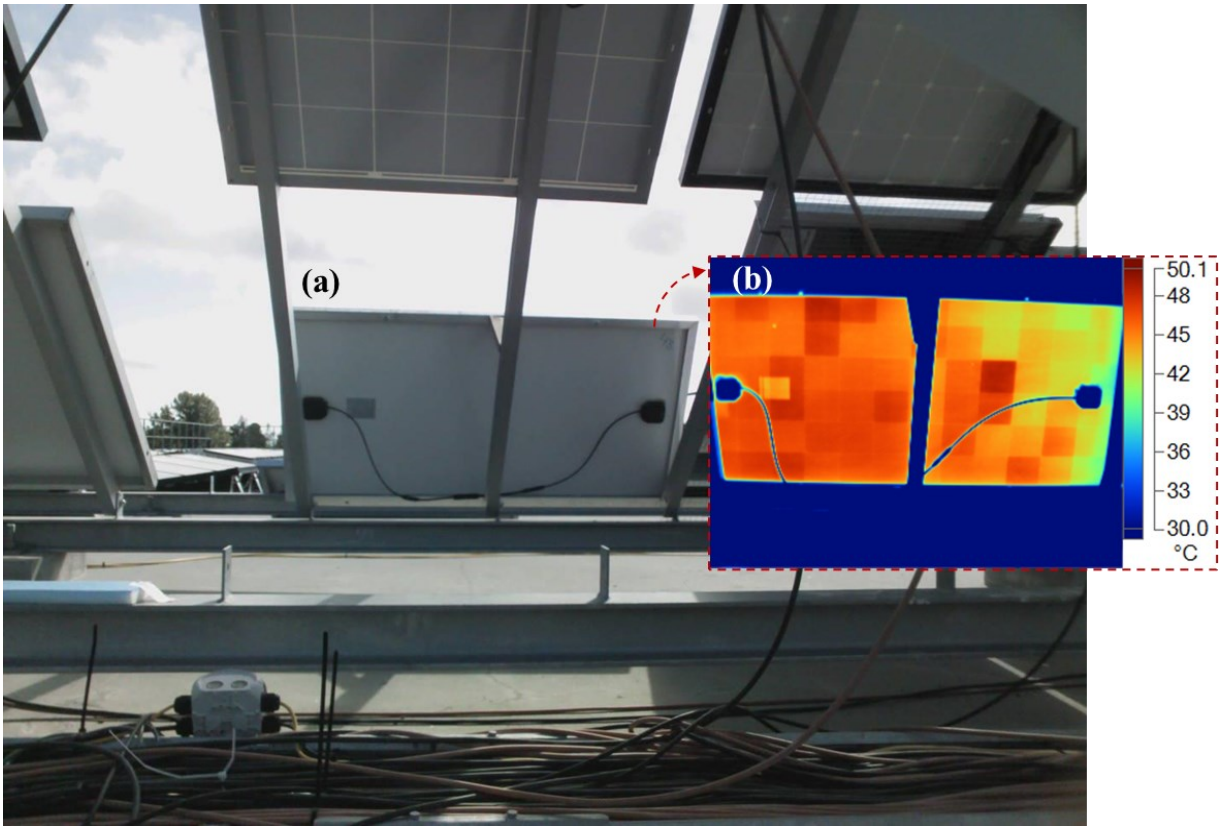

Figure 5. 4. The outdoor experimental set-up for IR-T investigation. (a) Visual image and (b) IR-T image (insert) from the rear side of the PV module. The open metal rack (supporting the solar panel) and the cables show their respective blue traces in the IR-T image.

For all measurements, the emissivity of the front glass and the TPT backsheet was set at 0.95 and 0.85, respectively [6, 161]. Details of the IR thermal imaging is presented in Paper A, D, E, and F.

5.2.6 Solar cell reclamation and microstructural analysis

The regions of interest (areas affected by microcracks and moisture ingress) were identified as per Sections 5.2.1 – 5.2.5 and were extracted using a Water Jet NC 3060D Beveljet cutting machine. The machine which is controlled by a CNC software employs a fine water jet with

abrasive under ultra-high pressure (about 4,000 bar) for sample cutting. The technique is very suitable when low cutting temperature is desired. The as cut samples (consisting of the front glass, encapsulant, copper ribbons, solar cell, and backsheet) were separated using toluene. The samples were immersed in the toluene at room temperature for 14 days. After 7 days, the front glass and front encapsulant were separated. However, the backsheet can be removed after 14 days. The extracted solar cells from the field-aged PV module were analyzed using a field emission scanning electron microscope (SEM) (JEOL 7200F) equipped with an energy dispersive X-ray spectrometer (Octane Elect EDS system from EDAX®-AMETEK®) to identify the MID products. The experimental procedure for the microstructural analysis is illustrated in Figure 5.5.

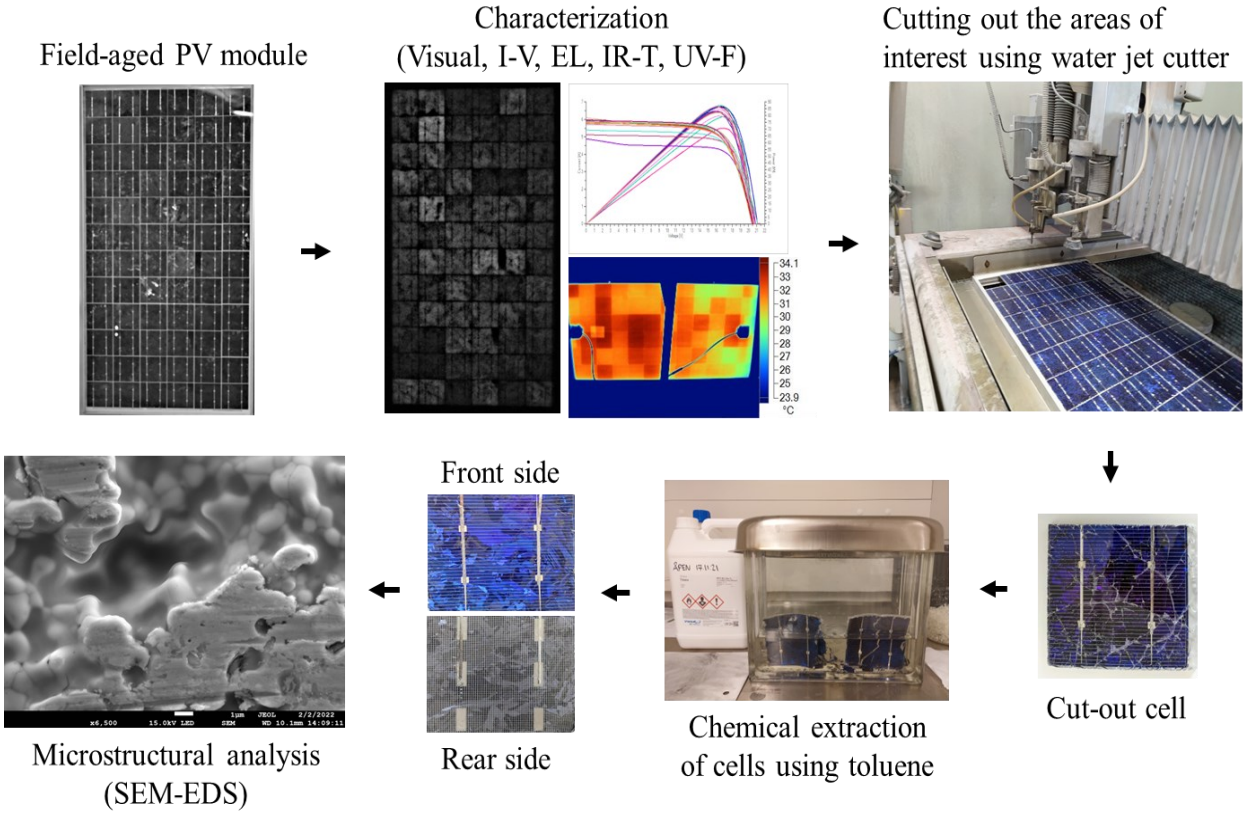

Figure 5. 5. Experimental procedure for the microstructural investigation of the MID products in the field-aged PV module, refer to Paper D.

Prior to the microstructural analysis, the extracted solar cell samples were rinsed carefully and thoroughly in isopropyl alcohol, then in deionized water, and finally, air dried. The components of the solar cell extracted from the field-aged PV module that were investigated are shown in Figure 5.6. This can also be found in Paper D. The copper busbars, located near the perimeter of the PV module, connect the Cu interconnect ribbons. They collect and deliver cumulative current to the junction boxes. The silver (Ag) fingers are perpendicular to the Cu ribbons whilst the Ag busbars lie beneath the Cu ribbons.

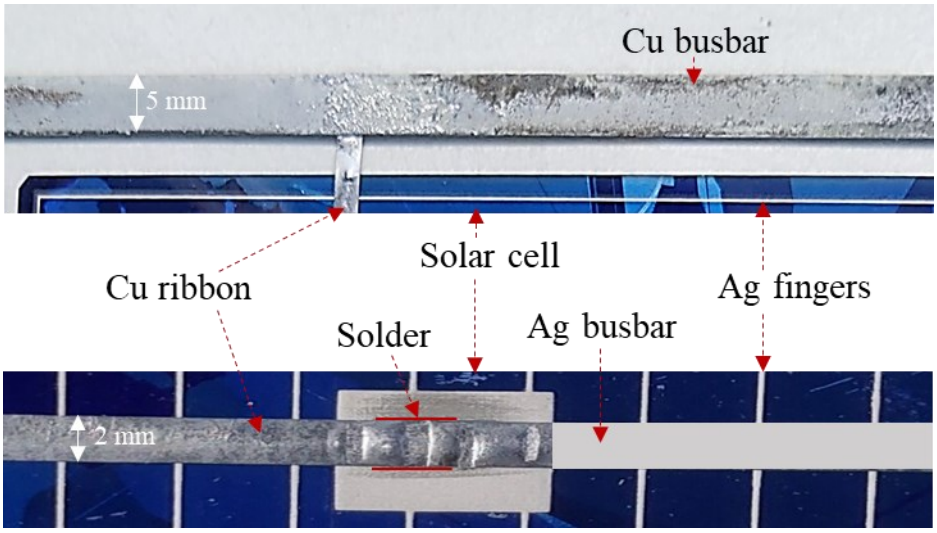

Figure 5. 6. Components of the field-aged PV module extracted for the SEM-EDS analysis, refer to Paper D [9].

The Cu ribbons are connected to the solar cells and the Ag grids with the solder, which is made up of lead (Pb) and tin (Sn). The effect of moisture ingress is more severe near the perimeter of PV modules [7, 11]. Hence, the solar cells and other components for the SEM-EDS investigation were extracted from the edge of the field-aged PV module.

5.2.7 Temperature coefficient profiling

On a clear sky sunny day in the summer, the PV modules were taken out to the outdoor measuring rack in turns from a storeroom where the modules were kept. The PV module and the reference device were shaded using cardboard. Measurement was initiated immediately after the shade was removed. The measurements on the modules were done on the same day between 12.30 and 14.30 hours and at wind speed less than 2 ms^{-1}. According to IEC 60891-4 standard, the temperature range of the data values should be at least 30 °C. However, this seems challenging in practical field measurements, especially for the investigation site. A graph of electrical parameters (P_{max}, V_{oc}, I_{sc}, FF, η_m, V_{mpp}, I_{mpp}) versus T_m was plotted and a least-squares-fit curve through each data set constructed to get the relative temperature coefficient (β_x). The resulting regression equation fits the general linear equation: $y = mx + c$, where y and x denote the electrical parameter, x, and T_m, respectively. m and c represent β_x and intercept, respectively. The β_x in %/°C was determined according to Equation (4.7). Details on determination of β_x was presented in Paper F, G, and H [145, 160].

Chapter 6

Main contribution

This chapter presents the summary of all the papers, Paper A – H, as regards their main contribution towards this thesis, refer to Figure 1.5.

Paper A

Defects and fault modes of field-aged photovoltaic modules in the Nordics

PV module durability and reliability influences its efficiency and return on investment. Hence, collection of ample and credible PV module reliability data in each climatic zone becomes increasingly essential. However, defects and reliability studies in the Nordics are rare or non-existent. In this work, defects, and fault modes of field-aged multicrystalline silicon PV modules installed outdoors in Grimstad from 2000 to 2011 are investigated. The investigations were done using visual inspection, current-voltage characterisation, temperature coefficient profiling, ultraviolet fluorescence, electroluminescence, infrared thermal imaging, and SEM-EDS analysis. Most PV modules show signs of microcracks, moisture ingress, corrosion, potential induced degradation, optical degradation, and irregular temperature sensitivities. Oxidised silver, tin, and lead were observed in the SEM-EDS results, which confirmed the remnants of moisture ingress. On average, the modules show power output of ~78 % and their efficiency dropped from 13 % to 10 %. The average temperature coefficient of efficiency of the modules was found to be about -0.5 %/°C, corresponding to an average degradation rate of 1.09 %/year over the 20 years period. However, the annual degradation rates when the modules were in the field and indoors were ~ 0.98 % and ~1.33 %, respectively. It is believed that limited evaporation of activated volatile carboxylic products under indoor conditions led to the formation and accumulation of carboxylic acids, hence higher rate of degradation. MID mechanisms underline the overall degradation in the PV modules' power output, especially over the later years. Apparently, this work provides an insight into the dominant types of defects and failure mechanisms associated with field-deployed solar PV plants in the Nordics, the first of its kind.

Published as:

O.K. Segbefia, N. Akhtar, T.O. Sætre, Defects and fault modes of field-aged photovoltaic modules in the Nordics, Energy Reports, 9 (2023) 3104-3119. https://doi.org/10.1016/j.egyr.2023.01.126.

Paper B

Moisture ingress in photovoltaic modules: A review

Moisture ingress in photovoltaic (PV) modules is the core of most degradation mechanisms that lead to PV module power degradation. Moisture in EVA encapsulant can lead to metal grids corrosion, delamination, and discolouration of encapsulants, potential induced degradation, optical and adhesion losses. This work is a review of literature on the causes, effects, detection, and mitigation techniques of moisture ingress in c-Si PV modules. Literature highlights on determining the diffusivity, solubility, and permeability of polymeric components of PV modules via water vapour transmission rate tests, gravimetric, and immersion methods, have been presented. Electroluminescence, photoluminescence, and ultraviolet fluorescence spectroscopy, as well as dark lock-in thermography are some techniques used to detect moisture ingress in modules. Encapsulants with excellent moisture barrier and adhesion characteristics, desiccant-stacked polyisobutylene sealants, imbedded moisture sensors, and PV designs with/without breathable backsheets are ways of preventing/detecting moisture ingression in PV modules. Areas of focus for future research activities have also been discussed. This work is the first of its kind to be published on the effect of moisture ingress on c-Si solar PV modules (though c-Si PV modules are the most established commercial technology in the PV community) and serves as a succinct working document for researchers in this field.

Published as:

O.K. Segbefia, A.G. Imenes, T.O. Saetre, Moisture ingress in photovoltaic modules: A review, Sol. Energy, 224 (2021) 889-906. https://doi.org/10.1016/j.solener.2021.06.055

Paper C

The effect of moisture ingress on titania antireflection coatings in field-aged photovoltaic modules

Titanium dioxide (TiO_2) or titania antireflection coating (ARC) enhances PV module efficiency. Yet, degraded TiO_2 can affect the performance reliability of PV modules. In this work, the effect of moisture ingress on the degradation of TiO_2 ARC in a field-aged multicrystalline silicon PV module is investigated. Scanning electron microscopy (SEM) and energy dispersive X-ray spectroscopy (EDS) analyses show degradation of the TiO_2 ARC. Disintegration of the TiO_2 nanoparticles (NPs) were also observed. The assumed Ti-O stoichiometry of the degraded TiO_2 ARC in the field-aged PV module was found to be higher than 1:2. It turned out that moisture ingress strongly influences the surface morphology and defects, crystallinity, and stoichiometry of TiO_2 ARC in the PV module during field operation. Silver and aluminium NPs migrate to and aggregate on the surfaces of the TiO_2 NPs which might likely lead to the formation of titania-metal complexes such as titania-alumina and silver-titania complexes. These degradation mechanisms affect the opto-electrical properties of the TiO_2 ARC, and hence, the P_{max} of the PV module. This work demonstrates the effect of moisture ingress TiO_2 ARC in field deployed solar PV modules. It also gives an insight into the likely moisture induced degradation of other PV module ARCs and its effect on PV module degradation. This work is the first published report on the effect of moisture on the degradation of ARCs used in field-deployed solar PV modules.

Published as:

O.K. Segbefia, N. Akhtar, T.O. Sætre, The effect of moisture ingress on titania antireflection coatings in field-aged photovoltaic modules, in: 2022 IEEE 49th Photovoltaics Specialists Conference (PVSC), IEEE, 2022, pp. 1237-1244. 10.1109/PVSC48317.2022.9938896.

Paper D

Moisture induced degradation in field-aged multicrystalline silicon photovoltaics modules

Moisture ingress is one of the key fault mechanisms responsible for PV devices degradation. Understanding moisture induced degradation (MID) mechanisms in field-aged PV modules is more reflective of the reality in the field. In the absence of moisture ingress (due to humidity exposure), formation of MID species is impossible, irrespective of the environmental stressors the PV module is exposed to. Moisture and MID products can attack the solar cell and the PV module components which can lead to solar cell degradation, corrosion, optical degradation, PID, solder bond and glass degradation. These degradation mechanisms have dire implications for the performance reliability of PV modules. In the Nordics, the issue of MID is of a greater concern due to extended periods of heavy rains, snow, and wind loads. With emerging PV applications such as floating PV and agro-PV at sight, understanding the mechanisms and effects of MID in PV modules under multiple real field environmental stressors is more important than ever. Up to now, research on the microstructural signatures of MID in PV modules appears to focus more on the EVA encapsulation, silver grids, solder, and copper ribbons. Most investigations ignore the effect of moisture ingress on the solar cell microstructure itself and its degradation mechanisms. In addition, only a few of these reports were carried out on field-aged PV modules. More importantly, none of the reports was done in the Nordics, where the effect of moisture ingress is a huge challenge.

In this work, the MID of reclaimed solar cells from 20-year-old field-aged mc-Si PV modules is investigated. The defective areas in the PV modules were identified using visual inspection, I-V characterization, EL, UV-F, and IR-T techniques. SEM-EDS analysis was used to elucidate the role of moisture on the observed degradation mechanisms. Degradation of the EVA encapsulation produces acetic acid, carbon dioxide, phosphorus, sulfur, fluorine, and chlorine. It was observed that under the influence of moisture ingress, leached metal ions e.g., Na, Ag, Pb, Sn, Cu, Zn, and Al migrate to the surface of the solar cells. When this happens, the formation of oxides, hydroxides, sulfides, phosphates, acetates, and carbonates of silver, lead, tin, copper, zinc, and aluminum is feasible. Also, other competing reactions can lead to the formation of stannates of copper, silver, sodium, and zinc. Another observation was that, in the presence of moisture and acetic acid, Pb is preferentially corroded (to form lead acetate complexes) instead of the expected sacrificial Sn in the solder. These MID species accounted for metal grids corrosion, cell cracks, optical degradation, and PID in the field-aged PV module. Consequently, these defects and fault modes lead to parasitic resistance losses which are witnessed by the 1.2 %/year degradation in the power output of the field-

aged PV module. This work is the first of its kind on the microstructural studies of MID mechanisms in field-deployed solar PV modules in the Nordics.

Published as:

O.K. Segbefia, N. Akhtar, T.O. Sætre, Moisture induced degradation in field-aged multicrystalline silicon photovoltaic modules. Sol. Energy Mater. Sol. Cells, 258 (2023) 112407. https://doi.org/10.1016/j.solmat.2023.112407.

Paper E

Temperature profiles of field-aged photovoltaic modules affected by optical degradation

Moisture ingress into solar PV module front encapsulation can affect the optical integrity of the PV module. Optical degradation can take the form of delamination, discolouration of encapsulant, metal grids oxidation, and trapped moisture or chemical species. This can influence the current transport properties in the PV module bulk and the module operating temperature. Mismatch losses due to optical degradation can influence the overall T_m. High T_m affects efficiency and induces other degradation processes. It is therefore important to understand the characteristics of defects and fault mechanisms that lead to optical degradation of PV devices in time for the prevention of further deterioration and evolution of other failure mechanisms.

In this work, the relationship between optical degradation and temperature sensitivity of 20 years old c-Si field-aged PV modules have been investigated using visual inspection, I-V characterization, temperature coefficients profiling, current resistivity profiling, IR-T, UV-F, and EL imaging. PV modules affected by optical degradation show weak fluorescence and luminescence signal intensities. The average difference in cell temperature (ΔT) between the warmest and coldest cell for the PV modules investigated was found to be around 10 ± 2 °C and the average power degradation rate was approximately 0.8 % per year. The underlying factor for the observed degradation is attributed to the degradation in the β_{Voc} and β_{Vmpp}. The average $\beta_{\eta m}$ of the modules was found to be around -0.5 %/°C. Finally, this work also demonstrates that extracting module temperature and temperature coefficients directly from IR thermal data of PV modules is possible, the first of its kind. The proposed model in

this work can be extended and integrated into IR thermography programs in IR thermal imagers for monitoring PV plants' reliability based on temperature sensitivity.

To be Published as:

O.K. Segbefia, Temperature profiles of field-aged photovoltaic modules affected by optical degradation. Manuscript submitted for publication. Preprint: http://dx.doi.org/10.2139/ssrn.4046700

Paper F

Investigation of the temperature sensitivity of 20-years old field-aged photovoltaic panels affected by potential induced degradation

One effect of moisture ingress on solar panels is potential induced degradation (PID). Solar panels affected by PID experience large leakage currents between the solar cells and the module's frame, which leads to substantial power degradation. In addition to power degradation, PID also induces mismatch losses due to non-uniform degradation. Degraded cells that are affected by PID cause current reverse biasing, which leads to local overheating or joule heating. This triggers hot spots, which influence the T_m, hence, the temperature sensitivity. The effect of T_m on power degradation due to mismatch losses is greatest at P_{max}: V_{mpp} and J_{mpp}. Hence, monitoring the effect of PID on β_{Vmpp} and β_{Jmpp} as diagnostic tool, will be interesting. Yet, there is no report on the influence of PID on β_{Vmpp} and β_{Jmpp} of PV modules.

In this work, the temperature coefficients of 3 old PV panels affected by PID were investigated. In the EL images, solar cells nearer to the edge of the modules appear darker due to ohmic shunting. IR thermal images acquired under clear sky outdoor conditions show that the majority of the warmer cells (hot spots) were located closer to the edge of the modules. The ΔT due to PID effect ranges from 7 °C to 15 °C for the 3 field-aged modules. The $\beta_{\eta m}$ was found to be −0.5%/°C. Also, it was observed that the β_{Voc} = −0.4%/°C, β_{Vmpp} = −0.5%/°C, and β_{FF} = −0.2%/°C, were the underlying factors for the degradation in the P_{max} of the old solar panels affected by PID. This accounted for an average 1.2 %/year overall degradation in the efficiency of these modules. Most notably, it was discovered that the PV modules affected by PID show negative β_{Jmpp} due to large leakage currents. The observed negative β_{Jmpp} is characteristic of PV panels affected by PID. This work is the first of its kind to document monitoring β_{Jmpp} as a diagnostic tool for detecting PV modules affected by PID.

Published as:

O.K. Segbefia, T.O. Sætre, Investigation of the Temperature Sensitivity of 20-Years Old Field-Aged Photovoltaic Panels Affected by Potential Induced Degradation, Energies, 15 (2022) 3865. https://doi.org/10.3390/en15113865.

Paper G

Temperature profiles of field-aged multicrystalline silicon photovoltaic modules affected by microcracks

In the field and under multiple environmental or climatic stressors, solar PV modules are susceptible to a variety of defects and failure modes including moisture ingress and solar cell cracks, which are co-defects. Usually, cracks in PV cells result in localized heating or joule heating due to ohmic resistance at cracked areas of the solar cell or module during field operation. This can serve as a conduit for other defects and failure modes, e.g., moisture ingress, PID, optical degradation, and hence, PV module degradation. Solar cells and PV modules with microcracks can be identified conveniently using I-V characteristics, EL and UV-F techniques. Another way of detecting modules affected by microcracks is using the temperature sensitivity of the affected PV module. There are a number of articles which have documented the general behaviour of solar cells and modules due to their characteristic temperature sensitivities which lead to corresponding power losses. However, none has reported on the unique temperature sensitivity of PV modules affected by solar cell cracks.

In this work, the temperature sensitivities of field-aged multicrystalline silicon PV modules affected by microcracks are investigated. ΔT due to microcracks ranges from 13 °C to 27 °C. In addition, the T_0 of the PV modules affected by microcracks were less than 270 °C. It was observed that estimation of the β_r of PV modules affected by microcracks from the Evans-Floschuetz efficiency ratio method may not always be valid. For solar PV modules affected by critical microcracks, $\beta_{\eta m}$ appears to be equivalent to β_{Vmpp}. Also, they are likely to show negative β_{Jmpp} just like PV modules affected by PID. Finally, it was observed that the temperature coefficients of the PV modules affected by microcracks depend on the crack characteristics, co-defects, and operating conditions. This work is the first of its kind to investigate the relationship between solar cell microcracks and their temperature coefficients.

Published as:

O.K. Segbefia, A.G. Imenes, I. Burud, T.O. Sætre, Temperature profiles of field-aged multicrystalline silicon photovoltaic modules affected by microcracks, in: 2021 IEEE 48th Photovoltaic Specialists Conference (PVSC), IEEE, 2021, pp. 0001-0006. 10.1109/PVSC43889.2021.9518939.

Paper H

Temperature coefficients of photovoltaic modules under partial shading conditions

Partial shading of photovoltaic (PV) modules leads to mismatch losses which cause local hot spots. Hot spots can lead to various failure mechanisms, hence, power degradation in PV plants. However, defects and failure modes also induce mismatch losses, and hence, local hot spots in solar PV modules. In high latitude countries, such as in the Nordics, both reliability issues are not uncommon. So, how can mismatch losses from partial shading and defects be differentiated from each other in a unique way? This has the potential of improving the accuracy in degradation estimates.

This work investigates the temperature sensitivity of field-aged c-Si PV modules under uniform partial shading conditions. Thermal images suggest that hot spots are localized to busbars in the shaded area. ΔT due to partial shading is between 32 °C to 45 °C. Under partial shading conditions, I_{sc}, I_{mpp}, and FF underline power degradation; about 50 % drop in I_{mpp} is possible. However, an increase in V_{mpp} (even above the nominal value) is also possible. The results estimate that, the average $\beta_{\eta m}$ and β_{Vmpp} of the field-aged PV modules is -0.5 %/°C. However, under partial shading conditions, the average $\beta_{\eta m}$ and β_{Vmpp} are -0.8 %/°C and -0.2 %/°C, respectively. In addition, under partial shading conditions, β_{Jsc} and β_{Jmpp} can be negative and large, whiles β_{FF} can also be positive. However, the severity of the temperature sensitivity under partial shading conditions also depends on defects, shade position/area, and operating conditions. This work is the first of its kind to investigate the temperature sensitivity of solar PV modules affected by different defects and fault modes.

Published as:

O.K. Segbefia, B.R. Paudyal, I. Burud, T.O. Sætre, Temperature Coefficients of Photovoltaic Modules under Partial Shading Conditions, 38th EU PVSEC, (2021) 1180 - 1186. 10.4229/EUPVSEC20212021-5CV.2.3.

Taken together, this thesis has unraveled the dominant defects and failure mechanisms in field-aged solar PV modules installed in Grimstad, Southern Norway. Moisture ingress underlines most of the defects and failure mechanisms. Microcracks: a co-defect of moisture ingress is also a major defect associated with the field-aged solar PV modules. Moisture ingress leads to the degradation of the EVA encapsulant into carboxylic acids (e.g., acetic acid) and MID species in the PV module. Moisture and MID species lead to corrosion, optical degradation, solar cell degradation, PID, solder bond and ARC degradation, and hence, increased parasitic resistance effects. This leads to the degradation and eventual failure of the PV modules. In addition, the temperature sensitivity of field-aged c-Si PV modules affected by microcracks, PID, and optical degradation has been reported. Finally, the temperature sensitivity of field-aged c-Si PV modules under partial shading conditions has been explored. There has not been any report dedicated to the detection of defects and fault modes in field-aged solar PV modules using a combination of visual, spectroscopic, microscopic, and temperature sensitivity profiling in the Nordics.

Field-aged solar PV modules are exposed to multiple environmental stressors such as high humidity, temperature, UV radiation, soiling, wind, and snow loads during their operation in the field. The role of these environmental stressors in the formation of MID species and subsequent degradation process in the PV module is significant and is the reality in the field. However, in the absence of moisture ingress (under humidity exposure), formation of MID species is impossible, irrespective of the environmental stressors the PV module is exposed to. Hence, understanding the mechanisms and effects of MID in field-aged solar PV modules is the best way to understand what happens in the field. Hence, the findings in this thesis can be a guide for performance reliability mitigation scheme for solar PV modules, especially in the Nordic countries.

Chapter 7

Conclusion and further work

7.1 Conclusion and outlook

This thesis has expanded the knowledge on the characteristics of moisture induced degradation (MID) mechanisms in mc-Si solar PV modules deployed in the Nordics (Grimstad, Norway). Defect and fault analysis on the field-aged PV modules indicates that the major failure mechanism is moisture ingress. Microstructural studies conducted on the samples of the field-aged solar PV modules suggest that the modules have been affected by moisture ingress. Characterization of the MID defects (e.g., microcracks, PID, and optical degradation) based on temperature sensitivity was also conducted. The investigations were done using visual inspection, current-voltage characterisation, temperature coefficient profiling, ultraviolet fluorescence, electroluminescence, infrared thermal imaging, and SEM-EDS analysis. A novel visual inspection in the dark with optimum light exposure was undertaken to identify moisture induced metal grids oxidation. In the pioneer review paper on moisture ingress in c-Si solar PV modules (Paper B), preventing moisture ingress in PV module is challenging, if not impossible. Hence, detection methods are preferred.

Degradation of the EVA encapsulation produces acetic acid, carbon dioxide, phosphorus, sulfur, fluorine, and chlorine. It was observed that under the influence of moisture ingress, leached metal ions e.g., Na, Ag, Pb, Sn, Cu, Zn, and Al migrate to the surface of the solar cells. This led to the formation of oxides, hydroxides, sulfides, phosphates, acetates, and carbonates of silver, lead, tin, copper, zinc, and aluminum. Also, other competing reactions can lead to the formation of stannates of copper, silver, sodium, and zinc. Another observation was that, in the presence of moisture and acetic acid, Pb is preferentially corroded (to form lead acetate complexes) instead of the expected sacrificial Sn in the solder. In the EL and UV-F images, these degradation species appeared as dark spots, and as hot spots in IR-T images. These MID species accounted for metal grids corrosion, cell microcracks, optical degradation, and potential induced degradation in the field-aged PV module. Consequently, these defects and fault modes lead to parasitic resistance losses which is witnessed by degradation in the power output of the field-aged solar PV modules.

On average, the modules show power output of ~78 % and their efficiency dropped from 13 % to 10 %. The average temperature coefficient of efficiency of the modules was found to be about -0.5 %/°C, corresponding to an average degradation rate of 1.09 %/year over the 20

years period. The difference in cell temperature (ΔT) depends on the type of defects present in the solar PV module and can range from 7 °C to 45 °C or even greater.

In addition, it was observed that the β_{Voc}, β_{Vmpp}, and β_{FF}, were the underlying factors for the degradation in the P_{max} of the field-aged PV modules. Most notably, it was discovered that the PV modules affected by PID show negative β_{Jmpp} due to large leakage currents. However, temperature sensitivity due to microcracks depends on the crack severity, co-defects, and operating conditions. Based on these findings, a new relationship between β_{Pmax}, β_{Vmpp}, and β_{Jmpp} was developed in Paper F. Also, a method for extracting temperature coefficients directly from measured IR thermal data of PV modules has been developed in Paper E. This thesis has expounded on the dominant defects and fault modes in field-aged mc-Si PV modules in Southern Norway. Using temperature sensitivity profiling for MID defect diagnosis has also been done.

In a Nordic environment with high CMI, the role of MID mechanisms in the degradation of field-aged solar PV modules is very significant. Investigation of MID mechanisms in field-aged solar PV modules is more reflective of the reality in the field. Though solar PV module materials and technology have evolved over the years, MID mechanisms in solar PV modules remain the same. Hence, insights from this thesis can guide decision making at the present and in the future as regards understanding the performance reliability of solar PV plants.

7.2 Challenges and further work

In this thesis, moisture ingress is observed as a challenging failure mechanism in mc-Si field deployed solar PV modules. The MID mechanisms were explored and the effects on the module degradation identified. MID defects such as microcracks, PID, and optical degradation were characterized using temperature sensitivity profiling. However, the full scope of MID (e.g., prediction and mitigation techniques) has not been explored. Even though there are some reports from other researchers on prediction and mitigation techniques, none was undertaken in the Nordics. Future work can explore these areas in the cold regions.

To have a comprehensive understanding of the effects of moisture ingress in solar PV modules, the effect on the other components such as the front glass and the polymeric encapsulation is important. The encapsulation materials of the field-aged solar PV modules are still state-of-the-art, maybe with minor variations in chemical formulations. However, in order to correlate the findings from the field-aged modules to the present trend, new modules are to be investigated as well. However, field degradation studies take longer (more than 3 years, typical of PhD research work) to be realized. In Paper E, a temperature dependent resistivity methods for mapping measured IR-T data to temperature coefficients is presented. However, further study on defect free and large number of PV modules is needed to verify the hypothesis.

Field-aged solar PV modules suffer from multiple defect mechanisms. In this work, efforts have been made to select modules with dominant defects for the investigation of specific defect mechanisms. Yet, the influence of other inherent defects on the overall investigation cannot be ruled out. At least three modules were used to investigate each defect category. However, future work can explore the possibility of using "forced" defects to reduce multi-defect effects. In Paper F, further studies on larger number of field-aged solar PV modules (with different technologies) affected by PID are needed to verify this hypothesis.

This thesis focuses on only crystalline silicon solar PV modules using experimental methods. Future work can also explore other PV module technologies and numerical modelling based on the experimental results from this work to improve and extend the findings in this work to other emerging technologies in solar PV modules as indicated in Table 3.2. In addition, the use of specialized solar module simulators can help to investigate the module temperature sensitivity over a broad range of module operating temperatures. In the present work, module operating temperatures during the outdoor investigations were below 60 °C due to limitations imposed by the ambient local conditions. Finally, detailed investigation into the role of moisture ingress and MID species on the development of solar cell microcracks will be important for solar PV performance reliability studies, especially in the Nordics.

Bibliography

[1] IEA, Net Zero by 2050, IEA, Paris https://www.iea.org/reports/net-zero-by-2050, (2021).
[2] IRENA, Renewable Capacity Statistics 2022, in, 2022.
[3] IEA, Renewables 2021, IEA, Paris https://www.iea.org/reports/renewables-2021 in, 2021.
[4] IEA, World Energy Outlook 2021, IEA, Paris https://www.iea.org/reports/world-energy-outlook-2021, in, 2021.
[5] IEA, Sustainable Recovery Tracker, IEA, Paris https://www.iea.org/reports/sustainable-recovery-tracker, in, 2022.
[6] M. Köntges, S. Kurtz, C. Packard, U. Jahn, K.A. Berger, K. Kato, T. Friesen, H. Liu, M. Van Iseghem, J. Wohlgemuth, Review of failures of photovoltaic modules, (2014).
[7] S. Kumar, R. Meena, R. Gupta, Finger and interconnect degradations in crystalline silicon photovoltaic modules: A review, Sol. Energy Mater. Sol. Cells, 230 (2021) 111296.
[8] O.K. Segbefia, N. Akhtar, T.O. Sætre, Defects and fault modes of field-aged photovoltaic modules in the Nordics, Energy Reports, 9 (2023) 3104-3119.
[9] O.K. Segbefia, N. Akhtar, T.O. Sætre, Moisture induced degradation in field-aged multicrystalline silicon photovoltaic modules, Sol. Energy Mater. Sol. Cells, 258 (2023) 112407.
[10] I. Duerr, J. Bierbaum, J. Metzger, J. Richter, D. Philipp, Silver grid finger corrosion on snail track affected PV modules–investigation on degradation products and mechanisms, Energy Procedia, 98 (2016) 74-85.
[11] S. Kumar, R. Meena, R. Gupta, Imaging and micro-structural characterization of moisture induced degradation in crystalline silicon photovoltaic modules, Sol. Energy, 194 (2019) 903-912.
[12] N. Kyranaki, A. Smith, K. Yendall, D.A. Hutt, D.C. Whalley, R. Gottschalg, T.R. Betts, Damp-heat induced degradation in photovoltaic modules manufactured with passivated emitter and rear contact solar cells, Prog. Photovoltaics Res. Appl., (2022).
[13] M.C.C. de Oliveira, A.S.A.D. Cardoso, M.M. Viana, V.d.F.C. Lins, The causes and effects of degradation of encapsulant ethylene vinyl acetate copolymer (EVA) in crystalline silicon photovoltaic modules: A review, Renew. Sust. Energ. Rev., 81 (2018) 2299-2317.
[14] M. Köntges, G. Oreski, U. Jahn, M. Herz, P. Hacke, K.-A. Weiß, Assessment of photovoltaic module failures in the field: International Energy Agency Photovoltaic Power Systems Programme: IEA PVPS Task 13, Subtask 3: report IEA-PVPS T13-09: 2017, International Energy Agency, 2017.
[15] I. Kaaya, J. Ascencio-Vásquez, K.-A. Weiss, M. Topič, Assessment of uncertainties and variations in PV modules degradation rates and lifetime predictions using physical models, Sol. Energy, 218 (2021) 354-367.
[16] D.C. Jordan, S.R. Kurtz, Photovoltaic degradation rates—an analytical review, Prog. Photovolt.: Res. Appl., 21 (2013) 12-29.
[17] H. Wang, X.L. Cheng, H. Yang, W.S. He, Z.L. Chen, L.H. Xu, D.Y. Song, Potential-induced degradation: Recombination behavior, temperature coefficients and mismatch losses in crystalline silicon photovoltaic power plant, Sol. Energy, 188 (2019) 258-264.
[18] N. Iqbal, D.J. Colvin, E.J. Schneller, T.S. Sakthivel, R. Ristau, B.D. Huey, X. Ben, J.-N. Jaubert, A.J. Curran, M. Wang, Characterization of front contact degradation in monocrystalline and multicrystalline silicon photovoltaic modules following damp heat exposure, Sol. Energy Mater. Sol. Cells, 235 (2022) 111468.
[19] M. Aghaei, A. Fairbrother, A. Gok, S. Ahmad, S. Kazim, K. Lobato, G. Oreski, A. Reinders, J. Schmitz, M. Theelen, Review of degradation and failure phenomena in photovoltaic modules, Renew. Sust. Energ. Rev., 159 (2022) 112160.

[20] V. Ramasamy, J. Zuboy, E. O'Shaughnessy, D. Feldman, J. Desai, M. Woodhouse, P. Basore, R. Margolis, US Solar Photovoltaic System and Energy Storage Cost Benchmarks, With Minimum Sustainable Price Analysis: Q1 2022, in, National Renewable Energy Lab.(NREL), Golden, CO (United States), 2022.
[21] IEA-PVPS, International Energy Agency. Snapshot of Global PV Markets - Task 1: Strategic PV Analysis and Outreach, in, 2022.
[22] B.L. Smith, M. Woodhouse, K.A. Horowitz, T.J. Silverman, J. Zuboy, R.M. Margolis, Photovoltaic (PV) Module Technologies: 2020 Benchmark Costs and Technology Evolution Framework Results, in, National Renewable Energy Lab.(NREL), Golden, CO (United States), 2021.
[23] B. Ehrler, E. Alarcon-Llado, S.W. Tabernig, T. Veeken, E.C. Garnett, A. Polman, Photovoltaics reaching for the Shockley–Queisser limit, in, ACS Publications, 2020.
[24] P. Campbell, M.A. Green, The limiting efficiency of silicon solar cells under concentrated sunlight, IEEE Transactions on Electron Devices, 33 (1986) 234-239.
[25] J.A. Tsanakas, L. Ha, C. Buerhop, Faults and infrared thermographic diagnosis in operating c-Si photovoltaic modules: A review of research and future challenges, Renew Sust Energ Rev, 62 (2016) 695-709.
[26] J.A. Tsanakas, L. Ha, C. Buerhop, Faults and infrared thermographic diagnosis in operating c-Si photovoltaic modules: A review of research and future challenges, Renew. Sust. Energ. Rev., 62 (2016) 695-709.
[27] O. Dupré, R. Vaillon, M.A. Green, Physics of the temperature coefficients of solar cells, Sol. Energy Mater. Sol. Cells, 140 (2015) 92-100.
[28] D.L. King, J.A. Kratochvil, W.E. Boyson, Temperature coefficients for PV modules and arrays: measurement methods, difficulties, and results, in: Conference record of the twenty sixth IEEE Photovoltaic Specialists Conference-1997, IEEE, 1997, pp. 1183-1186.
[29] E. Skoplaki, J.A. Palyvos, On the temperature dependence of photovoltaic module electrical performance: A review of efficiency/power correlations, Sol. Energy, 83 (2009) 614-624.
[30] D. Evans, Simplified method for predicting photovoltaic array output, Solar energy, 27 (1981) 555-560.
[31] M. Formolli, G. Lobaccaro, J. Kanters, Solar Energy in the Nordic Built Environment: Challenges, Opportunities and Barriers, Energies, 14 (2021) 8410.
[32] J. Wohlgemuth, T. Silverman, D.C. Miller, P. McNutt, M. Kempe, M. Deceglie, Evaluation of PV module field performance, in: 2015 IEEE 42nd Photovoltaic Specialist Conference (PVSC), IEEE, 2015, pp. 1-7.
[33] O.K. Segbefia, A.G. Imenes, T.O. Sætre, Moisture ingress in photovoltaic modules: A review, Sol. Energy, 224 (2021) 889-906.
[34] N. Bosco, S. Moffitt, L.T. Schelhas, Mechanisms of adhesion degradation at the photovoltiac module's cell metallization-encapsulant interface, Prog. Photovolt.: Res. Appl., 27 (2019) 340-345.
[35] M. Halwachs, L. Neumaier, N. Vollert, L. Maul, S. Dimitriadis, Y. Voronko, G. Eder, A. Omazic, W. Mühleisen, C. Hirschl, Statistical evaluation of PV system performance and failure data among different climate zones, Renew. Energy, 139 (2019) 1040-1060.
[36] D.C. Jordan, J.H. Wohlgemuth, S.R. Kurtz, Technology and climate trends in PV module degradation, in, National Renewable Energy Lab.(NREL), Golden, CO (United States), 2012.
[37] P. Malik, R. Chandel, S.S. Chandel, A power prediction model and its validation for a roof top photovoltaic power plant considering module degradation, Sol. Energy, 224 (2021) 184-194.
[38] M. Dhimish, A. Ahmad, A.M. Tyrrell, Inequalities in photovoltaics modules reliability: From packaging to PV installation site, Renewable Energy, 192 (2022) 805-814.

[39] M. Lamers, E. Özkalay, R. Gali, G. Janssen, A. Weeber, I. Romijn, B. Van Aken, Temperature effects of bifacial modules: Hotter or cooler?, Solar Energy Materials and Solar Cells, 185 (2018) 192-197.
[40] C. Baldus-Jeursen, A. Côté, T. Deer, Y. Poissant, Analysis of photovoltaic module performance and life cycle degradation for a 23 year-old array in Quebec, Canada, Renewable Energy, 174 (2021) 547-556.
[41] C.J. Willmott, J.J. Feddema, A more rational climatic moisture index, The Professional Geographer, 44 (1992) 84-88.
[42] L. Papargyri, M. Theristis, B. Kubicek, T. Krametz, C. Mayr, P. Papanastasiou, G.E. Georghiou, Modelling and experimental investigations of microcracks in crystalline silicon photovoltaics: A review, Renewable Energy, 145 (2020) 2387-2408.
[43] C. Osterwald, T. McMahon, History of accelerated and qualification testing of terrestrial photovoltaic modules: A literature review, Progress in Photovoltaics: Research and Applications, 17 (2009) 11-33.
[44] T. McMahon, Accelerated testing and failure of thin-film PV modules, Progress in Photovoltaics: Research and Applications, 12 (2004) 235-248.
[45] J. Tracy, D.R. D'hooge, N. Bosco, C. Delgado, R. Dauskardt, Evaluating and predicting molecular mechanisms of adhesive degradation during field and accelerated aging of photovoltaic modules, Prog. Photovolt.: Res. Appl., 26 (2018) 981-993.
[46] G.C. Eder, Y. Voronko, S. Dimitriadis, K. Knöbl, G. Újvári, K.A. Berger, M. Halwachs, L. Neumaier, C. Hirschl, Climate specific accelerated ageing tests and evaluation of ageing induced electrical, physical, and chemical changes, Progress in Photovoltaics: Research and Applications, (2018).
[47] D.C. Jordan, T.J. Silverman, B. Sekulic, S.R. Kurtz, PV degradation curves: non-linearities and failure modes, Prog. Photovolt.: Res. Appl., 25 (2017) 583-591.
[48] F. ISE, Certification Procedure: Tests for PV Module Certification, in.
[49] P. Hacke, M. Owen-Bellini, M. Kempe, D.C. Miller, T. Tanahashi, K. Sakurai, W.J. Gambogi, J.T. Trout, T.C. Felder, K.R. Choudhury, Combined and Sequential Accelerated Stress Testing for Derisking Photovoltaic Modules, in: Advanced Micro-and Nanomaterials for Photovoltaics, Elsevier, 2019, pp. 279-313.
[50] P.L. Hacke, M.D. Kempe, J. Wohlgemuth, J. Li, Y.-C. Shen, Potential-Induced Degradation-Delamination Mode in Crystalline Silicon Modules, in, National Renewable Energy Lab.(NREL), Golden, CO (United States), 2018.
[51] J.H. Wohlgemuth, S. Kurtz, Reliability testing beyond qualification as a key component in photovoltaic's progress toward grid parity, in: 2011 International Reliability Physics Symposium, IEEE, 2011, pp. 5E. 3.1-5E. 3.6.
[52] G. Oreski, B. Ottersböck, A. Omazic, Degradation Processes and Mechanisms of Encapsulants, in: Durability and Reliability of Polymers and Other Materials in Photovoltaic Modules, Elsevier, 2019, pp. 135-152.
[53] T.H. Kim, N.C. Park, D.H. Kim, The effect of moisture on the degradation mechanism of multi-crystalline silicon photovoltaic module, Microelectron. Reliab., 53 (2013) 1823-1827.
[54] M.D. Kempe, G.J. Jorgensen, K.M. Terwilliger, T.J. McMahon, C.E. Kennedy, T.T. Borek, Acetic acid production and glass transition concerns with ethylene-vinyl acetate used in photovoltaic devices, Solar Energy Materials and Solar Cells, 91 (2007) 315-329.
[55] A. Omazic, G. Oreski, M. Halwachs, G. Eder, C. Hirschl, L. Neumaier, G. Pinter, M. Erceg, Relation between degradation of polymeric components in crystalline silicon PV module and climatic conditions: A literature review, Solar Energy Materials and Solar Cells, 192 (2019) 123-133.
[56] C. Peike, I. Hädrich, K.-A. Weiß, I. Dürr, Overview of PV module encapsulation materials, Photovoltaics International, 19 (2013) 85-92.

[57] C. Yang, X. Xing, Z. Li, S. Zhang, A Comprehensive Review on Water Diffusion in Polymers Focusing on the Polymer–Metal Interface Combination, Polymers, 12 (2020) 138.
[58] H.E. Yang, Overview: Durability and Reliability of Common PV Module and Polymers/Materials, in: Durability and Reliability of Polymers and Other Materials in Photovoltaic Modules, Elsevier, 2019, pp. 23-45.
[59] J. Pern, Module encapsulation materials, processing and testing (presentation), in, National Renewable Energy Lab.(NREL), Golden, CO (United States), 2008.
[60] M.D. Kempe, Modeling of rates of moisture ingress into photovoltaic modules, Solar Energy Materials and Solar Cells, 90 (2006) 2720-2738.
[61] C. Han, Analysis of moisture-induced degradation of thin-film photovoltaic module, Solar Energy Materials and Solar Cells, 210 (2020) 110488.
[62] G. Van der Wel, O. Adan, Moisture in organic coatings—a review, Progress in organic coatings, 37 (1999) 1-14.
[63] S. Mitterhofer, C. Barretta, L.F. Castillon, G. Oreski, M. Topic, M. Jankovec, A Dual-Transport Model of Moisture Diffusion in PV Encapsulants for Finite-Element Simulations, IEEE J. Photovolt., 10 (2020) 94-102.
[64] M.D. Kempe, A.A. Dameron, M.O. Reese, Evaluation of moisture ingress from the perimeter of photovoltaic modules, Prog. Photovolt.: Res. Appl., 22 (2014) 1159-1171.
[65] M.D. Kempe, D.L. Nobles, L. Postak, J.A. Calderon, Moisture ingress prediction in polyisobutylene-based edge seal with molecular sieve desiccant, Prog. Photovolt.: Res. Appl., 26 (2018) 93-101.
[66] G. Mon, L. Wen, R. Ross, D. Adent, Effects of temperature and moisture on module leakage currents, in: 18th IEEE PVSC, 1985, pp. 1179-1185.
[67] G. Oreski, A. Mihaljevic, Y. Voronko, G.C. Eder, Acetic acid permeation through photovoltaic backsheets: Influence of the composition on the permeation rate, Polym. Test, 60 (2017) 374-380.
[68] T.J. Peshek, J.S. Fada, I.T. Martin, Degradation Processes in Photovoltaic Cells, in: Durability and Reliability of Polymers and Other Materials in Photovoltaic Modules, Elsevier, 2019, pp. 97-118.
[69] F.D. Novoa, D.C. Miller, R.H. Dauskardt, Adhesion and debonding kinetics of photovoltaic encapsulation in moist environments, Prog. Photovolt.: Res. Appl., 24 (2016) 183-194.
[70] G. Oreski, Co-extruded backsheets for PV modules: Past approaches and recent developments, in, NIST/UL Workshop on Photovoltaic Materials Durability Gaithersburg, USA, 2019.
[71] M. Thuis, N.M. Al Hasan, R.L. Arnold, B. King, A. Maes, D.C. Miller, J.M. Newkirk, L.T. Schelhas, A. Sinha, K. Terwilliger, A Comparison of Emerging Nonfluoropolymer-Based Coextruded PV Backsheets to Industry-Benchmark Technologies, IEEE Journal of Photovoltaics, 12 (2021) 88-96.
[72] M.D. Kempe, Y. Lyu, J.H. Kim, T. Felder, X. Gu, Fragmentation of photovoltaic backsheets after accelerated weathering exposure, Solar Energy Materials and Solar Cells, 226 (2021) 111044.
[73] A. Dadaniya, N.V. Datla, Water diffusion simulation in photovoltaic module based on the characterization of encapsulant material using in-situ gravimetric technique, Solar Energy Materials and Solar Cells, 201 (2019) 110063.
[74] M.O. Reese, A.A. Dameron, M.D. Kempe, Quantitative calcium resistivity based method for accurate and scalable water vapor transmission rate measurement, Review of Scientific Instruments, 82 (2011) 085101.
[75] M. Miyashita, S. Kawai, A. Masuda, Measuring method of moisture ingress into Photovoltaic modules, Jpn. J. Appl. Phys., 51 (2012) 10NF12.
[76] K. Nagayama, J. Kapur, B.A. Morris, Influence of two-phase behavior of ethylene ionomers on diffusion of water, J. Appl. Polym. Sci., (2020).

[77] T.S. Liang, M. Pravettoni, C. Deline, J.S. Stein, R. Kopecek, J.P. Singh, W. Luo, Y. Wang, A.G. Aberle, Y.S. Khoo, A review of crystalline silicon bifacial photovoltaic performance characterisation and simulation, Energy Environ. Sci., 12 (2019) 116-148.
[78] D. Wisniewski, R. Lv, S.V. Nair, J.N. Jaubert, T. Xu, H.E. Ruda, Measurement and modelling of water ingress into double-glass photovoltaic modules, Prog. Photovolt.: Res. Appl., 27 (2019) 144-151.
[79] P. Hülsmann, K.-A. Weiss, Simulation of water ingress into PV-modules: IEC-testing versus outdoor exposure, Solar Energy, 115 (2015) 347-353.
[80] P. Hülsmann, K.A. Weiß, M. Köhl, Temperature-dependent water vapour and oxygen permeation through different polymeric materials used in photovoltaic-modules, Prog. Photovolt.: Res. Appl., 22 (2014) 415-421.
[81] K. Hasan, S.B. Yousuf, M.S.H.K. Tushar, B.K. Das, P. Das, M.S. Islam, Effects of different environmental and operational factors on the PV performance: A comprehensive review, Energy Science & Engineering, 10 (2022) 656-675.
[82] M. Koehl, M. Heck, S. Wiesmeier, Modelling of conditions for accelerated lifetime testing of Humidity impact on PV-modules based on monitoring of climatic data, Solar Energy Materials and Solar Cells, 99 (2012) 282-291.
[83] F.D. Novoa, D.C. Miller, R.H. Dauskardt, Environmental mechanisms of debonding in photovoltaic backsheets, Solar Energy Materials and Solar Cells, 120 (2014) 87-93.
[84] T. Grossetête, A. Rivaton, J. Gardette, C.E. Hoyle, M. Ziemer, D. Fagerburg, H. Clauberg, Photochemical degradation of poly (ethylene terephthalate)-modified copolymer, Polymer, 41 (2000) 3541-3554.
[85] O.K. Segbefia, N. Akhtar, T.O. Sætre, The effect of moisture ingress on titania antireflection coatings in field-aged photovoltaic modules, in: 2022 IEEE 49th Photovoltaics Specialists Conference (PVSC), IEEE, 2022, pp. 1237-1244.
[86] J. Li, Y.-C. Shen, P. Hacke, M. Kempe, Electrochemical mechanisms of leakage-current-enhanced delamination and corrosion in Si photovoltaic modules, Sol. Energy Mater. Sol. Cells, 188 (2018) 273-279.
[87] M. Jankovec, E. Annigoni, C. Ballif, M. Topič, In-situ Determination of Moisture Diffusion Properties of PV Module Encapsulants Using Digital Humidity Sensors, in: 2018 IEEE 7th World Conference on Photovoltaic Energy Conversion, WCPEC 2018 - A Joint Conference of 45th IEEE PVSC, 28th PVSEC and 34th EU PVSEC, 2018, pp. 415-417.
[88] J. Slapšak, S. Mitterhofer, M. Topic, M. Jankovec, Wireless System for in Situ Monitoring of Moisture Ingress in PV Modules, IEEE J. Photovolt., 9 (2019) 1316-1323.
[89] N. Kim, C. Han, Experimental characterization and simulation of water vapor diffusion through various encapsulants used in PV modules, Solar energy materials and solar cells, 116 (2013) 68-75.
[90] R. Sander, Compilation of Henry's law constants (version 4.0) for water as solvent, Atmos. Chem. Phys, 15 (2015) 4399-4981.
[91] J. Crank, The mathematics of diffusion. Clarendon Press, Oxford, UK, The mathematics of diffusion. 2nd ed. Clarendon Press, Oxford, UK., (1975) -.
[92] G.M. Kimball, S. Yang, A. Saproo, Global acceleration factors for damp heat tests of PV modules, in: 2016 IEEE 43rd Photovoltaic Specialists Conference (PVSC), IEEE, 2016, pp. 0101-0105.
[93] M. Dhimish, Micro cracks distribution and power degradation of polycrystalline solar cells wafer: Observations constructed from the analysis of 4000 samples, Renewable Energy, 145 (2020) 466-477.
[94] M. Abdelhamid, R. Singh, M. Omar, Review of microcrack detection techniques for silicon solar cells, IEEE Journal of Photovoltaics, 4 (2013) 514-524.
[95] S. Kajari-Schršder, I. Kunze, M. Kšntges, Criticality of cracks in PV modules, Energy Procedia, 27 (2012) 658-663.

[96] Á. Fernández-Solas, L. Micheli, F. Almonacid, E.F. Fernández, Optical degradation impact on the spectral performance of photovoltaic technology, Renew. Sust. Energ. Rev., 141 (2021) 110782.
[97] C. Buerhop, D. Schlegel, M. Niess, C. Vodermayer, R. Weißmann, C. Brabec, Reliability of IR-imaging of PV-plants under operating conditions, Sol. Energy Mater. Sol. Cells, 107 (2012) 154-164.
[98] H.A. Al Mahdi, P.G. Leahy, A.P. Morrison, Predicting Early EVA Degradation in Photovoltaic Modules From Short Circuit Current Measurements, IEEE J. Photovoltaics, (2021).
[99] F. Pern, A. Czanderna, K. Emery, R. Dhere, Weathering degradation of EVA encapsulant and the effect of its yellowing on solar cell efficiency, in: The Conference Record of the Twenty-Second IEEE Photovoltaic Specialists Conference-1991, IEEE, 1991, pp. 557-561.
[100] International Standards Organization, ISO 17223:2014: Plastics — Determination of yellowness index and change in yellowness index, in, 2014.
[101] F. Rosillo, M. Alonso-García, Evaluation of color changes in PV modules using reflectance measurements, Sol. Energy, 177 (2019) 531-537.
[102] C. Dechthummarong, B. Wiengmoon, D. Chenvidhya, C. Jivacate, K. Kirtikara, Physical deterioration of encapsulation and electrical insulation properties of PV modules after long-term operation in Thailand, Sol. Energy Mater. Sol. Cells, 94 (2010) 1437-1440.
[103] M.C.C. de Oliveira, D.A. Cassini, A.S.A.C. Diniz, L.G. Soares, M.M. Viana, L.L. Kazmerski, V.d.F.C. Lins, Comparison and analysis of performance and degradation differences of crystalline-Si photovoltaic modules after 15-years of field operation, Sol. Energy, 191 (2019) 235-250.
[104] Q. Bao, X. Liu, S. Braun, J. Yang, Y. Li, J. Tang, C. Duan, M. Fahlman, The effect of oxygen uptake on charge injection barriers in conjugated polymer films, ACS applied materials & interfaces, 10 (2018) 6491-6497.
[105] D. Feldman, Polymer weathering: photo-oxidation, J. Polym. Environ., 10 (2002) 163-173.
[106] F. Pern, Luminescence and absorption characterization of ethylene-vinyl acetate encapsulant for PV modules before and after weathering degradation, Polym. Degrad. Stab., 41 (1993) 125-139.
[107] W. Stark, M. Jaunich, Investigation of Ethylene/Vinyl Acetate Copolymer (EVA) by thermal analysis DSC and DMA, Polym. Test., 30 (2011) 236-242.
[108] C. Peike, S. Hoffmann, P. Hulsmann, B. Thaidigsmann, K.A. Weiss, M. Koehl, P. Bentz, Origin of damp-heat induced cell degradation, Sol. Energy Mater. Sol. Cells, 116 (2013) 49-54.
[109] A.M. Jeffries, T. Nietzold, L.T. Schelhas, M.I. Bertoni, Corrosion of novel reactive silver ink and commercial silver-based metallizations in diluted acetic acid, Sol. Energy Mater. Sol. Cells, 223 (2021) 110900.
[110] H.P. Xiong, C.H. Gan, X.B. Yang, Z.G. Hu, H.Y. Niu, J.F. Li, J.F. Si, P.F. Xing, X.T. Luo, Corrosion behavior of crystalline silicon solar cells, Microelectronics Reliability, 70 (2017) 49-58.
[111] W. Oh, S. Kim, S. Bae, N. Park, Y. Kang, H.-S. Lee, D. Kim, The degradation of multi-crystalline silicon solar cells after damp heat tests, Microelectronics Reliability, 54 (2014) 2176-2179.
[112] P. Klemchuk, M. Ezrin, G. Lavigne, W. Holley, J. Galica, S. Agro, Investigation of the degradation and stabilization of EVA-based encapsulant in field-aged solar energy modules, Polymer degradation and stability, 55 (1997) 347-365.
[113] A. Kraft, L. Labusch, T. Ensslen, I. Dürr, J. Bartsch, M. Glatthaar, S. Glunz, H. Reinecke, Investigation of acetic acid corrosion impact on printed solar cell contacts, IEEE J. Photovolt., 5 (2015) 736-743.
[114] G.J. Jorgensen, K.M. Terwilliger, J.A. DelCueto, S.H. Glick, M.D. Kempe, J.W. Pankow, F.J. Pern, T.J. McMahon, Moisture transport, adhesion, and corrosion protection of PV module packaging materials, Solar Energy Materials and Solar Cells, 90 (2006) 2739-2775.
[115] J.H. Wohlgemuth, M.D. Kempe, Equating damp heat testing with field failures of PV modules, in: 2013 IEEE 39th Photovoltaic Specialists Conference (PVSC), IEEE, 2013, pp. 0126-0131.

[116] W. Luo, Y.S. Khoo, P. Hacke, V. Naumann, D. Lausch, S.P. Harvey, J.P. Singh, J. Chai, Y. Wang, A.G. Aberle, S. Ramakrishna, Potential-induced degradation in photovoltaic modules: a critical review, Energy & Environmental Science, 10 (2017) 43-68.
[117] J. Carolus, J.A. Tsanakas, A. van der Heide, E. Voroshazi, W. De Ceuninck, M. Daenen, Physics of potential-induced degradation in bifacial p-PERC solar cells, Solar Energy Materials and Solar Cells, 200 (2019) 109950.
[118] V. Naumann, T. Geppert, S. Grosser, D. Wichmann, H.J. Krokoszinski, M. Werner, C. Hagendorf, Potential-induced degradation at interdigitated back contact solar cells, Proceedings of the 4th International Conference on Crystalline Silicon Photovoltaics (Siliconpv 2014), 55 (2014) 498-503.
[119] U. Jahn, M. Herz, M. Köntges, D. Parlevliet, M. Paggi, I. Tsanakas, Review on infrared and electroluminescence imaging for PV field applications: International Energy Agency Photovoltaic Power Systems Programme: IEA PVPS Task 13, Subtask 3.3: report IEA-PVPS T13-12: 2018, International Energy Agency, 2018.
[120] V. Naumann, D. Lausch, A. Hahnel, J. Bauer, O. Breitenstein, A. Graff, M. Werner, S. Swatek, S. Grosser, J. Bagdahn, C. Hagendorf, Explanation of potential-induced degradation of the shunting type by Na decoration of stacking faults in Si solar cells, Solar Energy Materials and Solar Cells, 120 (2014) 383-389.
[121] Q. Bai, H. Yang, C. Nan, H. Wang, Z. Chen, Analysis of the electrochemical reactions and ions migration for crystalline silicon solar module under high system voltage, Sol. Energy, 225 (2021) 718-725.
[122] E.L. Meyer, E.E. Van Dyk, Assessing the reliability and degradation of photovoltaic module performance parameters, IEEE Transactions on reliability, 53 (2004) 83-92.
[123] P. Peng, A. Hu, W. Zheng, P. Su, D. He, K.D. Oakes, A. Fu, R. Han, S.L. Lee, J. Tang, Microscopy study of snail trail phenomenon on photovoltaic modules, RSC advances, 2 (2012) 11359-11365.
[124] S. Spataru, P. Hacke, D. Sera, C. Packard, T. Kerekes, R. Teodorescu, Temperature-dependency analysis and correction methods of in situ power-loss estimation for crystalline silicon modules undergoing potential-induced degradation stress testing, Progress in Photovoltaics, 23 (2015) 1536-1549.
[125] M.A. Islam, M. Hasanuzzaman, N. Abd Rahim, Investigation of the potential induced degradation of on-site aged polycrystalline PV modules operating in Malaysia, Measurement, 119 (2018) 283-294.
[126] X. Cheng, Y. Dong, T. Yang, T. Zhou, H. Wang, H. Yu, Investigation on Temperature Coefficients of Crystalline Silicon Solar Modules before and after Potential-induced Degradation, in: 2019 IEEE 46th Photovoltaic Specialists Conference (PVSC), IEEE, 2019, pp. 1942-1945.
[127] K.S. Oh, S. Bae, K.J. Lee, D. Kim, S.I. Chan, Mitigation of potential-induced degradation (PID) based on anti-reflection coating (ARC) structures of PERC solar cells, Microelectronics Reliability, 100 (2019) 113462.
[128] A. Virtuani, E. Annigoni, C. Ballif, One-type-fits-all-systems: Strategies for preventing potential-induced degradation in crystalline silicon solar photovoltaic modules, Progress in Photovoltaics, 27 (2019) 13-21.
[129] S. Pingel, O. Frank, M. Winkler, S. Daryan, T. Geipel, H. Hoehne, J. Berghold, Potential induced degradation of solar cells and panels, in: 2010 35th IEEE Photovoltaic Specialists Conference, IEEE, 2010, pp. 002817-002822.
[130] C.M. Oertel, S.P. Baker, A. Niklasson, L.-G. Johansson, J.-E. Svensson, Acetic Acid Vapor Corrosion of Lead–Tin Alloys Containing 3.4 and 15% Tin, J. Electrochem. Soc., 156 (2009) C414.

[131] S. Msallamova, M. Kouril, K.C. Strachotova, J. Stoulil, K. Popova, P. Dvorakova, M. Lhotka, Protection of lead in an environment containing acetic acid vapour by using adsorbents and their characterization, Heritage Science, 7 (2019) 1-9.
[132] A. Niklasson, L.-G. Johansson, J.-E. Svensson, Influence of acetic acid vapor on the atmospheric corrosion of lead, J. Electrochem. Soc., 152 (2005) B519.
[133] S. Marais, Q. Nguyen, D. Langevin, M. Metayer, Transport of water and gases through EVA copolymer films, EVA70/PVC, and EVA70/PVC/gluten blends, in: Macromolecular Symposia, Wiley Online Library, 2001, pp. 329-348.
[134] R. Czyzewicz, A. Smith, Next generation ionomer encapsulants for thin film technology, Proceedings of SPIE - The International Society for Optical Engineering, 8112 (2011).
[135] M.D. Kempe, Control of moisture ingress into photovoltaic modules, in: Conference Record of the Thirty-first IEEE Photovoltaic Specialists Conference, 2005., IEEE, 2005, pp. 503-506.
[136] K. Hardikar, T. Krajewski, K. Toivola, Assessing field performance of flexible PV modules for moisture induced degradation from accelerated testing, in: Conference Record of the IEEE Photovoltaic Specialists Conference, 2016, pp. 871-875.
[137] H. Morita, M. Miyashita, A. Masuda, Module composition for reliability test of organic photovoltaics, Jpn. J. Appl. Phys., 54 (2015).
[138] B.R. Paudyal, A.G. Imenes, Investigation of temperature coefficients of PV modules through field measured data, Sol. Energy, 224 (2021) 425-439.
[139] M. Seapan, Y. Hishikawa, M. Yoshita, K. Okajima, Detection of shading effect by using the current and voltage at maximum power point of crystalline silicon PV modules, Solar Energy, 211 (2020) 1365-1372.
[140] H. Mohammed, M. Kumar, R. Gupta, Bypass diode effect on temperature distribution in crystalline silicon photovoltaic module under partial shading, Solar Energy, 208 (2020) 182-194.
[141] O. Kunz, R.J. Evans, M.K. Juhl, T. Trupke, Understanding partial shading effects in shingled PV modules, Solar Energy, 202 (2020) 420-428.
[142] A. Woyte, J. Nijs, R. Belmans, Partial shadowing of photovoltaic arrays with different system configurations: literature review and field test results, Solar energy, 74 (2003) 217-233.
[143] A. Dolara, G.C. Lazaroiu, S. Leva, G. Manzolini, Experimental investigation of partial shading scenarios on PV (photovoltaic) modules, Energy, 55 (2013) 466-475.
[144] M.A. Green, General temperature dependence of solar cell performance and implications for device modelling, Prog. Photovoltaics Res. Appl., 11 (2003) 333-340.
[145] O.K. Segbefia, B.R. Paudyal, I. Burud, T.O. Sætre, Temperature Coefficients of Photovoltaic Modules under Partial Shading Conditions, 38th EU PVSEC, (2021) 1180 - 1186.
[146] M. Seapan, Y. Hishikawa, M. Yoshita, K. Okajima, Temperature and irradiance dependences of the current and voltage at maximum power of crystalline silicon PV devices, Solar Energy, 204 (2020) 459-465.
[147] M.A. Islam, M. Hasanuzzaman, N. Abd Rahim, A comparative investigation on in-situ and laboratory standard test of the potential induced degradation of crystalline silicon photovoltaic modules, Renewable Energy, 127 (2018) 102-113.
[148] C.R. Osterwald, M. Campanelli, G.J. Kelly, R. Williams, On the reliability of photovoltaic short-circuit current temperature coefficient measurements, in: 2015 IEEE 42nd Photovoltaic Specialist Conference (PVSC), IEEE, 2015, pp. 1-6.
[149] R. Dubey, P. Batra, S. Chattopadhyay, A. Kottantharayil, B.M. Arora, K. Narasimhan, J. Vasi, Measurement of temperature coefficient of photovoltaic modules in field and comparison with laboratory measurements, in: 2015 IEEE 42nd Photovoltaic Specialist Conference (PVSC), IEEE, 2015, pp. 1-5.

[150] C. Berthod, S.T. Kristensen, R. Strandberg, J.O. Odden, S. Nie, Z. Hameiri, T.O. Sætre, Temperature sensitivity of multicrystalline silicon solar cells, IEEE Journal of Photovoltaics, 9 (2019) 957-964.
[151] S.T. Kristensen, S. Nie, C. Berthod, R. Strandberg, J.O. Odden, Z. Hameiri, Temperature coefficients of crystal defects in multicrystalline silicon wafers, IEEE Journal of Photovoltaics, 10 (2020) 449-457.
[152] D. Evans, L. Florschuetz, Terrestrial concentrating photovoltaic power system studies, Solar Energy, 20 (1978) 37-43.
[153] O.K. Segbefia, A.G. Imenes, I. Burud, T.O. Sætre, Temperature profiles of field-aged multicrystalline silicon photovoltaic modules affected by microcracks, in: 2021 IEEE 48th Photovoltaic Specialists Conference (PVSC), IEEE, 2021, pp. 0001-0006.
[154] J. Zhao, A. Wang, S. Robinson, M. Green, Reduced temperature coefficients for recent high-performance silicon solar cells, Progress in Photovoltaics: Research and Applications, 2 (1994) 221-225.
[155] M. Keevers, M. Green, Extended infrared response of silicon solar cells and the impurity photovoltaic effect, Solar Energy Materials and Solar Cells, 41 (1996) 195-204.
[156] H. Garg, R. Agarwal, Some aspects of a PV/T collector/forced circulation flat plate solar water heater with solar cells, (1995).
[157] T. Våland, W. Bartholdsen, M. Ottestad, M. Våge, Grimstad renewable energy park, Agder University College, NO-4878 Grimstad, Norway. http://ieahia. org/pdfs/grimstad. pdf, (1997).
[158] H.E. Beck, N.E. Zimmermann, T.R. McVicar, N. Vergopolan, A. Berg, E.F. Wood, Present and future Köppen-Geiger climate classification maps at 1-km resolution, Scientific data, 5 (2018) 1-12.
[159] D. Verma, M. Tayyib, T.O. Saetre, O.-M. Midtgård, Outdoor Performance of 10 year Old a-Si and Poly-Si Modules in southern Norway conditions, in: 2012 38th IEEE Photovoltaic Specialists Conference, IEEE, 2012, pp. 002368-002371.
[160] O.K. Segbefia, T.O. Sætre, Investigation of the Temperature Sensitivity of 20-Years Old Field-Aged Photovoltaic Panels Affected by Potential Induced Degradation, Energies, 15 (2022) 3865.
[161] W. Herrmann, G. Eder, B. Farnung, G. Friesen, M. Köntges, B. Kubicek, O. Kunz, H. Liu, D. Parlevliet, I. Tsanakas, Qualification of photovoltaic (pv) power plants using mobile test equipment, IEA-PVPS T13-24: 2021, (2021).
[162] T. Potthoff, K. Bothe, U. Eitner, D. Hinken, M. Köntges, Detection of the voltage distribution in photovoltaic modules by electroluminescence imaging, Prog. Photovoltaics Res. Appl., 18 (2010) 100-106.

Appendices

The appended articles have been published or submitted for publication in peer-reviewed international journals and conference proceedings.

Paper A

Defects and fault modes of field-aged photovoltaic modules in the Nordics by O.K. Segbefia, N. Akhtar, and T.O. Sætre. Published in Energy Reports (2023).

Energy Reports 9 (2023) 3104–3119

Contents lists available at ScienceDirect

Energy Reports

journal homepage: www.elsevier.com/locate/egyr

Research paper

Defects and fault modes of field-aged photovoltaic modules in the Nordics

Oscar Kwame Segbefia *, Naureen Akhtar, Tor Oskar Sætre

Department of Engineering Sciences, University of Agder, 4879 Grimstad, Norway

ARTICLE INFO

Article history:
Received 25 August 2022
Received in revised form 29 November 2022
Accepted 31 January 2023
Available online xxxx

Keywords:
Moisture induced degradation
Microcrack
Silver acetate
Parasitic resistance
Temperature sensitivity

ABSTRACT

PV module durability and reliability influences its efficiency and return on investment. Hence, collection of ample and credible PV module reliability data in each climatic zone becomes increasingly essential. In this work, defects and fault modes of field-aged multicrystalline silicon PV modules installed outdoors in Grimstad from 2000 to 2011 are investigated. The investigations were done using visual inspection, current–voltage characterization, temperature coefficient profiling, ultraviolet fluorescence, electroluminescence, infrared thermal imaging, and SEM-EDS analysis. Most PV modules show signs of microcracks, moisture ingress, corrosion, potential induced degradation, optical degradation, and irregular temperature sensitivities. Oxidized silver, tin, and lead were observed in the SEM-EDS results, which confirmed the remnants of moisture ingress. On average, the modules show power output of ∼78% and their efficiency dropped from 13% to ∼10%. The average temperature coefficient of efficiency of the module was found to be ca. -0.5%/°C, corresponding to an average degradation rate of 1.09 %/year over the 20 years period. However, the annual degradation rates when the modules were in the field and indoors were ∼0.98% and ∼1.33 %, respectively. It is believed that limited evaporation of activated volatile carboxylic products under indoor conditions led to the formation and accumulation of carboxylic acids, hence higher rate of degradation. Moisture induced degradation (MID) mechanisms was the root cause for the overall degradation in the PV modules' power output, especially over the later years.

1. Introduction

The importance of solar energy in the Nordic countries is highlighted in Fig. 1 (IEA-PVPS, 2021). Usually, photovoltaic (PV) modules are expected to produce at least 90% and 80% of their rated power after 10 years and 25 years of operation, respectively (Köntges et al., 2014; Wohlgemuth et al., 2015). However, concerns of defects and fault modes associated with PV modules from environmental and climatic stressors such as temperature, humidity, ultraviolet radiation, wind and snow loads, soiling, etc. is worrying (Aghaei et al., 2022; Jordan and Kurtz, 2013; Wohlgemuth et al., 2015). These degradation and fault modes such as delamination, discolouration, metal grids corrosion, cracks, solar cell degradation, potential induced degradation (PID), interface adhesion losses, optical losses, and other material degradation affect modules' performance during their guarantee period of ca. 25 years or even more (Halwachs et al., 2019; Köntges et al., 2014; Liu et al., 2019; Wohlgemuth et al., 2015). These defects and fault modes lead to PV module degradation, and hence, power degradation (Jordan et al., 2012). About 2% of PV modules are predicted to fail after 11–12 years due to climatic stressors (Köntges et al., 2014). According to Jordan et al. (2012), PV plants

Abbreviations: Ag, silver; Al, aluminum; AM, air mass; ARC, antireflection coating; $C_{(x)}$, optical and material properties of the PV module; C, carbon; CMI, climate moisture index; CNC, Computer Numerical Control software; CO, carbon monoxide; CO_2, carbon dioxide; DH, damp heat; DSLR, digital single-lens reflex; E, east; EDS, energy dispersive X-ray spectroscopy; EL, electroluminescence spectroscopy; EVA, ethylene vinyl acetate; FEG, Field Emission Gun; *FF*, fill factor; FTIR, fourier transform infra-red; G_I, in-plane irradiance; H_2O, water; HF, humidity freeze; IEA, International Energy Agency; IEC, International Electrotechnical Commission; I_{mpp}, current at maximum power point; IR, infrared; I_{sc}, short circuit current; I–V, current–voltage; LCOE, levelized costs of electricity/energy; LED, light-emitting diode; *m*, meter; mc-Si, multicrystalline silicon; MI, moisture ingress; MID, moisture induced degradation; N, nitrogen; N, north; O, oxygen; Pb, lead; PID, potential induced degradation; P_{max}, maximum power; PV, photovoltaics; PVPS, Photovoltaic Power Systems Program; R_{ext}, external resistance; RH, relative humidity; R_{int}, internal resistance; SEM, scanning electron microscopy; Sn, tin; STC, Standard Test Conditions; T, temperature; TC, thermal cycling; Ti, titanium; T_m, module temperature; TPT, Tedlar® /Polyester/Tedlar®; UV, ultraviolet; UV-F, ultraviolet fluorescence spectroscopy; $V_{(x)}$, local voltage at a point *x*; VI, visual inspection; V_{mpp}, voltage at maximum power point; V_{oc}, open circuit voltage; V_T, thermal voltage; β_{FF}, temperature coefficient of fill factor; β_{Jsc}, temperature coefficient of I_{sc} density; β_{Pmax}, temperature coefficient of P_{max}; β_{Voc}, temperature coefficient of V_{oc}; $\beta_{\eta m}$, temperature coefficient of efficiency; η_m, PV module efficiency; η_{Tref}, PV module efficiency at reference temperature; $\phi_{(x)}$, local luminescence at a point *x*; ΔT, difference in cell temperature

* Corresponding author.
E-mail address: oscar.k.segbefia@uia.no (O.K. Segbefia).

https://doi.org/10.1016/j.egyr.2023.01.126

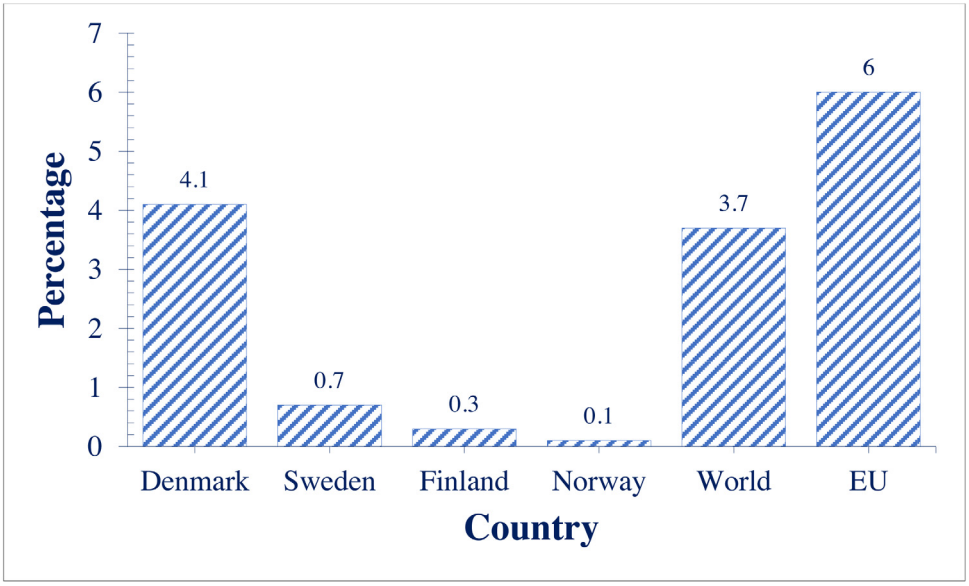

Fig. 1. Theoretical electricity contribution of PV to national energy mix, based on the PV capacity installed by the end of 2020 for the Nordics. Denmark is expected to exceed the world average electricity contribution from solar energy in the coming years.
Source: Extracted from IEA PVPS Snapshot of Global PV markets, 2021 (IEA-PVPS, 2021).

have an average degradation rate of 0.8%/year or more due to climatic defects.

PV module degradation can also be a function of the PV materials, usage, technology, assembling, and handling of PV modules (Aghaei et al., 2022; El Hammoumi et al., 2022; Halwachs et al., 2019; Jordan and Kurtz, 2013)). From packaging to installation, estimated power loss of up to 1.43% (mainly due to cracks) was reported (Dhimish et al., 2022). Also, roof mounted PV modules are likely to operate at higher temperatures due to reduced ventilation, and for that matter tend to degrade faster (Jordan and Kurtz, 2013; Jordan et al., 2012). Crystalline silicon solar cells have annual degradation rates of ca. 0.5% while thin film technologies show annual degradation rate of 1% but are predicted to improve over the coming years (Jordan and Kurtz, 2013). In environments with high humidity and wind loads (such as in the Nordics), the reliability of PV modules is more complicated (Halwachs et al., 2019; Köntges et al., 2014; Papargyri et al., 2020).

Corrosion can cause parasitic resistance losses whilst delamination and discolouration of encapsulants can also lead to loss of adhesion and optical efficiency (Bosco et al., 2019; Halwachs et al., 2019; Köntges et al., 2017). Moisture ingress can induce most defect and failure modes which lead to PV module degradation and eventual power loss (Köntges et al., 2014). A comprehensive review on the effect of moisture ingress on the degradation of crystalline PV modules is provided by Segbefia et al. (2021b). Some defects and failure modes affect the appearance of the PV module, and are easily detected using visual inspection (Wohlgemuth et al., 2015). However, some others such as microcracks are difficult to detect with the unaided eye and have no effect on the appearance of the module but can affect the power output (Köntges et al., 2014; Tsanakas et al., 2016). For defects and fault modes that cannot be detected with visual inspection, advanced spectroscopic and microscopic techniques are used for their detection. Some of these tools are current–voltage (I–V) characterization, electroluminescence (EL), photoluminescence (PL), fourier transform infra-red (FTIR), ultraviolet fluorescence (UV-F) spectroscopy, thermography, scanning electron microscopy (SEM), and energy dispersive spectroscopy (EDS). However, these tools are only useful after a defect or fault mode has occurred and some are destructive.

Kurtz et al. (2017) defined qualification tests to be tests which naturally provide a pass or fail outcome which reflects whether the test artefact exceeds a minimum acceptable key indicator. These tests are carried on a representative sample of 10 or less modules and the tests are relatively short in duration and are done to minimize the cost of testing. Since 1970s, the qualification, testing and standardization for PV cells, modules, and systems have evolved tremendously (McMahon, 2004; Osterwald and McMahon, 2009). However, these tests are limited in identifying wear out failures and PV durability and reliability over their lifetime (Hacke et al., 2019; Tracy et al., 2018; Trout et al., 2017). Additionally, they are not reliable in detecting all defects and failure modes e.g. potential induced degradation (PID) (Hacke et al., 2018).

Accelerated ageing tests are promising in predicting wear out failures (Osterwald and McMahon, 2009). These ageing tests include thermal cycling (TC) tests, ultraviolet (UV) exposure, humidity freeze (HF) test, damp heat (DH), mechanical load tests or a combination of two or more in climatic or environmental chambers to identify specific defects and failure modes. One single approach does not test for all degradation modes, rather, other components of the PV module end up being aged undesirably during the testing of another factor (Bosco et al., 2019; Eder et al., 2018; Trout et al., 2017). The accumulation of acetic acid and lead acetate in the ethylene vinyl acetate (EVA) encapsulant after prolonged damp heat exposure which predisposes the cell to corrosion and subsequent degradation is an example (Bosco et al., 2019; Tracy et al., 2018). Hence, selecting the most effective ageing approach in order not to over-accelerate or under-accelerate these degradation factors is the key. Moreover, as modules' reliability and durability has improved in recent years, accelerated testing appears to be losing its effectiveness (Aghaei et al., 2022). The use of physical models to forecast PV module's durability and reliability is fast, convenient, and cost-effective. However, these models are amenable to errors in estimating climatic variables, degradation rates, and PV module reliability. This can introduce up to 65% variation in the estimated degradation rate values (Kaaya et al., 2021).

One keyway of reducing the levelized costs of electricity (LCOE) of PV systems is increasing the durability and reliability of these systems (Aghaei et al., 2022; Kazem et al., 2020; Soto et al.,

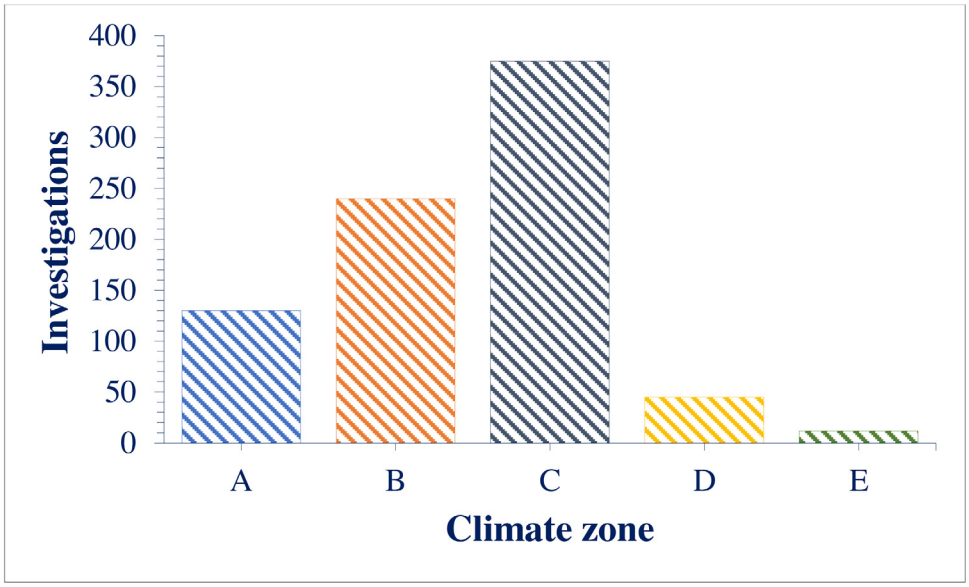

Fig. 2. Distribution of reported failure data on PV modules installed from the 1970s to the year 2015. Data is based on investigations that were done on the entire PV module as a unit.
Source: Extracted from Halwachs et al. (2019).

2022). According to a recent report by the researchers within the research project INFINITY in collaboration with the IEA PVPS Task 13 consortium and other multinational partners, there is an urgent need for collecting credible data on PV module performance and reliability globally (Halwachs et al., 2019). The report was collated based on the Köppen-Geiger climate zones: *A* (tropical), *B* (steppe/arid), *C* (temperate/moderate), *D* (cold/snow), and *E* (alpine/polar). The data for the study was collected on PV systems that were installed in the 1970s through to the year 2015. They found that most investigations were done in climate zones *B* and *C* except for investigations on PV module inverters. An extract of failure modes on investigations reported on the entire PV module as a unit is represented in Fig. 2. The Nordics fall in climate zone *D*, where the second fewest investigations were done over the study period, as expected.

Ample climatic failure data from each climate zone provides the platform for reliable correlation of expected failure mechanisms to specific climatic conditions and can provide useful insight into future investigations. Hence, practical field data from the cold regions (e.g., southern Norway) becomes ever more important. This work presents the main defects and failure modes associated with crystalline silicon PV modules deployed in Norway. To the best of our knowledge, we have not come across any such report from the same region. The work further investigates the underlying causes of the identified failure mechanisms using microstructural techniques. This distinguishes this study from the existing reports.

In the present work, the defects and fault modes of field-aged multicrystalline silicon (mc-Si) PV modules in a cold region are investigated. A catalogue of defects and fault modes together with the electrical performance data and temperature sensitivities of these modules is presented. In addition, the degradation rates of the PV modules over the initial 10 years of outdoor operation and the later 10 years when they were kept indoors is also presented. In Sections 2 and 3, a brief information on the Energy Park installed in Grimstad and the methods used for the defects and faults detection and diagnosis are presented, respectively. Finally, the results and insights from the investigation which demonstrated that cracks and moisture ingress are the main root causes for the observed degradation in the field-aged PV modules, is presented in Section 4.

2. Background of the Energy Park at Dømmesmoen

There have been research efforts within the University of Agder on outdoor monitoring of PV modules' performance and reliability over the years. One of these pioneer installations is the Grimstad Renewable Energy Park installed in Dømmesmoen, Grimstad. The Energy Park was officially commissioned in June 2000 and consists of 96 multicrystalline silicon (mc-Si) PV modules, amorphous silicon (a-Si) panels, and thermal collectors (Våland et al., 1997). According to the manufacturer, these solar PV modules were certified as per the existing IEC 1215 (presently, the IEC 61215) standards. Currently, 43 of the mc-Si modules are available for investigation. The main purpose of the Energy Park was to serve as a resource center for research and education in renewable energy. In 2011, the PV modules were decommissioned and kept securely for research purposes. At the time of decommissioning, the electrical performance data of these modules was investigated by Verma et al. (2012), and it was found that the PV modules were producing ∼90% of their rated power. However, their investigation on the mc-Si panels was solely on the electrical performance parameters, hence, the importance of the present study on the underlying defects and fault modes. A section of the park (mc-Si PV modules) and the geographical location of the installation site are shown in Fig. 3.

The climate in Grimstad (58.3447°N, 8.5949°E, 50 m above sea level for the installation site) is warm cold with monthly average temperature, relative humidity (RH), and air pressure ranges of −6.71 °C to 21.05 °C, 30% to 99%, and 97 kPa to 104 kPa, respectively. According to Köppen-Geiger climate classification, Grimstad is a humid continental climate, *Dfb* (−10 °C to +30 °C, with less than 90%), due to the constant stable marine air masses and heavy snow loads in winter (Beck et al., 2018). The optimum angle global irradiation is not more than 213 kWh/m^2. Average 1782 sunshine hours in a year with average wind speed between 3.4–5.3 m/s.

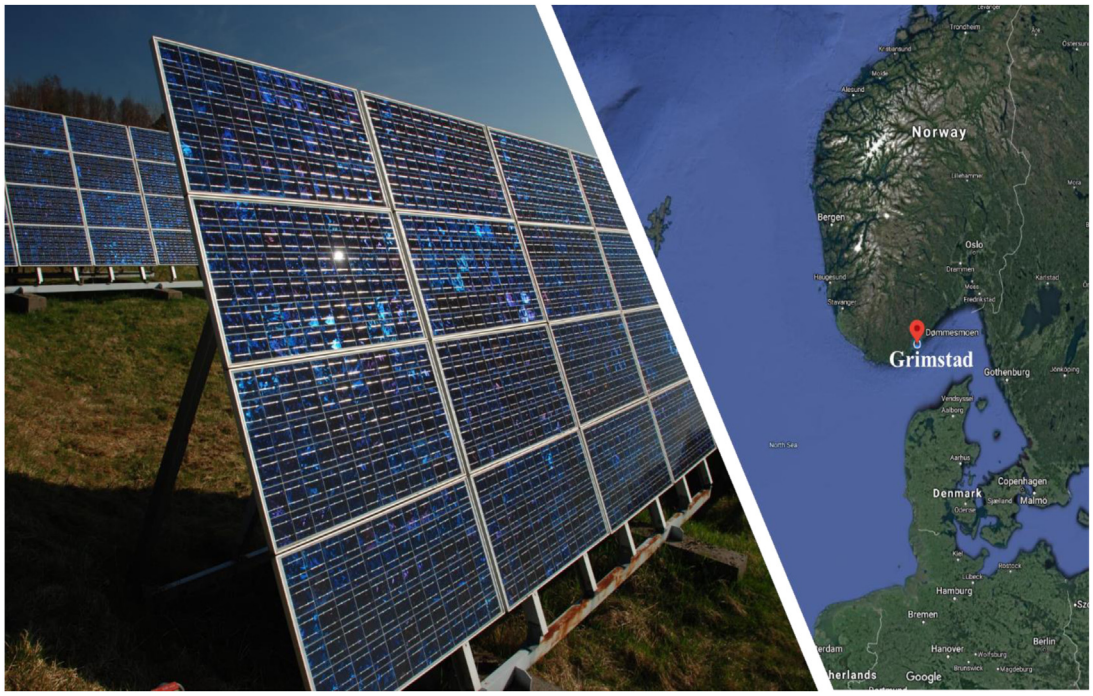

Fig. 3. A section of the mc-Si PV modules on the Energy Park at Dømmesmoen, Grimstad, showing the location of the site in southern Norway on the right.

3. Materials and methods

3.1. Materials

Defects and fault modes of the 43 field-aged mc-Si PV modules which have been installed in Grimstad between the years 2000 and 2011 are investigated using a combination of visual inspection (VI), current–voltage (I–V) characterization, ultraviolet fluorescence (UV-F), electroluminescence (EL), infrared (IR) thermal imaging, and scanning electron microscopy-energy dispersive spectroscopy (SEM-EDS) analysis. The schematic of the experimental method is illustrated in Fig. 4.

The technical specification of the solar cells and modules (as provided by the manufacturer in 2000) is summarized in Table 1. Details on the solar cell components and the module electrical layout was reported earlier (Segbefia et al., 2022; Segbefia and Sætre, 2022). By comparing the electrical performance characteristics to the information derived from the accompanying failure detection techniques, the underlying causes for power degradation of the PV modules were established. The characterization process took place partially indoors and outdoors.

3.2. Methods

3.2.1. Visual inspection

Visual inspection was conducted on all the PV panels (front and back) under clear sky outdoor and well-controlled light exposure conditions in the dark. This complementary procedure made it possible for a comprehensive logging of a variety of defects and fault modes which would not be possible with the conventional visual inspection alone. The visual inspection was done according to IEC 61215: 2016 standard.

3.2.2. I–V measurements

The current–voltage (I–V) characteristics (taken every two minutes) of all the PV panels was acquired using a handheld I–V 500w I–V Curve Tracer from HT® Instruments by following the IEC 60904- 1 standard. The electrical parameters acquired via the I–V characterization are the maximum power (P_{max}), short circuit current (I_{sc}), maximum power point current (I_{mpp}), open circuit voltage (V_{oc}), maximum power point voltage (V_{mpp}) and fill factor (FF). The data included information on the in-plane irradiance (G_I), module temperature (T_m), and the normalized values of all the electrical parameters to Standard Test Conditions (STC) of each PV module. STC specifies cell temperature (T_c) of 25 °C, solar irradiance of 1000 W/m^2 and air mass 1.5 (AM1.5) spectrum for commercial PV panels. The I–V characterization of all the modules proceeded under clear sky outdoor G_I conditions (960–1060 W/m^2), and the STC values were computed automatically by the I–V tracer used to minimize errors associated with data recording. The uncertainty of the Tracer for all the parameters (except the fill factor) measured is to the nearest hundredth. Moreover, the computed uncertainty is less than ±3% for all parameters measured. Hence, the values of all the parameters were approximated to the nearest tenth to accommodate the uncertainty in measurements. For the same reason, the FF and η_m are written in two significant figures. The PV module's efficiency (η_m) in the year 2020 was computed by multiplying the ratio of the normalized measured P_{max} values in the year 2020 to the datasheet P_{max} with the datasheet η_m value (13%). The relative temperature coefficients were determined using regression plots of electrical parameters (P_{max}, V_{oc}, I_{sc}, FF, η_m) versus T_m. The resulting regression equation fits the general linear equation: $y = mx + c$, where y and x denote the electrical parameter, x, and T_m, respectively. m and c represent the temperature coefficient (β_x) and intercept, respectively. The relative β_x in %/°C is then $\beta_x = m/c$. Details on the determination of β_x was presented earlier (Segbefia et al., 2021c; Segbefia and Sætre, 2022).

3.2.3. Ultraviolet fluorescence (UV-F) imaging

For the detection of moisture induced degradation (MID) defects and fault modes such as microcracks and optical degradation, the UV-F imaging technique is one of the handy tools. Moisture induced degraded PV module encapsulation materials

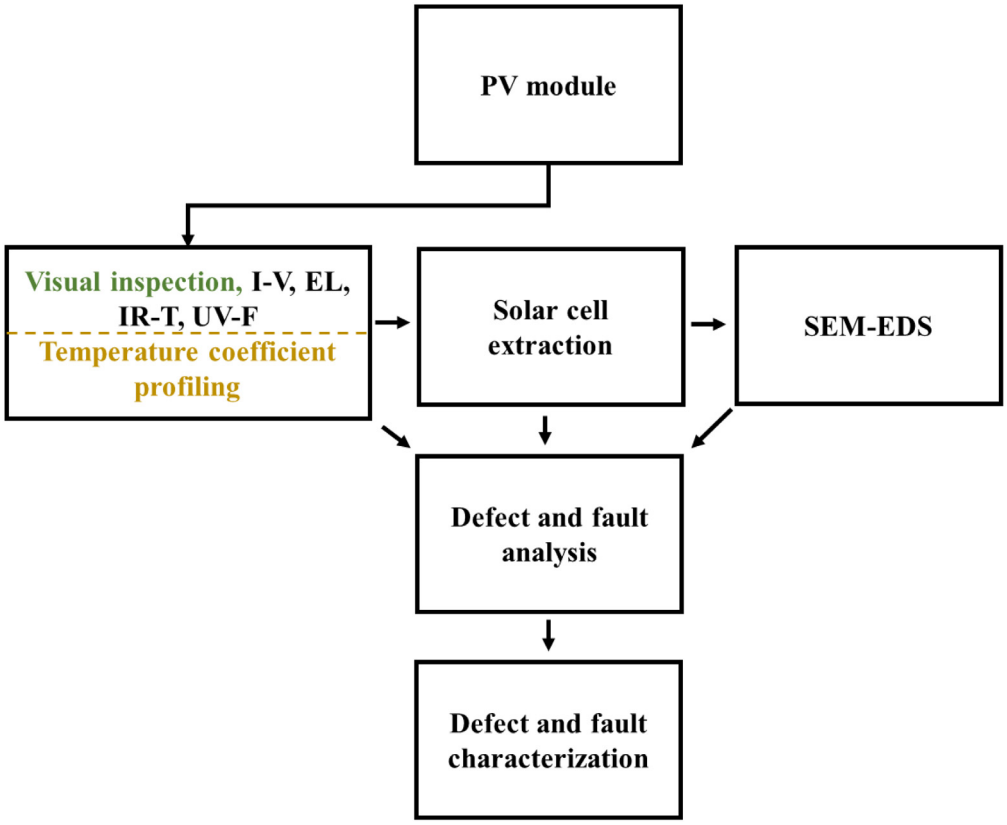

Fig. 4. Overview of the experimental methods.

Table 1
Solar module technical specification.

Module type	NESTE (NP100G12)
Power/efficiency (nameplate)	100 W ±10% (1000 W/m^2 and 25 °C) η = 13 % (total area), FF = 70% V_{oc} = 21.6 V, I_{sc} = 6.7 A, I_{mpp} = 6.0 A, V_{mpp} = 16.7 V
Cells	Multicrystalline silicon
Module dimension	Area: 129.3 × 65 = 8′405 cm^2 Depth: 3.4 cm (w. frame) Weight: 9.1 kg
Electrical layout	(12 x 2) x 3 = 72 cells in series
Front glass	Low iron content 3 mm tempered glass
Encapsulant	EVA (ethylene vinyl acetate)
Backsheet	Multi-layered TPT white (Tedlar® /Polyester/Tedlar®)
Junction box	2 weatherproof plastic casing, accommodating a bypass diode each
Frame	Full perimeter anodized aluminum (Al-) frame

(e.g., EVA) show weak UV fluorescence due to photoquenching. When these encapsulation materials are exposed to UV light, degraded areas show darker traces. The acquired UV-F information becomes useful for defect cataloguing and mitigation. Each of the PV module was characterized using a portable TROTEC® LED UV TorchLight 15F ($\lambda \approx 365$ nm) which is equipped with a Wolf eyes FD45 spectrum filter. The investigation was conducted in the dark by following the International Energy Agency (IEA) recommended procedure (Herrmann et al., 2021; Jahn et al., 2018).

3.2.4. Electroluminescence (EL) imaging

When a PV panel is forward biased, the solar cell signals in the infrared region can provide information on the degradation state of the PV panel. The EL characteristics of 15 sampled PV panels were acquired in a dark room using a BrightSpot EL Test Kit. The kit comprises of a 24 megapixels modified DSLR (digital single-lens reflex) Nikon D5600 camera, a DC power supply set, connecting cables, a flexible tripod stand, and computer with data acquisition and processing software. The investigation was conducted by following the IEC 60904- 13 standard and the IEA procedure (Herrmann et al., 2021; Jahn et al., 2018). The EL characterization of the PV modules was conducted using forward bias current densities of 10% of I_{sc} and 100% of I_{sc}. In this investigation, 100% of I_{sc} is 6.7 A (datasheet value for I_{sc}) and 10% of I_{sc} is 0.67 A at ca. 23.76 V (110% of V_{oc}), refer to Table 1.

According to Potthoff et al. (2010), the local luminescence, $\phi_{(x)}$ at a point x of a PV module is related to the local voltage, $V_{(x)}$ and the thermal voltage, V_T as

$$\phi_{(x)} = C_{(x)} exp\left(\frac{V_{(x)}}{V_T}\right), \quad for\ V_{(x)} \gg V_T \tag{1}$$

Where $C_{(x)}$ is the optical and material properties of the PV module and the camera system known as the local calibration factor. However, the operating voltage, V depends on $V_{(x)}$, the internal

resistance (R_{int}) between the metal grids and the solar cells and external resistance (R_{ext}) between the interconnectors and the solar cells of the PV module and can be written as (Potthoff et al., 2010)

$$V = V_{(x)} + R_{int}I_{(x)} + R_{ext}I \tag{2}$$

Where $I_{(x)}$ is the local current flowing through point x of the solar cell and I is the total current supplied to the PV module. If the solar cell or module is in good condition, then $C_{(x)} \approx$ C for all solar cells in series (N_c) and R_{int} is negligible and $R_{ext} \approx$ R, the total resistance within the PV module. Then V becomes (Potthoff et al., 2010)

$$V = V_T \cdot ln\left(\frac{\phi_{(x)}}{C}\right) + I \cdot \frac{R}{N_c} \tag{3}$$

For a good solar cell and module, R is negligible at current density below 10% of I_{sc} (Potthoff et al., 2010). That is, higher voltages come with higher resistances from electrical contacts rather than bulk material resistances, when the module is in a good condition. But, at lower injection levels, the material properties dominate the luminescence signal of the PV module. However, for bad solar cells at current density below 10% of I_{sc}, $R \approx R_{int}$, and Eq. (3) could be written in the form of Eq. (1) for each solar cell as

$$\phi_{(x)} = C_{(x)}exp\left(\frac{V_{(x)} + IR_{int}}{V_T}\right), \quad for\ V_{(x)} \gg V_T \tag{4}$$

In this case, the local luminescence is also influenced by the internal resistances as a result of cell cracks and other cell defects. In other words, when the cell is completely separated due to defects such as cracks, $I \approx I_{(x)} \approx 0$, and $V \approx V_{(x)}$ is maximum for the affected solar cell. However, moisture ingress can influence the luminescence signal due to photoquenching by degradation products, which is possible at open cracks or at the edges of the PV module.

That is, measurement at lower current density (ca. 10% of I_{sc}) is most appropriate for investigating degradation in material properties and measurements at higher current density (ca. 100% of I_{sc}) can be useful for evaluating the quality of the metal contacts. (Belmont et al., 2014; Jahn et al., 2018; Potthoff et al., 2010).

3.2.5. Infrared (IR) imaging

Defective PV panels under forward bias conditions can experience increased T_m due to the resistive losses. IR thermal information of the solar cells, and hence, the PV panel is useful for defects diagnostics. The IR thermal images of 15 sampled PV panels were acquired using the Fluke Ti400 Infrared Camera (measuring in the long-wave IR band: 650–1400 nm) by following the IEC 62446-3 standard. The investigation took place both indoors and outdoors. For the indoor investigation, the PV panels were investigated under I_{sc} forward bias conditions. IR images were taken 0.5, 2, and 5 min after current flow was initiated. For the outdoor investigation, the IR thermal images were acquired after soaking the PV panels in the sun for at least 15 min. For all measurements, the emissivity of the front glass and the TPT backsheet was set at 0.9 and 0.85, respectively. Details of the IR thermal imaging was presented earlier (Segbefia and Sætre, 2022).

3.2.6. Microstructural imaging of extracted solar cells

The defective areas were identified and extracted using a Water Jet NC 3060D Beveljet cutting machine. The Water Jet cutter uses a fine water jet stream with abrasive under ultra-high pressure (ca. 4,000 bar) for cutting a sample. This technique was preferred as low cutting temperatures was desired. The components of the as-cut cell sized samples were separated by treating it with toluene. The samples were immersed in the solvent in custom-made container at room temperature for 14 days. The microstructural information on the extracted solar cell samples was acquired using SEM-EDS analyses. The analysis was done using a field emission scanning electron microscope (SEM) (JEOL 7200F) equipped with an energy dispersive X-ray spectrometer (Octane Elect EDS system from EDAX® -AMETEK®). Prior to the microstructural analysis, the extracted solar cell samples were rinsed carefully and thoroughly in isopropyl alcohol, then in deionized water, and finally air dried.

4. Results and discussion

4.1. Optical degradation

Defects and fault modes that affect the optical properties of a PV module include delamination, discolouration of encapsulants and degradation of the front glass (Tsanakas et al., 2016). For the purpose of this work, we will restrict optical degradation to delamination and discolouration of encapsulants as none of the modules has broken front glass. All modules were dirty as they have been kept indoors for ten years. As expected, per the visual inspection, signs of moisture ingression into these modules dominate along with indications of delamination at cell edges, discolouration of encapsulants, metal grids oxidation, trapped chemical species, and adhesion loss (especially at the edges of the modules) as shown in Figs. 5 and 6.

Fig. 5a is a part of one of the field-aged modules showing delamination at the cell edges and discolouration of encapsulant. Figs. 5b and 5c are extracted cells from the panel in Fig. 5a. Figs. 5d and 5e show the edges of some of the modules with loose Al-frame and signs of moisture ingress, grids corrosion, discolouration, and delamination of encapsulants, respectively. Moisture ingress from the modules' edges appears to be one of the dominant fault mechanisms (Segbefia et al., 2020). This is responsible for the optical degradation and other defects in the affected modules (Segbefia et al., 2021b). Corrosion of the metal parts of the bypass diodes of some of the modules in the junction box (Fig. 5f) lends more credence to the influence of moisture ingress. This is not surprising considering the climatic conditions of the Nordics, especially in Grimstad with a global annual average climate moisture index (CMI) greater than 0.6 (Willmott and Feddema, 1992), together with high wind and snow loads. Fig. 6 highlights some of the defects and faults modes observed in photographs acquired on the PV modules in a dark room. This step makes it possible to detect and diagnose defects and fault modes which were not visible with the traditional outdoor visual inspection alone.

This visual inspection step highlights degradation of front glass (Fig. 6a), oxidation of metal grids, especially at the points where the busbars are attached to the cells (Fig. 6b), discolouration of encapsulants (Fig. 6c), and trapped degradation species (Fig. 6d). The oxidation and corrosion of metal grids, solar cell, solder bonds, and loss of optical transparency (due to delamination and discolouration of front encapsulants) characterized almost all modules. The I–V curves of the module depicted in Fig. 7a at different module operating temperatures is illustrated in Fig. 7c. This is compared with the data sheet values quoted for the module at 25 °C. After 20 years, Fig. 7a show ∼10% drop in the I_{sc} and ∼4% drop in the V_{oc} for measurements at ca. 25 °C. However, when module temperature increases, the I_{sc} increases but marginally and the V_{oc} decreases significantly. That is, there is permanent degradation in I_{sc}.

The drop in both I_{sc} and V_{oc} indicates that these modules are suffering from both series and shunt resistances. One reason for the observed degradation mechanism is optical degradation.

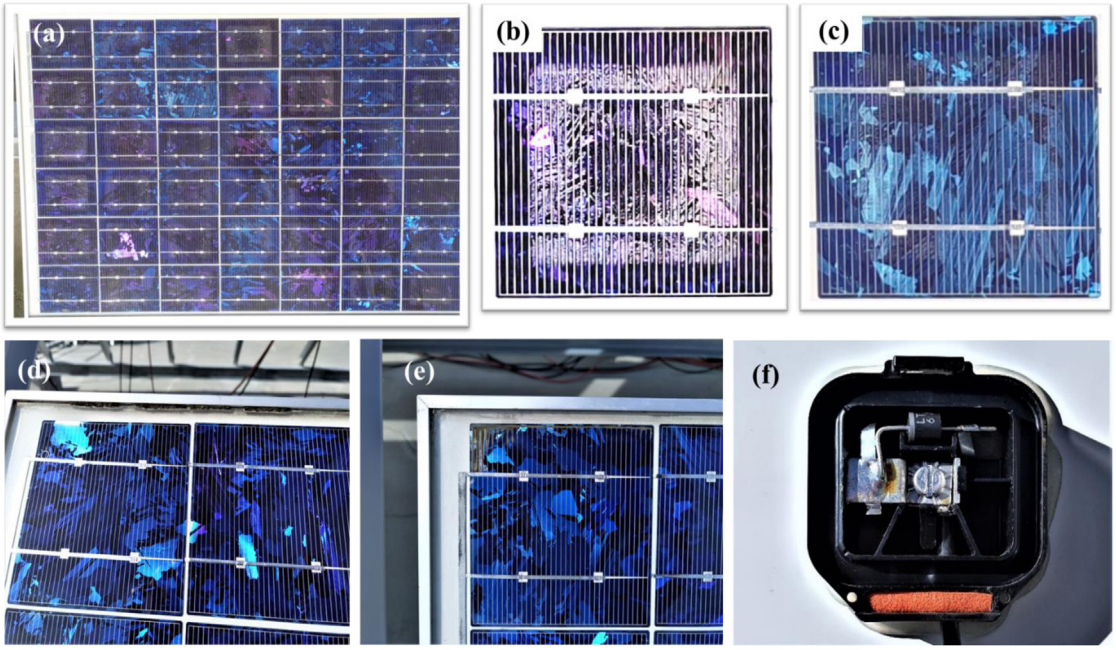

Fig. 5. Defects and fault modes from visual inspection. (a) A section of a field-aged PV module showing (b) delamination at cell edges, and (c) discolouration of encapsulant. Edges of modules with (d) loose Al-frames, and (e) signs of moisture ingress, grids corrosion, discolouration, and delamination of encapsulants. (f) A junction box showing signs of corrosion of the bypass diode and other metal interconnects. These images were acquired under clear sky outdoor conditions.

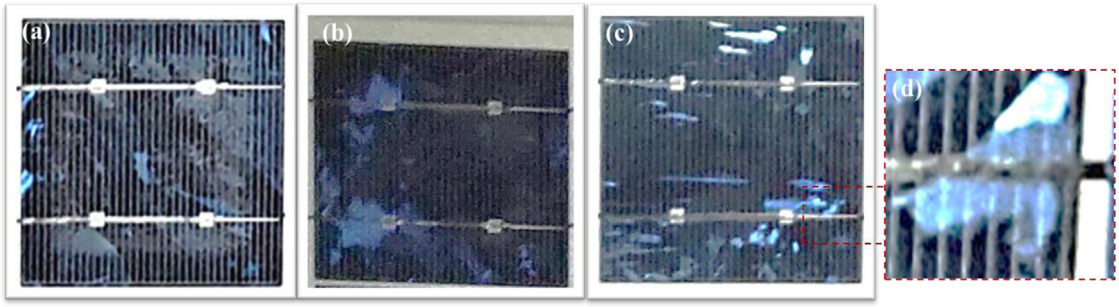

Fig. 6. Photographic images of cells from modules (taken in a dark room) showing signs of (a) corrosion of front glass, (b) oxidation of metal grids, (c) discolouration of encapsulants, and (d) metal grids corrosion and trapped degradation product in a zoomed-in image of the portion marked red in (c). (For interpretation of the references to colour in this figure legend, the reader is referred to the web version of this article.)

The main underlying cause of optical degradation is moisture ingress and UV radiation. However, optical degradation can also be a precursor for other fault mechanisms e.g., moisture ingress, microcracks, and corrosion which underline a degradation in V_{oc}. Of a greater concern is that optical degradation underlines short circuit (I_{sc}) degradation and can lead up to >50% drop in module efficiency (Al Mahdi et al., 2021). In addition, optical degradation can influence charge carrier absorption and transport properties within the PV module (Pern, 1993). This can lead to higher module temperature (degradation in temperature coefficients), and hence, a drop in efficiency (Dupré et al., 2015; Segbefia et al., 2021a).

4.2. Microcracks and cell degradation

Power loss due to cell cracks depends on several factors including the crack properties such as the crack size, geometry, location, orientation, and gravity. Cracks that damage the busbars and metal grids can result in power loss. A microcrack is a crack that has width less than 30 μm. However, the risk of power loss due to further degradation of microcracks into power sensitive cracks and defects under field operation is likely (Köntges et al., 2014; Papargyri et al., 2020). Moreover, cell cracks can induce other defects such as snail trails, moisture ingress, delamination, corrosion, PID, etc. (Ohdaira et al., 2023). Fig. 8 shows the EL images of some of the field-aged modules with their corresponding UV-F images of the red marked out areas. The zoomed-in portions of the areas marked red in the EL and the UV-F images are placed at the top of each corresponding image. In Fig. 8a–c, EL images acquired under 100% of I_{sc}, are shown. Images acquired under this current density highlight metal contact problems such as broken and corroded contacts in darker marks, refer to Eq. (4). However, under 10% of I_{sc}, materials problems which are in darker shades are highlighted, see Fig. 8d–f. The darker appearances are as a result of the inability of current to reach these parts of the module under forward bias conditions due to defects. These defects are metal grids corrosion, degraded solar cells and solder bonds. In Fig. 8a-c, these degradations are highlighted as darker spots over the PV modules, especially along the busbars. In Fig. 8d-f, more defective cells are highlighted, some which were not visible in the EL images in Fig. 8a-c.

The presence of randomly distributed darker spots (Fig. 8a-c) and darker cells (Fig. 8d-f) over the modules suggests cells and material degradation.

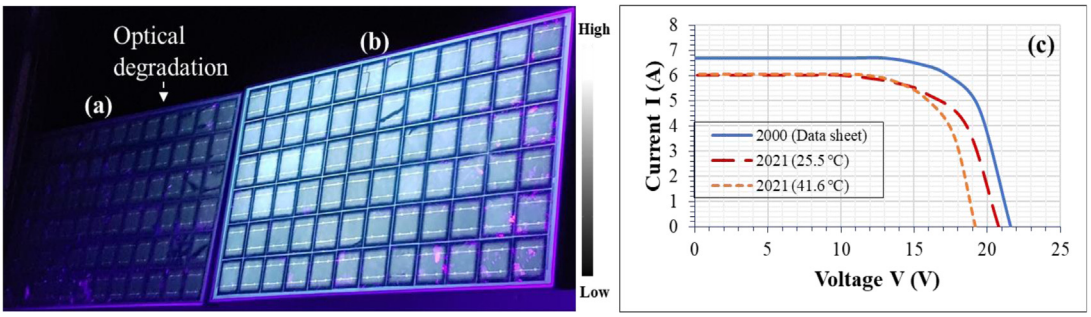

Fig. 7. UV-F images of (a) optically degraded and (b) fairly 'good' field-aged PV modules. (c) I–V characteristics of Fig. 7a at different module temperatures.

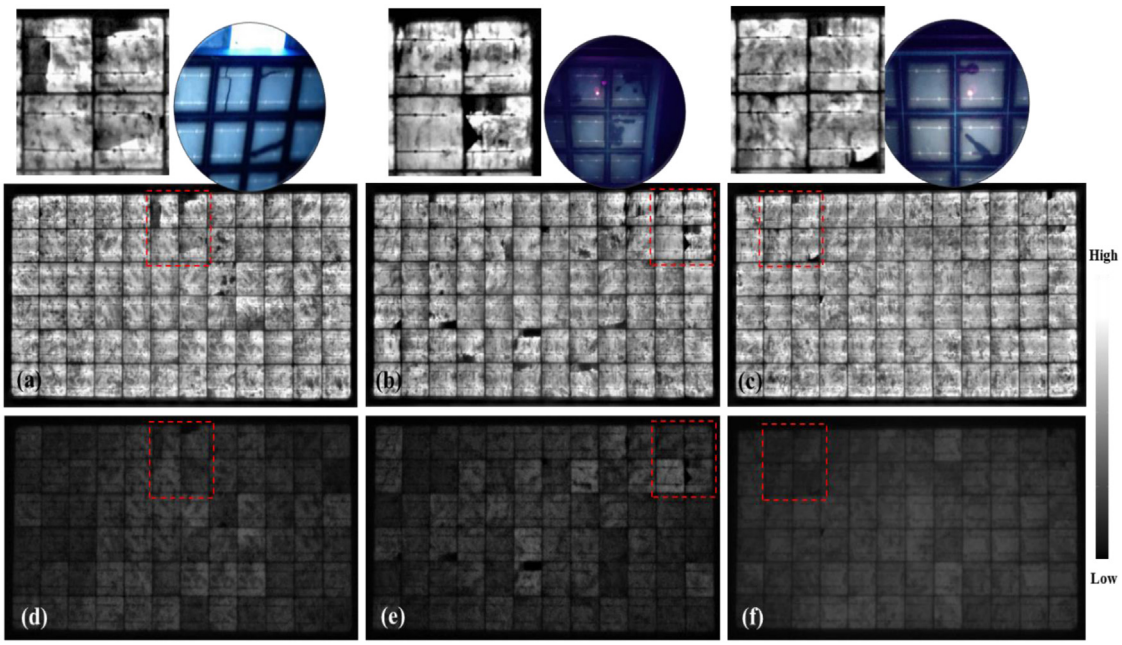

Fig. 8. EL images of 3 of PV panels under: (a)–(c) 100% of I_{sc} and (c)–(d) 10% of I_{sc} forward bias conditions. Areas marked in red are shown in corresponding zoomed-in EL images and UV-F images above.

One observation from Fig. 8d–f is that the majority of the less dark cells (better cells) are located in the middle parts of the PV module. Conversely, the majority of the darker cells (bad cells) are located at/near the edges of the module. Cells located at/near the perimeter of the modules are often more likely to be affected by moisture ingress. In addition, darker cells that are not located at the edge of the module appear to have underlining defect problem e.g., microcracks. This current accumulation at defective areas due to localized resistance leads to hotspots which can lead to accelerated ageing of the PV module. The observed defect patterns in the marked-out defective areas in the EL images are supported by the defect patterns in the UV-F images. The UV-F image of the marked-out portion of Fig. 8a shows critical micro-cracks. Moisture induced cell degradation is shown in the UV-F image of the marked-out portion of Fig. 8b. This cell degradation appears as a crack in the EL image, however. The UV-F image of the portion marked in Fig. 8c shows microcracks which have undergone further degradation due to moisture ingress.

Fig. 9 shows the IR thermal images of some of the field-aged modules. Fig. 9a-c are the IR thermal images acquired under real field outdoor conditions from the backside of the modules. The emissivity of the TPT backsheet was set at 0.85 for the outdoor measurements. Corresponding IR images acquired indoors under forward bias I_{sc} conditions after 5 min are shown in Fig. 9c–f. The indoor measurements were acquired from the front side of the modules with emissivity of the front glass set at 0.9. The areas marked in the images show the defective areas highlighted in the EL images (refer to Fig. 8). The IR thermal images of the module in Fig. 8a are shown in Figs. 9a and 9d and the IR thermal images of the module in Fig. 8b are shown in Figs. 9c and 9f.

Hotspots from broken metal grids, cell cracks, and other defects are depicted with blue–red colour codes: areas with severe shunts and material defects correspond with darker red colour (Tsanakas et al., 2016). In Fig. 9, the IR images show comparable defects (cracks) location on the PV module as shown in the EL images in Fig. 8. However, the thermal patterns for outdoor and indoor tests vary. In Fig. 9a-c, the exact position of the defects is indicated with associated hotspots. However, in Fig. 9d-f, the positions of defective cells are not very clear. Under outdoor conditions, the hotspots characteristics depend on the photon absorption, charge carrier generation, recombination, and transport properties. These mechanisms are highly material dependent. On the other hand, indoor IR thermal imaging is much more reliant on charge carrier recombination and transport characteristics. Hence, defects and fault mechanisms are better highlighted in outdoor IR imaging. It was also observed that IR images acquired under indoor conditions in relatively shorter time periods (∼1 min) could help to map out microcracks and other cell defects in PV modules. This could be done by comparing IR images taken at different time frames after the initiation of current

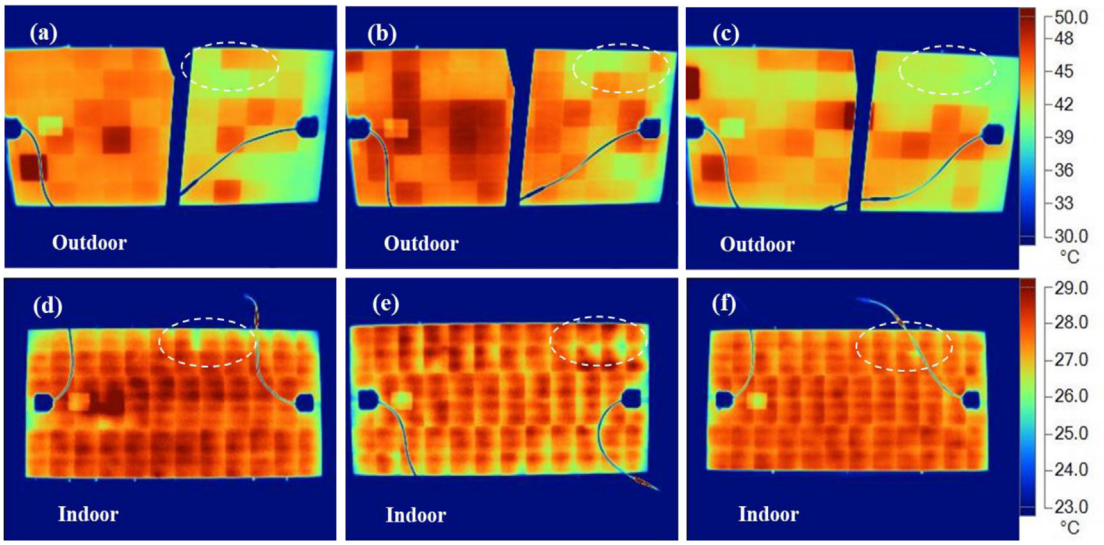

Fig. 9. IR thermal images acquired under (a)–(c) clear sky outdoor and (d)–(f) indoor forward bias I_{sc} conditions. Outdoor images were acquired after the modules were soaked in the sun for at least 15 min and the indoor images were taken 5 min after the forward bias current was initiated. The white marked areas show corresponding defective areas. The emissivity of the front glass (indoor measurements) and the TPT backsheet (outdoor measurements) was set at 0.9 and 0.85, respectively. The supporting frame (behind the PV module) in (a)–(c) and the cables show corresponding blue traces in the IR thermal images. (For interpretation of the references to colour in this figure legend, the reader is referred to the web version of this article.)

Table 2
Difference in cell temperature (ΔT) of different defect mechanisms that affected the PV modules under outdoor conditions.

Defect	ΔT (°C)	
	Result	Values from literature
Cracks	14 ± 2	2.5–45 (Buerhop et al., 2012; Tsanakas et al., 2016)
PID	7–15	7.5–30 (Jahn et al., 2018; Tsanakas et al., 2016)
Optical degradation	10 ± 2	6.0 ± 2 (Buerhop et al., 2012; Tsanakas et al., 2016)

flow. The temperature difference (ΔT) between the cell with the highest and lowest temperature in a PV module can be an indication of different defects and fault modes. It has to be noted, however, that ΔT values are also influenced by several factors including current characteristics and the ambient environment. In this regard, the ΔT values for the field-aged PV modules in each defect category was investigated. The average ΔT over the PV modules due to hotspots during the outdoor measurements was found for each defect category, see Table 2.

These values agree with observations elsewhere (Buerhop et al., 2012; Jahn et al., 2018; Tsanakas et al., 2016). According to Tsanakas et al. (2016), $\Delta T \approx 6 \pm 2$ °C indicates optical degradation such as delamination, trapped moisture bubbles, and discolouration of encapsulants. Critical solar cell cracks have been found to influence the thermal signatures of cells with ΔT values as high as ∼45 °C (Buerhop et al., 2012; Tsanakas et al., 2016). However, for these modules, the spots with microcracks show $\Delta T \approx 14 \pm 2$ °C. Yet, the modules with microcracks show the highest ΔT. The ΔT values of the surrounding cells indicates that these cracks may be critical to current flow in the affected regions. Defective bypass diodes can also be a reason for the observed hotspots in Fig. 9. However, an inspection on the bypass diodes revealed that the bypass diodes are in good condition. Hence, the hotspots are a result of microcracks, and moisture induced defects e.g., corrosion, optical degradation, PID, etc.

4.3. Potential induced degradation (PID)

Typically, PID of the shunting type (PID-s) cells are identified as warmer cells in IR thermal images and darker cells in EL images, see Fig. 10. In Fig. 10, the EL and IR thermal images of one of the PV modules affected by potential induced degradation (PID) are represented. EL images acquired under 100% of I_{sc} (Fig. 10a) and 10% of I_{sc} (Fig. 10b) are represented. In Fig. 10a, the luminescence intensity over the entire module is strong, though there are some localized darker spots, especially along the metal grids.

It is known that the electrical circuit is not always affected by corrosion and high series resistance. Hence, the effect of metal grids oxidation and the likes could be hidden in EL images if the grids are not significantly separated. Fig. 10b highlights PID and material defects localized to the edges of the module. The fact that a majority of the cells located nearer to the edges of the module are darker suggests that the degradation is due to moisture ingress from the perimeter of the module. This observation agrees with other reports on the influence of high humidity on the onset of PID (Ohdaira et al., 2023). In addition, the IR thermal image of this same module in Fig. 10c shows a fairly uniform distribution of temperature over its surface. It is therefore difficult to map out the defective cells or areas in Fig. 10c. In Fig. 10c, ΔT is ca. 3 °C. On the other hand, in Figs. 10b and 10d, the defective cells in the PV module correspond well and can be identified more easily. In Fig. 10d, ΔT is ca. 20 °C. The reason for the difference in the ΔT is due to the fact that the temperature sensitivity of defects is more highlighted under solar irradiation conditions than under induced current biasing conditions.

Also, the IR thermal images in Fig. 10d show cooler temperature regions around the cells, especially for cells at the edges of the module. Cooler temperature regions around cells in IR thermal images indicate PID-s degraded cells. It was also observed in the tests that, just at the initiation of current, cells and especially defective cells at the positive terminal show lower thermal profiles.

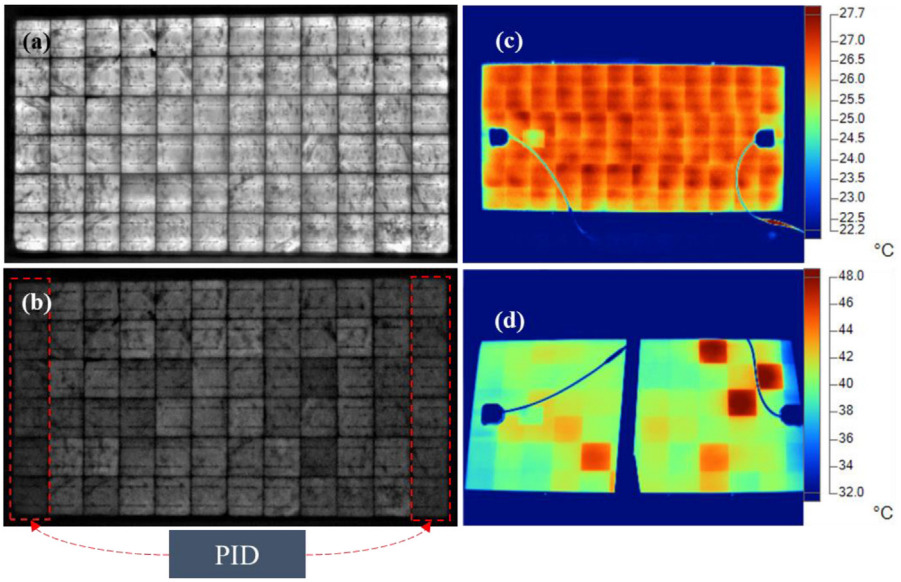

Fig. 10. A field-aged PV module affected by PID. EL images acquired under (a) 100% of I_{sc} and (b) 10% of I_{sc}. IR thermal image of the same module acquired under (c) indoor forward bias I_{sc} after 5 min and (d) clear sky outdoor conditions. In (c), ΔT =∼3 °C, and in (d), ΔT =∼20 °C. The supporting frame (behind the PV module) and the cables show corresponding blue traces in the IR thermal images.

4.4. Microstructural characteristics of the extracted solar cells

The EL signal in Fig. 10b could also be influenced by the interaction of moisture or moisture induced degradation (MID) chemical species. It is known that, water molecules absorb strongly in the near-infrared region (>0.70 microns) at ∼20 °C (Curcio and Petty, 1951). However, the absorption of water in the UV region is negligible but is influenced by the amount of dissolved oxygen and/or other chemicals (Mason et al., 2016). Hence, the darker cells in Fig. 10b could also be due to absorption of the IR signals by suspected ingressed moisture or/and trapped MID species. Usually, cracks and delaminated regions in the module serve as reservoirs for moisture and moisture induced degradation products e.g., acetic acids (Segbefia et al., 2021b).

Fig. 11 shows the micro-structural characteristics of the solar cell extracted from the edge of the PV panel. The images were acquired from different regions of the same solar cell. Fig. 11a, 11b, and 11c show the SEM images with their corresponding EDS analyses shown in Fig. 11d, 11e, and 11f, respectively. Fig. 11a shows the degradation state of the solar cell extracted from the edge of the module. Fig. 11d shows the EDS point analysis of the 2 points in Fig. 11a. Point 1 has more oxygen (O) than Point 2. The presence of carbon (C) in Point 2 (Fig. 11d) suggests the presence of carboxylic acids (e.g., acetic acid) on the surface of the solar cells. The presence of these acids might have consequences for further degradation processes. The presence of carbon might be due to the degradation of EVA encapsulation and/or through the ingress of carbon dioxide into the module. The presence of C could also be due to traces of EVA left on the cell after the reclamation. Corrosion (due to MID) was observed to make the EVA encapsulation adhere more strongly to the solar cell at the points of corrosion. Also, moisture ingress is responsible for the traces of aluminum (Al) and tin (Sn) observed at Points 1 and 2 (Fig. 11d), as observed elsewhere (Kumar et al., 2019). The titanium comes from the TiO_2 antireflection coating (ARC) used for the solar cells (Segbefia et al., 2022).

Fig. 11b displays the SEM image of the solder of the cell with corresponding EDS analysis given in Fig. 11e. Solder material consists of Pb and Sn as indicated by the arrows in Fig. 11b. However, EDS analysis evidenced the oxidation of Pb which appears as large bright flakes in the image. Migration of tin on the surface of the cell due to moisture (water and oxygen) ingress was also reported elsewhere (Kumar et al., 2019). The presence of oxygen at Point 1 in Fig. 11e confirms the observed oxidation around the metal grids as per the visual inspection (Fig. 6). Fig. 11c shows the state of the silver (Ag) grid of solar cells extracted from the edge of the field-aged PV modules. The Ag from the paste was oxidized as indicated by the presence of oxygen in the EDS analysis (Fig. 11f). This suggests that moisture ingress is the cause of the observed degradation modes. Similar degradation patterns were observed on polycrystalline silicon solar cells subjected to ca. 2500 h damp heat (DH) tests (Peike et al., 2013).

The degradation state of Ag and Pb and the presence of trace amounts of Sn, Al, C, and oxygen on the surface of the solar cells lend credence to the moisture induced degradation of these solar cells, see Fig. 11. Degradation of Ag and other elements in the Ag paste in the presence of moisture was also observed in other studies (De Rooij, 1989; Kumar et al., 2019; Moore and Codella, 1988; Nakano et al., 2016; Peike et al., 2013; Zheludkevich et al., 2004). According to Zheludkevich et al. (2004) and De Rooij (1989), the oxidation of Ag induces microcracks and flakes which facilitates the diffusion of oxygen, resulting in further degradation. Silver (I) oxide, AgO and silver (II) oxide, Ag_2O are the main MID products of silver in the case of PV application in the field (Kumar et al., 2019).

The presence of oxides of silver, lead, and other metals from the silver paste or solder on the surface of the cells lead to higher series resistance. In addition, the corrosion of the metal grids, solar cells, and the front glass due to the production of moisture induced degradation products is a precursor for shunts. Increased series resistance, reduced shunt resistance and degradation of the ARC lead to power degradation in the field-aged PV modules.

4.5. Power degradation

The distributions of the electrical characteristics (especially the P_{max}) can provide insight into the degradation state of PV modules. The I–V characteristics of PV modules were acquired under in-plane irradiance (960–1060 W/m^2) conditions, see Fig. 12. A clear spread in the P_{max} and I–V curves was observed. The difference in the electrical profiles' distribution is indicative of the degradation state of the modules after 20 years.

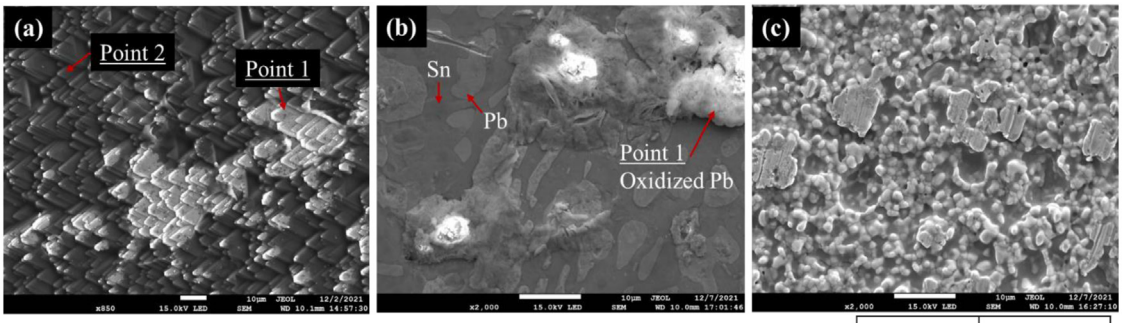

(d)

Element	Atomic %	
	Point 1	Point 2
C	0.0	25.3
O	15.0	8.9
Si	82.6	63.6
Al	0.6	0.3
Sn	0.1	0.1
Ti	1.8	1.8

(e)

Element	Atomic % (1)
C	0.0
O	74.4
Pb	20.8
Sn	4.8

(f)

Element	Atomic %
C	0.0
O	45.6
Si	2.3
Al	0.2
Ag	45.7
Pb	1.1
Ti	0.1
Sn	0.1

Fig. 11. SEM-EDS investigation of parts of solar cells extracted from the edge of the field-aged PV modules showing the effect of moisture ingress. Top row: (a) SEM image of solar cell showing degradation of the upper surface of the cell, (b) SEM image of the solder of the cell showing oxidation of lead (Pb), and (c) SEM image of the silver paste at the cell area where the grid is attached to the solar cell showing the state of the silver paste. Down row: Corresponding EDS analyses of (a), (b), and (c), respectively.

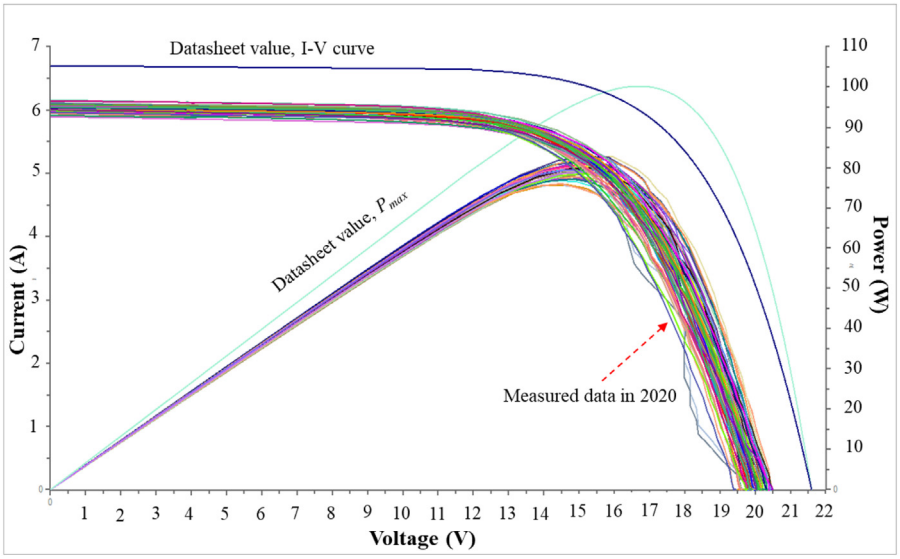

Fig. 12. Current–Voltage (I–V) and maximum power (P_{max}) curves of the PV modules under 960–1060 W/m^2 in-plane irradiance conditions normalized to STC.

The difference (Δ) in the electrical parameters of the PV modules was computed as the difference between the data sheet values and the values measured in the year 2020, according to a recommended procedure by Friesen et al. (2018) and Köntges et al. (2017). In Fig. 12, the difference in the I_{sc} (ΔI_{sc}) and V_{oc} (ΔV_{oc}) of the best and poorest PV modules are 4.9% and 4.31%, respectively. However, the change in P_{max} (ΔP_{max}) for the best and poorest modules was 14.8%. The value of ΔI_{sc} under the conditions in Fig. 12a is a strong indication of parasitic resistance losses which dominates at lower injection levels (Holman et al., 2012), as reported elsewhere (Dang et al., 2023). The average electrical parameters of the PV modules per technical data sheet from the manufacturer and measurements done in 2011 and 2020 are recorded in Table 3. The values for 2011 and 2020 are the average normalized values to STC.

In 2011, the modules were found to be producing ~90% of their nominal P_{max} (Verma et al., 2012). This value was within the tolerance limit (±10) specified by the manufacturer as in Table 1. However, after 20 years (10 years in the field and another 10 years indoors), these modules are found to be producing ~78% of their nominal P_{max}. The degradation in the electrical parameters of these modules in 2020 normalized to STC is illustrated in Fig. 13. Fig. 13a shows the distribution of the electrical parameters (V_{oc}, I_{sc}, and FF as a function P_{max}) of these modules using a scatter plot. The randomness of these parameters, especially

Table 3
Average electrical parameters of the field-aged PV modules normalized to STC.

Year	P_{max} (W)	V_{oc} (V)	V_{mp} (V)	I_{mp} (A)	I_{sc} (A)	FF (%)	η (%)
2000	100	21.6	16.7	6.0	6.7	70	13
2011	90.2	21.5	16.1	5.1	6.2	68	12
2020	78.2	19.7	14.7	5.3	6.0	66	10

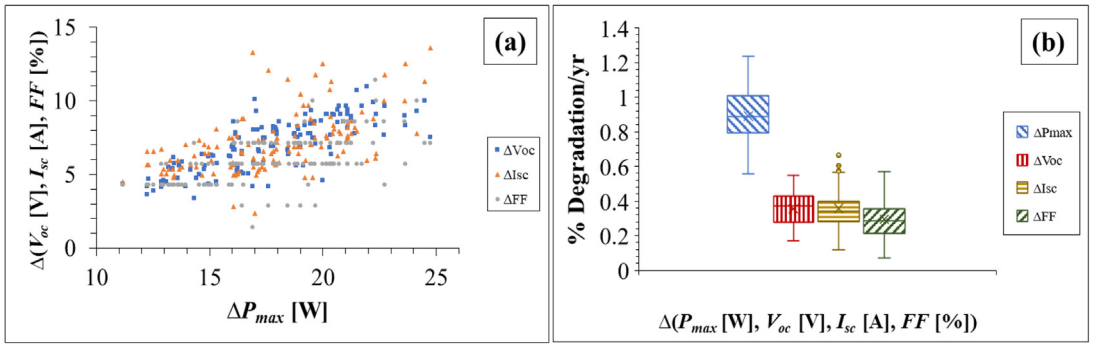

Fig. 13. Relative degradation in P_{max}, V_{oc}, I_{sc} and FF of the PV modules expressed as percentages. (a) A scatter plot showing the correlation among P_{max}, V_{oc}, I_{sc}, and FF degradation, (b) Box and whisker plots showing the five-number summary (that is the minimum, 25th percentile, median, 75th $_{max}$, V_{oc}, I_{sc}, and FF of the PV modules. The edges of the boxes indicate the lower and upper quartiles. The internal lines and x-marks in the boxes indicate the median and mean, respectively. Δ is the difference between data sheet and measured values in 2020. The electrical performance data was acquired under 960 W/m^2–1060 W/m^2 in-plane irradiance conditions, and then normalized to STC.

the I_{sc}, is uncharacteristic of 'good' PV cells or modules. Fig. 13b illustrates the degradation in the electrical parameters per year.

In Fig. 13b, the P_{max} degradation of all modules per year over the 20 years is above 0.5%; and more than 75% and 25% of the modules show annual degradation rates of >0.7% and >1.0% in P_{max}, respectively. Also, more than 75% of the modules showed an annual degradation rate of >0.2% in V_{oc} and I_{sc}, and more than 50% of them showed an annual degradation rate of more than 0.3% in V_{oc} and I_{sc}. However, only about 25% of the modules show an annual degradation rate of 0.3% or more in fill factor. Among all the electrical parameters, the V_{oc} and I_{sc} show mean degradation values just below and above their median values, respectively. This indicates that the V_{oc} and I_{sc} are skewed to the left (negatively skewed) and right (positively skewed), respectively. The difference in the mean and median values indicates degradation and this is the underlying cause of the overall P_{max} degradation, as observed elsewhere (Ohdaira et al., 2023; Virtuani et al., 2019). This also supports the observation in Fig. 14 which indicated a degradation in V_{oc} and I_{sc} as the underlying factors for P_{max} degradation.

It is known that P_{max} is linearly related to the V_{oc}, I_{sc}, and fill factor (FF) by:

$$P_{max} = V_{oc} \cdot I_{sc} \cdot FF \tag{5}$$

That is, any difference in the mean and median values of V_{oc} and I_{sc} affects the P_{max} of the PV modules. This is because V_{oc} and I_{sc} degradation also influence the FF degradation, and hence, leads to shunt losses (Annigoni et al., 2019; Halwachs et al., 2019; Köntges et al., 2014; Virtuani et al., 2019).

Fig. 14 highlights the degradation states of all the PV modules studied. A histogram of degradation rates per year showing the distribution of modules per their P_{max} degradation is shown in Fig. 14a. More than half (median or 50th percentile, P50) of the modules showed a degradation rate greater than 1.03 per year and not more than 10% (90th percentile, P90) of the modules showed a degradation below 1.17% per year. Over the entire 20 years, the annual degradation rate was computed to be 1.09%, a value which is greater than the 0.80%/year observed elsewhere (Jordan et al., 2012). Also, the average yearly degradation in the P_{max} of these PV modules over the first and second 10 years periods are ∼0.98% and ∼1.3%, respectively. These values are similar to the values reported for a similar climate by Belhaouas et al. (2022).

An average P_{max} of ∼78 watts with a standard deviation of ca. 1.49 was recorded for the PV modules in 2020. Meanwhile, in 2011, the average power output and standard deviation were found to be ∼90 watts and 0.41, respectively. This is also supported by the I–V curves of all the modules in 2011 and 2020, see Fig. 14b. Fig. 14b shows that the major factor for the degradation in P_{max} in 2011 is the degradation in the I_{sc}. This is due to high series resistance as reported elsewhere (Annigoni et al., 2019; Köntges et al., 2014). However, after these modules were kept indoors for a similar duration, degradation in V_{oc} dominates the underlying causes for P_{max} degradation. V_{oc} degradation is an indication of parasitic shunt losses which could be correlated to grave material degradation: metal grids corrosion, cracks, solder bond degradation, PID, etc. (Annigoni et al., 2019; Liu et al., 2019). According to Ohdaira et al. (2023), high humidity can induce PID-p. However, recovery of PID affected PV modules under sunshine is possible. These degradation mechanisms are due to moisture ingress, which is characteristic of the Nordics.

4.6. Degradation under indoor conditions

PV modules are expected to undergo minimal degradation (due to encapsulant discolouration) when kept indoors, where they are not exposed to any environmental stressor (Liu et al., 2019). It is known that optical degradation manifests itself in I_{sc} degradation (Annigoni et al., 2019; Köntges et al., 2014; Oh et al., 2019; Sinha et al., 2016). Yet, the I_{sc} degradation was minimal, and the degradation rates of the PV panels were higher when they were kept indoors. This degradation is mainly due to V_{oc} degradation, see Fig. 14b. It suggests that the higher degradation rate of the PV modules under indoor conditions after field exposure is mainly due to metal contact and material degradation issues. This also suggests FF degradation, refer to Fig. 13b. Degradation of the PV module components is due to the accumulation of volatile degradation products and subsequent formation of carboxylic acids (e.g., acetic acid) and other moisture induced degradation products during the later years.

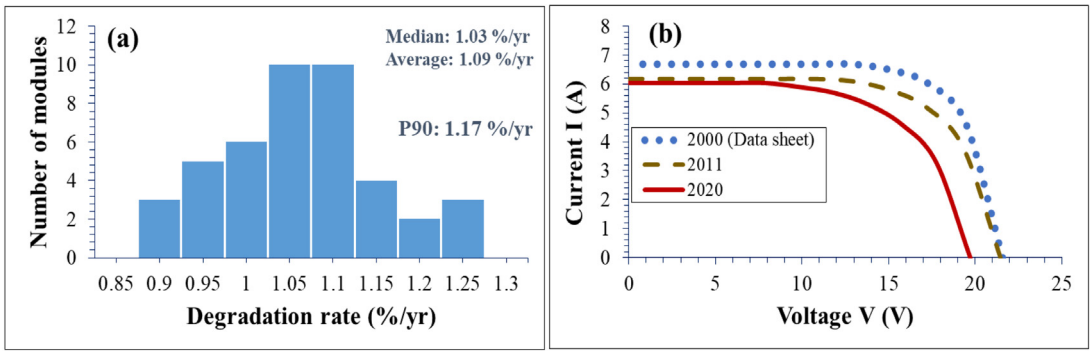

Fig. 14. (a) Degradation rates of all field-aged PV modules in 2020 showing the median, average, and 90th percentile (P90) values. (b) I–V curves of PV modules in 2000, 2011, and 2020.

Moisture (e.g., H_2O, O_2, CO_2, CO) ingress is the underlying cause of EVA degradation into acetic acid. The initial step in polymer (e.g., EVA) degradation is the formation of acetic acid, followed by polymer chain degradation (Allen et al., 2000; Oreski et al., 2017) and successive degradation of other PV module components. Yet, the formation of carboxylic acids such as acetic acids starts with the formation of carboxylic photoproducts (e.g., CO, CO_2, etc.) and moisture accumulation within the polymer substrate (Grossetête et al., 2000; Göpferich, 1996). Moreover, photodegradation products such as CO and CO_2 (which leads to the formation of acetic acids and its coproducts) are photo- and thermally unstable and oxidizes and evaporate at temperatures up to ca. 100 °C (Grossetête et al., 2000).

These modules were exposed to environmental stressors including high humidity conditions. Hence, the likelihood of the formation of photoproducts within the PV module during the field exposure is high. In the field, these volatile degradation products have the possibility to escape when the module heats up during operation. Conversely, under indoor conditions, evaporation of these volatile products is limited, and formation and accumulation of MID products is more feasible. The retention of these carboxylic radicals and ingressed moisture (during field exposure) within the module can result in the formation of carboxylic acids e.g., acetic acid (Oreski et al., 2017). This can induce defects and fault modes such as solar cell degradation, corrosion, delamination, and discolouration of encapsulants leading to considerable degradation in V_{oc} as observed elsewhere (Ohdaira et al., 2023). This is believed to be responsible for the significant power loss and higher degradation rate observed in 2020.

4.7. Temperature sensitivity of the PV modules

The effect of PV module's operating temperature on output power is well known (Dupré et al., 2015; Green, 2003; Skoplaki and Palyvos, 2009)). Moreover, PV cell parameters such as V_{oc}, I_{sc}, and *FF* tend to vary linearly when temperature varies (Dupré et al., 2015). So, from Eq. (5), the overall temperature coefficient of P_{max} (β_{Pmax}) could be expressed in terms of the temperature coefficients of open circuit voltage (β_{Voc}), short circuit current density (β_{Jsc}), and fill factor (β_{FF}). This can be written as

$$\beta_{Pmax} = \beta_{Voc} + \beta_{Jsc} + \beta_{FF} \tag{6}$$

However, each of these parameters in Eq. (6) depends on different loss mechanisms in the PV module (Green, 2003). In addition, Eq. (5) tells us that the fill factor influences the amount of power that could be extracted from a PV module with current–voltage tradeoffs . These tradeoffs mainly depend on the generation and recombination balances and the resistance losses at P_{max} (Dupré et al., 2015). Yet, the generation and recombination losses depend on material quality, which could be measured using the V_{oc}. That is, the V_{oc} of a PV cell is the measure of the carrier generation–recombination balance. So, the temperature sensitivity of a PV cell or module improves with increasing V_{oc}. In addition, it is known that the β_{Voc} of a solar cell accounts up to ∼90% of the overall temperature sensitivity of the solar cell (Dupré et al., 2015). Hence, degradation in the β_{Voc} affects P_{max} the most, and indicates some form of material degradation.

A graph of temperature sensitivities as a function of in-plane irradiance (G_I) and PV module operating temperature (T_m) of the PV modules are represented in Fig. 15. The dependence of the temperature coefficients on G_I is shown in Fig. 15a. The inconsistent spread in the β_{Pmax} and β_{FF} indicates that the modules are at various stages of degradation.

This is clearly evident in the Box and whisker plots in Fig. 15b, where the relative changes in the temperature coefficients are quantified. From Fig. 15b, the β_{Pmax} degradation depends strongly on the β_{FF}, β_{Voc}, and β_{Jsc} degradation. That is, the observed degradation in the β_{Pmax} is as a result of the β_{FF} degradation. β_{FF} depends mainly on β_{Voc} and β_{Jsc} characteristics which are products of parasitic resistance losses. Usually, temperature coefficients are normalized, refer to Eq. (6). Hence, any mechanism that influences the efficiency of the solar cell alters its temperature sensitivity, and vice versa. Fig. 15b suggests that the β_{Pmax} for the modules varies from 0.1–0.8%/°C. From Fig. 15b, over 75% of the PV modules show less than 0.1%/°C change in β_{Jsc} whiles the same fraction of the modules shows more than 0.1%/°C change in FF. Conversely, all the modules show a relative change in β_{Voc} which is greater than 0.1%/°C. It is obvious then that the major underlying factor for the degradation in both β_{Pmax} and β_{FF} is the β_{Voc} degradation, which usually comes from shunt losses due to the junction quality of solar cells.

The influence of temperature on the efficiency of the PV modules is illustrated in Fig. 16. A graph of the Evans–Floschuetz efficiency ratio (η_m/η_{Tref}) versus T_m is shown in Fig. 16a. According to Evans and Florschuetz (1978), this ratio can be used to determine the nominal or the data sheet temperature coefficient of efficiency ($\beta_{\eta m}$) value of crystalline silicon modules when the data sheet value for $\beta_{\eta m}$ is not available. For these PV modules, information on the temperature coefficients was not provided in the data sheet by the manufacturer. So, the Evans–Floschuetz efficiency ratio versus temperature plot was used to estimate the $\beta_{\eta m}$ of the modules. The normalized module efficiency versus T_m in the year 2020 is shown in Fig. 16b. Fig. 16a reflects the ideal temperature sensitivity of the modules when they were in a relatively good condition, and the temperature sensitivity of these modules in their current condition is reflected in Fig. 16b. This suggests that the nominal (data sheet) temperature coefficient of efficiency of the PV modules was ca. −0.4%/°C (Fig. 16a) and has degraded to ca. −0.5%/°C (Fig. 16b) over the 20 years period.

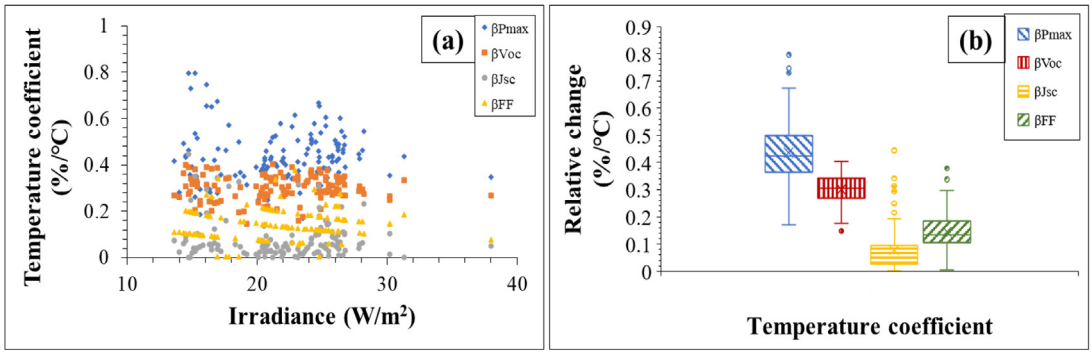

Fig. 15. Variation of (a) temperature coefficients with in-plane solar irradiance. (b) Variation in the temperature coefficients of electrical parameters of the PV modules. The edges of the boxes indicate the lower and upper quartiles and the internal lines and x-marks in the box indicate the median and mean, respectively. The electrical performance data was acquired under 960 W/m^2–1060 W/m^2 in-plane irradiance conditions, and then normalized to STC.

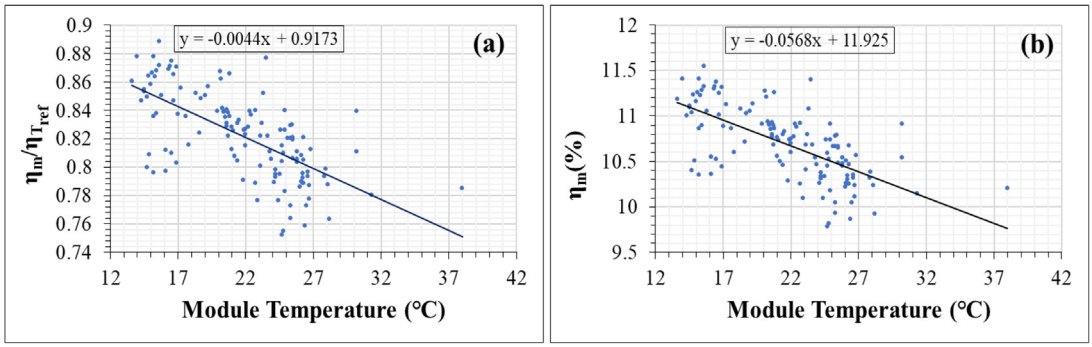

Fig. 16. The influence of temperature sensitivity on the efficiency of the PV modules. A graph of (a) Evans–Floschuetz efficiency ratio (η_m/η_{Tref}) and (b) normalized η_m versus T_m. The electrical performance data was acquired under 960 W/m^2–1060 W/m^2 in-plane irradiance conditions, and then normalized to STC.

Degradation in the temperature coefficients of the PV modules leads to linear degradation in P_{max}. Hence, the observed degradation in the temperature coefficients suggests that the modules have undergone significant degradation. Also, Fig. 16b suggests that when T_m is ∼25 °C and by extrapolation, the average efficiency of the modules reduces to ∼10%, which agrees with the value reported in Table 1 for the year 2020. However, when the T_m is 0 °C and by extrapolation, η_m is ca. 12% (refer to Fig. 16b). The η_m of the PV modules is not expected to be lower than the data sheet value (13%) if the PV modules are in good condition. This also supports the earlier evidence from the visual inspection, I–V characteristics, EL images, IR thermal images, and SEM-EDS analysis which points strongly to material degradation in the PV modules due to moisture ingress.

Taken together, these results suggest that the PV modules have been affected by a variety of defects and fault modes as a result of moisture ingress. In addition, the presence of microcrack can lead to moisture ingress, and vice versa. Hence, both have been observed as co-defects. Field-aged solar PV modules suffer from multiple defect mechanisms. In this work, efforts have been made to select modules with dominant defects for the investigation of specific defect mechanisms. Yet, the influence of other inherent defects on the overall investigation cannot be ruled out. At least three modules were used to investigate each defect category. In addition, over 20 years, PV technologies have revolved tremendously. More investigations in the cold regions utilizing newer and larger number of state-of-the-art technologies will be needed to improve and reemphasize the findings in this work.

Conclusion

PV plants are susceptible to varying degradation modes due to climatic and environmental stressors. As such, PV performance reliability studies is very important to develop credible climate specific protocols to ensure that PV plants produce optimal power consistently over their guaranteed lifetime. This will minimize the payback time on investment and levelized cost of electricity of PV plants and boost the confidence level in PV energy sources. Investigations on the 20 years old PV modules suggest that the major defects and fault modes affecting these modules is moisture ingress and microcracks (co-defects), which are precursors for other degradations modes. I–V characterization, UV-F, IR thermal, and EL imaging were used for defects and fault modes diagnosis. SEM-EDS analysis confirmed that the PV modules are affected by moisture ingress. The modules were found to be affected by MID defects such as microcracks, optical degradation, corrosion, PID, and the degradation of the solar cells and solder bonds.

It was observed that more than 93% of the modules were affected by optical degradation, and the average P_{max} of the modules decreased to ∼78%, a 22% degradation which is more than the 20% degradation limit specified for good PV modules. In addition, the temperature coefficient of efficiency of the modules has also degraded to −0.5%/°C after 20 years. *FF* and V_{oc} degradation appear to dominate the root cause of P_{max} degradation. However, the I–V characteristics suggest that the modules have been affected by both serial and shunt resistance losses. Also, it has been found that the average annual degradation rate of the modules was ∼1.09%. Yet, the degradation rates of the modules in the first 10 years (when they were in the field) and the later 10 years (when they were kept indoors) were ∼0.98%/year and ∼1.33%/year, respectively. Consequently, the average efficiency of the modules dropped from 13% to ∼10%. In summary, moisture ingress underlines the observed degradation in the electrical parameters in the PV modules.

CRediT authorship contribution statement

Oscar Kwame Segbefia: Conceptualization, Methodology, Investigation, Validation, Writing – original draft. **Naureen Akhtar:** Investigation, Validation, Writing – review & editing. **Tor Oskar Sætre:** Conceptualization, Supervision, Writing – review & editing, Funding acquisition.

Declaration of competing interest

The authors declare that they have no known competing financial interests or personal relationships that could have appeared to influence the work reported in this paper.

Data availability

Data will be made available on request.

Acknowledgement

The authors acknowledge the continuous support of the University of Agder, Norway.

References

Aghaei, M., Fairbrother, A., Gok, A., Ahmad, S., Kazim, S., Lobato, K., Oreski, G., Reinders, A., Schmitz, J., Theelen, M., 2022. Review of degradation and failure phenomena in photovoltaic modules. Renew. Sustain. Energy Rev. 159, 112160.

Al Mahdi, H.A., Leahy, P.G., Morrison, A.P., 2021. Predicting early EVA degradation in photovoltaic modules from short circuit current measurements. IEEE J. Photovolt..

Allen, N.S., Edge, M., Rodriguez, M., Liauw, C.M., Fontan, E., 2000. Aspects of the thermal oxidation, yellowing and stabilisation of ethylene vinyl acetate copolymer. Polym. Degrad. Stab. 71 (1), 1–14.

Annigoni, E., Virtuani, A., Caccivio, M., Friesen, G., Chianese, D., Ballif, C., 2019. 35 Years of photovoltaics: Analysis of the TISO-10-kW solar plant, lessons learnt in safety and performance—Part 2. Progr. Photovolt. Res. Appl. 27 (9), 760–778.

Beck, H.E., Zimmermann, N.E., McVicar, T.R., Vergopolan, N., Berg, A., Wood, E.F., 2018. Present and future Köppen-Geiger climate classification maps at 1-km resolution. Sci. Data 5 (1), 1–12.

Belhaouas, N., Mehareb, F., Kouadri-Boudjelthia, E., Assem, H., Bensalem, S., Hadjrioua, F., Aissaoui, A., Hafdaoui, H., Chahtou, A., Bakria, K., 2022. The performance of solar PV modules with two glass types after 11 years of outdoor exposure under the mediterranean climatic conditions. Sustain. Energy Technol. Assess. 49, 101771.

Belmont, J., Olakonu, K., Kuitche, J., TamizhMani, G., 2014. Degradation rate evaluation of 26-year-old 200 kW power plant in a hot-dry desert climate. In: 2014 IEEE 40th Photovoltaic Specialist Conference. PVSC, IEEE, pp. 3162–3166.

Bosco, N., Moffitt, S., Schelhas, L.T., 2019. Mechanisms of adhesion degradation at the photovoltiac module's cell metallization-encapsulant interface. Prog. Photovolt., Res. Appl. 27 (4), 340–345.

Buerhop, C., Schlegel, D., Niess, M., Vodermayer, C., Weißmann, R., Brabec, C., 2012. Reliability of IR-imaging of PV-plants under operating conditions. Sol. Energy Mater. Sol. Cells 107, 154–164.

Curcio, J.A., Petty, C.C., 1951. The near infrared absorption spectrum of liquid water. JOSA 41 (5), 302–304.

Dang, D.N., Le Viet, T., Takano, H., Duc, T.N., 2023. Estimating parameters of photovoltaic modules based on current–voltage characteristics at operating conditions. Energy Rep. 9, 18–26.

De Rooij, A., 1989. The oxidation of silver by atomic oxygen. ESA J. 13 (4), 363–382.

Dhimish, M., Ahmad, A., Tyrrell, A.M., 2022. Inequalities in photovoltaics modules reliability: From packaging to PV installation site. Renew. Energy 192, 805–814.

Dupré, O., Vaillon, R., Green, M.A., 2015. Physics of the temperature coefficients of solar cells. Sol. Energy Mater. Sol. Cells 140, 92–100.

Eder, G.C., Voronko, Y., Dimitriadis, S., Knöbl, K., Újvári, G., Berger, K.A., Halwachs, M., Neumaier, L., Hirschl, C., 2018. Climate specific accelerated ageing tests and evaluation of ageing induced electrical, physical, and chemical changes. Prog. Photovolt., Res. Appl..

El Hammoumi, A., Chtita, S., Motahhir, S., El Ghzizal, A., 2022. Solar PV energy: From material to use, and the most commonly used techniques to maximize the power output of PV systems: A focus on solar trackers and floating solar panels. Energy Rep. 8, 11992–12010.

Evans, D., Florschuetz, L., 1978. Terrestrial concentrating photovoltaic power system studies. Sol. Energy 20 (1), 37–43.

Friesen, G., Herrmann, W., Belluardo, G., Herteleer, B., 2018. Photovoltaic Module Energy Yield Measurements: Existing Approaches and Best Practice. Report IEA-PVPS T13-11 2018, pp. 25–26.

Göpferich, A., 1996. Mechanisms of polymer degradation and erosion. Biomaterials 17 (2), 103–114.

Green, M.A., 2003. General temperature dependence of solar cell performance and implications for device modelling. Prog. Photovolt. Res. Appl 11 (5), 333–340.

Grossetête, T., Rivaton, A., Gardette, J., Hoyle, C.E., Ziemer, M., Fagerburg, D., Clauberg, H., 2000. Photochemical degradation of poly (ethylene terephthalate)-modified copolymer. Polymer 41 (10), 3541–3554.

Hacke, P.L., Kempe, M.D., Wohlgemuth, J., Li, J., Shen, Y.-C., 2018. Potential-Induced Degradation-Delamination Mode in Crystalline Silicon Modules. National Renewable Energy Lab.(NREL), Golden, CO (United States).

Hacke, P., Owen-Bellini, M., Kempe, M., Miller, D.C., Tanahashi, T., Sakurai, K., Gambogi, W.J., Trout, J.T., Felder, T.C., Choudhury, K.R., 2019. Combined and sequential accelerated stress testing for derisking photovoltaic modules. In: Advanced Micro-and Nanomaterials for Photovoltaics. Elsevier, pp. 279–313.

Halwachs, M., Neumaier, L., Vollert, N., Maul, L., Dimitriadis, S., Voronko, Y., Eder, G., Omazic, A., Mühleisen, W., Hirschl, C., 2019. Statistical evaluation of PV system performance and failure data among different climate zones. Renew. Energy 139, 1040–1060.

Herrmann, W., Eder, G., Farnung, B., Friesen, G., Köntges, M., Kubicek, B., Kunz, O., Liu, H., Parlevliet, D., Tsanakas, I., 2021. Qualification of photovoltaic (pv) power plants using mobile test equipment. In: IEA-PVPS T13-24: 2021.

Holman, Z.C., Descoeudres, A., Barraud, L., Fernandez, F.Z., Seif, J.P., De Wolf, S., Ballif, C., 2012. Current losses at the front of silicon heterojunction solar cells. IEEE J. Photovolt. 2 (1), 7–15.

IEA-PVPS, 2021. International Energy Agency. 2021 Snapshot of global PV markets - task 1: strategic PV analysis and outreach.

Jahn, U., Herz, M., Köntges, M., Parlevliet, D., Paggi, M., Tsanakas, I., 2018. Review on Infrared and Electroluminescence Imaging for PV Field Applications: International Energy Agency Photovoltaic Power Systems Programme: IEA PVPS Task 13. Subtask 3.3: report IEA-PVPS T13-12: 2018, International Energy Agency.

Jordan, D.C., Kurtz, S.R., 2013. Photovoltaic degradation rates—an analytical review. Prog. Photovolt., Res. Appl. 21 (1), 12–29.

Jordan, D.C., Wohlgemuth, J.H., Kurtz, S.R., 2012. Technology and Climate Trends in PV Module Degradation. National Renewable Energy Lab.(NREL), Golden, CO (United States).

Kaaya, I., Ascencio-Vásquez, J., Weiss, K.-A., Topič, M., 2021. Assessment of uncertainties and variations in PV modules degradation rates and lifetime predictions using physical models. Sol. Energy 218, 354–367.

Kazem, H.A., Chaichan, M.T., Al-Waeli, A.H., Sopian, K., 2020. Evaluation of aging and performance of grid-connected photovoltaic system Northern Oman: Seven years' experimental study. Sol. Energy 207, 1247–1258.

Köntges, M., Kurtz, S., Packard, C., Jahn, U., Berger, K.A., Kato, K., Friesen, T., Liu, H., Van Iseghem, M., Wohlgemuth, J., 2014. Review of failures of photovoltaic modules.

Köntges, M., Oreski, G., Jahn, U., Herz, M., Hacke, P., Weiß, K.-A., 2017. Assessment of Photovoltaic Module Failures in the Field: International Energy Agency Photovoltaic Power Systems Programme: IEA PVPS Task 13. Subtask 3: Report IEA-PVPS T13-09: 2017, International Energy Agency.

Kumar, S., Meena, R., Gupta, R., 2019. Imaging and micro-structural characterization of moisture induced degradation in crystalline silicon photovoltaic modules. Sol. Energy 194, 903–912.

Kurtz, S., Repins, I.L., Hacke, P.L., Jordan, D., Kempe, M.D., Whitfield, K., Phillips, N., Sample, T., Monokroussos, C., Hsi, E., 2017. Qualification Testing Versus Quantitative Reliability Testing of PV-Gaining Confidence in a Rapidly Changing Technology. National Renewable Energy Lab.(NREL), Golden, CO (United States).

Liu, Z., Castillo, M.L., Youssef, A., Serdy, J.G., Watts, A., Schmid, C., Kurtz, S., Peters, I.M., Buonassisi, T., 2019. Quantitative analysis of degradation mechanisms in 30-year-old PV modules. Sol. Energy Mater. Sol. Cells 200, 110019.

Mason, J.D., Cone, M.T., Fry, E.S., 2016. Ultraviolet (250–550 nm) absorption spectrum of pure water. Appl. Opt. 55 (25), 7163–7172.

McMahon, T., 2004. Accelerated testing and failure of thin-film PV modules. Prog. Photovolt., Res. Appl. 12 (2–3), 235–248.

Moore, W.M., Codella, P.J., 1988. Oxidation of silver films by atomic oxygen. J. Phys. Chem. 92 (15), 4421–4426.

Nakano, M., Fujiwara, T., Koga, N., 2016. Thermal decomposition of silver acetate: physico-geometrical kinetic features and formation of silver nanoparticles. J. Phys. Chem. C 120 (16), 8841–8854.

Oh, W., Bae, S., Kim, S., Park, N., Chan, S.-I., Choi, H., Hwang, H., Kim, D., 2019. Analysis of degradation in 25-year-old field-aged crystalline silicon solar cells. Microelectron. Reliab. 100, 113392.
Ohdaira, K., Akitomi, M., Chiba, Y., Masuda, A., 2023. Potential-induced degradation of n-type front-emitter crystalline silicon photovoltaic modules—Comparison between indoor and outdoor test results. Sol. Energy Mater. Sol. Cells 249, 112038.
Oreski, G., Mihaljevic, A., Voronko, Y., Eder, G.C., 2017. Acetic acid permeation through photovoltaic backsheets: Influence of the composition on the permeation rate. Polym. Test. 60, 374–380.
Osterwald, C., McMahon, T., 2009. History of accelerated and qualification testing of terrestrial photovoltaic modules: A literature review. Prog. Photovolt., Res. Appl. 17 (1), 11–33.
Papargyri, L., Theristis, M., Kubicek, B., Krametz, T., Mayr, C., Papanastasiou, P., Georghiou, G.E., 2020. Modelling and experimental investigations of microcracks in crystalline silicon photovoltaics: A review. Renew. Energy 145, 2387–2408.
Peike, C., Hoffmann, S., Hülsmann, P., Thaidigsmann, B., Weiß, K., Koehl, M., Bentz, P., 2013. Origin of damp-heat induced cell degradation. Sol. Energy Mater. Sol. Cells 116, 49–54.
Pern, F., 1993. Luminescence and absorption characterization of ethylene-vinyl acetate encapsulant for PV modules before and after weathering degradation. Polym. Degrad. Stab. 41 (2), 125–139.
Potthoff, T., Bothe, K., Eitner, U., Hinken, D., Köntges, M., 2010. Detection of the voltage distribution in photovoltaic modules by electroluminescence imaging. Prog. Photovolt. Res. Appl 18 (2), 100–106.
Segbefia, O.K., Akhtar, N., Sætre, T.O., 2022. The effect of moisture ingress on titania antireflection coatings in field-aged photovoltaic modules. In: 2022 IEEE 49th Photovoltaics Specialists Conference. PVSC, IEEE, pp. 1237–1244.
Segbefia, O.K., Imenes, A.G., Burud, I., Sætre, T.O., 2021a. Temperature profiles of field-aged multicrystalline silicon photovoltaic modules affected by microcracks. In: 2021 IEEE 48th Photovoltaic Specialists Conference. PVSC, IEEE, pp. 0001–0006.
Segbefia, O.K., Imenes, A.G., Saetre, T.O., 2020. Outdoor fault diagnosis of field-aged multicrystalline silicon solar modules. In: 37th EU PVSEC.
Segbefia, O.K., Imenes, A.G., Sætre, T.O., 2021b. Moisture ingress in photovoltaic modules: A review. Sol. Energy 224, 889–906.
Segbefia, O.K., Paudyal, B.R., Burud, I., Sætre, T.O., 2021c. Temperature coefficients of photovoltaic modules under partial shading conditions. In: 38th EU PVSEC. pp. 1180–1186.
Segbefia, O.K., Sætre, T.O., 2022. Investigation of the temperature sensitivity of 20-years old field-aged photovoltaic panels affected by potential induced degradation. Energies 15 (11), 3865.
Sinha, A., Sastry, O., Gupta, R., 2016. Nondestructive characterization of encapsulant discoloration effects in crystalline-silicon PV modules. Sol. Energy Mater. Sol. Cells 155, 234–242.
Skoplaki, E., Palyvos, J.A., 2009. On the temperature dependence of photovoltaic module electrical performance: A review of efficiency/power correlations. Sol. Energy 83 (5), 614–624.
Soto, E.A., Arakawa, K., Bosman, L.B., 2022. Identification of target market transformation efforts for solar energy adoption. Energy Rep. 8, 3306–3322.
Tracy, J., D'hooge, D.R., Bosco, N., Delgado, C., Dauskardt, R., 2018. Evaluating and predicting molecular mechanisms of adhesive degradation during field and accelerated aging of photovoltaic modules. Prog. Photovolt., Res. Appl. 26 (12), 981–993.
Trout, T.J., Gambogi, W., Felder, T., Choudhury, K., Garreau-Iles, L., Heta, Y., Stika, K., 2017. PV Module Durability-connecting field results, accelerated testing, and materials. In: 2017 IEEE 44th Photovoltaic Specialist Conference. PVSC, IEEE, pp. 2312–2317.
Tsanakas, J.A., Ha, L., Buerhop, C., 2016. Faults and infrared thermographic diagnosis in operating c-Si photovoltaic modules: A review of research and future challenges. Renew. Sust. Energ. Rev. 62, 695–709.
Våland, T., Bartholdsen, W., Ottestad, M., Våge, M., 1997. Grimstad Renewable Energy Park. Agder University College, NO-4878 Grimstad, Norway. http://ieahia.org/pdfs/grimstad.pdf.
Verma, D., Tayyib, M., Saetre, T.O., Midtgård, O.-M., 2012. Outdoor performance of 10 year old a-Si and poly-Si modules in southern Norway conditions. In: 2012 38th IEEE Photovoltaic Specialists Conference. IEEE, pp. 002368–002371.
Virtuani, A., Caccivio, M., Annigoni, E., Friesen, G., Chianese, D., Ballif, C., Sample, T., 2019. 35 Years of photovoltaics: Analysis of the TISO-10-kW solar plant, lessons learnt in safety and performance—[part] 1. Progr. Photovolt. Res. Appl. 27 (4), 328–339.
Willmott, C.J., Feddema, J.J., 1992. A more rational climatic moisture index. Prof. Geogr. 44 (1), 84–88.
Wohlgemuth, J., Silverman, T., Miller, D.C., McNutt, P., Kempe, M., Deceglie, M., 2015. Evaluation of PV module field performance. In: 2015 IEEE 42nd Photovoltaic Specialist Conference. PVSC, IEEE, pp. 1–7.
Zheludkevich, M., Gusakov, A., Voropaev, A., Vecher, A., Kozyrski, E., Raspopov, S., 2004. Oxidation of silver by atomic oxygen. Oxid. Met. 61 (1), 39–48.

Paper B

Moisture ingress in photovoltaic modules: A review by O.K. Segbefia, A.G. Imenes, and T.O. Saetre. Published in Solar Energy (2021).

Solar Energy 224 (2021) 889–906

Contents lists available at ScienceDirect

Solar Energy

journal homepage: www.elsevier.com/locate/solener

Moisture ingress in photovoltaic modules: A review

Oscar Kwame Segbefia *, Anne Gerd Imenes, Tor Oskar Sætre

Department of Engineering Sciences, University of Agder, 4879 Grimstad, Norway

ARTICLE INFO

Keywords:
Moisture ingress
Diffusivity
Permeation
Encapsulation
Edge seal
Acetic acid

ABSTRACT

Moisture ingress in photovoltaic (PV) modules is the core of most degradation mechanisms that lead to PV module power degradation. Moisture in EVA encapsulant can lead to metal grids corrosion, delamination and discolouration of encapsulants, potential induced degradation, optical and adhesion losses. The present work is a review of literature on the causes, effects, detection, and mitigation techniques of moisture ingress in PV modules. Literature highlights on determining the diffusivity, solubility, and permeability of polymeric components of PV modules via water vapour transmission rate tests, gravimetric, and immersion methods, have been presented. Electroluminescence, photoluminescence, and ultraviolet fluorescence spectroscopy, as well as dark lock-in thermography are some techniques used to detect moisture ingress in modules. Encapsulants with excellent moisture barrier and adhesion characteristics, desiccant-stacked polyisobutylene sealants, imbedded moisture sensors, and PV designs with/without breathable backsheets are ways of preventing/detecting moisture ingression in PV modules. Areas of focus for future research activities have also been discussed.

1. Introduction

Durability and reliability of field installed photovoltaic (PV) modules over their useful lifetime of ca. 25 years (35 years proposed) with optimal energy output of not less than 80% of their rated capacity is one of the foremost concerns for all parties in the photovoltaic business (Köntges et al., 2014; Wohlgemuth et al., 2015). The long-term reliability of PV modules can be studied more accurately from the degradation mechanisms and the fault modes associated with PV modules in natural field operating conditions (Halwachs et al., 2019; Santhakumari and Sagar, 2019). This is because performance degradation of modules during real operating conditions are directly related to the environmental and climatic factors of the geographical area within which modules are deployed (Lyu et al., 2020). These degradation and reliability issues are in the form of solar cell metal grids corrosion (Asadpour et al., 2019; Peike et al., 2012), glass/antireflection coating

Abbreviations: A, preexponential factor; AES, Auger Electron Spectroscopy; AFM, atomic force microscopy; AR, antireflection coating; C Sensor, capacitance embedded sensor; C, carbon; Ca, calcium; CIGS, copper indium gallium selenide; c-Si, crystalline silicon; D, diffusivity; D_0, diffusion coefficient at infinity time; DH, damp heat; DLIT, dark lock-in thermography; DMA, dynamic mechanical analysis; DSC, differential scanning calorimetry; DVS, dynamic vapor sorption; E, Young's modulus; E_a, activation energy; E_D, activation energy for diffusivity; EDS, energy dispersive spectroscopy; EDX, energy-dispersive X-ray spectroscopy; EL, electroluminescence spectroscopy; E_p, activation energy for permeability; E_s, activation energy for solubility; ETFE, Ethylene tetrafluoroethylene; EVA, ethylene vinyl acetate; F, diffusion flux; FEM, finite element methods; FTIR, Fourier transform infrared spectroscopy; FTIR, fourier transform infrared spectroscopy; GC/MS, thermal desorption gas chromatography/mass spectrometry; GWFID, gas chromatography/flame ionization detection; HF, humidity freeze; IEC, International Electrotechnical Commission; I_{sc}, short circuit current; I-V, current-voltage; k, Boltzmann constant; *l*, layer thickness; LIT, lock-in thermography; mc, multicrystalline; MI, moisture ingress; N, nitrogen; n, number of samples; NIR, near infrared; NREL, National Renewable Energy Laboratory; O, oxygen; OTR, oxygen transmission rate; P, permeability; P_0, permeability constant; PA, polyamide; PCTFE, polychlorotrifluoroethylene; PDMS, polydimethylsiloxane; PET, polyethylene terephthalate; PIB, polyisobutylene; PID, potential induced degradation; PL, photoluminescence spectroscopy; POE, polyolefin elastomer; PPE, PVDF/PET/EVA; PV, photovoltaics; PVB, polyvinyl butyral; PVDF, polyvinylidene fluoride; PVF, polyvinyl fluoride; R, gas constant; RFID, radio-frequency identification; RH, relative humidity; S, solubility; S_0, solubility constant; SC, solar cell; SEM, scanning electron microscopy; SEM-EDS/EDX, scanning electron microscopy-energy dispersive (X-ray) spectroscopy; SOCT, spectroscopic optical coherence tomography; T, temperature; TC, temperature cycling; T_g, glass transition temperature; TGA, thermo-gravimetric analysis; TM, melting temperature; TPO, thermoplastic polyolefin elastomer; TPSE, thermoplastic silicone elastomer; TPT, Tedlar®/PET/Tedlar®; T_{TTF}, test-to-failure; UV, ultraviolet; UV-F, ultraviolet fluorescence spectroscopy; VA, vinyl acetate; V_{oc}, open circuit voltage; W_p, peak watt; WVTR, water vapour transmission rate; XPS, X-ray photoelectron spectroscopy.

* Corresponding author.
E-mail addresses: oscar.k.segbefia@uia.no (O.K. Segbefia), anne.g.imenes@uia.no (A.G. Imenes), tor.satre@uia.no (T.O. Sætre).

https://doi.org/10.1016/j.solener.2021.06.055
Received 30 October 2020; Received in revised form 14 June 2021; Accepted 21 June 2021
Available online 28 June 2021

(AR) degradation (Kudriavtsev et al., 2019), delamination (Kempe et al., 2014) and discolouration (La Mantia et al., 2016; Oreski and Wallner, 2005; Tracy et al., 2018) of encapsulants, solar cell degradation (Adams et al., 2015; Peike et al., 2012), potential induced degradation (PID) (Hacke et al., 2016; Mon et al., 1985; Virtuani et al., 2019a), interface adhesion losses (Bosco et al., 2019; Tracy et al., 2018), optical losses (McIntosh et al., 2011), and solder bond degradation (Asadpour et al., 2019; Kim et al., 2013). An overview of these failure mechanisms is shown in Fig. 1.

One of the major factors than links climatic conditions to module degradation is moisture ingress (Hülsmann and Weiss, 2015; Jankovec et al., 2016; KEMPE, 2006; Mon et al., 1985). This is true for environments with high humidity and temperature (Hülsmann et al., 2014; Schlothauer et al., 2012). According to Mon et al. (1985), moisture ingress together with ambient temperature play a vital role in determining the rate of many life-limiting processes such as corrosion and majority of materials deterioration in solar cells and modules. In addition to environmental and climatic factors, the properties of the polymeric materials and the module technology influence moisture ingress (KEMPE, 2006).

Usually, moisture ingress takes place through the polymeric materials, edges of the modules, and voids created by manufacturing, handling, and climatic stressors (Bosco et al., 2019; Crank, 1953; Han, 2020; Jankovec et al., 2018; Marais et al., 2001; Novoa et al., 2014). Once water comes into the PV module, the accumulated moisture within the module in the presence of other climatic stressors can lead to all forms of degradation modes in PV module's components and other packaging materials (Ballif et al., 2014; Kudriavtsev et al., 2019; Wohlgemuth and Kempe, 2013). The most common of these defects and failure modes are shown in Fig. 1. Fig. 2 shows an example of a PV module affected by moisture ingress.

The Fickian laws of diffusion are good model that forecasts moisture diffusion into encapsulation materials, and based on the water vapour transmission rate (WVTR) parameters determined experimentally, the moisture or gaseous barrier quality of a polymeric material could be predicted (Dadaniya and Datla, 2019; Oreski et al., 2017). Polymeric material here does not refer to organic or polymer-based PV devices. WVTR is the amount of water molecules that penetrates a given strip of encapsulant in a given time frame. This concept will be explained further in Section 4.1.

When it comes to testing moisture ingress reliability of PV modules, the common tests are damp heat test (DH), humidity freeze test (HF), and thermal cycling test (TC). These tests at times have negative impact

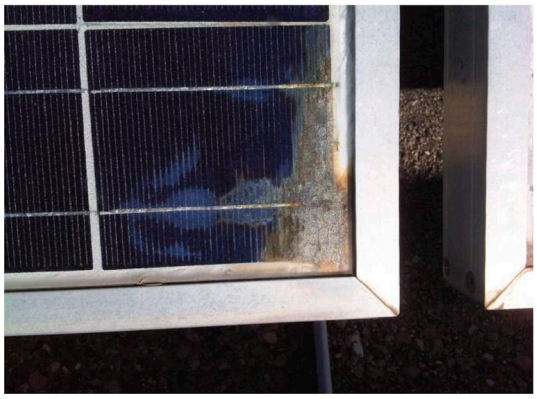

Fig. 2. A typical moisture ingressed PV module showing signs of corroded metal grids, delamination and discolouration of encapsulants. .
Adapted from Wohlgemuth et al. (2015)

on the test modules (Bosco et al., 2019; Eder et al., 2019; Lyu et al., 2020). Damp heat and humidity freeze tests sometimes predispose the polymeric components of the module to moisture ingress at elevated temperatures, reduces the optical properties of the module, and leads to the formation of acetic acid within the ethylene–vinyl acetate (EVA) encapsulant. Acetic acid accumulation in PV modules is a major precursor for interconnect corrosion in solar cells and modules (Eder et al., 2019; Kempe et al., 2007; Kim et al., 2013; Oreski et al., 2019). TC can induce thermomechanical stresses that can promote loss of adhesion at the encapsulant/PV-cell interfaces, cracks in solar cells, and other material induced degradations which also influence moisture ingress (Annigoni et al., 2015; Bosco et al., 2019; Tracy et al., 2018).

To this effect, several research groups across the globe in the field of photovoltaics are focused on PV reliability and durability studies (Halwachs et al., 2019; Köntges et al., 2014). Most of these investigations are focused on the performance monitoring, operation, and maintenance of PV plants (Annigoni et al., 2015; Eder et al., 2019). Even though there is yet to be any formal working documents on moisture ingress reliability of PV modules (Lyu et al., 2020), there have been a lot of work that have been done in this respect over the past decades (Dadaniya and Datla, 2019; KEMPE, 2006; Kumar et al., 2019; Mitterhofer et al., 2020; Annigoni et al., 2015; Jankovec et al., 2018). A collection of these works is represented in Fig. 3.

In 1953, Crank (1953) published an article on the diffusion in

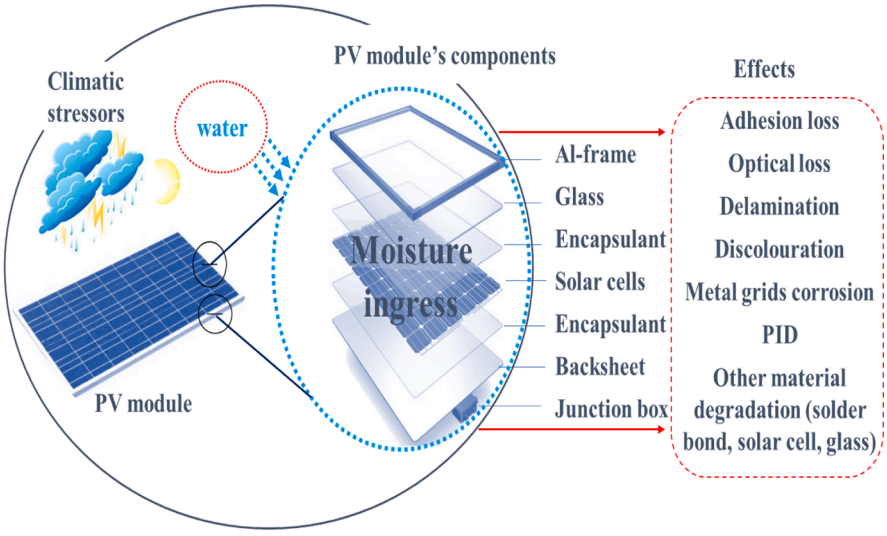

Fig. 1. Defects and failure modes associated with moisture ingress in PV devices. Under environmental and/or climatic stressors (e.g., high humidity, temperature, and UV radiation), PV modules can suffer from moisture ingress which can lead to PV module degradation.

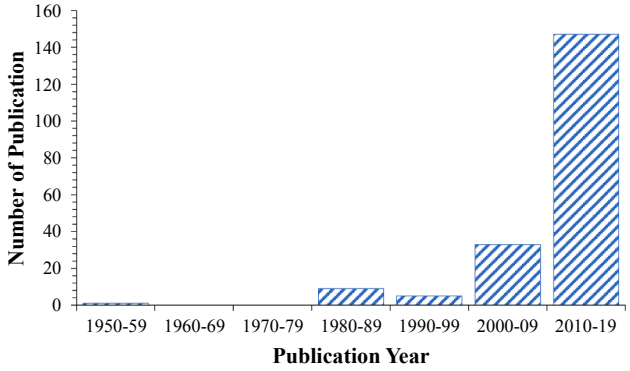

Fig. 3. Histogram of 195 published articles related to moisture ingress in PV devices. Data grouped into clusters based on the years of publication. The figure shows an exponential rise in the number of published articles related to moisture ingress in PV modules from the 1950s to 2019.

polymers due to their structure and stresses they are exposed to. Though it was not directly related to PV applications, it served as a foundation for investigating this phenomenon in PV devices as they are also made with polymeric materials. Since then, it took three decades for Mon et al. (1985) to publish an article on the "effect of temperature and moisture on module leakage currents" which marked the beginning of well-tailored research into the effect of moisture ingress in PV modules. However, for the past three decades more research attention is attached to this phenomenon, as illustrated in Fig. 3. The articles used for this review are obtain via the Scopus Document Download Manager using the word string: (*"moisture ingress" OR moisture AND photovoltaic OR solar AND module OR panel*) together with Google Scholar searches by using the phrase "*moisture ingress in photovoltaic modules*". The search flowchart is illustrated in Fig. 4. Articles published after 2019 are excluded from Fig. 3 to minimize challenge of benchmarking associated with new article publication process (Haustein et al., 2015). The results were further refined using research subject area, themes, and keywords, and a combination of analytical techniques to arrive at the most relevant articles for the purpose of this review. This was done with reference to the guideline proposed by Moher et al. (2009).

In literature, there are reviews on the general degradation mechanisms of PV devices (Halwachs et al., 2019; Jordan and Kurtz, 2013; Köntges et al., 2014; Santhakumari and Sagar, 2019), PV polymeric materials (de Oliveira et al., 2018; Omazic et al., 2019), and moisture ingress into polymeric films and coatings (Han and Kim, 2017; Van der Wel and Adan, 1999). However, to the best of our knowledge, there is yet to be a dedicated review article on moisture ingress in PV modules to guide further research work in this area.

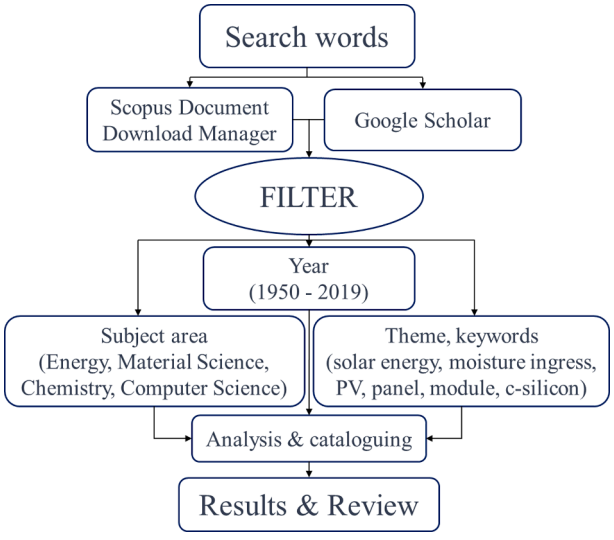

Fig. 4. Search flowchart for collecting relevant articles for this review.

The aim of this work is to reconcile the literature on moisture ingress regarding crystalline silicon (c-Si) PV modules. The effects, mechanism, and the predisposing factors of moisture ingress are presented and discussed, in that order. Test methods for assessing the moisture barrier propensity of PV encapsulants and diagnosing moisture ingressed PV modules are also examined. Finally, the mitigation techniques for moisture ingress in PV modules are discussed. It is anticipated that the present work thoroughly organizes the existing knowledge across the reported literature cogently and in an accessible way to serve as a guide for future work on moisture ingress in PV modules.

2. Components of crystalline silicon photovoltaic modules

Crystalline silicon (c-Si) PV modules usually consist of a superstrate solar glass covering, a polymeric encapsulating layer, silicon solar cells, a substrate polymeric backsheet material, aluminum frame, junction boxes, and other materials such as solder bonds, edge sealants and dielectric coating (de Oliveira et al., 2018; Omazic et al., 2019), see Fig. 1. These components, especially the polymeric elements of PV modules play vital roles in the durability and reliability of these devices (Peike et al., 2013b). Polymeric materials among other functions ensure optical coupling, electrical and physical insulation, give mechanical support and cohesion, serve as ancillary electrical connectors, and offer protection against climatic and environmental weathering (Peike et al., 2013b; Yang et al., 2020; Yang, 2019).

In order to perform these functions optimally, encapsulants are required to have high transparency, high resistance to UV degradation, and high adhesion characteristics (Cheacharoen et al., 2018; Lyu et al., 2020; Pern, 2008). In addition, encapsulants are expected to be cost-effective and environmentally benign (Lyu et al., 2020; Pern, 2008). For that matter, there are several material indicators that are evaluated when considering encapsulating materials for PV modules' applications (Peike et al., 2013b; Yang, 2019), some are listed in Table 1. Some of the methods that can be used to determine or characterize each encapsulant parameter (including differential scanning calorimetry- DSC, dynamic mechanical analysis- DMA, and dynamic multimode spectroscopy- DMS) are also highlighted in Table 1.

In addition to the optical transparency and glass transition temperature of the polymeric encapsulant under consideration, the electrical and mechanical properties are equally vital to ensure electrical insulation and resilience to mechanical and climatic stressors (Yang, 2019). Usually, a common limiting factor for modules' reliability and durability is the diffusion properties of PV encapsulation materials (Kempe et al., 2014; Lyu et al., 2020; Pern, 2008; Yang et al., 2020).

Encapsulation polymeric materials can either be thermoplastic or elastomeric in nature. The thermoplastics do not form cross-linked chemical bonds upon melting during processing, while the elastomers

Table 1
Some properties of PV module encapsulation materials and their means of evaluation.

Parameter	Technique	Importance
Diffusivity (WVTR/ OTR) (D)	Permeation, gravimetry	Moisture or gaseous barrier quality
Refractive index (η)	Refractometry	Optimizes optical efficiency
Volume resistivity (ρ_v)	Resistivity test	Electrical insulation
Glass transition temperature (T_g)	DSC, DMA, etc.	Reliability over the temperature range of application
Young's modulus (E)	DMA, tensile testing, etc.	Minimize mechanical stress on cells
Melting temperature (T_M)	DSC, DMS, etc.	Processing feasibility
Absorptivity (α)	FTIR spectroscopy	Optimizes optical efficiency

form cross-linked covalent bonds under high temperature, UV, or chemical processing conditions (Peike et al., 2013b). The cross-linking process improves on the mechanical, chemical, and electrical properties of these materials (Berghold et al., 2014).

Some of the popular encapsulation materials that are used for PV applications are listed in Table 2. Among these encapsulation materials are ethylene vinyl acetate (EVA), ionomer, polyvinyl butyral (PVB), silicone rubber (e.g. polydimethylsiloxane, PDMS), thermoplastic silicone elastomer (TPSE), polyolefin elastomer (POE), thermoplastic polyolefin elastomer (TPO), polyethylene terephthalate (PET), polyamide (PA), polyvinyl fluoride (PVF) or Tedlar®, polyvinylidene fluoride (PVDF) or Kynar®, ethylene tetrafluoroethylene (ETFE) or Halar®, and polychlorotrifluoroethylene (PCTFE) or Xylan® (Peike et al., 2013b; Yang, 2019).

The first encapsulation material used in the early days of PV industry was polydimethylsiloxane (PDMS) (Yang, 2019). However, the search for cost-effective encapsulants with optimal properties to meet the new dynamics of the PV applications has opened up the market for other encapsulants such as EVA, a dominant material in the PV market for decades (Peike et al., 2013b; Yang et al., 2020). This is because the choice of encapsulants are mostly based on trade-offs between material properties and cost (Yang, 2019). EVA encapsulants are cost-effective, and in addition, have high optical efficiency, good adhesion properties, high glass transition temperature, and optimal resistance to other climatic stressors (Novoa et al., 2016; Pern, 2008).

Backsheets are typically comprised of three main layers: a weathering resistant outer layer, an electrically insulating inner core layer, and an adhesion promoting cell side layer and can be used together with any suitable front encapsulation (Lyu et al., 2020), see Table 3. Fluoropolymer based backsheets are more common and takes up to 80% of the market base (Oreski, 2019). However, the non-fluoro-polymer based ones are slowly making their way into the market space. PET based backsheets have been mostly used for commercial PV module production over the years. These multilayered backsheets are thought to be cost-effective and have superior inter-layer adhesion properties, which are most suitable for outdoor PV applications (Oreski et al., 2019).

However, some commercial PA-based backsheets are susceptible to unexpected degradation (e.g. cracking) after a few years of outdoor exposure (Eder et al., 2019). These physico-chemical degradation processes largely depend on temperature, moisture (humidity), and UV irradiation (Han, 2020). This is because during field operation, PV modules under these climatic and environmental stressors are exposed to moisture and vaporous ingress, a precursor for most degradation mechanisms (KEMPE, 2006; Annigoni et al., 2015; Jankovec et al., 2018).

Table 2
. Properties of some PV module front encapsulation materials (Berghold et al., 2014; Peike et al., 2013b).

Polymer	Polymer class	Parameter			
		D [g/m^2/d]	η	T_g [℃]	ρ_v @ 23 ℃ [Ωcm]
EVA	Elastomer	8.38	1.48 to	−40 to	10^{14} to
Silicone		9 to 68	1.49	−34	10^{15}
rubber (eg.			1.38 to	−120 to	10^{14} to
PDMS)			1.58	−50	10^{15}
PVB	Thermoplastic	19.26	1.48	+12 to	10^{10} to
Ionomer		0.31	1.49	+ 20	10^{12}
				+40 to	10^{16}
				+ 50	
TPSE	Thermoplastic	38.50	1.42	−100 to	10^{16} to
TPO	elastomer	0.89	1.48	−5	10^{17}
				−60 to	10^{14} to
				−40	10^{18}

Table 3
Some commercially available backsheet designs. PVF is Tedlar®, PVDF is Kynar®, coating (C) is fluoro-polymer coating (e.g., Kynar, Xylan coatings). New backsheet designs substitute cell side EVA layer with olefins such as POE and TPO. The choice of a backsheet is independent of the front encapsulant chosen, and a backsheet could be a polymer or a combination of polymers.

Backsheet Design	TPT	TPE	KPK	KPE	PPE	KPC	PPC
Outer Layer (~100 μm)	PVF	PVF	PVDF	PVDF	PET	PVDF	PET
Inner core layer (~125 μm)	PET	PET	PET	PET	PET	PET	PET
Cell side layer (~30 μm)	PVF	EVA	PVDF	EVA	EVA	coating	coating

3. Moisture ingress in photovoltaic modules

Polymeric encapsulants and backsheets are important in PV modules because of the various functions they perform (Czanderna and Pern, 1996; Omazic et al., 2019; Peike et al., 2013b; de Oliveira et al., 2018; Pern, 2008; Yang, 2019). However, these polymeric components (as shown in Fig. 1) are not perfectly air-/water- tight, and are prone to permeation of gases, including moisture, oxygen, and other gaseous species from the ambient surrounding (KEMPE, 2006; Yang et al., 2020). Some of the predisposing factors are the climatic conditions, the age of the modules, the materials used for the PV module (especially the polymeric materials), and the solar cell and module technology (Mitterhofer et al., 2020; Peike et al., 2013b; Tracy et al., 2018).

Moisture within the EVA layer in the presence of other climatic stressors (temperature and UV radiation) leads to the formation of acetic acid and its related degradation products which lead to corrosion of metal contacts, delamination and discolouration of encapsulants (La Mantia et al., 2016; Omazic et al., 2019; Oreski et al., 2017). It has been observed that delamination and discolouration at the edges of the PV module is most critical to power degradation and also a catalyst for other failure modes, including moisture ingress (Bosco et al., 2019; Kempe et al., 2014; Tracy et al., 2018). Moisture ingress can also affect the optical efficiency of the module (Hoffmann and Koehl, 2014; Kim et al., 2013; Kudriavtsev et al., 2019; Peshek et al., 2019; Yang, 2019).

Water vapour transmission rate, WVTR tests (the most popular) (KEMPE, 2006), gravimetric (Dadaniya and Datla, 2019), capacitance (Miyashita et al., 2012; Reese et al., 2011), and water immersion methods (Nagayama et al., 2020) are usually employed to determine the moisture barrier characteristics of PV encapsulants. Usually, parameters for these material properties are used together with climatic data to predict moisture ingress into PV modules using finite element methods (Jankovec et al., 2018; Wisniewski et al., 2019). Mitigation methods use encapsulants with low diffusivity and good adhesion properties, desiccant-stacked polyisobutylene sealants, and PV designs with/without breathable backsheets to prevent or delay moisture ingress into PV modules (Hardikar et al., 2014b; Kempe et al., 2018; Miyashita et al., 2012; Morita et al., 2015; Reese et al., 2011).

3.1. Effects of moisture ingress

3.1.1. Material degradation

The degradation of all PV components into various forms can be classified as material degradation. In EVA encapsulation, the adhesion promoter is the least stable additive and hence limits the longevity of EVA encapsulants (Köntges et al., 2014). The loss of adhesion between the solar cells, encapsulants, glass, and other active layers due to environmental, climatic, and/or artificial mechanical stressors results in delamination (Bosco et al., 2019; Tracy et al., 2018; Yang, 2019). This can occur prior and/or after moisture ingress and can account for ≤4% loss in power output at a localized polymer/cell interface. However, the presence of delamination with its by-standing defects and failure modes

can lead to greater power losses in PV plants (Köntges et al., 2014).

Discolouration can also be a result of moisture ingress in PV modules (Han, 2020). Usually, the chemical reaction between moisture or gaseous species and encapsulation additives (including adhesion, UV, and thermal stabilizers) can lead to undesirable degradation products (Oreski et al., 2019; Tracy et al., 2018). In the field, these degradation products can take varying colouring forms depending on several complex reactions with moisture or gaseous species and UV radiation (Pern and Glick, 2000). Usually, discolouration can be detected with visual inspection, and can account for ca. 0.5% of the 0.8% power degradation per year for PV plants (Jordan and Kurtz, 2013). This loss is largely attributed to short circuit degradation (Jordan and Kurtz, 2013; Köntges et al., 2014). Fig. 5 shows some moisture ingress induced defects and fault modes of field-aged PV modules.

Delamination and discolouration cause optical performance losses (La Mantia et al., 2016), but of a greater concern is that they create voids within the module which serve as a suitable reservoir for moisture and gas accumulation (Yang, 2019). This can enhance the chances of corrosion of metal interconnects in modules and therefore may result in power loss (Peike et al., 2013a; Yang et al., 2020; Peike et al., 2012). Usually, these forms of material degradation are observed to occur around the cell interconnect ribbons and cell metallization (Hu and French, 2019), as in Fig. 5.

Particulate water trapped within encapsulants behaves as an optical barrier increasing absorption losses which has significant effect on the modules' quantum efficiency (Hoffmann and Koehl, 2014; Hülsmann et al., 2014; Peshek et al., 2019). For instance, Kudriavtsev et al. (2019) found a significant deterioration in the transmittance of a soda-lime glass sample after they were exposed to high humidity at 88 °C for two months. This optical loss can result in significant reduction in the quantum efficiency and therefore power output of the PV module. Using identical PV modules, McIntosh et al. (2011) investigated the effect of damp heat and UV ageing tests on the optical efficiency of EVA and silicone encapsulants by monitoring their absorption coefficients. After the damp heat test, they observed tiny absorption peaks within the 250–500 nm wavelength range which correlates to a drop in the PV module's efficiency of 0.39% and 0.14% for EVA and silicone encapsulants, respectively. In addition to the drop in the PV module's efficiency, the UV dose had insignificant effect on the absorption coefficients of both encapsulants.

In an earlier study, Vandyk et al. (2005) studied delamination induced degradation in a PV module over 30 months. They found that there was a small reversal in degradation during dryer periods of the year during their experiment. Hence, they concluded that the degradation in power was due to the presence of moisture in the delaminated regions of the module, as observed by increased series resistance with time. Also, Adams et al. (2015) believed that the presence of ingressed water at the hole extraction/active layer interface is the major denominator for PV device degradation.

The formation of acetic acid and its co-degradation products (such as lead acetate) in EVA encapsulants after prolonged damp heat tests have been observed and reported (Eder et al., 2019; Han, 2020; Kempe et al., 2007; Oreski et al., 2017, 2019). It is believed that the formation of these moisture assisted degradation products (and subsequent PV module material degradation) have direct correlation with extended exposure to high humidity, temperature and UV doses (Czanderna and Pern, 1996; de Oliveira et al., 2018; Omazic et al., 2019; Tracy et al., 2018; Wohlgemuth and Kempe, 2013).

3.1.2. Corrosion

Corrosion is the deterioration of materials due to reactions (chemical, electrochemical, physical, or physicochemical) with the environment. Traditionally, corrosion of metals occurs when there is an exchange of electrons between a metal and its environment. In the presence of oxygen and moisture, metals can experience electrochemical corrosion (Mon et al., 1985; Peshek et al., 2019; Tracy et al., 2018). Moreover, it is known that EVA produces acetic acid in the presence of moisture and other environmental stressors, which can lead to corrosion of metal grids and other components of PV modules (KEMPE, 2006; Kim et al., 2013; Oreski et al., 2017). Additionally, moisture ingress induces adhesion loss and creates voids in encapsulants and backsheets and therefore predisposes all components of the PV module to corrosion (Mon et al., 1985; Oreski and Wallner, 2005; Yang et al., 2020; Yang, 2019), see Fig. 5c.

Solar cell metal interconnect corrosion is known as a major cause for the overall module performance degradation (Annigoni et al., 2019; Bosco et al., 2019; Eder et al., 2019; Klemchuk et al., 1997; Virtuani et al., 2019b; Yang et al., 2020). Kim et al. (2013) studied three crystalline silicon PV modules under accelerated ageing conditions using I-V measurements, SEM-EDX, and Auger Electron Spectroscopy (AES) and found that the major effect of moisture ingress in PV modules is metal contact corrosion. Also, (Kraft et al., 2015) studied the corrosion of the screen-printed silver front-side contacts of silicon solar cells after damp heat test. They observed that the presence of acetic acid, a decomposition product of moisture ingressed EVA encapsulants, was responsible for the corrosion of the metal grids.

According to Peshek et al. (2019), the routes to corrosion are dominated by moisture ingress from the perimeter to the interior of the module. Earlier on, Jorgensen et al. (2006) studied the properties of module packaging materials, including moisture ingression, corrosion, and interfacial adhesion characteristics, under damp heat ageing conditions. They deposited an 80-nm-thick aluminum veneers onto a 100-cm^2 glass substrate and observed that the designs with the imbedded Al-glass laminates were effective in trapping deleterious species that catalyze moisture driven corrosion. These species they believed are low molecular weight PET fragments of carbonyl, carboxylic, and phenolic origins. Also, Wohlgemuth and Kempe (2013) performed series of damp heat tests on BP Solar modules to evaluate the effect of temperature and humidity on solar module degradation. They discovered that corrosion was the dominant degradation mechanism identified with the test

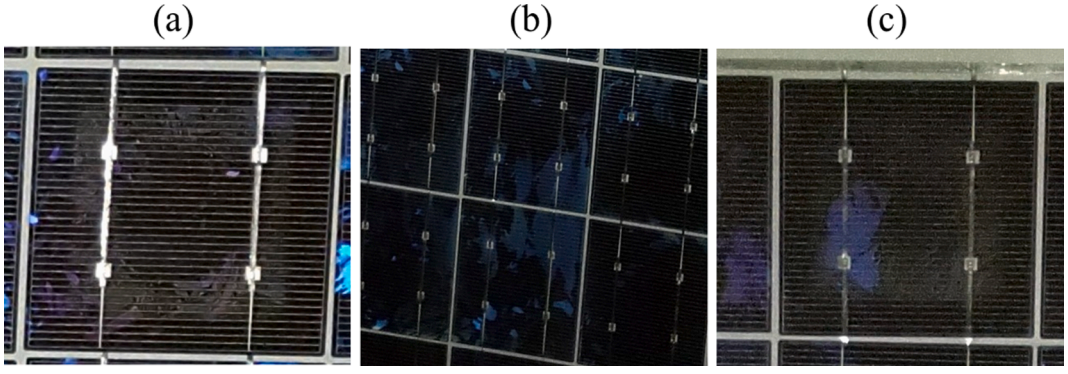

Fig. 5. (a) Delamination around solar cell edges, (b) discolouration of encapsulants, and (c) oxidation of metal grids as a result of moisture ingress.

modules. Later, Peike et al. (2013a) explored the origin of damp-heat induced cell degradation in c-Si PV modules under (80% / 80 °C and 80% / 90 °C RH) damp heat conditions using EL imaging and EDX. They concluded that the corrosion of the grids is the underlying cause for the degradation.

3.1.3. Potential induced degradation (PID)

PV modules are usually connected serially in grid-connected systems to increase voltage output and for safety purposes, modules frames are grounded. However, several factors can induce high potential difference between solar cells and the PV module frame due to electrochemical interactions (Carolus et al., 2019; Kwembur et al., 2020; Luo et al., 2017; Yamaguchi et al., 2020). Some of these factors include module encapsulation and design, solar cell's anti-reflection coating, PV system electrical topology and inverter type, environmental/climatic factors (such as humidity, temperature, UV radiation, soiling, etc.), and grounding conditions of the front glass (Carolus et al., 2019; Luo et al., 2017; Naumann et al., 2019). According to ongoing investigations, migration of sodium cations (Na^+) from the soda lime glass and/or the solar cell is responsible for the observed increased potential between the solar cell and module frame (Carolus et al., 2019; Kwembur et al., 2020). Fig. 6a shows the accumulation of Na^+ at the antireflection-silicon cell interfaces using time of flight (ToF) and secondary-ion mass spectrometry (SIMS). In a conventional multicrystalline silicon PV module, the possible conduits for leakage current from the module frame to the solar cells (or vice versa) are via the surface and bulk of the front glass and encapsulation (Luo et al., 2017; Yamaguchi et al., 2020). The electric potential difference lead to increased electrical conductivity and leakage currents from the solar cells to the module frame (or vice versa, depending on the state of the module in the string), which can lead to PID, and hence, power degradation (Carolus et al., 2019; Hacke et al., 2015; Hoffmann and Koehl, 2014; Luo et al., 2017; Mon et al., 1985; Naumann et al., 2019; Virtuani et al., 2019a).

It has been observed that humidity and temperature are the two most common environmental stressors that underpin PID which results in significant power degradation in PV modules (Kwembur et al., 2020; Luo et al., 2017; Naumann et al., 2019). High humidity and temperature drive moisture into PV modules and may lead to PID due to the electrochemical reactions of the antireflection coating and/or reduced bulk resistivity of the encapsulants (Fig. 6b and 5c) (Hacke et al., 2015; Luo et al., 2017; Pingel et al., 2010).

For instance, Hoffmann and Koehl (2014) in their experiment to explore the influence of temperature and humidity on the onset of PID using both indoor and outdoor exposures observed that humidity is the major denominator for the observed leakage current which causes PID. In another investigation, Hacke et al. (2015) employed accelerated degradation models (the Peck Equation and exponential models) to model temperature and humidity induced degradation in crystalline silicon solar modules. Their model was based on a semi-continuous statistical power degradation and leakage current data obtained via in-situ monitoring of modules undergoing PID in a climatic chamber. They found that the quantum of power transferred from the active cell circuit to the ground during the stress test has a linear correlation with time and the stress factors. Furthermore, Hacke et al. (2016) observed PID in cadmium telluride, CdTe PV modules after the modules were subjected to multiple stress factors. They concluded that the onset of the PID was as a result of moisture ingress.

Also, Virtuani et al. (2019a) in their investigation using sandwich structures with higher moisture barrier properties, found that limiting moisture ingress into the encapsulants helps in mitigating the incidence and impact of PID. In another work, Naumann et al. (2019) using damp heat test conditions (85 °C, 85% RH), found that moisture and soiling was the underlying cause for PID in test mini PV modules. According to Barth et al. (2019), moisture ingress is the major cause of PID, delamination and discolouration of encapsulants in PV modules.

In order to reduce the LCOE of PV projects, there are reports of PV plants operating at absolute voltages with at least 1000 V between the module frame and the solar cell, with a target of reaching maximum system voltage of ca. 1500 V (Carolus et al., 2019; Luo et al., 2017). This only indicates that the problem of PV module PID will be quite challenging with such high voltages going into the future. A critical review of PID in PV modules is given by Luo et al. (2017). Although mitigation techniques for the PID phenomenon at cell, module, and system levels have been proposed and demonstrated, these techniques are yet to be implemented commercially largely due to the complexity of PID (Carolus et al., 2019; Luo et al., 2017; Pingel et al., 2010). Also, the so-called PID-free modules may be susceptible to PID after long-term exposure to repeated mechanical stress and outdoor weathering which can cause microcracks and pinholes in the encapsulation. The increasing installations of floating PV power plants represent a challenge even for PID-free modules, as leakage currents increases with increasing localized humidity (Luo et al., 2017). This emphases the need for early-stage diagnostics of moisture ingress in PV plants.

3.2. Mechanism of moisture ingress

Moisture ingress refers to the diffusion of water molecules and other gaseous species (e.g., oxygen, nitrogen, carbon dioxide, etc.) into the interior of a PV module. Diffusion is initiated when water or gaseous molecules are adsorbed onto the surface of an encapsulant, and with an appropriate concentration gradient, are transported through and desorbed onto other components of the PV module (Kempe et al., 2014; Kim

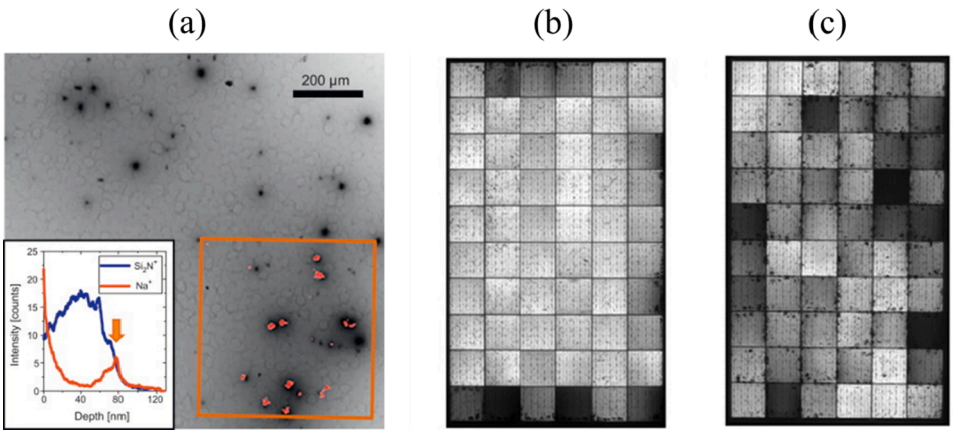

Fig. 6. (a) An EBIC image of a monocrystalline silicon solar cell acquired at an acceleration voltage of 30 kV showing a population of PID shunts. The insert is a ToF-SIMS image showing the distribution of Na^+ at the SiN_x-Si interface. Adapted from Naumann et al. (2014). (b)-(c) EL images of crystalline silicon PV modules after a high humidity and temperature (85 °C / 85% RH) PID tests. PID shunted solar cells turned dark. Adapted from Luo et al. (2017).

and Han, 2013). The process continues until equilibrium is established with the ambient humidity conditions as postulated by the Fickian laws (KEMPE, 2006), Eqs. (1)–(3). Fig. 7 is a scheme of moisture ingress phenomenon in PV modules. It illustrates the formation of photoproducts under the action of photons and formation of carboxylic acids in the presence of moisture in PV module. The diffused carboxylic acids and moisture initiate different degradation processes in the PV module (Grossetête et al., 2000; Kumar et al., 2019; Oreski et al., 2017).

Diffusion mechanisms could either be classified as Fickian or non-Fickian. Fickian diffusion models are those that obey the Fick's laws: Eqs. (1)–(3), otherwise, they are known as non-Fickian diffusion models (Kempe et al., 2018; Mitterhofer et al., 2020; Slapsak et al., 2019; Jankovec et al., 2018). According to Mitterhofer et al. (2020), the Fickian diffusion models can accurately model the behaviour of moisture or gaseous species across the interface, in channels and bulk of the polymeric material. However, in some special cases where the diffusion process is largely influenced by the channels within the polymeric material rather than the polymer bulk, the non-Fickian models such as dual transport models are more representative in modelling the profiles of the actual diffusion process (Slapsak et al., 2019; Jankovec et al., 2018).

The amount of moisture absorbed by a polymeric material depends on the temperature, concentration gradient, and also the material properties (Mitterhofer et al., 2020; Van der Wel and Adan, 1999). Some of the material properties that influence diffusion are polymer crystallinity, chemical morphology, polarity, free volume, voids in material, degree of cross-linking, ageing, and chemical additives (Mitterhofer et al., 2020).

It is believed that using materials of excellent moisture barrier properties is the best way to manage the challenge of moisture ingression into PV modules (KEMPE, 2006; Kempe et al., 2018). To this end, the diffusivity, permeability, and solubility properties of polymeric materials that are used for encapsulating PV modules are of greatest importance (Hülsmann and Weiss, 2015; Wisniewski et al., 2019). Hence, the majority of research work in understanding and preventing moisture ingress in PV modules are dedicated to investigating these material properties via experimental and theoretical methods (Hülsmann and Weiss, 2015; Jankovec et al., 2018; Kempe et al., 2018; Wisniewski et al., 2019).

3.3. Factors that influence moisture ingress

3.3.1. Module technology

PV modules can be fabricated in two configurations: modules with permeable and impermeable encapsulants, as illustrated in Fig. 8. With the impermeable encapsulants, usually referred to as glass-to-glass configuration, moisture and gases can diffuse in from the edges of the modules. This is the universal configuration for thin film PV and other emerging (e.g. organic PV) technologies (KEMPE, 2006), see Fig. 8a. This is because, thin films such as cadmium telluride (CdTe), amorphous silicon (a-Si), copper indium gallium selenide (CIGS) modules are highly vulnerable to moisture, which can lead to corrosion of metal grids, especially when these technologies are deployed in hot and humid environments (Han, 2020; Theelen et al., 2017). Similarly, low stability and moisture induced degradation in organic PVs makes the glass-to-glass encapsulation the most suitable for organic PVs and their related emerging technologies. Recent developments have also led to substantial growth in the bifacial market, where glass-glass based crystalline silicon modules are projected to become a leading technology (Liang et al., 2019).

The permeable configuration, known as "breathable" or glass-to-polymer configurations are universally associated with the traditional silicon crystalline technologies. Permeable designs are more prone to moisture ingress. According to Kempe et al. (2007), a typical EVA encapsulated module with permeable and impermeable backsheets can quickly equilibrate to pH values of 4.76–7.0 and <4.76, respectively under similar conditions (KEMPE, 2006). A scheme of this design is illustrated in Fig. 8b. Hence, this design is said to facilitate the acetic acid diffusion rate. Thus, it reduces acetic acid accumulation within the PV module (Oreski et al., 2017), which in turns prevents metal contacts corrosion.

In the same way, due to the relatively high moisture diffusivity in EVA encapsulants, it is largely challenging to completely prevent moisture ingress into modules (KEMPE, 2006). Even those with perfect hematic configurations are liable to moisture ingress through voids created (either via manufacturing, mechanical or climatic stressors) at the perimeter of the module (Jankovec et al., 2016; Wisniewski et al., 2019). Table 4 shows the major PV technologies available commercially.

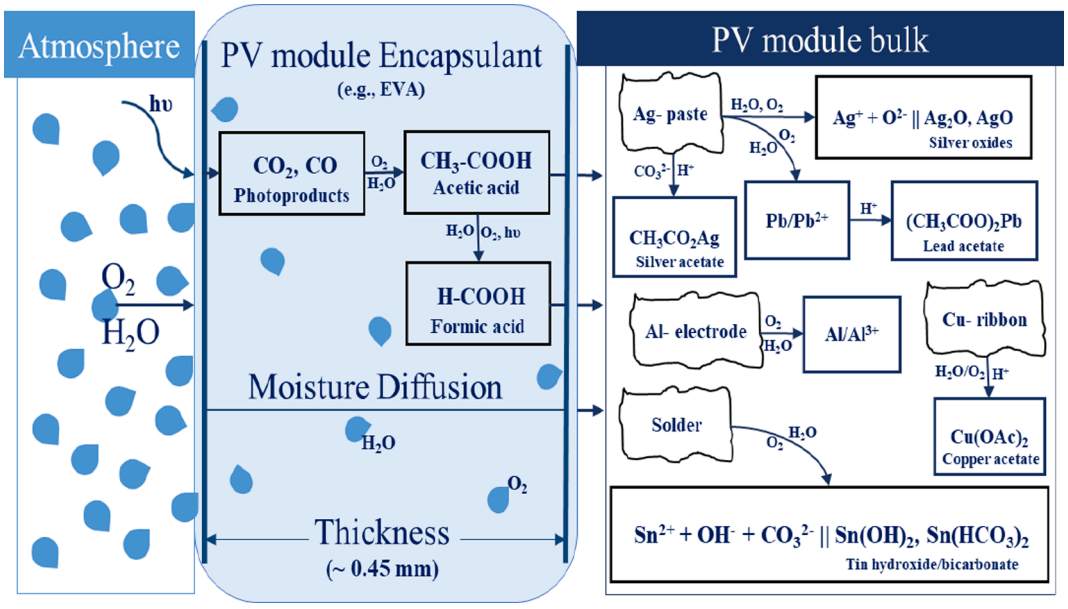

Fig. 7. Moisture ingress in PV devices. In the presence of sunlight (hυ), the encapsulant produces photoproducts (Grossetête et al., 2000), and interaction of the photoproducts with moisture can lead to the formation of carboxylic acids (Oreski et al., 2017). Moisture and the carboxylic acids diffuse into the PV module and initiate various degradation processes (Kumar et al., 2019). Silver (Ag) and lead (Pb) comes from the silver paste, and the solder and rear Al- electrode are the sources of tin (Sn) and aluminum (Al), respectively. Moisture is the electrolyte which sustains the degradation reactions in Fig. 7 (Kumar et al., 2019).

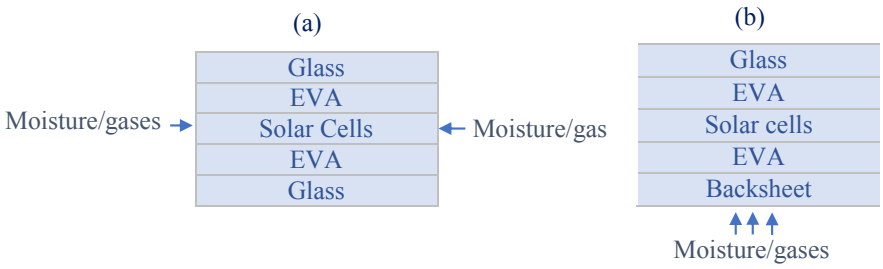

Fig. 8. PV module configurations: (a) impermeable and (b) permeable encapsulants.

Table 4
Types of commercial PV modules (Liang et al., 2019; Lopez-Garcia et al., 2018; Philipps and Warmuth, 2019).

PV module type	Characteristics	Encapsulation type
Monocrystalline (pure silicon)	- ca. 20% efficiency - relatively expensive - temperature coefficient: −0.3 to −0.5%/°C - blue in colour	Permeable (glass-to-polymer)
Polycrystalline or multicrystalline (fragments of molten Si crystals)	- ca. 15% − 17% efficiency - relatively low cost - temperature coefficient: −0.3 to −0.5%/°C - black in colour	Permeable (glass-to-polymer)
Thin film (CdTe, a-Si, CIGS, etc.)	- ca. 7% − 18% efficiency - lower cost - temperature coefficient: −0.1 to −0.4%/°C - blue/black in colour	Impermeable (glass-to-glass)
Crystalline silicon bifacial PV modules	- ca. 17% − 24% efficiency (front), 16% − 19% efficiency (rear), 0.70–0.9 bifaciality factor - lower LCOE - temperature coefficient: −0.3 to −0.4%/°C	Impermeable (glass-to-glass)
Emerging PV (e.g., Organic PV, Perovskites, etc.)	- relatively low efficiency - flexible, lightweight, and inexpensive - positive temperature coefficient - poor stability	Impermeable (glass-to-glass)

The effect of moisture ingress on thin film and organic PV devices is well documented in literature (Bag et al., 2016; Cheacharoen et al., 2018; Han, 2020; Morlier et al., 2013; Tanenbaum et al., 2012; Theelen et al., 2017; Weerasinghe et al., 2015a). The presence of moisture or gaseous species within the bulk of these modules result in photochemical reactions at the interfaces which leads to ultimate device degradation (Weerasinghe et al., 2015a, 2015b). However, there are efforts within the PV scientific community to develop suitable designs that will ensure the stability and reliability of these devices against moisture and gaseous ingress (Bag et al., 2016; Cheacharoen et al., 2018; Morlier et al., 2013; Tanenbaum et al., 2012). For the purpose of this review, we will focus on crystalline silicon PV module technologies, which are usually made with polymeric encapsulants. These technologies are not to be confused with emerging polymer-based PV modules which have the active materials of the solar cells made from polymeric materials or their blends: donor and hole transport materials (Tanenbaum et al., 2012).

3.3.2. *The material factor*

Material properties have been known to be the key factor to every device optimization, and this is not an exception in PV devices (Van der Wel and Adan, 1999). The material properties of the polymeric materials used as PV components are understood to be the limiting factor which predisposes PV modules to all forms of degradation and failure modes (Mitterhofer et al., 2020; Omazic et al., 2019), including moisture ingress (Kempe et al., 2014). Therefore, polymeric materials used as the component of the module have to be of desirable characteristic, especially as regards diffusivity, permeability, and solubility of gaseous species taking into consideration the economic and environmental concerns (Wisniewski et al., 2019). The most common parameter that is used is the diffusion coefficient which relies on both the permeability and solubility of moisture in a given polymeric material. Fig. 9 highlights some of the works in literature on the diffusion of moisture in different encapsulants and backsheets.

A close inspection of Fig. 9 shows that ionomer as an encapsulation material outperforms all other encapsulants including EVA, especially when it comes to resilience to moisture ingress. In contrast, PA is highly vulnerable to temperature changes. Similarly, it has been observed that the solubility and permeability of encapsulation materials follows the same trend. That is, the solubility and permeability of polymeric encapsulants increase significantly with increasing temperature (Hülsmann et al., 2014; Kim and Han, 2013; Köhl, 2013; Wisniewski et al., 2019).

Currently, EVA is the most preferred encapsulant material in crystalline silicon solar modules largely because of its cost effectiveness. However, EVA has a relatively high water diffusion coefficient and is liable to acetic acid production in the presence of moisture (Kempe et al., 2007). This and other factors open up the market for other encapsulation materials (Peike et al., 2013b). Even though these new polymeric encapsulants have their individual advantages, they all have some limitations in one way or the other, especially when it comes to PV applications (Peike et al., 2013b). Table 5 highlights some of the advantages and limitations of the most common PV encapsulants. Ionomer encapsulants, the most promising among the emerging PV encapsulants has a higher resilience to discolouration and PID, lower diffusivity, and higher optical transmittance among other properties. However, they are limited by higher costs, lower adhesion characteristics, and field data on their usage is limited (Tracy et al., 2020). The most vital parameter that is considered for the selection of an encapsulation material for PV module

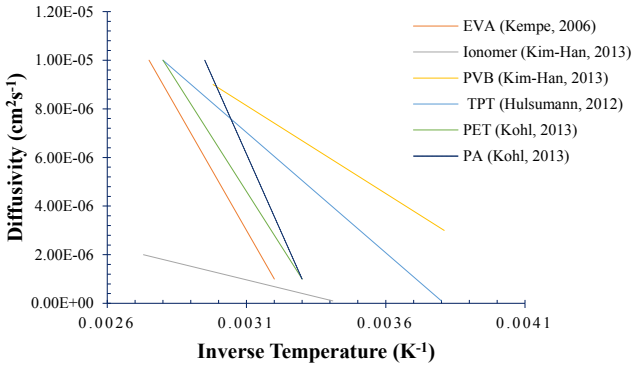

Fig. 9. Diffusion in different encapsulant materials. Data extracted from Kempe (2006), Kim and Han (2013), Hülsmann et al. (2014), and Köhl (2013).

Table 5
Advantages and limitations of some PV module's encapsulation materials.

Encapsulant	Advantages	Limitations
EVA	Cost-effective High adhesion	Acetic acid production UV instability High diffusivity
Ionomer	High volume resistivity High UV stability Low diffusivity High optical transparency High resilience to PID	High cost Poor adhesion Limited data High glass transition temperature
Silicone	High optical transparency High thermo-chemical stability Low thermal modulus High UV stability Low diffusivity	High cost High diffusivity High technical expertise
PVB	High UV stability and transparency Good adhesion	High diffusivity High cost High glass transition temperature
TPSE	High water repellent High thermo optic stability Easier recycling High volume resistivity	High cost
TPO	High volume resistivity Cost-effective High thermo-chemical stability Good resistance to hydrolysis	High diffusivity

application is cost (Peike et al., 2013b; Tracy et al., 2020; de Oliveira et al., 2018).

Czyzewicz and Smith (2011) carried out an investigation with several commercial grades of PVB, EVA and ionomer-based materials under repetitive 1000 hr damp heat ageing tests. Their findings, in part, led to the development of the commercially available cost-effective DuPont™ PV5300 and PV5400 ionomer-based encapsulants which exhibit superior moisture barrier quality as compared to EVA-based encapsulants.

Also, Kim and Han (2013) studied the amount of permeated moisture through an ionomer and PVB encapsulants and compared them with that of EVA encapsulants. They found that EVA has relatively lower diffusivity whilst ionomer encapsulants have relatively lower moisture retention capacity. Another study by Köhl (2013) using experimental and 2-dimensional finite element methods (FEM) in four different microclimates found that different encapsulants and backsheets behave differently under different climatic conditions. In a related work, Hülsmann et al. (2014) studied the behaviour of different encapsulants in different climates via simulation. They observed that in the same climatic condition, the solubility and permeability which account for the equilibrium moisture concentration is significantly influenced by the material composition. That is, additives, chemical structure, and morphology of the encapsulants affect moisture ingress reliability (Mitterhofer et al., 2020; Van der Wel and Adan, 1999).

In that respect, in order to protect the PV module over its useful lifetime against ingress of gaseous species, polymeric materials for making PV modules need to have good adhesion and lower diffusivity, solubility, and permeability characteristics to serve as good moisture or gaseous barrier materials (KEMPE, 2006; Miyashita and Masuda, 2013; Annigoni et al., 2015).

3.3.3. *Environmental and climatic factors*

In hot and humid climates, corrosion, delamination and discolouration of encapsulants as a result of ingress of moisture and gaseous species dominated old field deployed photovoltaic modules (Hülsmann and Weiss, 2015; Hülsmann et al., 2014; Schlothauer et al., 2012). Moisture ingress is also influenced by pressure and concentration gradients of diffusants, which are also functions of humidity and temperature. (Mitterhofer et al., 2020). In an investigation, Kempe et al. (2007) found that the ingress of water and oxygen into PV modules is highly influenced by temperature as compared to phase transitions (glass transition temperature, Tg or melting temperature, Tm) of the investigated materials. In addition, Koehl et al. (2012) investigated the impact of humidity on PV modules based on monitored climatic data at specific locations. Using phenomenological models, they estimated the moisture concentration at the surfaces of photovoltaic modules and concluded that degradation kinetics strongly depend on climatic locations.

In another study, Hülsmann et al. (2014) using a FEM simulation, studied the moisture ingress into wafer-based photovoltaic modules under extended periods of exposure in four different climatic conditions (namely *moderate climate* - Freiburg, Germany, *arid climate* - Negev desert, Israel, *alpine climate* - Zugspitze, Germany and *tropic climate* - Serpong, Indonesia), using polyethylene-terephthalate- (PET-) based and polyamide- (PA-) based backsheets and EVA as the encapsulating material. They observed a faster moisture ingress for warmer regions and higher moisture concentrations for moderate climate test sites. In a related report, Hülsmann and Weiss (2015) compared a simulated moisture uptake by PV modules under the standard IEC 61215 type approval ageing tests and moisture ingress into PV modules based on measured data sets from four different climatic zones using ethylene vinyl acetate, EVA as an encapsulant and polyvinyl fluoride/polyethylene terephthalate/polyvinyl fluoride (Tedlar®/PET/Tedlar®), TPT stack as a backsheet. They found that the standard IEC 61215 ageing tests causes twice as much moisture content in encapsulants than 20 years field exposure of modules. This is due to the dependency of diffusion (and solubility) on temperature and humidity and also the type of encapsulants, a trend highlighted in Fig. 9. They also compared their results to prior results in literature and found a good agreement among the results. Wisniewski et al. (2019) used a finite element model based on experimental data from WVTR tests to comprehend the moisture ingress into double glass modules and concluded that moisture ingress increases with increasing temperature. They also argued that the moisture content of the EVA can affect the diffusivity factor up to two folds.

According to Kempe et al. (2007) moisture ingress, acetic acid (due to ingressed moisture), and UV irradiation can lead to significant loss of adhesion of EVA encapsulants. Also, Novoa et al. (2014) developed a fracture kinetics model based on a quantitative characterization technique to study the effects of moisture, temperature, and mechanical stress on the adhesion characteristics of backsheets using ageing tests. They found that the delamination rate increased with test duration, temperature, and relative humidity. In another related study, the same group with the same model investigated the influence of humidity and temperature on the debonding kinetics of EVA and polyvinyl butyral (PVB) encapsulants and reported the same trend as observed with backsheets (Novoa et al., 2016). Similarly, Bosco et al. (2019) also investigated the influence of humidity and temperature on the delamination kinetics of the EVA/Si–PV cell boundary and concluded that electrochemical reactions dominated at higher humidity levels.

Kempe and Jordan (2017) investigated the possible influence of a manufacturing anomaly on the long-term reliability of a utility scale photovoltaic (PV) project. They subjected test modules to varying humidity and temperature conditions with periodic monitoring. They found that the degradation mechanism was dependent on the moisture content within the module due to damp heat test, and extrapolation to field scenarios forecasted minimal deviation for the project location. They also acknowledged the uncertainties in forecasting performance from damp heat tests. Thus, high humidity, temperature, and UV irradiation contribute significantly to loss of adhesion, solder bond and other material degradation which can lead to moisture ingress in PV devices.

Beside environmental and climatic factors in the field, the IEC 61215 type approval tests also have consequences of creating favourable routes for moisture ingress into PV modules. Humidity as an important stress factor for PV modules achieved through the Damp Heat test, as specified by IEC 61215 type approval testing under a 1000 hr at 85 °C and 85%

RH condition, can result in significant failures and damages to modules when not done according to standard specifications. These tests can serve as a precursor for other material degradation and fault modes. In one investigation, (Oreski and Wallner, 2005) observed chemical degradations in polyethylene terephthalate, polyvinylidene fluoride, and polyvinyl fluoride encapsulants after 85% / 85 °C damp heat tests.

Furthermore, Hoffmann and Koehl (2014) studied the effect of physical conditions (namely humidity, temperature, accelerated ageing scheme, and extreme voltage stress exposure in two different climatic zones) on the degradation mechanism of PV modules and found that accelerated ageing tests cause degradation in some orders of magnitude as compared with outdoor exposure. Later, Hülsmann and Weiss (2015) compared the simulated moisture ingress results of photovoltaic modules during accelerated ageing tests contained in the type approval standard IEC 61215 protocol and moisture ingress under real ambient outdoor conditions. They observed that the damp heat, thermal cycling, and humidity freeze tests as per the IEC 61215 standard resulted in twice as much moisture concentration in the encapsulant between the cell and glass than outdoor weathering over 20 years.

Recently, Tracy et al. (2020) investigated the resilience of ionomer and EVA encapsulants using both indoor and outdoor tests. Under 5000 h of accelerated aging at 65 °C/30% RH and 340 nm UV exposure, they observed significant discolouration in the EVA encapsulants and only a hazy discolouration in the ionomer encapsulants. They noted that the field-aged test samples did not experience any form of discolouration even under the same voltage exposure conditions of $\sim 8.0 \times 10^{-4}$ W·hr/m^2. Their result is shown in Fig. 10.

They also observed that EVA outperformed the ionomers as regards adhesion characteristics. They attributed these degradation processes partly to environmental and climatic factors which led to undesirable chemical reactions within the encapsulants.

Ultimately, all encapsulation materials are prone to moisture ingress at higher humidity, temperatures, and UV radiation conditions. These climatic or environmental stressors together with the encapsulants' properties (such as diffusivity, solubility, and permeability) and the PV module's design (permeable or impermeable) play a major role in the insurgence of moisture ingress. Optimization of these material properties and the module design to be resilient in all climatic conditions will be a key to achieving PV modules' durability and reliability.

4. Test methods for moisture ingress susceptibility

Moisture ingress is a tricky phenomenon that connects most material degradations in PV modules (Mon et al., 1985), and is a threat to module reliability. Hence, more effort must be put in place to address the incidence of moisture into PV modules. Unfortunately, we cannot control environmental factors but for the material properties and technology we can, especially when the failure mechanisms are well understood. To understand the role moisture plays in modules' failure mechanisms, all predisposing elements including the materials, the kinetics and the conditions in which modules operate must be well understood. The luminescence and fluorescence signals from moisture induced degradation products of PV modules are measured using electroluminescence (EL), photoluminescence (PL), and ultraviolent fluorescence (UV-F) spectroscopy, respectively. Dark lock-in thermography (DLIT) is based on the thermal signatures from degraded products from moisture ingress whilst scanning electron microscopy (SEM), energy dispersive spectroscopy (EDS), and fourier transform infra-red spectroscopy (FTIR) measure the chemical products (based on functional groups) associated with moisture ingress (Kim et al., 2013; Kumar et al., 2019).

Most often, the moisture diffusion characteristics of encapsulants such as EVA and backsheets is estimated using permeation-based techniques. The most common among these techniques is the water vapour transmission rate (WVTR) experiments, which can be derived from either the flux density (F), Equation (2) or permeability (P), Equation (3) in a polymeric material. Using the water transmission rates from the permeation tests, the overall mass transfer of water through the encapsulant can be determined. Normally, finite element models are used together with parameters from the gravimetric and permeation techniques in order to estimate the moisture absorption, retention, and transmission characteristics of the polymeric materials (Hülsmann and Wallner, 2017; Hülsmann and Weiss, 2015; Kim and Han, 2013; Meitzner and Schulze, 2016; Oreski et al., 2017; Wisniewski et al., 2019).

4.1. Predicting moisture ingress in polymeric materials

EVA is the most common encapsulant used in crystalline silicon solar modules currently, and several methods have been employed in order to understand and predict the moisture barrier characteristics of PV module encapsulants and backsheets. It is noteworthy that, determining the moisture concentration and mass transport characteristics of encapsulants (such as EVA) and backsheets under multiple moisture absorption and desorption conditions as in the case of real field operation is complex and challenging (Dadaniya and Datla, 2019; KEMPE, 2006; Novoa et al., 2016; Peike et al., 2013a). An overview of some of the methods that have been reported in literature are illustrated in Fig. 11. In Fig. 11, all the methods show a good agreement: diffusivity increases with increasing temperature. It has been shown that diffusion is more sensitive to temperature changes as compared to other environmental stressors and hence, influences the moisture barrier characteristics of materials the most (Dadaniya and Datla, 2019; KEMPE, 2006; Wisniewski et al., 2019).

According to Wisniewski et al. (2019), the material properties that determine the suitability of a polymeric material for encapsulants for PV applications are the permeability, mass concentration, solubility, and

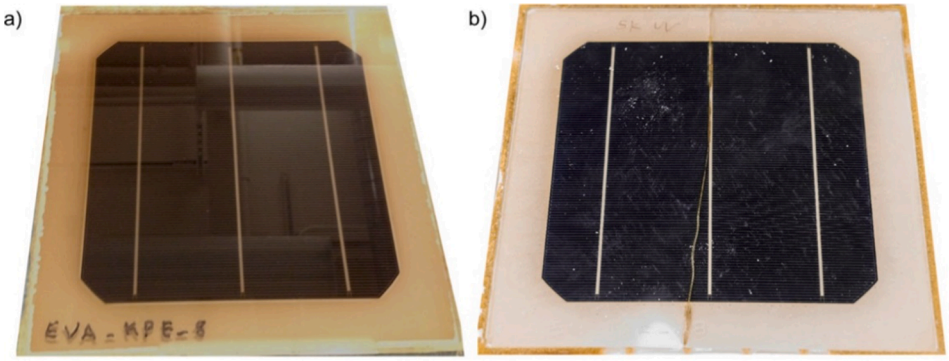

Fig. 10. Discoloration in (a) EVA and (b) ionomers encapsulants after 5000 h of accelerated aging (65 °C/30% RH, 340 nm UV) exposure. Ionomers showing greater resilience to discolouration as compared to EVA. .
Adapted from Tracy et al. (2020)

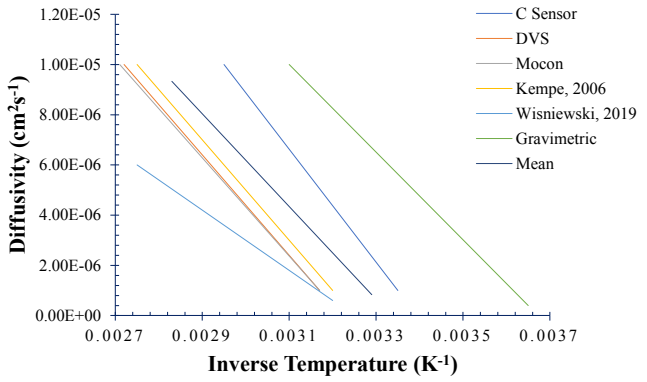

Fig. 11. Different approaches for determining the diffusion coefficient of EVA-water system. Data extracted from KEMPE (2006), Ballif et al. (2014), and Wisniewski et al. (2019), Dadaniya and Datla (2019) and the mean of these data points.

diffusivity of water through and within the EVA. In their work, they determined these parameters using a two-dimensional finite element model based on experimental data obtained via WVTR from Miami and Mumbai to forecast moisture ingress into solar modules during long-term outdoor exposure and laboratory accelerated tests. They argued that their model could be used to study specific regions on the module for degradation behaviour. More importantly, they concluded that the duration required for equilibrium could be much enhanced by controlling the initial moisture content of EVA.

Usually, the diffusion, permeability, solubility, and moisture concentration characteristics of encapsulants and backsheets are determined experimentally, and from these parameters, moisture or gaseous ingress profiles of these polymeric materials could be predicted with the Fickian laws, Equations (1) – (3), (Hülsmann and Weiss, 2015; KEMPE, 2006; Mitterhofer et al., 2020; Wisniewski et al., 2019; Jankovec et al., 2018). For an ideal thin film of polymeric material in the presence of moisture or gaseous species (assuming an ideal environment), the process dynamics could be represented with:

$$\frac{\partial C}{\partial t} = \nabla \cdot (D \nabla C), \tag{1}$$

where t is diffusion time, D is the diffusivity and C is the concentration of the species within the host material.

For isotropic diffusion (1-dimensional diffusion), that is, if the concentration gradient is assumed to be along the x-axis only, Equation (1) is the differential equation of the rate of flow of permeants per unit area, known as diffusion flux (F), and is given by

$$F = -D \cdot \frac{\partial C}{\partial x}, \tag{2}$$

where x is the space coordinate measured normal to the section, $-\partial C/\partial x$ is the driving force for the diffusion. The experimental measured value of F from Equation (2) could be taken as the *WVTR* of the material (Kim and Han, 2013; Wisniewski et al., 2019). For an ideal barrier material without voids, the behaviour of easily condensable permeating species could be represented by

$$P = S \cdot D, \tag{3}$$

where P is the permeability coefficient and S is the solubility (concentration proportionality constant). The solubility, S is usually known as the "Henry's coefficient", because it is based on the famous Henry's law (Sander, 2015), which describes the partial pressure of a solute-absorbent system. So, for the equilibrium between saturated moisture concentration, C_{sat} and ambient vapor pressure, p_v for a moisture–polymer system, the Henry's law could be expressed as $C_{sat} = S \cdot p_v$. For moisture and other gases, such as oxygen, that condense or interact with polymeric materials easily, permeability could be expressed in terms of flux density and solubility by comparing Equations (2) and (3) as

$$P = -\frac{F}{v/\partial x} \cdot S. \tag{4}$$

Thus, the *WVTR* of encapsulants or backsheets could be estimated from the experimental measured value of P (Hülsmann et al., 2014; KEMPE, 2006).

Assuming an ideal Fickian diffusion process, the transient $WVTR_{(t)}$ as a function of time, also known as the fractional mass of water, can be represented as (Crank, 1975)

$$WVTR_{(t)} = \frac{D \cdot C_{sat}}{l}\left[1 + 2\sum_{n=1}^{\infty}(-1)^n exp\left(\frac{-Dn^2 \cdot \pi^2 \cdot t}{l^2}\right)\right], \tag{5}$$

where n is the number of points in space, t is the time, and l is encapsulant film thickness. n takes values 0, 1, 2, … Usually, experimental results fit well with $n = 10$, but is best predicted with a real model with acceptable error values (Yang et al., 2020).

Using the permeability tests is often preferred when dealing with easily condensable fluids such as moisture and oxygen. This is because for these fluids, permeant flux is limited by the solubility of permeants in the polymeric material, which is due to the high degree of interaction of permeants with the polymeric material. This can result in alteration in the chemical morphology of the encapsulant (Luo et al. (2017). Moreover, the diffusion, solubility, and permeation processes are strongly influenced by temperature and are reliably described in a homogenous material with the Arrhenius equation as

$$X = X_0 exp\left(-\frac{E_X}{R \cdot T}\right), \tag{6}$$

where X, X_0, and E_X is the coefficient, the constant, and the activation energy of parameter X respectively (X = diffusivity, solubility, and permeability). R is the universal gas constant, and T is the absolute temperature (in kelvins). X_0 is also called the preexponential factor, which describes the relationship between temperature and the reaction rates. Using the definition of solubility, together with the *WVTR* fitted data derived from Equations (2), (4) and (5), the constants (D, S, and P) could be determined. The activation energy, E_a (E_X in Equation (6)) could be determined graphically and be used to evaluate the properties (diffusivity, permeability, and solubility) of the polymeric material at varying temperature conditions. For instance, using Equation (7), which is a linearized version of Equation (6) (KEMPE, 2006),

$$lnD = InD_0 - \frac{E_D}{R} \cdot \frac{1}{T}. \tag{7}$$

The diffusivity could be estimated for a given polymeric material at different operating temperatures. Assuming that the diffusion process is only influenced by a perfect linearized experimental temperature distribution in the polymeric encapsulant, D_0 and E_a (E_D) could be extracted from a fitted graph of (ln D) against ($1/T$). However, the Arrhenius equation assumes that the activation energy of the water diffusion process is independent of temperature and that water diffusion has insignificant influence on the physical properties of the polymeric material (Yang et al., 2020). In contrast, material properties such as chemical structure and morphology together with other additives can also influence the diffusion properties of polymeric materials (Van der Wel and Adan, 1999). So, at times, E_a (E_D in Equation (7)) is affected by unexpected chemical interactions due to temperature variations, and therefore a perfect linear relation between (ln D) and ($1/T$), in these cases, becomes largely unrealistic (Yang et al., 2020). In such circumstances, E_a could be determined using the difference in the diffusivity (D_1 and D_2) at two different temperatures (T_1 and T_2) respectively as (Yang et al., 2020)

$$ln\frac{D_1}{D_2} = \frac{E_a}{R}\left(\frac{1}{T_2} - \frac{1}{T_1}\right) \quad (8)$$

It is noteworthy that the equation above depends on the experimental methods and the error functions associated with these methods. According to Kimball et al. (2016), based on the Fickian and Arrhenius laws, the lifetime (t_{TTF}: test-to-failure in hours) of field deployed PV modules could be estimated based on the relative humidity (RH) in %, the humidity exponent (n), and the preexponential factor, A as

$$t_{TTF} = A \cdot exp^{\left(\frac{E_a}{R \cdot T}\right)} \cdot RH^{(n)}. \quad (9)$$

However, a few research findings have observed that the irreversible interactions between moisture or gaseous species and polymeric materials during real field operations may occur at higher humidity and temperature conditions (Mitterhofer et al., 2020). This can result in hydrothermal degradation due to some unforeseen chemical reactions which demonstrates some non-Fickian behaviours of these polymeric materials. Indeed, some researchers have shown that the Fickian models have not predicted the diffusion process in some encapsulants perfectly as compared to non-Fickian models. It is believed that moisture ingress could lead to the introduction of N-CO-N and C-O functional groups into the polymer chemical morphology or dehydration in some polymeric materials with significant additives, which can lead to many forms of degradation (Yang et al., 2020). These and other factors limit the reliability of the Fickian models. This has led to a search for a more reliable way of profiling the diffusion behaviours of PV module encapsulants.

Mitterhofer et al. (2020) developed a new non-Fickian 2-dimensional finite-element model using four different encapsulants based on in-situ humidity measurements after the encapsulants were exposed to transient humidity conditions. The scheme of their experiment by using humidity sensors is shown in Fig. 12. They argued that the simulation parameters from their experiment could be used to precisely define moisture ingress (20–80% RH) and egress (40–20% RH) profiles for PV devices. However, they also observed a deviation of the egress curves under higher humidity conditions. Immersion techniques have also been explored by a few researchers for the same purpose (Nagayama et al., 2020).

According to Ballif et al. (2014), apart from the permeation techniques, the capacitance embedded sensor measurements, FTIR, dynamic vapor sorption (DVS), and calcium (Ca) spot oxidation experiment could be used to determine the moisture ingress into PV modules. Nonetheless, they were quick to point out that all of these methods have their specific limitations. Capacitance embedded sensor methods are limited by long time drifts and lower operational temperatures (typically below 70℃) as the sensor needs to be imbedded in the encapsulant.

FTIR gives optimal results with only optically transparent samples and are ideal for PVB encapsulants. DVS is best for measuring moisture ingress in bulk materials and not in multilayered materials such as backsheets. Ca spot technique is best suited for materials with low WVTR such as ionomer encapsulants and as such excellent for qualitative, but not quantitative tests.

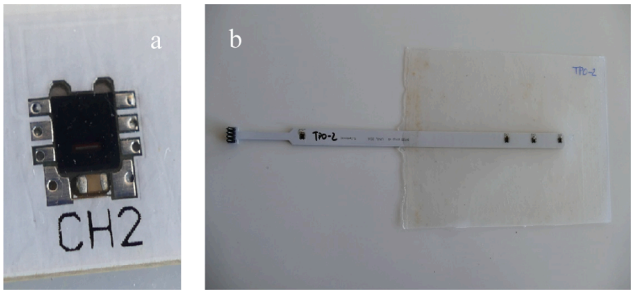

Fig. 12. A prototype in situ humidity sensor with (a) miniature sensor and (b) sensor strip in the encapsulant. .
Adapted from Mitterhofer et al. (2020)

4.1.1. Permeation based techniques

The water vapour transmission rate depends on the material properties (diffusivity, permeability, and solubility), thickness, temperature, and saturated water vapor pressure (Hu and French, 2019; Hülsmann and Wallner, 2017; Wisniewski et al., 2019).

KEMPE (2006) used water vapor transmission rate technique to measure several 12 cm diameter EVA films between 0.46 mm and 2.84 mm thickness. He used the data he obtained from these measurements together with meteorological data to perform a one-dimensional finite element analysis to determine the transient moisture concentration within a breathable backsheet and a double glass laminated PV module. He concluded that due to the high diffusivity of EVA, modules with EVA encapsulants are limited in preventing moisture ingress from the perimeter for the 20 – 30-year warranty lifetime of PV modules. He also argued that prevention of moisture ingress could only be achieved significantly by using encapsulants with very low diffusivity or perfect desiccant filled sealants. In another study, Hülsmann et al. (Köhl, 2013) employed a simulation based on parameters from WVTR tests to predict the moisture ingress into wafer-based PV modules under extended periods of exposure in four different climates. Their test modules were made from PET- based and PA- based backsheets and EVA as the encapsulating material. They observed a common similarity between their results and the results from already published articles (Jorgensen et al., 2006; KEMPE, 2006; Kim and Han, 2013).

In a related work, Hülsmann and Wallner (2017) using the WVTR tests studied the moisture permeability characteristics of different encapsulant and backsheet materials as a function of temperature. They found that WVTR tests are suitable for predicting moisture ingress in different encapsulants and under varying temperature conditions. Similarly, Wisniewski et al. (2019) also used the WVTR technique to determine the diffusivity, moisture concentration, solubility, and permeability of a 510 μm EVA film and concluded that moisture ingress depends on temperature and the moisture content of the EVA layer.

In addition, Meitzner and Schulze (2016) employed a gravimetric technique and the WVTR tests to investigate moisture barrier capability of polyvinyl butyral, PVB encapsulant. The parameters they obtained can be used for numerical simulation of the moisture ingress into PV modules when meteorological data is available.

4.1.2. Gravimetric methods

Gravimetry is when a sample is placed in a climate chamber and is intermittently taken out of the chamber to study the weight changes of the sample. Traditionally, gravimetric methods were used to determine the solubility and diffusivity of any encapsulant, for instance EVA. Then the moisture concentration within the encapsulant together with the moisture transmission rate can be determined directly from the measured solubility and diffusivity values (Dadaniya and Datla, 2019; Oreski et al., 2017). However, the moisture diffusion characteristics of polymeric materials, e.g., EVA is complex and cannot be determined reliably especially with the conventional gravimetric techniques without making considerations and adjustments. In one study, Swonke and Auer (2009) investigated the moisture barrier quality of different PV encapsulants, namely EVA, PVB, an ionomer, and thermoplastic polyurethane and silicone under varied climatic conditions. They observed that the water storage capacity of the silicone and the ionomer as compared to the other encapsulation materials is negligible.

In another work by Oreski et al. (2017), they employed an isostatic gravimetric method to investigate the influence of acetic acid transmission rates on laminates and single layers of backsheets (PET, PA, PVF, PVDF, and aluminum). They concluded that the acetic acid transmission rate strongly depends on temperature, layer thickness, and film composition. They also found that the acetic acid permeation rate of PET-core-backsheets is determined by the PET core layer, whilst an additional aluminum layer within the backsheet has insignificant barrier

effect. In addition, they observed that acetic acid retention by EVA layers in a PV module is insignificant due to the high acetic acid transmission rate of EVA. Finally, they argued that "breathable" backsheets enhance the diffusion of acetic acid out of a module, thereby enabling guarantee performance and reliability of PV modules of this design type over a longer time span.

More recently, Dadaniya and Datla (2019) employed a finite element method based on an in-situ gravimetric measurement technique to study the effects of temperature on the moisture ingress into PV modules. They demonstrated (using Delhi outdoor and accelerated environments) that moisture concentration at the edges of the modules depends strongly on the period and index of exposure. They also argued that, using their method, at a location 50 mm from the perimeter of the module, 1000 h of damp heat ageing can be equated to 339 days of outdoor exposure.

4.2. Detection methods based on degradation products

Permeation and gravimetric methods are used to predict the moisture and gaseous absorption characteristics of encapsulants and backsheets. However, these parameters are only used for material engineering purposes. More of a concern is the environmental and climatic conditions which are highly unpredictable and are almost impossible to control in real conditions. As a result, modules with even perfect hermetic designs are limited in preventing moisture ingress effectively (KEMPE, 2006; La Mantia et al., 2016; Hu and French, 2019). Therefore, diagnosis prior to degradation in electrical performance of the module is very important for predicting module durability and reliability (Köntges et al., 2020). As such, there have been efforts within the photovoltaic community towards early detection of moisture ingress into PV modules in order to put in place effective mitigation plans to avert the phenomenon and its effects (Kim et al., 2013; Klemchuk et al., 1997; Kumar et al., 2019; Schlothauer et al., 2012; Sinha et al., 2017).

Analytical methods for analyzing moisture ingress associated degradation (especially encapsulants, solar cells and other PV components degradation) on a molecular level are based on chemical degradation products (Köntges et al., 2014). These methods can be destructive or non-destructive in nature. Table 6 highlights some techniques for detecting moisture ingress in PV modules and their advantages.

Usually, visual inspection and I-V characterization are employed together with EL spectroscopy, PL spectroscopy, dark lock-in thermography (DLIT), ultraviolet fluorescence (UV-F) spectroscopy, and a variety of spectroscopic methods to investigate degradation mechanisms associated with moisture ingress and their effects (Kumar et al., 2019).

In the 1990s, Klemchuk et al. (1997) investigated the discolouration of several EVA based encapsulated field-aged modules and concluded that discolouration of encapsulants was due to chemical reactions between cross-linking peroxides and stabilizers and possible photobleaching of the encapsulants. They employed TGA, FTIR, Raman spectroscopy, GC/MS, GWFID, XPS, and SEM-EDX for their investigation.

In another study, Peike et al. (2011) studied the degradation behaviour of two EVA encapsulated c-Si PV modules after damp heat and combined humidity-UV tests using Raman spectroscopy. They observed lateral non-uniform fluorescence and C-H stretching vibration intensities of the EVA, and indication of additive degradation products of moisture. They concluded that their observation could be an indication of moisture diffusion into the encapsulant. Rashtchi et al. (2012) studied the practicability of using a combination of FTIR and spectroscopic optical coherence tomography (SOCT) to measure water concentration of the EVA layer within PV modules. They argued that absorbed water within different layers in the PV module could be quantified using SOCT which provides in-depth resolved spectral information on the state of the module. Furthermore, Kim and Han (2013) investigated the moisture-induced degradation mechanisms in multicrystalline silicon modules under accelerated test conditions using EL imaging, Dark I-V, Suns V_{oc} measurements, SEM-EDX and AES. They observed a power drop due to corrosion of the solder joints due to moisture ingress, and an increment in the oxide concentration on the metal electrodes after the accelerated ageing tests.

Recently, Kumar et al. (2019) explored the effects of moisture induced degradation in c-Si PV modules under damp heat ageing tests using electroluminescence, dark lock-in-thermography, and scanning electron microscopy-energy dispersive X-ray spectroscopy (SEM-EDS) imaging techniques. They observed moisture induced conditions such as tin migration at the finger-wafer interface and formation of silver oxide at cell cracks and edges as the dominant chemical mechanisms, and loss in interfacial adhesion between wafer, encapsulant and fingers. They also argued that the ribbon interconnects served as an active site for deposition of oxides from the solder material, and the aluminum electrode served as an electrolyte in the presence of moisture. They concluded that increase in series resistance is the main parameter that characterizes all forms of chemical degradation. Fig. 13 shows some of their SEM-EDS results.

Meyer and Van Dyk (2004) believe cell degradation may manifest itself in the form of high series resistance, shunting, and deterioration of the antireflection coating. EL and PL techniques are reliable for spatially resolved determination of the series resistance as both techniques rely on luminescence signals emitted from degradation products from polymeric components (Trupke et al., 2012). Fig. 14 shows an EL image from a test material after exposure to varying damp heat conditions illustrating corresponding dark regions due to solar cell and electrode degradation (Kim et al., 2013). This is because the degraded areas conduct little or no electrons.

In another study, Sinha et al. (2017) utilized a spatially resolved infrared thermography to investigate delamination, corroded interconnects and other electrical losses in a PV module. In the same work, they also used the EL imaging to estimate the severity of encapsulant discolouration, finger, and cell cracks. Similarly, Roy and Gupta (2019) employed EL and DLIT techniques to study the severity of shunts in commercial c-Si PV modules and argued that these techniques could be used to investigate the state of shunts in PV modules.

Most often, EL imaging requires an alteration in the system circuit layout, can only be done effectively in the night or at twilight, and applications in outdoor test facilities are still under investigation (Köntges et al., 2020; Trupke et al., 2012). Hence, PL imaging which is also based on the detection of degradation products of the polymeric encapsulant, usually EVA, is preferred (Morlier et al., 2017). However, it is highly reliant on the excitation source and can give unwanted luminescence contribution from spurious sources such as the antireflection coating (Paduthol et al., 2018). For the detection of defects and fault modes, including cracks and moisture ingress, the ultraviolet UV-F is very promising (Köntges et al., 2013; Morlier et al., 2018; Köntges et al., 2020).

In PV modules, the polymeric materials such as EVA can degrade into fluorescent species when exposed to environmental stressors and chemical species, see Fig. 15. In the presence of ingressed moisture and other gaseous species such as oxygen, the fluorescent degraded species

Table 6
Some techniques for detecting moisture ingress in PV modules.

Testing type	Testing techniques	Advantages of test type
Destructive	FTIR, Raman, XPS, SEM-EDX, AES, AFM, TGA, and SOCT spectroscopy	Well established Detailed investigation Assesses the effects of different testing methods on test coupons
Non-destructive (based on degradation products)	Visual inspection, I-V imaging, (EL, PL, UV-F) spectroscopy, DLIT	Equipment is easy to operate Defects can be detected without damaging test coupons Quick and accurate

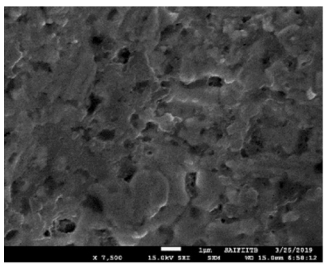

(a)

Element	Atomic%
Oxygen	41.83
Carbon	21.34
Silicon	4.41
Silver	28.04
Tin	0.00
Lead	0.11

(b)

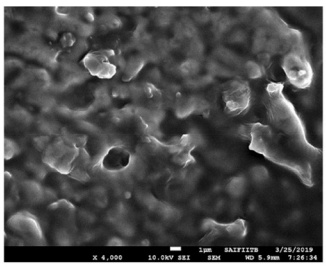

(c)

Element	Atomic%
Oxygen	20.80
Carbon	53.80
Silicon	3.29
Silver	20.46
Tin	0.00
Lead	1.43

(d)

Fig. 13. SEM-EDS results of DH testing of fingers on cell edge: (a) SEM image and (b) EDS results; and cracked regions on cell: (c) SEM image and (d) EDS results. Ingress of moisture and gases might have accounted for higher fractions of oxygen, silver, and carbon as shown in (b) and (d). .
Adapted from Kumar et al. (2019)

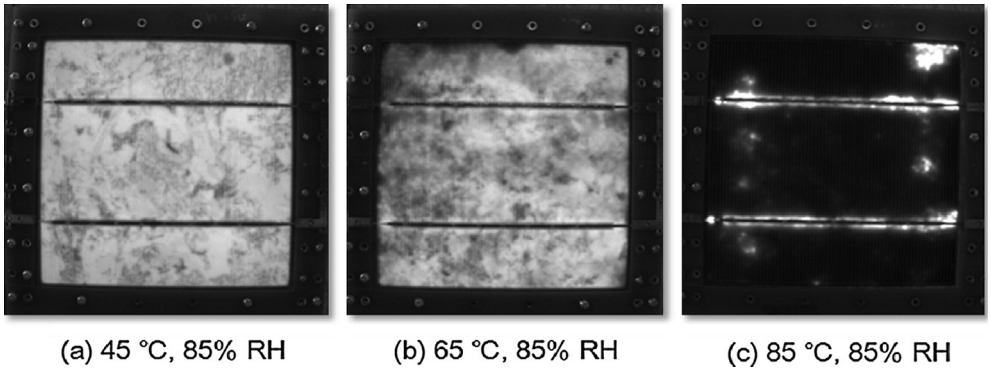

Fig. 14. An EL image of a test PV module after 3500 h damp heat tests. Darker areas indicate degradation, possibly due to moisture ingress, and cracks. .
Adapted from Kim et al. (2013)

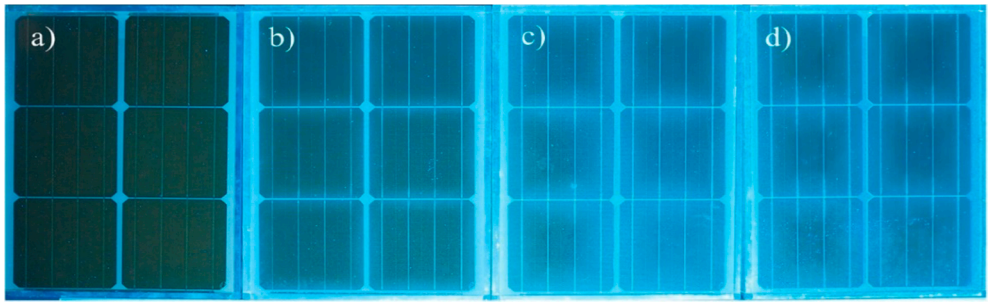

Fig. 15. UV-F signatures of a test PV encapsulants at 85℃ / 85% RH after: (a) original state, (b) 1000 h, (c) 2000 h, and (d) 3000 h tests. The increasing brightness of samples from left to right corresponds with increasing degraded fluorescent species with exposure time. .
Adapted from Eder et al. (2019)

undergo metamorphoses to nonfluorescent species, that is photobleaching (Morlier et al., 2018). These nonfluorescent species from the photobleaching marks areas around and within the module show darker traces when exposed to UV-F (Köntges et al., 2013; Morlier et al., 2017; Köntges et al., 2020).

This makes UV-F one of the most powerful tools that can be used to investigate defects and fault modes such as solar cell cracks, moisture ingress and its effects in PV modules based on the degraded products induced by the presence of moisture or gaseous species in the module.

5. Mitigation techniques

Controlling moisture ingression into PV modules will ensure the durability and reliability and therefore boost the marketability of PV devices substantially (KEMPE, 2006). There has been significant work within the scientific community to understand and develop possible mitigation strategies for preventing or delaying moisture ingress in PV modules. Investigations on the material properties of the major encapsulants (Kempe et al., 2014; Oreski and Wallner, 2005), the use of edge sealants (Bag et al., 2016; Kempe et al., 2018) and humidity sensors (Jankovec et al., 2016; Mitterhofer et al., 2020; Miyashita et al., 2012; Reese et al., 2011), developing intricate PV configurations with breathable backsheets (KEMPE, 2006), and making PV devices with high substrate adhesion and super hydrophobic materials on the surfaces have been explored and are still under serious investigation (Bosco et al., 2019; Novoa et al., 2016). A collection of some literature on barrier materials is illustrated in Fig. 16. The figure indicates that ionomer possesses the best moisture barrier potential has better prospects for PV applications.

In addition, the moisture barrier properties of encapsulants could be improved significantly when they are used together with edge seals such PIB sealants (Kempe et al., 2018), On the other hand, PA, PET, and TPT

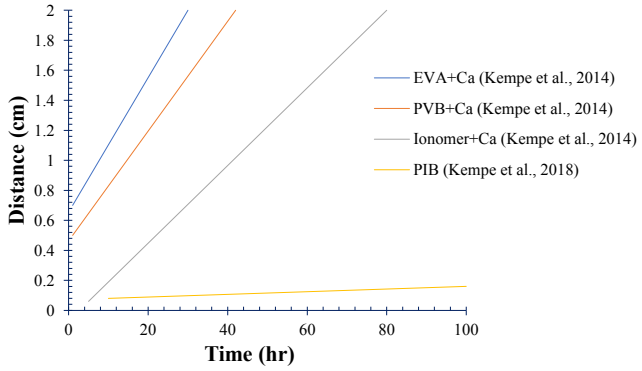

Fig. 16. Moisture barrier resilience of some edge sealants. Data extracted from Kempe et al. (2014) and Kempe et al. (2018).

encapsulants and backsheet have better moisture barrier properties than even a desiccant stacked edge sealed EVA (Hülsmann et al., 2014; Köhl, 2013). Marais et al. (2001) investigated the effect of moisture and gas (oxygen and carbon dioxide) transport through various blends of EVA with varying vinyl acetate (VA) contents. They found that, in the case of water, permeation rates increase with higher VA content whilst the gas permeation rate is unaffected even with varying contents of VA. As such, EVA with lower VA contents can limit the ingression of moisture into PV modules. In another study, Czyzewicz and Smith (2011) developed ionomer-based encapsulants with superior electrical, mechanical and moisture barrier properties with a possibility of making modules without supplementary edge seals. They argued that their developed ionomer-based encapsulant, with superior moisture barrier properties can be a solution to the problem of moisture ingression into PV modules.

Kim and Han (2013) studied the permeation rates in various encapsulants and observed that ionomer encapsulants are the best when considering only their lower moisture diffusivity, but EVA comes top when all characteristics and requirements of a good encapsulant is considered. In Fig. 16, the best moisture barrier material is the PIB base edge sealants proposed by Kempe et al. (2018), which can perform optimally over a vast temperature range. Additionally, Wisniewski et al. (2019) believe that PV modules with EVA films with lower initial water content can delay the time taken by the EVA to reach equilibrium with the ambient environment by two folds.

In an earlier work, Kempe (2005) evaluated the performance of desiccant edge-seal materials in a PV module. They employed an optical method where the reaction of water with calcium was used to quantify and compare moisture ingress into a PV module by exposing different test samples to humidity and heat. They concluded that desiccant filled PIB sealants have the potential to slow down moisture ingress in PV modules. In a related work by the same group, Reese et al. (2011) proposed a method of determining the moisture barrier properties of encapsulants based on the resistivity of Ca films when they undergo hydrolysis. In this process, the conductive Ca film changes to an insulator in the presence of moisture, and hence, the resistivity. Also, Miyashita et al. (2012) used colour changes in cobalt chloride, $CoCl_2$ paper to investigate moisture ingress into PV modules and found out that moisture ingress occurs from the back to the core of the module, but also depends on the WVTR of the backsheet.

Furthermore, Kempe et al. (2014) used a thin film of Ca between two laminated glass pieces for a variety of encapsulant and edge-seal materials to evaluate the ability of these configuration to prevent moisture ingress into PV modules. They found that the Ca-embedded structures are capable of preventing moisture ingress just like desiccant-stacked PIB sealants. They argued that since the best encapsulants are still permeable to moisture, low diffusivity encapsulants are reliable in preventing moisture ingress, in case edge sealants fail. In a related work by the same group, they developed permeation models that could be useful for field applications. They also concluded that molecular sieve desiccants can serve as a good moisture barrier materials when used in PIB based edge seals (Kempe et al., 2018). The synopsis of these results and other related reports in literature are illustrated in Fig. 16. Further, Hardikar et al. (2016, 2014a); (2014b;) using a theoretical framework, studied the moisture barrier performance of edge seals in PV modules based on accelerated testing and historical meteorological data. They concluded that edge sealants are capable of securing modules, even in aggressive environments.

In a related work, Morita et al. (2015) investigated the moisture barrier reliability of organic PV modules using the Ca method proposed by Kempe et al. (2014) and Reese et al. (2011). Test samples were connected to a data acquisition system via signal cables in order to test under varying environmental conditions. An edge card connector (with Ca film) was used to connect samples to the barrier material enabling easy switching of samples in and out of test. They observed a high moisture barrier resilience under conditions of 85 °C / 85% RH. However, they noticed a degradation (which was thought to be due to products from the encapsulant) of the modules, a condition which they believe could be improved by incorporating a vacuum process into the sample preparation procedure.

In other investigations, Jankovec et al. (2018, 2016) proposed an in-situ moisture measuring technique for PV modules using miniature digital humidity and temperature sensors embedded in encapsulants. They were able to test different encapsulants, backsheets, and edge sealants in different PV modules. They believed that using their monitoring technique, module's reliability and durability analysis could be done based on extracting the diffusion coefficients of encapsulants and backsheets after exposure to high humidity and temperature. In another study, Slapsak et al. (2019) developed an in-situ miniature digital relative humidity (RH) sensor based on a wireless radio-frequency identification (RFID) technology which could be used for monitoring moisture concentration in PV modules under indoor and outdoor conditions. They believe that the size of the sensors makes it possible to integrate them into any module design conveniently for reliable extraction of required data.

Most materials used for edge seals are limited by low fracture strength, and therefore are prone to mechanical failure (Han and Kim, 2017; Van der Wel and Adan, 1999; Yang et al., 2020). Hence, delamination or ripping can occur when edge seal environment of the module is subjected to even the slightest stress or strain (Bosco et al., 2019; Marais et al., 2001; Tracy et al., 2018). Kempe et al. (2016) investigated the adhesion characteristics of edge seals with a developed wedge test using glass substrates and PV encapsulants or edge-seal materials under accelerated ageing conditions. They concluded that edge seals barely provide mechanical integrity. Therefore, testing in the final product is necessary in selecting encapsulation materials with optimum barrier characteristics (Kempe et al., 2019; Novoa et al., 2016).

6. Conclusion

The effect of moisture ingress on PV modules has been reviewed. The major environmental and climatic factors such as temperature, humidity, and UV radiation influence moisture ingress into PV modules. In addition, the PV module design and the properties of the polymeric materials also determine how fast a material will equilibrate with ambient humidity conditions during operation. Usually, moisture can enter the module from the perimeter and through cracks and voids created either by manufacturing, transportation, or environmental/climatic stressors. The presence of moisture (inside or outside the PV module) together with high temperature and UV radiation can lead to delamination and discolouration of encapsulants, PID, corrosion of metal contacts, optical loss, solar cell degradation, adhesion loss, and other related material degradation culminating into PV module degradation and loss in power output.

WVTR tests, gravimetric, and immersion methods are used to

determine the diffusivity, solubility, permeability, and moisture concentration of polymeric components of PV modules. These parameters together with climatic data can be used in FEM models to predict the moisture barrier properties of PV encapsulation materials. Visual inspection, I-V characterization, (EL, PL, and UV-F) spectroscopy, and DLIT are some of the techniques that can be used to detect moisture ingress in PV devices. In addition, analytical tools such as SEM-EDS, Raman and FTIR spectroscopy have also been explored but are considered destructive techniques.

The use of encapsulant materials with excellent moisture barrier and adhesion characteristics, desiccant-stacked edge seals, and the use of permeable and impermeable PV designs are some of the proposed ways of preventing moisture ingress into PV modules. Embedded moisture sensors, calcium films (based on resistivity), and cobalt chloride paper strips (based on colour changes) could also be used for detecting moisture ingress in PV devices. Unfortunately, the complexity of the moisture ingress phenomenon itself, especially in real field operations under transient multiple factors, means there is yet to be an established reliable way to predict, detect, and prevent moisture and gaseous ingress into PV devices.

A solution to moisture ingress into PV devices will be a solution to most PV module degradation mechanisms. In this regard, focused research into encapsulant materials with optimal moisture barrier properties and desiccant-stacked edge seals for PV applications will be promising. When this is achieved, more power over the lifetime of PV modules can be expected, and hence, lower cost per peak watt (W_p) for electricity from PV devices.

Declaration of Competing Interest

The authors declare that they have no known competing financial interests or personal relationships that could have appeared to influence the work reported in this paper.

Acknowledgement

The authors acknowledge the continuous support of the University of Agder, Norway.

References

Adams, J., Salvador, M., Lucera, L., Langner, S., Spyropoulos, G.D., Fecher, F.W., Voigt, M.M., Dowland, S.A., Osvet, A., Egelhaaf, H.-J., Brabec, C.J., 2015. Water ingress in encapsulated inverted organic solar cells: Correlating infrared imaging and photovoltaic performance. Adv. Energy Mater. 5 (20), 1501065. https://doi.org/10.1002/aenm.201501065.

Annigoni, E., Jankovec, M., Galliano, F., Yu Li, H., Ballif, C., Sculati-Meillaud, F., 2015. Moisture ingress into pv modules: Long-term simulations and a new monitoring technique. The NREL PV Module Reliability Workshop.

Annigoni, E., Virtuani, A., Caccivio, M., Friesen, G., Chianese, D., Ballif, C., 2019. 35 years of photovoltaics: Analysis of the TISO-10-kW solar plant, lessons learnt in safety and performance—Part 2. Prog. Photovoltaics Res. Appl. 27 (9), 760–778.

Asadpour, R., Sun, X., Alam, M.A., 2019. Electrical signatures of corrosion and solder bond failure in c-Si solar cells and modules. IEEE J. Photovoltaics 9 (3), 759–767.

Bag, M., Banerjee, S., Faust, R., Venkataraman, D., 2016. Self-healing polymer sealant for encapsulating flexible solar cells. Sol. Energy Mater. Sol. Cells 145, 418–422.

Ballif, C., Li, H., Annigoni, E., Galliano, F., Escarre, J., Meillaud, F., Perret, L., CSEM, P., 2014. Impact of moisture ingress in PV modules on long-term performance: the role of EVA formulation, module design and climate. IEEE Photovoltaics 4(6), 1545-1551.

Barth, K.L., Morgante, J., Sampath, W.S., Shimpi, T.M., 2019. Progress Towards a Non-Lamination Encapsulation Technology to Improve Reliability and Reduce Costs, 2019 IEEE 46th Photovoltaic Specialists Conference (PVSC). IEEE 0495–0498.

Berghold, J., Koch, S., Frohmann, B., Hacke, P., Grunow, P., 2014. Properties of encapsulation materials and their relevance for recent field failures, 2014 IEEE 40th Photovoltaic Specialist Conference (PVSC). IEEE 1987–1992.

Bosco, Nick, Moffitt, Stephanie, Schelhas, Laura T., 2019. Mechanisms of adhesion degradation at the photovoltiac module's cell metallization-encapsulant interface. Prog. Photovoltaics Res. Appl. 27 (4), 340–345.

Carolus, Jorne, Tsanakas, John A., van der Heide, Arvid, Voroshazi, Eszter, De Ceuninck, Ward, Daenen, Michaël, 2019. Physics of potential-induced degradation in bifacial p-PERC solar cells. Sol. Energy Mater. Sol. Cells 200, 109950. https://doi.org/10.1016/j.solmat.2019.109950.

Cheacharoen, Rongrong, Boyd, Caleb C., Burkhard, George F., Leijtens, Tomas, Raiford, James A., Bush, Kevin A., Bent, Stacey F., McGehee, Michael D., 2018. Encapsulating perovskite solar cells to withstand damp heat and thermal cycling. Sustain. Energy Fuels 2 (11), 2398–2406.

Crank, J., 1953. A theoretical investigation of the influence of molecular relaxation and internal stress on diffusion in polymers. J. Polym. Sci. 11 (2), 151–168.

Crank, J., 1975. The mathematics of diffusion. Clarendon Press, Oxford, UK. The mathematics of diffusion. 2nd ed. Clarendon Press, Oxford, UK., -.

Czanderna, A.W., Pern, F.J., 1996. Encapsulation of PV modules using ethylene vinyl acetate copolymer as a pottant: a critical review. Sol. Energy Mater. Sol. Cells 43 (2), 101–181.

Czyzewicz, R., Smith, A., 2011. Next generation ionomer encapsulants for thin film technology. Proceedings of SPIE - The International Society for Optical Engineering 8112.

Dadaniya, Akhilesh, Datla, Naresh Varma, 2019. Water diffusion simulation in photovoltaic module based on the characterization of encapsulant material using in-situ gravimetric technique. Sol. Energy Mater. Sol. Cells 201, 110063. https://doi.org/10.1016/j.solmat.2019.110063.

de Oliveira, M.C.C., Cardoso, A.S.A.D., Viana, M.M., Lins, V.d.F.C., 2018. The causes and effects of degradation of encapsulant ethylene vinyl acetate copolymer (EVA) in crystalline silicon photovoltaic modules: A review. Renewable and Sustainable Energy Reviews 81, 2299-2317.

Eder, Gabriele C., Voronko, Yuliya, Dimitriadis, Simon, Knöbl, Karl, Újvári, Gusztáv, Berger, Karl A., Halwachs, Martin, Neumaier, Lukas, Hirschl, Christina, 2019. Climate specific accelerated ageing tests and evaluation of ageing induced electrical, physical, and chemical changes. Prog. Photovoltaics Res. Appl. 27 (11), 934–949.

Grossetête, T., Rivaton, A., Gardette, J.L., Hoyle, C.E., Ziemer, M., Fagerburg, D.R., Clauberg, H., 2000. Photochemical degradation of poly (ethylene terephthalate)-modified copolymer. Polymer 41 (10), 3541–3554.

Hacke, Peter, Spataru, Sergiu, Johnston, Steve, Terwilliger, Kent, VanSant, Kaitlyn, Kempe, Michael, Wohlgemuth, John, Kurtz, Sarah, Olsson, Anders, Propst, Michelle, 2016. Elucidating PID degradation mechanisms and in situ dark I-V monitoring for modeling degradation rate in CdTe thin-film modules. IEEE J. Photovoltaics 6 (6), 1635–1640.

Hacke, Peter, Spataru, Sergiu, Terwilliger, Kent, Perrin, Greg, Glick, Stephen, Kurtz, Sarah, Wohlgemuth, John, 2015. Accelerated testing and modeling of potential-induced degradation as a function of temperature and relative humidity. IEEE J. Photovoltaics 5 (6), 1549–1553.

Halwachs, M., Neumaier, L., Vollert, N., Maul, L., Dimitriadis, S., Voronko, Y., Eder, G.C., Omazic, A., Mühleisen, W., Hirschl, Ch., Schwark, M., Berger, K.A., Ebner, R., 2019. Statistical evaluation of PV system performance and failure data among different climate zones. Renewable Energy 139, 1040–1060.

Han, B., Kim, D.-S., 2017. Moisture ingress, behavior, and prediction inside semiconductor packaging: a review. J. Electron. Packag. 139 (1).

Han, Changwoon, 2020. Analysis of moisture-induced degradation of thin-film photovoltaic module. Sol. Energy Mater. Sol. Cells 210, 110488. https://doi.org/10.1016/j.solmat.2020.110488.

Hardikar, K., Krajewski, T., Toivola, K., 2016. Assessing field performance of flexible PV modules for moisture induced degradation from accelerated testing. Conf. Rec. IEEE Photovolt. Spec. Conf. 871–875.

Hardikar, K., Vitkavage, D., Saproo, A., Krajewski, T., 2014a. Establishing the long term moisture barrier performance of the edge seal from accelerated testing. 2014 IEEE 40th Photovoltaic Specialist Conference PVSC 2014, 2016–2020.

Hardikar, K., Vitkavage, D., Saproo, A., Krajewski, T., 2014b. Predicting edge seal performance from accelerated testing, Proceedings of SPIE - The International Society for Optical Engineering.

Haustein, S., Bowman, T.D., Costas, R., 2015. When is an article actually published? An analysis of online availability, publication, and indexation dates. arXiv preprint arXiv:1505.00796.

Hoffmann, Stephan, Koehl, Michael, 2014. Effect of humidity and temperature on the potential-induced degradation. Prog. Photovoltaics Res. Appl. 22 (2), 173–179.

Hu, Y., French, R.H., 2019. Degradation and Failure Mechanisms of PV Module Interconnects, Durability and Reliability of Polymers and Other Materials in Photovoltaic Modules. Elsevier, pp. 119-134.

Hülsmann, P., Wallner, G.M., 2017. Permeation of water vapour through polyethylene terephthalate (PET) films for back-sheets of photovoltaic modules. Polym. Test. 58, 153–158.

Hülsmann, Philip, Weiss, Karl-Anders, 2015. Simulation of water ingress into PV-modules: IEC-testing versus outdoor exposure. Sol. Energy 115, 347–353.

Hülsmann, Philip, Weiß, Karl-Anders, Köhl, Michael, 2014. Temperature-dependent water vapour and oxygen permeation through different polymeric materials used in photovoltaic-modules. Prog. Photovoltaics Res. Appl. 22 (4), 415–421.

Jankovec, M., Annigoni, E., Ballif, C., Topič, M., 2018. In-situ Determination of Moisture Diffusion Properties of PV Module Encapsulants Using Digital Humidity Sensors, 2018 IEEE 7th World Conference on Photovoltaic Energy Conversion, WCPEC 2018 - A Joint Conference of 45th IEEE PVSC, 28th PVSEC and 34th EU PVSEC. pp. 415-417.

Jankovec, M., Galliano, F., Annigoni, E., Li, H.Y., Sculati-Meillaud, F., Perret-Aebi, L.-E., Ballif, C., Topič, M., 2016. In-situ monitoring of moisture ingress in PV modules using digital humidity sensors. IEEE J. Photovoltaics 6 (5), 1152–1159.

Jordan, D.C., Kurtz, S.R., 2013. Photovoltaic degradation rates—an analytical review. Progress in photovoltaics: Research and Applications 21(1), 12-29.

Jorgensen, G., Terwilliger, K., Delcueto, J., Glick, S., Kempe, M., Pankow, J., Pern, F., Mcmahon, T., 2006. Moisture transport, adhesion, and corrosion protection of PV module packaging materials. Sol. Energy Mater. Sol. Cells 90 (16), 2739–2775.

Kempe, Michael, Korkmaz, Kaan, Postak, Lori, Booth, Dennis, Lu, Jerry, Kotarba, Casimir, Rupert, Lindsay, Molnar, Tawana, Aoki, Tsutomu, 2019. Using a butt joint test to evaluate photovoltaic edge seal adhesion. Energy Sci. Eng. 7 (2), 354–360.
Kempe, M., Wohlgemuth, J., Miller, D., Postak, L., Booth, D., Phillips, N., 2016. Investigation of a wedge adhesion test for edge seals, Proceedings of SPIE - The International Society for Optical Engineering.
Kempe, M.D., 2005. Control of moisture ingress into photovoltaic modules, Conference Record of the Thirty-first IEEE Photovoltaic Specialists Conference, 2005. IEEE, pp. 503-506.
KEMPE, M., 2006. Modeling of rates of moisture ingress into photovoltaic modules. Sol. Energy Mater. Sol. Cells 90 (16), 2720–2738.
Kempe, Michael D., Dameron, Arrelaine A., Reese, Matthew O., 2014. Evaluation of moisture ingress from the perimeter of photovoltaic modules. Prog. Photovoltaics Res. Appl. 22 (11), 1159–1171.
Kempe, Michael D., Jordan, Dirk C., 2017. Evaluation and modeling of the potential effects of a module manufacturing anomaly. Prog. Photovoltaics Res. Appl. 25 (12), 982–988.
Kempe, Michael D., Jorgensen, Gary J., Terwilliger, Kent M., McMahon, Tom J., Kennedy, Cheryl E., Borek, Theodore T., 2007. Acetic acid production and glass transition concerns with ethylene-vinyl acetate used in photovoltaic devices. Sol. Energy Mater. Sol. Cells 91 (4), 315–329.
Kempe, Michael D., Nobles, Dylan L., Postak, Lori, Calderon, Jose Alonzo, 2018. Moisture ingress prediction in polyisobutylene-based edge seal with molecular sieve desiccant. Prog. Photovoltaics Res. Appl. 26 (2), 93–101.
Kim, Namsu, Han, Changwoon, 2013. Experimental characterization and simulation of water vapor diffusion through various encapsulants used in PV modules. Sol. Energy Mater. Sol. Cells 116, 68–75.
Kim, T.H., Park, N.C., Kim, D.H., 2013. The effect of moisture on the degradation mechanism of multi-crystalline silicon photovoltaic module. Microelectron. Reliab. 53 (9-11), 1823–1827.
Kimball, G.M., Yang, S., Saproo, A., 2016. Global acceleration factors for damp heat tests of PV modules, 2016 IEEE 43rd Photovoltaic Specialists Conference (PVSC). IEEE, pp. 0101-0105.
Klemchuk, Peter, Ezrin, Myer, Lavigne, Gary, Holley, William, Galica, James, Agro, Susan, 1997. Investigation of the degradation and stabilization of EVA-based encapsulant in field-aged solar energy modules. Polym. Degrad. Stab. 55 (3), 347–365.
Koehl, Michael, Heck, Markus, Wiesmeier, Stefan, 2012. Modelling of conditions for accelerated lifetime testing of Humidity impact on PV-modules based on monitoring of climatic data. Sol. Energy Mater. Sol. Cells 99, 282–291.
Kraft, Achim, Labusch, Lutz, Ensslen, Tobias, Durr, Ines, Bartsch, Jonas, Glatthaar, Markus, Glunz, Stefan, Reinecke, Holger, 2015. Investigation of acetic acid corrosion impact on printed solar cell contacts. IEEE J. Photovoltaics 5 (3), 736–743.
Kudriavtsev, Yu., Hernandez, A.G., Asomoza, R., 2019. Solar cell degradation caused by glass superstrate corrosion. Sol. Energy 187, 82–84.
Kumar, Sagarika, Meena, Roopmati, Gupta, Rajesh, 2019. Imaging and micro-structural characterization of moisture induced degradation in crystalline silicon photovoltaic modules. Sol. Energy 194, 903–912.
Kwembur, I.M., Crozier McCleland, J.L., van Dyk, E.E., Vorster, F.J., 2020. Detection of potential induced degradation in mono and multi-crystalline silicon photovoltaic modules. Phys. B 581, 411938. https://doi.org/10.1016/j.physb:2019.411938.
Köhl, M., 2013. Simulation of water vapor ingress into PV-modules under different climatic conditions. Journal of Materials 2013.
Köntges, M., Kajari-Schröder, S., Kunze, I., 2013. Crack statistic for wafer-based silicon solar cell modules in the field measured by UV fluorescence. IEEE J. Photovoltaics 3 (1), 95–101.
Köntges, M., Kurtz, S., Packard, C., Jahn, U., Berger, K.A., Kato, K., 2014. Performance and reliability of photovoltaic systems: subtask 3.2: Review of failures of photovoltaic modules: IEA PVPS task 13: external final report IEA-PVPS. International Energy Agency, Photovoltaic Power Systems Programme.
Köntges, M., Morlier, A., Eder, G., Fleiß, E., Kubicek, B., Lin, J., 2020. Ultraviolet Fluorescence as Assessment Tool for Photovoltaic Modules. IEEE Journal of Photovoltaics.
La Mantia, F.P., Malatesta, V., Ceraulo, M., Mistretta, M.C., Koci, P., 2016. Photooxidation and photostabilization of EVA and cross-linked EVA. Polym. Test. 51, 6–12.
Liang, Tian Shen, Pravettoni, Mauro, Deline, Chris, Stein, Joshua S., Kopecek, Radovan, Singh, Jai Prakash, Luo, Wei, Wang, Yan, Aberle, Armin G., Khoo, Yong Sheng, 2019. A review of crystalline silicon bifacial photovoltaic performance characterisation and simulation. Energy Environ. Sci. 12 (1), 116–148.
Lopez-Garcia, Juan, Pavanello, Diego, Sample, Tony, 2018. Analysis of temperature coefficients of bifacial crystalline silicon PV modules. IEEE J. Photovoltaics 8 (4), 960–968.
Luo, Wei, Khoo, Yong Sheng, Hacke, Peter, Naumann, Volker, Lausch, Dominik, Harvey, Steven P., Singh, Jai Prakash, Chai, Jing, Wang, Yan, Aberle, Armin G., Ramakrishna, Seeram, 2017. Potential-induced degradation in photovoltaic modules: a critical review. Energy Environ. Sci. 10 (1), 43–68.
Lyu, Yadong, Fairbrother, Andrew, Gong, Mengyan, Kim, Jae Hyun, Gu, Xiaohong, Kempe, Michael, Julien, Scott, Wan, Kai-Tak, Napoli, Sophie, Hauser, Adam, O'Brien, Greg, Wang, Yu, French, Roger, Bruckman, Laura, Ji, Liang, Boyce, Kenneth, 2020. Impact of environmental variables on the degradation of photovoltaic components and perspectives for the reliability assessment methodology. Sol. Energy 199, 425–436.
Marais, S., Nguyen, Q., Langevin, D., Metayer, M., 2001. Transport of water and gases through EVA copolymer films, EVA70/PVC, and EVA70/PVC/gluten blends, Macromolecular Symposia. Wiley Online Library, pp. 329-348.
McIntosh, Keith R., Powell, Nick E., Norris, Ann W., Cotsell, James N., Ketola, Barry M., 2011. The effect of damp-heat and UV aging tests on the optical properties of silicone and EVA encapsulants. Prog. Photovoltaics Res. Appl. 19 (3), 294–300.
Meitzner, Rico, Schulze, Stefan-H., 2016. Method for determination of parameters for moisture simulations in photovoltaic modules and laminated glass. Sol. Energy Mater. Sol. Cells 144, 23–28.
Meyer, E.L., van Dyk, E.E., 2004. Assessing the reliability and degradation of photovoltaic module performance parameters. IEEE Trans. Reliab. 53 (1), 83–92.
Mitterhofer, Stefan, Barretta, Chiara, Castillon, Luis F., Oreski, Gernot, Topic, Marko, Jankovec, Marko, 2020. A dual-transport model of moisture diffusion in PV encapsulants for finite-element simulations. IEEE J. Photovoltaics 10 (1), 94–102.
Miyashita, Masanori, Kawai, Shinji, Masuda, Atsushi, 2012. Measuring method of moisture ingress into Photovoltaic modules. Jpn. J. Appl. Phys. 51 (10S), 10NF12. https://doi.org/10.7567/JJAP.51.10NF12.
Miyashita, M., Masuda, A., 2013. Correlation between moisture ingress and performance in photovoltaic modules. Proc. 28th European Photovoltaic Solar Energy Conf. Exhib.
Moher, David, Liberati, Alessandro, Tetzlaff, Jennifer, Altman, Douglas G., 2009. Preferred reporting items for systematic reviews and meta-analyses: the PRISMA statement. PLoS Med. 6 (7), e1000097.
Mon, G., Wen, L., Ross, R., Adent, D., 1985. Effects of temperature and moisture on module leakage currents, 18th IEEE PVSC. pp. 1179-1185.
Morita, Hideyuki, Miyashita, Masanori, Masuda, Atsushi, 2015. Module composition for reliability test of organic photovoltaics. Jpn. J. Appl. Phys. 54 (8S1), 08KF07. https://doi.org/10.7567/JJAP.54.08KF07.
Morlier, Arnaud, Cros, Stéphane, Garandet, Jean-Paul, Alberola, Nicole, 2013. Gas barrier properties of solution processed composite multilayer structures for organic solar cells encapsulation. Sol. Energy Mater. Sol. Cells 115, 93–99.
Morlier, A., Siebert, M., Kunze, I., Blankemeyer, S., Köntges, M., 2018. Ultraviolet fluorescence of ethylene-vinyl acetate in photovoltaic modules as estimation tool for yellowing and power loss. In: 2018 IEEE 7th World Conference on Photovoltaic Energy Conversion (WCPEC)(A Joint Conference of 45th IEEE PVSC, 28th PVSEC & 34th EU PVSEC). IEEE, pp. 1597–1602.
Morlier, Arnaud, Siebert, Michael, Kunze, Iris, Mathiak, Gerhard, Kontges, Marc, 2017. Detecting photovoltaic module failures in the field during daytime with ultraviolet fluorescence module inspection. IEEE J. Photovoltaics 7 (6), 1710–1716.
Nagayama, K., Kapur, J., Morris, B.A., 2020. Influence of two-phase behavior of ethylene ionomers on diffusion of water. J. Appl. Polym. Sci.
Naumann, V., Ilse, K., Pander, M., Tröndle, J., Sporleder, K., Hagendorf, C., 2019. Influence of soiling and moisture ingress on long term PID susceptibility of photovoltaic modules. AIP Conference Proceedings. AIP Publishing LLC, 090005.
Naumann, Volker, Lausch, Dominik, Hähnel, Angelika, Bauer, Jan, Breitenstein, Otwin, Graff, Andreas, Werner, Martina, Swatek, Sina, Großer, Stephan, Bagdahn, Jörg, Hagendorf, Christian, 2014. Explanation of potential-induced degradation of the shunting type by Na decoration of stacking faults in Si solar cells. Sol. Energy Mater. Sol. Cells 120, 383–389.
Novoa, Fernando D., Miller, David C., Dauskardt, Reinhold H., 2014. Environmental mechanisms of debonding in photovoltaic backsheets. Sol. Energy Mater. Sol. Cells 120, 87–93.
Novoa, Fernando D., Miller, David C., Dauskardt, Reinhold H., 2016. Adhesion and debonding kinetics of photovoltaic encapsulation in moist environments. Prog. Photovoltaics Res. Appl. 24 (2), 183–194.
Omazic, A., Oreski, G., Halwachs, M., Eder, G.C., Hirschl, C., Neumaier, L., Pinter, G., Erceg, M., 2019. Relation between degradation of polymeric components in crystalline silicon PV module and climatic conditions: a literature review. Sol. Energy Mater. Sol. Cells 192, 123–133.
Oreski, G., 2019. Co-extruded backsheets for PV modules: Past approaches and recent developments. NIST/UL Workshop on Photovoltaic Materials Durability Gaithersburg, USA.
Oreski, Gernot, Mihaljevic, Antonia, Voronko, Yuliya, Eder, Gabriele C., 2017. Acetic acid permeation through photovoltaic backsheets: Influence of the composition on the permeation rate. Polym. Test. 60, 374–380.
Oreski, G., Ottersböck, B., Omazic, A., 2019. Degradation processes and mechanisms of encapsulants, durability and reliability of polymers and other materials in photovoltaic modules. Elsevier 135–152.
Oreski, G., Wallner, G.M., 2005. Aging mechanisms of polymeric films for PV encapsulation. Sol. Energy 79 (6), 612–617.
Paduthol, Appu, Juhl, Mattias Klaus, Trupke, Thorsten, 2018. Addressing limitations of photoluminescence based external quantum efficiency measurements. J. Appl. Phys. 123 (2), 023105. https://doi.org/10.1063/1.5004193.
Peike, C., Hoffmann, S., Hülsmann, P., Thaidigsmann, B., Weiβ, K.A., Koehl, M., Bentz, P., 2013a. Origin of damp-heat induced cell degradation. Sol. Energy Mater. Sol. Cells 116, 49–54.
Peike, C., Hädrich, I., Weiß, K.-A., Dürr, I., 2013b. Overview of PV module encapsulation materials. Photovoltaics International 19, 85–92.
Peike, C., Hoffmann, S., Hülsmann, P., Weiß, K.-A., Koehl, M., Bentz, P., 2012. Permeation impact on metallization degradation, Reliability of Photovoltaic Cells, Modules, Components, and Systems V. International Society for Optics and Photonics, p. 84720U.
Peike, C., Kaltenbach, T., Weiß, K.-A., Koehl, M., 2011. Non-destructive degradation analysis of encapsulants in PV modules by Raman Spectroscopy. Sol. Energy Mater. Sol. Cells 95 (7), 1686–1693.

Pern, F.J., Glick, S.H., 2000. Photothermal stability of encapsulated Si solar cells and encapsulation materials upon accelerated exposures. Sol. Energy Mater. Sol. Cells 61 (2), 153–188.
Pern, J., 2008. Module encapsulation materials, processing and testing (presentation). National Renewable Energy Lab.(NREL), Golden, CO (United States).
Peshek, T.J., Fada, J.S., Martin, I.T., 2019. Degradation Processes in Photovoltaic Cells, Durability and Reliability of Polymers and Other Materials in Photovoltaic Modules. Elsevier 97–118.
Philipps, S., Warmuth, W., 2019. Photovoltaics Report Fraunhofer Institute for Solar Energy Systems, ISE with support of PSE GmbH November 14th.
Pingel, S., Frank, O., Winkler, M., Daryan, S., Geipel, T., Hoehne, H., Berghold, J., 2010. Potential induced degradation of solar cells and panels, 2010 35th IEEE Photovoltaic Specialists Conference. IEEE, pp. 002817-002822.
Rashtchi, S., Ruiz, P.D., Wildman, R., Ashcroft, I., 2012. Measurement of moisture content in photovoltaic panel encapsulants using spectroscopic optical coherence tomography: A feasibility study, Proceedings of SPIE - The International Society for Optical Engineering.
Reese, Matthew O., Dameron, Arrelaine A., Kempe, Michael D., 2011. Quantitative calcium resistivity based method for accurate and scalable water vapor transmission rate measurement. Rev. Sci. Instrum. 82 (8), 085101. https://doi.org/10.1063/1.3606644.
Roy, Subinoy, Gupta, Rajesh, 2019. Non-destructive approach for severity investigation of shunts in crystalline silicon photovoltaic modules by combination of electroluminescence imaging and lock-in thermography. Meas. Sci. Technol. 30 (4), 044009. https://doi.org/10.1088/1361-6501/ab0265.
Sander, R., 2015. Compilation of Henry's law constants (version 4.0) for water as solvent. Atmos. Chem. Phys 15 (8), 4399–4981.
Santhakumari, Manju, Sagar, Netramani, 2019. A review of the environmental factors degrading the performance of silicon wafer-based photovoltaic modules: Failure detection methods and essential mitigation techniques. Renew. Sustain. Energy Rev. 110, 83–100.
Schlothauer, Jan, Jungwirth, Sebastian, Köhl, Michael, Röder, Beate, 2012. Degradation of the encapsulant polymer in outdoor weathered photovoltaic modules: Spatially resolved inspection of EVA ageing by fluorescence and correlation to electroluminescence. Sol. Energy Mater. Sol. Cells 102, 75–85.
Sinha, A., Roy, S., Kumar, S., Gupta, R., 2017. Investigation of degradation in photovoltaic modules by infrared and electroluminescence imaging, Advances in Optical Science and Engineering. Springer, pp. 3-9.
Slapsak, Jan, Mitterhofer, Stefan, Topic, Marko, Jankovec, Marko, 2019. Wireless system for in situ monitoring of moisture ingress in PV Modules. IEEE J. Photovoltaics 9 (5), 1316–1323.
Swonke, T., Auer, R., 2009. Impact of moisture on PV module encapsulants. Components, and Systems II. International Society for Optics and Photonics, Reliability of Photovoltaic Cells, Modules, p. 74120A.
Tanenbaum, David M., Dam, Henrik Friis, Rösch, Roland, Jørgensen, Mikkel, Hoppe, Harald, Krebs, Frederik C., 2012. Edge sealing for low cost stability enhancement of roll-to-roll processed flexible polymer solar cell modules. Sol. Energy Mater. Sol. Cells 97, 157–163.
Theelen, Mirjam, Beyeler, Kyo, Steijvers, Henk, Barreau, Nicolas, 2017. Stability of CIGS solar cells under illumination with damp heat and dry heat: a comparison. Sol. Energy Mater. Sol. Cells 166, 262–268.
Tracy, Jared, Bosco, Nick, Delgado, Chris, Dauskardt, Reinhold, 2020. Durability of ionomer encapsulants in photovoltaic modules. Sol. Energy Mater. Sol. Cells 208, 110397. https://doi.org/10.1016/j.solmat.2020.110397.
Tracy, Jared, D'hooge, Dagmar R., Bosco, Nick, Delgado, Chris, Dauskardt, Reinhold, 2018. Evaluating and predicting molecular mechanisms of adhesive degradation during field and accelerated aging of photovoltaic modules. Prog. Photovoltaics Res. Appl. 26 (12), 981–993.
Trupke, T., Mitchell, B., Weber, J.W., McMillan, W., Bardos, R.A., Kroeze, R., 2012. Photoluminescence imaging for photovoltaic applications. Energy Procedia 15, 135–146.
van der Wel, G.K., Adan, O.C.G., 1999. Moisture in organic coatings—a review. Prog. Org. Coat. 37 (1-2), 1–14.
Vandyk, E., Chamel, J., Gxasheka, A., 2005. Investigation of delamination in an edge-defined film-fed growth photovoltaic module. Sol. Energy Mater. Sol. Cells 88 (4), 403–411.
Virtuani, Alessandro, Annigoni, Eleonora, Ballif, Christophe, 2019a. One-type-fits-all-systems: strategies for preventing potential-induced degradation in crystalline silicon solar photovoltaic modules. Prog. Photovoltaics Res. Appl. 27 (1), 13–21.
Virtuani, A., Caccivio, M., Annigoni, E., Friesen, G., Chianese, D., Ballif, C., Sample, T., 2019b. 35 years of photovoltaics: analysis of the TISO-10-kW solar plant, lessons learnt in safety and performance—Part 1. Prog. Photovoltaics Res. Appl. 27 (4), 328–339.
Weerasinghe, Hasitha C., Dkhissi, Yasmina, Scully, Andrew D., Caruso, Rachel A., Cheng, Yi-Bing, 2015a. Encapsulation for improving the lifetime of flexible perovskite solar cells. Nano Energy 18, 118–125.
Weerasinghe, Hasitha C., Watkins, Scott E., Duffy, Noel, Jones, David J., Scully, Andrew D., 2015b. Influence of moisture out-gassing from encapsulant materials on the lifetime of organic solar cells. Sol. Energy Mater. Sol. Cells 132, 485–491.
Wisniewski, David, Lv, Ruirui, Nair, Selvakumar V., Jaubert, Jean-Nicolas, Xu, Tao, Ruda, Harry E., 2019. Measurement and modelling of water ingress into double-glass photovoltaic modules. Prog. Photovoltaics Res. Appl. 27 (2), 144–151.
Wohlgemuth, J., Silverman, T., Miller, D.C., McNutt, P., Kempe, M., Deceglie, M., 2015. Evaluation of PV module field performance, 2015 IEEE 42nd Photovoltaic Specialist Conference (PVSC). IEEE, pp. 1-7.
Wohlgemuth, J.H., Kempe, M.D., 2013. Equating damp heat testing with field failures of PV modules, 2013 IEEE 39th Photovoltaic Specialists Conference (PVSC). IEEE 0126–0131.
Yamaguchi, Seira, Yamamoto, Chizuko, Ohshita, Yoshio, Ohdaira, Keisuke, Masuda, Atsushi, 2020. Influence of emitter position of silicon heterojunction photovoltaic solar cell modules on their potential-induced degradation behaviors. Sol. Energy Mater. Sol. Cells 216, 110716. https://doi.org/10.1016/j.solmat.2020.110716.
Yang, C., Xing, X., Li, Z., Zhang, S., 2020. A comprehensive review on water diffusion in polymers focusing on the polymer-metal interface combination. Polymers 12 (1), 138.
Yang, H.E., 2019. Overview: Durability and Reliability of Common PV Module and Polymers/Materials, Durability and Reliability of Polymers and Other Materials in Photovoltaic Modules. Elsevier, pp. 23-45.

Paper C

The effect of moisture ingress on titania antireflection coatings in field-aged photovoltaic modules by O.K. Segbefia, N. Akhtar, and T.O. Sætre. Published in the 49th IEEE Photovoltaics Specialists Conference (2022).

The effect of moisture ingress on titania antireflection coatings in field-aged photovoltaic modules

Oscar Kwame Segbefia[1], Naureen Akhtar[1], Tor Oskar Sætre[1]

[1]Department of Engineering Sciences, University of Agder, 4879 Grimstad, Norway

***Abstract*—Titanium dioxide (TiO_2) or titania antireflection coating (ARC) enhances photovoltaic (PV) module efficiency. Yet, degraded TiO_2 can affect the performance reliability of PV modules. In the present work, the effect of moisture ingress on the degradation of TiO_2 ARC in a field-aged multicrystalline silicon PV module is investigated. Scanning electron microscopy (SEM) and energy dispersive X-ray spectroscopy (EDS) analyses show degradation of the TiO_2 ARC. Disintegration of the TiO_2 nanoparticles (NPs) were also observed. The assumed Ti-O stoichiometry of the degraded TiO_2 ARC in the field-aged PV module was found to be higher than 1:2. It turned out that moisture ingress strongly influences the surface morphology and defects, crystallinity, and stoichiometry of TiO_2 ARC in the PV module during field operation. Silver and aluminium NPs migrate to and aggregate on the surfaces of the TiO_2 NPs which might likely lead to the formation of titania-metal complexes such as titania-alumina and silver-titania complexes. These degradation mechanisms affect the opto-electrical properties of the TiO_2 ARC in the PV module.**

Keywords— titanium dioxide, moisture ingress, degradation, morphology, titania-metal complex

I. INTRODUCTION

Crystalline silicon (c-Si) photovoltaic (PV) modules are made up of a framework of solar cells, front glass, antireflection coating, polymeric front encapsulation (e.g., ethylene vinyl acetate, EVA), backsheet (polymeric/glass), aluminum frame, and junction boxes [1, 2]. The solar cells convert sunlight to clean electricity via the photovoltaic effect. The other components play complementary roles to enhance performance reliability, and hence, optimize the PV module's efficiency [2, 3]. The presence of moisture within the PV module initiates different electrochemical reaction pathways [3]. This leads to different defects and fault mechanisms [4]. Some of these defects and fault modes are cracks, corrosion, optical degradation, and potential induced degradation [5, 6]. This leads to drop in power output of the PV modules [4-6].

In spite of the various degradation mechanisms, a major problem for low efficiency in c-Si solar cells is the high surface reflectivity of the polished silicon substrate [7-10]. Antireflection coating (ARC) improves the fraction of incident light reflection and coupling of the absorbed photon within the PV module. Hence, ARC is used in commercial PV modules to improve the device efficiency [11, 12]. Titanium dioxide or titania (TiO_2) ARC, in particular, is a well-established technology in the PV industry [7] and the most popular ARC used in photovoltaic devices [9, 13]. Stoichiometric TiO_2 films exhibit optimum refractive index, low absorption coefficient, excellent thermal and chemical stability, and is cost-effective [7]. However, it is known that the properties of the TiO_2 film depend on the sintering and deposition conditions [7, 12, 14, 15]. For instance, diffused moisture in porous TiO_2 films during deposition influences the refractive index [13, 16, 17].

It is also believed that TiO_2 possesses superior photocatalytic self-cleaning property under ultraviolet (UV) light (λ<400 nm). This property could be enhanced by doping TiO_2 with noble metals with its associated cost constraints [18]. The excellent photoactivity of TiO_2 can also lead to the formation of free radicals within the PV module bulk, hence, accelerated degradation of the polymeric encapsulation [19]. Moreover, the main limitation of TiO_2 ARC is that it possesses poor passivation characteristics [13]. Deficient passivation characteristics means degradation of TiO_2 ARC under UV radiation [20]. Besides, the morphology, surface defects, and presence of moisture can affect the efficiency of the TiO_2 ARC [21]. When moisture enters the PV module during operation in the field, degradation of the TiO_2 film is likely. In this case, the opto-electrical efficiency could also be compromised. Yet, we have not found any publication on the effect of moisture on the TiO_2 ARC in PV modules in the field.

In the present work, the effect of moisture on the degradation of the TiO_2 ARC in a field-aged multicrystalline silicon (mc-Si) PV module is investigated using scanning electron microscopy (SEM) and energy dispersive spectroscopy (EDS) techniques. Section 2 presents the experimental methods used for the investigation. This is followed by the discussion of the results on the effects of moisture on the TiO_2 ARC in Section 3.

II. MATERIAL AND METHODS

A field-aged PV module from a group of PV modules which were installed outdoors in Dømmesmoen, Grimstad (58.3° N, 8.59° E), Norway between the year 2000 and 2011 was chosen for this investigation [22]. The manufacture's data sheet and the measured average electrical data of the chosen field-aged PV module is presented in Table 1. The parameters measured were the maximum power (P_{max}), open circuit and maximum power point voltage (V_{oc}, V_{mpp}), short circuit and maximum power point current (I_{sc}, I_{mpp}), and fill factor (FF), The values in Table 1 are normalized to Standard Test Conditions (STC).

2022 IEEE 49th Photovoltaics Specialists Conference (PVSC) | 978-1-7281-6117-4/22/$31.00 ©2022 IEEE | DOI: 10.1109/PVSC48317.2022.9938896

The PV module was manufactured using anodized aluminium (Al-) frame, low iron tempered front glass, ethylene vinyl acetate (EVA) encapsulation, white multi-layered Tedlar®/Polyester/Tedlar® (TPT) backsheet, and 2 weatherproof plastic casing junction boxes (accommodating a bypass diode each). The screen-printed multicrystalline solar cells with dimensions of 100 x 100 mm^2 were made using a TiO_2 ARC and tinned copper (Cu) busbars. The PV module is an assembly of (12 x 2) series connected solar cells in 3 substrings. The cells were cut out from the panel using a water jet cutting machine and the cells were extracted by treating them with toluene.

A. I-V measurements

The selected field-aged PV module was taken through current-voltage (I-V) measurements using a handheld I-V 500w I-V Curve Tracer, following the IEC 60904- 1 standard. These measurements provided information on the electrical characteristics, irradiance, and module temperature characteristics at Standard Test Conditions (STC). STC specifies cell temperature of 25 °C, an irradiance of 1000 W/m^2 and air mass 1.5 (AM1. 5) spectrum for commercial PV modules. Measurements were done under clear sky in-plane irradiance (GI) (960 - 1060 W/m^2) conditions, and the I-V tracer used converted all measurements to STC automatically. This means the operating conditions were optimally resolved by the device to minimize errors in measuring and recording data.

TABLE I. AVERAGE ELECTRICAL PARAMETERS OF THE PV MODULE

Year	P_{max} (W)	V_{oc} (V)	V_{mpp} (V)	I_{mpp} (A)	I_{sc} (A)	*FF* (%)	η (%)
2000	100	21.6	16.7	6.0	6.7	70	13
2020	76.0	19.8	14.4	5.3	6.0	64	10

B. Microstructural Investigation

The as-cut solar cells (which comprised of the front glass, EVA, and backsheet) was immersed in toluene to extract the solar cells. The reclamation of the solar cells took 14 days under room temperature conditions. Finally, the extracted solar cell samples were investigated using SEM-EDS techniques to identify the effect of moisture on the TiO_2 ARC. The SEM-EDS analysis was done utilizing a field emission scanning electron microscope (SEM) (JEOL 7200F) equipped with an energy dispersive X-ray spectrometer (Octane Elect EDS system from EDAX®-AMETEK®). An overview of the experimental method is shown in Fig. 1.

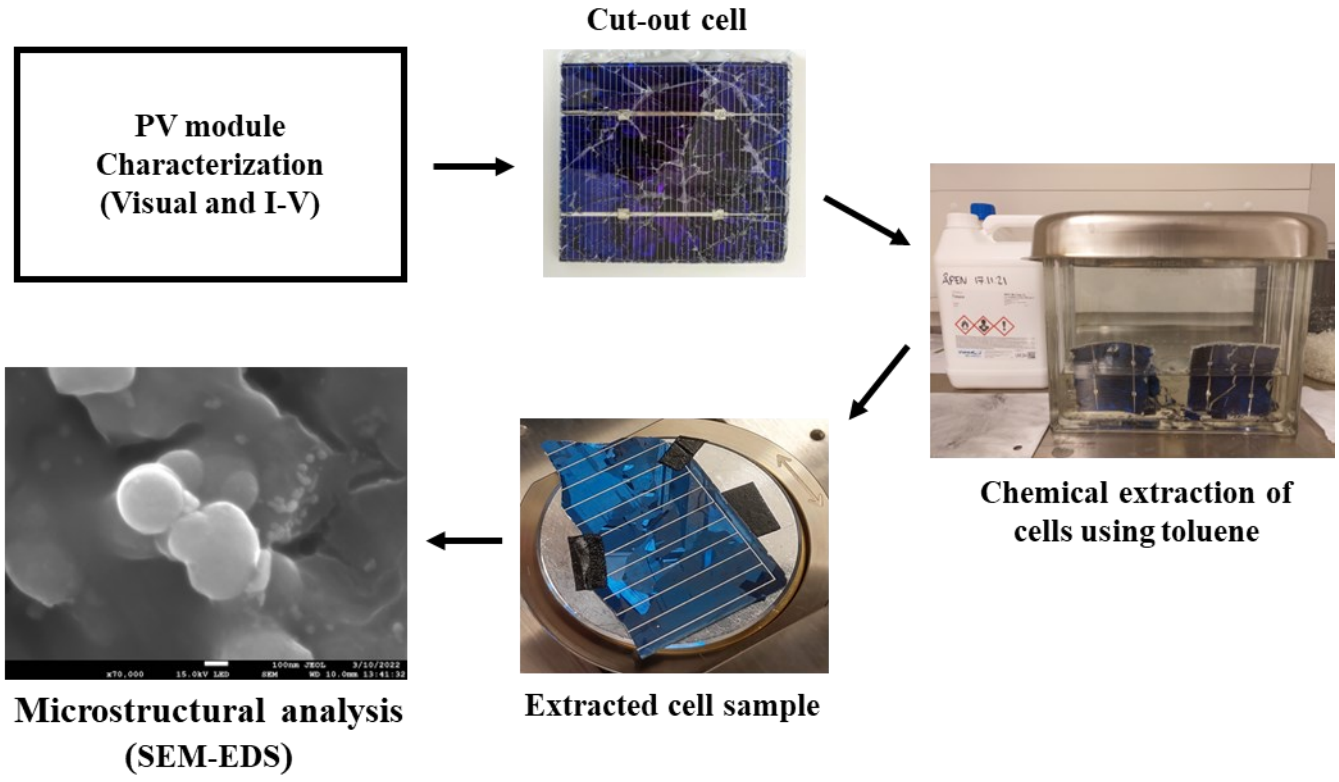

Fig. 1. Overview of the experimental method.

III. Results and Discussion

A. Visual inspection

Fig. 2 shows the results from the visual inspection of the field-aged PV module. Figs. 2a and 2b show signs of moisture ingress from the edges of the modules. Aside from influencing the optical and electrical efficiency of the ARC, the ingressed moisture can cause the production of acetic acid in the presence of ethylene vinyl acetate (EVA) encapsulant , and the presence of acidic species catalyzes TiO_2 degradation [19]. This can initiate several degradation mechanisms within the PV module [2, 3].

In Figs. 2a and 2b, there are clear indications of encapsulant discoloration, metal grid corrosion, and solar cell degradation. The front and the rear sides of the extracted cell after toluene treatments are shown in Fig. 2c and Fig. 2d, respectively. Some parts of the Cu busbars and the silver fingers appear to be darker than other parts of the same solar cell. It appears that the Cu busbars and the silver fingers have undergone some degradation. However, the focus of this paper is on the TiO_2 ARC. The degradation of Cu and other components of the solar cells is the subject of future investigation.

B. SEM-EDS characteristics

To investigate the effect of moisture on the degradation of the ARC, the extracted solar cells were taken through SEM-EDS analysis. Fig. 3 shows the SEM-EDS analyses from the region about 10 mm from the edge of a solar cell extracted from the field-aged PV module. The SEM micrograph in Fig. 3a and its corresponding EDS analyses is shown in Figs. 3b - d. The elemental mappings for oxygen (O) and titanium (Ti) of the SEM micrograph as displayed in Fig. 3a are shown in Figs. 3c and 3d, respectively. Highlighted in yellow circle, nanoparticles (NPs) of TiO_2 ARC, that appear bright in the SEM micrographs are randomly distributed on the surface of the solar cells, see Fig. 3a. The assumed titanium-oxygen (Ti-O) stoichiometry of TiO_2 is 1:2.

Fig. 3b represents the EDS elemental composition of the TiO_2 ARC in the field-aged PV module investigated. Obviously, silicon (Si) assumed the greatest abundance, as the TiO_2 ARC were deposited on multicrystalline silicon solar cells. The amount of oxygen in Fig. 3b suggests that the effect of moisture ingress on the solar cells is likely. The stoichiometry of Ti and O also confirms that the stoichiometric TiO_2 ARC has undergone oxidation. This observation agrees with other reports on the effect of moisture on TiO_2 [14, 23]. The presence of phosphorus (P) is thought to be from the degradation of the EVA encapsulant which contains phosphate stabilizing antioxidants [24].

The Ti-O elemental maps of oxygen (Fig. 3c) and titanium (Fig.3d) confirm that O and Ti are located along the same areas on the solar cells. It also shows the relative positions of O and TiO_2 NPs around the edges of the solar cell's microcrystals. This suggests that moisture induced degradation starts from the edges of the solar cells' crystals.

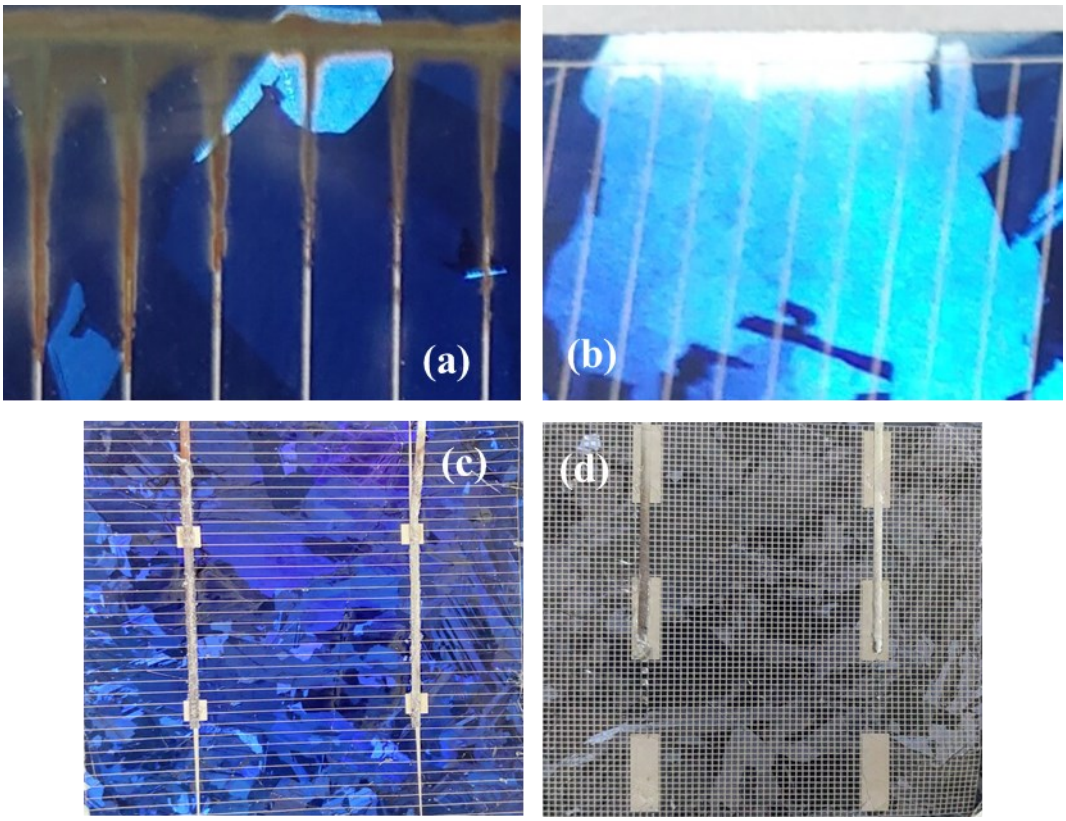

Fig. 2. Visual images of the field-aged PV module showing (a) - (b) signs of moisture ingress from the edges and the (c) front and (d) rear sides of the extracted solar cell.

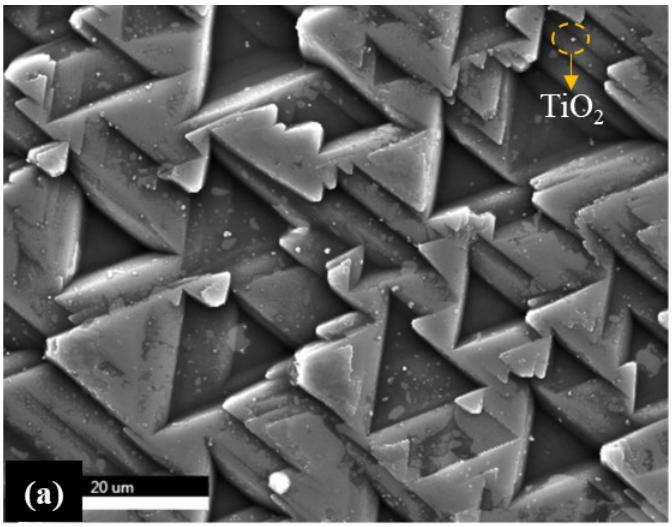

(b)

Element	Atomic %
O	11.6
Si	85.8
P	0.4
Ti	2.1

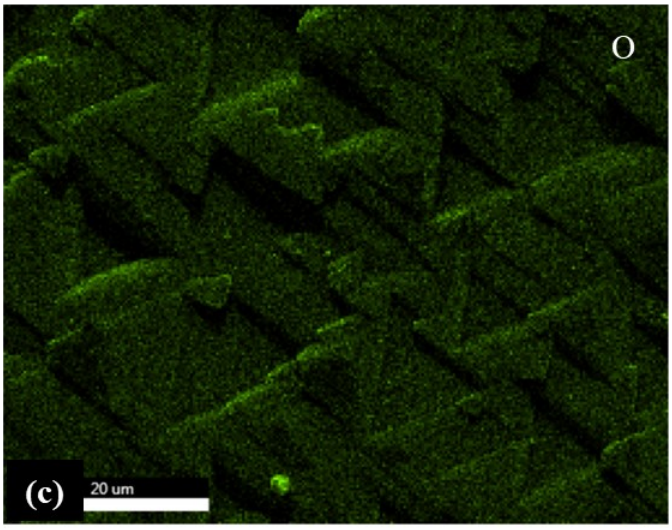

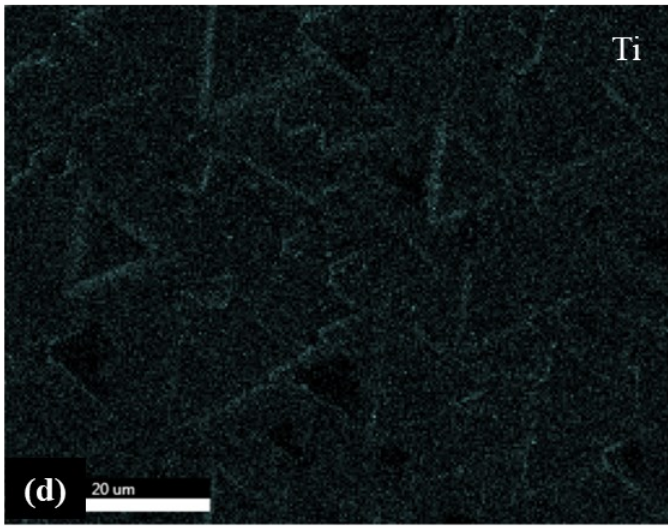

Fig. 3. (a) SEM micrograph and (b) EDS analysis and elemental mapping of (c) oxygen and (d) titanium of a solar cell extracted from the field-aged PV module. The data were taken from the middle of the solar cell, about 10 mm from the edge of the solar cell.

Fig. 4 shows the SEM-EDS analyses of a solar cell extracted from the edge of the field-aged PV module. Fig. 4a is the SEM micrograph with the corresponding EDS analyses in Figs. 4b - 4d. Figs. 4b and 4c show the relative positions of the TiO_2 NPs on the solar cell. It is evident that most of the oxygen content is associated with these particles. Also, it is clear from Fig. 4d that the dark spots correspond to the relative positions of the oxidized TiO_2 ARC NPs. This further suggests that these NPs are just not oxidized, but it is likely that the observed NPs form titania complexes with other elements. The EDS spectra and analysis of the SEM micrograph in Fig. 4a is shown in Figs. 5a and 5b, respectively. The Ti to O ratio as deduced from the quantification results shown in Fig. 5b is approximately 1:6, which is similar to what was observed in Fig. 3b. This suggests that the degradation of TiO_2 ARC appears to follow a general trend across the solar cells.

Leaching of aluminium (Al) from rear contacts of the solar cells under the influence of moisture ingress is also evident, see Figs. 5a and 5b. This agrees with other reports [25]. In Fig. 5a, the vertical and horizontal axes represent X-ray counts and electron energy (keV), respectively. Si shows the highest intensity. The EDS spectra in Fig. 5a corroborates with the elemental composition analysis in Fig. 5b. The higher amount of oxygen observed on the solar cells extracted from the edge of the PV module suggests that the influence of moisture ingress near the edges of the PV module is greater. Fig. 6 shows the high magnification SEM micrographs of some of the NPs of the TiO_2 ARC in their degraded forms. The surfaces of these NPs have been modified significantly. Fig. 7 shows the SEM-EDS analyses of some of the NPs of the TiO_2 ARC.

The presence of moisture can influence the Ti-O bond by introducing extra oxygen vacancies in the TiO_2 ARC [14]. In acetic acid environments, the morphology of TiO_2 NPs can change and become more porous, as observed elsewhere [26]. That is, degradation of the EVA encapsulant in the presence of moisture can further accelerate the degradation of the TiO_2 ARC. Another possible explanation for the observed degradation of the ARC might be the synergetic effect of UV radiation and moisture [23].

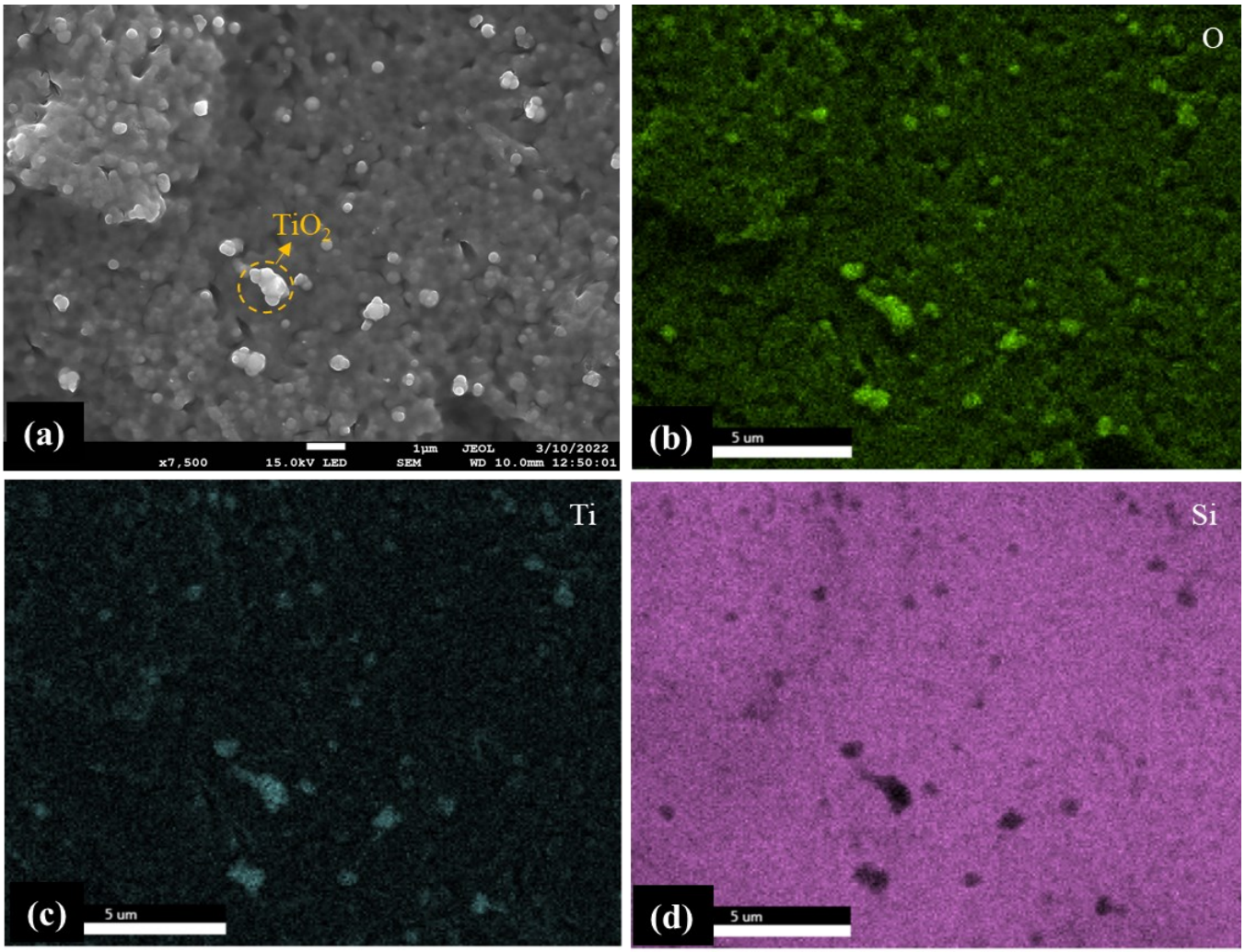

Fig. 4. (a) SEM micrograph and the corresponding EDS elemental mappings of (b) oxygen, (c) titanium, and (d) silicon of a solar cell extracted from the edge of the field-aged PV module.

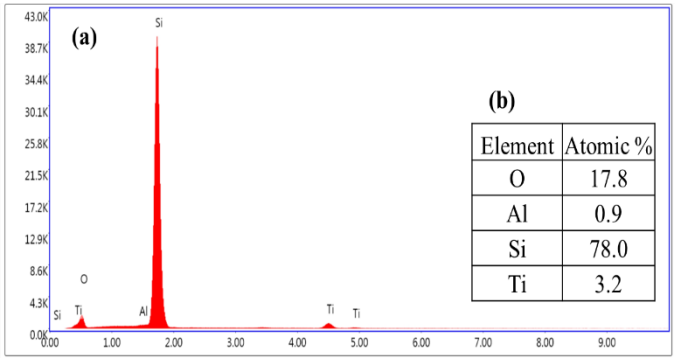

Fig. 5. (a) EDS spectra and (b) EDS analysis of the SEM micrograph in Fig. 4a.

Fig. 7c displays the EDS analysis of Fig. 7a and the EDS point analysis at Point 1 in Fig. 7b is shown in Fig. 7d. As expected, the observed Ti-O stoichiometry of TiO_2 ARC is significantly higher, which strongly suggests moisture induced degradation. Moreover, the morphologies of the two main phases of stoichiometric TiO_2: anatase and rutile; that are used in PV applications are different from what was observed in Figs. 6 and 7. Both phases of TiO_2 are more efficient in the crystalline phase [15, 23, 26]. The structural features of the TiO_2 ARC NPs are also modified substantially, see Fig. 7. The surface morphology and defects, crystallinity, and stoichiometry are known to affect the efficiency of TiO_2 NPs [15, 21]. Figs. 6 and 7 suggest that moisture ingress is the underlying factor for the observed disintegration of the TiO_2 NPs. In Fig. 7b, NPs of Ag (from the silver paste) were found to migrate to and aggregate on the surfaces of the TiO_2 ARC NPs under the influence of moisture ingress. This can lead to the formation of silver-titania (Ag-TiO_2) metal complexes. Other metal ions (e.g., lead, tin, sodium, and zinc) from the silver paste and solder are also capable of migrating to the surface of the TiO_2 ARC NPs under the influence of moisture ingress [27-29]. Moisture assisted migration of metal ions to the surface of the TiO_2 ARC can cause potential induced degradation [30].

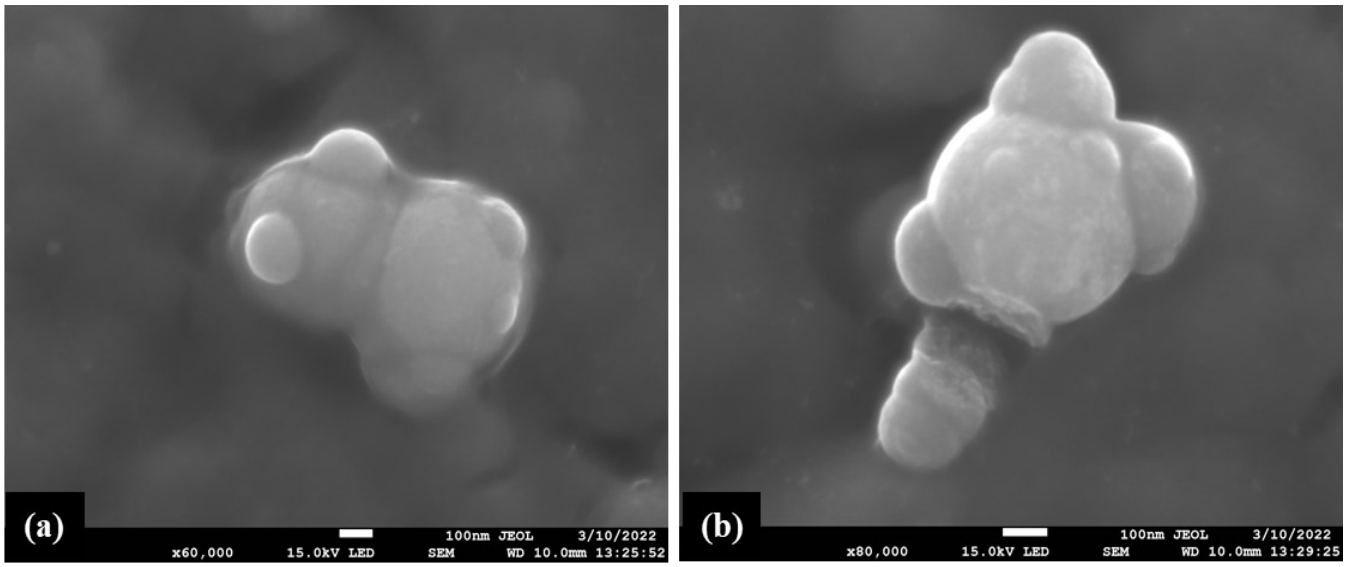

Fig. 6. Degraded TiO_2 ARC nanoparticles in the field-aged PV module.

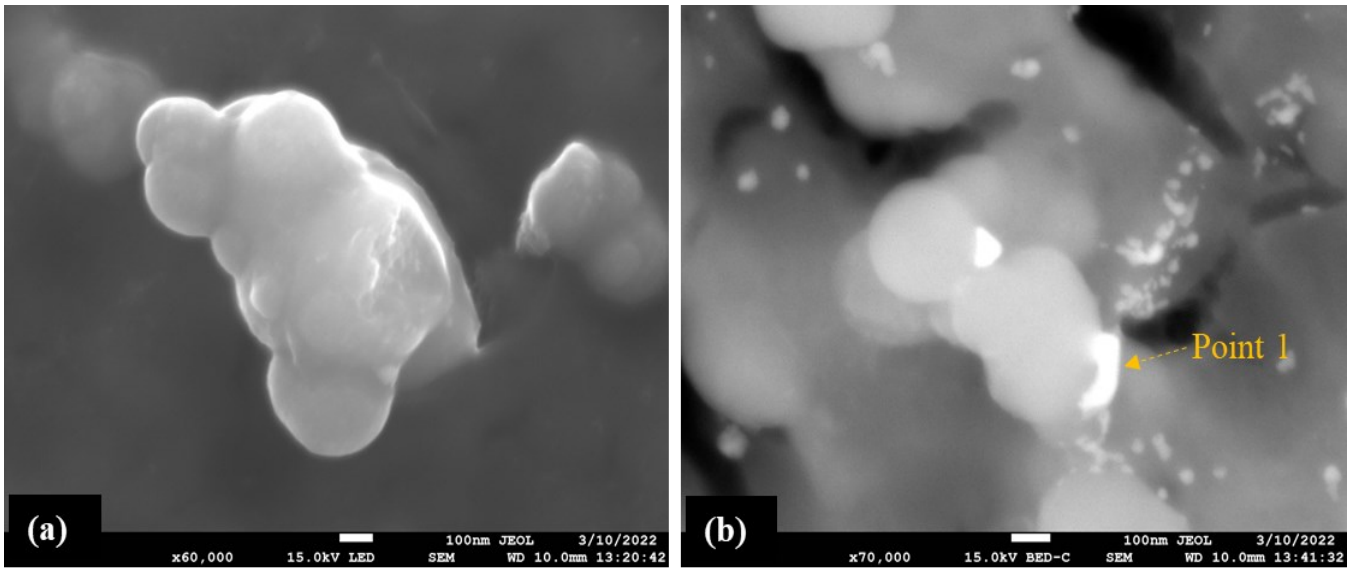

(c)

Element	Atomic %
O	58.2
Si	30.1
Ti	11.6

(d)

Element	Atomic %
O	35.2
Al	0.9
Si	55.2
Ag	2.1
Ti	6.6

Fig. 7. (a) - (b) High magnification SEM micrographs of TiO_2 ARC NPs in Fig. 4a and corresponding EDS (c) full area analysis of Fig. 7a and (d) point analysis at Point 1 in Fig. 7b.

One interesting observation from Figs. 5b and 7d is that the amount of Al (0.9 %) is the same. This suggests the formation of titania-alumina (Ti-O-Al) complexes under the influence of moisture ingress. The formation of these metal complexes can affect opto-electrical properties of the TiO_2 ARC [31]. That is, refractive index, scattering properties, and extinction coefficient of the TiO_2 ARC during field operation, are strongly influenced by moisture ingress.

IV. Conclusion

Titania (TiO_2) antireflection coatings play a vital role in enhancing PV module efficiency. However, in degraded form, TiO_2 can affect the performance reliability of PV modules. In the present work, the effect of moisture ingress on the degradation of TiO_2 ARC in a 20-year-old field-aged PV module is investigated. Visual inspection suggests the incidence of moisture ingress in the field-aged PV module. The SEM-EDS analyses show that moisture ingress leads to the degradation of the TiO_2 ARC. The assumed Ti-O stoichiometry of the oxidized TiO_2 ARC in the module was found to be higher than 1:2. Also, the surface morphology of the TiO_2 ARC NPs appeared to be modified under the influence of moisture. Finally, Ag and Al-NPs were observed to migrate to and aggregate on the surfaces of the TiO_2 ARC NPs which can induce the formation of titania-metal complexes e.g., titania-alumina and silver-titania complexes. These metal complexes can influence the opto-electrical properties of the TiO_2 ARC, hence, the performance reliability of PV modules. Specifically, moisture ingress strongly influences the refractive index, scattering properties, and extinction coefficient of the TiO_2 ARC in PV modules during field operation. This could be an important cause of the observed 1.2 %/year degradation in the P_{max} of the field-aged PV module, refer to Table I.

References

[1] M. C. C. de Oliveira, A. S. A. D. Cardoso, M. M. Viana, and V. d. F. C. Lins, "The causes and effects of degradation of encapsulant ethylene vinyl acetate copolymer (EVA) in crystalline silicon photovoltaic modules: A review," Renew. Sust. Energ. Rev., vol. 81, pp. 2299-2317, 2018, doi: https://doi.org/10.1016/j.rser.2017.06.039.

[2] M. Köntges et al., "Review of failures of photovoltaic modules," 2014.

[3] O. K. Segbefia, A. G. Imenes, and T. O. Saetre, "Moisture ingress in photovoltaic modules: A review," (in English), Sol. Energy, vol. 224, pp. 889-906, Aug 2021, doi: 10.1016/j.solener.2021.06.055.

[4] O. K. Segbefia, A. G. Imenes, and T. O. Saetre, "Outdoor Fault Diagnosis of Field-Aged Multicrystalline Silicon Solar Modules," in 37th EU PVSEC, 2020, 2020.

[5] O. K. Segbefia, A. G. Imenes, I. Burud, and T. O. Sætre, "Temperature profiles of field-aged multicrystalline silicon photovoltaic modules affected by microcracks," in 2021 IEEE 48th Photovoltaic Specialists Conference (PVSC), 2021: IEEE, pp. 0001-0006, doi: 10.1109/PVSC43889.2021.9518939.

[6] O. K. Segbefia and T. O. Sætre, "Investigation of the Temperature Sensitivity of 20-Years Old Field-Aged Photovoltaic Panels Affected by Potential Induced Degradation," Energies, vol. 15, no. 11, p. 3865, 2022. [Online]. Available: https://www.mdpi.com/1996-1073/15/11/3865.

[7] B. S. Richards, "Single-material TiO2 double-layer antireflection coatings," (in English), Sol. Energy Mater. Sol. Cells, vol. 79, no. 3, pp. 369-390, Sep 15 2003, doi: 10.1016/S0927-0248(02)00473-7.

[8] D. Bouhafs, A. Moussi, A. Chikouche, and J. M. Ruiz, "Design and simulation of antireflection coating systems for optoelectronic devices: Application to silicon solar cells," (in English), Sol. Energy Mater. Sol. Cells, vol. 52, no. 1-2, pp. 79-93, Mar 16 1998, doi: Doi 10.1016/S0927-0248(97)00273-0.

[9] S. Chhajed, M. F. Schubert, J. K. Kim, and E. F. Schubert, "Nanostructured multilayer graded-index antireflection coating for Si solar cells with broadband and omnidirectional characteristics," (in English), Appl. Phys. Lett., vol. 93, no. 25, p. 251108, Dec 22 2008, doi: Artn 25110810.1063/1.3050463.

[10] W. Kern and E. Tracy, "Titanium-Dioxide Antireflection Coating for Silicon Solar-Cells by Spray Deposition," (in English), Rca Review, vol. 41, no. 2, pp. 133-180, 1980.

[11] A. S. Sarkın, N. Ekren, and Ş. Sağlam, "A review of anti-reflection and self-cleaning coatings on photovoltaic panels," Sol. Energy, vol. 199, pp. 63-73, 2020, doi: https://doi.org/10.1016/j.solener.2020.01.084.

[12] M. Murozono, S. Kitamura, T. Ohmura, K. Kusao, and Y. Umeo, "Titanium dioxide antireflective coating for silicon solar cells by spinning technique," Jpn. J. Appl. Phys., vol. 21, no. S2, p. 137, 1982, doi: https://doi.org/10.7567/JJAPS.21S2.137.

[13] N. Shanmugam, R. Pugazhendhi, R. M. Elavarasan, P. Kasiviswanathan, and N. Das, "Anti-Reflective Coating Materials: A Holistic Review from PV Perspective," (in English), Energies, vol. 13, no. 10, p. 2631, May 2020, doi: https://doi.org/10.3390/en13102631.

[14] T. Fuyuki, T. Kobayashi, and H. Matsunami, "Effects of Small Amount of Water on Physical and Electrical-Properties of Tio2 Films Deposited by Cvd Method," (in English), J. Electrochem. Soc., vol. 135, no. 1, pp. 248-250, Jan 1988, doi: Doi 10.1149/1.2095566.

[15] Y. Leprince-Wang and K. Yu-Zhang, "Study of the growth morphology of TiO2 thin films by AFM and TEM," (in English), Surface & Coatings Technology, vol. 140, no. 2, pp. 155-160, May 30 2001, doi: Doi 10.1016/S0257-8972(01)01029-5.

[16] V. N. Van et al., "Growth of Low and High Refractive-Index Dielectric Layers as Studied by in-Situ Ellipsometry," (in English), Thin Solid Films, vol. 253, no. 1-2, pp. 257-261, Dec 15 1994, doi: https://doi.org/10.1016/0040-6090(94)90331-X.

[17] J. P. Borgogno et al., "Refractive index and inhomogeneity of thin films," Appl Opt, vol. 23, no. 20, p. 3567, Oct 15 1984, doi: 10.1364/ao.23.003567.

[18] M. S. Mozumder, A. H. I. Mourad, H. Pervez, and R. Surkatti, "Recent developments in multifunctional coatings for solar panel applications: A review," (in English), Sol. Energy Mater. Sol. Cells, vol. 189, pp. 75-102, Jan 2019, doi: 10.1016/j.solmat.2018.09.015.

[19] S. L. Cashmore, A. J. Robinson, and D. A. Worsley, "The Effect Of Humidity On Titanium Dioxide Photocatalysed PVC Degradation," (in English), Coatings for Corrosion Protection, vol. 25, no. 29, pp. 95-104, 2010, doi: 10.1149/1.3327228.

[20] A. G. Aberle, "Surface passivation of crystalline silicon solar cells: A review," (in English), Prog Photovoltaics, vol. 8, no. 5, pp. 473-487, Sep-Oct 2000, doi: Doi 10.1002/1099-159x(200009/10)8:5<473::Aid-Pip337>3.3.Co;2-4.

[21] T. Luttrell, S. Halpegamage, J. Tao, A. Kramer, E. Sutter, and M. Batzill, "Why is anatase a better photocatalyst than rutile?-Model studies on epitaxial TiO2 films," Scientific reports, vol. 4, no. 1, pp. 1-8, 2014, doi: https://doi.org/10.1038/srep04043.

[22] O. K. Segbefia, A. G. Imenes, I. Burud, and T. O. Sætre, "Temperature profiles of field-aged photovoltaic modules affected by optical degradation. Manuscript submitted for publication. Department of Engineering Sciences, University of Agder.," Sol. Energy Mater. Sol. Cells, 2022.

[23] P. C. Ricci et al., "Anatase-to-rutile phase transition in TiO2 nanoparticles irradiated by visible light," (in English), J. Phys. Chem. C., vol. 117, no. 15, pp. 7850-7857, Apr 18 2013, doi: 10.1021/jp312325h.

[24] I. Duerr, J. Bierbaum, J. Metzger, J. Richter, and D. Philipp, "Silver grid finger corrosion on snail track affected PV modules–investigation on degradation products and mechanisms," Energy Procedia, vol. 98, pp. 74-85, 2016.

[25] N. Kyranaki, J. Zhu, R. Gottschalg, and T. Betts, "Investigating the degradation of front and rear sides of c-Si PV cells exposed to acetic acid," 2018.

[26] X. Zhang, X. Ge, and C. Wang, "Synthesis of titania in ethanol/acetic acid mixture solvents: phase and morphology variations," Crystal growth & design, vol. 9, no. 10, pp. 4301-4307, 2009.

[27] S. Kumar, R. Meena, and R. Gupta, "Imaging and micro-structural characterization of moisture induced degradation in crystalline silicon photovoltaic modules," (in English), Sol. Energy, vol. 194, pp. 903-912, Dec 2019, doi: 10.1016/j.solener.2019.11.037.

[28] T. H. Kim, N. C. Park, and D. H. Kim, "The effect of moisture on the degradation mechanism of multi-crystalline silicon photovoltaic module," (in English), Microelectronics Reliability, vol. 53, no. 9-11, pp. 1823-1827, Sep-Nov 2013, doi: 10.1016/j.microrel.2013.07.047.

[29] N. Park, C. Han, and D. Kim, "Effect of moisture condensation on long-term reliability of crystalline silicon photovoltaic modules," (in English), Microelectronics Reliability, vol. 53, no. 12, pp. 1922-1926, Dec 2013, doi: 10.1016/j.microrel.2013.05.004.

[30] J. Bauer, V. Naumann, S. Großer, C. Hagendorf, M. Schütze, and O. Breitenstein, "On the mechanism of potential ‐ induced degradation in crystalline silicon solar cells," physica status solidi (RRL) ‐ Rapid Research Letters, vol. 6, no. 8, pp. 331-333, 2012.

[31] M. Waleczek et al., "Influence of Alumina Addition on the Optical Properties and the Thermal Stability of Titania Thin Films and Inverse Opals Produced by Atomic Layer Deposition," Nanomaterials (Basel), vol. 11, no. 4, p. 1053, Apr 20 2021, doi: 10.3390/nano11041053.

Paper D

Moisture induced degradation in field-aged multicrystalline silicon photovoltaics modules by O.K. Segbefia, N. Akhtar, and T.O. Sætre. Published in Solar Energy Materials and Solar Cells (2023).

Solar Energy Materials & Solar Cells 258 (2023) 112407

Contents lists available at ScienceDirect

Solar Energy Materials and Solar Cells

journal homepage: www.elsevier.com/locate/solmat

Moisture induced degradation in field-aged multicrystalline silicon photovoltaic modules

Oscar Kwame Segbefia *, Naureen Akhtar, Tor Oskar Sætre

Department of Engineering Sciences, University of Agder, 4879, Grimstad, Norway

ARTICLE INFO

Keywords:
Moisture ingress
Lead oxide
Metal stannate
Silver acetate
Metal-ligand
Photosensitive

ABSTRACT

Moisture ingress is one of the key fault mechanisms responsible for photovoltaic (PV) devices degradation. Understanding moisture induced degradation (MID) mechanisms in field-aged PV modules is more reflective of the reality in the field. In the present work, MID products of reclaimed solar cells from 20-year-old field-aged silicon PV modules is investigated. The defective areas in the PV modules were identified using visual inspection, electroluminescence (EL), ultraviolet fluorescence (UV–F), and infrared thermal (IR-T) techniques. SEM-EDS analysis is used to elucidate the role of moisture on the observed degradation mechanisms. Degradation of the ethylene vinyl acetate (EVA) encapsulation produces acetic acid, carbon dioxide, phosphorus, sulfur, fluorine, and chlorine. Migration of metal ions under the influence of moisture ingress makes the formation of oxides, hydroxides, sulfides, phosphates, acetates, and carbonates of silver, lead, tin, copper, zinc, and aluminum feasible. Also, other competing reactions can lead to the formation of stannates of copper, silver, sodium, and zinc. Another observation is that, in the presence of MID species, Pb is preferentially corroded (to form lead acetate complexes) instead of the expected sacrificial Sn in the solder. These MID species account for different defects and fault modes that lead to parasitic resistance losses. This is witnessed by the 1.2%/year degradation in the P_{max} of the PV module.

1. Introduction

Moisture ingress is one of the key routes to photovoltaic (PV) devices degradation [1–5]. In the field, and under environmental stressors (e.g., high temperature, humidity, ultraviolet radiation), moisture can enter the PV modules from the edges, 'breathable' backsheets, and via cracks or voids [3,4,6]. These channels of diffusion for moisture (water, oxygen, and carbon oxides), are created during manufacturing, transportation, handling, and installation [4,7–9]. Long periods of heavy snow and wind loads complicate the situation in the Nordics. In the Nordics, the global annual average climate moisture index (CMI) is greater than 0.5 [5]. CMI is the measure of moisture availability at a specific place and time based on the precipitation and moisture absorption of the local atmosphere [10]. Hence, the CMI can be an indicator of the degree of moisture susceptibility of electronic devices (including solar panels) in a particular place.

There are efforts within the PV community as regards preventing, detecting, and mitigating moisture ingress and its effects in PV modules. The use of encapsulation materials with high adhesion and moisture barrier qualities, desiccant stacked sealants, and imbedded moisture sensors are some of the ways of achieving this objective [4,11]. In hermetic PV module configurations (e.g., double glass PV modules), moisture ingress into the modules is limited. However, the escape of moisture induced degradation (MID) or corrosion species is also limited. This can therefore lead to accelerated degradation of field deployed solar panels. A comprehensive review on moisture ingress in crystalline silicon PV modules has been provided by Segbefia et al. [4]. In the field, PV modules are exposed to multiple environmental stressors such as high humidity, temperature, UV radiation, and soiling during their operation in the field. The role of these environmental stressors in the formation of MID species and subsequent degradation processes in the PV module is significant and is the reality in the field. However, in the absence of moisture ingress (under humidity exposure), formation of MID species is impossible, irrespective of the environmental stressors the PV module is exposed to. Hence, understanding the mechanisms and effects of MID in field-aged solar PV modules is the best way to understand what happens in the field.

Once moisture enters the PV module bulk, electrochemical reactions

* Corresponding author. Department of Engineering Sciences, University of Agder, 4879, Grimstad, Norway.
E-mail address: oscar.k.segbefia@uia.no (O.K. Segbefia).

https://doi.org/10.1016/j.solmat.2023.112407
Received 2 March 2023; Received in revised form 16 May 2023; Accepted 30 May 2023
Available online 11 June 2023

are initiated. The ethylene vinyl acetate (EVA) encapsulation when exposed to moisture and light, can produce acetic acid [4,8,12]. In the presence of excess moisture and light, the acetic acid can breakdown to formic acid, and the incidence of corrosion is more likely [4]. Moisture and acetic acid can attack the metal grids to form their respective metal oxides, acetates, hydroxides, and bicarbonates [13–17]. The copper ribbon, lead, and zinc (from the silver paste) can also degrade into copper (Cu), lead (Pb), and zinc (Zn) acetates, respectively in the presence of acetic acid and moisture [14,16,18]. Recently, Jeffries et al. [14] reported silver acetate as the main product of acetic acid corrosion in PV modules. Moreover, it was reported that the corrosion of intermetallic compounds (IMC) in acetic acid depend on the concentration of Ag in the paste [14]. These degradation products can also lead to the degradation of the solar cells, corrosion, and optical degradation [12–19].

In the presence of moisture, aluminum (Al) and sodium (Na) ions can also leach from the Al- frame and the front glass, respectively into emitter regions in the solar cells and modules, hence, cause potential induced degradation (PID) [20,21]. These MID processes can also lead to the incidence of microcracks and/or snail trails, optical degradation, and antireflection coating (ARC) degradation, among others [8,22–24]. These degradation mechanisms affect the efficiency and performance reliability of PV plants [25,26]. For instance, silver oxides deposited on the metal grids lead to increased series resistance [14,17,18,27]. Degradation of the encapsulation and the silver grids in the presence of moisture can lead to the formation of silver carbonates, sulfides and phosphates which are precursors for snail trails [13]. The silver carbonate can reflect, absorb, and scatter light photons [28]. This influences the charge carrier generation, transport, and recombination in the module bulk. Resistance effects leads to localized hotspots and increased module temperature, and hence, a drop in the power output [29]. MID products such as lead, silver, copper oxides, acetates, and carbonates appear as dark spots in electroluminescence (EL) and ultraviolet fluorescence (UV–F) images, and in infrared thermal (IR-T) images, they are seen as hotspots [12,14,17,19,30].

Electroluminescence, photoluminescence (PL), infrared thermal, ultraviolet fluorescence, dark lock-in thermography (DLIT), current-voltage (I–V), and visual inspection techniques have been used to detect these defects and fault mechanisms in PV plants [4,12,17]. The collective advantage of these techniques is that they are non-destructive. However, these techniques are incapable of establishing the microstructural causes of the observed degradation mechanisms. Hence, investigations to unravel the root causes of these degradation mechanisms (based on degradation products) employ microscopic and spectroscopic methods. MID species can be detected using scanning electron microscopy (SEM), energy dispersive spectroscopy (EDS), electron beam induced current (EBIC), fourier transform infrared (FTIR) spectroscopy, X-ray photoelectron spectroscopy (XPS), atomic force microscopy (AFM), thermo-gravimetric analysis (TGA), Raman spectroscopy, etc. [4,8,12,31]. Even though these techniques are destructive, they are well established. The prospects of employing both the destructive and non-destructive methods to detect MID mechanisms have been reported [8,12,16,17,28,32]. In these investigations, efforts were made to understand the MID observed in non-destructive methods at the microstructural level. Indeed, this twin approach employs the strengths of both methods for defects and fault diagnosis.

Most recently, the present authors reported the effect of moisture on the morphological degradation of titania antireflection coatings (ARCs) [33]. The influence of the degradation of these coatings on the efficiency of the PV module is important. With emerging PV applications such as floating PV and agro-PV at sight, understanding the mechanisms and effects of MID in PV modules under multiple real field environmental stressors is more important than ever. Up to now, research on the microstructural signatures of MID in PV modules appear to focus more on the EVA encapsulation, silver grids, solder, and copper ribbons [8, 12–19,32,34]. Most investigations ignore the effect of moisture ingress on the solar cell microstructure itself and its degradation mechanisms. In addition, only a few of these reports were carried out on field-aged PV modules [12,13,15,32,34]. Moreover, we have not come across any published work on the effects of MID on silicon solar cells. Additionally, none of the reports on the effect of MID on solar PV modules was done in the Nordics, where the effect of moisture ingress is a huge challenge, due to the high CMI in this climate. Hence, a holistic investigation on all the solar cell components: solar cell, silver grids, solder, and copper ribbons in the Nordic is necessary. The effect of moisture ingress on the degradation of the EVA encapsulation is not presented in this work, as it is the subject of another investigation.

In the present work, the MID of reclaimed solar cells from a 20-year-old field-aged multicrystalline silicon (mc-Si) PV module is investigated. The electrical characteristics of the PV module were acquired via I–V characterization. The defective areas in the PV modules were identified using visual inspection, EL, IR-T, and UV-F techniques. The microstructural characterization of the reclaimed solar cells employed SEM-EDS techniques. A brief description of the PV modules and the methods used for the investigation are given in Section 2, followed by the findings and the discussions in Section 3.

2. Material and methods

The field-aged NESTE NP100G12 PV Module X for this investigation was chosen from a batch of PV modules which were installed on a Renewable Energy Park in Dømmesmoen, Grimstad (58.3447° N, 8.5949° E), Norway in the year 2000. However, the PV modules on the Energy Park were decommissioned in 2011 and were kept securely for research purposes. The manufacture's data sheet and the measured average electrical data of the 43 field-aged PV modules and the PV module selected for this study is summarized in Table 1. Details of the Energy Park and the catalogue of the defects and failure modes of these PV modules was reported earlier [5].

The module comprises of a (0.1 × 0.1) m^2 mc-Si solar cells with screen printed aluminum (Al-) grids at the back and titania (TiO_2) ARC. The cell is sandwiched between ethylene vinyl acetate (EVA) encapsulant. The front glass and the backsheets were made from a low iron tempered glass and white multi-layered Tedlar®/Polyester/Tedlar® (TPT), respectively. The rest of the module's components are 2 junction boxes, each containing a bypass diode and an anodized Al- frame. Tinned copper was used for the interconnect ribbons. The panel is made up of 72 cells connected serially in 3 parallel substrings [21]. The suspected areas were extracted using a water jet cutting technique, followed by subsequent solvent treatment. The reclaimed solar cell samples (from the defective areas) were then taken through SEM-EDS analyses. The experimental procedure for the study is illustrated in Fig. 1. Table 1 suggests that, after 20 years, the electrical characteristics of PV Module X is similar to the average electrical characteristics of the 43 field-aged PV modules. Hence, the degradation mechanisms in these field-aged PV modules might be identical.

2.1. Visual inspection

A comprehensive visual inspection on the solar PV panel was

Table 1
The manufacturer's data sheet and the measured average electrical parameters of the 43 solar PV modules and PV Module X in 2020 normalized to Standard Test Conditions (STC).

Year	P_{max} (W)	V_{oc} (V)	V_{mpp} (V)	I_{mpp} (A)	I_{sc} (A)	FF (%)	η (%)
2000 (Data sheet)	100	21.6	16.7	6.0	6.7	70	13
2020 (43 modules)	78.2	19.7	14.7	5.3	6.0	66	10
2020 (Module *X*)	76.0	19.8	14.4	5.3	6.0	64	10

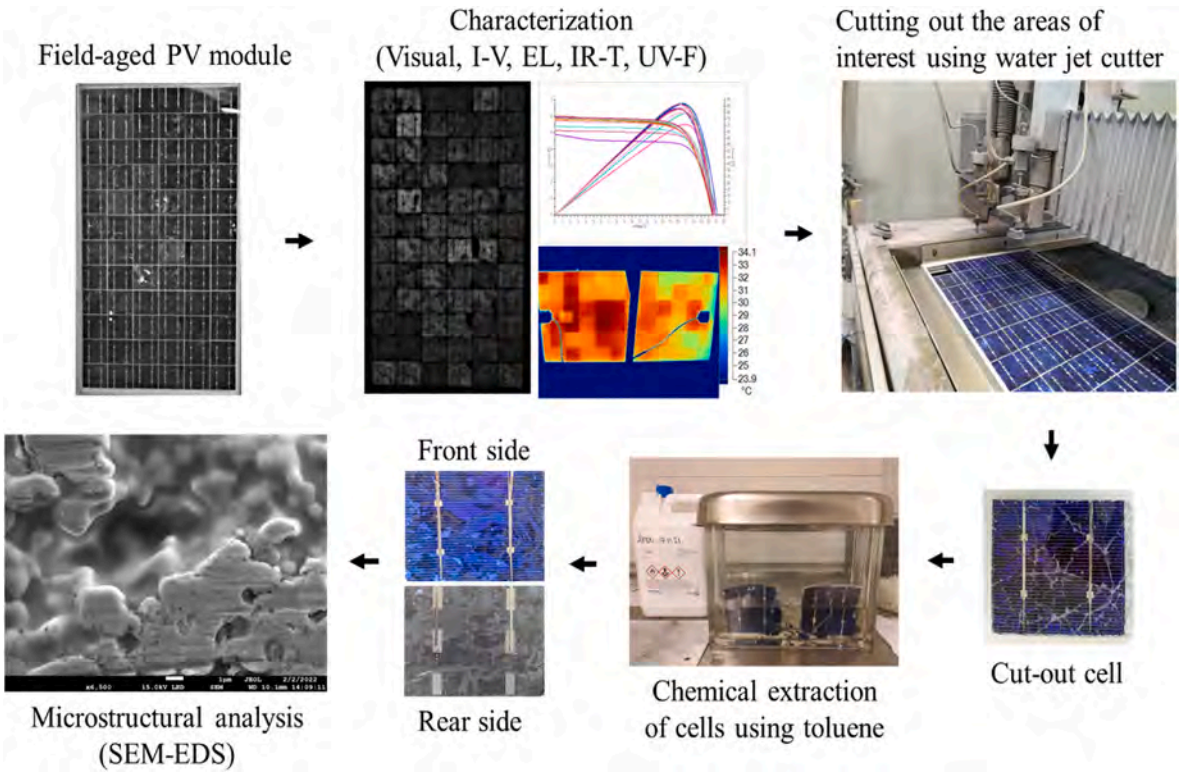

Fig. 1. Experimental procedure for the microstructural investigation of the moisture induced degradation products in the field-aged PV module.

conducted under clear sky outdoor conditions. We also acquired high-resolution photographs from the panel: front and rear sides in a dark room with optimized light exposure. This extra step was invaluable in identifying defects which were hidden in the conventional visual inspection method. The IEC 61215: 2016 standard was adhered to in collecting and reporting the data from the visual inspection of the solar panel.

2.2. I–V measurements

Information on the electrical parameters was acquired from the solar panel using a handheld I–V 500w I–V Curve Tracer as per the IEC 60904-1 standard. The measurements were done under Standard Test Conditions (STC) and data on the maximum power (P_{max}), short circuit current (I_{sc}), open circuit voltage (V_{oc}), fill factor (FF), maximum power point voltage (V_{mpp}), maximum power point current (I_{mpp}), module temperature (T_m), and in-plane irradiance (G_I) characteristics of the panel was documented. STC specifies cell temperature (25 °C), an in-plane irradiance (1000 W/m^2) and air mass 1.5 (AM1. 5) spectrum for commercial PV panels. The experiments were performed under clear sky in-plane irradiance (960–1040 W/m^2) and wind speed (<2 ms^{-1}) conditions. The I–V Tracer converted data points to STC automatically to minimize errors related to data recording and processing. The temperature coefficient (β_x) of each electrical parameter (x) was computed using regression plots: a graph of T_m versus electrical parameter, x. Details of the temperature coefficient measurement was presented earlier [21,35].

2.3. Ultraviolet fluorescence (UV–F) imaging

UV-F imaging is a handy tool for detecting cracks and moisture induced degradation (e.g., cell and optical degradation) in PV plants [36,37]. In the presence of ingressed moisture (e.g., water and oxygen), fluorescent degraded species (in the solar panel's encapsulation) undergo photochemical transformations into nonfluorescent species [37]. Under UV light, degraded areas show darker traces due to defects photoquenching. This helps to differentiate defective areas from healthy areas in the solar PV panel [36]. UV-F images of PV module X was acquired in a dark room using a TROTEC® LED UV TorchLight 15F ($\lambda \approx$ 365 nm) equipped with a Wolf eyes FD45 spectrum filter. The experiments were done as per the International Energy Agency (IEA) recommended procedure [25,38].

2.4. Electroluminescence (EL) imaging

EL imaging is a suitable tool for quantifying resistive losses in old PV modules affected by cracks and severed metal grids. EL characteristics of the solar panel was acquired in a dark room using the BrightSpot EL Test Kit: a 24 megapixels modified DSLR (digital single-lens reflex) Nikon D5600 camera, a DC power supply device set, and a laptop computer equipped with data acquisition and processing software. The measurements were done as per the IEC 60904- 13 standard and the IEA prescribed method [26]. The EL characterization was performed under I_{sc} and 0.1I_{sc} forward bias conditions in a dark room as reported earlier [5,21].

2.5. Infrared thermal (IR-T) imaging

The field-aged PV module was taken through IR-T measurements using the Fluke Ti400 Infrared Camera ($\lambda \approx$ 650–1400 nm) as per the IEA prescribed procedure [26] and the IEC 62446- 3 standard. Details of the experimental set up for the outdoor investigation under clear sky outdoor conditions at the Rooftop facility was reported earlier [21]. For these measurements, the IR thermal images were acquired after soaking the solar panel in the sun for at least 15 min.

2.6. Solar cell reclamation and microstructural analysis

The regions of interest (areas affected by microcracks and moisture ingress) were extracted using a Water Jet NC 3060D Beveljet cutting machine. The machine which is controlled by a CNC software employs a

fine water jet with abrasive under ultra-high pressure (ca. 4000 bar) for sample cutting. The technique is very suitable when low cutting temperature is desired. The as cut samples (consisting of the front glass, encapsulant, copper ribbons, solar cell, and backsheet) was separated using toluene. The samples were immersed in the toluene at room temperature for 14 days, refer to Fig. 1. After 7 days, the front glass and front encapsulant were separated. However, the backsheet could be removed after 14 days. The extracted solar cells from the field-aged PV module were analyzed using a field emission scanning electron microscope (SEM) (JEOL 7200F) equipped with an energy dispersive X-ray spectrometer (Octane Elect EDS system from EDAX®-AMETEK®) to identify the MID products. The components of the solar cell extracted from the field-aged PV module that were investigated are shown in Fig. 2.

The copper busbars, located around the perimeter of the PV module, connect the Cu interconnect ribbons. They collect and deliver cumulative current to the junction boxes. The silver fingers are perpendicular to the Cu ribbons whilst the Ag busbars lie beneath the Cu ribbons. The Cu ribbons are connected to the solar cells and the Ag grids with the solder, which is made up of lead and tin. The effect of moisture ingress is more severe around the perimeter of PV modules [12,30]. Hence, the solar cells and other components for the SEM-EDS investigation were extracted from the edge of the field-aged PV module.

3. Results and discussion

3.1. Visual inspection

Fig. 3 shows some of the results from the visual inspection of the PV module. Fig. 3a shows the photographic images of a pair of solar cells acquired under clear sky outdoor conditions highlighting signs of optical degradation e.g., delamination and discolouration of the encapsulation. Fig. 3b and c are images acquired from the same area of the field-aged PV module under clear sky outdoor and dark room conditions, respectively. Fig. 3b and c shows complementary signs of MID degradations, which could not be seen in either of these Figs. alone.

Moisture induced discoloration is shown in the upper left corner in Fig. 3b whilst Fig. 3c shows accumulation of MID species around the solder joint. Fig. 3d and e shows the inner side of the TPT backsheets of solar cells extracted from the middle and the edge of the field-aged PV Module X, respectively. Fig. 3d is not discolored whereas Fig. 3e is discolored. Discoloration of the backsheets is a typical sign of degradation due to UV radiation. Yet, the effect of UV radiation is expected to be uniform across the backsheet in the same PV module. Hence, we believe that the degradation of the EVA encapsulation and the TPT backsheets of the PV module is due to moisture ingress. In Section 3.6, SEM-EDS analyses will be used to support this observation. Dark discolored backsheets were also observed in optically degraded PV modules

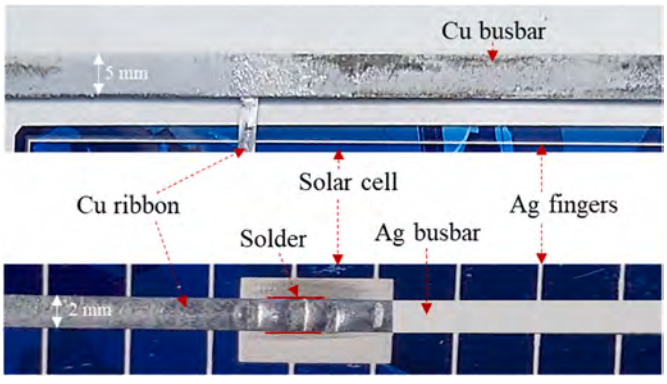

Fig. 2. Components of the field-aged PV module extracted for the SEM-EDS analysis.

by other researchers [39]. Fig. 4 shows the visual images acquired from the same area of a solar cell close to the edge of field-aged PV Module X showing the degradation state of a Cu ribbon. Fig. 4a was acquired under clear sky outdoor conditions and Fig. 4b was acquired under optimized dark room conditions. The figure shows corrosion and oxidation of the metal grids, and trapped moisture and MID species, especially around the solder joint. Corrosion of metal grids around the solder joint area due to moisture ingress was also reported by other authors [17–19,23]. Fig. 4 suggests that Module X has been affected by moisture induced defects.

Corrosion at the solder joint is attributed to the dissolution of lead and tin (main components of solder) in moisture and acetic acid due to galvanic corrosion [17]. This could be due to low adhesion at the solder joint or the presence of defects during the soldering process [18]. The observed corrosion at the solder joint region could also be as a result of MID of the Ag grids [8]. However, this corrosion mechanism is only feasible in the presence of moisture. It can be seen in Fig. 4 that the metal grids have been masked out by MID species. The optical integrity of these areas in Fig. 4 appears to be compromised as well. Earlier investigation by the present authors established that more than 90% of these field-aged PV modules were affected by optical degradation, though other stressors such as UV radiation also can play significant roles [5,40]. This observation agrees with other reports on the role of MID products in optical degradation of PV modules [13,14,16,27].

3.2. I–V characteristics of the field-aged PV module

Fig. 5 shows the electrical characteristics of field-aged PV Module X. Degradation in the P_{max}, V_{oc}, and I_{sc} due to increased series resistance (R_S), low shunt resistance (R_{SH}), and reduced fill factor are illustrated. The annual degradation in P_{max}, V_{oc}, and I_{sc} for PV Module X were found to be approximately 1.2%, 0.4%, and 0.5%, respectively. The degradation in PV Module X is similar to the average degradation in all the field-aged PV modules. Corrosion of metal grids, optical degradation, and PID due to moisture ingress are known to be the underlying causes of resistance losses, hence, power degradation [4,25]. Considering the location of the present investigation, the influence of MID mechanisms on the degradation of these PV modules is high [5]. MID products such as acetic acid, acetates, oxides and hydroxides of silver, lead, silver, tin, and copper were reported to be responsible for increased series resistance and shunting [12,14,30].

It was reported that increased series resistance, shunting, and ARC degradation are the three key fault mechanisms that lead to power degradation [8,22]. The effect of moisture ingress on the degradation of the ARC in PV Module X was reported earlier [33]. On the other hand, increased series and decreased shunt resistances due to a variety of defects and fault modes lead to increased module operating temperature (T_m) [29,40]. The temperature coefficients of the PV module can therefore be an indicator of the effect of resistance losses [29,41,42]. Table 2 summarizes the average relative temperature coefficients of PV Module X. The average temperature coefficient of efficiency ($\beta_{\eta m}$) of the field-aged PV module was found to be approximately −0.5%/°C, which is equivalent to the average $\beta_{\eta m}$ of all the field-aged PV modules [5].

$\beta_{\eta m}$ is the cumulative contributions from the temperature coefficients of V_{oc} (β_{Voc}), I_{sc} (β_{Jsc}), fill factor (β_{FF}), V_{mpp} (β_{Vmpp}), and I_{mpp} (β_{Jmpp}). The β_{Jsc} among other factors, depends strongly on the collection fraction (f_c) [29,43]. The f_c is the fraction of photogenerated charge carriers within the solar cell that could be extracted from the solar cell as photocurrent [44]. Hence, the f_c depends on the resistive losses due to optical degradation and parasitic absorption within the solar cell [29].

From Table 2, the β_{Jsc} for PV Module X is relatively low, indicating increased resistance losses. The β_{Jsc} from other reports were higher, with $\beta_{Jsc} > 0.06$ [42,45]. The observed lower β_{Jsc} for the field-aged PV module suggests degradation due to reduced f_c [29]. Strikingly, the β_{Jmpp} is negative as reported earlier by Segbefia and Sætre [21] for field-aged PV modules affected by PID. Migration of cations e.g., Na ions to the emitter regions of solar cells are responsible for PID [9]. Moisture ingress has

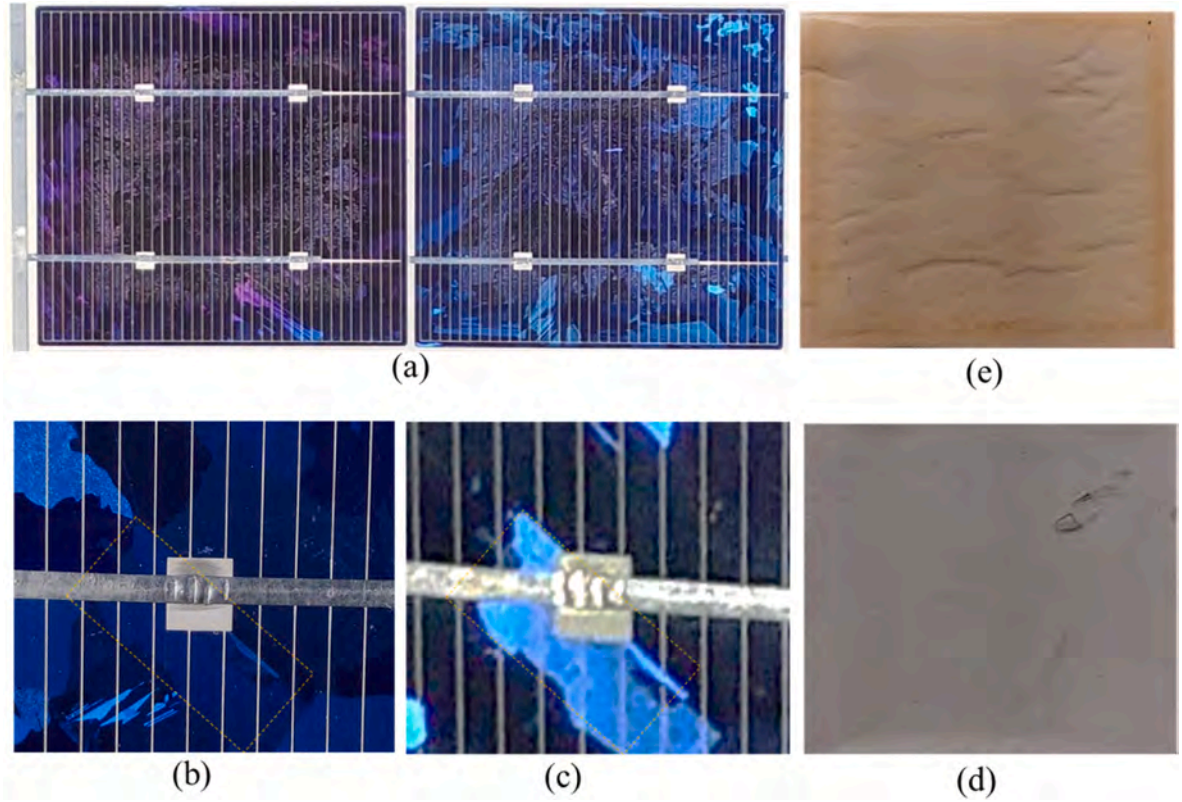

Fig. 3. Visual images of the field-aged PV module. Photographic images of a (a) pair of solar cells showing signs of delamination and discolouration of encapsulation, a copper ribbon under (b) clear sky outdoor and (c) optimized light exposure in dark room conditions, and the inner side of the backsheet of a solar cell (d) not affected and (e) affected by moisture ingress.

Fig. 4. Part of a solar cell and degraded copper ribbon showing signs of moisture ingress. Images were acquired under (a) clear sky outdoor and (b) optimized light exposure dark room conditions from the same area of the solar cell.

been reported for the migration of these ions to sensitive areas such as the emitter of solar cells [46]. Hence, it is likely that PV Module X is suffering from PID as well due to moisture ingress, as will be demonstrated with the EL, IR-T, and SEM-EDS characteristics.

3.3. Electroluminescence (EL) characteristics

Fig. 6 shows the EL and UV-F images of field-aged PV Module X. Fig. 6a and b are the EL images acquired under I_{sc} and $0.1I_{sc}$ forward bias conditions, respectively. Fig. 6a shows the presence of microcracks and darker regions at the edges of the solar cells. Microcracks are conduits and reservoir for moisture ingress [4]. Darker marks at the edges of the solar cells suggest that degradation at the cell edges is more severe [26]. From Fig. 6b, it can be seen that the majority of the solar cells around the edge of the module are darker than those in the middle of the module. Dark cell patterns (especially around the edge of the module) indicate the presence of MID products such as metal oxides and acetates [12,14,19,30]. In addition, most of the darker cells are located nearer to the perimeter of the PV module. Degraded cells around the edges of the PV module indicate moisture induced PID, as indicated by the β_{Jmpp}. This observation is in line with other reports [25,26]. The satellite cells in the areas affected by cracks also show darker patterns.

3.4. Ultraviolet fluorescence (UV–F) characteristics

PV Module X shows weak fluorescence and luminescence signals, which align with earlier investigations by the present authors [35,40]. The majority of the batch of field-aged PV modules from which PV

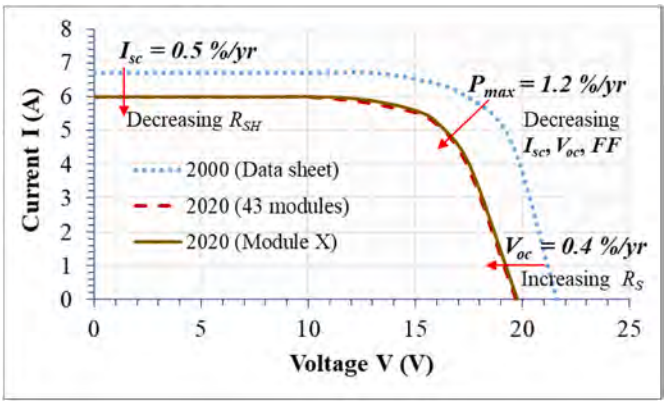

Fig. 5. Electrical characteristics of the solar PV module. Degradation per year (yr) in P_{max}, V_{oc}, and I_{sc} as well as the effect of the series resistance (R_S), shunt resistance (R_{SH}), and fill factor (FF) are illustrated.

Table 2
Average relative temperature coefficients of solar PV Module X.

Temperature coefficient (%/°C)					
β_{Voc}	β_{Jsc}	β_{FF}	$\beta_{\eta m}$	β_{Vmpp}	β_{Jmpp}
−0.4	0.05	−0.2	−0.5	−0.5	−0.07

Module X was chosen were found to show weak fluorescence and luminescence signal intensities [5]. Fig. 6c, d, and 6e are the UV-F images of the corresponding marked out areas in Fig. 6a showing the evidence of microcracks and MID. Although most of the defective areas (microcracks) in the UV-F images correspond with the observation in the EL image (Fig. 6a), some microcracks were hidden in the EL images. Defects that do not affect current flow are not seen in EL images [26,47]. On the other hand, only degraded encapsulation areas are seen as dark areas in UV-F images [36,37].

Usually, these microcracks are located around the perimeter of the PV module. One reason for this observation is that, during manufacturing, handling and transportation of PV modules, the likelihood for microcracks formation is high. The thermal processing steps especially induces thermochemical stress, and hence, microcracking in the solar cells. Usually, some of the microcracks formed during the manufacturing phase of the production process are not detected. So, in the field, environmental and climatic stressors can make these microcracks degrade further, even into macrocracks. Very high and low ambient temperatures can induce microcracks in solar cells due to thermochemical stress. In addition, in environments with high humidity conditions, moisture can enter the PV module. Moisture ingress is more feasible where there are microcracks and other voids around the edges of the PV module. Moisture ingress can also initiate new microcracks or make existing microcracks degrade further [48].

Formation and degradation of microcracks under the influence of moisture ingress is one possible reason for the observed microcracks in

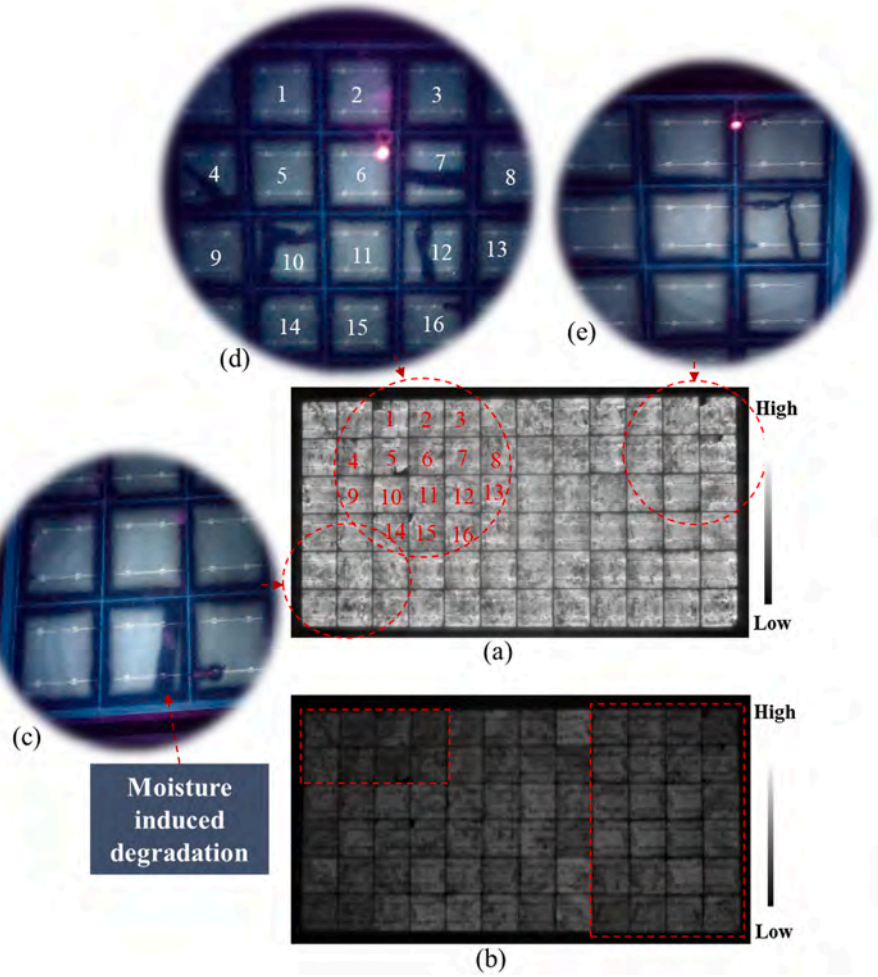

Fig. 6. EL characteristics of PV Module X acquired under (a) I_{sc} and (b) 0.1I_{sc} forward bias conditions. (c)–(e) UV-F characteristics of various parts of PV Module X showing signs of microcracks and MID. All images were acquired in a dark room.

Fig. 6c, d, and 6e. Specifically, the geometry of the microcracks and the presence of some of the microcracks was not very clear in the EL images. In Fig. 6c, the copper ribbon in the defective area appears unbroken. Hence, the position of the defect in Fig. 6c is not very clear in the EL images (Fig. 6a and b). This defect is likely a moisture induced degradation. In Fig. 6d, the copper ribbons of the defective cells (e.g., Cells 4, 7, 10 and 12) appear to be completely broken. These microcracks are also multidimensional to the busbars and are more critical to power loss. Since these microcracks are located close to the edge of the PV module, the influence of moisture ingress on the microcracks formation and degradation cannot be ruled out. The geometry and positions of the microcracks in Cells 4, 7, 10, and 12 are not very clear in Fig. 6a, however. Hence, UV-F technique is better suited for detecting moisture induced defects and fault modes.

In addition, the nature of the microcracks (e.g., crack width) in Fig. 6c and d shows further degradation of the microcrack regions which might be due to the influence of moisture ingress under multiple real field environmental stressors. The microcrack patterns in Fig. 6c and d are broader in width and extend beyond the immediate crack regions. However, the microcrack in Fig. 6e is narrower and suggests that the effect of moisture ingress on this crack region is less severe. In Fig. 6e, even though the microcrack is located at edge of the PV module, the microcrack appears to be opened inwards away from the Al- frame. However, in Fig. 6c, the microcrack opens towards the Al- frame. In Fig. 6c, the influence of moisture ingress from the edge of the module is greater than in Fig. 6e. In an earlier investigation on these field-aged PV modules, PV modules with strong fluorescence and luminescence signals show sharper crack patterns [40]. The effect of moisture on the degradation of microcracks was also observed elsewhere [48]. Moisture ingress induce the formation of silver and lead acetates, oxides, sulfides, and phosphates in the affected areas in PV modules [13,28]. These degradation products are witnessed as dark areas in EL and UV-F images [13,14,16].

3.5. Infrared thermal (IR-T) characteristics

Defective cells cause mismatch losses, hence, lead to inhomogeneous distribution of cell temperature (T_c) throughout the PV module. Defective cells operate at higher T_c and become hotspots. This in turn influences the T_m of the PV module. The difference in the T_c (ΔT) of the cell with the highest and lowest T_c can be an indication of the presence of specific defects and fault mechanisms [26,47,49]. Fig. 7a shows the IR-T image of PV Module X. The respective zoomed-in EL images of the marked-out areas in Fig. 7a are shown in Fig. 7b, c, and 7d. The marked-out areas in Fig. 7a are closer to the frame of the module and show the most critical hotspots. This is an indication of the occurrence of large leakage current during operation. There are other hotspots all over the module, however. The respective location of the hotspot cells closer to the frame of the PV module supports the observations in the EL images. The number of hotspot cells suggests that the majority of the cells in field-aged PV Module X are at different stages of degradation.

In Fig. 7b, no obvious crack was observed. Yet, the corresponding area in Fig. 7a shows hotspots. The observed hotspots in Fig. 7a might be due to metal grids corrosion and/or solar cell degradation. Fig. 7c shows the presence of microcracks and the warmest cells were observed in this area in the IR-T image, see Fig. 7a. On the other hand, Fig. 7d shows some cracks. However, the hotspots of its corresponding area in the IR-T image were not as high as the hotspots in Fig. 7c. The criticality of cracks to current flow underpins the occurrence and severity of the hotspots observed in Fig. 7c [25,26]. The ΔT of PV Module X was found to be ~8.2 ± 2 °C. The presence of MID products such as acetic acid, oxides and acetates of silver, lead, and copper could also influence the formation and the characteristics of the hotspots [12].

3.6. Microstructural characteristics

3.6.1. Solar cells

Fig. 8 shows the SEM micrographs of a multicrystalline silicon solar cell extracted from the edge of PV Module X. Fig. 8a shows two distinct surface morphology of the silicon microcrystal structures present in the solar cell. Area 1 appears to be the characteristic surface morphology of alkaline anisotropic etching of crystalline silicon [50]. On the other hand, Area 2 depicts the surface morphology of isotropic etching using acidic solutions [50]. As a multicrystalline silicon solar cell, the cell is made up of different crystals with random crystallographic orientations. It is known that etching rate depends on the etchant, crystal type and orientation. Hence, the crystal type and orientations might be the reason for the difference in the surface morphology in Fig. 8a.

According to Li et al. [51], in the presence of moisture and light, the EVA encapsulation can produce acidic or basic environments in the solar

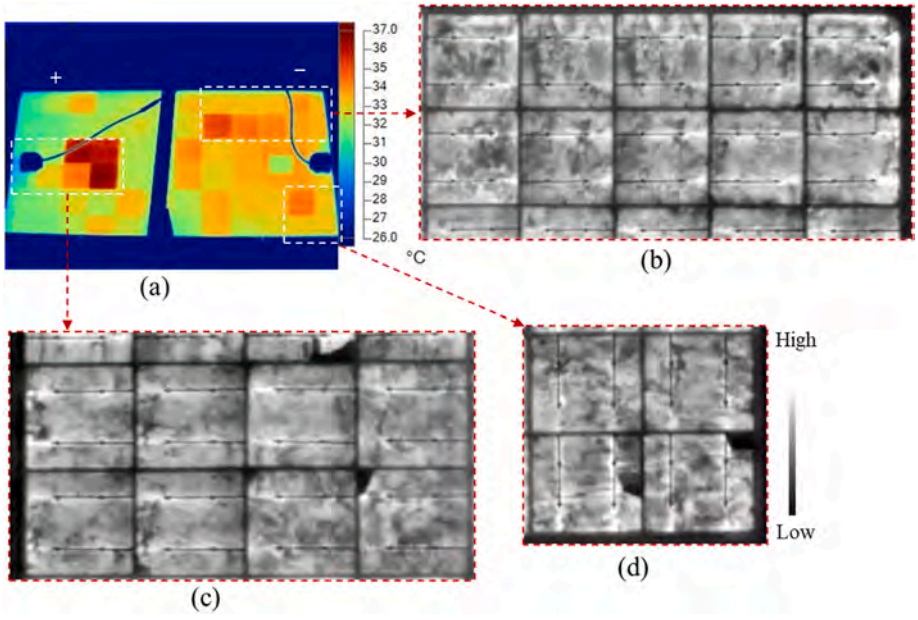

Fig. 7. (a) IR-T characteristics of PV Module X acquired under clear sky outdoor conditions. (b)–(d) EL characteristics acquired under I_{sc} bias conditions of the corresponding marked areas in (a).

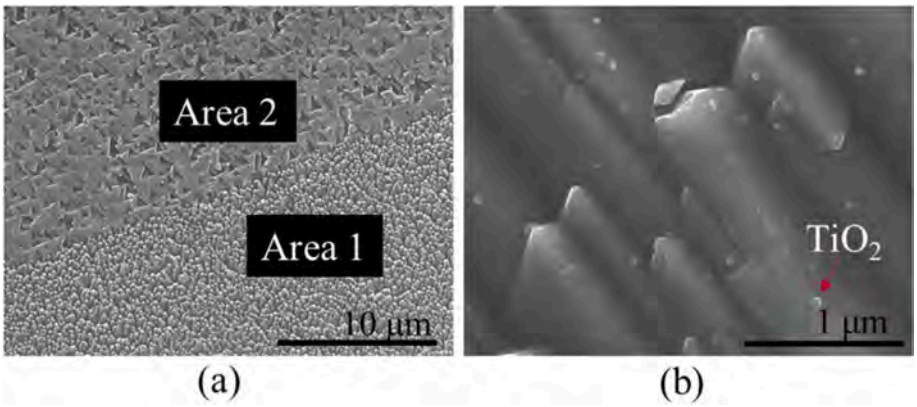

Fig. 8. SEM micrographs of a solar cell extracted from PV Module X showing (a) the types of micro crystallographic features and (b) high magnification micrograph of Area 1.

panel bulk depending on the voltage bias in the field. Under negative bias, as typical of solar panels affected by PID, the EVA under moisture ingress can produce basic environment in the panel. High basic environment can make degradation of the silicon solar cell, antireflection coating, and corrosion of the metal grids feasible. However, under negative bias, the effect of basic environments on the corrosion of Ag metallization is negligible [51]. Yet, the amount of moisture accumulation within the solar panel is the rate determining step for the resulting basic or acidic environment in the panel. Moreover, since the solar cells used for the present investigation were extracted from the edge of the module, the influence of voltage bias (i.e., PID) on the degradation mechanisms in the module cannot be ruled out. Fig. 6b shows that the module might be affected by PID. Therefore, it is likely that the EVA encapsulation degraded and provided both acidic and basic environments inside Module X. This suggests that degradation of different crystals in the solar cell to different degrees is possible. This is likely one of the reasons for the differences in the surface morphologies observed in Fig. 8a.

In the high-magnification micrograph of Area 1 (Fig. 8b), the state of the microcrystals of the solar cells is clearer. Some portions of the microcrystals have disintegrated and undergone morphological changes. In this situation, the consequences for parasitic resistance losses and power degradation cannot be ruled out. The role of moisture ingress in the degradation of the solar cell appears to be significant. The white particles in Fig. 8b are the titanium dioxide (TiO_2) ARCs used on the surface of the solar cells to optimize efficiency. The effect of moisture on the degradation of the TiO_2 ARCs in field-aged PV Module X was reported earlier [33]. The TiO_2 ARCs were found to be oxidized, highly porous, and aggregation of silver nanoparticles (NPs) on the surfaces of the TiO_2 ARC particles were observed. Hence, the formation of titania metal complexes (e.g., silver-titania and titania-alumina complexes) is feasible [33]. Degradation of the TiO_2 ARC due to moisture ingress in field deployed PV modules was also reported by Baldus-Jeursen et al. [23]. In addition, migration of metal ions to the surface of the ARC leads to leakage currents, and hence, PID [23,52].

Fig. 9 shows the SEM micrographs and EDS analyses of a solar cell extracted from the edge of the module. Fig. 9a and c are the respective SEM and EDS analyses acquired approximately 10 mm from the edge of the solar cell. In Fig. 9b and d, the SEM micrograph and EDS analysis taken from the edge of the cell are shown, respectively. The EDS

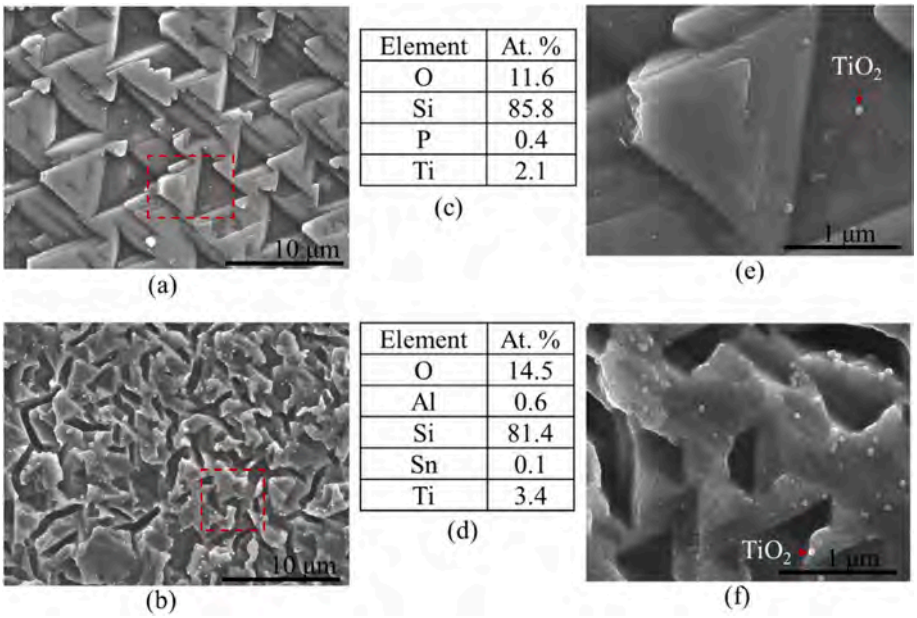

Fig. 9. SEM micrographs and EDS analyses of a solar cell extracted from the edge of PV Module X. (a)–(b) SEM micrographs and (c)–(d) EDS analyses acquired ca. 10 mm from the edge and just at the edge of the solar cell. SEM micrographs of the marked-out areas in (a) and (b) are shown in (e) and (f), respectively. The EDS analyses are represented in atomic % (at. %).

analyses show the composition of oxygen (O), silicon (Si), phosphorus (P), titanium (Ti), aluminum (Al), tin (Sn), and lead (Pb) in atomic % (at. %). Fig. 9e and f are the SEM micrographs of the marked-out areas in Fig. 9a and b, respectively. The microcrystal structures in Fig. 9a are similar to what was observed in Fig. 8a, Area 2. However, the microcrystal structures in Fig. 9b are completely different from what was observed in Fig. 8. The microcrystalline features of the solar cell in Fig. 9b appear to be more amorphous. The EDS analyses in Fig. 9c and d shows that the amount of oxygen is higher in the results acquired from the edge of the field-aged PV module. It is clear from Fig. 9e and f that the region of the solar cell in Fig. 9f is more amorphous than what is observed in Fig. 9e. The presence of oxygen in Fig. 9e and f suggests that there is a general trend of degradation across the solar cell. With these microcrystalline structures, poor charge carrier generation and high parasitic recombination in the solar cells is expected. This is likely one of the key factors for the observed degradation in P_{max} of the field-aged PV module, refer to Fig. 5. Phosphorus (P) in Fig. 9c is believed to come from the MID of the EVA encapsulation [23].

Phosphorus containing additives are used as secondary antioxidants to stabilize the encapsulation materials against peroxide degradation [13]. Hence, formation of phosphate compounds under the influence of moisture ingress is possible. At the edges and areas in the PV module where the influence of moisture ingress is more pronounced, formation of degradation compounds (e.g., Al_2O_3) is likely, see Fig. 9d. Formation of aluminum oxides due to the influence of moisture and acetic acid was also reported elsewhere [18]. More significantly, the number and proportion of chemical species increase in the EDS data acquired from the edge of the solar cell due to moisture ingress. For instance, the amount of Ti in Fig. 9c is less than what is observed in Fig. 9d. Migration and aggregation of TiO_2 nanoparticles (NPs) around the solar cell edges under the influence of moisture ingress is a possible explanation for this observation.

Fig. 9d shows the presence of Al and Sn. Aluminum can leach from the back contact of the cell or from the Al- frame of the PV module to the cell surface under the influence of moisture ingress [16,20]. Galvanic corrosion of the Al back contact, under the influence of moisture and acetic acid, causes optical degradation and deposits oxide films on the electrodes, especially around the solder joint [18]. This is because Al has the least potential (−1.662 V) among the metals in the Ag paste and solder material and is preferentially corroded in the presence of moisture and acetic acid [17,18].

According to Bai et al. [20], in the presence of moisture, Al ions are capable of migrating to the surface of the solar cell via hydrolysis. In addition, Sn from the solder or the tinned Cu ribbon can migrate under moisture ingress (Fig. 9d), as observed elsewhere [16]. This appears to confirm the observation that degradation is more severe around the edges and cracked areas of the PV module [12]. This is because moisture ingress takes place through microcracks, voids, and the edges of PV modules [4]. Fig. 10 shows the SEM-EDS elemental mappings of oxygen, sodium, silicon, titanium, and carbon, for a sample of the solar cell extracted from Module X. Fig. 10 suggests some amount of oxygen is present, which is one of the main moisture ingress species. That is, formation of chemical complexes between oxygen and the elements in Fig. 10 is feasible. Fig. 10c suggests that the migration of sodium (Na^+) ions under the influence of moisture ingress cannot be ruled out. The presence of these ions at the emitter regions of the solar cell leads to PID [9]. Also, the formation of sodium hydroxides and bicarbonates is possible. This observation agrees with the leaching behaviour of Na^+ ions in the presence of moisture reported by Smets and Lommen [53] and Hoffmann and Koehl [46]. Moisture induced migration of Na^+ ions lead to the solar cell degradation [24].

From Fig. 10b and d, distribution of oxygen across the surface of the cell can be observed. The black spots and traces around the pyramids of the Si microcrystals are the traces of oxidized TiO_2 ARC NPs around these areas. This was also observed elsewhere [16]. Fig. 10e also suggests that beside the TiO_2 ARC NPs, traces of Ti were observed across the cell area. The traces of carbon (Fig. 10f) indicate that the presence of acidic species e.g., acetic acid in the module is possible. EVA encapsulants produce acetic acid under the influence of moisture and light [4]. The presence of carboxylic acids led to further degradation of Si in these

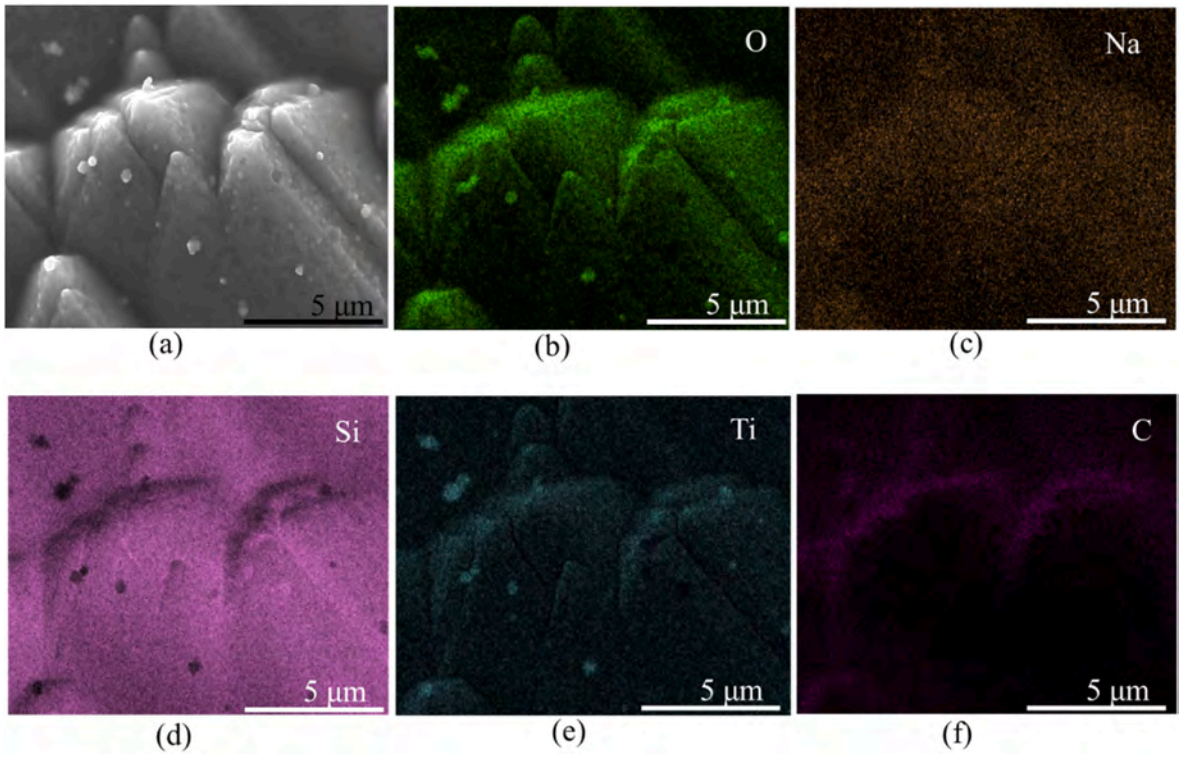

Fig. 10. (a) SEM micrograph and EDS element mappings of (b) oxygen, (c) sodium, (d) silicon, (e) titanium, and (f) carbon acquired from the edge of a solar cell extracted from PV Module X.

areas, see Fig. 10d and f.

The presence of carbon could also be due to the diffusion of carbon dioxide (CO_2) from the edge of the module or/and through cracks created in the module during field operation [4]. Fig. 11 shows the SEM micrograph and the respective EDS analyses of a cell area close to the Ag fingers of a solar cell extracted from the edge of Module X. The SEM micrograph in Fig. 11a suggests that the front surface of the solar cell and the Ag finger have undergone substantial degradation.

This observation is supported by the EDS full area analysis (Fig. 11b) and spot analyses in Fig. 12c and d. The presence and amount of oxygen in the EDS analysis in Fig. 11b suggest the influence of moisture ingress on the observed cell degradation. There is migration of cations of sodium, aluminum, lead, silver, potassium, and titanium to the surface of the solar cell under the influence of moisture ingress. Subsequently, the spot analysis of Point 1 shows that the silicon solar cell has been oxidized, see Fig. 11c. Interestingly, the amount of Si at Point 2 is the least due to the presence of C and O, see Fig. 11d. Moreover, the presence and amount of carbon in Point 2 indicates the presence of MID products of EVA such as acetic acid.

The release of chlorine and phosphorus in the degradation process of the EVA encapsulation material is also possible, see Fig. 11b. Not long ago, Kumar et al. [12] also observed about 0.28 atomic % of chlorine in a field-aged PV module that was deployed in India. The presence of moisture and acetic acid accounts for the observed degradation of the solar cell and Ag grid in Fig. 11a. Ingressed moisture activates the surface of the Ag followed by reaction of the activated Ag grid with acetic acid to form silver acetate [13,14,16]. The formation of silver acetate leads to optical degradation [27]. Fig. 12 shows the EDS mappings of oxygen, silicon, carbon, and phosphorus of the SEM micrograph in Fig. 11a.

Fig. 12a shows that oxygen is found across the surface of the solar cell. In Fig. 12b, it appears that Points 1 and 2 are at different vertical heights on the solar cell, compare with Fig. 11a. The Si mapping shows crevices or pits at the regions where carbon is present. The crevices appear dark in the EDS maps, see Fig. 12. These crevices appear to serve as reservoirs for moisture and MID products, refer to Fig. 11d. In that regard, acetic acid might accumulate and contribute to further degradation in the localized areas of Point 2 which can result in the observed crevices in Fig. 11. In addition, Fig. 12c shows that carbon is present across the surface of the solar cell, even on the Ag grids, except at Point 1 (as in Fig. 11a). Point 1 is therefore appears to have undergone full carboxylic acid degradation, and hence, the presence of carbon in these regions is negligible. This is because it is unlikely that the diffusion of moisture and its degradation species will be restricted to Point 2 (refer to Fig. 11a) alone. Furthermore, MID products such as Ag ions tend to absorb CO_2 to form their respective carbonates and acetates [13,54]. This could reduce the concentration of C at Point 1, and hence, could not be present in the EDS analyses of this area. Moreover, the production and accumulation of phosphorus across the solar cell-Ag grid boundary is consistent, see Fig. 12d. It is believed that MID processes of the solar cell and the encapsulation release phosphorus to form silver phosphates [13]. In addition, the accumulation of phosphorus at the cell-Ag grid boundary is greatest nearer to Point 1 (where C is absent). Production and accumulation of phosphorous in the PV module can be correlated to the degree of EVA encapsulation degradation in the presence of moisture [8,55]. The silver phosphates (Ag_3PO_4) degradation products lead to optical degradation [13,55].

3.6.2. *Degradation of the silver grids*

One of the most important components of the solar cell is the silver grids: fingers and busbars, refer to Fig. 2. Yet, the Ag grids are prone to degradation in the presence of moisture and acetic acid [13,14,17]. Fig. 13 shows the SEM micrographs and EDS spectra of the Ag finger grid on a newly acquired commercial mc-Si solar cell. Trace amounts of

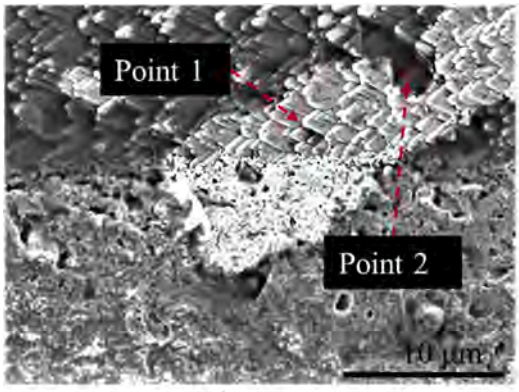

(a)

(b)

Element	At. %
O	20.8
Na	3.6
Al	0.5
Si	54.4
P	1.0
Pb	0.4
Cl	0.3
Ag	16.7
K	0.4
Ti	1.7

Point 1

Element	At. %
O	15.0
Al	0.6
Si	82.6
Sn	0.1
Ti	1.8

(c)

Point 2

Element	At. %
C	38.2
O	9.9
Na	0.2
Al	0.6
Si	49.6
Ti	1.5

(d)

Fig. 11. (a) SEM micrograph of front surface of solar cell and (b) EDS analyses of the full area of SEM micrograph in (a). (c) Point 1, and (d) Point 2 of the Ag–Si region of a solar cell extracted from the edge of the field-aged PV module showing degradation of the solar cell and the Ag finger.

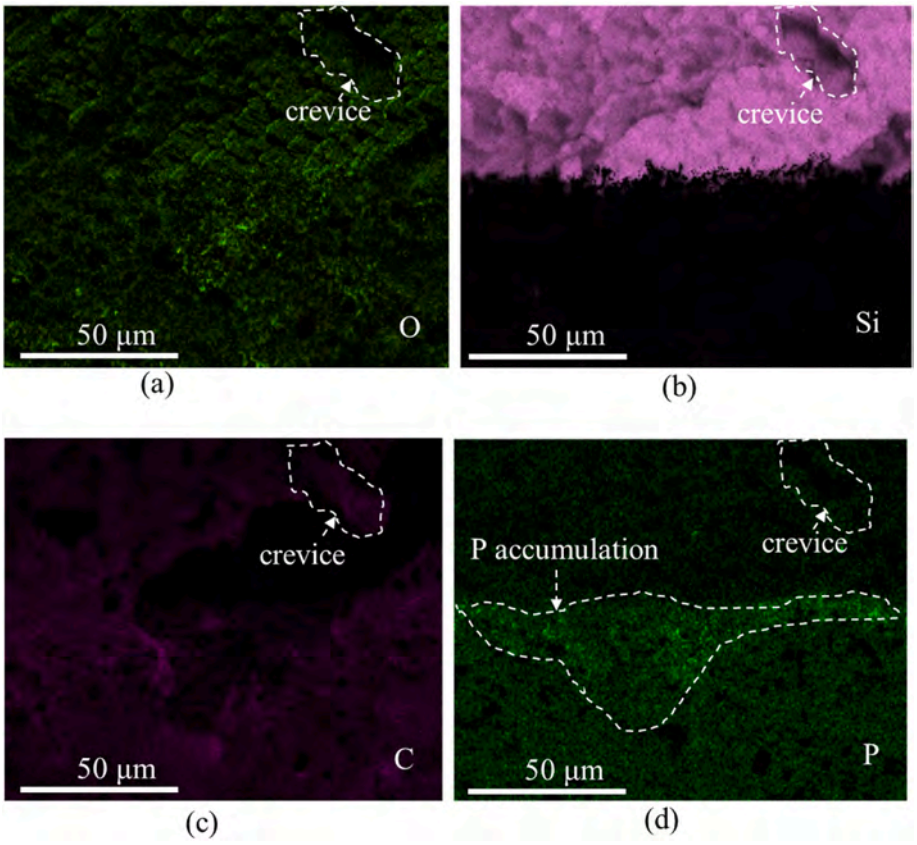

Fig. 12. EDS element mappings of (a) oxygen, (b) silicon, (c) carbon, and (d) phosphorus of the SEM micrograph in Fig. 11a.

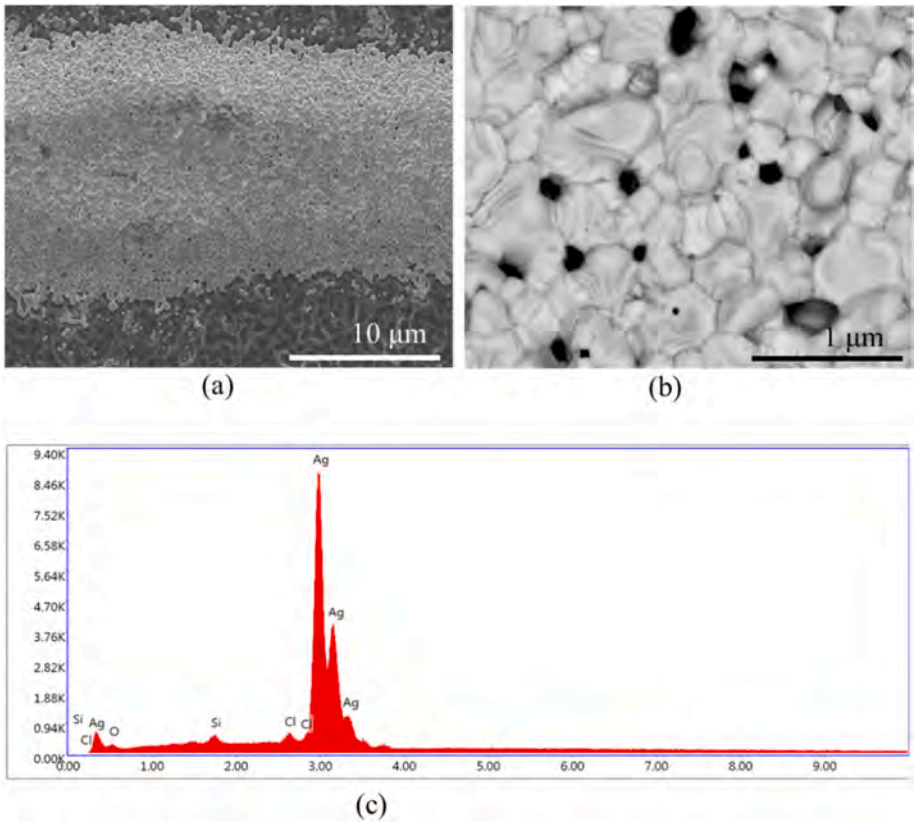

Fig. 13. (a)–(b) SEM micrographs of the Ag finger grid on a newly acquired commercial multicrystalline silicon solar cell and (c) EDS spectra of (b).

impurity Cl and O in Fig. 13c comes from the silicon production process.

In Fig. 13b, the morphology of the Ag grid shows a compact and well-ordered microstructure. The neck of the Ag micro-clusters is thicker as compared to the pore sizes. The pore density of the Ag micro-clusters is low as well. Fig. 14 shows the SEM micrographs and the EDS analysis of the Ag finger of a solar cell extracted from the edge of field-aged PV Module X. Fig. 14a and b shows the morphologies of the Ag grid of the solar cell and the EDS analysis is shown in Fig. 14c. The microstructure of the Ag grid in Fig. 14a is coarser than what is observed in Fig. 13a. Also, the neck of the Ag micro-clusters in this case are thinner and irregular, see Fig. 14b. The pore density is also higher as compared to what was observed in Fig. 13b. In addition, white micro crystallites were observed on the Ag NPs. These white crystallites are expected to be the acetates of silver or lead. These observed morphological changes agree with other reports in literature [13,14]. Duerr et al. [13] observed coarse Ag finger grids, white silver acetate crystals, and more porous Ag clusters in crystalline silicon modules affected by snail trails.

Jeffries et al. [14], observed thinner Ag cluster necks, larger and more pores, and irregular bumps, and white spot crystallites after a commercial Ag paste was subjected to 3000 h of acetic acid exposure. Moreover, Fig. 14c suggests that the Ag grids have been oxidized. This suggests that the formation of zinc, silicon, lead, and silver oxides is feasible. Fig. 15 shows the SEM micrographs and EDS analyses of the Ag busbar (refer to Fig. 2) of a solar cell extracted from the field-aged PV module. The analysis was carried out in the region nearer to the solder joint of the solar cell.

Fig. 15a shows that degradation of the Ag grid is possibly minimal. However, the EDS analysis of Fig. 15a suggests that Ag_2O is the main degradation product, see Fig. 15c. Fig. 15b is the SEM micrograph of the marked-out area in Fig. 15a, which highlights the degradation of the Ag grid better. This observation is supported by the corresponding EDS analysis in Fig. 15d, where the main degradation product expected in this area is AgO. A further EDS analysis at Point 1 in Fig. 15b suggests that the Ag grid could be present in a more severe degraded form, see Fig. 15e. The presence of fluorine in the EDS analysis in Fig. 15e might be coming from the degradation of the EVA encapsulant. The migration of Na, Al, and Pb to the surface of Ag grid is due to moisture ingress, as observed elsewhere [12,13,15–17,19]. Zinc, a component of Ag paste, is one of the degradation products responsible for optical degradation [13,28]. Zinc oxide (ZnO) was reported to be the intermediate compound for the formation of silver carbonate and silver hydroxide [54]. In this reaction mechanism, ZnO catalyzes the adsorption of ingressed CO_2 onto the Ag grid [13,54,56]. CO_2 could also be the byproduct of EVA degradation [4,13].

It was reported that under the influence of moisture, Ag has affinity for phosphorus, silicon, and sulfur [55]. Fig. 16 shows the SEM-EDS element mappings of oxygen, sodium, sulfur, lead, and zinc of the Ag busbar around the solder joint. The SEM micrograph in Fig. 16a shows a degradation trend similar to what was observed in Fig. 15b. The observed degradation is likely due to the presence of moisture and MID species on the Ag busbar region. The EDS element maps suggest that the formation of the oxides and sulfides of sodium, lead, and zinc cannot be ruled out.

Secondary organosulfur antioxidants, adhesion promoters, and stabilizers are used in the processing and/or stabilization of PV module backsheets [8,13,55]. These encapsulation materials release sulfur and phosphorus under the influence of moisture, and hence, lead to the formation of metal sulfides and phosphates [55]. These chemical species are highly photosensitive and can influence the opto-electrical characteristics of the PV module. The presence of oxygen and cell cracks can accelerate the formation of Ag_2S, and subsequent optical degradation [13,55]. In the visual inspection, it was observed that the field-aged PV module has undergone optical degradation. This observation is in line with the report by Duerr et al. [13]. Photosensitive Ag_2S appears as dark and hotspots in EL/UV-F and IR-T images, respectively.

3.6.3. Degradation of the copper ribbons

Fig. 17 shows the SEM micrographs and EDS analyses of the top and rear surfaces of the tinned Cu ribbon extracted from the field-aged PV module. The surface of the Cu ribbon is seen with microcracks which accelerate moisture ingress and degradation, see Fig. 17a. The observed oxidized layers along the crack contours suggest the influence of moisture ingress. It also indicates the role of moisture ingress in the development of microcracks. Cracks on Cu ribbons during thermal cycling has been observed and reported previously [15,57,58]. Point 1 shows erosion of the tin-plated surface on the Cu ribbon, see Fig. 17a. The EDS analysis of this region is shown in Fig. 17b indicating the presence of Cu. The EDS analysis of Point 2 shows the 'uneroded' surface of the tin-plated Cu ribbon in Fig. 17c, in which Cu is absent. The amount of Sn in Fig. 17b is higher than the amount of Sn in Fig. 17c. On the other hand, the amount of oxygen, silicon and lead are higher in Fig. 17c. In the first place, migration of O, Na, Ti, Si, and Pb elements to the surface of tinned Cu ribbon is normally due to moisture ingress. The amount of oxygen in Fig. 17b and c suggests that the surfaces of the tinned Cu ribbon are more oxidized due to the formation of surface oxide layers of Sn and Pb in the presence of moisture. That is, Sn and Pb of the tinned plated component of the Cu ribbon were oxidized preferentially to protect the Cu ribbon from degradation. This is likely the reason for the lower amount of Sn observed in Fig. 17c. However, when a large chunk of the protective oxidized Sn is removed, Cu could be found in a greater amount with lesser amount of oxygen, see Fig. 17b. Fig. 17d is the SEM micrograph of the rear surface of the tinned Cu ribbon and the corresponding EDS analysis is shown in Fig. 17e. The SEM-EDS analyses of the rear surface of the Cu ribbon suggest that this region has also undergone degradation due to moisture ingress.

The substantial amount of oxygen, aluminum, and the presence of carbon suggest the effect of moisture ingress and subsequent formation of carboxylic acids in this region. The presence of moisture together with acetic acid means that the formation of copper oxides, hydroxides, and acetates is feasible. In addition, the formation of metal complexes such

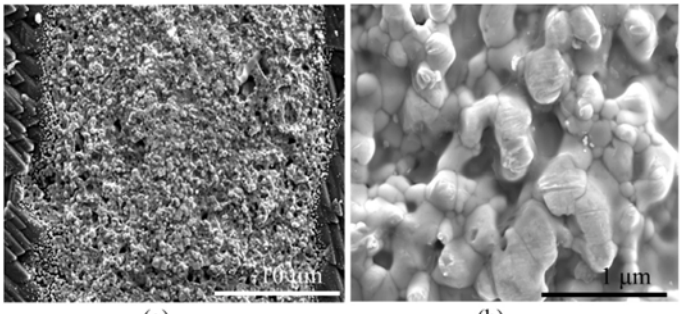

Element	At. %
O	39.5
Zn	3.1
Si	2.7
Pb	0.7
Ag	54.0

(c)

Fig. 14. (a)–(b) SEM micrographs of the Ag finger of a solar cell extracted from the edge of the field-aged PV module and (c) EDS analysis of the SEM micrograph in (b).

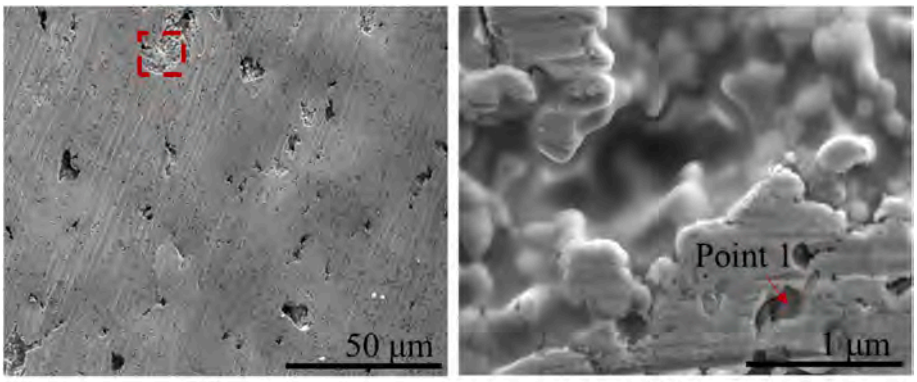

(a) (b)

Element	At. %
O	34.0
Na	8.5
Al	1.1
Si	2.3
Pb	0.8
Ag	53.4

(c)

Element	At. %
O	43.1
Si	2.6
Pb	1.4
Ag	48.5
Zn	4.4

(d)

Point 1

Element	At. %
O	60.9
F	1.7
Al	0.4
Si	6.5
Pb	4.0
Ag	14.3
Zn	12.3

(e)

Fig. 15. (a) SEM micrograph of the Ag busbar from the region nearer to the solder joint of the field-aged solar cell. (b) High magnification SEM micrograph of the marked-out area in (a). (c)–(e) EDS analyses of the SEM micrograph areas in (a), (b), and point analysis at Point 1, respectively.

as copper stannates and silver stannates around this region cannot be ruled out. These complexes have detrimental effect on the optoelectrical properties of the PV module [57].

Other competing reactions in this region can lead to the formation of aluminum and lead oxides and hydroxides [18]. In addition, it was observed that more elements were found on the rear surface of the Cu ribbon, see Fig. 17e. It is expected that these species migrated to the rear surface of the Cu ribbon under the influence of moisture ingress. However, the ratios of oxygen and copper in Fig. 17b and e are approximately 2:1 in both cases. This suggests that the degradation of the Cu ribbon in the PV module under the influence of moisture ingress is similar.

Fig. 18 shows the SEM-EDS analyses of the Ag busbar (refer to Fig. 2) of a solar cell at the solder joint extracted from the field-aged PV module. During PV module fabrication, the solar cells are stringed together with the Ag busbar underneath the Cu ribbon. SEM-EDS analyses were acquired from the region of the Ag busbar at the solder joint of the solar cell. Fig. 18a shows that after the Cu ribbon was detached from the solar cell, a large chunk of the tinned Cu ribbon remained on the solar cell and masked out the Ag busbar. This suggests that the Cu ribbon has undergone degradation leaving behind significant remnants of the tinned Cu ribbon. In this case, the possible influence of moisture ingress in the Cu ribbon degradation cannot be ruled out. This is supported by the presence and amount of copper, tin, and oxygen in the EDS analysis, see Fig. 18b.

Degradation of the Cu ribbon might also be accelerated by the presence of acetic acid, as observed in Fig. 17d and e. The Cu ribbon degradation due to the presence of acetic acid was reported elsewhere [15–17,27]. Formation of oxides of copper, tin, lead, aluminum, and silver in such areas is feasible, and underlines parasitic resistance losses.

3.6.4. Degradation of the solder bonds

Fig. 19 shows the SEM-EDS analyses of the solder bond in the solar cell extracted from the field-aged PV module. Fig. 19a shows the SEM micrograph and Fig. 19b shows the corresponding EDS analysis of the SEM micrograph in Fig. 19a. Fig. 19 indicates that the major component of the solder is lead and tin. Apart from Pb and Sn, migration of chemical species under the influence of moisture ingress is the reason for the observed oxygen, sodium, aluminum, silver, calcium, and copper in Fig. 19b. Point analyses for Pb and Sn in Fig. 19a show that Pb was more oxidized. The amount of oxygen at areas where Pb was observed was higher than areas where Sn was observed (not shown here). Yet, Sn remained largely unoxidized, even though Sn has lower potential.

It is known that solder degradation in the presence of moisture and acetic acid obeys the galvanic corrosion reaction [17,18]. In the presence of moisture and acetic acid, Pb is preferentially corroded [59]. Acetic acid catalyzes the degradation of the Pb in the solder in the presence of moisture [60]. Under atmospheric conditions, a nanometer sized protective lead oxide passive layer is formed on the surface of Pb according to the following reaction mechanisms:

$$\text{Anode (oxidation)} : Pb \rightarrow Pb^{+2} + 2e^{-} \quad (1)$$

$$\text{Cathode (reduction)} : \frac{1}{2}O_2 + H_2O + 2e^{-} \rightarrow 2OH^{-} \quad (2)$$

$$\text{Passive PbO layer} : Pb^{+2} + 2OH^{-} \rightarrow PbO + H_2O \quad (3)$$

The passivation lead oxide (PbO) layer protects the Pb metal from further corrosion and degradation. However, in the presence of moisture and acetic acid, the PbO protective layer is susceptible to dissolution, and hence, degradation. The acidified electrolyte (consisting of several MID products) in the PV module permeates into cracks and defects in the PbO protective layer and reacts with the Pb to form soluble lead acetate complexes according to the following reaction mechanisms [61]:

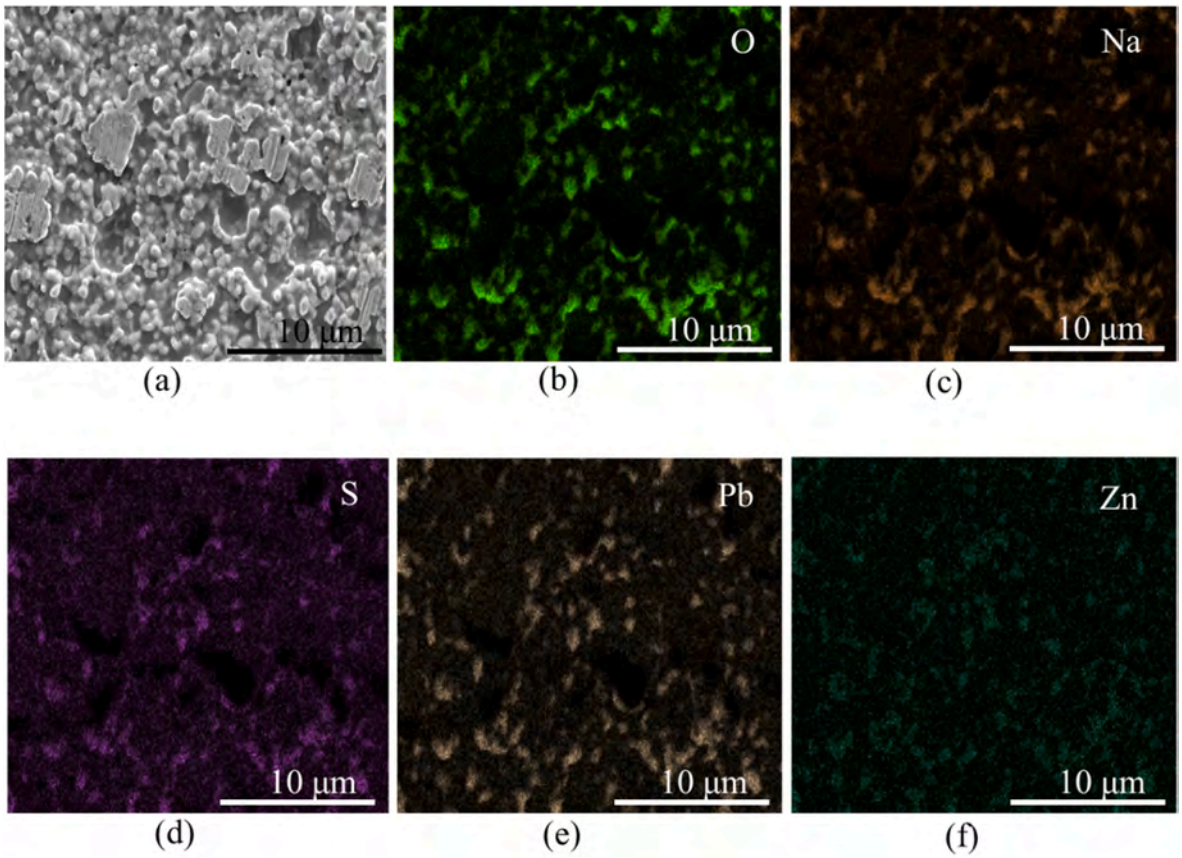

Fig. 16. (a) SEM micrograph and EDS element mappings of oxygen (O), sodium (Na), sulfur (S), lead (Pb), and zinc (Zn) of the Ag busbar at the solder joint of the extracted solar cell.

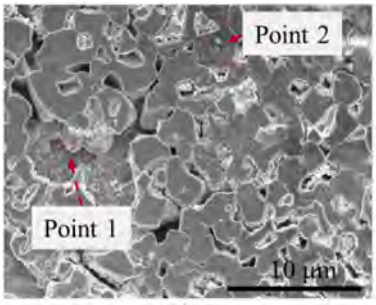

Point 1

Element	At. %
Ti	6.2
O	37.9
Si	6.6
Pb	5.7
Sn	25.5
Cu	18.1

(b)

Point 2

Element	At. %
O	66.7
Na	5.2
Si	9.3
Pb	16.6
Sn	2.3

(c)

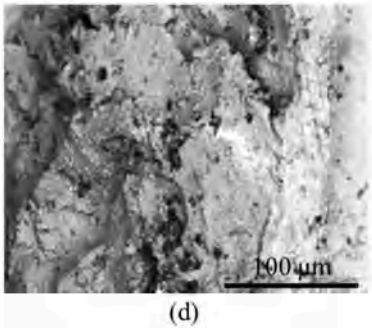

Element	At. %
C	6.9
O	45.7
Cu	25.1
Al	4.1
Si	2.3
Pb	8.9
Sn	7.0

(e)

Fig. 17. (a) SEM micrograph of the top surface of the Cu ribbon and the corresponding EDS analyses of (b) Point 1 and (c) Point 2. (d) SEM micrograph and (e) corresponding EDS analysis of the rear surface of the Cu ribbon. Data was acquired from the field-aged PV module.

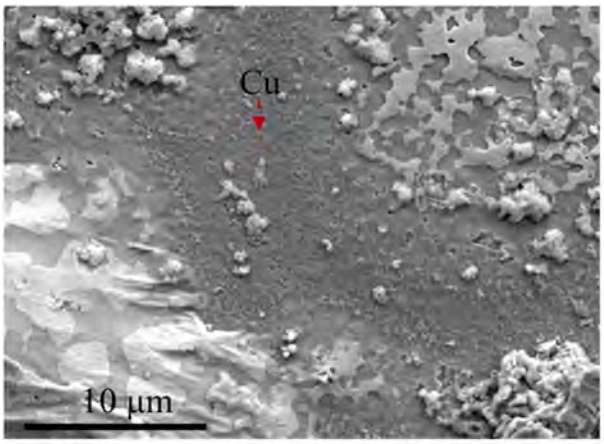

Element	At. %
O	19.3
Al	3.1
Pb	7.8
Ag	2.2
Sn	22.0
Cu	45.4

(b)

Fig. 18. (a) SEM micrograph and (b) EDS analysis of the Ag busbar beneath the Cu ribbon of the solar cell at the solder joint extracted from the PV module.

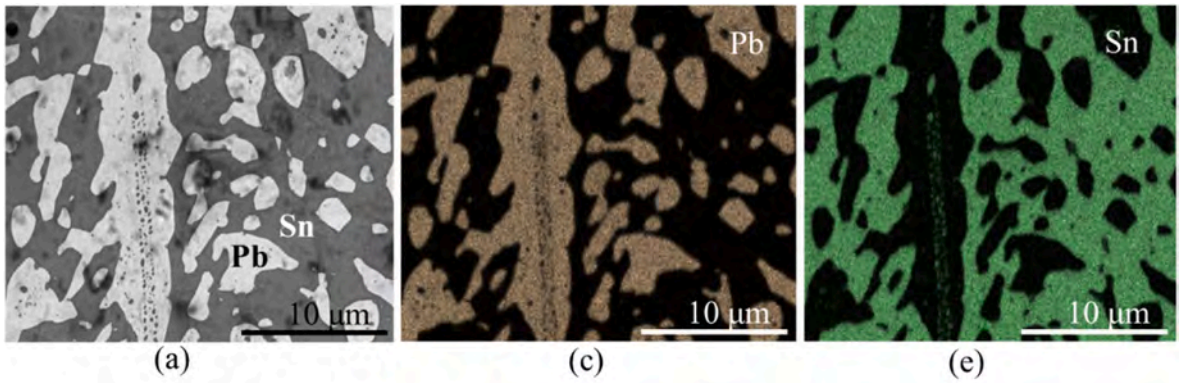

(b)

Element	At. %
O	10.7
Na	1.8
Al	0.3
Si	2.3
Pb	20.6
Ag	1.1
Sn	60.6
Ca	2.5
Cu	0.2

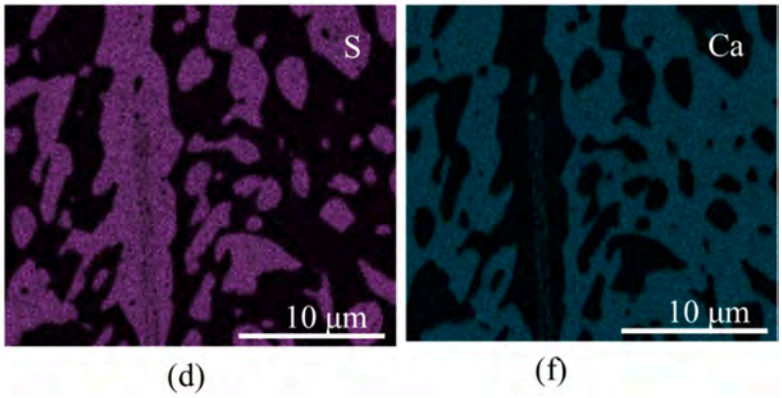

Fig. 19. (a) SEM micrograph and (b) EDS analyses of the solder bond in the solar cell extracted from the field-aged PV module. EDS element mappings of (c) lead, (d) sulfur, (e) tin, and (f) calcium indicating formation of metal complexes due to moisture ingress.

$$\text{PbO layer dissolution}: PbO + 2CH_3COOH \rightarrow Pb^{+2} + 2CH_3COO^{-} + H_2O \quad (4)$$

$$2PbO + Pb^{+2} + 2CH_3COO^{-} + H_2O \rightarrow Pb(CH_3COO)_2 \bullet 2PbO \bullet H_2O \quad (5)$$

To understand other competing reactions, elemental maps were acquired from Fig. 19a. It was observed that the mappings of Pb and sulfur were similar, see Fig. 19c and d. On the other hand, the mappings of Sn and calcium were also similar, see Fig. 19e and f. Interestingly, the elemental mappings of the minor elements (e.g., Na, Al, Si, P, and Cu) were similar to the mappings of Pb and sulfur. These elemental mappings suggest that the formation of lead sulfides and phosphates is feasible. Formation of other Sn-metal complexes such as calcium, copper, and sodium stannates is also expected, see Fig. 19e and f.

Taken together, moisture ingress is the underlying factor for the formation of oxides, hydroxides, sulfides, phosphates, acetates, and carbonates of silver, lead, tin, copper, zinc, and aluminum in the field-aged PV modules. Notably, moisture can induce the formation of photosensitive metal-ligand complexes of silver, tin, and titanium. The solar cells also undergo consequential degradation when exposed to moisture and its degradation products. These MID products lead to the observed corrosion, cracks, optical degradation, and PID in the field-

aged PV module. Subsequently, these defects and fault modes cause parasitic resistance losses, and hence, power degradation in the field-aged PV module.

4. Conclusion

In the present work, the effect of moisture ingress on the degradation of reclaimed solar cells from a 20-year-old field-aged mc-Si PV module was investigated. Visual inspection, I–V characterization, EL, UV-F, and IR-T imaging techniques show that the PV module has undergone substantial degradation. To elucidate the role of moisture ingress on the observed degradation mechanisms, microstructural analyses were conducted on the extracted solar cells from the PV module using SEM-EDS techniques. Visual inspection demonstrated that the EVA encapsulation has undergone optical degradation and the extracted cells show dark discolored TPT backsheets. Corrosion at the solder joint was dominant and is attributed to the dissolution of lead and tin (main components of solder) and the Ag grids in moisture and acetic acid due to galvanic corrosion.

Moisture ingress, in the presence of light, in the field-aged PV module led to the degradation of the EVA encapsulation, and hence, the formation of carboxylic acids such as acetic acid and degradation products such as CO, CO_2, phosphorus, sulfur, fluorine, and chlorine. In the presence of moisture and acetic acid, the solar cells, metal grids, solder bonds, and the antireflection coatings undergo different forms of degradation. The solar cell and ARC become oxidized under the influence of moisture ingress. Moisture ingress influences the migration of metal ions e.g., Na, Ag, Pb, Sn, Cu, Zn, and Al to the surface of the solar cells, and hence, leads to PID. Silver and zinc ions originate from the degradation of the silver paste used for the Ag grids and busbars. Whilst Pb and Sn ions come from the solder, the copper ribbon is the source of Cu and also Sn ions. The Al and Na ions migrate from the Al- frame and/or rear solar cell contact and the soda lime front glass, respectively.

In this regard, the formation of oxides, hydroxides, sulfides, phosphates, acetates, and carbonates of silver, lead, tin, copper, zinc, and aluminum have been observed. Degradation of the front and rear surfaces of the copper ribbons appears to be similar. However, degraded remnants of the Cu ribbon can mask out the silver busbar, leading to parasitic resistive losses. Also, other competing reactions can lead to the formation of stannates of copper, silver, sodium, and zinc. Similarly, migration of silver and aluminum to the surfaces of the TiO_2 ARC NPs can lead to the formation of titania-alumina and silver-titania complexes. It was observed that, in the presence of moisture and acetic acid, Pb is preferentially corroded (to form lead acetate complexes) instead of the expected sacrificial Sn in the solder.

These MID species may account for the observed metal grids corrosion, cell cracks, optical degradation, and PID in the field-aged PV module. In the EL and UV-F images, these degradation species appear as dark spots, and as hotspots in IR-T images. It is well known that these defects and fault modes can lead to parasitic resistance losses which was witnessed by the overall 1.2%/year degradation in the P_{max} of the field-aged PV module. The relative temperature coefficient of efficiency of the examined PV module was found to be −0.5%/°C. In a Nordic environment with high CMI, the role of these MID mechanisms in the degradation of field-aged solar PV modules is very significant. Investigation of MID mechanisms in field-aged solar PV modules is more reflective of the reality in the field. Though solar PV module materials and technology have evolved over the years, MID mechanisms in solar PV modules appear to follow a similar trend. Hence, insights from this work can guide decision making at the present and in the future as regards understanding the performance reliability of solar PV plants.

CRediT authorship contribution statement

Oscar Kwame Segbefia: Writing – original draft, Validation, Methodology, Investigation, Formal analysis, Conceptualization. **Naureen Akhtar:** Writing – review & editing, Validation, Investigation, Formal analysis. **Tor Oskar Sætre:** Writing – review & editing, Supervision, Funding acquisition, Conceptualization.

Declaration of competing interest

The authors declare that they have no known competing financial interests or personal relationships that could have appeared to influence the work reported in this paper.

Data availability

Data will be made available on request.

Acknowledgement

The authors acknowledge the continuous support of the University of Agder, Norway and Dr. Odin Kvam of the Department of Engineering Sciences, University of Agder for his role in the solar cell samples' reclamation for this investigation.

References

[1] A. Dadaniya, N.V. Datla, Water diffusion simulation in photovoltaic module based on the characterization of encapsulant material using in-situ gravimetric technique, Sol. Energy Mater. Sol. Cell. 201 (2019), 110063.
[2] C. Han, Analysis of moisture-induced degradation of thin-film photovoltaic module, Sol. Energy Mater. Sol. Cell. 210 (2020), 110488.
[3] M.D. Kempe, Modeling of rates of moisture ingress into photovoltaic modules, Sol. Energy Mater. Sol. Cell. 90 (2006) 2720–2738.
[4] O.K. Segbefia, A.G. Imenes, T.O. Sætre, Moisture ingress in photovoltaic modules: a review, Sol. Energy 224 (2021) 889–906.
[5] O.K. Segbefia, N. Akhtar, T.O. Sætre, Defects and fault modes of field-aged photovoltaic modules in the Nordics, Energy Rep. 9 (2023) 3104–3119.
[6] N. Kim, C. Han, Experimental characterization and simulation of water vapor diffusion through various encapsulants used in PV modules, Sol. Energy Mater. Sol. Cells 116 (2013) 68–75.
[7] D. Wisniewski, R. Lv, S.V. Nair, J.N. Jaubert, T. Xu, H.E. Ruda, Measurement and modelling of water ingress into double-glass photovoltaic modules, Prog. Photovoltaics Res. Appl. 27 (2019) 144–151.
[8] C. Peike, S. Hoffmann, P. Hulsmann, B. Thaidigsmann, K.A. Weiss, M. Koehl, P. Bentz, Origin of damp-heat induced cell degradation, Sol. Energy Mater. Sol. Cells 116 (2013) 49–54.
[9] V. Naumann, D. Lausch, A. Hahnel, J. Bauer, O. Breitenstein, A. Graff, M. Werner, S. Swatek, S. Grosser, J. Bagdahn, C. Hagendorf, Explanation of potential-induced degradation of the shunting type by Na decoration of stacking faults in Si solar cells, Sol. Energy Mater. Sol. Cell. 120 (2014) 383–389.
[10] C.J. Willmott, J.J. Feddema, A more rational climatic moisture index, Prof. Geogr. 44 (1992) 84–88.
[11] S. Mitterhofer, C. Barretta, L.F. Castillon, G. Oreski, M. Topic, M. Jankovec, A dual-transport model of moisture diffusion in PV encapsulants for finite-element simulations, IEEE J. Photovoltaics 10 (2020) 94–102.
[12] S. Kumar, R. Meena, R. Gupta, Imaging and micro-structural characterization of moisture induced degradation in crystalline silicon photovoltaic modules, Sol. Energy 194 (2019) 903–912.
[13] I. Duerr, J. Bierbaum, J. Metzger, J. Richter, D. Philipp, Silver grid finger corrosion on snail track affected PV modules–investigation on degradation products and mechanisms, Energy Proc. 98 (2016) 74–85.
[14] A.M. Jeffries, T. Nietzold, L.T. Schelhas, M.I. Bertoni, Corrosion of novel reactive silver ink and commercial silver-based metallizations in diluted acetic acid, Sol. Energy Mater. Sol. Cells 223 (2021), 110900.
[15] J.S. Jeong, N. Park, C. Han, Field failure mechanism study of solder interconnection for crystalline silicon photovoltaic module, Microelectron. Reliab. 52 (2012) 2326–2330.
[16] N. Kyranaki, A. Smith, K. Yendall, D.A. Hutt, D.C. Whalley, R. Gottschalg, T. R. Betts, Damp-heat induced degradation in photovoltaic modules manufactured with passivated emitter and rear contact solar cells, Prog. Photovoltaics Res. Appl. 30 (9) (2022) 1061–1071.
[17] T.H. Kim, N.C. Park, D.H. Kim, The effect of moisture on the degradation mechanism of multi-crystalline silicon photovoltaic module, Microelectron. Reliab. 53 (2013) 1823–1827.
[18] H.P. Xiong, C.H. Gan, X.B. Yang, Z.G. Hu, H.Y. Niu, J.F. Li, J.F. Si, P.F. Xing, X. T. Luo, Corrosion behavior of crystalline silicon solar cells, Microelectron. Reliab. 70 (2017) 49–58.
[19] W. Oh, S. Kim, S. Bae, N. Park, Y. Kang, H.-S. Lee, D. Kim, The degradation of multi-crystalline silicon solar cells after damp heat tests, Microelectron. Reliab. 54 (2014) 2176–2179.

[20] Q. Bai, H. Yang, C. Nan, H. Wang, Z. Chen, Analysis of the electrochemical reactions and ions migration for crystalline silicon solar module under high system voltage, Sol. Energy 225 (2021) 718–725.
[21] O.K. Segbefia, T.O. Sætre, Investigation of the temperature sensitivity of 20-years old field-aged photovoltaic panels affected by potential induced degradation, Energies 15 (2022) 3865.
[22] E.L. Meyer, E.E. Van Dyk, Assessing the reliability and degradation of photovoltaic module performance parameters, IEEE Trans. Reliab. 53 (2004) 83–92.
[23] C. Baldus-Jeursen, A. Côté, T. Deer, Y. Poissant, Analysis of photovoltaic module performance and life cycle degradation for a 23 year-old array in Quebec, Canada, Renew. Energy 174 (2021) 547–556.
[24] K. Matsuda, T. Watanabe, K. Sakaguchi, M. Yoshikawa, T. Doi, A. Masuda, Microscopic degradation mechanisms in silicon photovoltaic module under long-term environmental exposure, Jpn. J. Appl. Phys. 51 (2012) 10NF07.
[25] M. Köntges, S. Kurtz, C. Packard, U. Jahn, K.A. Berger, K. Kato, T. Friesen, H. Liu, M. Van Iseghem, J. Wohlgemuth, Review of Failures of Photovoltaic Modules, 2014.
[26] U. Jahn, M. Herz, M. Köntges, D. Parlevliet, M. Paggi, I. Tsanakas, Review on Infrared and Electroluminescence Imaging for PV Field Applications: International Energy Agency Photovoltaic Power Systems Programme: IEA PVPS Task 13, International Energy Agency, 2018. Subtask 3.3: report IEA-PVPS T13-12: 2018.
[27] N. Iqbal, D.J. Colvin, E.J. Schneller, T.S. Sakthivel, R. Ristau, B.D. Huey, X. Ben, J.-N. Jaubert, A.J. Curran, M. Wang, Characterization of front contact degradation in monocrystalline and multicrystalline silicon photovoltaic modules following damp heat exposure, Sol. Energy Mater. Sol. Cells 235 (2022), 111468.
[28] P. Peng, A. Hu, W. Zheng, P. Su, D. He, K.D. Oakes, A. Fu, R. Han, S.L. Lee, J. Tang, Microscopy study of snail trail phenomenon on photovoltaic modules, RSC Adv. 2 (2012) 11359–11365.
[29] O. Dupré, R. Vaillon, M.A. Green, Physics of the temperature coefficients of solar cells, Sol. Energy Mater. Sol. Cells 140 (2015) 92–100.
[30] S. Kumar, R. Meena, R. Gupta, Finger and interconnect degradations in crystalline silicon photovoltaic modules: a review, Sol. Energy Mater. Sol. Cells 230 (2021), 111296.
[31] M.C.C. de Oliveira, A.S.A.D. Cardoso, M.M. Viana, V.d.F.C. Lins, The causes and effects of degradation of encapsulant ethylene vinyl acetate copolymer (EVA) in crystalline silicon photovoltaic modules: a review, Renew. Sustain. Energy Rev. 81 (2018) 2299–2317.
[32] W. Oh, S. Bae, S. Kim, N. Park, S.-I. Chan, H. Choi, H. Hwang, D. Kim, Analysis of degradation in 25-year-old field-aged crystalline silicon solar cells, Microelectron. Reliab. 100 (2019), 113392.
[33] O.K. Segbefia, N. Akhtar, T.O. Sætre, The effect of moisture ingress on titania antireflection coatings in field-aged photovoltaic modules, in: 2022 IEEE 49th Photovoltaics Specialists Conference (PVSC), IEEE, 2022, pp. 1237–1244.
[34] D.J. Colvin, N. Iqbal, J.H. Yerger, F. Li, A. Sinha, G. Vicnansky, G. Brummer, N. Zheng, E.J. Schneller, J. Barkaszi, Degradation of monocrystalline silicon photovoltaic modules from a 10-year-old Rooftop system in Florida, IEEE J. Photovoltaics 13 (2) (2023) 275–282.
[35] O.K. Segbefia, B.R. Paudyal, I. Burud, T.O. Sætre, Temperature Coefficients of Photovoltaic Modules under Partial Shading Conditions, 38th EU PVSEC, 2021, pp. 1180–1186.
[36] M. Köntges, A. Morlier, G. Eder, E. Fleiß, B. Kubicek, J. Lin, Ultraviolet Fluorescence as Assessment Tool for Photovoltaic Modules, IEEE J. Photovolt., 2020.
[37] A. Morlier, M. Siebert, I. Kunze, S. Blankemeyer, M. Köntges, Ultraviolet fluorescence of ethylene-vinyl acetate in photovoltaic modules as estimation tool for yellowing and power loss, in: 2018 IEEE 7th World Conference on Photovoltaic Energy Conversion (WCPEC)(A Joint Conference of 45th IEEE PVSC, 28th PVSEC & 34th EU PVSEC), IEEE, 2018, pp. 1597–1602.
[38] W. Herrmann, G. Eder, B. Farnung, G. Friesen, M. Köntges, B. Kubicek, O. Kunz, H. Liu, D. Parlevliet, I. Tsanakas, Qualification of Photovoltaic (Pv) Power Plants Using Mobile Test Equipment, 2021. IEA-PVPS T13-24: 2021.
[39] R. Meena, S. Kumar, R. Gupta, Comparative investigation and analysis of delaminated and discolored encapsulant degradation in crystalline silicon photovoltaic modules, Sol. Energy 203 (2020) 114–122.
[40] O.K. Segbefia, A.G. Imenes, I. Burud, T.O. Sætre, Temperature profiles of field-aged multicrystalline silicon photovoltaic modules affected by microcracks, in: 2021 IEEE 48th Photovoltaic Specialists Conference (PVSC), IEEE, 2021, pp. 1–6.
[41] E. Skoplaki, J.A. Palyvos, On the temperature dependence of photovoltaic module electrical performance: a review of efficiency/power correlations, Sol. Energy 83 (2009) 614–624.
[42] D.L. King, J.A. Kratochvil, W.E. Boyson, Temperature coefficients for PV modules and arrays: measurement methods, difficulties, and results, in: Conference Record of the Twenty Sixth IEEE Photovoltaic Specialists Conference-1997, IEEE, 1997, pp. 1183–1186.
[43] M.A. Green, General temperature dependence of solar cell performance and implications for device modelling, Prog. Photovoltaics Res. Appl. 11 (2003) 333–340.
[44] G. Segev, H. Dotan, D.S. Ellis, Y. Piekner, D. Klotz, J.W. Beeman, J.K. Cooper, D. A. Grave, I.D. Sharp, A. Rothschild, The spatial collection efficiency of charge carriers in photovoltaic and photoelectrochemical cells, Joule 2 (2018) 210–224.
[45] G.A. Landis, Review of solar cell temperature coefficients for space, in: XIII Space Photovoltaic Research and Technology Conference, SPRAT XIII, 1994, p. 385.
[46] S. Hoffmann, M. Koehl, Effect of humidity and temperature on the potential-induced degradation, Progress in Photovoltaics 22 (2014) 173–179.
[47] J.A. Tsanakas, L. Ha, C. Buerhop, Faults and infrared thermographic diagnosis in operating c-Si photovoltaic modules: a review of research and future challenges, Renew. Sustain. Energy Rev. 62 (2016) 695–709.
[48] S. Kajari-Schršder, I. Kunze, M. Kšntges, Criticality of cracks in PV modules, Energy Proc. 27 (2012) 658–663.
[49] C. Buerhop, D. Schlegel, M. Niess, C. Vodermayer, R. Weißmann, C. Brabec, Reliability of IR-imaging of PV-plants under operating conditions, Sol. Energy Mater. Sol. Cells 107 (2012) 154–164.
[50] W. Chen, Y. Liu, L. Yang, J. Wu, Q. Chen, Y. Zhao, Y. Wang, X. Du, Difference in anisotropic etching characteristics of alkaline and copper based acid solutions for single-crystalline Si, Sci. Rep. 8 (2018) 1–8.
[51] J. Li, Y.-C. Shen, P. Hacke, M. Kempe, Electrochemical mechanisms of leakage-current-enhanced delamination and corrosion in Si photovoltaic modules, Sol. Energy Mater. Sol. Cells 188 (2018) 273–279.
[52] J. Bauer, V. Naumann, S. Großer, C. Hagendorf, M. Schütze, O. Breitenstein, On the mechanism of potential-induced degradation in crystalline silicon solar cells, Phys. Status Solidi Rapid Res. Lett. 6 (2012) 331–333.
[53] B. Smets, T. Lommen, The leaching of sodium containing glasses: ion exchange or diffusion of molecular water? J. Phys. Colloq. 43 (1982). C9-649-C649-652.
[54] R. Wiesinger, S. Schnöller, H. Hutter, M. Schreiner, C. Kleber, About the formation of basic silver carbonate on silver surfaces–An in situ IRRAS study, Open Corrosion J. 2 (2009).
[55] S. Meyer, S. Timmel, M. Gläser, U. Braun, V. Wachtendorf, C. Hagendorf, Polymer foil additives trigger the formation of snail trails in photovoltaic modules, Sol. Energy Mater. Sol. Cells 130 (2014) 64–70.
[56] H.-J. Freund, M.W. Roberts, Surface chemistry of carbon dioxide, Surf. Sci. Rep. 25 (1996) 225–273.
[57] C. Oh, A. Kim, J. Kim, J. Bang, J. Ha, W.-S. Hong, Bonding copper ribbons on crystalline photovoltaic modules using various lead-free solders, J. Mater. Sci. Mater. Electron. 26 (2015) 9721–9726.
[58] P. Chaturvedi, B. Hoex, T.M. Walsh, Broken metal fingers in silicon wafer solar cells and PV modules, Sol. Energy Mater. Sol. Cells 108 (2013) 78–81.
[59] C.M. Oertel, S.P. Baker, A. Niklasson, L.-G. Johansson, J.-E. Svensson, Acetic acid vapor corrosion of lead–tin alloys containing 3.4 and 15% tin, J. Electrochem. Soc. 156 (2009) C414.
[60] S. Msallamova, M. Kouril, K.C. Strachotova, J. Stoulil, K. Popova, P. Dvorakova, M. Lhotka, Protection of lead in an environment containing acetic acid vapour by using adsorbents and their characterization, Heritage Science 7 (2019) 1–9.
[61] A. Niklasson, L.-G. Johansson, J.-E. Svensson, Influence of acetic acid vapor on the atmospheric corrosion of lead, J. Electrochem. Soc. 152 (2005) B519.

Paper E

Temperature profiles of field-aged photovoltaic modules affected by optical degradation by O.K. Segbefia. Manuscript to be submitted for publication. Preprint: http://dx.doi.org/10.2139/ssrn.4046700.

Temperature profiles of field-aged photovoltaic modules affected by optical degradation

Oscar Kwame Segbefia

Department of Engineering Sciences, University of Agder, 4879 Grimstad, Norway

*Corresponding author (oscar.k.segbefia@uia.no)

Abstract

Moisture ingress into PV module in the presence of ultraviolet radiation, high temperature, and other environmental stressors can affect the optical integrity of the PV module. Optical degradation can take the form of delamination, discolouration of encapsulant, metal grids corrosion, and trapped moisture or chemical species. This can influence the photon absorption and current transport properties in the PV module bulk, which can affect the module operating temperature. In the present work, the relationship between optical degradation and temperature sensitivity of 20-year-old multicrystalline silicon field-aged PV modules have been investigated. The selected PV modules were characterized using visual inspection, current-voltage (I-V) characterization, temperature coefficients profiling, current resistivity profiling, infrared (IR) thermal, ultraviolet fluorescence (UV-F), and electroluminescence (EL) imaging. PV modules affected by optical degradation show weak fluorescence and luminescence signal intensities. The average difference in cell temperature (ΔT) between the warmest and coldest cell for the PV modules investigated was found to be around 10 ± 2 ℃ and the average power degradation rate was approximately 0.8 % per year. The underlying factor for the observed degradation is attributed to the degradation in the temperature coefficients of open circuit voltage (β_{Voc}) and maximum power point voltage (β_{Vmpp}). The average temperature coefficient of efficiency ($\beta_{\eta m}$) of the modules was found to be around -0.5 %/℃. Finally, a temperature dependent resistivity method for extracting temperature coefficients from IR thermal data of PV modules has been proposed.

Keywords: optical degradation, resistivity, temperature coefficient, thermal imaging, co-defect

1 Introduction

One of the most critical characteristics of good photovoltaic (PV) front encapsulation materials is optimum optical transmission efficiency [1, 2]. However, in the field, PV modules are exposed to a variety of environmental stressors: high temperature, humidity, ultraviolet radiation, wind and snow loads, and soiling [3-5]. In the presence of these environmental stressors, moisture can diffuse into the bulk of the solar panel through the edge, back of the panel, and/or voids (e.g., cracks) created in the panel [4, 5]. Moisture and moisture induced degradation (MID) products in

the PV module initiate several degradation processes in the ethylene vinyl acetate (EVA), which is the most popular PV module front encapsulation material [4]. MID products include oxides, acetates, carbonates of metal grids e.g., silver, lead, tin, copper, and aluminum [5]. For instance, MID of the EVA encapsulation produces acetic acid, and possibly, silver acetate [6]. The MID species can lead to delamination and discolouration of encapsulants, snail trails, potential induced degradation (PID), loss of adhesion, corrosion of metal grids and other components of the PV module [1, 6]. These degradation mechanisms have also been found to serve as a precursor for other degradation mechanisms in PV plants [1, 4, 7].

More importantly, the majority of these reliability issues affect the optical efficiency of the front encapsulant, and hence, constitute optical degradation [3]. For instance, metal grids corrosion and PID can lead to optical degradation and vice versa [8]. The route to optical degradation of PV modules due to moisture ingress is illustrated in Fig. 1. Over time, the issue of optical degradation becomes more pronounced and can in the most severe cases constitute more than 50 % degradation in the rated power output of the PV module [7]. The loss of power output is due to increased optical reflection due to "light decoupling" with reduced photon absorption in the active PV material [1, 7, 9]. This has dire implications for PV module efficiency and costs for operating PV plants over their guaranteed lifetime. The optical transparency can be quantified by the "yellowness index". According to the International Standards Organization [10], "yellowness index" is a measure of the deviation in polymer hue from colourless or whiteness toward yellow.

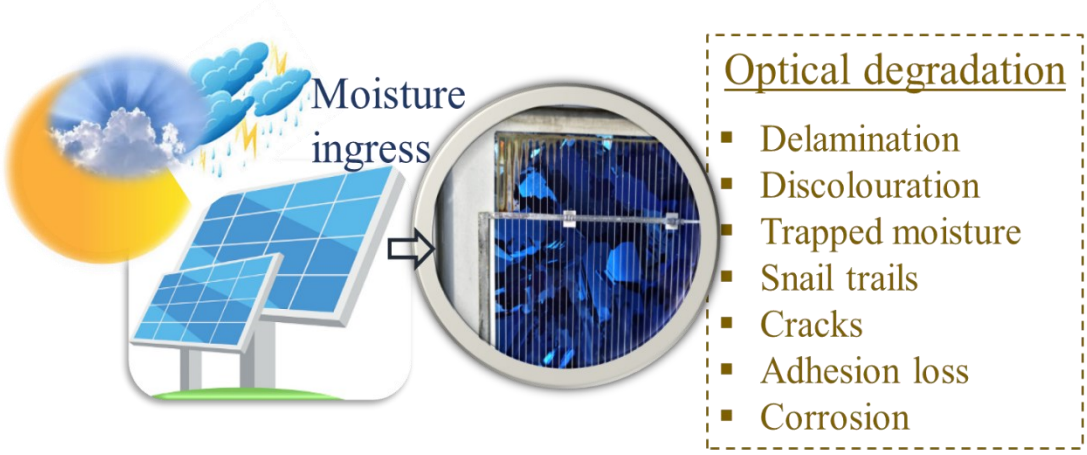

Fig. 1. PV module in the field. Under environmental stressors e.g., high humidity, temperature, and UV radiation, moisture can enter the PV module. Moisture ingress can lead to optical degradation [5].

Pern et al. [9] observed ca. 50 % reduction in the efficiency of PV modules as the encapsulant colour changed to dark brown. Rosillo and Alonso-García [11] reported up to 3 % reduction in the maximum power (P_{max}) of silicon crystalline PV modules due to high yellowness index. Dechthummarong et al. [3] investigated the relationship between encapsulant degradation and electrical insulation properties of field-aged single crystalline silicon PV modules that were deployed in Thailand. They observed that the modules with lower yellowness index possessed better electrical insulation properties. However, sometimes, the use of the "yellowness index" as

a measure of optical degradation can be misleading [12]. For instance, de Oliveira et al. [12] observed up to 0.5 %/year loss in power for ~15 years field-aged PV modules with insignificant discolouration. In addition, degradation in power due to optical degradation also depends on other attendant defects and fault mechanisms within the module [13-16]. It is therefore important to understand the characteristics of defects and fault mechanisms that lead to optical degradation of PV devices in time for the prevention of further deterioration and evolution of other failure mechanisms.

Several studies on detecting optical degradation in PV plants using visual inspection, infrared (IR) thermal imaging, electroluminescence (EL) imaging, and reflectance measurements have been carried out and documented [11, 12]. Some reports also investigated the optical integrity of the front encapsulant and glass using fourier transform attenuated total reflectance (ATR-FTIR), differential scanning calorimetry (DSC), scanning electron microscopy (SEM) and energy dispersive X-ray spectroscopy (EDS), scanning auger electron microscopy (SAM), X-ray photoelectron spectroscopy (XPS), and secondary ion mass spectroscopy (SIMS) [11, 12, 17].

Hypothetically, variations in the module temperature coefficients can be traced to optical and/or electrical degradation [18]. According to earlier reports, optical degradation affects the electrical performance characteristics: especially the short circuit current (I_{sc}) and the fill factor (FF) of the PV modules, which lead to subsequent power degradation [1, 7]. Optical degradation influences the electronic charge transport properties in the PV module bulk [19, 20]. In addition, optical degradation increases the number of UV absorption chromophoric species in the encapsulant [21, 22]. These chromophores increase the UV absorption efficiency of the encapsulant with its attendant increased module operating temperature [23]. Moreover, the chromophores can also absorb/block visible light, hence, reduce the amount of useable photons reaching the active solar cell materials [7, 24]. This leads to accumulation of current in the affected areas accompanied with high localized inhomogeneous cell temperatures known as hotspots in defective modules [13, 17]. For 'good' modules, the temperature distribution is homogeneous [13].

IR thermal imaging provides information on the temperature distribution over the PV module surface and the position of the defect or fault mode, hence, the defective cell or cells [17]. The temperature difference (ΔT) between the solar cell with the lowest temperature, T_{cL}, and the solar cell with the highest temperature, T_{cH}, can be an indicator of a specific defect or fault mechanism [13]. The nature of the hotspots depends on the characteristics of the defect and fault modes [2, 13, 17]. Also, the thermal profile of the module depends on the degree, defect density, and the areas affected by the hotspots [25]. Depending on the degree of optical degradation, the ΔT can be up to 6 °C or even higher [13]. High ΔT underpins mismatch losses [2, 17, 26]. Mismatch losses due to optical degradation can influence the overall PV module operating temperature (T_m) [2, 13, 22]. High T_m affects the PV module efficiency (η_m) and induces other degradation processes [4, 13]. The best way to understand the effect of these degradation mechanisms on performance reliability is using field-aged PV modules which are exposed to multiple environmental stressors during operation. The effect of T_m on PV module performance is illustrated in Fig. 2.

In normal operation, the module voltage reduces significantly whilst the current increases but only slightly when temperature increases [27]. This affects the fill factor and efficiency of the module.

Hence, η_m depends on T_m [18, 28, 29]. Moreover, the microscopic effect of temperature can accurately be traced to the temperature coefficients of the PV device [27, 30]. The use of temperature coefficients for PV module fault diagnostics is non-destructive, fast, reliable, cost-effective, and can be done conveniently anytime. Studies on PV module temperature coefficients are well documented [18, 27, 28, 31, 32]. Dubey et al. [31] found that there is a good agreement between the temperature coefficients of different solar panel technologies measured in the field with the values obtained in the laboratory. Dupré et al. [27] reported that the physics of the temperature coefficients of solar cells depends on the loss mechanisms. Paudyal and Imenes [18] investigated the degradation of the temperature coefficients of solar panels installed in a Nordic climate using 8-years field data and found no degradation. Segbefia et al. [28] investigated the temperature sensitivities of 20-year-old field-aged multicrystalline silicon solar panels affected by microcracks. They observed ca. 1.2%/year in the efficiency of panels due to the degradation of the temperature coefficients. A review on the dependence of solar panels' electrical performance on their temperature sensitivity is presented by Skoplaki and Palyvos [32].

The prospect of extracting the temperature coefficients from IR thermal data of PV modules is interesting, but non-existent. An additional analysis of temperature coefficients could make PV module fault diagnosis using IR thermal imaging more efficient, reliable, and cost-effective. To the best of our knowledge there is no report on characterizing PV module optical degradation using temperature coefficients profiling presently.

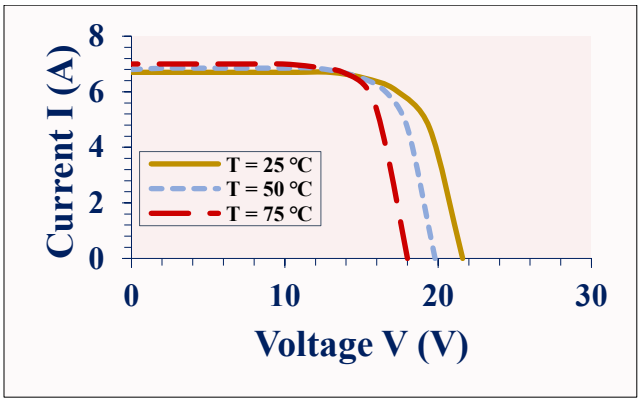

Fig. 2. Effect of temperature on electrical characteristics of a normally operating PV module.

In the present work, field-aged multicrystalline silicon (mc-Si) PV modules affected by optical degradation are investigated using temperature profiling. The selected PV modules were characterized using visual inspection, current-voltage (I-V) characteristics, temperature coefficients profiling, infrared (IR) thermal, ultraviolent fluorescence (UV-F), and electroluminescence (EL) imaging. The temperature coefficients of maximum power (P_{max}), open circuit voltage (V_{oc}), short circuit current (I_{sc}), fill factor (FF), and module efficiency (η_m) were studied. In addition, the temperature coefficients of the maximum power point voltage (V_{mpp}) and current (I_{mpp}) were also examined. In Section 2, brief background information on the field-aged multicrystalline silicon (mc-Si) PV modules and the methods used for the investigation are presented. The results and the discussion follow in Section 3. A proposed temperature dependent resistivity technique for defects and faults diagnosis in PV modules is presented in Section 4.

2 Material and methods

In Summer of the year 2000, the Renewable Energy Park located at Dømmesmoen (58.3447° N, 8.5949° E) in Norway was commissioned as a resource center for research and education in renewable energy. The Park contained 96 NESTE NP100G12 mc-Si PV panels (in a red circle), as well as amorphous silicon (a-Si) panels (extreme right and left) and thermal collectors (immediate left) as shown in Fig. 3. The mc-Si panels were rated 100 watts each [33]. However, in 2011, the park was decommissioned, and the PV panels were kept securely indoors for research purposes. At the time of decommissioning, the maximum power of the mc-Si panels had dropped to ca. 90 % [34]. In an earlier reports on the field-aged modules, about 90 % of the mc-Si panels have been affected by optical degradation [5].

Fig. 3. The Renewable Energy Park located at Dømmesmoen. The mc-Si PV modules under study are shown in a red circle.

In the present study, 3 of these field-aged PV modules (A, B, and C) which have been affected by optical degradation have been selected for investigation. The electrical characteristics of the 3 selected modules and the manufacture's data sheet values are presented in Table 1. The information on the modules and solar cells has been presented earlier [5, 35].

Table 1

Average electrical parameters of the 3 selected field-aged PV modules, normalized to STC.

PV module		P_{max} (W)	V_{oc} (V)	I_{sc} (A)	V_{mpp} (V)	I_{mpp} (A)	FF (%)	η (%)
2000 (Data sheet)		100	21.6	6.7	16.7	6.0	70	13.0
2011 (Average)		90.2	21.5	6.2	16.1	5.1	68	12.0
2021	**A**	82.2	20.9	6.0	15.6	5.3	66	10.7
	B	84.1	20.9	6.0	15.9	5.3	67	10.9
	C	82.1	20.7	5.9	15.5	5.3	67	10.7

2.1 Visual inspection

The field-aged PV modules were taken through a thorough visual inspection program in a clear sky outdoor environment. In addition, high-resolution photographs of each PV module were taken in a dark room under well-controlled light exposure. The visual inspection in the dark room reduced the undesired glare or gloss effect of the front glass. This made it possible to identify some details of the defects which are not easily seen with the traditional visual inspection technique alone. This ensures a comprehensive cataloguing of all visible defects and fault modes. The International Electrotechnical Commission: IEC 61215: 2016 standard was duly adhered to in collecting and reporting the data from the visual inspection of the PV modules.

2.2 I-V measurements

The field-aged PV modules were each taken through current-voltage (I-V) curve electrical performance measurements using a handheld I-V 500w I-V Curve Tracer, following the procedure according to IEC 60891 and the IEC 60904- 1 series. These measurements provided information on the P_{max}, V_{oc}, V_{mpp}, I_{sc}, I_{mpp}, FF, in-plane irradiance (G_I), and temperature characteristics of each module at Standard Test Conditions (STC). STC specifies cell temperature of 25 °C, an irradiance of 1000 W/m^2 and air mass 1.5 (AM1. 5) spectrum for commercial PV modules. Measurements were done under in-plane irradiance conditions (970 - 1130 W/m^2), and the I-V tracer used converted all measurements to STC automatically. This means the operating conditions were optimally resolved by the device to minimize errors in measuring and recording data. The difference in each electrical parameter, x (Δx), was computed as the difference between data sheet values and measured values in the year 2021.

2.3 Temperature coefficient profiling

To measure the temperature coefficients, the PV modules were taken out to the outdoor measuring rack one after the other from a storeroom where the modules were kept at room temperature. The PV module and the reference device were then covered with a shade (cardboard), and the measurement initiated immediately after the shade was removed. Module temperature was measured with an PT300N probe (PT1000) attached to the backside of the PV module. The

measurements on all modules were done on the same day between 12.30 and 14.30 hours on a clear sky day and at wind speed less than 2 ms^{-1}. In all cases, the PV modules were sun soaked for at least 30 minutes before the measurements were taken to allow sufficient time for the modules to reach thermal equilibrium. The IEC 60891-4 standard was followed during the investigation. However, according to this standard, the temperature range of the data values should be at least 30 °C. This seems practically challenging on the investigation site. The electrical parameters (P_{max}, V_{oc}, I_{sc}, FF, η_m, V_{mpp}, I_{mpp}) were plotted as functions of PV module's temperature (T_m) and a least-squares-fit curve through each set of data was constructed. The regression equation for such a relation can be represented as $y = mx + c$, where m and c are the slope and the intercept, respectively. The relative temperature coefficient of parameter X (β_x) in %/°C was calculated by dividing the slope (m) of parameter X by the intercept (c) of parameter X. That is, $\beta_x = m/c$. Details of this measurement procedure was reported earlier [26, 35].

2.4 Ultraviolet fluorescence (UV-F) imaging

In the detection of defects and fault modes, including cracks and optical degradation, the UV-F imaging is one of the most suitable tools [36, 37]. PV components, especially polymeric materials degrade into fluorescent species when exposed to environmental stressors and chemical species. In the presence of ingressed moisture or other gaseous species such as oxygen, the fluorescent degraded species undergo metamorphoses to nonfluorescent species via photobleaching or photoquenching [36]. These nonfluorescent species form photobleaching marks around and within the defective areas in the module and show darker traces when exposed to UV-F [37]. UV-F images of the field-aged PV modules were taken in a dark room using a TROTEC® LED UV TorchLight 15F ($\lambda \approx 360$ nm) together with a Wolf eyes FD45 spectrum filter. The IEA prescribed procedure was followed in the investigation [15, 38].

2.5 Electroluminescence (EL) imaging

EL imaging works on the principle that when a PV module is forward biased, the solar cells glow in the near-infrared (NIR) region; peaking around 1150 nm for silicon cells [25]. This signal could be captured with an infrared camera, and the degradation state of the cells and the balance of system (BoS) materials could be extracted from the EL images. EL imaging is interesting especially for quantifying resistive losses in old PV modules affected by cracks and severed metal grids. Moreover, the technique could also be very useful in detecting encapsulant degradation [39]. Degraded encapsulant reduces the luminescence signal that gets through to the detection camera. The PV modules were taken through the EL characterization in a dark room using the BrightSpot EL Test Kit. The kit comprises a 24 megapixels modified DSLR (digital single-lens reflex) Nikon D5600 camera, power supply set, and computer with data acquisition and post processing software. The image acquisition and processing were done according to the IEA procedure [15, 25] and the IEC TS 60904-13 standard. The EL characterization of the sampled PV modules was done indoors using 10 % and 100 % of the I_{sc} 5 minutes after the current was initiated.

2.6 Infrared (IR) thermal imaging

When a PV module is forward biased, current accumulates on cell areas affected by defects and fault modes. This leads to localized hotspots or joule heating which raises the PV module's

temperature and increases the intensity of the emitted IR radiation. This signal could be captured with an infrared thermal camera, and the thermal state of the cells could be extracted from the IR thermal images. The PV modules were taken through infrared measurements using the Fluke Ti400 Infrared Camera (measuring in the long-wave IR band: 650 - 1400 nm) by following the IEA prescribed procedure [25] and IEC TS 62446-3 standard. Measurements were done under clear sky outdoor conditions. The experimental set up for the IR thermal imaging is illustrated in Fig. 4. IR thermal images were acquired after soaking the PV modules in the sun for at least 15 minutes.

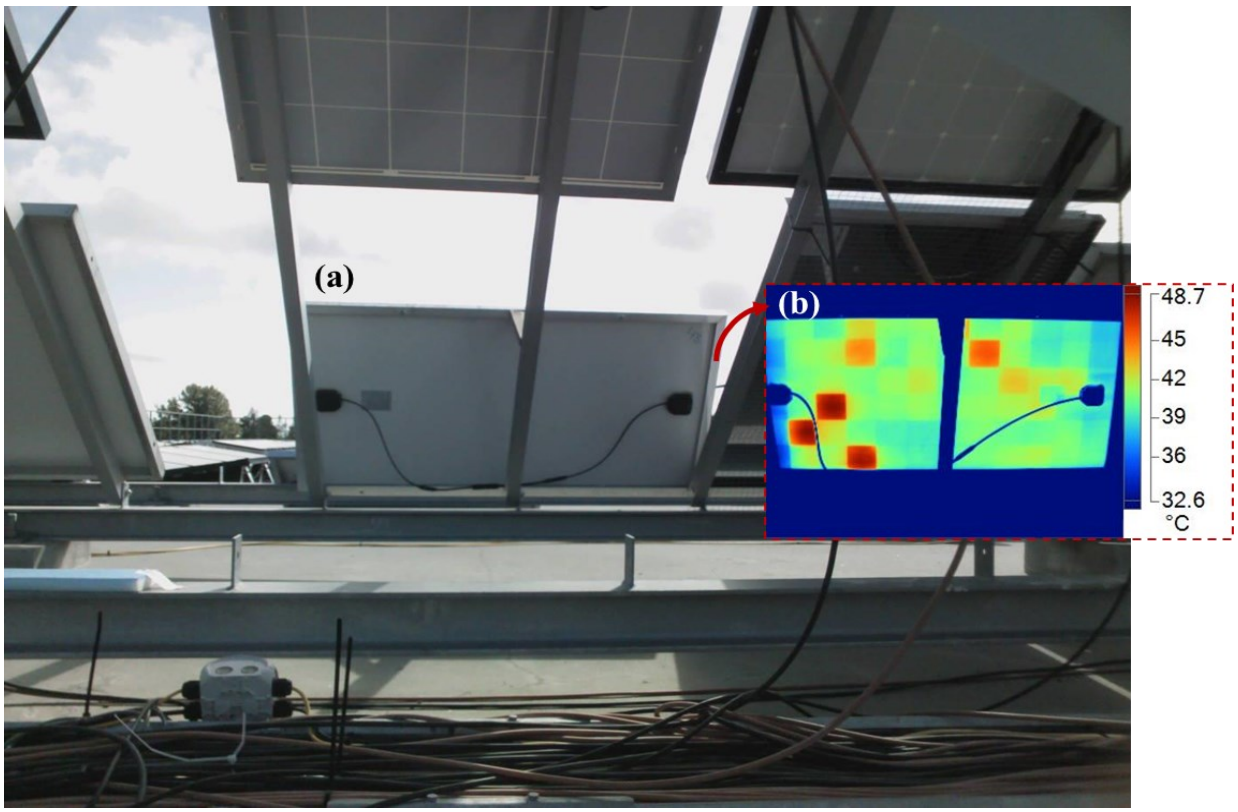

Fig. 4. (a) Visual image and (b) IR thermal image (insert) of a PV module from the backside during IR thermal imaging. The metal support (behind the PV module) and the cables show corresponding blue traces in the IR thermal image.

3 Results and Discussion

3.1 Visual inspection

A change in the colour of encapsulant towards yellow and dark brown indicates optical degradation [1, 7, 11]. However, the effect of optical degradation could precede the change in the colour of the encapsulant [12]. Yet, the most established technique for detecting optical degradation is the visual inspection [1, 15]. Fig. 5 shows some of the results from the visual inspection. Fig. 5a is a photographic image of one of the field aged PV acquired under clear sky conditions. The field-aged PV modules show cells with delamination at the cell edges (Fig. 5b), discolouration of the EVA encapsulant (Fig. 5c), front glass degradation (Fig. 5d), oxidation of metal grids at the solder

joints (Fig. 5e), and trapped moisture induced degradation (MID) species around the solar cell edges (Fig. 5f), as reported earlier [6]. Also, some of the modules have loose aluminium (Al) frames and microcracks which served as a conduit for moisture ingress, as reported earlier [5]. These defect and fault mechanisms are the underlying factor for the degradation mechanisms observed in the field-aged PV modules, as reported in other studies [4, 8].

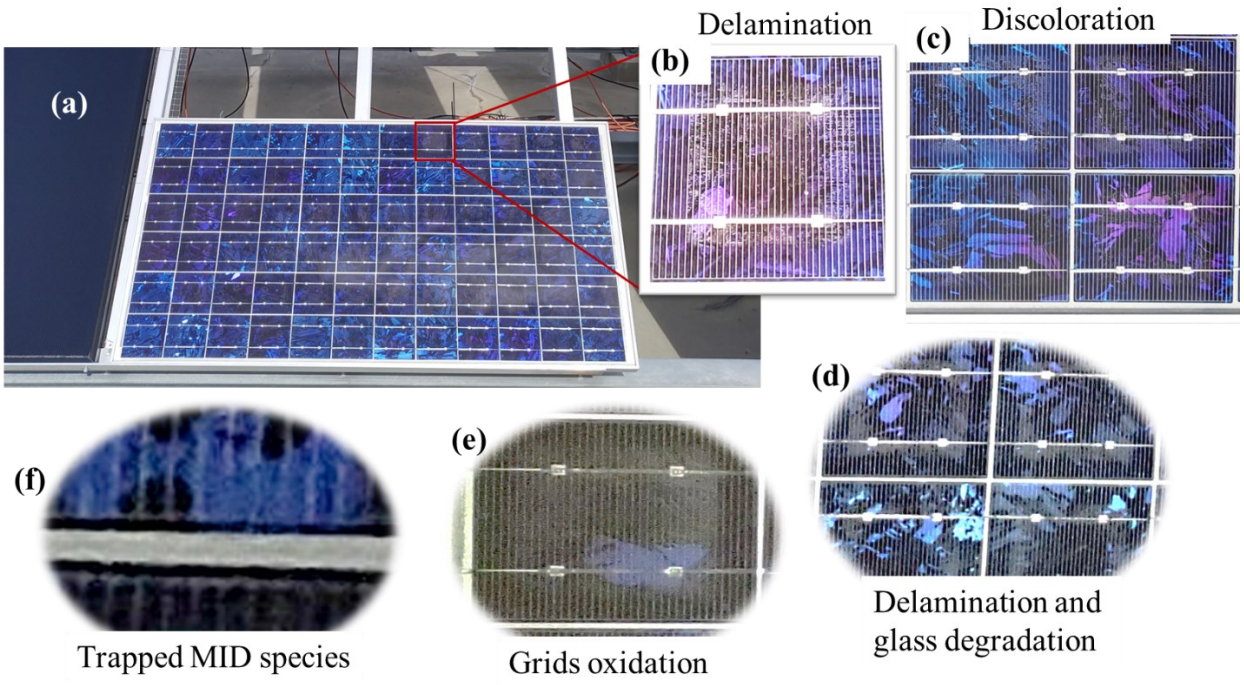

Fig. 5. Defects and fault modes of the field-aged PV modules affected by optical degradation. Photographic images showing (a) one of the PV modules, (b) a solar cell affected by delamination around the solar cell edges, (c) discolouration of the front encapsulant, (d) delamination around the solar cell edges and front glass degradation, (e) metal grids oxidation at the solder joints, (f) trapped moisture induced degradation (MID) species around the solar cell edges.

According to Tsanakas et al. [13] optical degradation includes encapsulant discolouration, delamination, glass breakage, and trapped moisture or bubbles. However, in this work, none of the field-aged PV modules under investigation have visible broken glass. The denominator for the observed optical degradation is moisture ingress considering the climatic conditions of the installation site [4, 5, 16].

3.2 Ultraviolet fluorescence (UV-F) characteristics

Fig. 6 shows UV-F images of the two classes of the PV modules investigated as per their fluorescence intensity. Based on the fluorescence signal intensity from the front encapsulation of the field-aged PV modules, the PV modules were classified into 2 classes, as reported earlier by the same authors [5]. For this purpose, the focus is on the response of the front encapsulant to UV-F light in order to determine which modules have been affected by optical degradation and which are not. Hence, we ignore other defects (e.g., cracks) that appear in the UV-F images of the PV

modules. Class I modules (Fig. 6a) show very weak fluorescence intensity, and their surfaces appear uniformly darker. Class II modules (Fig. 6b) show relatively strong fluorescence intensity and appear brighter under the UV light. Class I PV modules constitute more than 90 % of the field-aged PV modules. This indicates that the front encapsulation of the class of PV modules in Fig. 6b are in relatively better condition. It is noteworthy that both classes of PV modules do not differ significantly in terms of physical appearance and power output [5]. This suggests that the power degradation in the PV modules is not due to optical degradation alone.

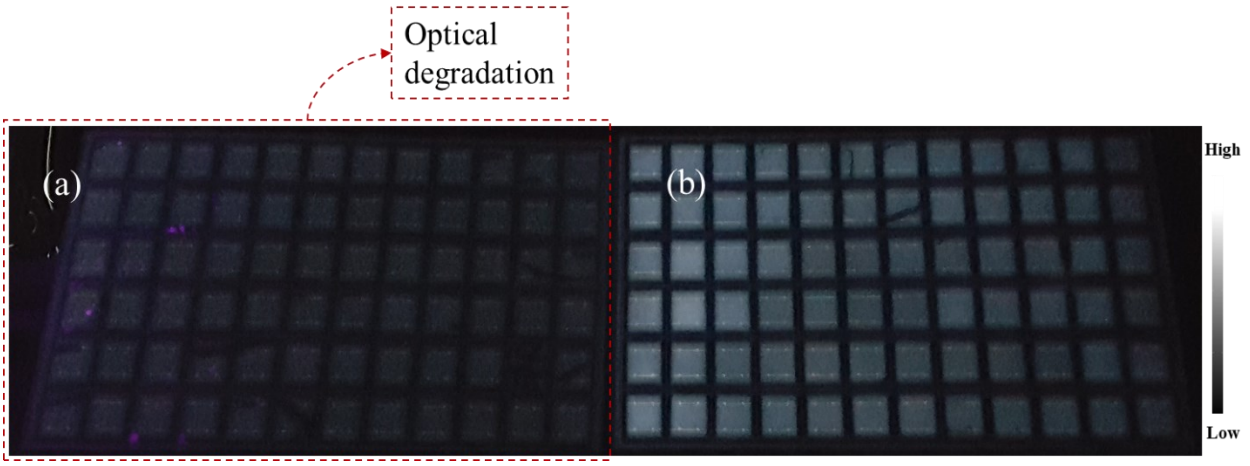

Fig. 6. Ultraviolet fluorescence (UV-F) images of two field-aged PV modules showing the two classes of modules: (a) optical degradation (Class I) and (b) 'good' front encapsulant (Class II). The 3 field-aged PV modules under this study belong to Class I.

3.3 Electroluminescence images

In a PV module with 'good' encapsulation, a strong luminescence signal intensity is recorded by the near IR (NIR) camera. That is, EL intensity can be an indicator of PV module degradation. Fig. 7 shows a 'good' PV module imaged under 100 % of I_{sc} and 10 % of I_{sc} forward bias conditions, respectively. A close inspection of both images shows that the front encapsulant of this PV module is in good condition, even though the luminescence signal intensity in Fig. 7b is weaker. The strong luminescence signal intensity for good encapsulant in Fig. 7 is due to the fact that good encapsulants have high optical transparency, hence, majority of the luminescence signal passed through the encapsulant and were detected by the NIR camera. The relatively weak luminescence signal recorded in Fig. 7b is due to reduced forward bias current: 10 % of I_{sc} with high voltage [13]. The defects that are highlighted in Fig. 7a; the EL image acquired under I_{sc} forward bias conditions are also highlighted in Fig. 7b; the EL image acquired under 10 % I_{sc} forward bias conditions. These defects (marked in red) are related to cell degradation during production, transportation, and handling since this module is yet to be installed outdoors. In addition, under 10 % I_{sc}, more material (cell) degradation issues are highlighted, as observed elsewhere [25, 40]. On the other hand, in PV modules affected by encapsulant degradation, the intensity and profiles of the luminescence signal could be different [40]. This is true for field-aged PV modules which have undergone significant degradation due to exposure to several environmental stressors.

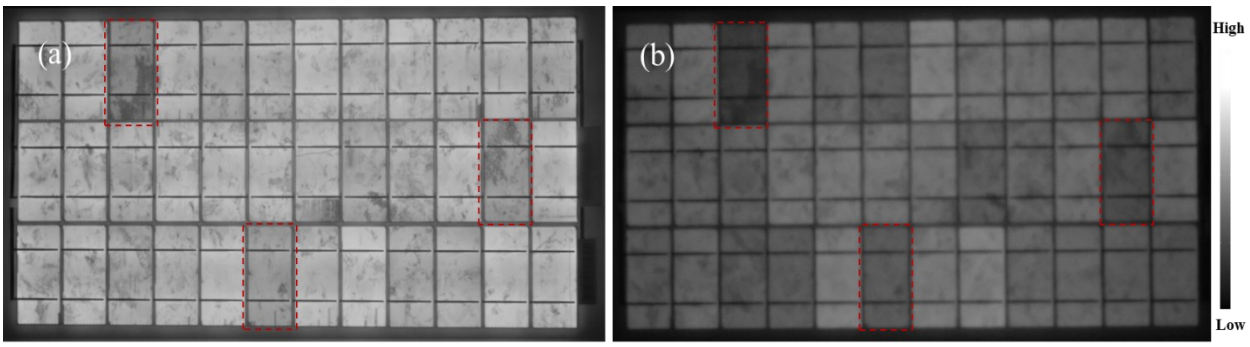

Fig. 7. EL images of a new silicon mini-PV module under (a) 100 % of I_{sc} and (b) 10 % of I_{sc} conditions. Corresponding cell degradation areas are marked in red.

The EL images of the 3 field-aged PV modules acquired under 100 % I_{sc} (Figs. 8a-c) and 10 % I_{sc} (Figs. 8d-f) are shown in Fig. 8. PV modules affected by optical degradation show randomly distributed small darker spots all over the PV modules in the EL images acquired under 100 % I_{sc}. In addition, localized hotspots along the busbars are also distributed randomly over the PV modules. Except for the cells affected by cracks (Figs. 8a-c), the darker cells in the EL images acquired under 100 % I_{sc} do not clearly correspond with the darker cells in the EL images acquired under 10 % of I_{sc} conditions.

According to Sinha et al. [17], the observed darker cells in EL images is due to resistance losses emanating from optical degradation and electrical mismatch. The extra darker cells observed in the EL images acquired under 10 % I_{sc} indicate cell degradation [25]. The dark spots indicate areas of cell cracks, corrosion, delamination, and discolouration of encapsulants and other material degradation e.g., solder bond degradation [41]. Accumulation of current at the shunts of defect areas gives rise to the darker spots [40]. The weaker luminescence signal intensity recorded in Fig. 8 for the field-aged PV modules is due to the fact that the encapsulants of these modules have undergone optical degradation, hence, blocking the greater portion of the luminescence signal from the cells.

The degradation of the solar cells could also be the reason for the observed weaker EL intensity in Fig. 8. However, defective cells e.g., cells affected by cracks show characteristic darker patterns, refer to Figs. 8d-f and Fig. 7. Moreover, Figs. 7 and 8 were acquired under the same forward bias I_{sc} conditions. However, the quality of the EL images in Figs. 7 and 8 are totally different. This is as a result of the degradation states of the field-aged PV modules, see Fig. 8. The quality of the EL images in Fig. 8 is affected by the optical characteristics of the front encapsulation material and the solar cells due to degradation.

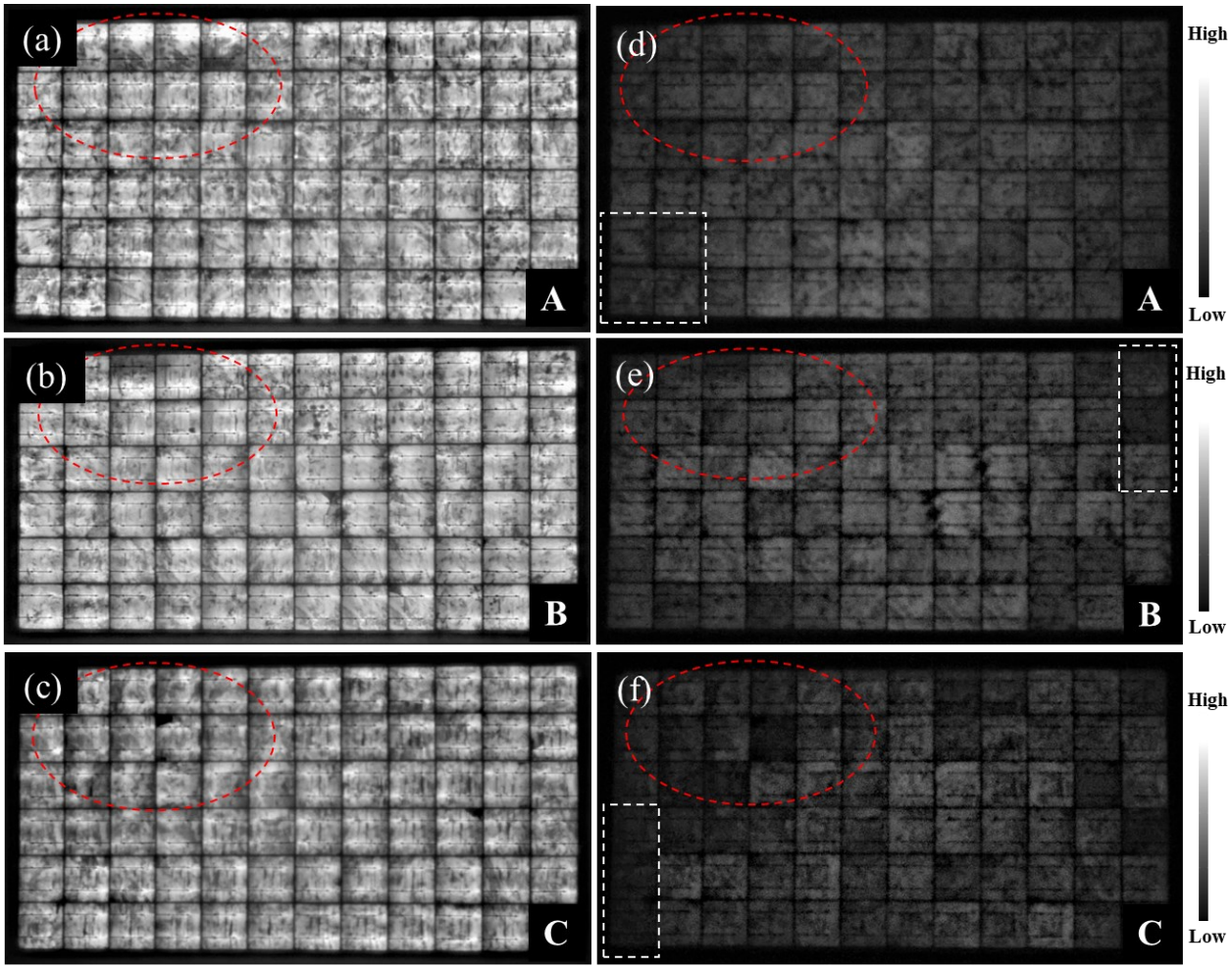

Fig. 8. EL images of the 3 field-aged PV modules under (a) - (c) 100 % of I_{sc} and (d) - (f) 10 % of I_{sc} forward bias conditions. Corresponding defect areas in both EL images are circled in red. Areas marked in white are the corresponding areas marked in the IR thermal images in Fig. 9.

3.4 IR thermal images

The infrared thermal images of the 3 field-aged PV modules are shown in Fig. 9. The solar cells with the highest temperature (T_{cH}), which correspond to hotspots, spread randomly over the PV modules. A close comparison of the IR thermal images (Fig. 9) to the EL images (Fig. 8) suggests that the hotter cells correlate to the areas where the darker spots were observed in the EL images. The observed hotspot cells in the IR thermal images underline the observation of cell degradation as confirmed in the EL images [2, 25]. Also, due to the uniform optical degradation of the modules, the observed randomly distributed hotspots are possible since optical degradation also leads to other degradation modes e.g., moisture ingress, PID, corrosion, solder bond degradation, etc. The bypass diodes of these modules were found to be in good condition [26]. An interesting observation is that some of the darker cells located at the edges of the PV modules in the EL images (Fig. 8) show lower cell temperatures in the IR thermal images (Fig. 9). A possible explanation for this observation is that these defect cells might be short circuited to the aluminium frames due to

degradation mechanisms such as corrosion [25]. In an earlier microstructural investigation on these PV modules, the presence of MID species was observed, especially on the perimeter cells which show similar characteristics. These MID species lead to corrosion, optical degradation, PID, etc., and hence, shunting and other parasitic resistance loss mechanisms [6]. Changes in the T_m due to optical degradation leads to reduced bulk resistivity, hence, PID [15, 42]. Moreover, optical degradation predisposes the module to moisture ingress which can lead to PID [5].

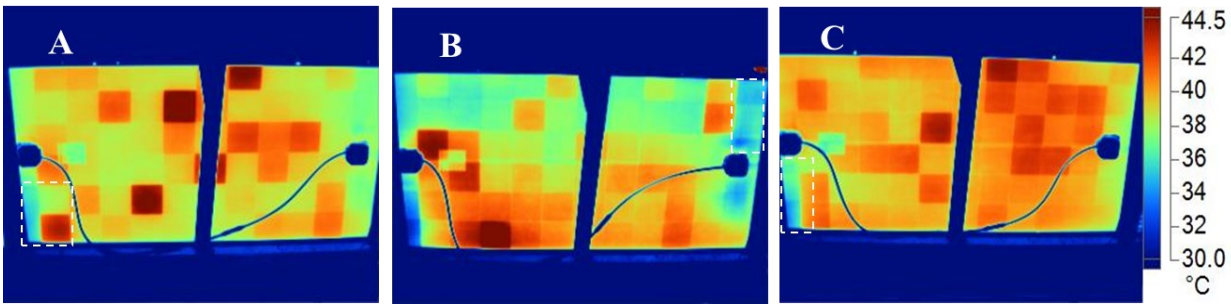

Fig. 9. IR thermal images of the 3 field-aged PV modules under clear sky outdoor conditions. Corresponding defect areas in Fig. 8 are marked out in white.

The shunts (due to optical degradation) created by the short circuits create alternative path for current [42]. That is, PV modules with optically degraded encapsulation can also serve as conduits for current leakages [43]. The marked defect cells in Fig. 9 might be reverse biased to the bypass diodes and therefore may possibly be operating under reverse bias conditions. Also, electrically isolated cells can show lower cell temperature (T_c) since current cannot get to these areas easily [25]. Degradation of these cells into inactive areas around the perimeter of the PV modules might be due to moisture induced degradation of these cells. Around the perimeter of the PV modules, moisture ingress is likely, and can cause further degradation of the cells and its components [8]. In these situations, the defect cells may not show hotspots [25, 37, 38]. To further explore the relationship between optical degradation and PV module temperature sensitivity, data on the solar cells with the highest temperature (T_{cH}) and lowest temperature (T_{cL}) for each PV module over time was extracted and the difference in cells' temperature (ΔT) was computed. That is,

$$\Delta T = T_{cH} - T_{cL} \quad (1)$$

Table 2 shows the average values of T_{cH}, T_{cL}, and ΔT for the 3 field-aged PV modules. The average ΔT due to optical degradation was found to be ~10 ± 2 ℃.

Taking an error margin of ±2 ℃ into account, the observed ΔT values for the 3 field-aged PV modules agree with reported ΔT values that underlines optical degradation. In literature, ΔT due to optical degradation was found to be ca. ~6.0 ± 2 ℃ or higher, based on the degree of the optical degradation and/or the presence of other defect/fault modes [2, 13]. Optical degradation induces other failure mechanisms [4, 17]. The presence of other defects in these PV modules (mainly due to moisture ingress) was reported by Segbefia et al. [5], [6]. This observation was also reported elsewhere [17]. The location of majority of the darker cells in the EL images (Fig. 8) and warmer cells in the IR thermal images (Fig. 9) along the edges of the PV modules suggests that the presence

of PID in these PV modules is likely [14, 15, 38]. According to Segbefia and Sætre [35], some of these modules have been affected by PID as well.

Table 2

Difference in temperature (ΔT) of the solar cells with the highest temperature (T_{cH}) and lowest temperature (T_{cL}) for each field-aged PV module. Measurements were made under clear sky outdoor conditions.

PV module	Temperature (°C)		ΔT (°C)
	T_{cH}	T_{cL}	
A	47.7	36.2	11.5
B	52.3	41.7	10.6
C	44.2	33.7	10.5

3.5 I-V characteristics

Optical degradation influences photon absorption efficiency and current flow in the PV module bulk, especially in the areas affected by the optical defect. This constitutes current mismatch, which can cause local hotspots over the PV module [13]. High T_m affects V_{oc} and hence, fill factor (FF) and P_{max} [29]. The field-aged PV modules show a drop in the P_{max} due to decrease in optical efficiency. The efficiency of all the 3 modules decreased from 13 % to less than 11 %, refer to Table 1. This translates into a degradation rate of 0.8 % per year in the module efficiency. Fig. 10 shows the I-V characteristics of the 3 PV modules at two different T_m, normalized to STC.

All the 3 field-aged PV modules show similar electrical characteristics. Strikingly, the drop in the I_{sc} remains fairly constant under both T_m conditions. On the other hand, the V_{oc} decreases substantially when T_m increases. Yet, at ca. 25 °C, the drop in V_{oc} appears fairly minimal. This suggests that the underlying cause for the drop in V_{oc} at ca. 40 °C is higher T_m. The increase in I_{sc} when T_m increases is almost insignificant for the 3 modules, especially for PV Module B. This supports the earlier observation per the visual inspection that PV module B appears to be the most affected by optical degradation. Loss of optical transparency means that reduced amount of light gets to the solar cells during field operation. This usually manifests itself in reduced I_{sc} even when in-plane irradiance and T_m increases (see Module B in Fig. 10). There is an insignificant improvement in the I_{sc} even when T_m increases from 25.4 °C to 40 °C. In addition, optical degradation enhances the absorption and retention efficiency of UV light in the PV modules [23]. This leads to higher T_m and hence, a drop in P_{max} due to module hotspots [21]. Also, optical degradation induces other defects and fault modes which influence charge carrier absorption, generation, mobility, and recombination in the PV module bulk. These mechanisms influence T_m and hence, a drop in V_{oc} [27].

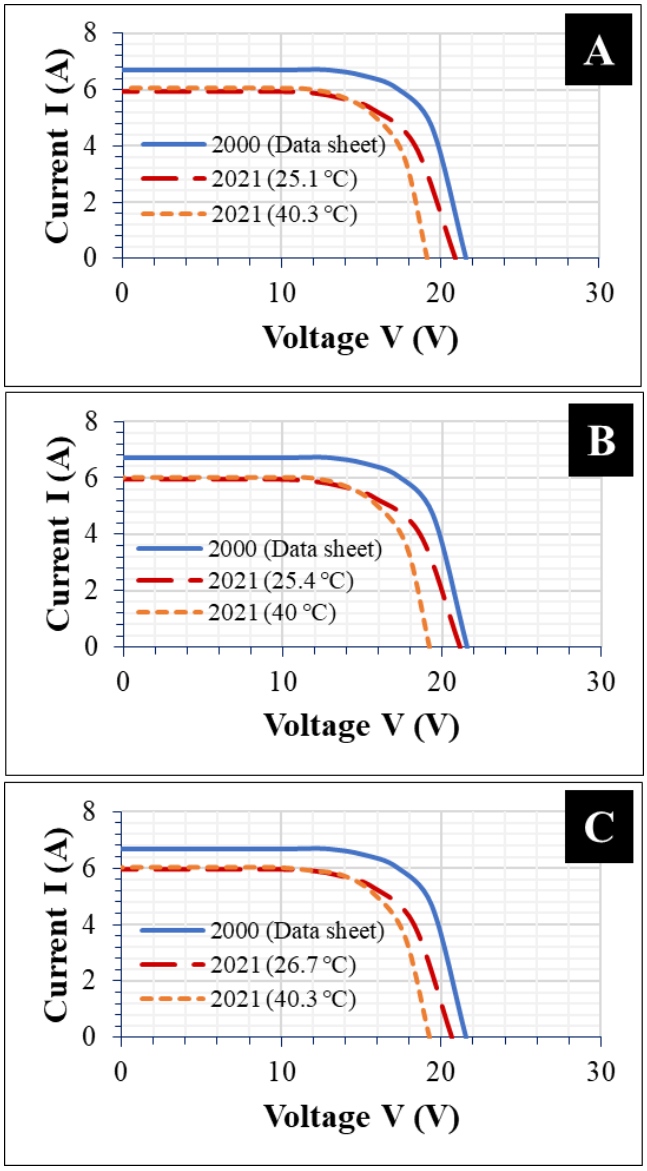

409

410 **Fig. 10**. I-V profiles of the 3 field-aged PV modules. Permanent degradation in I_{sc} even when T_m
411 increases indicate optical degradation.

412 **3.6 Temperature sensitivity**

413 Figs. 11a-c illustrate the evolution of the electrical parameters and Figs. 11d-f show the
414 corresponding temperature coefficients of the 3 field-aged PV modules using Box and Whisker
415 plots. PV Module A appears to be the most degraded among the 3 field-aged PV modules, possibly
416 due to other co-defects [5, 28]. The variation in the electrical parameters, especially in the V_{oc}, FF,
417 and V_{mpp}, is the highest, see Fig. 11a.

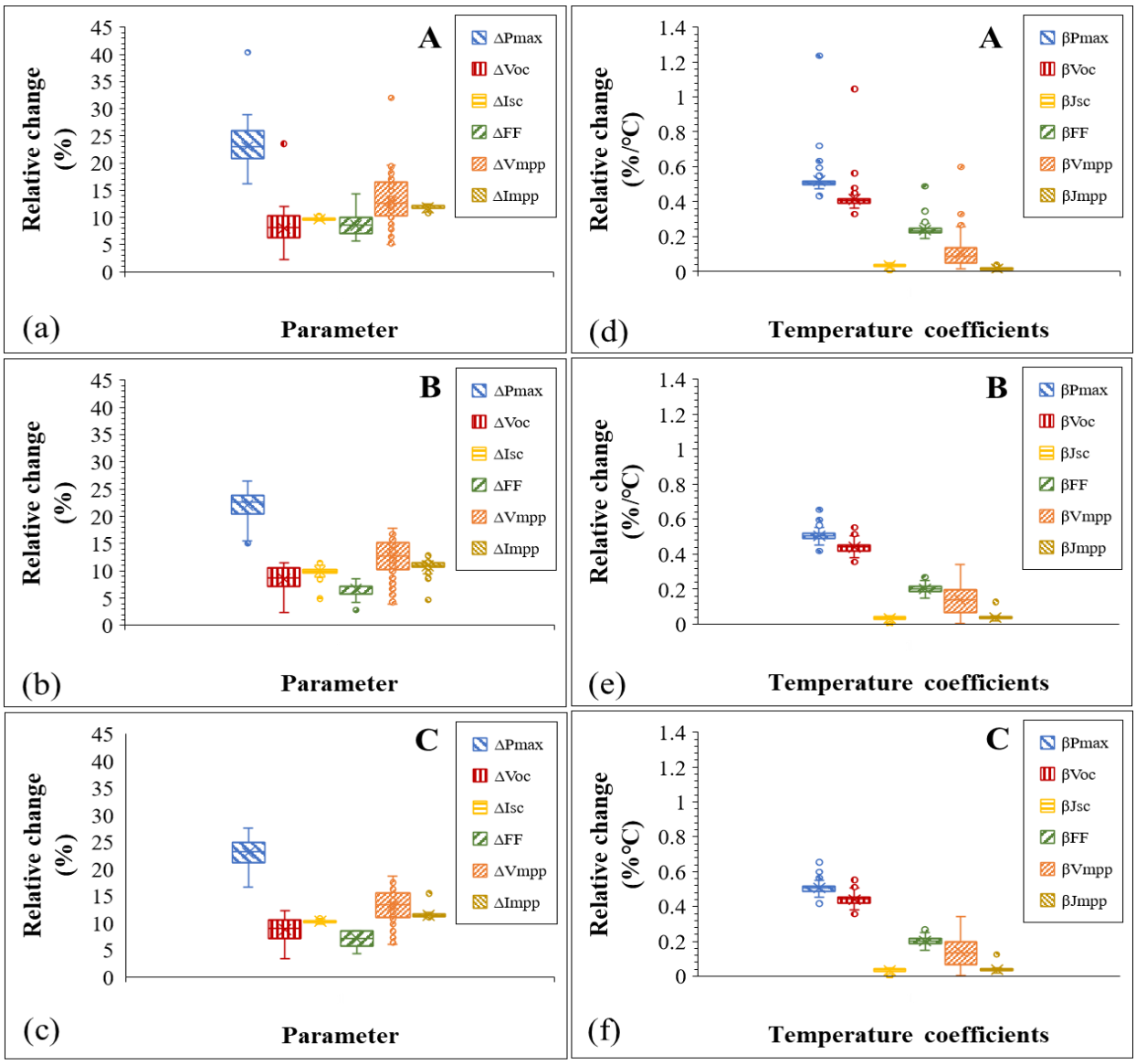

Fig. 11. Evolution of electrical characteristics (a) - (c) and temperature coefficients (d) - (f) of the 3 field-aged PV modules, normalized to STC. The ends of the boxes are the lower and upper quartiles (interquartile range), the internal lines and *x*-marks indicate the median and mean, respectively.

A close inspection of the electrical parameters shows that the relative change in P_{max} (ΔP_{max}) depends more on the relative change in V_{oc} (ΔV_{oc}) and V_{mpp} (ΔV_{mpp}). On average, the relative percent change in P_{max}, V_{oc}, and V_{mpp} for the 3 modules are >22 %, >8 %, and >12 %, respectively. The relative change in the fill factor (ΔFF) was also observed to be high, however. The higher ΔFF is due to carrier generation-recombination induced resistance losses and its variation with T_m [27]. A closer look at the evolution of the temperature coefficients of the modules (Figs. 11d-f) corresponds with the relative changes observed in the electrical parameters of the modules (Figs. 11a-c). That is, the relative change in the temperature coefficient of P_{max} (β_{Pmax}) depends more on the relative changes in the temperature coefficients of V_{oc} (β_{Voc}) and V_{mpp} (β_{Vmpp}). However, the

temperature coefficients predict the effects on P_{max} better. That is, the profile of β_{Pmax} matches that of β_{Voc} and β_{Vmpp} far better than the degree to which ΔP_{max} matches ΔV_{oc} and ΔV_{mpp}.

The relative changes in the temperature coefficients of I_{sc} (β_{Jsc}) and I_{mpp} (β_{Jmpp}) are far lower. However, the relative effect of β_{Jsc} and β_{Jmpp} is expected to be significant. The average β_{Pmax}, β_{Voc}, and β_{Vmpp} were >0.5 %/°C, >0.4 %/°C, and >0.1 %/°C, respectively. On average, the relative change in the temperature coefficients of *FF* (β_{FF}) for the 3 optically degraded PV modules, except Module A, is ca. 0.2 %/°C. The variation in β_{Pmax} and β_{Voc} appear to be closely identical for all the 3 PV modules. In PV modules affected by PID, the β_{Pmax} was found to be closely identical to both β_{Voc} and β_{FF}. However, for the modules affected by PID, the variation in β_{FF} was observed to be greater than 0.3 %/°C [35]. To understand the degree of correlation of these electrical parameters to P_{max}, regression plots of the temperature coefficients were carried out. The results from the regression plots of PV module C are shown in Fig. 12.

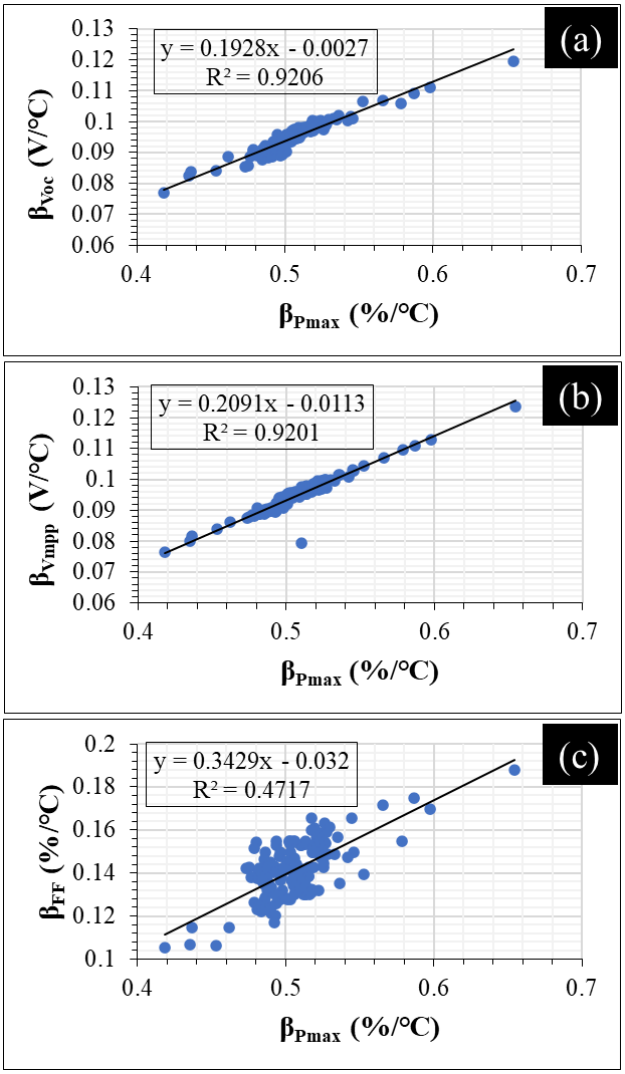

Fig. 12. Dependence of β_{Pmax} on (a) β_{Voc}, (b) β_{Vmpp}, and (c) β_{FF}. Strong correlation of β_{Voc} and β_{Vmpp} to β_{Pmax} (i.e., high $R^2 > 0.9$) value. Weak correlation of β_{Jsc}, β_{Jmpp} and β_{FF} to β_{Pmax} (i.e., low $R^2 < 0.5$) value.

Fig. 12 suggests that even though β_{FF} appears to influence ΔP_{max}, the degree of correlation is weak with $R^2 < 0.5$. The R^2 for both β_{Jsc} and β_{Jmpp} is even lower. However, β_{Voc} and β_{Vmpp} show a strong correlation to ΔP_{max} with $R^2 > 0.9$ for both. These trends in the temperature sensitivity support the observed V_{oc} drop in the I-V characteristics for the optically degraded field-aged PV modules, see Fig. 10. This suggests that optical degradation in PV modules could be monitored more precisely using PV module's β_{Voc} and β_{Vmpp}. However, the effect of β_{Voc} and β_{Vmpp} on β_{Pmax} also depends on other co-defects [26, 35]. The regression plots of PV module efficiency (η_m) versus T_m for the optically degraded PV modules are shown in Fig. 13.

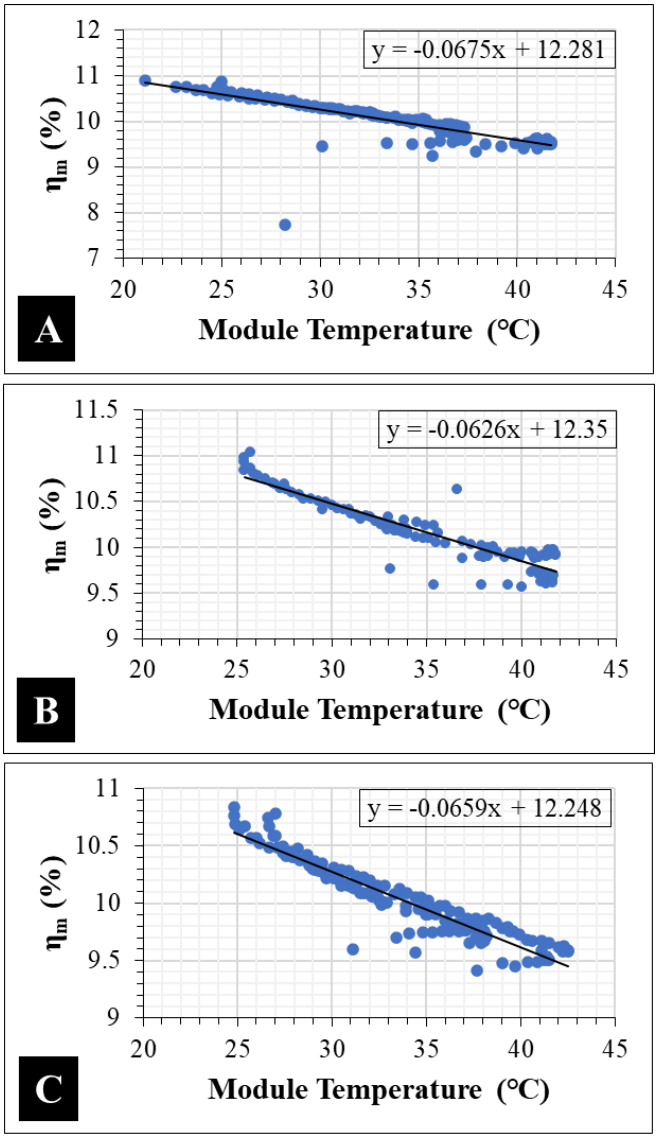

Fig. 13. Temperature coefficient of efficiency, $\beta_{\eta m}$ of the 3 field-aged PV modules

In literature, the temperature coefficient of efficiency for mc-Si PV modules is 0.4 %/°C [27, 30-32]. By extrapolation, Fig. 13 suggests that the PV module efficiency (η_m) for each optical degraded module at 0 °C is ca. 12 %. The average temperature coefficients of the 3 optically degraded PV modules are recorded in Table 3. Our values for β_{Voc}, β_{Jsc}, and β_{Vmpp} agree with the

values reported by King et al. [30]. In Table 3, unlike all the other parameters, the difference in the β_{Jmpp} values appears to be large for the 3 PV modules. The difference in the β_{Jmpp} is due to the degree of optical degradation in each of the PV modules. That is PV Module B (worst optically degraded module) show the highest β_{Jmpp} of 0.07 %/°C. Probably, the most striking is the negative β_{Jmpp} for PV Module C.

Table 3

Average temperature coefficients of the 3 field-aged PV modules. These values are in good agreement with earlier reports [30, 31].

PV module	Temperature coefficient (%/°C)					
	β_{Voc}	β_{Jsc}	β_{FF}	$\beta_{\eta m}$	β_{Vmpp}	β_{Jmpp}
A	-0.4	0.04	-0.2	-0.5	-0.6	0.03
B	-0.4	0.06	-0.2	-0.5	-0.6	0.07
C	-0.4	0.04	-0.2	-0.5	-0.5	-0.01

Fig. 14a is an EL image of PV Module C with its corresponding zoomed in image of the marked area in Fig. 14b. Fig. 14c is an UV-F image of the corresponding area in Fig. 14b. The figure highlights other defects in addition to optical degradation. Figs. 14a-c show microcracks and broken or severed metal grids. Fig. 14d is a visual image taken in a dark room and Fig. 14e is a visual image acquired under a clear sky outdoor environment. In both visual images, it appears that there is a sign of trapped MID species in the areas affected by cracks (as shown in Fig. 14b). However, Fig. 14d revealed more details than Fig. 14e. These defect mechanisms can influence the behaviour of current transport in the module. From the experiments, we observed that the negative β_{Jmpp} by Module C is due to reverse bias current from a critical hotspot(s) which turns the bypass diode into a heat sink. In other words, PV Module C appears to have a defective busbar due to the presence of other defects e.g., cracks, see Fig. 14. Cracks are conduit for moisture ingress, hence, can accelerate optical degradation [4, 14, 15]. In addition, moisture ingress can also cause PID [14, 15, 38]. PV modules affected by PID were found to show characteristic negative β_{Jmpp} [35]. It was observed in Sections 3.3 and 3.4 that PV Module C was affected by PID. PID leads to large leakage currents [25].

So, during operation, current accumulates and forms hotspots along the defective busbar. As the T_m of the PV module increases, the ΔT of the module also increases, and the bypass diode on the string is activated which reverse bias the cells on the defective busbar. So, as the T_m continues to increase, the current from the cells on the defective busbars is dissipated via joule heating, according to the relation:

$$P = I^2R = I^2 \frac{\rho_D \cdot l_D}{A_D} \tag{2}$$

$$\rho_D = R \cdot \frac{A_D}{l_D} \tag{3}$$

Where P is the power dissipated into heat due to defect, I is the current flowing through the cell, R and ρ are the resistance and resistivity in the defective cell, respectively across defect length (l_D) and defect area (A_D). Assuming that each defect contributes to increased resistivity in ohm-meter (Ωm), the resistivity (ρ_D) due to defects and fault modes depends on the defect type, defect concentration, and resistance of the solar cell or module materials. Hence, the T_m due to dissipated energy at defective areas in the PV module depends on these factors. In defective cell or module, R increases significantly, and hence, the power dissipation into heat increases linearly. Therefore, ρ_D can be represented as a ratio of the electric field (E_D) to the current density (J_D) due to defects.

$$\rho_D = \frac{E_D}{J_D} \tag{4}$$

Whenever T_m increases, β_{Jmpp} decreases and hence, P_{max} also decreases [26, 30]. A negative β_{Jmpp} was also observed by King et al. [30].

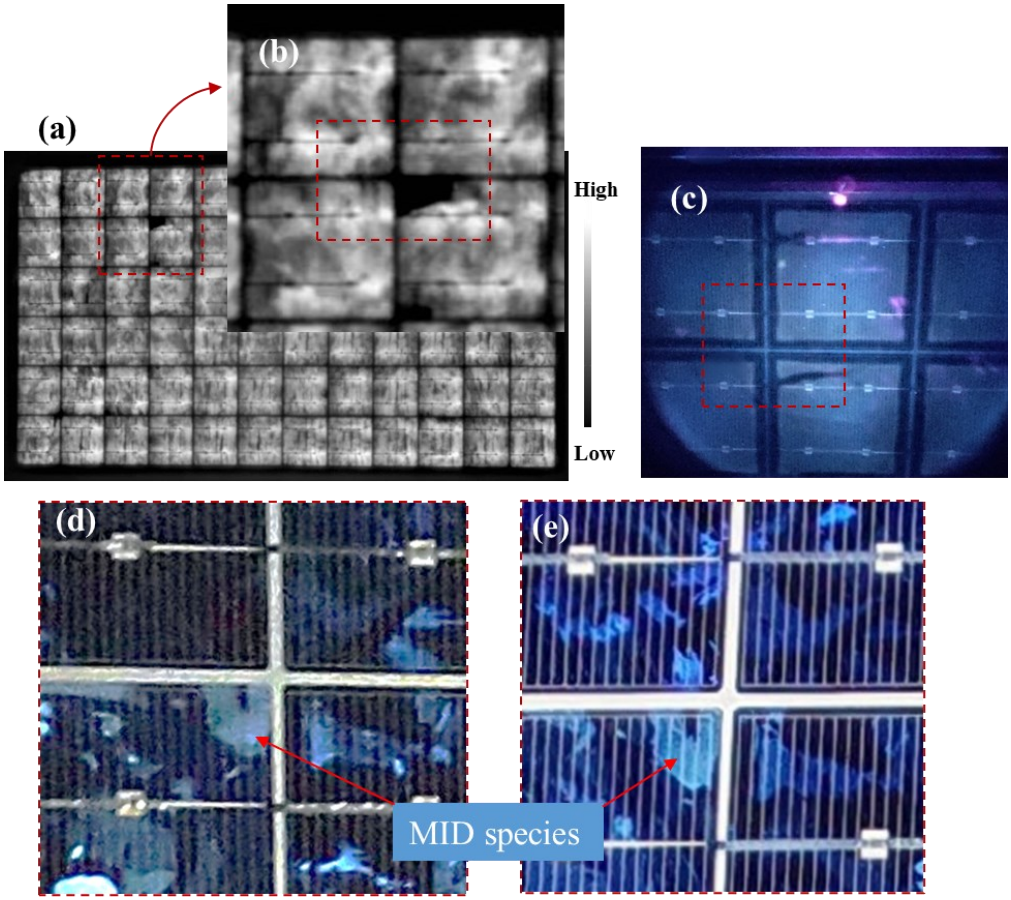

Fig. 14. (a) EL image of PV Module C, with a corresponding (b) zoomed-in area and (c) UV-F image showing cracks (marked in red). Visual image in a (d) dark room and (e) clear sky outdoor environment showing the areas marked red in (b) and (c). These images revealed that this module is affected by other defects. Cracks can accelerate optical degradation.

4 Temperature-current dependent resistivity profiling

The resistivity (ρ) of a material determines how easily electricity can flow through it. In the case of PV modules, the solar cells are made of semiconducting materials with specific resistivity values [44]. When a hotspot occurs in a PV module, the ρ can increase. The increase in ρ of the solar cells due to hotspots causes a local increase in the R of the PV module. This increased R can lead to an imbalance in current flow across the module. That is, the hotspot cells may experience a decrease in current flow (due to higher ρ), while the cells around them experience an increase in current flow (due to lower ρ). This is because during operation, the voltage across the module remains constant, but the ρ in the hotspot region increases. To further explore the correlation among defect mechanisms, current flow, and T_m, we explored the relationship between cell temperature (T_c) and ΔT obtained from IR thermal images as defined by Eq. (1). This is done to understand temperature dependent resistivity in the field-aged PV modules. To this end, several IR thermal images were taken for each PV module, the T_{cH} and T_{cL} values were extracted and the ΔT values for each module was computed.

Fig. 15 shows the regression plot of T_c versus ΔT for PV Module A. The correlation of the cell with the highest T_c (T_{cH}) and the cell with the lowest T_c (T_{cL}) to ΔT is shown. The correlation for T_{cH} is significantly higher ($R^2 > 0.8$). This suggests that the model predicts more accurately using the T_c of defect areas i.e., hotspot areas. By extrapolation, Fig. 15 suggests that, when $\Delta T = 0$, then the T_c for both T_{cH} and T_{cL} is equal. That is, when $\Delta T = 0$, then the T_c for all the PV cells in the module is equal, hence, $T_c = T_m$ (assuming all transient mechanisms are negligible). For 'good' PV modules, ΔT is negligible and can be assumed as $\Delta T \approx 0$. As a function of efficiency, T_m depends largely on in-plane irradiance.

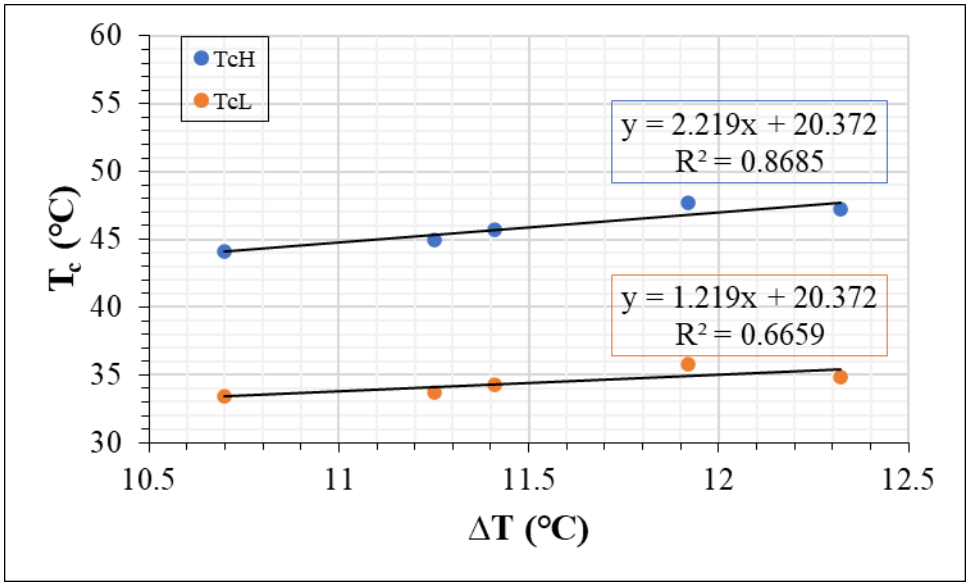

Fig. 15. Dependence of T_c on difference in cell temperature (ΔT). The values were extracted from IR thermal images acquired under clear sky outdoor conditions for the cell with the highest temperature (T_{cH}) and cell with the lowest temperature (T_{cL}). In this case, T_{cH} is the hotspot cell.

The extracted information for the graph in Fig. 15 for the 3 optically degraded PV modules is recorded in Table 4. The slopes of the cell with the lowest T_c (m_{cL}) and highest T_c (m_{cH}) and T_m of the modules are presented. Interestingly, the values for m_{cL}, m_{cH}, and T_m were observed to be constant under similar in-plane irradiance conditions.

Generally, the regression equations in Fig. 15 can be represented as

$$T_c = m_c \cdot \Delta T + T_m \quad => \quad \frac{\partial T_c}{\partial \Delta T} = m_c \tag{5}$$

where m_c is the slope of T_{cL} (m_{cL}) or T_{cH} (m_{cH}) versus ΔT. Fig. 15 evaluates the behaviour of current flow in the module (resistivity) as a function of temperature changes. Considering a PV module with a hotspot (due to defects), it can be assumed that during operation, the voltage across the module is constant, and that the ρ of the hotspot cell is higher than the ρ of the surrounding cells, which are in a better condition. Hence, the power dissipated into heat in the T_{cH} will be greater than the power dissipated into heat in the T_{cL} and surrounding cells due to defects induced resistivity, refer to Eq. (2). Hence, the m_c extracted from Fig. 15 can be used to assess current resistivity (Ωm) due to defects when temperature varies. A high m_c value indicates high resistivity (low conductivity), and vice versa. This is evident in Fig. 15 and Table 4 where m_{cH} is higher than m_{cL} for all the field-aged PV modules. This because ρ_D depends on A_D in defective PV cell or module, referring to Eq. (3). So, a negative m_c value indicates an inverse relationship between T_c (current flow) and ΔT. This means when ΔT increases, T_c decreases due to current dissipation by a critical defect such as cracks. A negative m_{cL} (-0.563 Ωm) for PV Module C supports the earlier observation where this same module showed a negative β_{Jmpp}. This behaviour is characteristic of a cell with the lowest temperature in the string, since this indicates that the bypass diode is active and has been activated. On the other hand, the same module showed a positive m_{cH} (0.437 Ωm) for the hotspot, since in this case, the bypass diode might have kicked in as the reaction threshold of the bypass diode might have been exceeded.

Table 4

Slopes of m_{cL}, m_{cH}, and T_m of the 3 field-aged PV modules.

PV module	Slope		T_m (°C)
	m_{cL} (Ωm)	m_{cH} (Ωm)	
A	1.22	2.22	20
B	2.69	3.69	8.7
C	-0.563	0.437	40

One observation from Table 4 is that PV Module C which showed the lowest m_c (lowest resistivity) among the 3 modules also showed the highest T_m though the measurements were done under similar irradiance conditions for the 3 PV modules. This observation supports our earlier assertion that PV Module C has critical defects that inhibit current flow. Also, Module B (the worst optically degraded module) showed the highest m_c with corresponding lowest T_m of ca. 9 °C. It is noteworthy

that m_c quantifies the bulk resistivity in the PV module. This also goes to emphasize our earlier views on the behaviour of β_{Jsc} and β_{Jmpp} due to the presence of co-defects in the module.

Fig. 16 illustrates the relationship between m_{cH} and m_{cL} for 10 selected field-aged PV modules, including the 3 modules chosen for this investigation. Each of the 10 selected modules has been identified to be affected by at least one of the defect mechanisms: optical degradation, cracks, or PID. This is to compare the resistivity due to the T_{cH} and T_{cL} of the PV modules affected by these defect mechanisms. It appears that this technique can predict the resistivity in PV modules precisely as it shows a perfect correlation of $R^2 = 1$. The 3 field-aged PV modules affected by optical degradation are highlighted in bold red dots as A, B, and C. The blue dots represent the rest of the 7 modules. The 10 PV modules are distributed in Quadrants 1, 2, and 3. The PV modules with the least and highest resistivity are located in Quadrants 1 and 3, respectively.

PV Modules A and B are located in Quadrant 1 while PV Module C is located in Quadrant 2. In Quadrant 1, Module B is located well above Module A. This suggests that Module B had the least resistance to current flow when in operation. That is, Module B appears to be the least affected by parasitic resistive current flow. On the other hand, Module C experienced the highest resistance to current flow in its bulk, which suggests that it has been affected by much more critical defects due to MID mechanisms e.g., corrosion, cracks, PID, etc. In general, it has been observed that PV modules affected by defects which are severely critical to current flow are located in Quadrants 2 and 3, hence, show negative β_{Jmpp}. For instance, PV modules affected by critical cracks are located in Quadrant 3. This confirms the assertion that the severity of power loss due to optical degradation also depends on the presence of other defects.

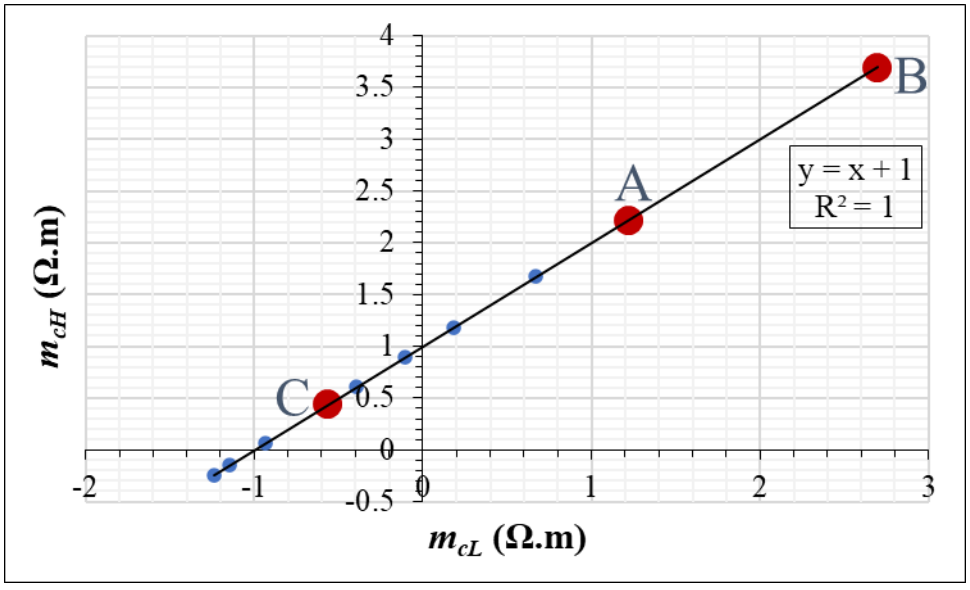

Fig. 16. A graph of m_{cH} versus m_{cL} (extracted from IR thermal images) for 10 selected field-aged PV modules. The 10 selected PV modules are affected by different defects: optical degradation, cracks, and PID. The 3 modules affected by optical degradation are labelled A, B, and C with their position on the regression line marked in bold red dots.

In situations where optical degradation is caused by other defects due to MID mechanisms, the current flow in the module bulk could be influenced by the characteristics of the other co-defects such as cracks, corrosion, PID, etc. Fig. 16 suggests that the m_{cH} versus m_{cL} graph for a defect free PV module will have a slope of 1 and will be located in Quadrant 1 only. On the other hand, a module affected by uniformly distributed defects which contribute to resistance equally (rare case) will have a slope of 1 but will be located in Quadrants 1 or 3. In both of these scenarios, the $m_c = 1$. In the case of non-uniform defect types and distribution, ρ_D is likely to be non-uniform. Hence, the graph for m_{cH} versus m_{cL} will be located in Quadrants 2 or 4. The upward shift of the intercept of the graph at m_{cH} (i.e., $m_{cH} > 0$), indicates the influence of resistance to current flow in the module bulk due to defect induced hotspots. The model for PV cell efficiency (η_c) or η_m is

$$\eta_c = \eta_r[1 - \beta(T_c - T_r)] \tag{6}$$

When $\Delta T = 0$ or for 'good' PV module, $T_c \approx T_m$, then Eq. (6) becomes

$$\eta_m = \eta_r[1 - \beta(T_m - T_r)] \tag{7}$$

where η_r is the cell/module reference efficiency at cell/module temperature (T_c or T_m) and reference temperature (T_r) of 25 °C. The T_m in Eq. (7) is estimated from Fig. 15. Accounting for temperature effects, the resistivity due to defects (ρ_D) in a PV module can be written as

$$\rho_D = \rho_r[1 - \beta(T_D - T_r)] \tag{8}$$

where ρ_r is the cell/module reference resistivity at the defect temperature (T_D) and reference cell/module temperature (T_r) of 25 °C. β is the temperature coefficient of the PV cell or module. For a defective PV module, T_D can be assumed to be T_m. Hence, using Eq. (8), the temperature coefficient (β) of a PV module could be estimated from the IR thermal data of the PV module.

Next, we explore the relationship between the information obtained from IR thermal images, $\beta_{\eta m}$ and β_{Vmpp} for 10 field-aged PV modules (including the 3 modules affected by optical degradation). This was done using regression plots as shown in Fig. 17.

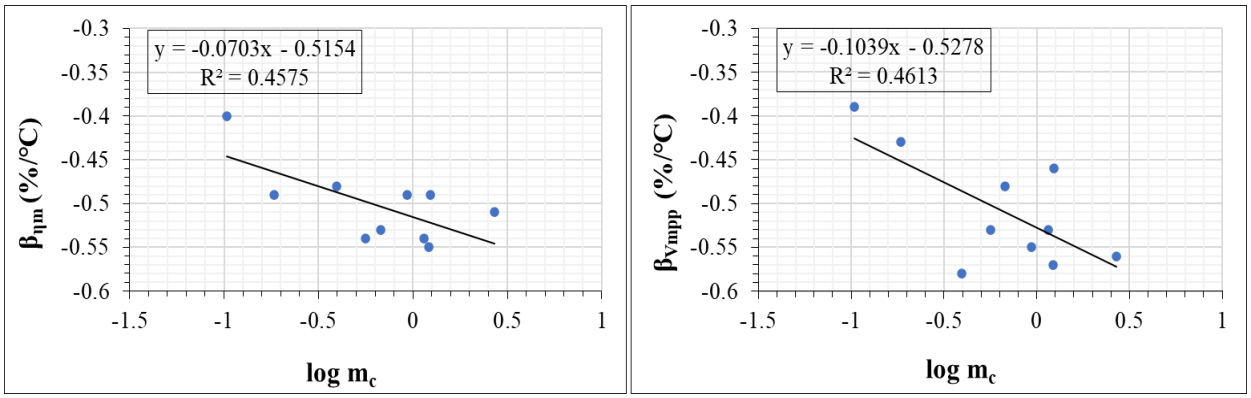

Fig. 17. Relationship between m_c and $\beta_{\eta m}$ and β_{Vmpp}, respectively. m_c is the slope of the graph of T_c versus ΔT (extracted from IR thermal images) for 10 PV modules. m_{cH} for the PV modules were used as they were more characteristic of the defects and fault modes.

Remember, m_c is the slope of T_c versus ΔT, refer to Eq. (5). The correlation between m_c and the temperature coefficients is weak with $R^2 < 0.5$. However, by extrapolation, when $log\ m_c = 0$ (i.e., when $m_c = 1$), $\beta_{\eta m} \approx$ -0.5 %/°C and $\beta_{Vmpp} \approx$ -0.5 %/°C. From Table 3, these are the average values for these parameters at STC. It is known that the temperature sensitivity and resistivity of PV modules are highly dependent on materials properties, defect types and defects concentration, refer to Eqs. (2) and (8). Hence, it appears the degradation states of the PV modules also influenced the degree of correlation as represented in Fig. 17. For instance, the regression graphs of $log\ m_c$ versus $\beta_{\eta m}$ and β_{Vmpp} for PV Modules A, B, and C alone give R^2 values greater than 0.5, but less than 0.6. The improved R^2 value is likely due to the fact that these 3 modules are affected by a similar defect mode: optical degradation. In addition, higher polynomial regression models can be useful for understanding the relationship between the degradation-induced temperature information and the module characteristics better [45]. For instance, when a sixth order polynomial fit is used for the data in Fig. 17, the R^2 value is greater than 0.8. Yet, the use of higher polynomial regression models can be misleading. In solar PV modeling, the model tends to be more sensitive to small changes in G_I when the degree of polynomial increases. The number of PV modules used may also be a factor for the low R^2 obtained. Further studies on a larger number of defect free modules will be needed to verify and improve on the current hypothesis. Nevertheless, the use of these temperature dependent information together with other module characteristics can improve the understanding of fault diagnostics in PV plants.

Conclusion

3 field-aged PV modules that have been affected by optical degradation were investigated. The investigation made use of visual inspection, current-voltage (I-V) characterization, temperature sensitivity profiling, current resistivity profiling, ultraviolet fluorescence (UV-F), electroluminescence (EL), and infrared (IR) thermal imaging. The results show that over the 20 years (10 years outdoor operation followed by 10 years indoor storage at room temperature), the EVA encapsulants of the field-aged PV modules have undergone optical degradation: delamination, discolouration of encapsulant, metal grids oxidation and corrosion, trapped moisture/chemical species, and glass corrosion.

Visual inspection in the dark (under well controlled light exposure) as a complementary tool to the visual inspection under clear sky conditions was also used. PV modules affected by optical degradation show weak fluorescence and luminescence signal intensities. The average ΔT for the 3 PV modules investigated was found to be ~10 ± 2 °C. The average degradation rate in the efficiency of the 3 PV modules was 0.8 % per year. This is due to the degradation in I_{sc} due to loss of optical efficiency and the drop in V_{oc} due to high module operating temperature. It is also observed that degradation in β_{Pmax} due to optical degradation can be traced to degradation in β_{Voc} and β_{Vmpp}. The average β_{Voc}, β_{Vmpp}, β_{Jsc}, β_{FF} and $\beta_{\eta m}$ for the 3 modules studies were -0.4 %/°C, -0.6 %/°C, 0.05 %/°C, -0.2 %/°C, and -0.5 %/°C, respectively.

A method of using the cell temperatures extracted from IR thermal imaging to estimate the degree of resistance to current flow within the PV module is also proposed. Using the temperature dependent resistivity graphs, defective modules could be identified based on the effect of defect mechanisms on current flow in the PV module. In addition, a method of extracting PV module

operating temperature (T_m) from IR thermal images is put forward. Finally, this work also demonstrates that extracting temperature coefficients directly from IR thermal data of PV modules is possible. The model for 10 field-aged PV modules with different defects and fault modes showed a weak correlation of $R^2 < 0.5$. However, the model for the 3 PV modules affected by optical degradation showed $R^2 > 0.5$. The proposed model in this work can be explored further and integrated into IR thermography programs in IR thermal imagers for monitoring PV plants' reliability based on temperature sensitivity. Though these field-aged PV modules have been affected by multiple defect mechanisms, efforts were made to select these 3 modules with similar characteristics. Besides, the best way to understand degradation mechanisms in PV modules is using field-aged PV modules which are exposed to multiple environmental stressors, and hence, suffer from multiple defect and fault mechanisms. This work has the potential of improving upon the existing knowledge on faults diagnostics in PV plants.

Acknowledgement

The author acknowledges the support of the Department of Engineering Sciences, University of Agder, Norway. The author also acknowledges the supervisors' invaluable support, suggestions, and feedback.

References

[1] Á. Fernández-Solas, L. Micheli, F. Almonacid, E.F. Fernández, Optical degradation impact on the spectral performance of photovoltaic technology, Renew. Sust. Energ. Rev., 141 (2021) 110782.
[2] C. Buerhop, D. Schlegel, M. Niess, C. Vodermayer, R. Weißmann, C. Brabec, Reliability of IR-imaging of PV-plants under operating conditions, Sol. Energy Mater. Sol. Cells, 107 (2012) 154-164.
[3] C. Dechthummarong, B. Wiengmoon, D. Chenvidhya, C. Jivacate, K. Kirtikara, Physical deterioration of encapsulation and electrical insulation properties of PV modules after long-term operation in Thailand, Sol. Energy Mater. Sol. Cells, 94 (2010) 1437-1440.
[4] O.K. Segbefia, A.G. Imenes, T.O. Sætre, Moisture ingress in photovoltaic modules: A review, Sol. Energy, 224 (2021) 889-906.
[5] O.K. Segbefia, N. Akhtar, T.O. Sætre, Defects and fault modes of field-aged photovoltaic modules in the Nordics, Energy Reports, 9 (2023) 3104-3119.
[6] O.K. Segbefia, N. Akhtar, T.O. Sætre, Moisture induced degradation in field-aged multicrystalline silicon photovoltaic modules, Sol. Energy Mater. Sol. Cells, 258 (2023) 112407.
[7] H.A. Al Mahdi, P.G. Leahy, A.P. Morrison, Predicting Early EVA Degradation in Photovoltaic Modules From Short Circuit Current Measurements, IEEE J. Photovoltaics, (2021).
[8] C. Peike, S. Hoffmann, P. Hülsmann, B. Thaidigsmann, K. Weiβ, M. Koehl, P. Bentz, Origin of damp-heat induced cell degradation, Sol. Energy Mater. Sol. Cells, 116 (2013) 49-54.
[9] F. Pern, A. Czanderna, K. Emery, R. Dhere, Weathering degradation of EVA encapsulant and the effect of its yellowing on solar cell efficiency, in: The Conference Record of the Twenty-Second IEEE Photovoltaic Specialists Conference-1991, IEEE, 1991, pp. 557-561.
[10] International Standards Organization, ISO 17223:2014: Plastics — Determination of yellowness index and change in yellowness index, in, 2014.
[11] F. Rosillo, M. Alonso-García, Evaluation of color changes in PV modules using reflectance measurements, Sol. Energy, 177 (2019) 531-537.

[12] M.C.C. de Oliveira, D.A. Cassini, A.S.A.C. Diniz, L.G. Soares, M.M. Viana, L.L. Kazmerski, V.d.F.C. Lins, Comparison and analysis of performance and degradation differences of crystalline-Si photovoltaic modules after 15-years of field operation, Sol. Energy, 191 (2019) 235-250.
[13] J.A. Tsanakas, L. Ha, C. Buerhop, Faults and infrared thermographic diagnosis in operating c-Si photovoltaic modules: A review of research and future challenges, Renew. Sust. Energ. Rev., 62 (2016) 695-709.
[14] M. Köntges, G. Oreski, U. Jahn, M. Herz, P. Hacke, K.-A. Weiß, Assessment of photovoltaic module failures in the field: International Energy Agency Photovoltaic Power Systems Programme: IEA PVPS Task 13, Subtask 3: report IEA-PVPS T13-09: 2017, International Energy Agency, 2017.
[15] M. Köntges, S. Kurtz, C. Packard, U. Jahn, K.A. Berger, K. Kato, Performance and reliability of photovoltaic systems: subtask 3.2: Review of failures of photovoltaic modules: IEA PVPS task 13: external final report IEA-PVPS, International Energy Agency, Photovoltaic Power Systems Programme, 2014.
[16] O.K. Segbefia, N. Akhtar, T.O. Sætre, The effect of moisture ingress on titania antireflection coatings in field-aged photovoltaic modules, in: 2022 IEEE 49th Photovoltaics Specialists Conference (PVSC), IEEE, 2022, pp. 1237-1244.
[17] A. Sinha, O. Sastry, R. Gupta, Nondestructive characterization of encapsulant discoloration effects in crystalline-silicon PV modules, Sol. Energy Mater. Sol. Cells, 155 (2016) 234-242.
[18] B.R. Paudyal, A.G. Imenes, Investigation of temperature coefficients of PV modules through field measured data, Sol. Energy, 224 (2021) 425-439.
[19] Q. Bao, X. Liu, S. Braun, J. Yang, Y. Li, J. Tang, C. Duan, M. Fahlman, The effect of oxygen uptake on charge injection barriers in conjugated polymer films, ACS applied materials & interfaces, 10 (2018) 6491-6497.
[20] R. Di Pietro, D. Fazzi, T.B. Kehoe, H. Sirringhaus, Spectroscopic investigation of oxygen-and water-induced electron trapping and charge transport instabilities in n-type polymer semiconductors, J. Am. Chem. Soc., 134 (2012) 14877-14889.
[21] D. Feldman, Polymer weathering: photo-oxidation, J. Polym. Environ., 10 (2002) 163-173.
[22] A. Pareek, R. Meena, R. Gupta, Analysis of encapsulant discoloration effect on the temperature of photovoltaic module, (2022).
[23] F. Pern, Luminescence and absorption characterization of ethylene-vinyl acetate encapsulant for PV modules before and after weathering degradation, Polym. Degrad. Stab., 41 (1993) 125-139.
[24] W. Stark, M. Jaunich, Investigation of Ethylene/Vinyl Acetate Copolymer (EVA) by thermal analysis DSC and DMA, Polym. Test., 30 (2011) 236-242.
[25] U. Jahn, M. Herz, M. Köntges, D. Parlevliet, M. Paggi, I. Tsanakas, Review on infrared and electroluminescence imaging for PV field applications: International Energy Agency Photovoltaic Power Systems Programme: IEA PVPS Task 13, Subtask 3.3: report IEA-PVPS T13-12: 2018, International Energy Agency, 2018.
[26] O.K. Segbefia, B.R. Paudyal, I. Burud, T.O. Sætre, Temperature Coefficients of Photovoltaic Modules under Partial Shading Conditions, 38th EU PVSEC, (2021) 1180 - 1186.
[27] O. Dupré, R. Vaillon, M.A. Green, Physics of the temperature coefficients of solar cells, Sol. Energy Mater. Sol. Cells, 140 (2015) 92-100.
[28] O.K. Segbefia, A.G. Imenes, I. Burud, T.O. Sætre, Temperature profiles of field-aged multicrystalline silicon photovoltaic modules affected by microcracks, in: 2021 IEEE 48th Photovoltaic Specialists Conference (PVSC), IEEE, 2021, pp. 0001-0006.
[29] J.L. Bryan, T.J. Silverman, M.G. Deceglie, Z.C. Holman, Thermal model to quantify the impact of sub-bandgap reflectance on operating temperature of fielded PV modules, Sol. Energy, 220 (2021) 246-250.
[30] D.L. King, J.A. Kratochvil, W.E. Boyson, Temperature coefficients for PV modules and arrays: measurement methods, difficulties, and results, in: Conference record of the twenty sixth IEEE Photovoltaic Specialists Conference-1997, IEEE, 1997, pp. 1183-1186.

[31] R. Dubey, P. Batra, S. Chattopadhyay, A. Kottantharayil, B.M. Arora, K. Narasimhan, J. Vasi, Measurement of temperature coefficient of photovoltaic modules in field and comparison with laboratory measurements, in: 2015 IEEE 42nd Photovoltaic Specialist Conference (PVSC), IEEE, 2015, pp. 1-5.
[32] E. Skoplaki, J.A. Palyvos, On the temperature dependence of photovoltaic module electrical performance: A review of efficiency/power correlations, Sol. Energy, 83 (2009) 614-624.
[33] T. Våland, W. Bartholdsen, M. Ottestad, M. Våge, Grimstad renewable energy park, Agder University College, NO-4878 Grimstad, Norway. http://ieahia. org/pdfs/grimstad. pdf, (1997).
[34] D. Verma, M. Tayyib, T.O. Saetre, O.-M. Midtgård, Outdoor Performance of 10 year Old a-Si and Poly-Si Modules in southern Norway conditions, in: 2012 38th IEEE Photovoltaic Specialists Conference, IEEE, 2012, pp. 002368-002371.
[35] O.K. Segbefia, T.O. Sætre, Investigation of the Temperature Sensitivity of 20-Years Old Field-Aged Photovoltaic Panels Affected by Potential Induced Degradation, Energies, 15 (2022) 3865.
[36] A. Morlier, M. Siebert, I. Kunze, S. Blankemeyer, M. Köntges, Ultraviolet fluorescence of ethylene-vinyl acetate in photovoltaic modules as estimation tool for yellowing and power loss, in: 2018 IEEE 7th World Conference on Photovoltaic Energy Conversion (WCPEC)(A Joint Conference of 45th IEEE PVSC, 28th PVSEC & 34th EU PVSEC), IEEE, 2018, pp. 1597-1602.
[37] M. Köntges, A. Morlier, G. Eder, E. Fleiß, B. Kubicek, J. Lin, Ultraviolet fluorescence as assessment tool for photovoltaic modules, IEEE J. Photovoltaics, 10 (2020) 616-633.
[38] W. Herrmann, G. Eder, B. Farnung, G. Friesen, M. Köntges, B. Kubicek, O. Kunz, H. Liu, D. Parlevliet, I. Tsanakas, Qualification of photovoltaic (pv) power plants using mobile test equipment, IEA-PVPS T13-24: 2021, (2021).
[39] R. Meena, M. Kumar, R. Gupta, Investigation of dominant degradation mode in field-aged photovoltaic modules using novel differential current-voltage analysis approach, Prog. Photovoltaics Res. Appl., 30 (2022) 1312-1324.
[40] T. Potthoff, K. Bothe, U. Eitner, D. Hinken, M. Köntges, Detection of the voltage distribution in photovoltaic modules by electroluminescence imaging, Prog. Photovoltaics Res. Appl., 18 (2010) 100-106.
[41] S. Deitsch, V. Christlein, S. Berger, C. Buerhop-Lutz, A. Maier, F. Gallwitz, C. Riess, Automatic classification of defective photovoltaic module cells in electroluminescence images, Sol. Energy, 185 (2019) 455-468.
[42] W. Luo, Y.S. Khoo, P. Hacke, V. Naumann, D. Lausch, S.P. Harvey, J.P. Singh, J. Chai, Y. Wang, A.G. Aberle, Potential-induced degradation in photovoltaic modules: a critical review, Energy & environmental science, 10 (2017) 43-68.
[43] J. Berghold, O. Frank, H. Hoehne, S. Pingel, B. Richardson, M. Winkler, Potential induced degradation of solar cells and panels, 25th EUPVSEC, (2010) 3753-3759.
[44] A. Augusto, A. Srinivasa, S.G. Bowden, Influence of the bulk resistivity on silicon heterojunction solar cells and module reliability, Sol. RRL, 6 (2022) 2100519.
[45] A.M. Pavan, A. Mellit, D. De Pieri, S.A. Kalogirou, A comparison between BNN and regression polynomial methods for the evaluation of the effect of soiling in large scale photovoltaic plants, Appl. Energy, 108 (2013) 392-401.

Paper F

Investigation of the Temperature Sensitivity of 20-Years Old Field-Aged Photovoltaic Panels Affected by Potential Induced Degradation by O.K. Segbefia and T.O. Sætre. Published in Energies (2022).

energies

MDPI

Article

Investigation of the Temperature Sensitivity of 20-Years Old Field-Aged Photovoltaic Panels Affected by Potential Induced Degradation

Oscar Kwame Segbefia * and Tor Oskar Sætre

Department of Engineering Sciences, University of Agder, 4879 Grimstad, Norway; tor.satre@uia.no
* Correspondence: oscar.k.segbefia@uia.no; Tel.: +47-4637-9399

Abstract: One effect of moisture ingress on solar panels is potential induced degradation (PID). Solar panels affected by PID experience large leakage currents between the solar cells and the module's frame, which leads to substantial power degradation. In the present work, the temperature coefficients of 3 old PV panels affected by PID were investigated. In the electroluminescence images, solar cells nearer to the edge of the modules appear darker due to ohmic shunting. IR thermal images acquired under clear sky outdoor conditions show that the majority of the warmer cells (hotspots) were located closer to the edge of the modules. The difference in cell temperature (ΔT) due to PID effect ranges from 7 °C to 15 °C for the 3 field-aged modules. The average temperature coefficient of efficiency ($\beta_{\eta m}$) was found to be −0.5%/°C. Also, it was observed that the temperature coefficients of open circuit voltage (β_{Voc} = −0.4%/°C), maximum power point voltage (β_{Vmpp} = −0.5%/°C), and fill factor (β_{FF} = −0.2%/°C), were the underlying factors for the degradation in the P_{max} of the old solar panels affected by PID. This accounted for an average 1.2%/year overall degradation in the efficiency of these modules. Most notably, it was discovered that the PV modules affected by PID show negative temperature coefficients of maximum power point current (β_{Jmpp}) due to large leakage currents. This observed negative β_{Jmpp} we believe is characteristic of PV panels affected by PID.

Keywords: potential induced degradation; shunting; temperature coefficient; leakage current; field-aged

Citation: Segbefia, O.K.; Sætre, T.O. Investigation of the Temperature Sensitivity of 20-Years Old Field-Aged Photovoltaic Panels Affected by Potential Induced Degradation. *Energies* **2022**, *15*, 3865. https://doi.org/10.3390/en15113865

Academic Editors: Pedro Dinis Gaspar, Pedro Dinho da Silva and Luís C. Pires

Received: 20 April 2022
Accepted: 14 May 2022
Published: 24 May 2022

1. Introduction

One of the underlying effects of moisture ingress on photovoltaic (PV) modules is potential induced degradation (PID) [1–7]. PID occurs when there is an increased material conductivity and leakage current between the PV module's frame and the cells [8–15]. This has severe consequences for PV module power reliability and can constitute up to 100% of power loss in PV plants [16].

According to Naumann et al. [10], high surface defect density on interdigitated back contact (IBC) solar cells results in decreased field effect passivation. Decreased field effect passivation leads to high surface recombination, and hence, causes PID of polarization/passivation (PID-p) type. However, PID-p is temporary and reversible [10,17–19]. Investigations revealed that the transport of mobile ions, especially sodium (Na+) ions, within the PV module bulk is responsible for the PID of shunting (PID-s) type [2,15,20,21]. High conductivity of sodium decorated stacking faults across the solar cell emitter leads to shunting, hence, PID-s [2,20]. PID-s manifests itself in the degradation in the open circuit voltage, short circuit current, and fill factor [2,3]. Hence, PID-s type appears to be the key problem in the field [17].

There have been efforts to prevent PID at the cell and module manufacturing levels, installation, and during operation [2,5,22]. Current-voltage (I-V) characterization, electroluminescence (EL), and infrared (IR) thermography could be used to detect and monitor the onset of PID in PV plants under sunlight or in the dark with external bias conditions [2,21]. PID-s cells are identified as warmer cells in IR thermal images and darker

cells in EL images [3,6,15]. According to Carolus et al. [14], Current-voltage (I-V) and external quantum efficiency (EQE) measurements could be used to differentiate PID-s from PID-p. Proposed methods for reversing the PID effect appears to be saddled with other limitations [8,22]. Indeed, the TS IEC 62804-1 standard exists to ensure PID reliability of commercial PV modules. However, the PID effect continues to be a challenge for the PV community [2,6,20,23,24].

In addition to power degradation, PID also induces mismatch losses due to non-uniform degradation [9,20,25,26]. Degraded cells that are affected by PID cause current reverse biasing, which leads to local overheating or joule heating [14,27]. This triggers hotspots, which influence the PV module operating temperature (T_m), hence, the temperature sensitivity [20,25,28]. According to Islam et al. [23], PID in polycrystalline solar panels can accelerate cell crack propagation and can lead to the degradation in the temperature coefficient of efficiency. In addition, Wang et al. [24] observed an increased temperature coefficient of maximum power (P_{max}) in PV modules affected by PID. Extensive research on the influence of the temperature sensitivity on PV modules main electrical parameters is available in literature [25,26,28–31]. However, studies on the influence of PID on the temperature coefficients of PV modules are rare [20,25,26,28]. Moreover, only a few were done on field-aged PV modules [23,24]. Yet, we have not found any report on the influence of PID on the temperature coefficients of the maximum power point voltage (β_{Vmpp}) and current (β_{Jmpp}) of PV modules.

A procedure for detecting PID based on temperature coefficient profiling of PID affected field-aged multicrystalline silicon (mc-Si) PV modules is presented in this contribution. I-V characterization, EL, and IR thermal imaging were used for the investigation. It turned out that PV modules affected by PID could be detected by monitoring the temperature coefficient of maximum power point current (β_{Jmpp}). Section 2 presents the material and methods used for the investigation and the results and the insights from the investigation are presented in Section 3.

2. Materials and Methods

In the present work, field-aged NESTE NP100G12 multicrystalline silicon (mc-Si) PV modules affected by PID were investigated. The 3 solar panels (namely A, B, and C) were chosen from a batch of solar panels which were installed on a Renewable Energy Park in Dømmesmoen, Grimstad (58.3447° N, 8.5949° E), Norway in the year 2000. However, the PV modules on the Energy Park were decommissioned in 2011 and were kept securely for research purposes [32]. In an earlier report on the types of defects and faults modes of these old solar panels by the present authors, EL and IR thermal data of PV panel C was used to show that some of the old PV panels were affected by PID. The manufacture's data sheet and the measured electrical data on the 3 old PV panels (namely A, B, and C) is summarized in Table 1.

Table 1. Technical data sheet (2000) and the measured electrical parameters (2021) of old solar panels normalized to Standard Test Conditions (STC).

PV Module		P_{max} (W)	V_{oc} (V)	I_{sc} (A)	V_{mpp} (V)	I_{mpp} (A)	*FF* (%)	η (%)
2000 (Data sheet)		100	21.6	6.7	16.7	6.0	70	13.0
2021	A	75.0	19.5	5.9	14.3	5.2	65	9.7
	B	75.9	19.3	6.1	14.2	5.3	65	9.9
	C	78.3	19.6	6.1	14.7	5.3	66	10.2

The PV modules were made using anodized aluminum (Al-) frame, low iron tempered front glass, ethylene vinyl acetate (EVA) encapsulation, white multi-layered Tedlar®/Polyester/Tedlar® (TPT) backsheet, and 2 weatherproof plastic casing junction boxes (accommodating a bypass diode each). Each PV module consists of (12 × 2) series connected solar cells and 3 substrings, refer to Figure 1. The solar cells feature a full area screen-printed Al-grid rear surface with dimensions of 100 × 100 mm^2 and a titania antireflective coating (ARC).

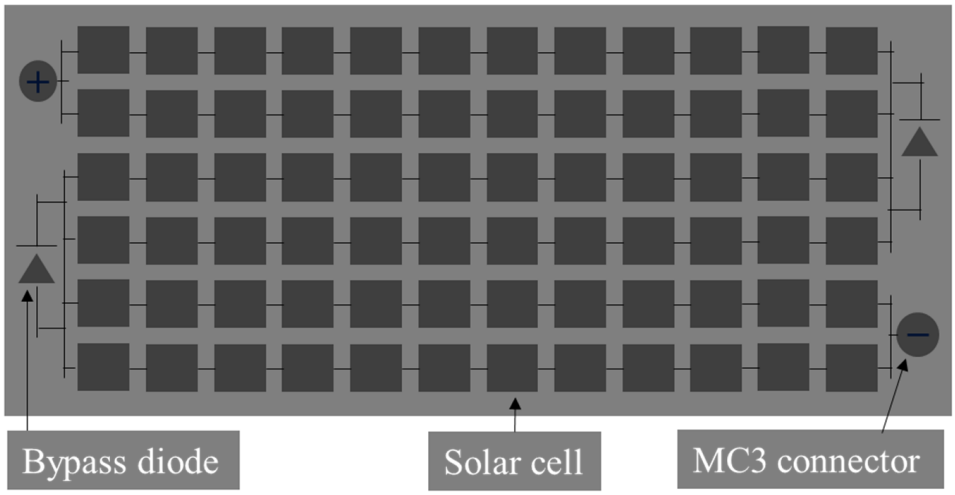

Figure 1. Electrical layout of the field-aged PV modules. Three serially circuited substrings; each consisting of a pair of 12 series connected solar cells in 3 series connected substrings.

2.1. I-V Measurements

The sampled old solar panels were each taken through electrical performance measurements using an HT® Instruments I-V 500 w I-V Curve Tracer. This was done by following the IEC 60904-1 standard. By these measurements, information on the maximum power (P_{max}), open circuit voltage (V_{oc}), maximum power point voltage (V_{mpp}), short circuit current (I_{sc}), maximum power point current (I_{mpp}), fill factor (FF), in-plane irradiance (G_I), and module temperature characteristics of each panel at Standard Test Conditions (STC) was acquired. STC indicates solar cell temperature at 25 °C, G_I at 1000 W/m^2 and air mass 1.5 (AM1. 5) spectrum for commercial solar PV panels. The entire experimental procedure was carried out under clear sky in-plane irradiance conditions (960–1060 W/m^2). The I-V tracer converted all measurements to STC automatically to minimize errors associated with data acquisition.

2.2. Temperature Coefficient Profiling

On a clear sky sunny day in the summer, the PV modules were taken out to the outdoor measuring rack in turns from a storeroom where the modules were kept. The PV module and the reference device were shaded using a cardboard. Measurement was initiated immediately after the shade was removed. The measurements on the 3 field-aged PV modules were done on the same day between 12.30 and 14.30 h and at wind speed less than 2 ms^{-1}. According to IEC 60891-4 standard, the temperature range of the data values should be at least 30 °C. However, this seems challenging in practical field measurements, especially for the investigation site.

A graph of electrical parameters (P_{max}, V_{oc}, I_{sc}, FF, η_m, V_{mpp}, I_{mpp}) versus PV module's temperature (T_m) was plotted and a least-squares-fit graph through each data set was acquired to get the relative temperature coefficients. The regression equation for such relation can be represented as $y = mx + c$, where m and c are the slope (temperature coefficient) and the intercept (the value of the electrical parameter at 0 °C), respectively [33]. The relative temperature coefficient of parameter X (β_x) in%/°C was calculated by dividing the slope of parameter X by the intercept of parameter X. That is, $\beta_x = m/c$.

2.3. Electroluminescence (EL) Tomography

EL tomography is interesting especially for characterizing old PV panels affected by PID. The 3 sampled PV panels were taken through the EL characterization in a dark room using the BrightSpot EL Test Kit, see Figure 2. The kit comprises of a 24 megapixels modified DSLR (digital single-lens reflex) Nikon D5600 camera, DC power supply set, and computer with data acquisition and image processing software. The image acquisition and processing were done

according to the IEC 60904-13 standard and the IEA procedure [3,15]. The EL characterization of the PV modules was done under $0.1I_{sc}$ and at I_{sc} current density conditions.

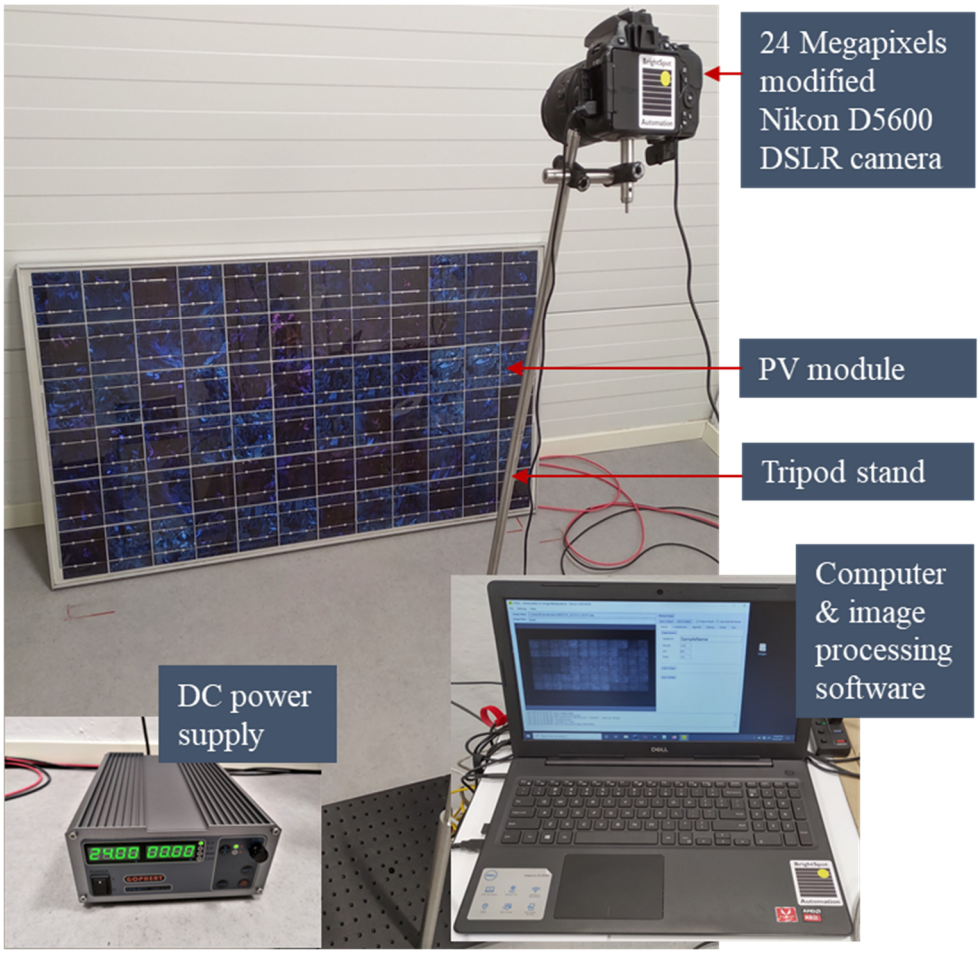

Figure 2. Experimental setup of the EL imaging system. The system runs on a DC power supply.

2.4. Infrared (IR) Thermal Imaging

The sampled solar panels were also taken through IR thermography using the Fluke Ti400 Infrared Camera ($\lambda \approx 650$ nm) as per the IEA recommended procedure [15] and the IEC 62446-3 standard. Figure 3 shows the outdoor experimental setup. Measurements were done under clear sky field conditions. The IR thermal images were acquired after soaking the PV modules in the sun for at least 15 min, as prescribed by the IEC 62446-3 standard.

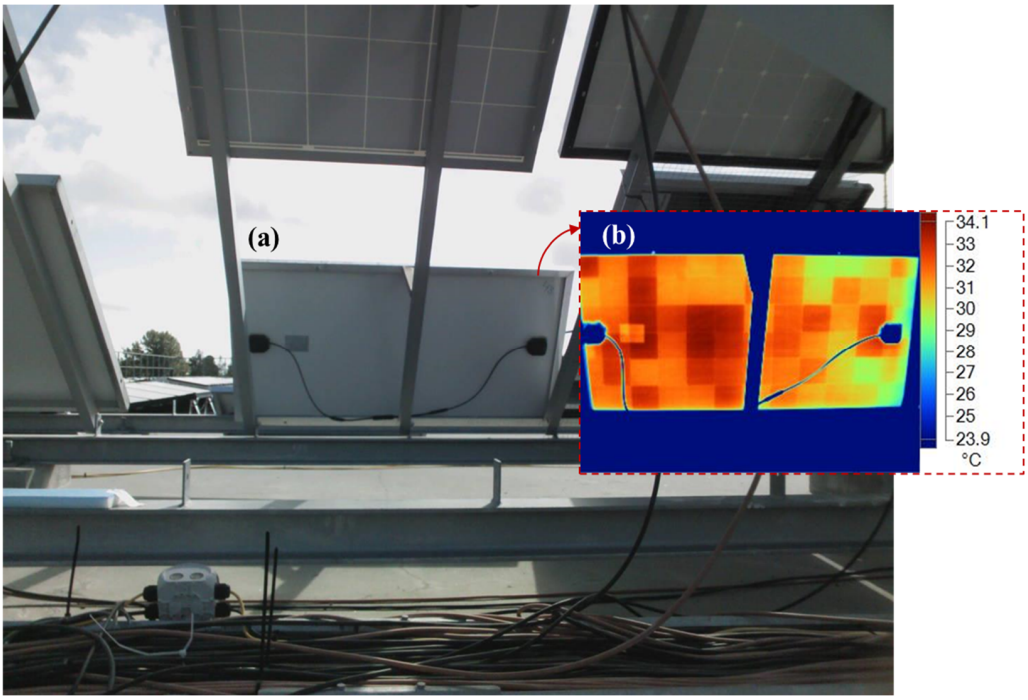

Figure 3. (**a**) Visual image and (**b**) IR thermal image (insert) of a PV module measured from the backside during the outdoor IR thermal imaging. The supporting metal trestle (behind the PV module) and the cables in the visual image show corresponding blue traces in the IR thermal image.

3. Results and Discussion

3.1. I-V Characteristics of the PV Panels

Figure 4 illustrates the I-V characteristics of the field-aged PV Modules A, B, and C. The I-V curve for the manufacturer's data sheet in 2000 illustrates the I-V characteristics of the panels when they were new, i.e., when they were not affected by PID. However, in 2021, when the solar panels were affected by PID, the 3 panels show similar degradation trend in electrical characteristics. There was ca. 10% degradation in both I_{sc} and V_{oc} and ca. 24% degradation in P_{max} over the 20 years. That is, annual degradation of ca. 0.5% in I_{sc} and V_{oc} and ca. 1.2% in P_{max}, which agrees with observation elsewhere [34]. This resulted in the decrease in fill factor (F) of ca. 0.3%/year and a drop in efficiency of ca. 1.2%/year, see Table 1. A drop in the P_{max}, I_{sc}, V_{oc}, and FF was also observed by other researchers [3,14,15,29].

It was reported that the effect of PID is more severe under lower irradiation conditions as compared to STC [3,16]. This means that PV modules deployed in the cold regions are more susceptible to the PID effect than those deployed in climates with high regular irradiance conditions. Low irradiance and shading conditions predispose PV modules to mismatch losses, hence, hotspots [33]. These hotspots can induce the onset of PID [16,20,35]. For the 3 field-aged PV modules, the average degradation in the V_{mpp} and I_{mpp} were 0.7% and 0.6% per year, respectively (refer to Table 1). Figure 5 illustrates the relative change (Δ) in the electrical parameters of the old solar panels affected by PID over the 20 years. The relative change (Δ) in the electrical parameters of the PID affected old solar panels was computed as the difference between the datasheet values (2000) and the values measured in the year 2021, a recommended procedure by Köntges et al. [17].

The position of the box indicates the percentage degradation, and the dots show the outliers. The degree of deviation of the electrical parameter from the mean value is indicated by the length of the box. The degradation in the electrical parameters of the 3 old solar panels follow a similar trend. P_{max} shows more than 20% degradation over the 20 years, refer to Table 1. It appears from Figure 5 that the underlying cause of the P_{max} degradation is the degradation in all electrical parameters, especially degradation in V_{oc}

and V_{mpp}. Yet, it is blurry as to the degree of contribution from each electrical parameter to the overall degradation in P_{max}.

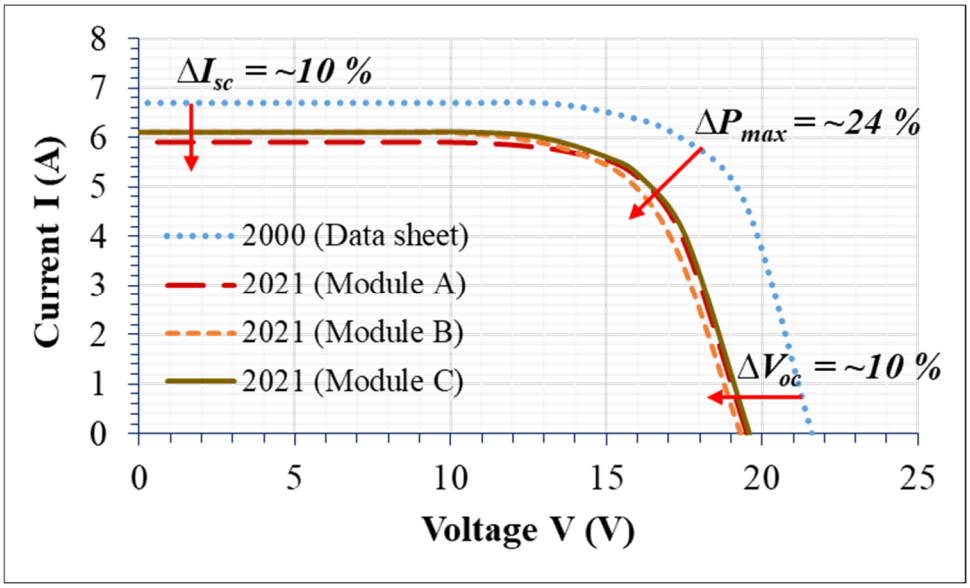

Figure 4. Normalized I-V characteristics of the 3 old PV panels (A, B, C). The data sheet curve by the manufacturer in the year 2000 is also shown.

It is known that P_{max} is directly related to the maximum power point voltage (V_{mpp}) and the maximum power point current (I_{mpp}) by the following relation:

$$P_{max} = V_{mpp} \cdot I_{mpp} \quad (1)$$

However, fill factor (FF) of a PV module could also be written as

$$FF = \frac{V_{mpp} \cdot I_{mpp}}{V_{oc} \cdot I_{sc}} \quad (2)$$

So, the maximum power output of a PV panel is related to the fill factor as

$$P_{max} = V_{oc} \cdot I_{sc} \cdot FF \quad (3)$$

The PV module efficiency (η_m) is related to the P_{max}, module's area (A_m), and the input power (P_{in}) as

$$\eta_m = \frac{P_{max}}{A_m \cdot P_{in}} \quad (4)$$

That means, any drop or degradation in V_{oc}, I_{sc}, FF, V_{mpp}, and I_{mpp} affects the P_{max} or η_m of the PV module directly, refer to Figure 4. Since the P_{in} for η_m calculations is assumed as 1 kWm^{-2}, $P_{max} \approx \eta_m / A_m$. A_m is the product of the solar cell's area and the number of solar cells in the module. From Table 2, the regression plots (which indicates the degree of correlation) for P_{max} versus V_{oc} and V_{mpp} gave $R^2 > 97$. On the other hand, the $R^2 < 0.6$ for I_{sc} and I_{mpp}. Resistance losses due to PID is the reason for the higher R^2 values for the fill factor (FF) of the modules, especially for solar panels A and C. The I-V curves of the modules in Figure 4 support this observation. Solar panel C appears to be the least affected by PID, hence, shows the weakest R^2 in both ΔI_{sc} and ΔI_{mpp}, refer to Table 2. This is because PID alters the current flow characteristics of the PV module [5,8,13]. When PID is caused by negative bias, it can induce optical degradation [5]. This is why most of these old solar panels were found to be affected by optical degradation as well.

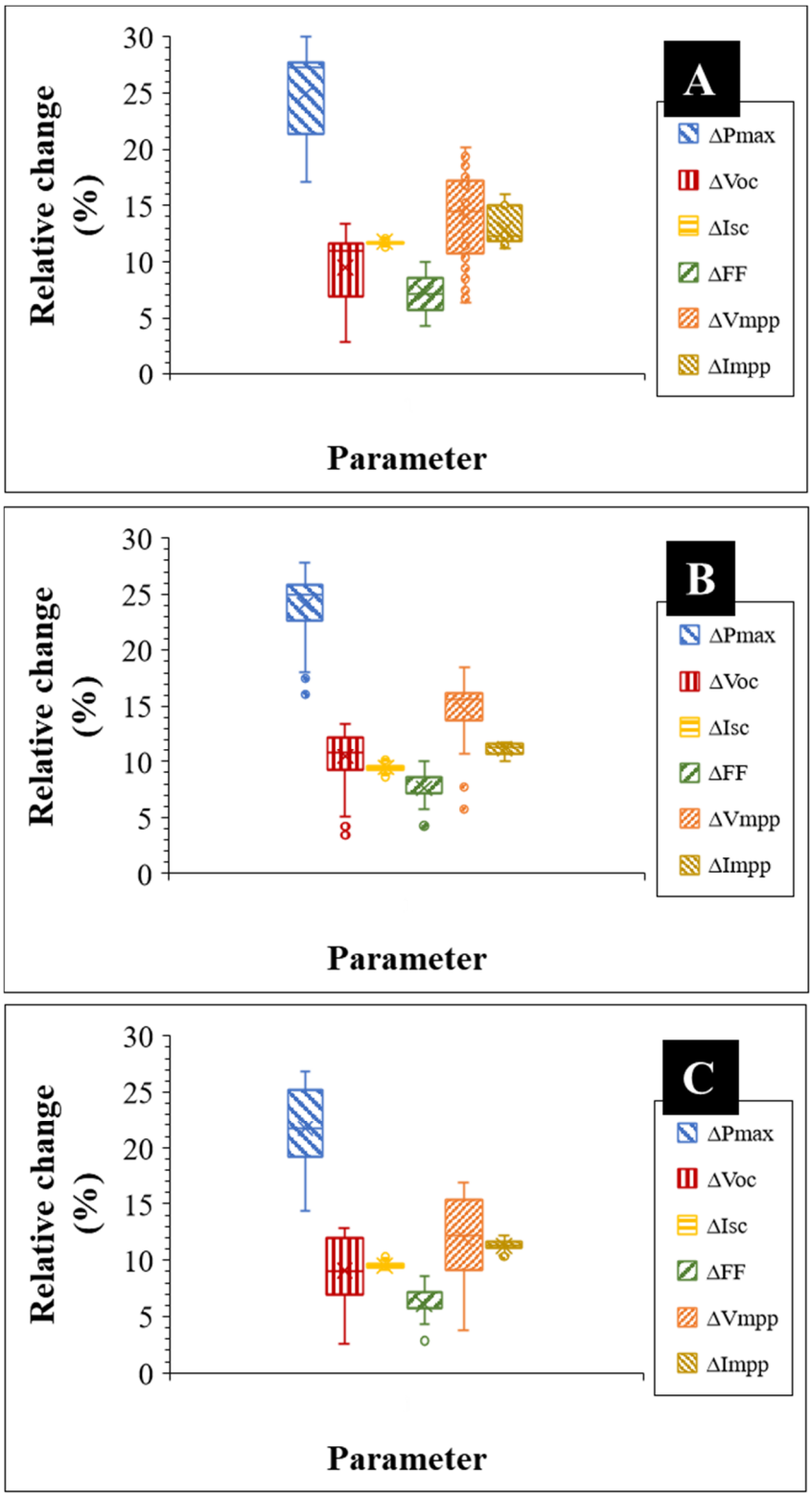

Figure 5. Degradation in the electrical parameters of the old PV panels under STC conditions using Box and Whisker plots. The tips of the boxes show the interquartile ranges. The internal lines show the median and the *x*-marks show mean. Δ is the difference between data sheet (2000) and measured (2021) values. Measurements were done under 960–1060 W/m^2 in-plane irradiance conditions.

Table 2. Correlation of the degradation in PV modules electrical parameters to the degradation in P_{max} due to PID. R^2 indicates the degree of correlation.

PV Module	R^2				
	ΔV_{oc}	ΔV_{mpp}	ΔFF	ΔI_{mpp}	ΔI_{sc}
A	0.98	0.99	0.86	0.23	0.47
B	0.98	0.98	0.57	0.55	0.17
C	0.99	0.99	0.88	0.06	0.04

Degradation in P_{max}, V_{oc}, V_{mpp}, and FF due to PID was also reported by other authors [3,14,16,29]. They believed that the loss in P_{max} due to PID could be up to 100% in severe cases [16]. The I-V characteristics of the old solar panels suggest that they are suffering from PID, as reported in other investigations [2,3,5,8,13,14,16,20,21,24,35].

3.2. Electroluminescence Characteristics

Figure 6 shows the EL analyses of the solar panels. The EL images were acquired under I_{sc} (Figure 6a–c) and $0.1I_{sc}$ (Figure 6d–f) forward bias conditions, respectively. The red marked out areas on the images in Figure 6 show some of the areas affected by PID in each PV module. In Figure 6a–c, apart from some darker spots, these images give little or no information on the areas affected by PID. This is because EL under I_{sc} conditions highlights metal contact or shunt issues [3,15]. In fact, contact issues such as cracks and corrosion are highlighted as darker spots in Figure 6a–c. Hence, EL under I_{sc} conditions are less suitable for detecting PID in PV modules, as observed in other studies [3,13,15].

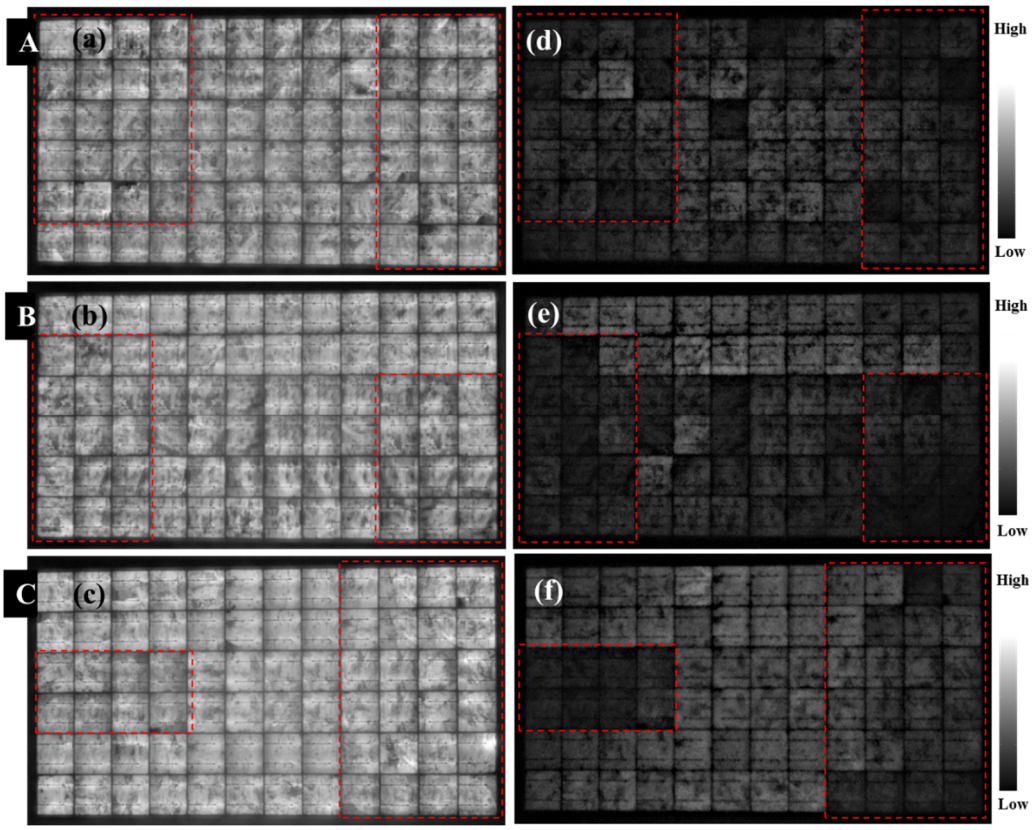

Figure 6. EL analyses of the 3 old solar panels under I_{sc} (**a–c**) and $0.1I_{sc}$ (**d–f**) conditions, respectively. Corresponding PID affected areas in EL images under both bias conditions are marked out in red. EL at $0.1I_{sc}$ revealed PID affected areas better.

On the other hand, under $0.1I_{sc}$ conditions, the effect of PID in the field-aged PV modules are well highlighted, see Figure 6d–f. The effect of PID manifests itself in the degradation of the solar cells located closer to the perimeter of the solar panel [8,22]. This accelerated degradation of the cells nearer to the frame of the PV module is due to high leakage currents associated with the PID effect [2,7,24]. Degraded solar cells appear as darker cells in the EL analyses due to strong ohmic shunting of the cell with the panel's Al-frame [24,27].

The PID affected areas in the solar panels are marked out in red. The trend in Figure 6 is that majority of the darker cells are located close to the edge of the old solar panels. The degradation pattern in Figure 6 suggests that these PV modules are affected by PID, as reported by other authors [3,9,14,15,35].

3.3. IR Thermal Image Characteristics

In IR thermal images, solar cells affected by PID appear as warmer cells or hotspots [16,36]. Figure 7 shows the IR thermograms of the 3 old solar panels (A, B, and C). In Figure 7, the areas marked out in white corresponds to the areas marked out in Figure 6. They show some of the areas in the PV modules that have been affected by PID. Figure 7 shows that majority of the warmer cells are located nearer to the perimeter of the old solar panels, as observed elsewhere [3,15,20,35].

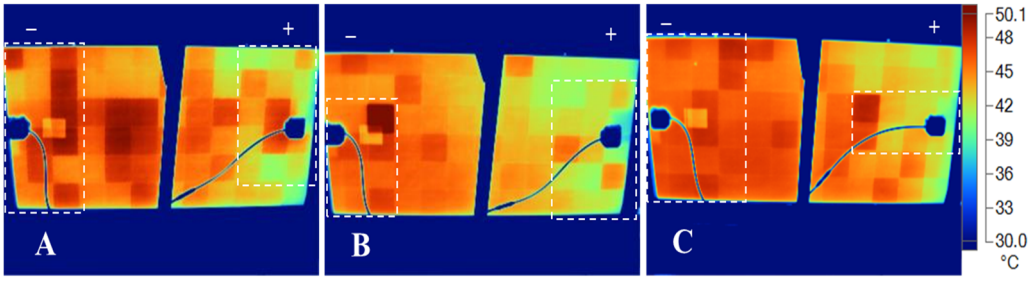

Figure 7. IR thermograms of the 3 old solar panels (**A**–**C**) affected by PID under clear sky outdoor conditions. Corresponding defects areas in Figure 6 are marked in white. The negative terminal (**left**) and the positive terminal (**right**) are indicated above the modules.

It could be seen that the locations of the warmer cells in the IR thermal images (Figure 7) correspond with the locations of the darker cells in the EL images, refer to Figure 6. Another observation from Figure 7 is that the cells which are closer to the negative terminal (left) of the field-aged PV modules are warmer than the cells which are located nearer to the positive terminal (right), especially those cells that are closer to the Al- frame. This was also reported by other researchers [9,15,35]. This is due to the direction of current flow in a PV module under illumination. Under in-plane radiation, current move by diffusion from the negative to the positive terminal. In PID affected areas, there is high resistance to current flow culminating into high module temperature localized to these areas [20,26,28], as observed in Figure 7.

This is opposite to the direction of current flow when the IR thermal imaging is done under forward bias (drift) conditions, as it is done in EL imaging. This also explains why the defective solar cells are clearly seen at the areas closer to the negative terminal in the field-aged PV modules. Also, high negative leakage current accelerates PID degradation [5,9,20,24,35]. Table 3 shows the extracted solar cells' temperatures of the old solar panels from the IR thermograms. The difference in the solar cells' temperature (ΔT) extracted from the IR thermograms of each solar panel was calculated according to Equation (4):

$$\Delta T = T_{cH} - T_{cL}, \quad (5)$$

where T_{cH} is the solar cell with the highest temperature and T_{cL} is the solar cell with the lowest temperature. ΔT due to PID for the 3 modules which have been affected by PID

ranges from 7 °C to 15 °C. Our results for these old panels agrees with the ΔT values reported in literature [15]. The reported ΔT values for solar panels affected by PID is in the range of ca. 7.5–30 °C depending on the severity of the PID effect [3,15,16].

Table 3. Difference in temperature (ΔT) of the solar cells with the highest temperature (T_{cH}) and lowest temperature (T_{cL}) for PV Modules A, B, and C which were affected by PID.

PV Module	Temperature (°C)		ΔT (°C)
	T_{cH}	T_{cL}	
A	36.9	29.5	7.4
B	51.3	36.7	14.6
C	49.5	40.5	9.0

The severity of the PID effect depends on the module materials- antireflection coating and encapsulation [6,21], module configuration [3,11], climatic conditions such as temperature and humidity [4,24,26], and voltage stress [5,9].

3.4. Temperature Coefficient Characteristics

Figure 8 illustrates the characteristics of the relative temperature coefficients of P_{max} (β_{Pmax}), V_{oc} (β_{Voc}), I_{sc} (β_{Jsc}), FF (β_{FF}), V_{mpp} (β_{Vmpp}), and I_{mpp} (β_{Jmpp}) of solar panels A, B, and C. Figure 8 compares the variation of each electrical parameter from the average value measured in the year 2021. Degradation in electrical parameters stems from the degradation in the relative temperature coefficients of PV modules [25,26,29]. That is, PID increases recombination in the emitter region of the solar cell [10,11,17–19], and this leads to a drop in the V_{oc} [25]. A drop in the V_{oc} influence the temperature characteristics of the solar panel [30,37]. A change in the V_{oc} accounts for more than 80% of the temperature sensitivity of the PV modules [25]. From Figure 8, the main root causes for the observed degradation in P_{max} became clearer, unlike in Figure 5. That is, the β_{Voc} and β_{Vmpp} of the PV modules are the main underlying causes of the P_{max} degradation.

Figure 8 also suggests that degradation in β_{FF} is significantly responsible for the degradation in P_{max}. This supports the earlier observation in Figure 5 that the solar panels affected by PID experience large resistance losses. Degradation in β_{Voc} and β_{FF} due to PID effects were reported earlier [20,26,28]. Figure 8 also shows clear outliers for β_{Pmax}, β_{Voc}, β_{Vmpp}, and β_{FF}. It could be seen that the majority of these outliers are correlated to higher temperature coefficient values which results from higher T_m [38]. This suggests that when T_m increases, the reliability of PV modules affected by PID decreases, as observed elsewhere [24,39].

Conceptually, the effect of T_m on P_{max} could be derived from Equation (3) because PV module parameters (V_{oc}, I_{sc}, FF) depend strongly on T_m [30,32,40]. Hence, could be represented as

$$\beta_{Pmax} = \beta_{Voc} + \beta_{Jsc} + \beta_{FF} \quad (6)$$

Interestingly, each of these parameters in Equation (5) depends on different loss mechanisms in the PV module [25,35]. These loss mechanisms mainly depend on the effects of different defects and fault mechanisms on the charge carrier generation-recombination balances at maximum power point (MPP) [35,41]. Therefore, Equations (1) and (5) could be represented in terms of V_{mpp} and I_{mpp} as

$$\beta_{Pmax} = \beta_{Vmpp} + \beta_{Jmpp} \quad (7)$$

The V_{oc} is the charge carrier generation-recombination characteristic of a solar panel. So, the temperature sensitivity of a solar panel improves when the V_{oc} increases [40,42]. Moreover, the β_{Voc} of a PV module accounts for 80–90% of the β_{Pmax} of the PV module [25]. For that matter, and inferring from Equation (6), β_{Vmpp} could be assumed to have the greatest impact on the degradation in β_{Pmax}, and hence, on P_{max} degradation. The corre-

lation of values of β_{Voc} and β_{Vmpp} to β_{Pmax} degradation is shown in Figure 9. In Figure 9, the regression plots show high correlation of $R^2 > 90$ and $R^2 > 88$ for β_{Voc} and β_{Vmpp}, respectively. Indeed, Figures 8 and 9 suggest that the root causes of degradation in the PV modules affected by PID are more accurately profiled using their temperature coefficients. They suggest that the β_{Voc} and β_{Vmpp} are the underlying factors for the degradation in the efficiency of the solar panels.

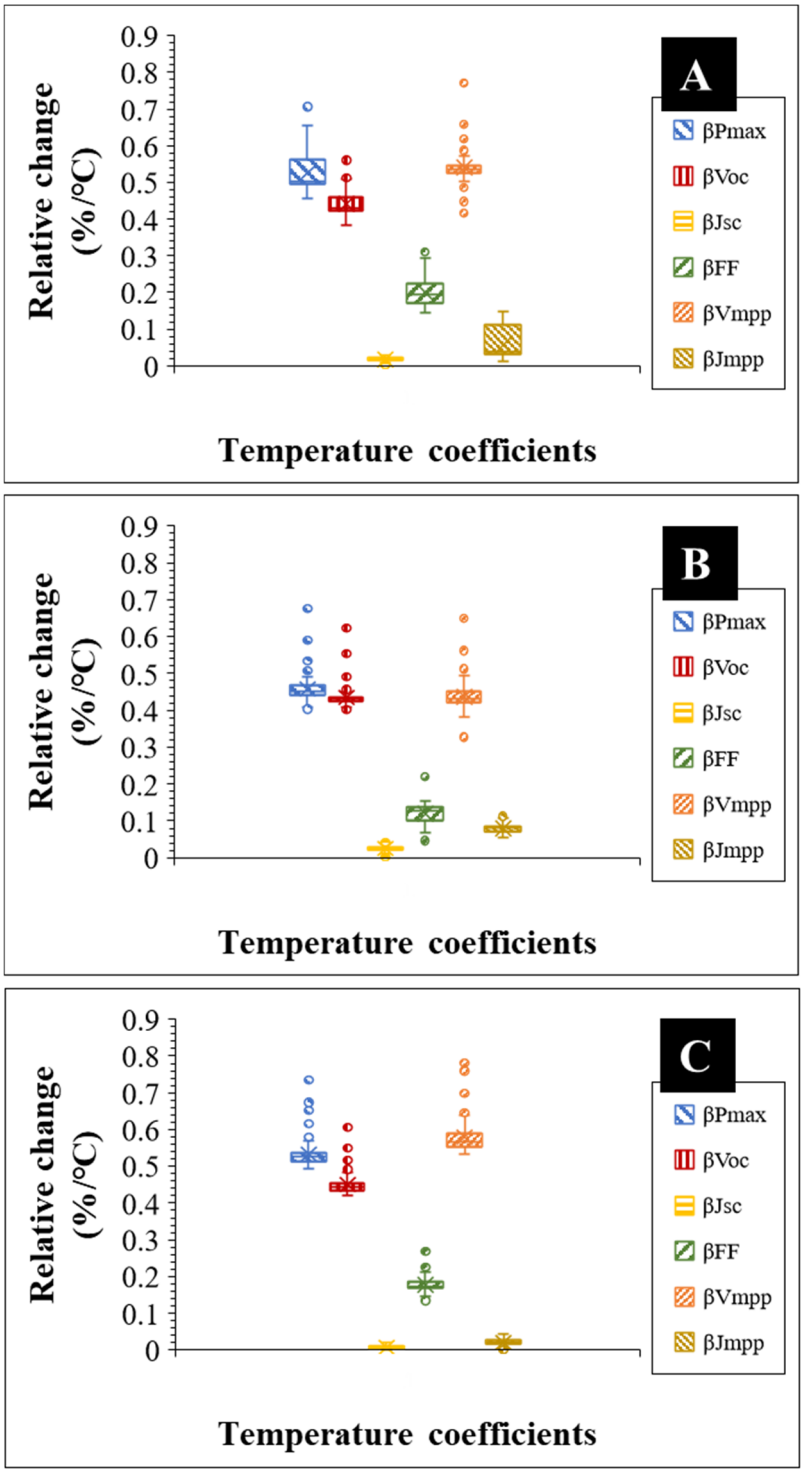

Figure 8. Change in the relative temperature coefficients of the 3 solar panels under STC conditions. The tips of the boxes show the interquartile ranges. The internal lines show the median and the *x*-marks show the mean. Measurements were done under 960 W/m^2–1060 W/m^2 in-plane irradiance conditions.

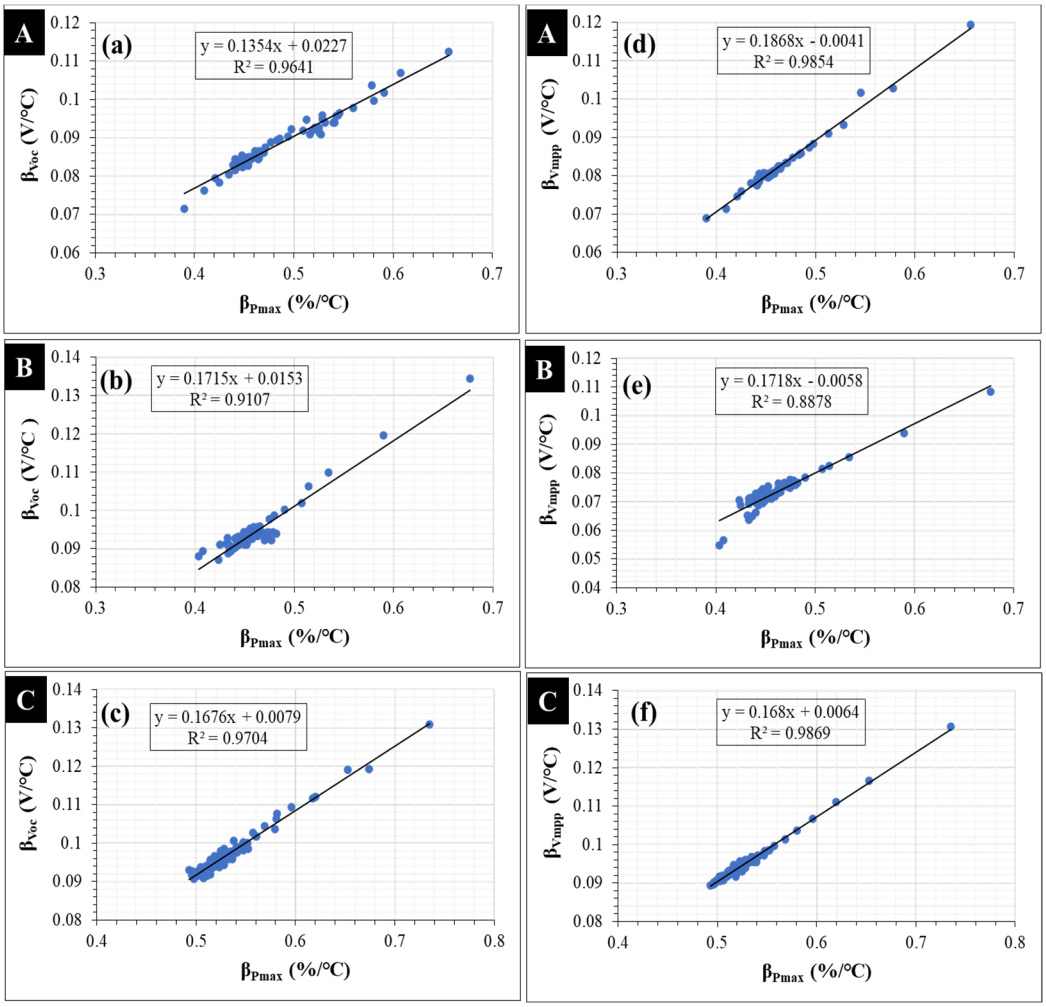

Figure 9. Dependence of absolute β_{Pmax} on absolute β_{Voc} (**a**–**c**) and β_{Vmpp} (**d**–**f**) of the 3 solar panels affected by PID. R^2 indicates the degree of correlation.

In Figure 9a,d, the slopes of the regression plots for PV Module A are 0.14 and 0.19 for β_{Voc} and β_{Vmpp}, respectively. However, the average of the slope values of β_{Voc} and β_{Vmpp} is ca. 0.17. Interestingly, from Figure 9, the slopes of PV Modules B and C for both β_{Voc} and β_{Vmpp} regression plots are ca. 0.17. Also, the slopes of the regression plots for β_{Vmpp} are closer to the average 0.17 value. Hence, we can predict the behaviour of β_{Pmax} better with the slopes of β_{Vmpp} for the PV modules affected by PID. This suggests that a unit change in β_{Pmax} is accounted for by 0.17 change in either β_{Voc} or β_{Vmpp} for each PV module affected by PID. The values of the slopes from the regression plots of β_{Pmax} versus β_{Voc} and β_{Vmpp} can be used to monitor PID severity in solar panels. On that basis, Figure 9 suggest that the effect of PID on PV Module A is the severest. Another observation from Figure 9d–f is that, when β_{Pmax} is zero, then by extrapolation, β_{Vmpp} will be ca. 0.4%/°C, 0.6%/°C, and 0.6%/°C for PV Module A, B, and C, respectively. These values are very close to the β_{Vmpp} values for the 3 field-aged PV modules in Table 4.

Table 4. Average temperature coefficients of the 3 solar panels.

PV Module	Temperature Coefficient (%/°C)					
	β_{Voc}	β_{Jsc}	β_{FF}	$\beta_{\eta m}$	β_{Vmpp}	β_{Jmpp}
A	−0.4	0.02	−0.2	−0.5	−0.5	**−0.06**
B	−0.4	0.03	−0.1	−0.5	−0.4	**−0.09**
C	−0.4	0.01	−0.2	−0.5	−0.5	**−0.02**

Figure 10 shows the profiles of the temperature coefficients of efficiency, η_m ($\beta_{\eta m}$) of the 3 solar panels. The average of $\beta_{\eta m}$ has been found to be ca. −0.5%/°C for the 3 field-aged PV modules. In literature, the $\beta_{\eta m}$ for mc-Si PV modules is 0.4%/°C [25,26,28–30]. PV modules in good conditions are expected to be more efficient when PV module operating temperature (T_m) drops below 25 °C [30,32]. However, by extrapolation when T_m is equal to zero, η_m < 13%, refer to Figure 10. This is characteristic of degraded PV modules which are suffering from resistive losses [20,26,40].

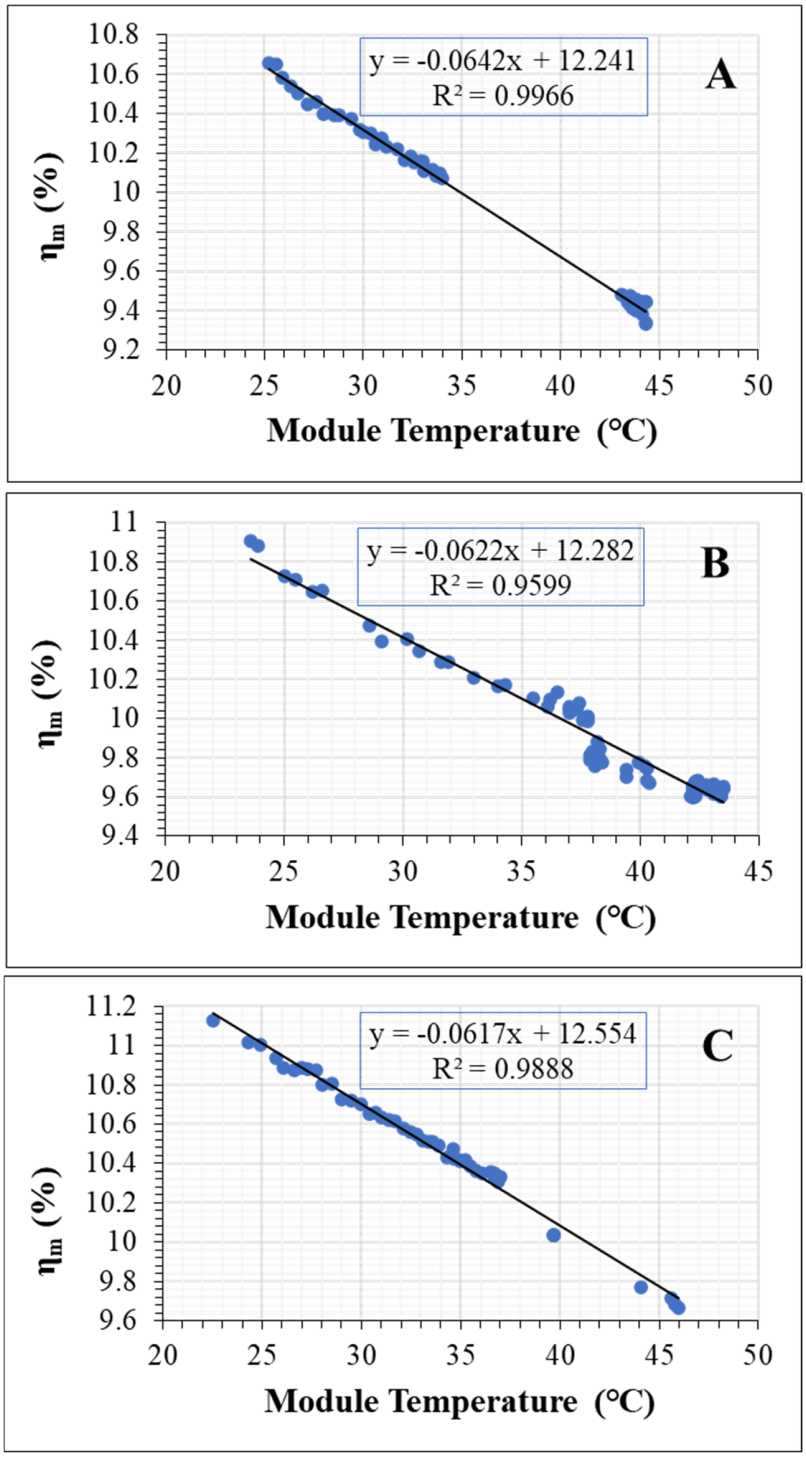

Figure 10. The relationship among the efficiency (η_m), module temperature, and temperature coefficient of efficiency($\beta_{\eta m}$) of the 3 solar panels. R^2 indicates the degree of correlation.

The average temperature coefficients of the 3 solar panels are shown in Table 4. The observed values for β_{Voc} and β_{Vmpp} agree with the values reported by King et al. [30] for conventional mc-Si PV modules. However, the β_{Voc} values are far less than the $-1.2\%/^{\circ}C$ reported by Cheng et al. [38] and the $-0.7\%/^{\circ}C$ reported by Wang et al. [24] for PV modules affected by PID. On the other hand, the β_{Jsc} values are relatively lower for these PV modules that have been affected by PID than observed elsewhere [24,38]. This suggests that in solar panels affected by PID, the contribution from thermally generated electrons towards the overall current density is less.

In addition, the β_{FF} values for the 3 field-aged PV modules are lower than the $-0.4\%/^{\circ}C$ reported for β_{FF} by Cheng et al. [38] for solar panels affected by PID. The fact that the modules studied by Cheng et al. [38] were aged artificially whiles our modules were field aged should not be ignored. Comparison of lab and field results are to be done with caution due to factors of uncertainty [43,44]. Our values are also in a good agreement with the $-0.2\%/^{\circ}C$ reported for β_{FF} by Wang et al. [24] for solar panels affected by PID.

Interestingly, the β_{Jmpp} of all the 3 solar panels show negative values. It is believed that the negative β_{Jmpp} values observed for the 3 old solar panels is due to the large leakage current experienced by PV modules affected by PID. Indeed, earlier investigation on the temperature profiles of solar panels affected by optical degradation indicated that negative β_{Jmpp} values are likely when the electrical circuit of the module is affected. However, in such cases, the β_{Jmpp} values are relatively higher and the β_{Jsc} values are by far higher as well. In that investigation, one of the modules affected by optical degradation showed a β_{Jmpp} of $-0.01\%/^{\circ}C$ and an average β_{Jsc} for the 3 modules was $0.05\%/^{\circ}C$. Moreover, a majority of the darker cells in the EL and warmer cells in IR thermal images were closer to the edge of the PV module affected by optical degradation. This suggests that the module in question is affected by at least optical degradation and PID. It is known that PID can lead to optical degradation and vice versa [5].

Furthermore, an earlier investigation on some of the solar panels under partial shading conditions, negative β_{Jmpp} values were observed for the modules investigated. However, under partial shading conditions, beside the peculiar I-V characteristics, the degradation in the P_{max} strongly depends mainly on the degradation in the β_{Jmpp} and β_{FF}. Moreover, under partial shading conditions, the effect on $\beta_{\eta m}$ becomes far higher, with $\beta_{\eta m} \geq -0.6\%/^{\circ}C$ [33]. It therefore suggests that an effective, quick, and reliable method of detecting PID in solar panels is to monitor the temperature coefficients, and specifically, the β_{Jmpp} of PV panels.

4. Conclusions

The temperature coefficients of 20 years old field-aged mc-Si PV modules which were affected by PID were investigated. Characterization utilized I-V characterization, EL imaging, IR thermal imaging, and temperature coefficient profiling. The results showed that the field-aged PV modules were indeed affected by PID. EL images acquired under $0.1I_{sc}$ indoor conditions show degraded darker cells located closer to the perimeter of the PV modules. The weak signal of the cells closer to the edge of the modules is due to strong ohmic shunting of the solar cells with the PV module's Al- frame. In the IR thermal images acquired under clear sky conditions, majority of the warmer cells (hotspots) were seen closer to the perimeter of the modules. In addition, areas closer to the negative terminals were also observed to be warmer than areas closer to the positive terminals. Our results show that the module ΔT due to PID ranges from 7 °C to 15 °C for the 3 old solar panels.

The modules show an average degradation of 0.5%/year in both I_{sc} and V_{oc}, 1.2%/year in P_{max}, and 0.3%/year in fill factor. For the 3 field-aged PV panels, the average degradation in the V_{mpp} and I_{mpp} were 0.7% and 0.6% per year, respectively. It turns out that the key underlying causes for PID in the field-aged PV modules and the subsequent degradation is degradation in V_{oc}, V_{mpp}, and FF. The average temperature coefficients of $\beta_{\eta m}$, β_{Voc}, β_{Jsc}, β_{FF}, β_{Jmpp}, and β_{Vmpp} were found to be $-0.5\%/^{\circ}C$, $-0.4\%/^{\circ}C$, $0.02\%/^{\circ}C$, $-0.2\%/^{\circ}C$, $-0.06\%/^{\circ}C$, and $-0.5\%/^{\circ}C$, respectively. This shows that all the temperature coefficients of the field-aged modules have undergone some form of degradation. However, it was

observed that the β_{Voc}, β_{Vmpp}, and β_{FF} were the primary factors for the degradation in the P_{max} for the old solar PV panels affected by PID. This translated into an average 1.2%/year overall degradation in the efficiency of these modules.

Most interestingly, it was observed that solar panels affected by PID show negative β_{Jmpp} due to large leakage currents. Hence, PID could be detected decisively by monitoring the β_{Jmpp} of solar PV panels. These findings have the potential of enhancing the existing knowledge on defects and faults diagnostics in PV arrays.

Author Contributions: Conceptualization, O.K.S.; methodology, O.K.S.; validation, O.K.S.; investigation, O.K.S.; resources, T.O.S.; writing—original draft preparation, O.K.S.; writing—review and editing, T.O.S.; supervision, T.O.S.; funding acquisition, T.O.S. All authors have read and agreed to the published version of the manuscript.

Funding: This research was funded by the University of Agder, Norway.

Institutional Review Board Statement: Not applicable.

Informed Consent Statement: Not applicable.

Data Availability Statement: The data presented in this study are available on request from the corresponding author. The data are not publicly available at this time as the data also forms part of an ongoing study.

Acknowledgments: The authors acknowledge the continuous support of the University of Agder, Norway.

Conflicts of Interest: The authors declare no conflict of interest.

References

1. Segbefia, O.K.; Imenes, A.G.; Saetre, T.O. Moisture ingress in photovoltaic modules: A review. *Sol. Energy* **2021**, *224*, 889–906. [CrossRef]
2. Luo, W.; Khoo, Y.S.; Hacke, P.; Naumann, V.; Lausch, D.; Harvey, S.P.; Singh, J.P.; Chai, J.; Wang, Y.; Aberle, A.G.; et al. Potential-induced degradation in photovoltaic modules: A critical review. *Energy Environ. Sci.* **2017**, *10*, 43–68. [CrossRef]
3. Köntges, M.; Kurtz, S.; Packard, C.; Jahn, U.; Berger, K.A.; Kato, K. *Performance and Reliability of Photovoltaic Systems: Subtask 3.2: Review of Failures of Photovoltaic Modules: IEA PVPS Task 13: External Final Report IEA-PVPS*; International Energy Agency, Photovoltaic Power Systems Programme: Paris, France, 2014.
4. Hoffmann, S.; Koehl, M. Effect of humidity and temperature on the potential-induced degradation. *Prog. Photovolt.* **2014**, *22*, 173–179. [CrossRef]
5. Hacke, P.; Terwilliger, K.; Smith, R.; Glick, S.; Pankow, J.; Kempe, M.; Bennett, S.K.I.; Kloos, M. System voltage potential-induced degradation mechanisms in PV modules and methods for test. In Proceedings of the 2011 37th IEEE Photovoltaic Specialists Conference, Seattle, WA, USA, 19–24 June 2011; pp. 000814–000820.
6. Virtuani, A.; Annigoni, E.; Ballif, C. One-type-fits-all-systems: Strategies for preventing potential-induced degradation in crystalline silicon solar photovoltaic modules. *Prog. Photovolt.* **2019**, *27*, 13–21. [CrossRef]
7. Lausch, D.; Naumann, V.; Breitenstein, O.; Bauer, J.; Graff, A.; Bagdahn, J.; Hagendorf, C. Potential-Induced Degradation (PID): Introduction of a Novel Test Approach and Explanation of Increased Depletion Region Recombination. *IEEE J. Photovolt.* **2014**, *4*, 834–840. [CrossRef]
8. Pingel, S.; Frank, O.; Winkler, M.; Daryan, S.; Geipel, T.; Hoehne, H.; Berghold, J. Potential induced degradation of solar cells and panels. In Proceedings of the 2010 35th IEEE Photovoltaic Specialists Conference, Honolulu, HI, USA, 20–25 June 2010; pp. 002817–002822.
9. Hylský, J.; Strachala, D.; Vyroubal, P.; Čudek, P.; Vaněk, J.; Vanýsek, P. Effect of negative potential on the extent of PID degradation in photovoltaic power plant in a real operation mode. *Microelectron. Reliab.* **2018**, *85*, 12–18. [CrossRef]
10. Naumann, V.; Geppert, T.; Grosser, S.; Wichmann, D.; Krokoszinski, H.J.; Werner, M.; Hagendorf, C. Potential-induced degradation at interdigitated back contact solar cells. In Proceedings of the 4th International Conference on Crystalline Silicon Photovoltaics (Siliconpv 2014), 's-Hertogenbosch, The Netherlands, 25–27 March 2014; Volume 55, pp. 498–503.
11. Yamaguchi, S.; Yamamoto, C.; Ohshita, Y.; Ohdaira, K.; Masuda, A. Influence of emitter position of silicon heterojunction photovoltaic solar cell modules on their potential-induced degradation behaviors. *Sol. Energy Mater. Sol. Cells* **2020**, *216*, 110716. [CrossRef]
12. Schütze, M.; Junghänel, M.; Koentopp, M.B.; Cwikla, S.; Friedrich, S.; Müller, J.W.; Wawer, P. Laboratory study of potential induced degradation of silicon photovoltaic modules. In Proceedings of the 2011 37th IEEE Photovoltaic Specialists Conference, Seattle, WA, USA, 19–24 June 2011; pp. 000821–000826.

13. Kwembur, I.M.; McCleland, J.L.C.; van Dyk, E.E.; Vorster, F.J. Detection of Potential Induced Degradation in mono and multi-crystalline silicon photovoltaic modules. *Phys. B—Condens. Matter* **2020**, *581*, 411938. [CrossRef]
14. Carolus, J.; Tsanakas, J.A.; van der Heide, A.; Voroshazi, E.; de Ceuninck, W.; Daenen, M. Physics of potential-induced degradation in bifacial p-PERC solar cells. *Sol. Energy Mater. Sol. Cells* **2019**, *200*, 109950. [CrossRef]
15. Jahn, U.; Herz, M.; Köntges, M.; Parlevliet, D.; Paggi, M.; Tsanakas, I. *Review on Infrared and Electroluminescence Imaging for PV Field Applications: International Energy Agency Photovoltaic Power Systems Programme: IEA PVPS Task 13, Subtask 3.3: Report IEA-PVPS T13-12*; International Energy Agency: Paris, France, 2018.
16. Tsanakas, J.A.; Ha, L.; Buerhop, C. Faults and infrared thermographic diagnosis in operating c-Si photovoltaic modules: A review of research and future challenges. *Renew. Sustain. Energy Rev.* **2016**, *62*, 695–709. [CrossRef]
17. Köntges, M.; Oreski, G.; Jahn, U.; Herz, M.; Hacke, P.; Weiß, K.-A. *Assessment of Photovoltaic Module Failures in the Field: International Energy Agency Photovoltaic Power Systems Programme: IEA PVPS Task 13, Subtask 3: Report IEA-PVPS T13-09*; International Energy Agency: Paris, France, 2017.
18. Halm, A.; Schneider, A.; Mihailetchi, V.D.; Koduvelikulathu, L.J.; Popescu, L.M.; Galbiati, G.; Chu, H.F.; Kopecek, R. Potential-induced degradation for encapsulated n-type IBC solar cells with front floating emitter. In Proceedings of the 5th International Conference on Silicon Photovoltaics, SiliconPV 2015, Konstanz, Germany, 25–27 March 2015; pp. 356–363.
19. Swanson, R.; Cudzinovic, M.; DeCeuster, D.; Desai, V.; Jürgens, J.; Kaminar, N.; Mulligan, W.; Rodrigues-Barbarosa, L.; Rose, D.; Smith, D. The surface polarization effect in high-efficiency silicon solar cells. In Proceedings of the 15th PVSEC, Shanghai, China, 10–15 October 2005.
20. Naumann, V.; Lausch, D.; Hahnel, A.; Bauer, J.; Breitenstein, O.; Graff, A.; Werner, M.; Swatek, S.; Grosser, S.; Bagdahn, J.; et al. Explanation of potential-induced degradation of the shunting type by Na decoration of stacking faults in Si solar cells. *Sol. Energy Mater. Sol. Cells* **2014**, *120*, 383–389. [CrossRef]
21. Oh, K.S.; Bae, S.; Lee, K.J.; Kim, D.; Chan, S.I. Mitigation of potential-induced degradation (PID) based on anti-reflection coating (ARC) structures of PERC solar cells. *Microelectron. Reliab.* **2019**, *100*, 113462. [CrossRef]
22. Masuda, A.; Akitomi, M.; Inoue, M.; Okuwaki, K.; Okugawa, A.; Ueno, K.; Yamazaki, T.; Hara, K. Microscopic aspects of potential-induced degradation phenomena and their recovery processes for p-type crystalline Si photovoltaic modules. *Curr. Appl. Phys.* **2016**, *16*, 1659–1665. [CrossRef]
23. Islam, M.A.; Hasanuzzaman, M.; Rahim, N.A. Investigation of the potential induced degradation of on-site aged polycrystalline PV modules operating in Malaysia. *Measurement* **2018**, *119*, 283–294. [CrossRef]
24. Wang, H.; Cheng, X.L.; Yang, H.; He, W.S.; Chen, Z.L.; Xu, L.H.; Song, D.Y. Potential-induced degradation: Recombination behavior, temperature coefficients and mismatch losses in crystalline silicon photovoltaic power plant. *Sol. Energy* **2019**, *188*, 258–264. [CrossRef]
25. Dupré, O.; Vaillon, R.; Green, M.A. Physics of the temperature coefficients of solar cells. Solar energy materials and solar cells. *Sol. Energy Mater. Sol. Cells* **2015**, *140*, 92–100. [CrossRef]
26. Dubey, R.; Batra, P.; Chattopadhyay, S.; Kottantharayil, A.; Arora, B.M.; Narasimhan, K.; Vasi, J. Measurement of temperature coefficient of photovoltaic modules in field and comparison with laboratory measurements. In Proceedings of the 2015 IEEE 42nd Photovoltaic Specialist Conference (PVSC), New Orleans, LA, USA, 14–19 June 2015; pp. 1–5.
27. Kaden, T.; Lammers, K.; Moller, H.J. Power loss prognosis from thermographic images of PID affected silicon solar modules. *Sol. Energy Mater. Sol. Cells* **2015**, *142*, 24–28. [CrossRef]
28. Mattei, M.; Notton, G.; Cristofari, C.; Muselli, M.; Poggi, P. Calculation of the polycrystalline PV module temperature using a simple method of energy balance. *Renew. Energy* **2006**, *31*, 553–567. [CrossRef]
29. Skoplaki, E.; Palyvos, J.A. On the temperature dependence of photovoltaic module electrical performance: A review of efficiency/power correlations. *Sol. Energy* **2009**, *83*, 614–624. [CrossRef]
30. King, D.L.; Kratochvil, J.A.; Boyson, W.E. Temperature coefficients for PV modules and arrays: Measurement methods, difficulties, and results. In Proceedings of the Conference Record of the Twenty Sixth IEEE Photovoltaic Specialists Conference-1997, Anaheim, CA, USA, 29 September–3 October 1997; pp. 1183–1186.
31. Evans, D.; Florschuetz, L. Terrestrial concentrating photovoltaic power system studies. *Sol. Energy* **1978**, *20*, 37–43. [CrossRef]
32. Segbefia, O.K.; Imenes, A.G.; Sætre, T.O. Outdoor Fault Diagnosis of Field-Aged Multicrystalline Silicon Solar Modules. In Proceedings of the 37th EU PVSEC, Lisbon, Portugal, 7–11 September 2020.
33. Segbefia, O.K.; Paudyal, B.R.; Burud, I.; Sætre, T.O. Temperature Coefficients of Photovoltaic Modules under Partial Shading Conditions. In Proceedings of the 38th EU PVSEC, Lisbon, Portugal, 6–10 September 2021; pp. 1180–1186.
34. Islam, M.A.; Hasanuzzaman, M.; Rahim, N.A. A comparative investigation on in-situ and laboratory standard test of the potential induced degradation of crystalline silicon photovoltaic modules. *Renew. Energy* **2018**, *127*, 102–113. [CrossRef]
35. Green, M.A. General temperature dependence of solar cell performance and implications for device modelling. *Prog. Photovolt. Res. Appl.* **2003**, *11*, 333–340. [CrossRef]
36. Buerhop, C.; Schlegel, D.; Niess, M.; Vodermayer, C.; Weigmann, R.; Brabec, C.J. Reliability of IR-imaging of PV-plants under operating conditions. *Sol. Energy Mater. Sol. Cells* **2012**, *107*, 154–164. [CrossRef]
37. Segbefia, O.K.; Imenes, A.G.; Burud, I.; Sætre, T.O. Temperature profiles of field-aged multicrystalline silicon photovoltaic modules affected by microcracks. In Proceedings of the 2021 IEEE 48th Photovoltaic Specialists Conference (PVSC), Fort Lauderdale, FL, USA, 20–25 June 2021; pp. 0001–0006.

38. Cheng, X.; Dong, Y.; Yang, T.; Zhou, T.; Wang, H.; Yu, H. Investigation on Temperature Coefficients of Crystalline Silicon Solar Modules before and after Potential-induced Degradation. In Proceedings of the 2019 IEEE 46th Photovoltaic Specialists Conference (PVSC), Chicago, IL, USA, 16–21 June 2019; pp. 1942–1945.
39. Spataru, S.; Hacke, P.; Sera, D.; Packard, C.; Kerekes, T.; Teodorescu, R. Temperature-dependency analysis and correction methods of in situ power-loss estimation for crystalline silicon modules undergoing potential-induced degradation stress testing. *Prog. Photovolt.* **2015**, *23*, 1536–1549. [CrossRef]
40. Green, M.; Emery, K.; Blakers, A. Silicon solar cells with reduced temperature sensitivity. *Electron. Lett.* **1982**, *18*, 97–98. [CrossRef]
41. Dupré, O.; Vaillon, R.; Green, M.A. Experimental assessment of temperature coefficient theories for silicon solar cells. *IEEE J. Photovolt.* **2015**, *6*, 56–60. [CrossRef]
42. Zhao, J.; Wang, A.; Robinson, S.; Green, M. Reduced temperature coefficients for recent high-performance silicon solar cells. *Prog. Photovolt. Res. Appl.* **1994**, *2*, 221–225. [CrossRef]
43. Reise, C.; Müller, B.; Moser, D.; Belluardo, G.; Ingenhoven, P. *Uncertainties in PV System Yield Predictions and Assessments*; IEA: Paris, France, 2018.
44. Berghold, J.; Koch, S.; Böttcher, A.; Ukar, A.; Leers, M.; Grunow, P. Potential-induced degradation (PID) and its correlation with experience in the field. *Photovolt. Int.* **2013**, *19*, 87–93.

Paper G

Temperature profiles of field-aged multicrystalline silicon photovoltaic modules affected by microcracks by O.K. Segbefia, A.G. Imenes, I. Burud, and T.O. Sætre. Published in the 48th IEEE Photovoltaic Specialists Conference (2021).

Temperature profiles of field-aged multicrystalline silicon photovoltaic modules affected by microcracks

Oscar Kwame Segbefia[1], Anne Gerd Imenes[1], Ingunn Burud[2], Tor Oskar Sætre[1]

[1]Department of Engineering Sciences, University of Agder, 4879 Grimstad, Norway
[2]Department of Physics, Norwegian University of Life Sciences, 1433 Ås, Norway

2021 IEEE 48th Photovoltaic Specialists Conference (PVSC) | 978-1-6654-1922-2/21/$31.00 ©2021 IEEE | DOI: 10.1109/PVSC43889.2021.9518939

***Abstract*—In this work, the temperature sensitivities of field-aged multicrystalline silicon PV modules affected by microcracks are investigated. It is found that the temperature coefficient of efficiency of all modules has increased more than 10 times over the 20 years period, mainly due to a degradation in the temperature coefficients of fill factor. Temperature coefficient of efficiency of PV modules affected by microcracks changed from -0.44 %/°C to -1.51 %/°C under solar irradiance conditions at 1010 - 1030 W/m². Inconsistent values for the Evans–Floschuetz efficiency ratio versus temperature plots for the microcrack affected modules were also observed.**

Keywords— microcrack, temperature coefficient, degradation, efficiency, solar irradiation

I. INTRODUCTION

Photovoltaic (PV) modules are reliable tools for harvesting clean electrical energy from the sun [1]. However, studies show that PV modules can degrade in the field under multiple environmental or climatic stressors such as temperature, humidity, ultraviolet radiation, wind, and snow loads [2-4]. This leads to reliability issues such as cracks, moisture ingress, corrosion, delamination, discolouration, and optical degradation which can induce power degradation in these devices [3, 5, 6]. In particular, high module temperature apart from inducing varieties of reliability issues can also cause direct power loss in PV plants [7-9]. A good understanding of the temperature behaviour of PV modules under varying conditions can give insight into the efficiency status of the PV module [10-13]. That is, temperature profiles of PV plants can be an indicator for PV module reliability status during field operation [8, 10-12, 14-17].

Several articles have documented the general behaviour of solar cells and modules due to their characteristic temperature sensitivities which lead to corresponding power losses [7-10]. However, these studies were on the PV cell or module without detailed investigation into the contribution of individual defects (such as microcracks) to the general temperature sensitivity of PV cells or modules. Usually, cracks in PV cells result in localized heating or joule heating due to ohmic resistance at cracked areas of the solar cell or module during operation which can influence the temperature sensitivity [5, 6, 18]. PV modules affected by microcracks can be conveniently detected with luminescence and fluorescence techniques without any destruction to the PV module or string for temperature sensitivity studies [18, 19].

Data on the temperature coefficients of PV modules with a variety of defect and fault modes under different climatic conditions can be integrated into models for monitoring and forecasting the performance and reliability status of PV plants. This will reduce investigation time and overhead cost on investment and boost confidence in PV energy resources.

The present work investigates the temperature sensitivity of field-aged multicrystalline silicon PV modules affected by solar cell microcracks. Temperature coefficients of the affected modules were studied under varying irradiance conditions.

II. METHODS

In the year 2000, 50 silicon multicrystalline PV modules were installed in Dømmesmoen, Grimstad in Norway. In 2011, the electrical performance data were documented, and the PV modules were decommissioned and kept securely for research purposes [20]. At the time, the PV modules' average power dropped to 90.16 W from 100 W. The electrical performance data of sampled 43 field-aged PV modules were used to evaluate the corresponding temperature sensitivities and degradation states of these modules. Microcrack affected modules among the field-aged modules were identified using ultraviolet fluorescence (UV-F) and infrared (IR) thermal imaging. The selected PV modules were then taken through a comprehensive study and results compared with other "fairly good" field-aged PV modules.

Data for the analysis is acquired by way of current-voltage (I-V) curve electrical performance measurements on all 43 field-aged PV modules using a handheld I-V 500w I-V Curve Tracer, following the procedure according to the IEC 60904- 1 series. These measurements provided information on the maximum power (P_{max}), open circuit and maximum power point voltage (V_{oc}, V_{mpp}), short circuit and maximum power point current (I_{sc}, I_{mpp}), fill factor (FF), irradiance, and module temperature characteristics of each module at Standard Test Conditions (STC). STC specifies cell temperature of 25 °C, an irradiance of 1000 W/m² and air mass 1.5 (AM1. 5) spectrum for commercial PV modules. Measurements were done at varying irradiance conditions (540 - 1060 W/m²), and the I-V tracer used converts all measurements to STC automatically. This means the operating conditions were optimally resolved by the device to minimize errors in measuring and recording data. The relative temperature coefficients were determined using regression plots

of electrical parameters (P_{max}, V_{oc}, I_{sc}, FF) and PV module's efficiency versus PV module's temperature.

UV-F images of the 43 field-aged PV modules were taken in a dark room using a TROTEC® LED UV TorchLight 15F ($\lambda \approx$ 365 nm) together with a Wolf eyes FD45 spectrum filter. The IEA prescribed procedure was followed in the investigation [5]. Additionally, sampled 15 field-aged PV modules were taken through infrared measurements using the Fluke Ti400 Infrared Camera by following the IEA prescribed procedure [18]. Measurements were done in a dark room using a power supply to forward bias the current into the solar cells. IR thermal images were taken after 0.5, 2, and 5 minutes when current flow was initiated.

III. Results and Discussion

Table I summarizes the results from the I-V measurement of the field-aged PV modules and indicates that over the 20 years period, the efficiency of the modules has reduced significantly due to degradation in V_{oc}, I_{sc}, and FF. n is the representative number of PV modules for a specific category. One of the most common defects and fault modes that affected these field-aged modules is solar cell microcracks (crack* as in Table I). 3 of the field-aged PV modules affected by characteristic microcracks have been chosen for this investigation and are shown in Fig. 1 with their infrared thermal and I-V characteristics. However, the PV modules show a similar trend, but slightly varying magnitude, in the degradation in electrical parameters since they have different crack characteristics. Hence, only one is represented in Table I to illustrate a common trend of power degradation.

TABLE I. Average Electrical Parameters of PV Modules.

Year	n	P_{max} (W)	V_{oc} (V)	I_{sc} (A)	FF (%)	η (%)
2000	50	100	21.60	6.70	70.00	13.00
2011	20	90.16	21.46	6.18	68.00	11.80
2020	43	78.19	19.71	6.04	65.65	10.10
Crack*	1	75.60	19.62	6.07	63.00	9.80

Cracks are known to be detrimental to PV module power outputs [5] and this is confirmed in Table I. It appears that the extent to which an electrical parameter is affected depends on the type and severity of the microcracks in the module [6]. Fig. 1 shows a PV module that appears to be affected by microcracks. The microcracks in Fig. 1a appears to affect the I_{sc} more than the V_{oc}, while the ones in Fig. 1b affect the V_{oc} more than the I_{sc}, see Fig. 1e However, the modules with the microcrack patterns in Figs. 1a and 1c show a FF of 65 % each with varying P_{max} values of 77.43 W and 77.97 W, respectively. This might be due to the number, nature, and position of the microcracks in the PV module [5]. However, the module with the microcracks in Fig. 1b (which is represented as Crack* in Table I) shows the least P_{max} among all the modules affected by microcracks. This suggests that the star shaped microcracks has a higher possibility of damaging the metal grids and hence pose higher danger to power loss [5, 6].

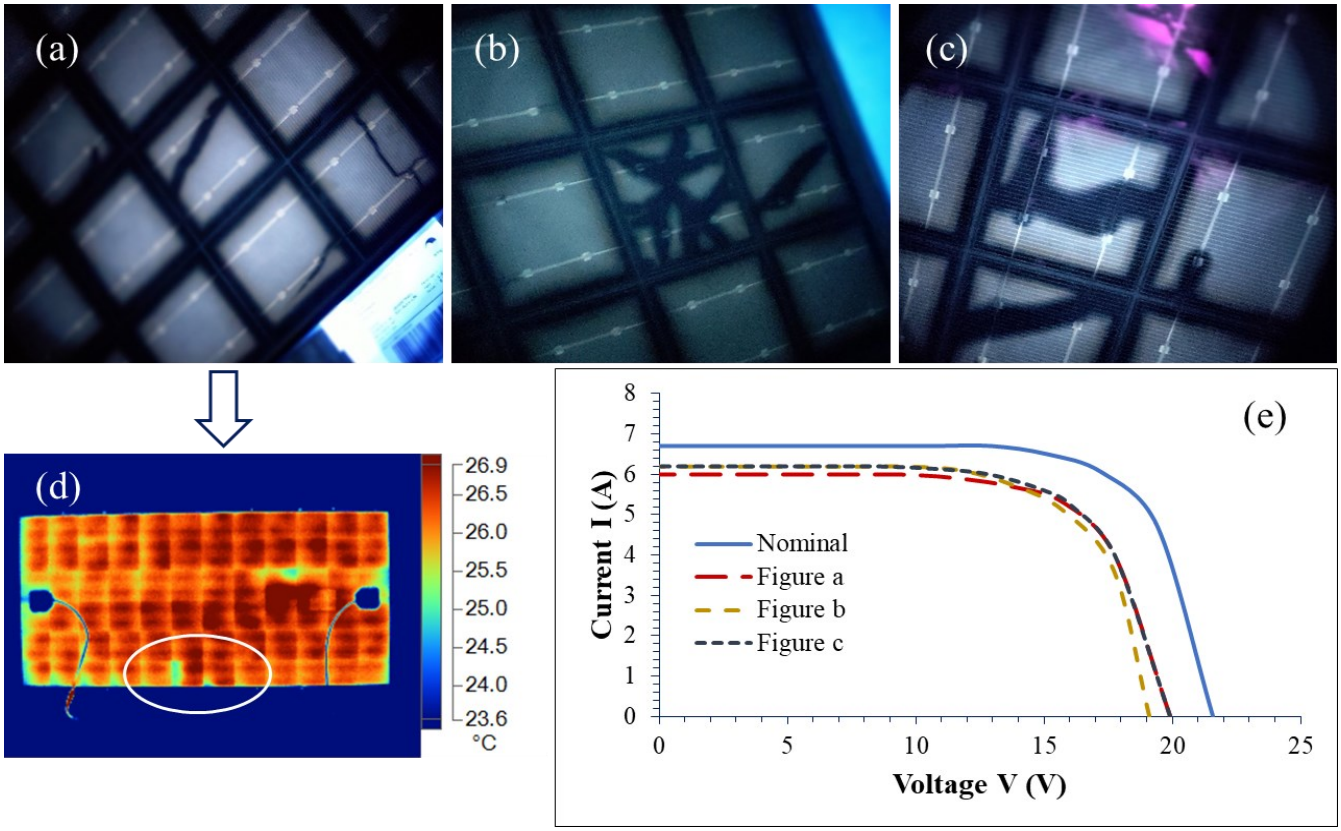

Fig. 1. (a) - (c) UV-F images of some of the field-aged PV modules showing patterns of different kinds of microcracks, (d) IR thermal image showing the corresponding portion, in a circle, of (a), (e) respective I-V curves of (a) - (c).

Interestingly, infrared thermal images of most of the field-aged PV modules show fairly uniform temperature distribution over the modules investigated. However, there were areas which show slightly higher temperature profiles but did not show any direct correlation with the cracks observed. Instead, areas affected by cracks show lower temperature profiles, refer to the area in circle in Fig. 1d. The change in temperature (ΔT) over the PV modules due to defects induced hotspots is ca. 6.0 ± 2 °C, which agrees with observation elsewhere [19]. According to Tsanakas et al. (2016), this range of ΔT values correlate to optical degradation: delamination and discolouration of encapsulants [19]. Solar cell cracks with ΔT as high as ~40 °C are critical to power output [18, 19]. However, for these field-aged modules, areas with cracks show ΔT of ~2.0 ± 0.5 °C, although neighboring cells show higher ΔT values. The higher temperature profiles of the nearby cells indicate that these cracks are certainly critical to current flow in the affected regions and PV module. However, the lower ΔT values for the areas affected by cracks suggests that these modules might be suffering from other failure mechanisms (e.g., moisture ingress) as well. Moisture degraded areas influence the flow of current to the affected areas which also impacts the ΔT profiles [18].

The effect of these cracks on the PV modules' electrical characteristics are illustrated in Fig. 1e. The microcracks in Fig. 1a separate the cells completely and damage the metal grids, and hence, affect both the I_{sc} and V_{oc} almost equally. In contrast, the microcracks in in Fig. 1b affect the V_{oc} more than the I_{sc}. Interestingly, indeed, the cracks in Fig. 1c assumes a power characteristics, combining the best characteristics of the PV modules affected by cracks in Fig. 1a and Fig. 1b.

To understand the contribution of microcracks to the overall power degradation further, a comprehensive temperature profiling of the modules was undertaken with a special focus on the modules that have been affected by microcracks. The influence of operating temperature on the power degradation in PV module is well documented in literature [7, 8, 12, 15, 17]. Interestingly, PV cell parameters (V_{oc}, I_{sc}, FF) apparently vary linearly with temperature [7, 8, 13]. Hence, the overall temperature coefficient of P_{max} (β_{Pmax}) depends directly on the temperature coefficients of V_{oc} (β_{Voc}), short circuit current density (β_{Jsc}), and fill factor (β_{FF}) [7, 8, 13]:

$$\beta_{Pmax} = \beta_{Voc} + \beta_{Jsc} + \beta_{FF} \quad (1)$$

Yet, each of the parameters in (1) depends on different loss mechanisms based on the generation and recombination characteristics in the PV module at P_{max} [8]. Box and whisker diagrams of temperature sensitivities of all the field-aged PV modules and a selected number of the modules which are suffering from microcracks are presented in Fig. 2. In Fig. 2, it appears that the absolute variation in the temperature coefficients of PV modules is greater under lower irradiance conditions than under STC conditions. This suggests that modules operating under lower irradiance conditions can be susceptible to higher degradation rates as observed elsewhere [12, 17]. However, more investigations with more extended data are under way to better understand the behaviour of these modules under lower irradiance conditions, especially as illustrated in Fig. 2c. Efforts will be made to understand the observation in Fig. 2c as regards its deviation from (1).

It has also been observed that current density is more affected at higher irradiance conditions (>1020 W/m^2) due to local hotspots created by defects. This is largely manifested in β_{FF} degradation [8], see Fig. 2d. In addition, Fig. 2 suggests that the increase in the temperature coefficient of power (β_{Pmax}) is mainly due to the corresponding increase in the temperature coefficient of fill factor (β_{FF}). β_{FF} is also known to be a function of the temperature coefficients of open circuit voltage (β_{Voc}) and short circuit current density (β_{Jsc}) [7, 8]. Increased β_{Voc} and β_{Jsc} characteristics are known to be a function of parasitic resistance losses which affect the fill factor [7]. The fill factor is a measure of the quality of the contacts [8], hence, a high β_{FF} in these PV modules suggests a possible degradation in the PV materials such as the solar cell and corrosion of metal grids [18].

Fig. 2c suggests that under lower irradiance conditions, the variation in β_{Jsc} is almost negligible unlike what is observed in Fig. 2a under similar conditions. It also appears from Fig. 2c that the contribution of β_{Voc}, β_{Jsc}, and β_{FF} to β_{Pmax} variation is minimal in modules affected by cracks under low irradiance conditions. However, at STC, the absolute variation of β_{FF} is almost equivalent to the absolute variation in β_{Pmax}. The high absolute variation in β_{FF} can be traced to the obvious material degradation in cracked solar cells, see Fig. 2. Also, the relative proportions of the temperature coefficients in Fig. 2c appears to deviate from Equation (1) as microcracks influence the loss mechanisms. Another observation from Figs. 2c and 2d suggests that the temperature sensitivity of PV modules affected by microcracks is identical under STC conditions significantly and approaches a minimum value. In Figs. 2a and 2b, the average absolute variation in β_{Pmax} reduced to 0.35 % which is far higher than the 0.14 % improvement in β_{Pmax} in Figs. 2c and 2d. It is obvious then that the major underlying factor for the degradation in both β_{Pmax} and β_{FF} is the β_{Voc} degradation (the greatest victim of high temperature sensitivity), which usually comes from shunt losses due to the junction quality of the solar cells [8]. It therefore suggests that in cold climates, power losses from I_{sc} degradation dominates while V_{oc} degradation dominates power losses in warm climates for PV modules affected by microcracks.

The influence of the temperature coefficient on the efficiency of the field-aged PV modules is shown in Fig. 3, with evolution of the (a) Evans–Floschuetz efficiency ratio (η_m/η_{Tref}) [16] and (b) normalized efficiency with operating temperature. η_{Tref} is the module efficiency at reference temperature at 25 °C. The Evans–Floschuetz efficiency ratio versus temperature plot can be used to determine the reference temperature coefficient of efficiency of PV modules. The efficiency (η_m) of the PV modules was computed by multiplying the nominal module efficiency (η=13.00 %) with the ratio of the normalized P_{max} and the nominal P_{max} (100 W). Fig. 3a reflects the calculated nominal temperature sensitivity (β_{ref}) of the modules when they were in a relatively good condition and their β_{ref} in their current condition is depicted in Fig. 3b.

That is, we can assume that the nominal temperature coefficient of efficiency of the PV modules (β_{ref}) was ca. -0.44 %/°C in the year 2000 and has now increased to ca. -5.68 %°C, almost 10 times. We also realized that the β_{ref} could be estimated from the ratio of the β_{Pmax} (the slope of the P_{max}-temperature plot) and P_{ref} (reference P_{max}) of the PV modules.

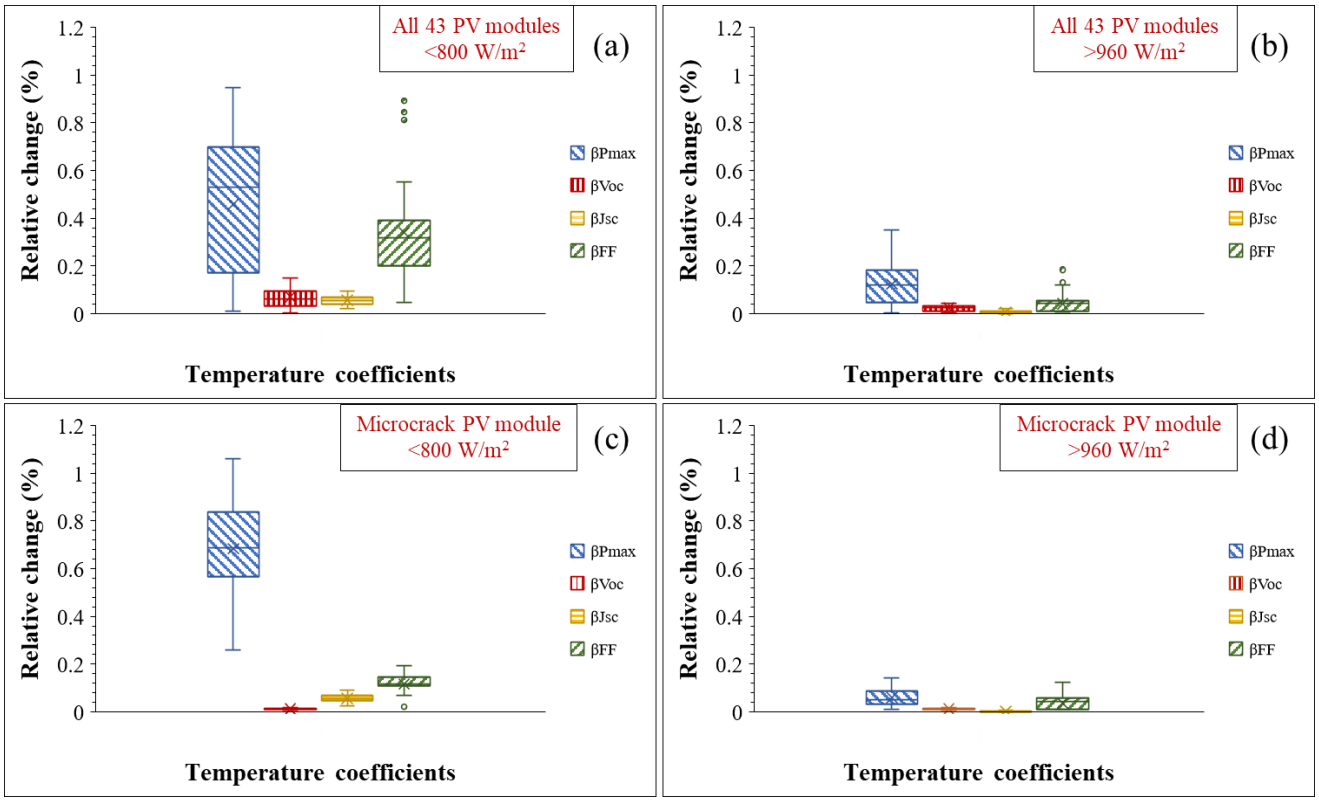

Fig. 2. Evolution of temperature coefficients of (a)-(b) all field-aged PV modules and (c)-(d) PV modules affected by microcracks. (a) & (c) and (b) & (d) were done under irradiance conditions at 540 - 790 W/m^2 and 960 - 1060 W/m^2, respectively. The ends of the boxes are the lower and upper quartiles (interquartile range), the internal lines and x-marks indicate the median and mean, respectively. The y-axis is the absolute difference between the average value measured in 2020 and each temperature point value, *x* measured in 2020.

That is

$$\beta_{ref} = \frac{\beta_{Pmax}}{P_{ref}} \qquad (2)$$

Under lower temperature or irradiance conditions, the effect of the temperature coefficient of module's normalized efficiency ($\beta_{\eta m}$) on the efficiency of good modules is relatively lower [8, 12]. This is because the temperature sensitivity of a PV module depends on material properties and technology. T_0, the temperature at which the efficiency of a PV module reduces to zero is introduced in modelling [15, 21]. 270 °C has been adapted for crystalline silicon solar cells [16]. According to Evans and Florschuetz (1978), β_{ref} is related to T_0 and the reference module temperature (T_{ref}), which is typically 25 °C, as [16]

$$\beta_{ref} = \frac{1}{T_0 - T_{ref}} \qquad (3)$$

It should be pointed out, however, that T_0 typically is an extrapolated value given by data at lower temperatures. This may introduce errors and values of T_0 should this be adopted carefully. Eq. (3) tells us that a higher β_{ref} correlates to a lower T_0, because T_{ref} is constant for a given PV module [15]. From (3), a PV module with an absolute β_{ref} ca. 0.44 %/°C will have $T_0 \approx 252$ °C. However, Fig. 3b suggests that the average efficiency of the field-aged PV modules approximates to zero at ~210 °C which indicates possible module degradation. This suggests that T_0 could be lower for PV modules affected by cracks. T_0 could be far lower depending on the types and number of defects and faults modes that affect the module [8, 15]. For instance, modules affected by microcracks tend to show positive $\beta_{\eta m}$ even under lower irradiance conditions, see Fig. 4. In addition, the average efficiency of the modules reduces to ~11.93 % at 0 °C, see Fig. 3b. However, according to Fig. 4b, η_m reduces to ~10.50 % at 0 °C for PV modules affected by microcracks.

It has also been observed that PV modules affected by microcracks show either negative or positive temperature coefficients of efficiency. A distribution of such observation is shown in Fig. 4a (without a trendline). This could be due to the different crack characteristics, codefects, and/or operating conditions of the PV modules. The magnitude of the $\beta_{\eta m}$ of PV modules with different crack characteristics also differs slightly. The temperature coefficient of efficiency profiles of the PV module affected by the microcrack pattern in Fig. 1a is shown in Fig. 4. Under higher irradiance conditions (ca. STC), all PV modules affected by microcracks show the same trend in the $\beta_{\eta m}$, but with varying magnitudes, see Fig. 4b. Clearly, more investigations are needed to make any valid conclusions on the $\beta_{\eta m}$ behaviour of these PV modules, especially under lower irradiance conditions.

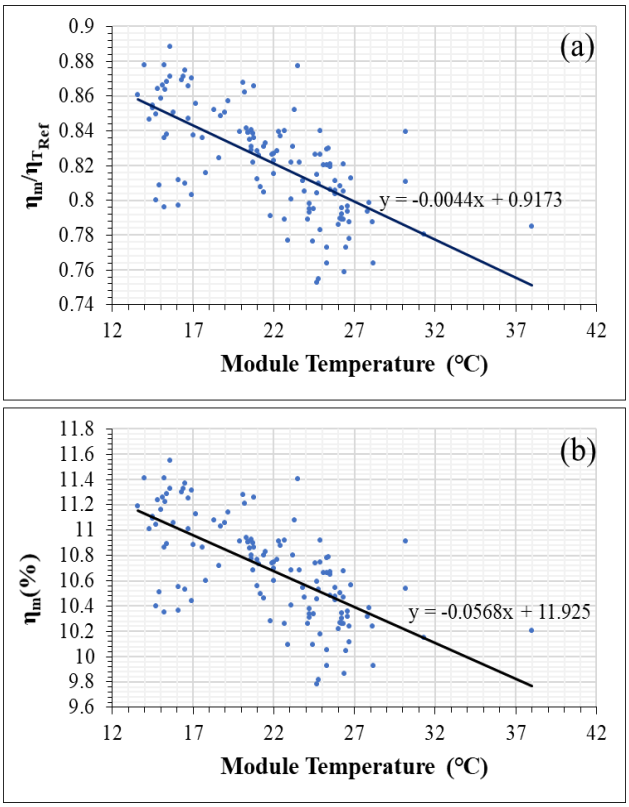

Fig. 3. A graph of temperature sensitivity of efficiency ($\beta_{\eta m}$) of the field-aged PV modules using the (a) Evans–Floschuetz efficiency ratio and (b) normalized PV module efficiency (η_m) under STC.

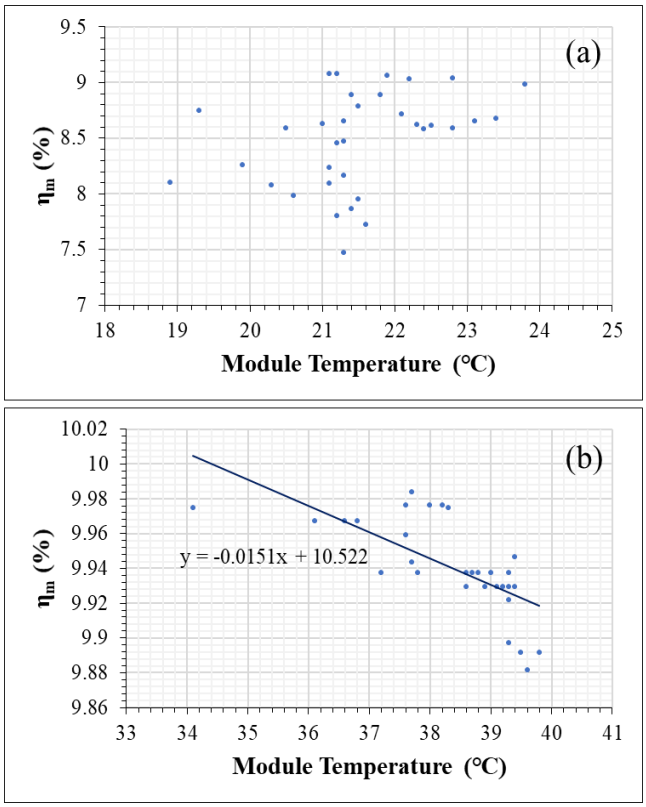

Fig. 4. The temperature coefficients of efficiency of a typical PV module affected by microcracks at irradiance conditions at (a) 710 - 860 W/m^2 and (b) 1010 - 1030 W/m^2.

However, in Fig. 4b, the $\beta_{\eta m}$ of PV modules affected by microcracks show ca. -1.51 %/°C under solar irradiance conditions at 1010 - 1030 W/m^2. This implies that the effect of microcracks on the ultimate temperature sensitivity of PV modules is dependent on climatic, and hence, irradiance conditions. The cause of the significant degradation in efficiency of the field-aged modules is due to fundamental losses (absorption, recombination, thermalization, resistance, etc.) which increase with temperature [7, 8].

The recombination losses include radiative, Shockley-Read-Hall, Auger, surface, and shunts processes [7]. As temperature increases, the equilibrium carrier concentration is altered due to an increased recombination rate. This results into a negative temperature sensitivity of the absorption-emission rate balance of the solar cell, which is the source of higher temperature sensitivity of PV cells and modules [8]. That is, most degradation mechanisms including solar cell microcracks influence the temperature sensitivity of PV modules, and hence their power output and lifespan.

IV. Conclusion

The temperature sensitivity of field-aged multicrystalline silicon PV modules has been examined with a special focus on PV modules affected by solar cell microcracks. The temperature coefficients of efficiency ($\beta_{\eta m}$) of the field-aged modules were found to degrade from ca. -0.44 %/°C to ca. -5.68 %/°C over 20 years. However, the temperature coefficients of PV modules affected by microcracks appears to depend on the crack characteristics, codefects, and/or operating conditions. Under lower irradiance conditions, a trend in the $\beta_{\eta m}$ of the PV modules is inconsistent and can be better understood with more data. Yet, PV modules affected by microcracks show a $\beta_{\eta m}$ of ca. -1.51 %/°C under solar irradiance conditions at 1010 - 1030 W/m^2. It is observed that under higher irradiance conditions (>1020 W/m^2), modules affected by microcracks experience greater hotspots effects (due to instability in current flow) which affect the fill factor. This might be due to the higher voltage gain by virtue of high resistive losses experienced by modules affected by microcracks.

It is also observed that increase in β_{FF} is the major root cause for the increase in the overall temperature sensitivities of the field-aged modules, especially those that have been affected by microcracks. In addition, it has been found that estimation of the β_{ref} of PV modules affected by microcracks from a plot of the Evans–Floschuetz efficiency ratio and temperature may not always be valid. However, investigations are under way to explore these observations comprehensively. Finally, it is suggested that the temperature sensitivity of PV modules could be useful for detecting and analyzing defects and fault modes such as solar cell microcracks.

Acknowledgment

The authors acknowledge the continuous support of the University of Agder, Norway.

REFERENCES

[1] M. Halwachs et al., "Statistical evaluation of PV system performance and failure data among different climate zones," Renewable Energy, vol. 139, pp. 1040-1060, 2019.

[2] D. C. Jordan and S. R. Kurtz, "Photovoltaic degradation rates—an analytical review," Progress in photovoltaics: Research and Applications, vol. 21, no. 1, pp. 12-29, 2013.

[3] D. C. Jordan, J. H. Wohlgemuth, and S. R. Kurtz, "Technology and climate trends in PV module degradation," National Renewable Energy Lab.(NREL), Golden, CO (United States), 2012.

[4] J. Wohlgemuth, T. Silverman, D. C. Miller, P. McNutt, M. Kempe, and M. Deceglie, "Evaluation of PV module field performance," in 2015 IEEE 42nd Photovoltaic Specialist Conference (PVSC), 2015: IEEE, pp. 1-7.

[5] M. Köntges, S. Kurtz, C. Packard, U. Jahn, K. A. Berger, and K. Kato, Performance and reliability of photovoltaic systems: subtask 3.2: Review of failures of photovoltaic modules: IEA PVPS task 13: external final report IEA-PVPS. International Energy Agency, Photovoltaic Power Systems Programme, 2014.

[6] S. Kajari-Schršder, I. Kunze, and M. Kšntges, "Criticality of cracks in PV modules," Energy Procedia, vol. 27, pp. 658-663, 2012.

[7] M. A. Green, "General temperature dependence of solar cell performance and implications for device modelling," Progress in Photovoltaics: Research and Applications, vol. 11, no. 5, pp. 333-340, 2003.

[8] O. Dupré, R. Vaillon, and M. A. Green, "Physics of the temperature coefficients of solar cells," Solar energy materials and solar cells, vol. 140, pp. 92-100, 2015.

[9] K. Emery et al., "Temperature dependence of photovoltaic cells, modules and systems," in Conference Record of the Twenty Fifth IEEE Photovoltaic Specialists Conference-1996, 1996: IEEE, pp. 1275-1278.

[10] R. Dubey et al., "Measurement of temperature coefficient of photovoltaic modules in field and comparison with laboratory measurements," in 2015 IEEE 42nd Photovoltaic Specialist Conference (PVSC), 2015: IEEE, pp. 1-5.

[11] J. Zhao, A. Wang, S. Robinson, and M. Green, "Reduced temperature coefficients for recent high‐performance silicon solar cells," Progress in Photovoltaics: Research and Applications, vol. 2, no. 3, pp. 221-225, 1994.

[12] C. Whitaker, T. Townsend, H. Wenger, A. Iliceto, G. Chimento, and F. Paletta, "Effects of irradiance and other factors on PV temperature coefficients," in The Conference Record of the Twenty-Second IEEE Photovoltaic Specialists Conference-1991, 1991: IEEE, pp. 608-613.

[13] C. Berthod et al., "Temperature sensitivity of multicrystalline silicon solar cells," IEEE Journal of Photovoltaics, vol. 9, no. 4, pp. 957-964, 2019.

[14] H. Zondag, "Flat-plate PV-Thermal collectors and systems: A review," Renewable and Sustainable Energy Reviews, vol. 12, no. 4, pp. 891-959, 2008.

[15] E. Skoplaki and J. A. Palyvos, "On the temperature dependence of photovoltaic module electrical performance: A review of efficiency/power correlations," Solar energy, vol. 83, no. 5, pp. 614-624, 2009.

[16] D. Evans and L. Florschuetz, "Terrestrial concentrating photovoltaic power system studies," Solar Energy, vol. 20, no. 1, pp. 37-43, 1978.

[17] D. L. King, J. A. Kratochvil, and W. E. Boyson, "Temperature coefficients for PV modules and arrays: measurement methods, difficulties, and results," in Conference record of the twenty sixth IEEE Photovoltaic Specialists Conference-1997, 1997: IEEE, pp. 1183-1186.

[18] U. Jahn, M. Herz, M. Köntges, D. Parlevliet, M. Paggi, and I. Tsanakas, Review on infrared and electroluminescence imaging for PV field applications: International Energy Agency Photovoltaic Power Systems Programme: IEA PVPS Task 13, Subtask 3.3: report IEA-PVPS T13-12: 2018. International Energy Agency, 2018.

[19] J. A. Tsanakas, L. Ha, and C. Buerhop, "Faults and infrared thermographic diagnosis in operating c-Si photovoltaic modules: A review of research and future challenges," Renewable and sustainable energy reviews, vol. 62, pp. 695-709, 2016.

[20] D. Verma, M. Tayyib, T. O. Saetre, and O.-M. Midtgård, "Outdoor Performance of 10 year Old a-Si and Poly-Si Modules in southern Norway conditions," in 2012 38th IEEE Photovoltaic Specialists Conference, 2012: IEEE, pp. 002368-002371.

[21] H. Garg and R. Agarwal, "Some aspects of a PV/T collector/forced circulation flat plate solar water heater with solar cells," 1995.

Paper H

Temperature Coefficients of Photovoltaic Modules under Partial Shading Conditions
by O.K. Segbefia, B.R. Paudyal, I. Burud, and T.O. Sætre. Published in the 38th EU PVSEC (2021).

TEMPERATURE COEFFICIENTS OF PHOTOVOLTAIC MODULES UNDER PARTIAL SHADING CONDITIONS

Oscar Kwame Segbefia[1], Basant Raj Paudyal[1], Ingunn Burud[2], Tor Oskar Sætre[1]
[1]Department of Engineering Sciences, University of Agder, 4879 Grimstad, Norway
[2]Department of Physics, Norwegian University of Life Sciences, 1433 Ås, Norway

ABSTRACT: Partial shading of photovoltaic (PV) modules leads to mismatch losses which cause local hotspots. Hotspots can lead to various failure mechanisms, hence, power degradation in PV plants. This work investigates the temperature sensitivity of field-aged multicrystalline silicon PV modules under uniform partial shading conditions. Thermal images suggest that hotspots are localized to busbars at the shaded area. The results estimate that, the temperature coefficient of V_{mpp} (β_{Vmp}) of the field-aged PV modules under STC ranges from -0.41 %/°C to -0.48 %/°C. However, under partial shading conditions, the absolute variation in the β_{Vmp} is >2.00 %/°C for the 3 field-aged PV modules studied. The results for the temperature coefficient of I_{mpp} (β_{Jmp}) ranges from ca. -0.08 %/°C to 0.01 %/°C and ca. -1.00 %/°C to -0.90 %/°C under non-shading and partial shading conditions, respectively. However, the severity of the temperature sensitivity under partial shading conditions also depends on the degradation state of the PV modules.
Keywords: partial shading, hotspot, temperature coefficient, efficiency

1 INTRODUCTION

Solar irradiance conditions influence the overall efficiency, reliability, and lifespan of photovoltaic (PV) devices [1-3]. Partial shading has been identified as a denominator for the reduction in power and degradation in PV plants since the 1990s [4]. Shading of PV plants is an issue in all parts of the world, depending on the local surroundings/obstacles near the installation, even under optimum solar irradiation conditions [5]. However, shading can be more difficult to avoid and have a greater impact on yield at high latitudes, due to low solar incidence angles in the winter [4]. Partial shading, one of the main factors of mismatch losses, induces several reliability issues in PV devices [6]. These reliability issues can lead to significant power losses and accelerated degradation in PV plants, which in turn can lead to higher levelized cost of energy (LCOE) of PV power [6, 7].

Usually, mismatched cells due to shading may become reverse biased which leads to local hot spots or joule heating [1]. Hence, PV modules are equipped with bypass diodes to mitigate the effect of reverse biasing [7]. Yet, it has been discovered that bypass diodes are limited in preventing hot spots entirely [7, 8]. The problem of local hot spots in PV plants is yet to be fully resolved [1, 6].

Algorithms based on the Shockley diode equation have been propounded for optimizing the performance of bypass diodes via maximum power point tracking (MPPT) mechanisms [5, 6]. When a bypass diode is activated, a whole string of solar cells is typically bypassed. The I-V curve will also change in a characteristic way, giving a substantial loss of power for the panel.

A good understanding of the influence of temperature variations under different climatic (irradiance) conditions is vital for developing mitigation techniques for monitoring PV module performance and reliability [2, 3, 5, 7, 9, 10]. According to Sun et al. (2018, 2019), the Suns-V_{mpp} technique could be used to monitor and diagnose PV array failure mechanisms at maximum power point (MPP) [11]. However, the method depends on data sheet information (which is sometimes unavailable in the case of old PV plants) and numerical fitting. Recently, a technique was proposed for detecting partial shading effects on a PV module using the temperature corrected maximum power point current - voltage (I_{mpp} - V_{mpp}) curves [8].

Temperature profiles of PV devices can be an indicator of the degradation state of a PV module during field operation [10, 12-14]. Temperature effects on PV devices are accurately accounted for by their temperature coefficients: change in device parameter per unit change in temperature [15, 16]. Hence, incorporating the temperature coefficients of PV modules under partial shading conditions in mitigation algorithms for diagnosing and resolving mismatch losses, due to hot spots has the potential of improving diagnostic methods for solar power plants [15, 16].

In the present work, the temperature sensitivity of field-aged multicrystalline silicon PV modules operating under custom-made uniform partial shading conditions is investigated. The temperature sensitivity of the modules is investigated by evaluating the temperature coefficients of maximum power, efficiency, open circuit voltage, short circuit current and maximum power point voltage (V_{mpp}) and current (I_{mpp}) of the field-aged PV modules under both non-shading and partial shading conditions.

2 METHODS

In the year 2000, 50 multicrystalline silicon PV modules were installed in Dømmesmoen, Grimstad (58.3447° N, 8.5949° E) in Norway. In 2011, the PV modules were decommissioned and kept securely for research purposes. At the time of decommissioning, the PV modules' average power was 90.16 W: about 10 % decrease in nominal power of 100 W [17]. In the present work, the temperature profiles of 3 of these field-aged PV modules have been investigated under a custom-made uniform partial shading conditions in real field operating conditions. In the entire investigation, the shade is placed at the same position of the PV module, shading ca. 3.40 % of the PV module area. With this shading procedure, 6 cells out of the 72 cells of the PV module are partially shaded simultaneously during each measurement. Each PV module consists of (12 x 2) series connected cells and 3 substrings with 2 bypass diodes.

The 3 sampled PV modules were taken through infrared (IR) thermal imaging using the Fluke Ti400 Infrared Camera by following the IEA prescribed procedure [18]. Measurements were done in real field outdoor conditions for both non-shading and shading

conditions. IR thermal images were taken after the PV modules were sun soaked for at least 30 minutes.
Performance data for the analysis was acquired by way of current-voltage (I-V) curve electrical measurements on the 3 selected field-aged PV modules using a handheld I-V 500w I-V Curve Tracer, following the procedure according to the IEC 60904- 1. These measurements provided information on the maximum power (P_{max}), open circuit and maximum power point voltage (V_{oc}, V_{mpp}), short circuit and maximum power point current (I_{sc}, I_{mpp}), fill factor (FF), irradiance, and module temperature characteristics of each module at Standard Test Conditions (STC). STC specifies cell temperature of 25 °C, an irradiance of 1000 W/m^2 and air mass 1.5 (AM 1. 5) spectrum for commercial PV modules. Measurements were done at varying irradiance conditions (700 - 1030 W/m^2), and the I-V tracer used converts all measurements to STC automatically. This means the operating conditions were optimally resolved by the device to minimize errors in measuring and recording data. However, the guidelines of IEC 61853-1 were observed to ensure that the wind speed and in-plane irradiance (G_I) during the measurements were within the recommended limits to ensure the accuracy of the results [19]. The distribution of the G_I and PV module operating temperature (T_m) during the measurement period is illustrated in Figure 1. The in-plane irradiance during the studies ranges from 700 - 1030 W/m^2, which falls within the ± 30 % limit specified in the IEC 61853-1 protocol [19].

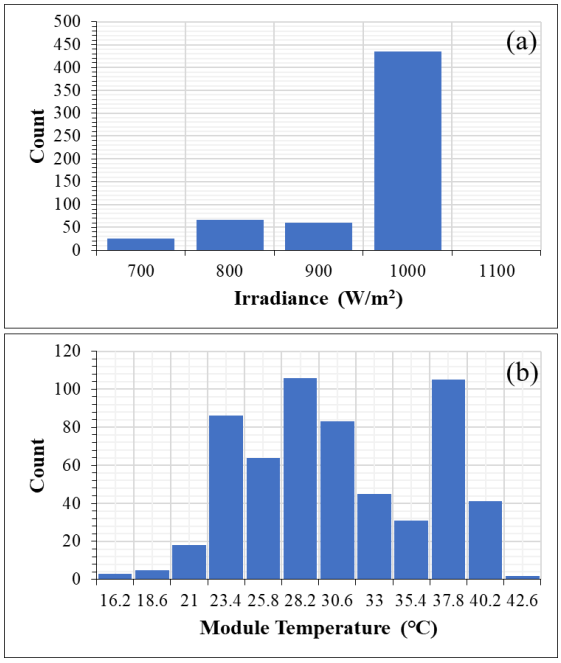

Figure 1: Distribution of (a) in-plane irradiance and (b) the corresponding PV module operating temperatures during the outdoor studies.

The model for terrestrial PV module assumes that, under MPP conditions, the PV module efficiency (η_m) assumes a linear function of the PV module temperature (T_m) and in-plane solar irradiance (G_I) [13, 20, 21].

$$\eta_m = \eta_r[1 - \beta_r(T_m - T_r) + \gamma log_{10} G_I] \quad (1)$$

Where η_r and β_r are the module reference efficiency and temperature coefficient, respectively at reference temperature, T_r. γ is the solar radiation absorption coefficient: the ratio of transmitted to incident solar radiation. However, high solar absorptivity is desired of PV devices [22]. So, most often, the γ is considered negligible and taken as zero [13, 20, 21]. Hence, (1) approximates to

$$\eta_m = \eta_r[1 - \beta_r(T_m - T_r)] \quad (2)$$

The slope of the linear regression plot of η_m versus (T_m - T_r) in (2) gives $\eta_r\beta_r$. That is, a graph of a parameter x which obeys (2), versus T_m fits the linear equation $y = mx + c$, with a slope, m related to β_x and the intercept, $c = \eta_r$ as

$$\beta_x = {}^{m}/_{c} \quad (3)$$

The value from (3) gives the temperature coefficient of x (β_x) in °C^{-1} [23]. The relative temperature coefficients are determined using regression plots of the electrical parameters (P_{max}, V_{oc}, I_{sc}, FF, V_{mpp}, I_{mpp}, and η_m) versus T_m. The temperature coefficients of the PV modules under the partial shading and non-shading conditions are then compared.

3 RESULTS AND DISCUSSION

Table I summarizes the results from the current-voltage (I-V) measurement of one of the field-aged PV modules in its present state and indicates that over the 20 years period, the efficiency of the module has reduced significantly due to degradation in P_{max}, V_{oc}, I_{sc}, FF, V_{mpp}, I_{mpp}, and η_m. However, under partial shading conditions for the given case shown in Figure 2a, the power reduction was more than 60 % for the PV module.

Generally, P_{max} degradation for all the 3 PV modules investigated under partial shading (PS) conditions was more than 50 %. From Table I and Figure 2b, it seems partial shading conditions affect I_{sc} more than the V_{oc}. Even so, the degradation in P_{max} is directly related to the value of current and voltage at maximum power point, which are I_{mpp} and V_{mpp}, respectively. That is

$$P_{max} = I_{mpp} \cdot V_{mpp} \quad (4)$$

Under partial shading conditions, see Figure 2b, both I_{mpp} and V_{mpp} are far lower. According to Xiao et al. [24], 2020,

Table I: Average electrical parameters of field-aged PV module C in the year 2021 at STC. Measurements were done at 991 - 1019 W/m^2: 22.4 - 37.6 °C and 995 - 1027 W/m^2: 22.5 - 39.1 °C for non-shading and shading conditions, respectively.

Parameter	P_{max} (W)	V_{oc} (V)	I_{sc} (A)	V_{mpp} (V)	I_{mpp} (A)	FF (%)	η (%)
Data sheet	100	21.60	6.70	16.70	6.00	70	13.00
No shading	77.16	19.96	5.97	15.09	5.11	65	10.03
Partial shading	37.45	19.68	5.31	13.16	2.86	36	4.87

degraded Schottky contacts produce localized hotspots, which leads to bypass diode failure and hence, power degradation and possible permanent damage to panel. Degradation in P_{max} due to localized hotspots was also observed elsewhere [5, 9]. That is, the value of P_{max} reduces according to (4) when I_{mpp} and V_{mpp} decrease.

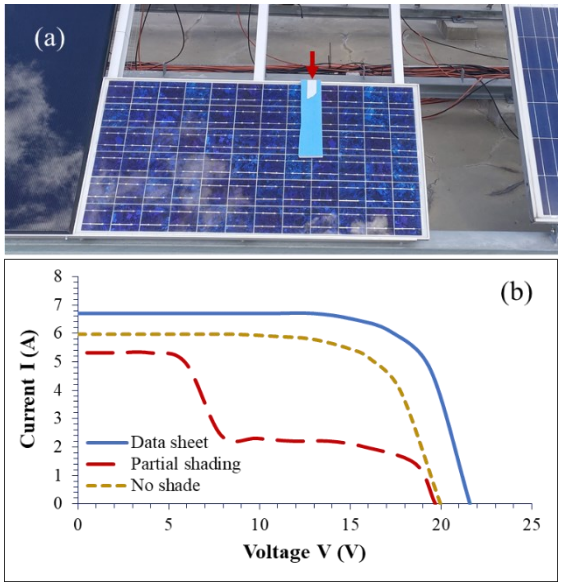

Figure 2: (a) Photographic image and (b) electrical profiles of a PV module C partially shaded intentionally during the investigation.

The P_{max} degradation as a result of lower I_{mpp} and V_{mpp} is known to be due to the temperature profiles of the PV modules under different shading conditions; which induces hotspots [3, 5]. In addition, the asymmetrical temperature distribution in PV modules can be a precursor for other degradation mechanisms which can affect the long-term performance reliability of PV modules [5, 7]. This is evident in the values reported in Table I. The values for both I_{mpp} and V_{mpp} are far lower under partial shading conditions.

The IR thermal images of the 3 field-aged PV modules are shown in Figure 3. The thermal profile of the modules under non-shading conditions varies for each PV module due to different defects and fault modes affecting each of the modules, see Figures 3a, 3b, and 3c. The defect cells show darker red colours in the thermal image due to localized hotspots [10]. Figures 3d, 3e, and 3f are the corresponding thermal images of PV modules A, B, and C, respectively under partial shading conditions. Figure 3 suggests that under partial shading conditions, hotspots are formed around the shaded area, but along the affected busbars. That is, in Figures 3d, 3e, and 3f, the hotspots are restricted to the upper left side of the PV module where the shade covers. The lower portion of the modules appears to be less affected due to the partial shading at the upper part of the module. This is because the busbars at the lower parts of the modules are not covered by the shade.

Another observation from Figure 3 is that, under partial shading conditions, formation of hotspots due to defects and fault modes decreases. This is because reversed biased current at the shaded area, hence, less or no current flows through the rest of the modules, including defect affected areas. This means that a combination of thermal imaging and shading could be used to isolate PV module material defects and fault modes from other defects such as soiling. This is because material defects will not show significant thermal signatures under partial shading conditions. In addition, the presence of defect and fault mode types can also influence the geometry or distribution of hotspots around the shade affected area of the PV module. The shape of the hotspots formed under partial shading conditions for the 3 modules is different and appears to depend on the type of defect at the shaded area, see Figure 3.

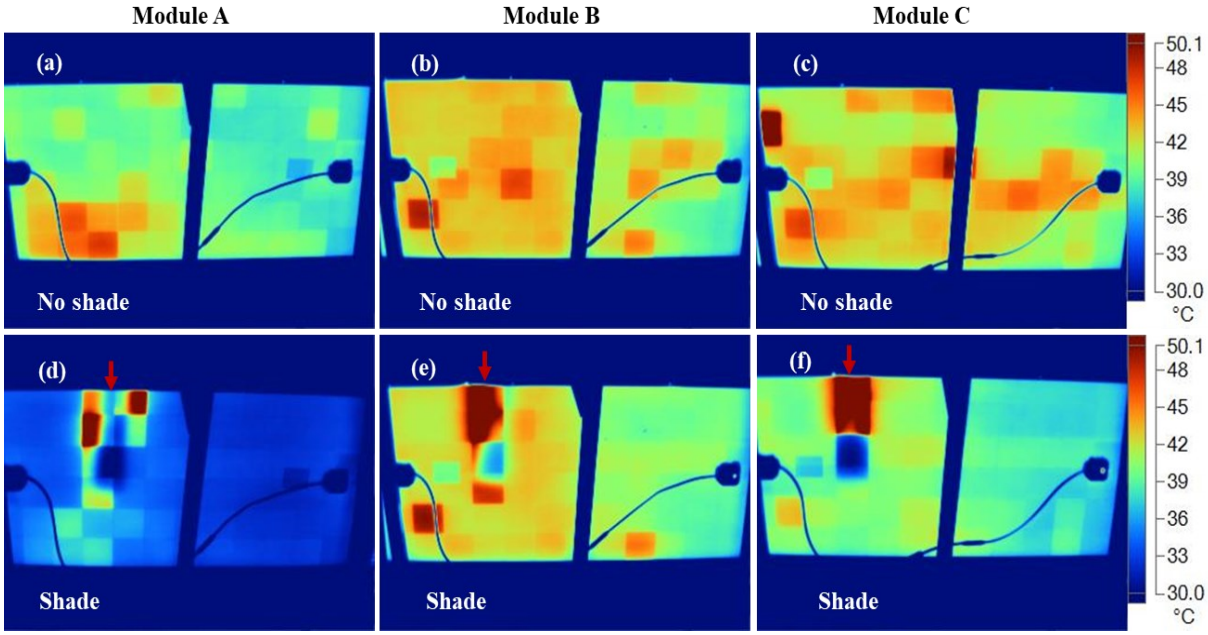

Figure 3: IR thermal images of the 3 field-aged PV modules under (a) - (c) non-shading and (d) - (f) partial shading conditions, respectively. The red arrow in (d) - (f) shows the position of the customized shade (as shown in Figure 2a) during the measurements. The measurements were done in real field outdoor conditions. The thick vertical blue line in the middle of each image is due to the metal frame of the rack (behind the module) used for holding the PV modules in place during measurements.

The dependence of I_{mpp} and V_{mpp} on the PV module temperature and irradiance conditions is well known [3, 8, 25]. Figure 4 illustrates the influence of varying irradiance conditions on the PV module operating temperature (T_m), P_{max}, V_{mpp}, and I_{mpp} under nominal operating conditions in non-shading and partial shading conditions. The values of ΔP_{max}, ΔV_{mpp}, and ΔI_{mpp} are the differences between the respective measured values under each condition (as in Figure 4) and the average value under nominal conditions in Figure 4a. Figure 4 suggests that T_m increases with increasing G_I, even under partial shading conditions, but reveals opposite effects on P_{max}, V_{mpp}, and I_{mpp}.

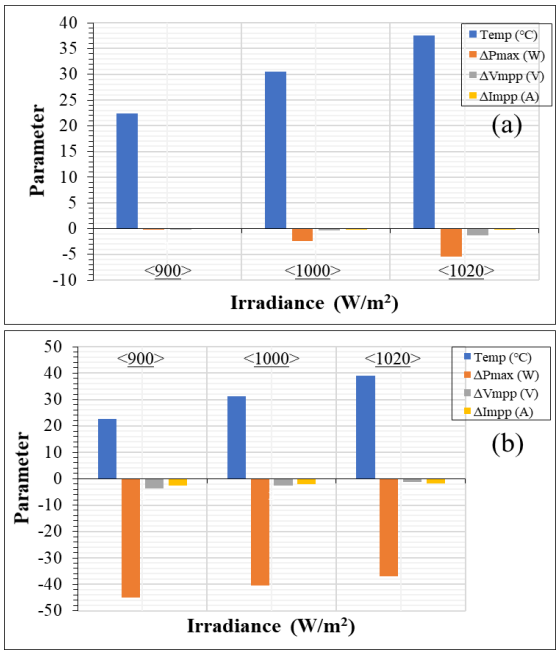

Figure 4: Evolution of PV module operating temperature, P_{max}, V_{mpp}, and I_{mpp} under varying irradiance conditions under (a) non-shading and (b) partial shading conditions. Δ is the difference between a parameter x and the average x-value in Figure 4a.

It appears the drop in P_{max}, V_{mpp}, and I_{mpp} increases with increasing temperature and irradiance in the absence of shading effects, see Figure 4a. However, under partial shading conditions, the drop in P_{max}, V_{mpp}, and I_{mpp} decreases when T_m and in-plane irradiance (G_I) increases. Another observation is that, under partial shading conditions, the percentage degradation in I_{mpp} becomes more critical to the degradation in P_{max} and worsen under higher G_I and T_m.

The dependence of P_{max} and FF on T_m of the field-aged PV modules is shown in Figure 5. In Figure 5a, the P_{max} and T_m profiles of the field-aged PV modules show relative dependence on each other in the absence of any shading condition. The FF also does not show any significant variation as T_m increases. However, under partial shading conditions, the trend is different, see Figure 5b.

Under partial shading conditions, the P_{max} and FF curves are not as smooth as compared to how they appear when the module is not affected by any shading condition. It is observed that the unsteadiness of current flow under partial shading conditions makes the P_{max} and FF curves are less smooth. Figure 5b suggests that the effect of T_m on P_{max} and FF degradation is more critical under partial shading conditions. As much as the P_{max} and FF depend on T_m, they are influenced by the in-plane irradiance (G_I) as well [2, 3]. The influence of T_m appears to be more pronounced under partial shading conditions which resulted in the surge in the P_{max} and FF profiles at $T_m > 30$ °C, see Figure 5b.

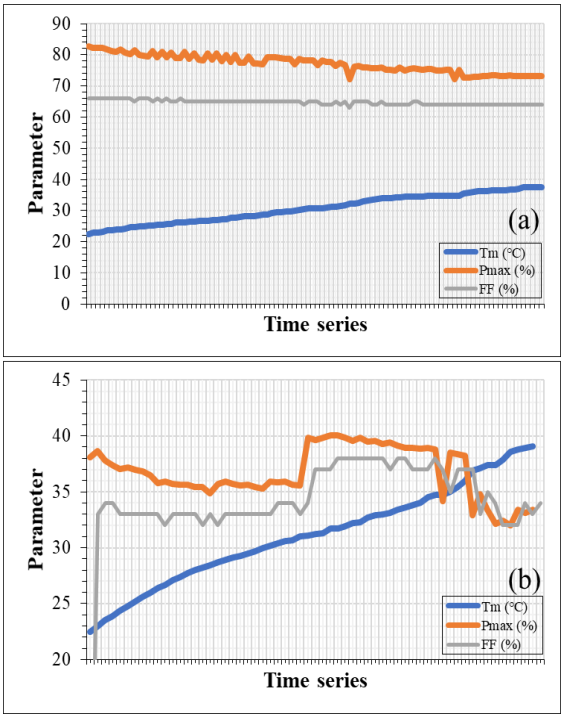

Figure 5: Profiles of a field-aged PV module's P_{max} and fill factor (FF) at varying T_m under (a) non-shading and (b) partial shading conditions in time series.

Hot spots from mismatch losses arise from uneven temperature distributions over the PV cell/module due to reverse biasing [6]. Figure 6 is Box and Whisker plots of the evolution of the temperature sensitivity of a field-aged PV module in the absence of shading and in the presence of partial shading conditions. Figure 6a is the absolute variation in the temperature coefficients of P_{max} (β_{Pmax}), V_{oc} (β_{Voc}), I_{sc} (β_{Isc}), and FF (β_{FF}) of the field-aged PV module at STC in the absence of any shading condition. The absolute variation in the temperature coefficients under partial shading and low irradiance conditions are represented in Figure 6b and Figure 6c, respectively.

According to Figure 6, the absolute variation in the β_{Pmax}, β_{Voc}, β_{Isc}, and β_{FF} increases under partial shading conditions. However, the variation in β_{FF} dominates the cause for the variation, hence, the higher variation in β_{Pmax} [3, 7, 8]. Figure 6 also suggests that at STC, the influence of β_{Voc} in the degradation in β_{Pmax} is fairly constant even under partial shading conditions. In contrast, under partial shading conditions, β_{Isc} is more affected than β_{Voc}, see Figure 6c. Figure 6 also suggests that the β_{Isc} of the partially shaded modules under both STC and lower irradiance conditions remains fairly constant.

Partial shading effects could be better diagnosed from the I_{mpp} and V_{mpp} characteristics of a PV module [8]. Previous investigations reported a minimal influence of temperature on I_{mpp}, ca. <0.04 %/K [3, 9, 14, 23, 25].

However, the temperature sensitivity of a PV module could be influenced by different degradation modes [26]. Therefore, the temperature sensitivity of P_{max}, hence, I_{mpp} and V_{mpp} of a PV module could be influenced by different degradation modes such as cracks and moisture induced

degradations [16, 27]. The temperature coefficients of V_{mpp} (β_{Vmp}) and I_{mpp} (β_{Jmp}) of one of the field-aged PV modules is presented in Figure 7. The experimental investigation on the field-aged PV modules were done under the conditions ca. STC (980 - 1030 W/m^2).

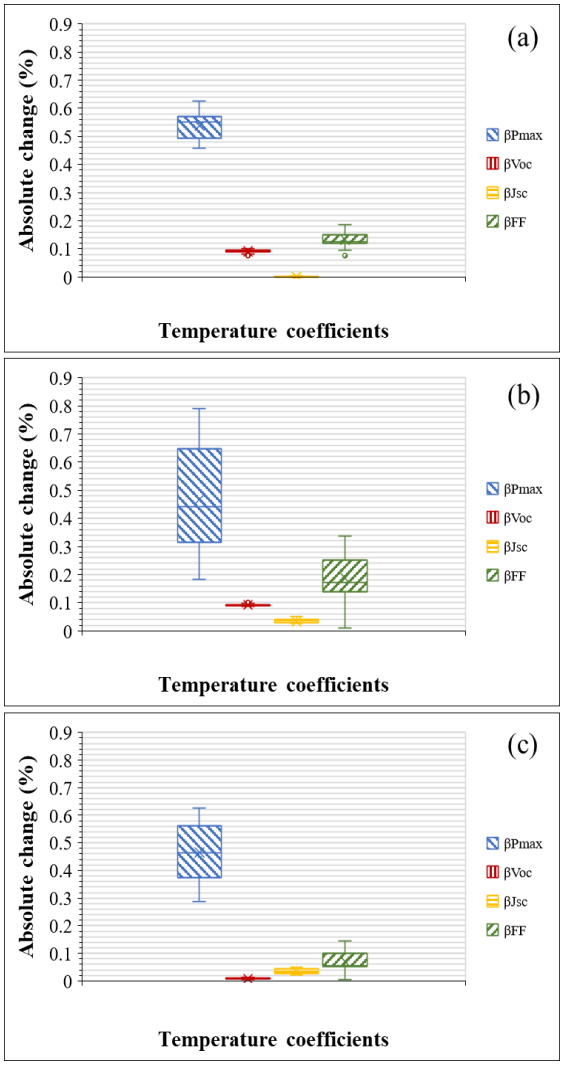

Figure 6: Evolution of temperature coefficients of a field-aged PV module under (a) STC conditions (in the absence of shading), (b) STC and (c) 700 - 800 W/m^2 conditions, but under partial shading conditions. The ends of the boxes are the lower and upper quartiles (interquartile range), the internal lines and *x*-marks indicate the median and mean, respectively.

Under non-shading conditions (in the absence of shading), the outdoor experiments estimate the β_{Vmp} and β_{Jmp} to be -0.0681 V/°C (-0.41 %/°C) and -0.0041 A/°C (-0.08 %/°C), respectively, see Figure 7a. The outdoor experimental studies on the same module under partial shading conditions give the results in Figure 7b. This estimates the β_{Vmp} and β_{Jmp} to be -0.0875 V/°C (-0.44 %/°C) and -0.0194 A/°C (-0.66 %/°C), respectively. Table II summarizes the results from the temperature sensitivity profiling of the 3 selected field-aged PV modules under non-shading and partial shading conditions.

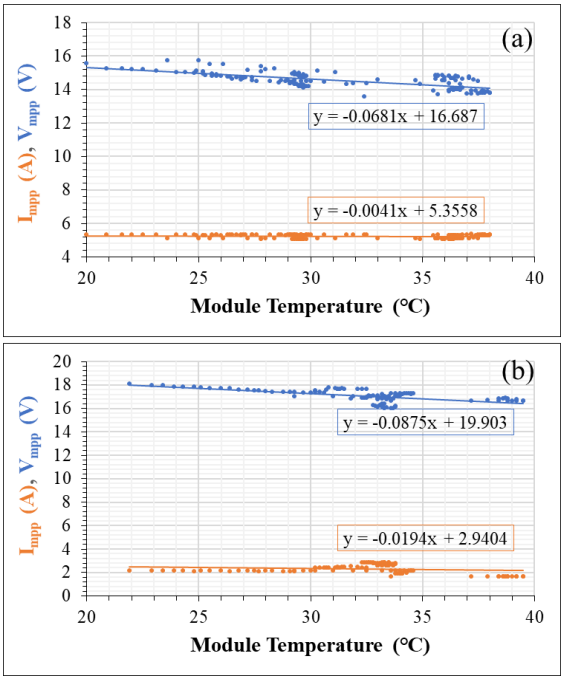

Figure 7: Evolution of temperature coefficients of I_{mpp} (β_{Jmp}) and V_{mpp} (β_{Vmp}) of a field-aged PV module under (a) non-shading and (b) partial shading conditions.

The results estimate the β_{Vmp} to be between ca. -0.41 %/°C and -0.48 %/°C under nominal conditions, which agrees with previous findings [3, 14, 25]. These results indicate that over the 20 years, the β_{Vmp} remains largely constant, and is not affected by the different defects that affected the PV modules. Yet, under partial shading conditions, the estimate for the PV module β_{Vmp} ranges from ca. -0.44 %/°C to 2.66 %/°C, see Table II. Increase in V_{mpp} under partial shading conditions was also observed elsewhere [8]. The disparity in β_{Vmp} is due to different defect mechanisms which trigger different characteristic current flux in the field-aged PV modules [8, 28]. This was observed during outdoor experiments on the field-aged PV modules when the in-plane irradiance is >1020 W/m^2, irrespective of the T_m. Strikingly, the β_{Vmp} for PV module C is positive under partial shading conditions, probably due to specific defect(s), see Table II. Comprehensive investigation on the typical effect of different defects mechanisms on the temperature profiles of the field-aged PV modules is underway.

In contrast, the results for the β_{Jmp} ranges from ca. -0.08 %/°C to 0.01 %/°C under non-shading conditions. These results differ from the 0.04 %/°C reported previously for multicrystalline silicon PV modules [3, 14,

Table II: Temperature coefficients of I_{mpp} (β_{Jmp}) and V_{mpp} (β_{Vmp}) of the field-aged PV modules investigated.

PV module	A		B		C	
Parameter (%/°C)	β_{Jmp}	β_{Vmp}	β_{Jmp}	β_{Vmp}	β_{Jmp}	β_{Vmp}
Partial shading*	-1.00	-0.36	-0.66	-0.44	-0.90	2.66
No shade	0.01	-0.41	-0.08	-0.41	0.01	-0.48

25]. Variation in the β_{Jmp} with irradiance is reported in other studies [12, 14]. Surprisingly, PV module B shows a negative β_{Jmp} under nominal conditions, most likely due to degradation issue(s).

Also, under partial shading conditions, the estimate for the β_{Jmp} for the modules ranges from ca. -1.00 %/°C to -0.90 %/°C, see Table II. The β_{Jmp} appears to be negative for all the modules measured under partial shading conditions. Obviously, this could be caused by the defects (e.g., cracks, moisture ingress, optical degradation, potential induced degradation, etc.) that has affected the field-aged PV modules. More importantly, the results show that the β_{Vmp} and β_{Jmp} increase under partial shading conditions, hence, affect P_{max}. β_{Jmp} is negative due to its dependence on FF which has a negative temperature dependence [25]. It is assumed that the degradation in both β_{Vmp} and β_{Jmp} stems from parasitic series and shunt resistance losses emanating from different moisture induced failure mechanisms affecting the field-aged PV modules as reported elsewhere [25, 29].

The influence of the temperature coefficients of efficiency ($\beta_{\eta m}$) on one of the field-aged PV modules under non-shading and shading conditions is shown in Figure 8.

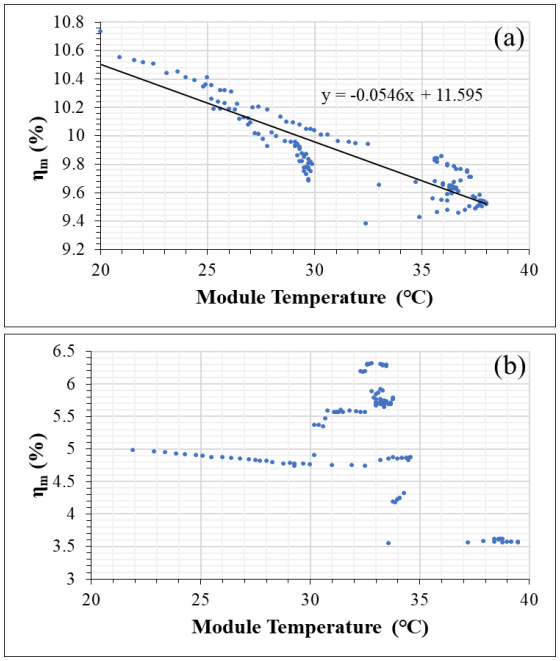

Figure 8: The temperature coefficients of efficiency of a field-aged PV module at ca. STC under (a) non-shading and (b) partial shading conditions.

The figure suggests that PV modules are more sensitive to temperature effects under partial shading conditions. That is, under STC and in the absence of any form of shading, the $\beta_{\eta m}$ is ca. -0.47 %/°C, refer to Figure 8a and (3). However, under partial shading conditions, the $\beta_{\eta m}$ is estimated to be ca. -0.92 %/°C, refer to Figure 8b and (3). The estimated $\beta_{\eta m}$ for the 3 field-aged PV modules is recorded in Table III.

The $\beta_{\eta m}$ under non-shading and shading conditions ranges from -0.41 to -0.48 %/°C and -0.59 to -1.18 %/°C, respectively for the 3 field-aged PV modules. In addition, Figure 8 estimates that at STC (i.e., at 25 °C), the PV module efficiency (η_m) reduces to 10.23 % and 5.62 % for non-shading and partial shading conditions, respectively.

Table III: Temperature coefficients of efficiency, η_m ($\beta_{\eta m}$) of the 3 field-aged PV modules investigated.

PV module $\beta_{\eta m}$ (%/°C)	**A**	**B**	**C**
Shade	-1.18	-0.92	-0.59
No shade	-0.41	-0.47	-0.48

4 CONCLUSIONS

The temperature coefficients of 20 years field-aged PV modules have been investigated under real field operation conditions in Grimstad, southern Norway. Thermal images show that hotspots are mostly localized to the busbars that are closer to the shade affected area of the module. The results show that, under partial shading conditions, drop in the temperature coefficient of fill factor (β_{FF}) dominates for power degradation, especially under partial shading conditions. Furthermore, it is estimated that under partial shading conditions, degradation in P_{max}, V_{mpp}, and I_{mpp} decreases when the PV module operating temperature (T_m) and in-plane irradiance increases, due to the dependence of V_{mpp}, and I_{mpp} on fill factor. That is, under partial shading conditions, the dependence of P_{max} on the T_m could be different from what is known.

Also, the results estimate that, the temperature coefficient of V_{mpp} (β_{Vmp}) of the field-aged PV modules under STC is ca. -0.41 %/°C to -0.48 %/°C, which agrees with previous findings [3, 25]. The results suggest that, over the 20 years, the β_{Vmp} of the modules remains largely constant and is not affected by the degradation state of the PV modules. However, under partial shading conditions, the absolute variation in the β_{Vmp} is >2.00 %/°C for the 3 field-aged PV modules studied. The results for the temperature coefficient of I_{mpp} (β_{Jmp}) ranges from ca. -0.08 %/°C to 0.01 %/°C and ca. -1.00 %/°C to -0.90 %/°C under non-shading and partial shading conditions, respectively. The disparity in the β_{Jmp} values from the 0.04 %/°C reported previously for multicrystalline silicon PV modules could be due to the degradation states of the field-aged PV modules.

The results suggest that the PV modules have undergone some form of degradation over the 20 years. More importantly, the studies demonstrate that the temperature coefficients of field-aged PV modules increase under partial shading conditions. Yet, the severity of the temperature sensitivity under partial shading conditions also depends on the degradation state of the PV modules. It appears that thermal images under partial shading conditions could be useful for identifying PV modules affected by material defects from those affected by other defects such as dirt. However, more investigations are underway to explore the full scope of these observations. This may have the potential in the future to be used as a diagnostic tool in field installations.

REFERENCES

[1] A. Dolara, G. C. Lazaroiu, S. Leva, and G. Manzolini, "Experimental investigation of partial shading

scenarios on PV (photovoltaic) modules," *Energy,* vol. 55, pp. 466-475, 2013.
[2] B. R. Paudyal and A. G. Imenes, "Investigation of temperature coefficients of PV modules through field measured data," *Solar Energy,* vol. 224, pp. 425-439, 2021.
[3] M. Seapan, Y. Hishikawa, M. Yoshita, and K. Okajima, "Temperature and irradiance dependences of the current and voltage at maximum power of crystalline silicon PV devices," *Solar Energy,* vol. 204, pp. 459-465, 2020.
[4] A. Woyte, J. Nijs, and R. Belmans, "Partial shadowing of photovoltaic arrays with different system configurations: literature review and field test results," *Solar energy,* vol. 74, no. 3, pp. 217-233, 2003.
[5] H. Mohammed, M. Kumar, and R. Gupta, "Bypass diode effect on temperature distribution in crystalline silicon photovoltaic module under partial shading," *Solar Energy,* vol. 208, pp. 182-194, 2020.
[6] O. Kunz, R. J. Evans, M. K. Juhl, and T. Trupke, "Understanding partial shading effects in shingled PV modules," *Solar Energy,* vol. 202, pp. 420-428, 2020.
[7] K. A. Kim and P. T. Krein, "Reexamination of photovoltaic hot spotting to show inadequacy of the bypass diode," *IEEE Journal of Photovoltaics,* vol. 5, no. 5, pp. 1435-1441, 2015.
[8] M. Seapan, Y. Hishikawa, M. Yoshita, and K. Okajima, "Detection of shading effect by using the current and voltage at maximum power point of crystalline silicon PV modules," *Solar Energy,* vol. 211, pp. 1365-1372, 2020.
[9] M. Zaimi, H. El Achouby, A. Ibral, and E. Assaid, "Determining combined effects of solar radiation and panel junction temperature on all model-parameters to forecast peak power and photovoltaic yield of solar panel under non-standard conditions," *Solar Energy,* vol. 191, pp. 341-359, 2019.
[10] O. K. Segbefia, A. G. Imenes, I. Burud, and T. O. Sætre, "Temperature profiles of field-aged multicrystalline silicon photovoltaic modules affected by microcracks," in *2021 IEEE 48th Photovoltaic Specialists Conference (PVSC)*, 2021: IEEE, pp. 0001-0006.
[11] X. Sun, R. V. K. Chavali, and M. A. Alam, "Real-time monitoring and diagnosis of photovoltaic system degradation only using maximum power point—the Suns-Vmp method," *Progress in Photovoltaics: Research and Applications,* vol. 27, no. 1, pp. 55-66, 2019.
[12] R. Dubey *et al.*, "Measurement of temperature coefficient of photovoltaic modules in field and comparison with laboratory measurements," in *2015 IEEE 42nd Photovoltaic Specialist Conference (PVSC)*, 2015: IEEE, pp. 1-5.
[13] E. Skoplaki and J. A. Palyvos, "On the temperature dependence of photovoltaic module electrical performance: A review of efficiency/power correlations," *Solar energy,* vol. 83, no. 5, pp. 614-624, 2009.
[14] D. L. King, J. A. Kratochvil, and W. E. Boyson, "Temperature coefficients for PV modules and arrays: measurement methods, difficulties, and results," in *Conference record of the twenty sixth IEEE Photovoltaic Specialists Conference-1997*, 1997: IEEE, pp. 1183-1186.
[15] M. A. Green, "General temperature dependence of solar cell performance and implications for device modelling," *Progress in Photovoltaics: Research and Applications,* vol. 11, no. 5, pp. 333-340, 2003.
[16] O. Dupré, R. Vaillon, and M. A. Green, "Physics of the temperature coefficients of solar cells," *Solar energy materials and solar cells,* vol. 140, pp. 92-100, 2015.
[17] D. Verma, M. Tayyib, T. O. Saetre, and O.-M. Midtgård, "Outdoor Performance of 10 year Old a-Si and Poly-Si Modules in southern Norway conditions," in *2012 38th IEEE Photovoltaic Specialists Conference*, 2012: IEEE, pp. 002368-002371.
[18] U. Jahn, M. Herz, M. Köntges, D. Parlevliet, M. Paggi, and I. Tsanakas, *Review on infrared and electroluminescence imaging for PV field applications: International Energy Agency Photovoltaic Power Systems Programme: IEA PVPS Task 13, Subtask 3.3: report IEA-PVPS T13-12: 2018*. International Energy Agency, 2018.
[19] I. 61853-1, "Photovoltaic (PV) module performance testing and energy rating–Part 1: Irradiance and temperature performance measurements and power rating," 2011.
[20] M. Siegel, S. Klein, and W. Beckman, "A simplified method for estimating the monthly-average performance of photovoltaic systems," *Solar Energy,* vol. 26, no. 5, pp. 413-418, 1981.
[21] D. Evans, "Simplified method for predicting photovoltaic array output," *Solar energy,* vol. 27, no. 6, pp. 555-560, 1981.
[22] M. Keevers and M. Green, "Extended infrared response of silicon solar cells and the impurity photovoltaic effect," *Solar Energy Materials and Solar Cells,* vol. 41, pp. 195-204, 1996.
[23] B. H. King, C. W. Hansen, D. Riley, C. D. Robinson, and L. Pratt, "Procedure to determine coefficients for the Sandia Array Performance Model (SAPM)," *SAND2016-5284,* vol. 1256510, 2016.
[24] C. Xiao, P. Hacke, S. Johnston, D. B. Sulas-Kern, C. S. Jiang, and M. Al-Jassim, "Failure analysis of field-failed bypass diodes," *Progress in Photovoltaics: Research and Applications,* vol. 28, no. 9, pp. 909-918, 2020.
[25] M. Kasu, J. Abdu, S. Hara, S. Choi, Y. Chiba, and A. Masuda, "Temperature dependence measurements and performance analyses of high-efficiency interdigitated back-contact, passivated emitter and rear cell, and silicon heterojunction photovoltaic modules," *Japanese Journal of Applied Physics,* vol. 57, no. 8S3, p. 08RG18, 2018.
[26] E. L. Meyer and E. E. Van Dyk, "Assessing the reliability and degradation of photovoltaic module performance parameters," *IEEE Transactions on reliability,* vol. 53, no. 1, pp. 83-92, 2004.
[27] C. Buerhop, D. Schlegel, M. Niess, C. Vodermayer, R. Weißmann, and C. Brabec, "Reliability of IR-imaging of PV-plants under operating conditions," *Solar Energy Materials and Solar Cells,* vol. 107, pp. 154-164, 2012.
[28] E. Molenbroek, D. Waddington, and K. Emery, "Hot spot susceptibility and testing of PV modules," in *Photovoltaic Specialists Conference*, 1991, vol. 1: Las Vegas, pp. 547-552.
[29] O. K. Segbefia, A. G. Imenes, and T. O. Sætre, "Moisture ingress in photovoltaic modules: A review," *Solar Energy,* vol. 224, pp. 889-906, 2021.